

A drug to treat spinal
cord injury pp. 285 & 347

Arctic warming and
summer heat waves p. 324

Science

\$10
17 APRIL 2015
sciencemag.org

AAAS

A lasting bond

The secrets of our
deep ties with dogs
pp. 274, 280, & 333



CONTENTS

17 APRIL 2015 • VOLUME 348 • ISSUE 6232



285 & 347

Treating spinal
cord injury



270

NEWS

IN BRIEF

264 Roundup of the week's news

IN DEPTH

268 MEAGER SNOWS SPELL TROUBLE AHEAD FOR SALMON

Without snowmelt, streams in the western U.S. could reach lethal temperatures *By R. F. Service*

269 WOMEN BEST MEN IN STUDY OF TENURE-TRACK HIRING

Female candidates twice as likely to get top rating *By R. Bernstein*

270 U.S. LAYS OUT ITS AMBITIONS FOR LEADERSHIP IN THE ARCTIC

Climate, marine conservation, and renewable energy priorities as U.S. ascends to chair of Arctic Council *By C. Gramling*

► EDITORIAL P. 263

271 MOON-FORMING IMPACT LEFT SCARS IN DISTANT ASTEROIDS

Planetary collision dated through analysis of meteorites *By E. Hand*

► REPORT P. 321

272 FOR TOILETS, MONEY MATTERS

New work suggests that, subsidies to the poor to buy latrines could help end open defecation *By J. Kaiser*

► SCIENCE EXPRESS REPORT BY R. GUITERAS ET AL. 10.1126/science.aaa0491

273 JAPAN ACCELERATOR POISED TO GO FULLY OPERATIONAL

Closure after radiation leak ended up hampering some teams more than others *By D. Normile*

FEATURES

274 DAWN OF THE DOG

An unprecedented collaboration may solve one of the greatest mysteries of domestication *By D. Grimm*

277 How the wolf became the dog

By D. Grimm

► PERSPECTIVE P. 280; REPORT P. 333; PODCAST

INSIGHTS

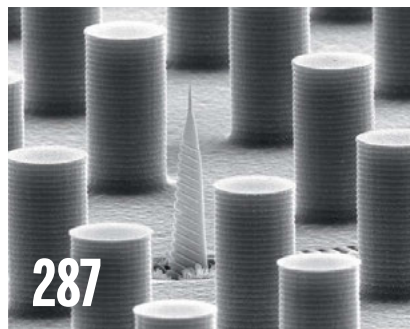
PERSPECTIVES

280 DOGS HIJACK THE HUMAN BONDING PATHWAY

Oxytocin facilitates social connections between humans and dogs

By E. L. MacLean and B. Hare

► NEWS STORY P. 274; REPORT P. 333; PODCAST



287

282 COMBATING EMERGING VIRAL THREATS

Broad-spectrum antiviral drugs are under development to treat emerging viral diseases such as Ebola and dengue for which no specific, licensed treatments exist *By E. Bekerman and S. Einar*

284 A SCAR IS BORN: ORIGINS OF FIBROTIC SKIN TISSUE

A fibroblast lineage is characterized by an inherent ability to form scar tissue in skin *By R. Sennett and M. Rendl*

► RESEARCH ARTICLE P. 302

285 SYSTEMICALLY TREATING SPINAL CORD INJURY

A drug that crosses the blood-brain barrier has therapeutic potential for central nervous system trauma

By A. P. Tran and J. Silver

► REPORT P. 347

287 NANOPLASMONIC SENSING AND DETECTION

Enhanced optical fields in nanoplasmonic systems provide efficient sensing and detection

By M. I. Stockman

288 MITORIBOSOME ODDITIES

The mitochondrial ribosome has evolved structural differences from its cytosolic counterpart *By R. Beckmann and J. M. Herrmann*

► REPORT P. 303

290 ESCAPE BY DILUTION

Dissolved organic matter in much of the deep ocean is too dilute to be consumed by microbes

By J. J. Middelburg

► REPORT P. 331

291 IMPROVE CUSTOMS SYSTEMS TO MONITOR GLOBAL WILDLIFE TRADE

Widely used trade codes lack taxonomic granularity

By H.-K. Chan et al.

BOOKS ET AL.

294 ARRESTING CONTAGION

By A. L. Olmstead and P. W. Rhode, reviewed by D. Grace

295 ETERNAL EPHEMERA

By N. Eldredge, reviewed by J. Endersby

CONTENTS

17 APRIL 2015 • VOLUME 348 • ISSUE 6232



303

Mitochondrial ribosome
fingers tRNA

LETTERS

296 SHAPING THE FUTURE OF SYNTHETIC BIOLOGY

By T. Kuiken

296 COMBATING THE NEXT LETHAL EPIDEMIC

By P. J. Hotez

297 OUTSIDE THE TOWER: MORE THAN A SCIENCE CAMP

By L. Gastón Morosi

297 TECHNICAL COMMENT ABSTRACTS

RESEARCH

IN BRIEF

298 From *Science* and other journals

REVIEW

301 VERTEBRATE EVOLUTION

Evolutionary innovation and ecology in marine tetrapods from the Triassic to the Anthropocene *N. P. Kelley and N. D. Pyenson*

REVIEW SUMMARY; FOR FULL TEXT:

dx.doi.org/10.1126/science.aaa3716

RESEARCH ARTICLES

302 SKIN FIBROSIS

Identification and isolation of a dermal lineage with intrinsic fibrogenic potential *Y. Rinkevich et al.*

RESEARCH ARTICLE SUMMARY; FOR FULL TEXT:

dx.doi.org/10.1126/science.aaa2151

► PERSPECTIVE P. 284

303 RIBOSOME

The complete structure of the 55S mammalian mitochondrial ribosome *B. J. Greber et al.*

► PERSPECTIVE P. 288

REPORTS

308 SURFACE STRUCTURE

Subatomic resolution force microscopy reveals internal structure and adsorption sites of small iron clusters *M. Emmrich et al.*

311 ACTIVE GALAXIES

A strong magnetic field in the jet base of a supermassive black hole *I. Martí-Vidal et al.*

314 GALAXY EVOLUTION

Evidence for mature bulges and an inside-out quenching phase 3 billion years after the Big Bang *S. Tacchella et al.*

317 SUPERCONDUCTIVITY

Quasiparticle mass enhancement approaching optimal doping in a high- T_c superconductor *B. J. Ramshaw et al.*

321 LUNAR FORMATION

Dating the Moon-forming impact event with asteroidal meteorites *W. F. Bottke et al.*

► NEWS STORY P. 271

324 CLIMATE CHANGE

The weakening summer circulation in the Northern Hemisphere mid-latitudes *D. Coumou et al.*

327 ICE SHEETS

Volume loss from Antarctic ice shelves is accelerating *F. S. Paolo et al.*

331 OCEAN CHEMISTRY

Dilution limits dissolved organic carbon utilization in the deep ocean *J. M. Arrieta et al.*

► PERSPECTIVE P. 290

333 SOCIAL EVOLUTION

Oxytocin-gaze positive loop and the coevolution of human-dog bonds *M. Nagasawa et al.*

► NEWS STORY P. 274; PERSPECTIVE P. 280; PODCAST

336 PLANT ECOLOGY

Anthropogenic environmental changes affect ecosystem stability via biodiversity *Y. Hautier et al.*

340 STEM CELLS

Asymmetric apportioning of aged mitochondria between daughter cells is required for stemness *P. Katajisto et al.*

344 PROTEIN STRUCTURE

Engineering of a superhelicase through conformational control *S. Arslan et al.*

► REPORT P. 352

347 AXONAL REGENERATION

Systemic administration of epothilone B promotes axon regeneration after spinal cord injury *J. Ruschel et al.*

► PERSPECTIVE P. 285

352 PROTEIN STRUCTURE

Direct observation of structure-function relationship in a nucleic acid-processing enzyme *M. J. Comstock et al.*

► REPORT P. 344



DEPARTMENTS

263 EDITORIAL

One Arctic *By Fran Ulmer*

► NEWS STORY P. 270

366 WORKING LIFE

En pointe *By Elisabeth Pain*

ON THE COVER



As dogs gaze into our eyes, and we into theirs, we form a bond similar to that we share with our own infants. Now, a large collaboration of archaeologists and geneticists may help us understand where

and when this special relationship began to form. See pages 274, 280, and 333.

Photo: © Arco Images GmbH/Alamy

Science Staff	262
New Products	355
Science Careers	359

SCIENCE (ISSN 0036-8075) is published weekly on Friday, except the last week in December, by the American Association for the Advancement of Science, 1200 New York Avenue, NW, Washington, DC 20005. Periodicals mail postage (publication No. 484460) paid at Washington, DC, and additional mailing offices. Copyright © 2015 by the American Association for the Advancement of Science. The title SCIENCE is a registered trademark of the AAAS. Domestic individual membership and subscription (51 issues): \$153 (\$74 allocated to subscription). Domestic institutional subscription (51 issues): \$1282; foreign postage extra: Mexico, Caribbean (surface mail) \$55; other countries (air assist delivery) \$85. First class, airmail, student, and emeritus rates on request. Canadian rates with GST available upon request. GST #R1254 88122. Publications Mail Agreement Number 1069624. Printed in the U.S.A. Change of address: Allow 4 weeks, giving old and new addresses and 8-digit account number. Postmaster: Send change of address to AAAS, P.O. Box 96178, Washington, DC 20090-6178. Single-copy sales: \$10.00 current issue, \$15.00 back issue prepaid includes surface postage; bulk rates on request. Authorization to photocopy material for internal or personal use under circumstances not falling within the fair use provisions of the Copyright Act is granted by AAAS to libraries and other users registered with the Copyright Clearance Center (CCC) Transactional Reporting Service, provided that \$30.00 per article is paid directly to CCC, 222 Rosewood Drive, Danvers, MA 01923. The identification code for Science is 0036-8075. Science is indexed in the Reader's Guide to Periodical Literature and in several specialized indexes.

Editor-in-Chief Marcia McNutt

Executive Editor Monica M. Bradford **News Editor** Tim Appenzeller

Managing Editor, Research Journals Katrina L. Kelner

Deputy Editors Barbara R. Jasny, Andrew M. Sugden(UK), Valda J. Vinson, Jake S. Yeston

Research and Insights

SR. EDITORS Caroline Ash(UK), Gilbert J. Chin, Lisa D. Chong, Julia Fahrenkamp-Uppenbrink(UK), Pamela J. Hines, Stella M. Hurlley(UK), Paula A. Kiberstis, Marc S. Lavine(Canada), Kristen L. Mueller, Ian S. Osborne(UK), Beverly A. Purnell, L. Bryan Ray, Guy Riddihough, H. Jesse Smith, Jelena Stajic, Peter Stern(UK), Phillip D. Szuroni, Brad Wible, Nicholas S. Wigginton, Laura M. Zahn **ASSOCIATE EDITORS** Brent Grocholski, Sacha Vignieri **ASSOCIATE BOOK REVIEW EDITOR** Valerie B. Thompson **ASSOCIATE LETTERS EDITOR** Jennifer Sills **CHIEF CONTENT PRODUCTION EDITOR** Cara Tate **SR. CONTENT PRODUCTION EDITORS** Harry Jach **CONTENT PRODUCTION EDITORS** Jeffrey E. Cook, Chris Filiatreau, Cynthia Howe, Lauren Krnec, Barbara P. Ordway **SR. EDITORIAL COORDINATORS** Carolyn Kyle, Beverly Shields **EDITORIAL COORDINATORS** Ramatoulaye Diop, Joi S. Granger, Lisa Johnson, Anita Wynn **PUBLICATIONS ASSISTANTS** Aneera Dobbins, Jeffrey Hearn, Dona Mathieu, Le-Toya Mayne Flood, Shannon McMahon, Scott Miller, Jerry Richardson, Rachel Roberts(UK), Alice Whaley(UK), Brian White **EXECUTIVE ASSISTANT** Anna Bashkirova **ADMINISTRATIVE SUPPORT** Janet Clements(UK), Monika Magon(UK, Intern), Lizanne Newton(UK), Maryrose Madrid, John Wood(UK)

News

NEWS MANAGING EDITOR John Travis **INTERNATIONAL EDITOR** Richard Stone **DEPUTY NEWS EDITORS** Daniel Clery(UK), Robert Coontz, Elizabeth Culotta, David Grimm, David Malakoff, Leslie Roberts **CONTRIBUTING EDITORS** Martin Enserink(Europe), Mara Hvistendahl **SR. CORRESPONDENTS** Jeffrey Mervis, Elizabeth Pennisi **NEWS WRITERS** Adrian Cho, John Cohen, Jennifer Couzin-Frankel, Carolyn Gramling, Eric Hand, Jocelyn Kaiser, Kelly Servick, Robert F. Service, Erik Stokstad(Cambridge, UK), Emily Underwood **INTERNS** Emily Conover, David Shultz, Jia You **CONTRIBUTING CORRESPONDENTS** Pallava Bagla(South Asia), Michael Balter(Paris), John Bohannon, Ann Gibbons, Sam Kean, Richard A. Kerr, Eli Kintisch, Kai Kupferschmidt(Berlin), Andrew Lawler, Christina Larson(Beijing), Mitch Leslie, Charles C. Mann, Eliot Marshall, Virginia Morell, Dennis Normile(Tokyo), Heather Pringle, Tania Rabesandratana(Brussels), Gretchen Vogel(Berlin), Lizzie Wade(Mexico City) **CAREERS** Jim Austin(Editor), Donisha Adams, Rachel Bernstein **COPY EDITORS** Kara Estelle, Nora Kelly, Jennifer Levin **ADMINISTRATIVE SUPPORT** Scherraine Mack

Executive Publisher Rush D. Holt

Publisher Kent R. Anderson **Chief Digital Media Officer** Rob Covey

BUSINESS OPERATIONS AND ADMINISTRATION DIRECTOR Deborah Rivera-Wienhold **BUSINESS SYSTEMS AND FINANCIAL ANALYSIS DIRECTOR** Randy Yi **MANAGER OF FULFILLMENT SYSTEMS** Neal Hawkins **SYSTEMS ANALYST** Nicole Mehmedovich **ASSISTANT DIRECTOR, BUSINESS OPERATIONS** Eric Knott **MANAGER, BUSINESS OPERATIONS** Jessica Tierney **BUSINESS ANALYSTS** Cory Lipman, Cooper Tilton, Celeste Troxler **FINANCIAL ANALYST** Jeremy Clay **RIGHTS AND PERMISSIONS ASSISTANT DIRECTOR** Emilie David **PERMISSIONS ASSOCIATE** Elizabeth Sandler **RIGHTS, CONTRACTS, AND LICENSING ASSOCIATE** Lili Kiser

MARKETING DIRECTOR Ian King **MARKETING MANAGER** Julianne Wielga **MARKETING ASSOCIATE** Elizabeth Sattler **SR. MARKETING EXECUTIVE** Jennifer Reeves **SR. ART ASSOCIATE, PROJECT MANAGER** Tzeitel Sorrosa **ART ASSOCIATE** Seil Lee **ASSISTANT COMMERCIAL EDITOR** Selby Frame **MARKETING PROJECT MANAGER** Angelissa McArthur **SR. WRITER** Bill Zimmer **PROGRAM DIRECTOR, AAAS MEMBER CENTRAL** Peggy Mihlthel **FULFILLMENT SYSTEMS AND OPERATIONS** membership@aaas.org **MANAGER, MEMBER SERVICES** Pat Butler **SPECIALISTS** LaToya Casteel, Javia Flemmings, Latasha Russell **MANAGER, DATA ENTRY** Mickie Napoleoni **DATA ENTRY SPECIALISTS** JJ Regan, Jaimee Wise, Fiona Giblin **DIRECTOR, SITE LICENSING** Tom Ryan **DIRECTOR, CORPORATE RELATIONS** Eileen Bernadette Moran **SR. PUBLISHER RELATIONS SPECIALIST** Kiki Forsythe **PUBLISHER RELATIONS MANAGER** Catherine Holland **PUBLISHER RELATIONS, EASTERN REGION** Keith Layson **PUBLISHER RELATIONS, WESTERN REGION** Ryan Rexroth **MANAGER, SITE LICENSE OPERATIONS** Iquo Edem **FULFILLMENT ANALYST** Lana Guz **ASSOCIATE DIRECTOR, MARKETING** Christina Schlecht **MARKETING ASSOCIATES** Thomas Landreth, Minah Kim

DIRECTOR OF WEB TECHNOLOGIES Ahmed Khadr **SR. DEVELOPER** Chris Coleman **DEVELOPERS** Dan Berger, Jimmy Marks **SR. PROJECT MANAGER** Trista Smith **SYSTEMS ENGINEER** Luke Johnson **PRODUCT MANAGER** Walter Jones

CREATIVE DIRECTOR, MULTIMEDIA Martyn Green **DIRECTOR OF ANALYTICS** Enrique Gonzales **SR. WEB PRODUCER** Sarah Crespi **WEB PRODUCER** Alison Crawford **VIDEO PRODUCER** Nguyen Nguyen **SOCIAL MEDIA PRODUCER** Meghna Sachdev

DIRECTOR OF OPERATIONS PRINT AND ONLINE Elizabeth Harman **DIGITAL/PRINT STRATEGY MANAGER** Jason Hillman **QUALITY TECHNICAL MANAGER** Marcus Spiegel **DIGITAL PRODUCTION MANAGER** Lisa Stanford **ASSISTANT MANAGER DIGITAL/PRINT** Rebecca Doshi **DIGITAL MEDIA SPECIALIST** Tara Kelly **SENIOR CONTENT SPECIALISTS** Steve Forrester, Antoinette Hodal, Lori Murphy, Anthony Rosen **CONTENT SPECIALISTS** Jacob Hedrick, Kimberley Oster

DESIGN DIRECTOR Beth Rakouskas **DESIGN EDITOR** Marcy Atarod **SENIOR SCIENTIFIC ILLUSTRATORS** Chris Bickel, Katharine Sutliff **SCIENTIFIC ILLUSTRATOR** Valerie Altounian **SENIOR ART ASSOCIATES** Holly Bishop, Preston Huey **SENIOR DESIGNER** Garvin Grullón **DESIGNER** Chrystal Smith **SENIOR PHOTO EDITOR** William Douthitt **PHOTO EDITOR** Leslie Blizard

DIRECTOR, GLOBAL COLLABORATION, CUSTOM PUBLICATIONS, ADVERTISING Bill Moran **EDITOR, CUSTOM PUBLISHING** Sean Sanders: 202-326-6430 **ASSISTANT EDITOR, CUSTOM PUBLISHING** Tianna Hicklin: 202-326-6463 **ADVERTISING MARKETING MANAGER** Justin Sawyers: 202-326-7061 **science_advertising@aaas.org** **ADVERTISING MARKETING ASSOCIATE** Javia Flemmings **ADVERTISING SUPPORT MANAGER** Karen Foote: 202-326-6740 **ADVERTISING PRODUCTION OPERATIONS MANAGER** Deborah Tompkins **SR. PRODUCTION SPECIALIST/GRAPHIC DESIGNER** Amy Hardcastle **PRODUCTION SPECIALIST** Yuse Lajiminmuhip **SR. TRAFFIC ASSOCIATE** Christine Hall **SALES COORDINATOR** Shirley Young **ASSOCIATE DIRECTOR, COLLABORATION, CUSTOM PUBLICATIONS/CHINA/TAIWAN/KOREA/SINGAPORE** Ruolei Wu: +86-186 0822 9345, rwu@aaas.org **COLLABORATION/CUSTOM PUBLICATIONS/JAPAN** Adarsh Sandhu + 81532-81-5142 asandhu@aaas.org **EAST COAST/E. CANADA** Laurie Faraday: 508-747-9395, FAX 617-507-8189 **WEST COAST/W. CANADA** Lynne Stickrod: 415-931-9782, FAX 415-520-6940 **MIDWEST** Jeffrey Dembski: 847-498-4520 x3005, Steven Loerch: 847-498-4520 x3006 **UK EUROPE/ASIA** Roger Goncalves: TEL/FAX +41 43 243 1358 **JAPAN** Katsuyoshi Fukamizu(Tokyo): +81-3-3219-5777 fukamizu@aaas.org **CHINA/TAIWAN** Ruolei Wu: +86-0882-9345

WORLDWIDE ASSOCIATE DIRECTOR OF SCIENCE CAREERS Tracy Holmes: +44 (0) 1223 326525, FAX +44 (0) 1223 326532 tholmes@science-int.co.uk **CLASSIFIED advertise@sciencecareers.org** **U.S. SALES** Tina Burks: 202-326-6577, Nancy Toerna: 202-326-6578 **SALES ADMINISTRATOR** Marci Gallun **EUROPE/ROW SALES** Axel Gesatzki, Sarah LeLarge **SALES ASSISTANT** Kelly Grace Japan Hirokyuki Mashiki(Kyoto): +81-75-823-1109 hsmashiki@aaas.org **CHINA/TAIWAN** Ruolei Wu: +86-186 0882 9345 rwu@aaas.org **MARKETING MANAGER** Allison Pritchard **MARKETING ASSOCIATE** Aimee Aponte

AAAS BOARD OF DIRECTORS **RETIRING PRESIDENT, CHAIR** Gerald R. Fink **PRESIDENT** Geraldine (Geri) Richmond **PRESIDENT-ELECT** Barbara A. Schaaf **TREASURER** David Evans Shaw **CHIEF EXECUTIVE OFFICER** Rush D. Holt **BOARD** Bonnie L. Bassler, May R. Berenbaum, Carlos J. Bustamante, Stephen P.A. Fodor, Claire M. Fraser, Michael S. Gazzaniga, Laura H. Greene, Elizabeth Loftus, Mercedes Pascual

SUBSCRIPTION SERVICES For change of address, missing issues, new orders and renewals, and payment questions: 866-434-AAAS (2227) or 202-326-6417, FAX 202-842-1065. Mailing addresses: AAAS, P.O. Box 96178, Washington, DC 20090-6178 or AAAS Member Services, 1200 New York Avenue, NW, Washington, DC 20005

INSTITUTIONAL SITE LICENSES 202-326-6755 **REPRINTS:** Author Inquiries 800-635-7181 **COMMERCIAL INQUIRIES** 803-359-4578 **PERMISSIONS** 202-326-6765, permissions@aaas.org **AAAS Member Services** 202-326-6417 or <http://membercentral.aaas.org/discounts>

Science serves as a forum for discussion of important issues related to the advancement of science by publishing material on which a consensus has been reached as well as including the presentation of minority of conflicting points of view. Accordingly, all articles published in Science—including editorials, news and comment, and books reviews—are signed and reflect the individual views of the authors and not official points of view adopted by AAAS or the institutions with which the authors are affiliated.

INFORMATION FOR AUTHORS See pages 678 and 679 of the 6 February 2015 issue or access www.sciencemag.org/about/authors

SENIOR EDITORIAL BOARD

Gary King, Harvard University
Susan M. Rosenberg, Baylor College of Medicine, Ali Shilatifard, Northwestern University
Feinberg School of Medicine, Michael S. Turner, U. of Chicago

BOARD OF REVIEWING EDITORS (Statistics board members indicated with \$)

Adriano Aguzzi, U. Hospital Zürich
Takuzo Aida, U. of Tokyo
Leslie Aiello, Wenner-Gren Foundation
Judith Allen, U. of Edinburgh
Sonia Altizer, U. of Georgia
Sebastian Amigorena, Institut Curie
Kathryn Anderson, Memorial Sloan-Kettering Cancer Center
Meinrat O. Andreae, Max-Planck Inst. Mainz
Paola Arlotta, Harvard U.
Johan Auwerx, EPFL
David Awschalom, U. of Chicago
Jordi Bascompte, Estación Biológica de Doñana CSIC
Facundo Batista, London Research Inst.
Ray H. Baughman, U. of Texas, Dallas
David Baum, U. of Wisconsin
Carlo Beenakker, Leiden U.
Kamran Behnia, ESPCI-ParisTech
Yasmine Belkaid, NIAID, NIH
Philip Benfey, Duke U.
Stephen J. Benkovic, Penn State U.
May Berenbaum, U. of Illinois
Gabriele Bergers, U. of California, San Francisco
Bradley Bernstein, Massachusetts General Hospital
Peer Bork, EMBL
Bernard Bourdon, Ecole Normale Supérieure de Lyon
Chris Bowler, Ecole Normale Supérieure
Ian Boyd, U. of St. Andrews
Emily Brodsky, U. of California, Santa Cruz
Ron Brookmeyer, U. of California Los Angeles (\$)
Christian Büchel, U. Hamburg-Eppendorf
Joseph A. Burns, Cornell U.
Gyorgy Buzsaki, New York U. School of Medicine
Blanche Capel, Duke U.
Mats Carlsson, U. of Oslo
David Clapham, Children's Hospital Boston
David Clary, U. of Oxford
Joel Cohen, Rockefeller U., Columbia U.
Jonathan D. Cohen, Princeton U.
James Collins, Boston U.
Robert Cook-Deegan, Duke U.
Alan Cowman, Walter & Eliza Hall Inst.
Robert H. Crabtree, Yale U.
Roberta Croce, Vrije Universiteit
Janet Currie, Princeton U.
Jeff L. Dangl, U. of North Carolina
Tom Daniel, U. of Washington
Frans de Waal, Emory U.
Stanislas Dehaene, Collège de France
Robert Desimone, MIT
Claude Desplais, U. of Nijmegen
Ap Dijksterhuis, Radboud U. of Nijmegen
Dennis Discher, U. of Pennsylvania
Gerald W. Dorn II, Washington U. School of Medicine
Jennifer A. Doudna, U. of California, Berkeley
Bruce Dunn, U. of California, Los Angeles
Christopher Dye, WHO
Todd Ehlers, U. of Tuebingen
David Ehrhardt, Carnegie Inst. of Washington
Tim Elston, U. of North Carolina at Chapel Hill
Gerhard Ertl, Fritz-Haber-Institut, Berlin
Barry Everitt, U. of Cambridge
Ernst Fehr, U. of Zurich
Anne C. Ferguson-Smith, U. of Cambridge
Michael Feuer, The George Washington U.
Kate Fitzgerald, U. of Massachusetts
Peter Fratzl, Max-Planck Inst.
Elaine Fuchs, Rockefeller U.
Daniel Geschwind, UCLA
Andrew Gewirth, U. of Illinois
Karl-Heinz Glassmeier, TU Braunschweig
Ramon Gonzalez, Rice U.
Julia R. Greer, Caltech
Elizabeth Grove, U. of Chicago
Nicolas Gruber, ETH Zurich
Kip Guy, St. Jude's Children's Research Hospital
Taekjip Ha, U. of Illinois at Urbana-Champaign
Christian Haass, Ludwig Maximilians U.
Steven Hahn, Fred Hutchinson Cancer Research Center
Michael Hasselmo, Boston U.
Martin Heimann, Max-Planck Inst. Jena
Yia-Hai He, U. of Cambridge
James A. Hendler, Rensselaer Polytechnic Inst.
Janet G. Hering, Swiss Fed. Inst. of Aquatic Science & Technology
Kai-Uwe Hinrichs, U. of Bremen
Kei Hirose, Tokyo Inst. of Technology
David Hodell, U. of Cambridge
David Holden, Imperial College
Lora Hooper, UT Southwestern Medical Ctr. at Dallas
Raymond Huey, U. of Washington
Steven Jacobsen, U. of California, Los Angeles
Kai Jonsson, EPFL Lausanne
Peter Jonas, Inst. of Science & Technology (IST) Austria
Matt Kaerberlein, U. of Washington
William Kaelin Jr., Dana-Farber Cancer Inst.
Daniel Kahne, Harvard U.
Daniel Kammen, U. of California, Berkeley
Masashi Kawasaki, U. of Tokyo
Joel Kingsolver, U. of North Carolina at Chapel Hill
Robert Kingston, Harvard Medical School
Etienne Kochlin, Ecole Normale Supérieure
Alexander Koldkin, Johns Hopkins U.
Alberto R. Kornblihtt, U. of Buenos Aires
Leonid Kruglyak, UCLA
Thomas Langer, U. of Cologne
Mitchell A. Lazar, U. of Pennsylvania
David Lazer, Harvard U.
Thomas Lecuit, IBDM
Virginia Lee, U. of Pennsylvania
Stanley Lemon, U. of North Carolina at Chapel Hill
Ottoline Leyser, Cambridge U.
Marcia C. Linn, U. of California, Berkeley
Jianguo Liu, Michigan State U.
Luis Liz-Marzan, CIC bioGUNE
Jonathan Losos, Harvard U.
Ke Lu, Chinese Acad. of Sciences
Christian Lüscher, U. of Geneva
Laura Machesky, CRUK Beatson Inst. for Cancer Research
Aime Magurran, U. of St. Andrews
Oscar Marin, CSIC & U. Miguel Hernández
Charles Marshall, U. of California, Berkeley
C. Robertson McClung, Dartmouth College
Graham Medley, U. of Warwick
Yasushi Miyashita, U. of Tokyo
Mary Ann Moran, U. of Georgia
Richard Morris, U. of Edinburgh
Allison Møntsgaard-Reif, NC State U. (\$)
Sean Munro, MRC Lab. of Molecular Biology
Thomas Murray, The Hastings Center
James Nelson, Stanford U. School of Med.
Daniel Neumark, U. of California, Berkeley
Timothy W. Nilsen, Case Western Reserve U.
Pär Nordlund, Karolinska Inst.
Heila Nowotny, European Research Advisory Board
Ben Oken, MIT
Jens Olsen, U. of California
Berkeley & Lawrence Berkeley National Lab
Harry Orr, U. of Minnesota
Andrew Oswald, U. of Warwick
Steve Palumbi, Stanford U.
Jane Parker, Max-Planck Inst. of Plant Breeding Research
Giovanni Parmigiani, Dana-Farber Cancer Inst. (\$)
Donald R. Paul, U. of Texas, Austin
John H. J. Petrini, Memorial Sloan-Kettering Cancer Center
Joshua Plotkin, U. of Pennsylvania
Albert Polman, FOM Institute AMOLF
Philippe Poulin, CNRS
Jonathan Pritchard, Stanford U.
David Randell, Colorado State U.
Colin Renfrew, U. of Cambridge
Felix Rey, Institut Pasteur
Trevor Robbins, U. of Cambridge
Jim Roberts, Fred Hutchinson Cancer Research Ctr.
Barbara A. Romanowicz, U. of California, Berkeley
Jens Rostrup-Nielsen, Haldor Topsøe
Mike Ryan, U. of Texas, Austin
Mitinori Saitou, Kyoto U.
Shimon Sakaguchi, Kyoto U.
Miguel Salmeron, Lawrence Berkeley National Lab
Jürgen Sandkühler, Medical U. of Vienna
Alexander Schlier, Harvard U.
Randy Seeley, U. of Cincinnati
Vladimir Shalae, Purdue U.
Robert Siliciano, Johns Hopkins School of Medicine
Joseph Silk, Institut d'Astrophysique de Paris
Denis Simion, Arizona State U.
Alison Smith, John Innes Centre
Richard Smith, U. of North Carolina (\$)
John Speakman, U. of Aberdeen
Allan C. Spradling, Carnegie Institution of Washington
Jonathan Sprent, Garvan Inst. of Medical Research
Eric Steig, U. of Washington
Paula Stephan, Georgia State U. and National Bureau of Economic Research
Molly Stevens, Imperial College London
V. S. Subrahmanian, U. of Maryland
Ira Tabas, Columbia U.
Sarah Teichmann, Cambridge U.
John Thomas, North Carolina State U.
Shubha Tole, Tata Institute of Fundamental Research
Christopher Tyler-Smith, The Wellcome Trust
Sanger Inst.
Herbert Virgin, Washington U.
Bert Vogelstein, Johns Hopkins U.
Cynthia Volkert, U. of Göttingen
Douglas Wallace, Dalhousie U.
David Wallace, Weizmann Inst. of Science
Ian Walsmsley, U. of Oxford
David A. Wardle, Swedish U. of Agric. Sciences
David Waxman, Fudan U.
Jonathan Weissman, U. of California, San Francisco
Chris Wikle, U. of Missouri (\$)
Ian A. Wilson, The Scripps Res. Inst. (\$)
Timothy D. Wilson, U. of Virginia
Rosemary Wyse, Johns Hopkins U.
Jan Zaenen, Leiden U.
Kenneth Zaret, U. of Pennsylvania School of Medicine
Jonathan Zehr, U. of California, Santa Cruz
Len Zon, Children's Hospital Boston
Maria Zuber, MIT

BOOK REVIEW BOARD

David Bloom, Harvard U. Samuel Bowring, MIT, Angela Creager, Princeton U., Richard Swedder, U. of Chicago, Ed Wasserman, DuPont

One Arctic

This month, the United States takes over the chairmanship of the Arctic Council, a position it last held in 1998. Since then, global interest in the Arctic has increased, and the council has evolved considerably. What has spurred that interest, and what will the council focus on under U.S. leadership?

Increased interest in the Arctic is being driven by dramatic change in a region that is both valuable and vulnerable: a warming climate (sea-ice retreat, thawing permafrost, and coastal erosion); globalization and the demand for resources (increasing population and an expanding middle class); and geopolitics (claims on extended continental shelves and potential northern shipping routes). Taken together, these factors create opportunities and challenges, all of which require preparation, informed by knowledge acquired through Arctic research.

The Arctic Council was formed in 1996 by the eight Arctic nations (Canada, Denmark/Greenland, Finland, Iceland, Norway, Russia, Sweden, and the United States) as a forum to address sustainable development and environmental issues. The council promotes cooperation and collaboration among its member states and indigenous peoples' organizations and with formally recognized observers. The council has produced well-regarded reports, such as the Arctic Climate Impact Assessment and the Arctic Marine Shipping Assessment, which stimulated cross-border science and the adoption of best practices.

In recent years, discussion initiated by the council led to the creation of two multilateral agreements on search and rescue and on marine oil pollution preparedness and response. A third agreement, to increase international scientific cooperation, is in progress. Last year, the council created the Arctic Economic Council, an independent organization that facilitates economic

development in the region.

The U.S. theme for the chairmanship is One Arctic: Shared Opportunities, Challenges and Responsibilities. Three areas of focus are: Ocean Safety, Security, and Stewardship; Improving Economic and Living Conditions of Arctic People; and Addressing the Impacts of Climate Change. Specific initiatives will be conducted under each focus area by the council's working groups (see www.arctic-council.org).



“This month, the United States takes over the chairmanship of the Arctic Council...”

Are the Arctic Eight still working well together? Yes. There is more political alignment in the Arctic than in many other places, as evidenced by good relations at council events and by similar national objectives. Each member nation has its own strategy for the Arctic, with remarkably similar goals: international cooperation, national security, environmental stewardship, and economic and social benefits for the people of the region. In January 2015, President Obama issued an Executive Order to focus federal efforts in the Arctic under the U.S. National Strategy for the Arctic Region, as aug-

mented by an implementation plan, and a 5-year Arctic research program plan. These documents recognize federal responsibilities in the region and offer hope for increased coordination and efficiency to meet evolving challenges. U.S. chairmanship initiatives will advance these goals and will require the support of Congress, the State of Alaska, and local and tribal entities to be successful.

Scientific observations and research provide the knowledge base for prudent decisions. The initiatives proposed for the U.S. chairmanship require resources and coordinated effort. An essential ingredient is continued federal investment in Arctic science and technology. If the United States is to lead in these next 2 years and beyond, then it must have the capability and commitment to do so.

– Fran Ulmer

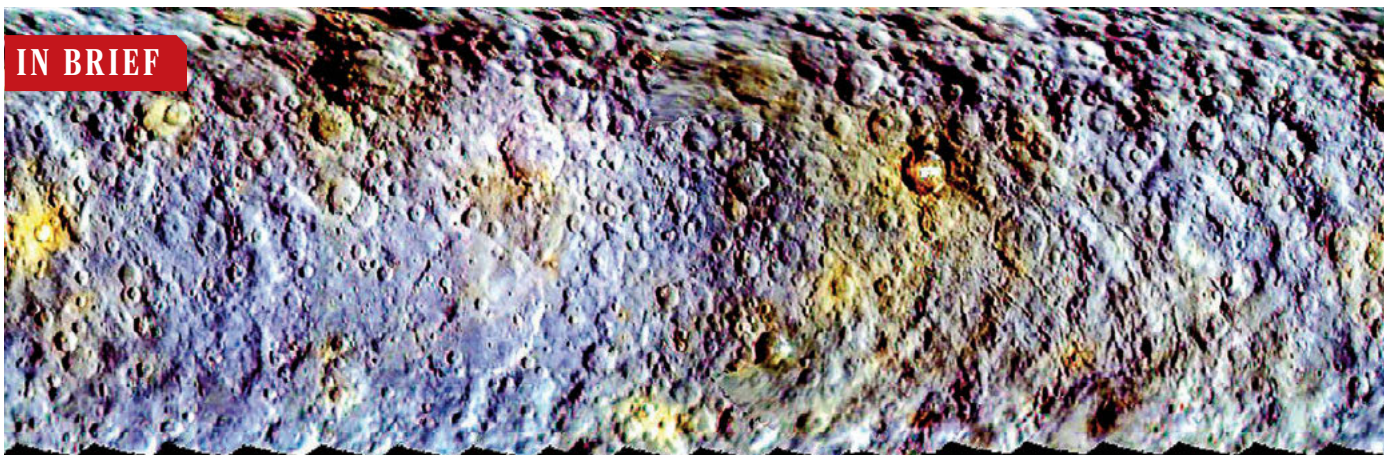


Fran Ulmer is chair of the U.S. Arctic Research Commission, which has offices in Washington, DC, and Anchorage, Alaska. E-mail: fran.ulmer@arctic.gov

“I’m 110% committed to being a scientist ... [but] 110% effort may not be enough if I can’t afford to get to the conferences where I may meet somebody that gives me [a] job.”

Marine sociologist Edward Hind: his #SciSpends survey asked scientists what they spend to advance their careers. <http://scim.ag/SciSpends>

IN BRIEF



A dwarf planet’s mysterious mottled landscape

About 20 years ago, the Hubble Space Telescope observed several curious bright spots on the surface of the dwarf planet Ceres, the largest object in the asteroid belt between Mars and Jupiter. Now, scientists are getting a much closer look. NASA’s Dawn spacecraft, which was captured by Ceres’s gravity on 6 March, has been offering the first close-up look at the surface of a dwarf planet in a series of images it took last month. The images offered evidence that the spots might be plumes of ice

bursting out of the dwarf planet’s surface. But new images from the spacecraft, released this week at the annual meeting of the European Geosciences Union in Vienna, paint a more complex picture. A false-color map of Ceres’s surface (pictured) shows that only some of the bright spots remain visible at infrared wavelengths, which could suggest different origins than the icy plumes. The map also reveals that the dwarf planet’s surface has fewer large craters—a possible sign of geologic activity—than researchers expected.

AROUND THE WORLD

WHO backs trial result access

GENEVA, SWITZERLAND | The movement to make results from clinical trials publicly available has found an important new ally. On 14 April, the World Health Organization (WHO) issued a statement calling for the public release of all key clinical trial outcomes within a year after data collection ends and for publication of the findings in a peer-reviewed journal within 2 years. Recent research has shown that many studies still go unpublished, says WHO’s Vasee Moorthy. This can harm patients and research volunteers, waste money, and distort scientists’ understanding of the state of the art of their science. “It’s unethical to conduct clinical research without reporting

the results,” Moorthy says. WHO also called for the publication of results from older, finished trials that have never been made public. http://scim.ag/_WHOtrials

GM eucalyptus approved in Brazil

SÃO PAULO, BRAZIL | Commercial planting of genetically modified eucalyptus

trees has been approved for the first time anywhere by the National Biosafety Technical Commission of Brazil. The trees were developed by FuturaGene of São Paulo, a subsidiary of Suzano Pulp and Paper. The trees grow about 20% more wood than standard ones—a feature the company expects will allow it to reduce its carbon emissions by cutting the distance

the wood must travel to mills. Development began in 2001, and the trees have been in field trials since 2006. Commercial planting was approved on 10 April, shortly



Test plot of FuturaGene’s GM eucalyptus.

after a meeting of the commission was canceled due to protests by the Brazil Landless Workers' Movement. The protesters also destroyed GM seedlings at FuturaGene's research station in Itapetininga, 170 kilometers west of São Paulo.

Monkey deaths prompt new probe

SOUTHBOROUGH, MASSACHUSETTS | The U.S. Department of Agriculture has launched an investigation into Harvard University's New England Primate Research Center after several suspicious deaths at the facility. The inquiry coincides with a series of articles published by *The Boston Globe*, which has uncovered potential animal welfare violations at the center, including a dozen dehydrated squirrel monkeys found dead in their cages or euthanized because of poor health between 1999 and 2011. In several cases it appears that the animals were not given water or were unable to drink due to malfunctioning water lines. Some of these animals were the subject of a 2014 *Veterinary Pathology* paper on the impact of dehydration on lab animals. The journal says it is investigating this study. The primate center is set to close at the end of next month—although, the *Globe* notes, the university blames finances, not animal care problems.

NEWSMAKERS

Three Q's

Scientific labs generate a lot of waste, a fact that bothered biomedical engineer **Joshua Resnikoff** (also co-founder of eco-friendly company Cuppow!). So last October, he founded Labconscious (www.labconscious.com), an open community where scientists can share tips and tricks to help each other green their labs.

Q: How did you get interested in reducing lab waste?

A: I'm a biomedical engineer by training. In life science, there's an unbelievable amount of waste that comes out of the lab. I'm a big environmentalist—I take the time to sort my recycling at home. It's always been a hard juxtaposition to go from biking to work to throwing all of this plastic away.

Q: What's the purpose of the blog?

A: We don't pretend to be the experts in the room about any of this stuff. The real goal of the blog is to get the conversation going and raise awareness so that people can trade tips and best practices



New species of 'terror bird' discovered

Famed for their large hooked beaks and a presumed taste for meat, flightless "terror birds" (above, in an artist's representation) were among South America's top predators before going extinct about 2.5 million years ago. Now, paleontologists have unearthed one of the most complete fossils of a terror bird—known as a phorusrhacid—to date. The skeleton of the new species is nearly 95% complete, giving scientists the ability to study a terror bird's anatomy in unprecedented detail. So far, researchers say, the most interesting information has come from CT scans of the bird's inner ear, which show that it had a much lower range of hearing than its closest relatives. The fossil, missing only a few wing and toe bones and the tip of its stubby tail, was excavated in northeastern Argentina in 2010 from material laid down as sediment about 3.5 million years ago. <http://scim.ag/terrorbird>

BY THE NUMBERS

3.3
million

Age, in years, of the earliest known human tools. The tools were found at a site in Kenya, scientists reported this week at the Paleoanthropology Society's annual meeting in San Francisco, California.

\$13
million

The largest education donation to the Smithsonian Institution's National Museum of Natural History to date, made to support the museum's science education center, Q?rius.



A panel nixed Japanese research whaling in the Antarctic. (This minke whale was landed north of Japan.)

Panel: Thumbs-down to Japan's plan to hunt minke whales

Experts on a review panel gave a thumbs-down to Japan's latest proposal to resume hunting minke whales in the Antarctic for scientific research. The panel, which was convened by the Scientific Committee of the International Whaling Commission (IWC), released its nonbinding report this week from a February meeting in Tokyo. From 1987 to 2014, Japan killed 10,000 whales in the Antarctic under a special IWC clause that permits "scientific whaling." But in March 2014, the International Court of Justice ruled that Japan's whaling was not "for purposes of scientific whaling." Japan agreed to revise its research plan. But the panel has concluded that Japan's new proposal to harpoon nearly 4000 additional minke whales over the next 12 years fails to demonstrate why its scientists need to kill any whales to achieve their research objectives. Japan's fisheries officials say they are open to revising their proposal, although they did not give details. If Japan abides by the panel's recommendations, it will collect samples nonlethally next year during its proposed whale hunting season.

and better products that they've discovered on their own.

Q: Can you share a few quick tips?

A: One, recycle your pipette tip boxes—don't throw them into the biohazard bin. Two, shut the sash on your bio hood and chemical fume hood when it's not in use to save energy. And look for vendors that have green product alternatives.

Artificial trachea pioneer cleared

Paolo Macchiarini, a thoracic surgeon who attracted widespread attention for transplanting artificial tracheae into patients—and then faced charges of scientific misconduct—has been found not guilty in the first of two investigations into his work. The ethics council of the

Karolinska Institute in Stockholm began its investigation after receiving concerns last year about misrepresentation of results in Macchiarini's papers. In its report, released 14 April, the council dismissed the issues. "We are now happy that everything has been cleared," Macchiarini says. Pierre Delaere, a head and neck surgeon at UZ Leuven in Belgium who brought the case against Macchiarini, says he is "stunned." Another ongoing investigation claims that Macchiarini did not get properly informed consent from patients, a charge he denies. Macchiarini, who splits his time between the Karolinska Institute and Kuban State Medical University in Krasnodar, Russia, says his team has "moved forward" and no longer works on tracheae. <http://scim.ag/artiftrach>

#IAmAScientistBecause ...

A cheerful meme swept through the Twitter science community last week: Biologists, physicists, geologists, and others proclaimed why they love their work. See some of our favorites below and at <http://scim.ag/scientistbec>.

... there are moments when I learn something in the lab and think, I'm the only human that knows this right now

@DrWorms (Brian D. Ackley)

... my honest answer to "what would you want to do all day if you didn't need money" is "what I actually am doing"

@WhySharksMatter (David Shiffman)

... Science turns "I don't know" into "I don't know... yet" and you won't find anything more empowering than that.

@orzalc (Chad Orzel)

FINDINGS

Vampire bats prefer bacon

Examining animal droppings is not glamorous—even if you're studying vampires. But for scientists interested in the diet of the common vampire bat (*Desmodus rotundus*), it's one of the few ways to learn what they eat. In a new study in the *Journal of Mammalogy*, researchers used DNA from the bats' feces to learn whose blood they suck and which blood they like best. They found that more than 60% of their viable samples—collected from 18 villages in the Amazon—contained chicken DNA, while just 30% contained pig DNA. After accounting for the relative scarcity of pigs, the scientists found that swine took the prize: Vampire bats were seven times more likely to feed on pigs than chance would predict. <http://scim.ag/vampirebacon>

PHOTO: KYODO/NEWSCOM

63

• KNOWLEDGE FOR A BETTER WORLD •
north



Photo: Carl-Erik Eriksson

Trondheim is the ancient Viking capital of Norway. The Nidelva River flows through the city, and you can even fish for salmon during your lunch break. You'll find hiking, alpine and cross-country skiing, cycling and more within a 10-minute drive of the city centre.

Research adventure at 63 degrees north

Remote yet modern. Beautiful and peaceful. Quality and equality. All that combined with long-term government research funding and the UN's ranking as one of the best countries to live in. Welcome to Trondheim and NTNU. The best minds, world-class research, and just the right size city for a great life.

We welcome top scientists from all cultures and nations who want to contribute to our goal: Knowledge for a better world.

**TOP RESEARCH DEMANDS BRILLIANT MINDS
– WE'RE ALWAYS LOOKING FOR THE BEST**



Photo: Geir Mogen/Kavli Institute for Systems Neuroscience

NTNU neuroscientists May-Britt and Edvard Moser were awarded the Nobel Prize in Medicine or Physiology in December 2014.



NTNU – Trondheim
Norwegian University of
Science and Technology

www.ntnu.edu



CONSERVATION

Meager snows spell trouble ahead for salmon

Without snowmelt, streams in the western U.S. could reach lethal temperatures

By Robert F. Service

Although record snowfall in the north-eastern United States grabbed the headlines this winter, the mountains throughout much of the western United States remained unusually bare. Early to mid-April in the West typically marks the high point of the snowpack, which serves as a critically important water bank that doles out reserves as the snow melts over the dry summer months. But this year the bank is nearly empty, and drought-stricken farms and cities in California can expect little relief. And for endangered salmon migrations, a calamity is looming. "It's going to be a Katrina for fish," says Dan Isaak, a fisheries scientist at the U.S. Forest Service's Rocky Mountain Research Station in Boise.

He and others predict that when salmon swim up western rivers to spawn this summer, their eggs and young will perish in shallow, warm water. That could threaten already meager endangered stocks, particularly in California's Central Valley, which faced similar disastrous conditions last summer.

A map of snowpack

totals in the Pacific Northwest shows mostly light and dark red dots, indicating snow levels 50% of normal and below. A smattering of white dots indicates no measured snow at all. California's Sierra Nevada is in even worse shape, as those mountains now hold only 5% of their normal snowpack. The state's reservoirs are also only about half full. Faced with this combination, earlier this month California Governor Jerry Brown mandated an across-the-board 25% cutback in water deliveries to urban water users.

Ironically, river and stream flows are still robust, at least outside California. According

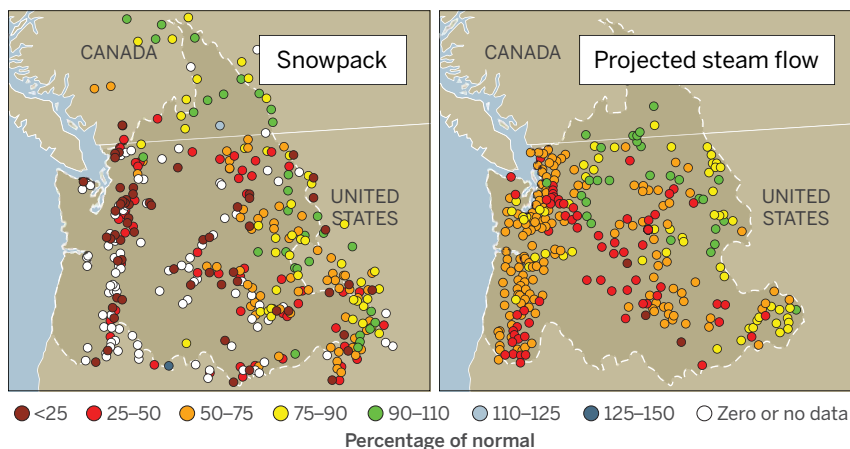
to interactive stream flow maps maintained by the National Oceanic and Atmospheric Administration (NOAA), water levels in rivers that are prime salmon habitat across the Pacific Northwest are surging. The maps are peppered with pale blue and deep blue dots, indicating flow levels 125% to 175% of normal. But that's because for most of the winter, temperatures across the region were 3°C to 6°C above normal, says Kevin Berghoff, a senior hydrologist with NOAA's Northwest River Forecast Center (NRFC) in Portland, Oregon. As a result, most of the precipitation in the Northwest fell as rain rather than snow, swelling spring runoff volumes.

Flows are likely to drop dramatically in the summer, according to NRFC. With the exception of a few river basins in central and eastern Washington, Idaho, and British Columbia, virtually all the rivers in the Northwest are expected to have flow levels far below normal.

When summertime heat sets in, water temperatures in those rivers are likely to spike. In many inland streams in California's Central Valley, as well as central Oregon and Washington, river temperatures are expected to crest

Mapping the threats to endangered stocks

Mild winter temperatures in the Pacific Northwest caused most precipitation to fall as rain instead of snow. That has left a snowpack far below normal (left) and is expected to cause low stream levels this summer (right).



above 20°C, the upper limit for migrating salmon. Above that, salmon eggs, fry, and juveniles typically perish, says Chris Caudill, a fisheries ecologist at the University of Idaho, Moscow. Adult fish sometimes survive those temperatures by halting their migrations and holing up in any colder water tributaries they can find. Yet doing so can bring other problems. For starters, the fish don't eat during spawning, so extended layovers can sap the energy reserves they need to complete their trip. And as the fish wait, they face increased predation and disease. "When water temperatures rise, none of the options is good," Caudill says.

Water managers can combat high summer stream temperatures by slowly releasing cold water from summertime snowmelt captured in reservoirs. But without a significant snowpack, that strategy can only work for so long. Last year, for example, water managers in northern California tried that approach at Shasta Dam in an effort to keep water temperatures below 20°C in the Sacramento River, home to endangered winter-run Chinook salmon that migrate upriver during the summer. But the supply of cold water behind the dam ran out in early September, and river temperatures soared. As a result, an estimated 95% of the eggs, fry, and juvenile winter-run Chinook died, says Peter Moyle, a fisheries biologist at the University of California, Davis. Right now, Shasta Lake holds roughly the same volume of cold water as it did at this time last year, Moyle says. "Chances are good we'll see a repeat of last year."

Even if the skies open up and water fills reservoirs throughout the West, young salmon that do make it out to sea face a potentially even larger problem. That's because river travel represents only the first of their challenges. Equally important to the health of the fish is the availability of food in the ocean. That food depends on the upwelling of cold, nutrient-rich waters off the West coast. Yet this year there has been less upwelling than usual because of a layer of unusually warm surface water (*Science*, 3 April, p. 17), which has already led to a crash in sardine and seabird populations. So if and when young salmon manage to escape the warm, low river levels, "they will face an ocean with not a lot of food," Moyle says. That's likely to further jeopardize the more than one dozen fish runs already listed as either threatened or endangered.

Adding to these troubles, long-term climate change, which is expected to produce more hot and dry years like this one, is likely to wipe out all the remaining California salmon stocks by the end of the century, Moyle says. At this point, Moyle says, "it looks inevitable." ■

FACULTY HIRING

Women best men in study of tenure-track hiring

Female candidates twice as likely to get top rating

By Rachel Bernstein

Wendy Williams and Stephen Ceci believe they have crossed one factor off the list of obstacles facing women in academia: the hiring committee. To their own surprise, the Cornell University psychologists have found that a highly qualified woman applying for a tenure-track faculty position in STEM (science, technology, engineering, and mathematics) at a U.S. university is twice as likely to be hired as an equally qualified man.

The results run counter to widely held perceptions and suggest that this is a good time for women to pursue an academic career. Some observers, however, say the study—which involved actual faculty members rating hypothetical candidates—does not reproduce real-world hiring. And they worry the results may leave the incorrect impression that universities have achieved gender parity in STEM fields. Still, says psychologist Virginia Valian of Hunter College in New York City, "it will definitely make people think more thoroughly and more subtly" about the issue.

The researchers invented three hypothetical candidates for an assistant professorship: an extremely well-qualified woman, an extremely well-qualified man, and a slightly less qualified man. For each candidate, they wrote a summary that included a search committee's impression of the candidate, quotes from recommendation letters, and a score for the candidate's job talk and interview. Then they asked 873 tenure-track faculty from four fields, roughly divided between men and women, to rank the candidates. Overall, raters in most fields were twice as likely to tag the woman as the best candidate, the researchers reported online this week in the *Proceedings of the National Academy of Sciences*.

Williams and Ceci say they were shocked

at the outcome. And although they did not investigate the potential causes, they suspect it may be due to some combination of training programs on gender and hiring, a growing belief about the importance of gender balance among STEM faculty, and the retirement of older faculty.

The candidates' marital status and whether they had children made little difference to the outcome, except in one case.

When the female candidate was described as having had a child during graduate school, male raters preferred a candidate who took a 1-year parental leave, whereas female raters preferred the one who did not take a leave.

"I almost wonder if there's a bit of paternalism going on" among the male raters, says University of Mississippi, Oxford, business professor H. Kristl Davison. Perhaps "there's a female bias present in terms of, 'I struggled through grad school without taking leave; I think others should do so as well.'"

But Davison also wonders whether the study's main result "would translate to the real world." She and others note that bias can enter the hiring process well before the final selection round. Men and women can be perceived differently during preliminary interviews, for instance, based on personality traits that have nothing to do with merit.

Others note that obstacles may emerge later, after a woman is hired. "I think it's fair to say that the women who have run the gauntlet and gotten advanced STEM degrees will find the labor market quite welcoming," writes Jennifer Glass, a sociologist at

the University of Texas, Austin, in an e-mail. "What happens once they are [hired] is another matter entirely." She says studies suggest that women still have higher attrition rates in some STEM careers.

Valian agrees. Despite the apparent good news, she says, "it's too soon to say: 'OK, problem solved.' " ■

Who chose the female candidate?

67.3
%, overall

69.2
%, biology

66.7
%, engineering

72.5
%, psychology

58.6
%, economics

ARCTIC POLICY

U.S. lays out its ambitions for leadership in the Arctic

Climate, marine conservation, and renewable energy priorities as U.S. ascends to chair of Arctic Council

By Carolyn Gramling

The United States plans to launch an ambitious Arctic agenda next week as it begins a 2-year stint as chair of the Arctic Council, an eight-nation group that aims to foster cooperation on research and policy in the rapidly changing polar region.

Concerns about the Arctic have escalated since the first U.S. chairmanship from 1998 to 2000. This time, officials say they will emphasize the need to take action on climate change, expand marine conservation, and

of the International Arctic Program at the Ocean Conservancy in Washington, D.C. But implementation is another matter, he says, because the recommendations are “not always business-friendly and politically palatable.”

The council was created in 1996 by the “Arctic 8” nations that claim territory above the Arctic Circle—Canada, Denmark, Finland, Iceland, Russia, Sweden, Norway, and the United States. Early on, it became known for producing detailed reports, some with “pretty specific recommendations,” says Fran Ulmer, head of the U.S.

ince). The U.S. agenda, announced in October, includes a call for nations to enhance studies of climate-related processes such as the deposition of tiny particulates known as black carbon, which is accelerating the warming and melting of the region; emissions of methane, a potent warming gas, from permafrost and the seabed; and the acidification of the Arctic Ocean. The United States also wants to make progress on creating an Arctic network of marine protected areas and equipping Arctic villages with renewable energy sources.

The list marks “probably the most forward-leaning, ambitious program that’s been proposed [for] the chairmanship of Arctic Council,” said Admiral Robert Papp, a former commandant of the U.S. Coast Guard who is now the Obama administration’s special representative for the Arctic, at a March event at the Brookings Institution think tank in Washington, D.C. Papp and others also hope to use the position to remind Americans that the United States is an Arctic nation with a big stake in the region’s future.



U.S. seeks more research on soot particles that are accelerating melting on Greenland’s ice sheet (left) and methane bubbling from frozen Arctic lakes (right).

promote renewable energy. “They’ve laid out a very ambitious, good agenda,” says Lisa Speer, director of the International Oceans Program at the nonprofit Natural Resources Defense Council in Washington, D.C. She and others say the U.S. emphasis on climate will come as a marked contrast to outgoing chair Canada, which downplayed the issue and focused on economic development for indigenous people.

But some observers warn against lofty expectations, noting that the council doesn’t issue rules, only recommendations for action by the member governments. The group is often very good at identifying solutions, says Whit Sheard, director

Arctic Research Commission in Anchorage, Alaska, and the State Department’s special adviser on Arctic science and policy. But in recent years, she says the council has begun to broker binding agreements. A 2011 pact, for instance, focused on coordinating search and rescue operations, while a 2013 deal dealt with responding to oil spills. Negotiations on a third agreement, on international cooperation in Arctic research, are nearing completion, she says (see Editorial, p. 263).

The United States hopes to add to that record after it takes the gavel at a 24 to 25 April ministerial meeting in Iqaluit, Nunavut (Canada’s northernmost prov-

“The chairmanship is falling at a key time,” Speer notes. Climate change is having an increasingly noticeable impact on Arctic ecosystems, industry is ramping up interest in the region, and nations have been jostling to stake territorial claims. Against that backdrop, efforts to forge agreements on marine conservation, for example, “could really break new ground,” Speer says. “A regional seas agreement combined with a network of protected areas throughout the Arctic could be a huge legacy” left by a U.S. leadership team.

But the clock is ticking. “Two years isn’t much time,” Speer says. “I hope they’ll hit the ground running.” ■



The giant impact that formed the moon may have flung copious debris into the solar system.

PLANETARY SCIENCE

Moon-forming impact left scars in distant asteroids

Planetary collision dated through analysis of meteorites

By **Eric Hand**

It was the biggest cataclysm the solar system has ever seen. About 100 million years after the planets began to take shape, a Mars-sized body crashed into the proto-Earth, creating a halo of hot debris that coalesced into the moon.

There was collateral damage, it turns out. Scientists now suspect that fragments of the giant impact were flung all the way to the fledgling asteroid belt. When this planetary shrapnel crashed into bodies there, it shock heated them, leaving an imprint that can still be detected billions of years later in meteorites. On page 321, planetary scientists show that these shock-heating signatures provide a new way to date the moon's formation, pegging it at 105 million years after the beginning of the solar system 4.6 billion years ago.

The result could help settle debates about the age of the moon and suggests that meteorites, which are mostly fragments of asteroids, could harbor other evidence of tumult in the inner solar system. "The asteroid belt is almost primordial," says Bill Bottke, a planetary scientist at Southwest Research Institute in Boulder, Colorado, and lead author of the new study. "A lot of objects there have been witness to activity in the inner solar system. We now have a

way to probe that."

Scientists have long tried to pin down the age of the moon by analyzing lunar samples returned from the Apollo missions. But because of disagreements about the isotope systems used for dating, the calculated ages vary from about 30 million years after the start of the solar system to 100 million or even 200 million years younger. A more precise age would help scientists work out when the bumper-car process of planet formation began winding down. The moon-forming impact is thought to have come late in the process, because the composition of Earth's mantle reflects only a short period of impacts by smaller bodies after the mammoth collision.

Researchers who study the giant impact have typically ignored the bits that didn't end up in the moon. But Bottke realized that an event so large would have created fragments moving fast enough to escape the collective gravity of the Earth-moon system. "You create this huge swarm of material," he says. His models suggest

that 10 billion kilometer-sized bodies would have been flung out into the solar system—where many of them could strike asteroids.

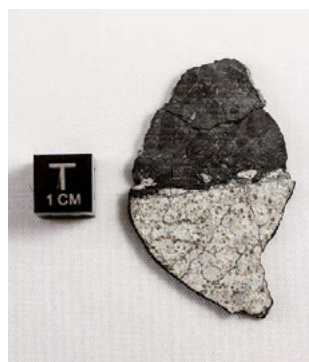
Asteroids constantly collide with each other, but at relatively slow speeds. Some high-speed projectiles from the giant impact, in contrast, would have struck at speeds upward of 10 kilometers a second, melting and transforming asteroid minerals into darker, glassy materials. The shock heating would also have altered a standard radioactive "clock" used for dating, in which a radioactive isotope of potassium decays into argon that remains trapped in the crystal structure of the rock. "If you heat it up enough, argon moves through the crystal structures, and you can reset [the clock]," says study co-author Tim Swindle, director of the Lunar and Planetary Laboratory at the University of Arizona in Tucson.

Searching through the literature for meteorites that had already been dated, the team found 34 samples that fit their profile: those with shock-heating alteration and ancient argon ages. A significant fraction of these 34 samples have ages that cluster around 105 million years after the solar system began; that, the team believes, is the age of the moon-forming impact.

Other scientists are excited about the method but worried about the small sample size. The authors used their own judgment to identify meteorites with the right type of shock heating, and their 34 meteorite samples could hail from as few as five or six parent asteroid bodies. "Is that really representative of everything the asteroid belt saw?" asks Sarah Stewart, a planetary scientist at the University of California, Davis. "It's not a robust conclusion, but it's a robust method."

Swindle says the new moon age estimate—a signal "strong enough to look like more than a curiosity"—will improve as his lab and others calculate dates for more shock-heated meteorites. And Bottke hopes the method will be used for more than just dates. He says meteoriticists should return to these 34 samples and inspect them carefully. Perhaps amid the veins of glassy materials are

fragments of the giant impactor, or the proto-Earth itself. "There may still be traces of the primordial Earth in the asteroid belt, and they may be in our meteorite collections today," Bottke says. "To me that's fun." ■



Dark impact melt (top) in a meteorite that fell near Chelyabinsk, Russia, may have been created by projectiles from the moon-forming impact.



In Bangladesh, some people still use “hanging latrines” that dump feces into a body of water.

SANITATION

For toilets, money matters

New work suggests that subsidies to the poor to buy latrines could help end open defecation

By Jocelyn Kaiser

When nature calls, about 1 billion people in the developing world still head to an open field, the bushes, or a body of water to defecate. The practice has contributed to high rates of diarrheal diseases, especially in India, where more than half of people don't use latrines. Prime Minister Narendra Modi, who took power last May, has pledged to build 111 million toilets as part of the Clean India mission, a sanitation campaign. One goal is to end open defecation by October 2019.

But exactly how to get there is surprisingly controversial. Some nongovernmental organizations and government officials in developing countries have long pushed for education campaigns—teaching people about the health benefits of using toilets. Others advocate subsidizing latrine costs for the poor, but some economists argue that financial aid for cheap toilets could backfire by discouraging those who don't receive it from buying latrines on their own for a higher price.

Now, one of the largest controlled experiments to examine sanitation strategies, conducted in India's neighbor Bangladesh and published online this week in *Science* (<http://scim.ag/RGuiteras>), comes down strongly in favor of cash. After comparing three policies in more than 100 villages, the authors found that the key to getting people to build latrines

is to subsidize the cost. They also found that funding poor villagers to install latrines can encourage their unsubsidized neighbors to follow suit in a beneficial spillover effect.

“Given the enormous emphasis Prime Minister Modi has placed on eliminating open defecation in India, these results should be of great interest to [the Indian government]. It tells us that cutting the price of quality toilets is the single most powerful instrument in getting people to stop defecating outside,” says economist Abhijit Banerjee of the Massachusetts Institute of Technology in Cambridge, who was not involved in the study. Others caution, however, that building toilets doesn't always mean people will use them or be healthier, or that findings in Bangladesh will be relevant to culturally different India.

The experiment, funded by the Bill & Melinda Gates Foundation in Seattle, Washington, took place in the Tanore, a poor, rural district in northwest Bangladesh. Although open defecation rates are only 3% overall in Bangladesh, in Tanore, about one-third of adults still follow the practice or use unhygienic latrines, such as “hanging” latrines that empty into waterways. Yale University economists Mushfiq Mobarak and James Levinsohn and Raymond Guiteras of the University of Maryland, College Park, chose 107 villages with 18,254 poor households. Some villages received education on the importance of sanitation, and some received only information on buying and installing

a latrine. In a third program, 25% to 75% of villagers received vouchers through a lottery. Each voucher was good for about 50% off the \$29 to \$58 cost of an installed pour flush latrine—a design that carries feces to a sealed pit.

The vouchers made all the difference, the researchers found 13 months later. Education alone or information on how to acquire a latrine did not significantly increase the portion of people who owned or had access to a hygienic latrine. But education plus vouchers resulted in significant change—for example, a rise in hygienic latrine ownership from 22% in the control group to 45% in villages where half the households received vouchers and education. The study also found a reduction of 14% in open defecation in these same villages.

The big surprise was that even people who didn't receive a voucher were more inclined to buy a latrine at full price if their neighbors received vouchers. This effect was stronger when a higher proportion of households received vouchers. People were also more likely to use their vouchers in neighborhoods where more households received vouchers. For policymakers, the message is clear, Mobarak says: “If you are going to use subsidies, it makes sense to allocate them in a coordinated manner so that many people in a community all get subsidies jointly.”

Varad Pande, an economist with the Dalberg consulting firm in Mumbai, India, who has advised the Indian government and the World Bank about sanitation policies, says the results “resonate with our experience on the ground. ... Both [subsidies and education] need to happen in a well-orchestrated sequence.” To Sumeet Patil, an epidemiologist and economist with the Network for Engineering and Economics Research and Management in Mumbai, the result should settle the debate over toilet subsidies.

But others say an encouraging result in Bangladesh may not say much about India, where the hygiene problem is much bigger. A survey released last year by the Research Institute for Compassionate Economics (RICE) in New Delhi found that many Indians who have access to a hygienic latrine still prefer open defecation, particularly Hindus, who were not represented in the Bangladesh study. The reasons may involve Hindu caste system beliefs that allowing feces to accumulate in a latrine is impure and that only an “untouchable” can remove them, says RICE Executive Director Dean Spears. He adds: “I would just say we should be very careful about generalizing [the *Science* findings] to Hindu rural north India.” ■

PHOTO: © KAREN KASMAUSKI/CORBIS

Japan accelerator poised to go fully operational

Closure after radiation leak ended up hampering some teams more than others

By Dennis Normile

Japan's premier particle accelerator will soon be back in business after a long shutdown that frustrated entire physics communities.

On 23 May 2013, a malfunction at the Japan Proton Accelerator Research Complex (J-PARC) in Tokai, 110 kilometers northeast of Tokyo, directed an unexpectedly strong pulse of protons from its 50 giga-electronvolt synchrotron at a gold target in the Hadron Experimental Facility. Radioactive vapors escaped into the hall and outside the building. The leak was minor, exposing staff to doses equivalent to medical x-rays, and radiation was barely detectable at the campus boundary (*Science*, 7 June 2013, p. 1155). But the entire lab was closed for safety upgrades, hitting some research groups harder than others.

The proton beam feeds three separate experimental halls. In addition to the hadron facility where researchers study exotic subatomic particles, a second hall focuses on materials and life sciences, and a third is dedicated to a world-leading neutrino experiment. The life sciences and neutrino experiments were brought back online a year ago. Because the leak occurred in the hadron hall, it faced greater scrutiny and its experiments suffered a more crippling delay. If it passes a final safety inspection scheduled for 17 April, the hadron facility should soon resume operations as well.

Shuttering the hadron work for 2 years “had a big impact,” says Shin’ya Sawada, a physicist with Japan’s High Energy Accelerator Research Organization (KEK) in Tsukuba, which operates J-PARC along with the Japan Atomic Energy Agency. It “has been a very difficult period.” The unique facility produces kaons, pions, muons, and other particles and directs them to several specially built secondary beamlines. These subatomic particles are at the heart of questions about the formation of atomic nuclei immediately after the big bang.

When the accident occurred, several hadron experiments were ongoing. Some groups were able to publish based on limited data. Others were less fortunate, including a planned hunt for a rare form of particle decay that might offer clues to one of the great mysteries of physics: why there is more matter than antimatter in the universe. J-PARC had built a beamline for the experiment, known as KOTO, which aimed to observe neutral kaons decaying into neutral pions plus pairs of neutrinos. This decay violates a symmetry between matter and antimatter known as charge-parity (CP) symmetry. It is predicted to be vanishingly rare, so an observation would upend the standard theory of

direct the proton beam from the synchrotron at a graphite target, which produces neutrinos that wing their way from J-PARC to the Super-Kamiokande neutrino detector, 295 kilometers west. T2K began taking data in 2010, but lost a year to repairs after the 2011 Tohoku earthquake. The experiment’s primary objective was to catch muon neutrinos changing into electron neutrinos in flight—a phenomenon called oscillation that holds clues to the vanishingly small masses of the three neutrino varieties. At the time of the accident, the accumulated data were “enough to show electron neutrino appearance,” says Tsuyoshi Nakaya, T2K spokesman and a Kyoto University physicist. T2K researchers

announced these world-first findings in 2013.

The synchrotron, fed by a newly upgraded linear accelerator, came back online last year; T2K began taking data again that May. The team is now studying anti-neutrinos for insights into another aspect of CP violation. Nakaya says they will announce new results this summer. But the team is warily watching Fermilab’s NOvA, an experiment that came online last fall and will also probe CP violation. By delaying the Japanese project, the J-PARC shutdown “brought us [into]

severe competition with NOvA,” says Takashi Kobayashi, a T2K physicist with KEK.

Investigators traced the accident to faulty equipment and human error in the hadron hall. J-PARC has added devices to minimize equipment glitches, installed air-tight membranes on the radiation shielding surrounding the beamline, and fitted exhaust fans with filters to prevent any radioactive gas from escaping to the environment. Construction is complete; after a safety inspection by an independent agency, a final green light must come from Japan’s Nuclear Regulation Authority.

Yamanaka is philosophical about the delay. Re-establishing trust with local authorities and the public “is a very difficult business,” he says. “But I’m glad the experiment is coming back online.” ■



To contain any future radiation mishap, J-PARC installed an air-tight barrier topped by a rubber sheet and spacers (shown) in its Hadron Experimental Facility.

CP violation, which alone cannot explain the matter-antimatter imbalance.

After nearly a decade of preparation and instrument development, the KOTO team started taking data on 18 May 2013, just 5 days before the radiation leak shut them down. Taku Yamanaka, an Osaka University particle physicist who leads KOTO, says they have tried to put their downtime to good use, for instance by building an additional detector that screens out background noise and steering Ph.D. candidates to focus their theses on detector development. Other groups are working on related themes, Yamanaka says, but “we don’t have any direct competitors, so that’s good.”

Scientists involved in the Tokai to Kamioka (T2K) neutrino experiment were luckier, though they still suffered a setback. They

FEATURES

DAWN OF THE DOG

An unprecedented collaboration may solve one of the greatest mysteries of domestication

By David Grimm, in Columbus, Ohio

A prehistoric dog is about to go to the dentist. Ardern Hulme-Beaman, a lanky 27-year-old Irish postdoc, pulls on a white face-mask and lifts a small 5000-year-old jawbone from a cardboard box. He places a gloved hand over one of the molars and gently tugs from side to side until it pops out. The jagged top of the tooth is yellowish white, but the roots are dirty brown. Hulme-Beaman powers on a drill, and a circular blade screeches into a root. The scent of burning hair fills the air. “That’s a good sign,” he says. “It means there’s DNA here.”

Hulme-Beaman has spent the past 6 months traveling the world in search of ancient dog bones like this one. He’s found plenty in this Ohio State University archaeology laboratory. Amid boxes stacked high with Native American artifacts, rows of plastic containers filled with primate teeth, and a hodgepodge of microscopes, calipers, and research papers, a few shoe and cigar boxes hold the jigsaw pieces of a dozen canines: skulls, femurs, mandibles, and vertebrae.

It’s all a bit of a jumble, which seems appropriate for a field that’s a bit of a mess itself. Dogs were the very first thing humans domesticated—before any plant, before any other animal. Yet despite decades of study, researchers are still fighting over where and

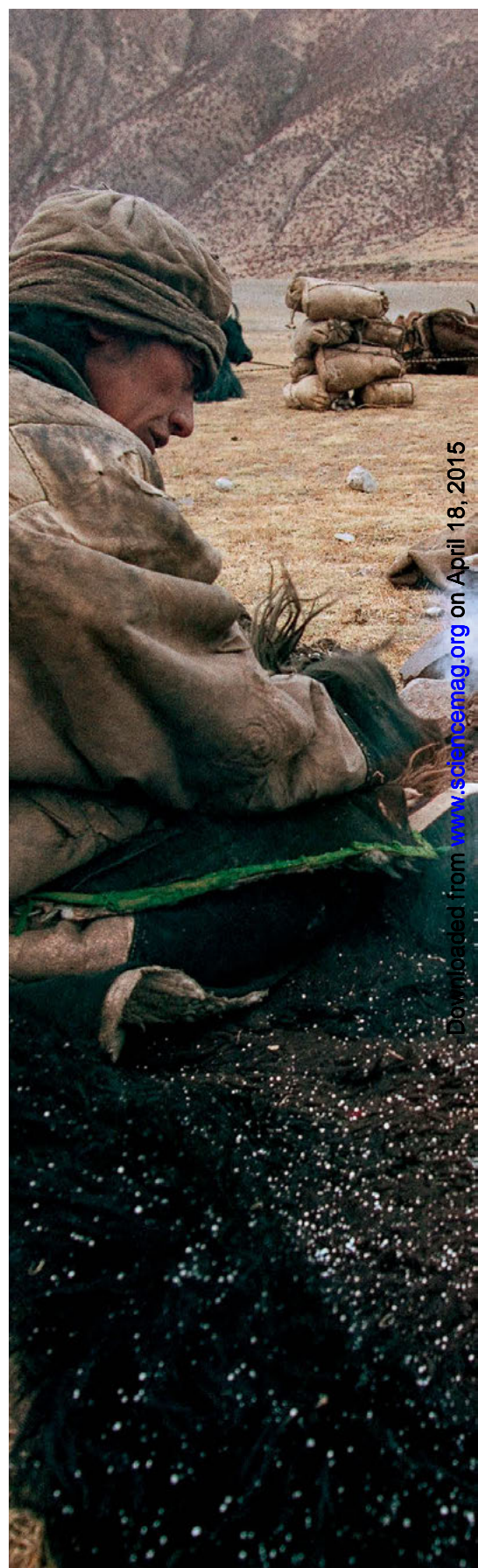
when wolves became humans’ loyal companions. “It’s very competitive and contentious,” says Jean-Denis Vigne, a zooarchaeologist at the National Museum of Natural History in Paris, who notes that dogs could shed light on human prehistory and the very nature of domestication. “It’s an animal so deeply and strongly connected to our history that everyone wants to know.”

And soon everyone just might. In an unprecedented truce brokered by two scientists from outside the dog wars, the various factions have started working together. With the help of Hulme-Beaman and others, they’re sharing samples, analyzing thousands of bones, and trying to set aside years of bad blood and bruised egos. If the effort succeeds, the former competitors will uncover the history of man’s oldest friend—and solve one of the greatest mysteries of domestication.

CHARLES DARWIN fired the first shot in the dog wars. Writing in 1868 in *The Variation of Animals and Plants under Domestication*, he wondered whether dogs had evolved from a single species or from an unusual mating, perhaps between a wolf and a jackal. Decades of speculation followed, until in the late 1990s, genetic analyses finally confirmed that dogs had descended from gray wolves. (The two share 99.9% of their DNA.)

MORE ONLINE

For a video, quiz, and more, see <http://scim.ag/k9science>.



Downloaded from www.sciencemag.org on April 18, 2015



Dogs have helped humans since prehistory. Here they accompany a caravan transporting salt in Tibet.

But just when and where this transition happened was a mystery. In 1977, scientists discovered a puppy buried in the arms of a human under a 12,000-year-old home in northern Israel, suggesting that dogs were domesticated in the Middle East, shortly before people took up farming. But later finds—skulls recovered from Russian caves and from ancient encampments in Germany—pushed canine origins back another 4000 years, indicating that dogs accompanied people in Eurasia while they were still hunters and gatherers.

Genetic investigations have only complicated the picture. A 1997 analysis of DNA from more than 300 modern dogs and wolves tallied genetic differences, aiming to use these as a measure of time since dogs began to diverge from their wolf ancestor. It concluded that dogs may have been domesticated as early as 135,000 years ago. Later studies argued for a more recent origin—less than 30,000 years ago—but the exact time and location remained unclear.

“There were lots of books written, and they all said something completely different,” says Peter Savolainen, a geneticist at the Royal Institute of Technology in Stockholm. Savolainen had become interested in the topic in the early 1990s as a master’s student in a government forensics lab, where he set up the world’s first canine DNA database to help police with two unsolved murders. Dog hair had been found on the bodies, and by collecting genetic material from 100 canines across the globe, he helped the officers determine the type of dog the murderer owned.

Savolainen knew that DNA had been used to pinpoint Africa as the place where modern humans emerged, and he wondered if a similar approach could help him home in on the birthplace of dogs. “Already in our small database, I saw a pattern,” he says. East Asian breeds were more genetically diverse—a hallmark of more ancient origins. As Savolainen continued to build his database, the pattern remained. In 2009, he published a genetic analysis of more than 1500 dogs from around the world, concluding that the animals had likely arisen in a region south of China’s Yangtze River less than 16,300 years ago—a time when humans were transitioning from hunting and gathering to rice farming. These early canines, his team speculated, may have been raised for meat. “The data are very clear and distinct,” he says. “For me, the basic question is solved.”

Not for Robert Wayne, an evolutionary biologist at the University of California, Los Angeles. The elder statesman of canine ge-



netics, Wayne began working on dog DNA in the early 1980s, when genetic sequencing was still in its infancy. Like Savolainen, he's interested in where dogs came from. But the two have come to very different conclusions and have been sparring in papers and the press for more than a decade.

That's largely because Wayne thinks looking at modern DNA is a mistake. "We have this image of dogs living in our homes and going on walks with us," he says. "But that's not the way it was in the past." Dogs regularly interbred with wolves and canines from other regions—especially in China, he says, where traffic along major trade routes likely brought in breeds from Europe, the Middle East, and elsewhere in Asia. Any genetic diversity in modern Asian dogs, he says, may simply be a result of all of these far-flung animals mating. "It would be like concluding that humans arose in the United States because there's so much genetic diversity here."

Instead, Wayne focuses more on ancient DNA, hoping to peer back to a time when dog populations were relatively isolated from one another. In 2013, he and his colleagues published the most extensive analysis of ancient dog and wolf genomes to date. Comparing the DNA of 18 dog- and wolflike bones from Eurasia and America to that of modern dogs and wolves from around the world, the study found that the DNA of ancient dogs most closely matched that of European wolves, and the DNA of today's dogs most closely matched that of ancient wolves.

That led the group to conclude that dogs evolved from a now-extinct group of wolves in Europe, somewhere between 19,000 and 32,000 years ago. These early dogs may have resembled Siberian huskies on steroids—their hunting prowess and ability to carry heavy loads a boon to ice age humans as they pursued mammoths and other large game across a frigid continent.

Savolainen pounced on the study, calling it "geographically biased" in a 2013 story in *The New York Times*, because Wayne's group hadn't used any samples from Southeast Asia. "It's like studying the geographical origins of humans without including a single sample from Africa," he says. Wayne shot back, saying he hadn't included ancient specimens from China because there were none—a fact, he said, that cast further doubt on the view that dogs had originated there. "I think we've reached an impasse," Wayne says. "We don't interact much."

Gregor Larson holds a wolf skull at the Oxford Museum of Natural History (*top*). Arden Hulme-Beaman (*bottom*) examines an ancient dog jawbone (*middle*).

PHOTOS: © JOHN CAIRNS (3); (PREVIOUS PAGE) © KAZUYOSHI NOMACHI/CORBIS

Geneticists aren't the only ones brawling. In 2009, paleontologist Mietje Germonpré reported finding an unusual skull in the archives of her museum, the Royal Belgian Institute of Natural Sciences in Brussels. Though the scientist who had originally unearthed the skull from Goyet Cave in southern Belgium pegged it as a wolf cranium, Germonpré's measurements indicated that it belonged to a dog. Radiocarbon dating revealed that the skull was 32,000 years old—so much older than other ancient dog remains known at the time that it could have finally stamped a time and place on canine beginnings.

Critics chomped, calling Germonpré's analysis "premature" and "misleading." They said the specimen, like some other ancient putative dog skulls, could merely be a strange-looking wolf. Germonpré responded that the creature may have been an early dog that didn't give rise to today's canines—a primitive attempt at domestication that hit a dead end. "It's a very combative field," she sighs. "More than any other subject in prehistory."

ENTER GREGER LARSON and Keith Dobney. The two had met in the early 1990s in Turkmenistan, where Dobney and a large group of other British archaeologists were excavating an early farming village. Larson—fresh out of college in California—showed up unannounced, wearing a baseball cap and loafers. The archaeologists, in their floppy hats and scruffy trousers, "thought he was just another preppy American," Dobney says. Yet Larson quickly impressed the scientists, asking a volley of incisive questions about their work. "It was a bit irritating, but his enthusiasm was infectious," Dobney says. Within a few days, Larson was shotgunning beers with his new pals.

The two began working together a few years later when Larson was a Ph.D. student at the University of Oxford and Dobney was back at the University of Aberdeen, both in the United Kingdom. Both were interested in the domestication of the pig—an animal that, like the dog, had played a crucial role in early human history but whose origins were murky. Their initial work, based on modern DNA, suggested that humans had independently domesticated wild boar in several locations. But when they combined ancient DNA with a relatively new technique known as geometric morphometrics—which involves taking thousands of measurements of bones to see how their shapes differ between individuals—they discovered that a long history of trading and interbreeding had created the impression of numerous domestication events when there were likely only one or two.



A gray wolf.

How the wolf became the dog By David Grimm

Scientists who study canine origins seem to fight about everything: where dogs arose, when this happened, and even the best way to find these answers. But there's one thing most of them agree on: *how* dogs became domesticated. Still, it's taken almost a century to get here, and the details are still emerging.

In 1907, the English scientist Francis Galton suggested that dogs first entered our lives when our ancestors nabbed some wolf pups, brought them back to camp, and raised them as pets. If you've ever seen a baby wolf, with its big eyes and oversized ears, the idea doesn't seem so far-fetched—and, indeed, Galton's hypothesis reigned for decades. But scientists eventually realized that domestication is a long, messy process that can take hundreds or even thousands of years. These early humans may have started with a cute pup, but they would have ended up with a wild animal.

So what did happen? Most experts now think dogs domesticated themselves. Early humans left piles of discarded carcasses at the edges of their campsites—a veritable feast, the thinking goes, for wolves that dared get close to people. Those wolves survived longer and produced more pups—a process that, generation by generation, yielded ever-bolder animals, until finally a wolf was eating out of a person's hand. Once our ancestors realized the utility of these animals, they initiated a second, more active phase of domestication, breeding early canines to be better hunters, herders, and guardians.

A massive collaboration that's trying to figure out where and when dogs emerged (see main story, p. 274) has found some intriguing insights into the second phase of dog domestication. A comparison of thousands of ancient dog and wolf skeletons, for example, has revealed flattening of the dorsal tips of ancient dog vertebrae, suggesting that the animals hauled heavy packs on their backs. The team has also spotted missing pairs of molars near the rear of the jaw in ancient dogs, which may indicate that the animals wore some sort of bridle to pull carts. These services, in addition to dogs' hunting prowess, may have proved critical for human survival, potentially allowing modern humans to outcompete our Neandertal rivals and even eventually settle down and become farmers.

Now, a study on page 333 helps explain how man and dog took the next step to become best friends. Takefumi Kikusui, an animal behaviorist at Azabu University in Sagamihara, Japan, and his colleagues have found that when dogs and humans gaze into each other's eyes, both experience a rise in oxytocin—a hormone that has been linked to trust and maternal bonding. The same rise in oxytocin occurs when human mothers and infants stare at each other, suggesting that early dogs may have hijacked this response to better bond with their new human family.

The oxytocin study and the skeletal data from the new collaboration go beyond clarifying the origin of the family pet, says collaboration leader Greger Larson, an evolutionary biologist at the University of Oxford in the United Kingdom. "The more that we know about the process of how dogs became associated with people, the more we learn about the origins of civilization." ■

A dog skull sits on a disk, as scientists prepare to photograph it for geometric morphometrics.



“When all these dog papers started coming out, we got really frustrated,” says Larson, now an evolutionary biologist at Oxford. “We felt we had done more with pigs.” He thought that Wayne hadn’t accurately distinguished between ancient wolf and dog bones and that his samples were too geographically limited. Yet he also faulted Savolainen for trying to use modern DNA as a window into the past. “It’s like a giant tomato soup with just one color,” he says. “You can’t go back and figure out what the ingredients are.”

Larson and Dobney wanted to take a lesson from their pig work—analyzing as many samples as possible from as many places as possible and combining ancient DNA analysis with geometric morphometrics. But in order to do this, they were going to have to bring everyone together.

Money proved a great motivator. Though dogs loom large in the public consciousness, they don’t tend to loosen the purse strings of funding organizations. As a result, many scientists work on them as only a hobby or side project, piggybacking on funding from other grants. But Larson and Dobney made a strong case to European funding agencies in 2012, arguing that the domestication of dogs set the stage for taming an entire host of plants and animals. “We said, without dogs

you don’t have any other domestication,” Larson says. “You don’t have civilization.”

The approach worked. The duo secured \$3 million and began calling people up. “We told them, ‘We’re going to do this. We have the finances. We want you on board,’” Larson says. His personality helped. “Everybody likes him,” Dobney says. “People don’t

see him as a rival.” Larson also took ego out of the equation. “I told everyone, ‘I don’t give a shit where I am as an author on these papers—I just want to get them out.’”

By the end of 2013, Larson and Dobney had attracted 15 collaborators, including Wayne, Savolainen, and Germonpré. In a 2-day conference in December, they ham-

mered out the details of the project. “You could feel the tension in the room,” Dobney recalls. But Larson soothed the small crowd. “Everything is water under the bridge,” he told them. “We all have a stake in this.”

Savolainen was intrigued by the opportunity to delve into new data sets. “There’s always more to learn,” he says. And Wayne was excited to analyze more samples. “Greger won the trust and confidence of a lot of people,” he says. “That’s a real skill.” Now, they just had to get their hands on thousands of bones.

BACK AT OHIO STATE, Hulme-Beaman is drilling into a second dog molar, but this time he seems nervous. The tooth has a hairline crack, and he’s worried it will fracture or explode: precious DNA lost in the dust, an irreplaceable museum specimen destroyed. But he gets lucky; the root saws clean off, and the rest of the molar remains intact. Hulme-Beaman plugs

Wolf versus dog

Traditionally, researchers used the traits below to distinguish wolves from dogs, but geometric morphometrics may reveal new nuances.

Dogs have a relatively shorter snout.

Canines are generally smaller, finer in dogs.

The wolf snout slopes down gently, whereas the dog snout has a kink in front of the eyes.

Wolf teeth tend to be less crowded.

Dog



Wolf



the tooth back into its mandible and slots the root into a tiny Ziploc bag, where it will be shipped to the United Kingdom for genetic analysis. “That’s about as good as it can go,” he exhales.

The postdoc has made 11 trips as one of the dog collaboration’s two main sample hunters, traveling from his home base at the University of Aberdeen to other universities, museums, and even private collections. “I’m on a plane or train every 2 to 3 weeks,” he says. He’s probed wolf skulls in Serbia, cradled dog bones in Sweden, and scoured the archives of the Smithsonian Institution in Washington, D.C. Most of the destinations come from scanning the scientific literature, talking to experts, and putting up posters at professional and amateur archaeology conferences. “There’s a huge amount that’s hidden in desk drawers,” he says.

Hulme-Beaman is at Ohio State because of a call Larson received from Paul Sciulli, a retired physical anthropologist who heard about the collaboration. He told Larson he had access to a bunch of ancient Native American dogs, some of which he had dug up himself in unexpected places. “There are sites where you find nothing,” says Sciulli, who has swung by to check on Hulme-Beaman’s progress. “No houses, no signs of village life. Just graves. And it’s just people and dogs.” Most of the dogs were about the size of beagles, and some were buried with their owners, one under a person’s arm. “These weren’t wild animals,” he says. “They were part of the family.”

Sciulli watches as Hulme-Beaman moves on to another specimen, gingerly removing a yellow-brown cranium the size of a pineapple from a plastic bag. He places the sample on a record-size disk, beneath a camera attached to a jointed mechanical arm. Then he slowly rotates the disk, snapping a picture every 2 seconds as the images appear on a nearby laptop. “We’re tricking the computer into thinking that we’re walking around the object,” he explains. By the time the disk has done a 360, he has taken more



The skeletons of a human and dog (upper left) discovered underneath a 12,000-year-old home in northern Israel are early evidence of the human-canine bond.

than 200 shots, and a three-dimensional rendering of the skull pops up on the screen, rotating to expose every nook and cranny—a carbon copy cranium Hulme-Beaman can bring anywhere.

The computer can now do something no archaeologist can: perform geometric morphometric analysis of the skull. The thousands of measurements it will take will go far beyond mere length and width to determine actual shapes: the precise circles of eye sockets, the jut and jag of every tooth. Ancient DNA, Hulme-Beaman says, can tell you where an animal came from, but only such morphometric data can show you domestication in progress—the sharper angling of the snout, for example, that took place as wolves morphed into dogs.

“For the first time, we’re going to be able to look at some of these strange skulls like the Goyet skull and figure out how strange they really are,” he says. “Are they wolves

becoming dogs, or are they just unusual wolves?” Combining the two approaches, he says, should allow the collaboration to home in on just where dogs came from—and when this happened.

“Archaeology is storytelling,” Hulme-Beaman says. “I think we’re going to be able to tell a great story.”

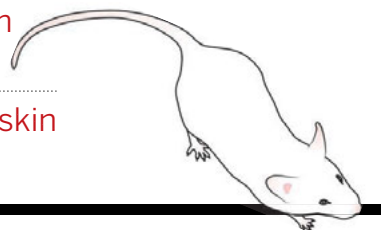
AT THE END OF THE DAY, Hulme-Beaman packs up his laptop and samples and prepares for his next trip, likely to Istanbul. Sciulli suggests a detour, mentioning a museum in Cleveland that has “hundreds of bones” from a local site; he says he can put the curator in touch. Hulme-Beaman looks tired, but he smiles. “Sure,” he says, “give me his number.”

A continent away, Larson and Dobney have continued to make phone calls. Their collaboration has now swelled to 50 scientists from around the world—experts on dogs, domestication, zooarchaeology, and genetics. Larson estimates that the team has analyzed more than 3000 wolf, dog, and mystery specimens so far, and he expects the group to submit its first paper this summer. “I’ve been really encouraged by how everyone has been getting

along,” he says. “We have a lot more in common than we thought.”

Larson feels confident that the work will solve the mystery of dog domestication once and for all, though some experts aren’t so sure. Just throwing a lot of data at an enigma won’t necessarily unravel it, warns Richard Meadow, the director of the zooarchaeology laboratory at Harvard University’s Peabody Museum. “The more samples you get, the more complicated things get.” And Hulme-Beaman points out that even if there is an answer, it’s likely to disgruntle some of the collaborators.

Still, the formerly warring camps seem sanguine. “I’m willing to accept a different result,” Savolainen says. “If I’m wrong, it will be a bit embarrassing,” he laughs, “but science is about trying to find the truth.” Wayne agrees. “Even if what we find contradicts my hypothesis, I’d be very happy,” he says. “I just want an answer.” ■



PERSPECTIVES



Look into my eyes. Changes in oxytocin concentration in a dog might elicit similar changes in a human and vice versa.

EVOLUTION

Dogs hijack the human bonding pathway

Oxytocin facilitates social connections between humans and dogs

By **Evan L. MacLean**^{1,2} and **Brian Hare**^{1,2,3}

Tens of thousands of years ago, a wolf-like predator gave rise to a more docile lineage, which soon became our trusted fireside companions (1). How did dogs become so embedded in human societies? Why do we feel genuine friendship, love, and social attachment in our relationships with dogs? On page 333 in this issue, Nagasawa *et al.* (2) reveal a powerful mechanism through

which dogs win our hearts—and we win theirs in return.

Until recently, most research on human social and cognitive evolution concentrated on our closest primate relatives. Meanwhile, sitting at our feet was a remarkable case of evolutionary convergence. Inspired by developmental psychologists studying human infants, comparative psychologists began studying family dogs. It quickly became apparent that dogs have much more to tell us about cognition, and ourselves,

than many might have imagined (3). This is particularly true when it comes to how dogs understand the social world. Even as puppies, dogs spontaneously respond to cooperative human gestures, such as pointing cues, to find hidden food or toy rewards. By contrast, great apes must have extensive experience with people to show similar skills (4). This use of social cues extends to a wide range of social gestures, including gaze direction and even the use of arbitrary communicative markers. Such

abilities provide humans with a social foundation for word learning, another area in which dogs have been surprisingly adept (5). Incredibly, dogs' attention to social information leads not only to skillful problem solving, but also to the same socially mediated errors that young children make. For example, both dogs and children are likely to interpret eye contact as communicative, even in contexts when it is not (6). Thus, dogs exhibit many of the same cognitive flexibilities and biases that characterize our own species.

The domestication hypothesis suggests that humanlike tendencies in dogs are the result of selection for easygoing temperaments, which allowed dogs to interact with humans much like conspecific partners (7). Direct comparisons with wolves show that like great apes, but unlike dog puppies, wolves are only skilled with human gestures when heavily socialized. Unlike dogs, wolves—who do not expect humans to be cooperative social partners—do not look to humans for help when faced with an unsolvable problem (8). Wolves also ignore the ostensive social cues that lead human infants and dogs to make predictable errors in certain cognitive tasks (6). Therefore, the evidence to date suggests that the set of unusual traits found in dogs is not simply inherited from wolves.

If dog psychology was shaped by domestication, what biological mechanisms were affected? How do these mechanisms make possible an interspecies relationship that is surprisingly successful from an evolutionary perspective? The neuropeptide oxytocin has long been known for its role in affiliative social behavior, and the formation of bonds between members of a species. But can oxytocin facilitate social relationships between species? Comparisons of humans and dogs before and after they interact with each other have revealed notable increases in circulating oxytocin, as well as endorphins, dopamine, and prolactin, in both species (9). In addition, exogenous administration of oxytocin causes dogs to initiate more social contact with other dogs and humans (10), and allows dogs to tune into human social cues even more faithfully (11). These findings suggest not only an interspecies effect of oxytocin, but also the exciting possibility of a feedback loop—that is, shifts in oxytocin concentration in a dog might elicit similar changes in a human and vice versa—just as is seen when a mother bonds with her infant.

Nagasawa *et al.* report the strongest test yet of the idea that humans and dogs are locked in an oxytocin feedback loop that is mediated in part through mutual gaze—sustained eye contact between human and dog (see the figure). The authors observed 30 dog owners (24 female, 6 male) interacting with their dogs (15 females and 15 males of varying breeds and ages) and measured changes in both the dogs' and owners' urinary oxytocin concentrations before and after the two interacted. In previous work, the authors found that owners who report the highest relationship satisfaction with their

“Why do we feel genuine friendship, love, and social attachment...with dogs?”

dogs also have dogs who maintain mutual gaze with them the most (12). Nagasawa *et al.* demonstrated that dog owners whose dogs gazed at them the most had the largest change in urinary oxytocin after interacting with their canine companions (2, 12). Their dogs, in return, experienced a similar oxytocin increase, the magnitude of which correlated with that of the owner. When they carried out a similar experiment with wolves, there was no evidence of this type of relationship, even though the wolves were tested with the people who had raised them as pups.

But is there a causal relationship between mutual gazing and oxytocin release? Nagasawa *et al.* administered oxytocin to a new group of dogs before they interacted with their owners. Not only did the authors see an increase in the extent of mutual gaze between owners and dogs, but they also detected an increase in oxytocin in the dog owners as a result. Oxytocin administered to dogs increased oxytocin concentration in their owners through increased mutual gaze—however, this effect occurred only with female dogs. Collectively these findings mirror studies demonstrating that oxytocin administration to human parents can have parallel effects in their infants, as a result of increased affiliative parental behavior (13).

Evolution is notoriously thrifty, often recycling old mechanisms for new purposes. Nagasawa *et al.*'s findings suggest that dogs have taken advantage of our parental sensitivities—using behaviors such as staring into our eyes—to generate feelings of social reward and caretaking behavior. Because these processes are bidirectional, dogs themselves likely experience similar rewards, ensuring that the feedback loop

is propagated. From an evolutionary perspective, the challenge for dogs may simply have been to express a behavioral (and morphological) repertoire that mimicked the cues that elicit caregiving toward our own young. Indeed, these juvenile characteristics of dogs are known to carry a selective advantage with respect to human preferences (14). Once dogs were capable of eliciting such responses in humans, interspecific bonds could be maintained through the feedback loop, which originally evolved to promote bonding between mother and child. Recent brain imaging studies have also demonstrated that when human mothers view images of their child or their dog, a common network of brain areas related to emotion, reward, and affiliation is activated (15). Thus, diverse aspects of our biology appear to be tuned into dogs and children in remarkably similar ways.

If they stand the test of time, the implications of these findings are far-reaching. In addition to providing clues about how dogs became a part of human history, the results also help to elucidate the proximate mechanisms through which our relationships with dogs may be salubrious. For example, the benefits of assistance dogs for individuals with autism or posttraumatic stress disorder—conditions for which oxytocin is currently being used as an experimental treatment—may arise partly through these social pathways. Thus, an important future challenge will be to probe the extent to which these findings generalize to diverse populations. In the meantime, Nagasawa *et al.* have provided more evidence that when your dog is staring at you, she may not just be after your sandwich. ■

REFERENCES

1. D. Grimm, *Science* **348**, 274 (2015).
2. M. Nagasawa *et al.*, *Science* **348**, 333 (2015).
3. B. Hare, V. Woods, *The Genius of Dogs: How Dogs Are Smarter Than You Think* (Dutton Adult, New York, 2013).
4. B. Hare, M. Brown, C. Williamson, M. Tomasello, *Science* **298**, 1634 (2002).
5. J. Kaminski, J. Call, J. Fischer, *Science* **304**, 1682 (2004).
6. J. Topál, G. Gergely, A. Erdohegyi, G. Csibra, A. Miklósi, *Science* **325**, 1269 (2009).
7. B. Hare, M. Tomasello, *Trends Cogn. Sci.* **9**, 439 (2005).
8. A. Miklósi, E. Kubinyi, J. Topál, M. Gácsi, Virányi, V. Csányi, *Curr. Biol.* **13**, 763 (2003).
9. J. S. Ondaal, R. A. Meintjes, *Vet. J.* **165**, 296 (2003).
10. T. Romero, M. Nagasawa, K. Mogi, T. Hasegawa, T. Kikusui, *Proc. Natl. Acad. Sci. U.S.A.* **111**, 9085 (2014).
11. J. Oliva, J.-L. Rault, B. Appleton, A. Lill, *Anim. Cogn.* **10.1007/s10071-015-0843-7** (2015).
12. M. Nagasawa, T. Kikusui, T. Onaka, M. Ohta, *Horm. Behav.* **55**, 434 (2009).
13. O. Weisman, O. Zagoory-Sharon, R. Feldman, *Biol. Psychiatry* **72**, 982 (2012).
14. B.M. Waller, K. Peirce, C.C. Caeiro, L. Scheider, A.M. Burrows, S. McCune, J. Kaminski, *PLOS ONE* **8**, e82686 (2013).
15. L. E. Stoeckel, L. S. Palley, R. L. Gollub, S. M. Niemi, A. E. Evans, *PLOS ONE* **9**, e107205 (2014).

¹Duke Canine Cognition Center, Duke University, Durham, NC, USA. ²Department of Evolutionary Anthropology, Duke University, Durham, NC, USA. ³Center for Cognitive Neuroscience, Duke University, Durham, NC, USA. E-mail: b.hare@duke.edu

INFECTIOUS DISEASE

Combating emerging viral threats

Broad-spectrum antiviral drugs are under development to treat emerging viral diseases such as Ebola and dengue for which no specific, licensed treatments exist

By Elena Bekerman and Shirit Einav

Although hundreds of viruses are known to cause human disease, antiviral therapies are approved for fewer than 10. Most approved antiviral drugs target viral enzymes, most commonly proteases and polymerases. Such direct acting antivirals (DAAs) have shown considerable success in the treatment of HIV and hepatitis C virus (HCV) infections. However, this approach does not scale easily and is limited particularly with respect to emerging and reemerging viruses against which no vaccines or antiviral therapies are approved.

A major limitation of the commonly developed DAAs is their narrow spectrum of coverage. Given an average cost of over 2 billion dollars and an 8- to 12-year timeline to develop a new drug (1), targeting viruses individually makes drug development expensive and slow. Moreover, given the unpredictable nature of virus emergence, this approach cannot provide adequate global health protection and national security preparedness. Finally, resistance to conventional DAA monotherapy typically emerges rapidly.

Emerging and reemerging pathogens for which no specific, licensed treatments exist include the flavivirus dengue, estimated to infect 400 million people annually; the coronaviruses SARS-CoV and MERS-CoV, associated with outbreaks of severe acute respiratory syndrome in 2002 and Middle East respiratory syndrome in 2012, respectively; and the filovirus Ebola, responsible for the current large-scale epidemic in Africa. There is an urgent need for novel drugs against these and many other viral diseases. This need is unlikely to be met solely by the prevailing drug-development approach.

Broad-spectrum drugs can play a role in addressing this need (see the figure). They drastically reduce the time and cost associated with the early stages of drug development per approved indication and diminish the clinical risks in the more ad-

“Repurposing approved drugs that target host functions required by several viruses is a cost- and time-effective route to broad-spectrum antivirals.”

vanced phases. Off-label use of approved broad-spectrum antivirals against new viral indications can provide further economic incentives as well as facilitate readiness for future outbreaks of emerging pathogens. A broad-spectrum therapeutic could also be administered before a viral threat has been accurately diagnosed, increasing likelihood of viral control.

The concept of broad-spectrum antivirals was first introduced in the 1970s with the discovery of ribavirin, which inhibits viral RNA or DNA synthesis as one of its mechanisms of action. Ribavirin was reported to benefit the resolution of many emerging viral infections preclinically (2) but yielded marginal to no benefit in the clinic. In the U.S., ribavirin is commonly administered together with DAAs or the soluble immune factor interferon for HCV treatment. Although interferon is active against most vertebrate-infecting viruses (3), it has shown partial success rates in the clinic, requires intramuscular injections, has serious side effects, and is expensive.

More promising, next-generation nucleotide and nucleoside analogs have been recently developed. For example, the synthetic adenosine analog BCX4430 inhibits replication of more than 20 RNA viruses in nine families, including coronaviruses and flaviviruses, both in vitro and in animal models (4). It protects nonhuman primates from filovirus disease and has a favorable preliminary preclinical safety profile. T-705 (favipiravir), another nucleoside analog, also has in vitro and in vivo efficacy against several RNA viral families (5). Human trials for the treatment of both influenza and Ebola with T-705 are ongoing. CMX001 (brincidofovir), a

lipid conjugate of the nucleotide analog cidofovir, shows in vitro activity against multiple DNA viruses, including herpesviruses and papillomavirus (6). It has a favorable pharmacokinetic profile and has advanced to phase III trials. However, because of the extensive sequence and structural diversity of virally encoded proteins, design of broad-spectrum DAAs is seldom feasible. Thus far, only one class of molecules, nucleoside inhibitors, has shown promise in the clinic.

A different broad-spectrum antiviral strategy is to target the host (see the figure). Host proteins or pathways required by multiple viruses are attractive targets for broad-spectrum antivirals, with an often added benefit of a higher genetic barrier to resistance. The most clinically advanced representatives of this class are the cyclophilin A inhibitors DEB025 (alisporivir) and SCY-635 (7). These compounds act in a multifaceted way that includes impairing protein folding and augmenting innate immune responses. They inhibit a diverse group of RNA and DNA viruses, including HCV, dengue virus, HIV, influenza, and SARS-CoV, both in vitro and in animal models, and have shown promise as anti-HCV drugs in phase II/III trials.

Endoplasmic reticulum α -glucosidase is another host protein that serves as a broad-spectrum antiviral target. Glycoproteins of many enveloped viruses depend on host glucosidases to achieve proper folding. Iminosugars, such as celgosivir, are competitive substrates for α -glucosidases with activity against multiple unrelated viruses both in tissue culture and in rodents (8). Little to no efficacy has been found thus far with celgosivir in clinical studies, but further investigation of glucosidase inhibitors is warranted.

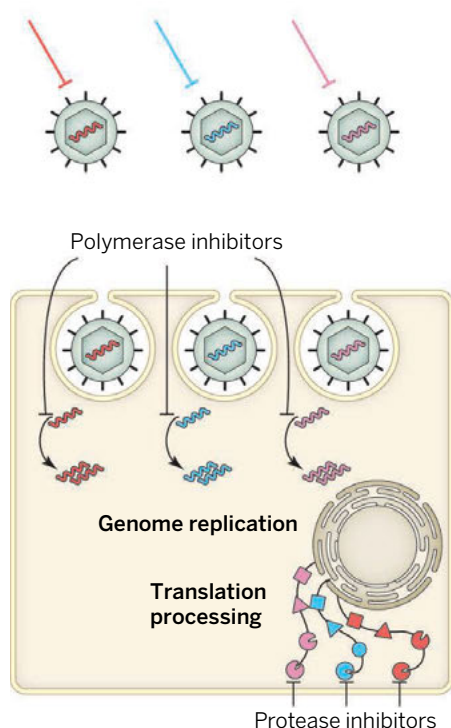
Repurposing approved drugs that target host functions required by several viruses is a cost- and time-effective route to broad-spectrum antivirals. One area of investigation targets host factors involved in regulating intracellular viral trafficking. For example, the host kinases cyclin G associated kinase (GAK) and AP2-associated protein kinase 1 (AAK1) regulate viral trafficking during entry,



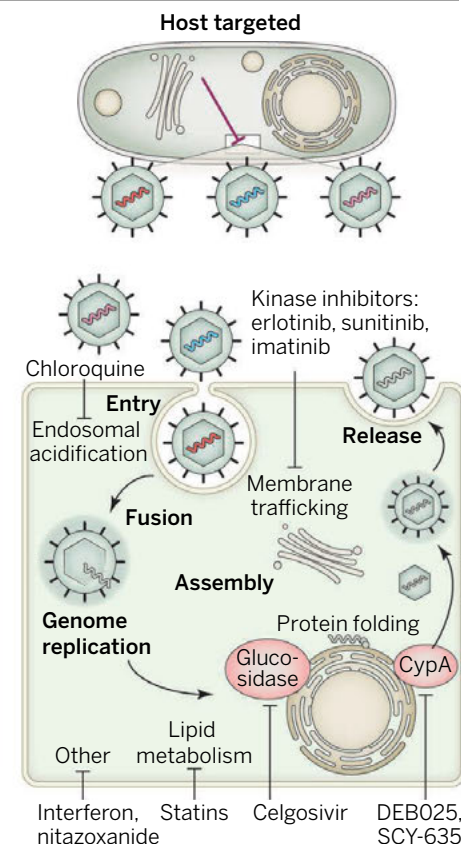
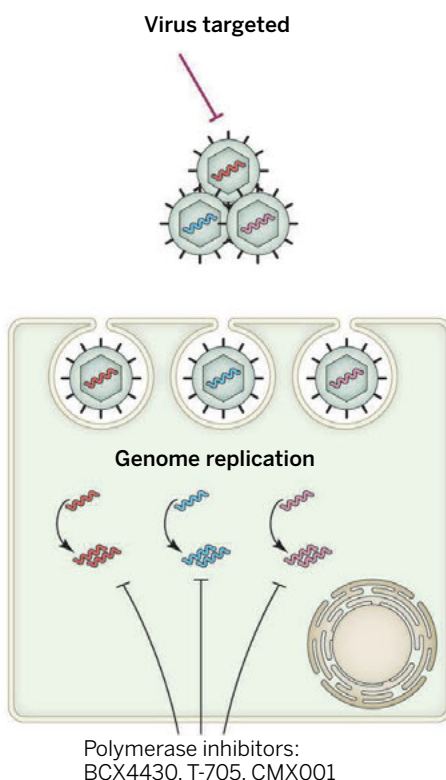
INFECTIOUS DISEASE SERIES

Department of Medicine, Division of Infectious Diseases and Geographic Medicine, and Department of Microbiology and Immunology, Stanford University School of Medicine, Stanford, CA, USA. E-mail: seinav@stanford.edu

"One drug, one bug"



"One drug, multiple bugs"



Toward broad-spectrum antivirals. Antiviral drugs that selectively inhibit unique viral proteins provide a "one drug, one bug" solution (left), whereas broad-spectrum drugs can restrict multiple viruses by inhibiting either common viral enzymatic functions or host factors commonly required by several viruses (right). Each panel depicts specific stages of the viral life cycle (bold) often targeted by the two classes of drugs. Examples of broad-spectrum compounds are connected to the corresponding targeted proteins or pathways by blunt arrows. CypA, cyclophilin A.

assembly, and release of unrelated viruses (9). The approved anticancer drugs erlotinib and sunitinib potently inhibit GAK and AAK1, respectively, and show in vitro activity against HCV, several flaviviruses, Ebola virus, and HIV (9). The combination of erlotinib and sunitinib protects mice from lethal dengue and Ebola virus challenges and is being advanced into clinical trials for dengue and Ebola. The kinase inhibitors dasatinib, imatinib, and nilotinib are additional approved anticancer drugs with broad antiviral activity (10, 11).

Another drug that may be repurposed is nitazoxanide, approved by the U.S. Food and Drug Administration (FDA) for the treatment of parasitic diarrhea. It inhibits replication of respiratory viruses, HIV, HCV, flaviviruses, and other viruses and has reduced the duration of flu symptoms

in clinical studies (12). Nitazoxanide blocks maturation of the influenza hemagglutinin, but the target remains unknown. Further approved drugs whose therapeutic potential against emerging viruses is being evaluated include chloroquine, an antimalarial agent (13), and cholesterol-lowering drugs, like statins (14).

Focusing on host functions is a useful expansion of potential antiviral drug targets, but this approach faces its own challenges. Cellular proteins function in a complex network of interactions, and a complete understanding of the drug's mechanism of action is often elusive. Moreover, the antiviral effect observed in vitro often cannot be reproduced in vivo. Toxicity is another major concern. Nevertheless, it may be feasible to identify a therapeutic window where the drug level is sufficient to inhibit viral replication with minimal cellular toxicity. Furthermore, shifting from an indication requiring long-term therapy (e.g., months to years for cancer) to a shorter duration sufficient to treat most acute viral infections can help limit toxicity. Emergence of resistance typical of DAA monotherapy can also complicate treatment with host-targeted approaches, as in the case of the chemokine receptor 5 (CCR5) antagonist maraviroc (15). Nevertheless, the time to resistance with other host-targeted approaches ap-

pears longer and the level of resistance lower than with DAAs, as exemplified by treatment with cyclophilin inhibitors (7).

Taken together, meeting the clinical needs presented by emerging viruses will best be achieved by a combinatorial approach that includes discovery of novel broadly acting DAAs and host-targeted therapies as well as repurposing of already approved drugs. ■

REFERENCES

1. Tufts Center for the Study of Drug Development. (2014). Cost to Develop and Win Marketing Approval for a New Drug Is \$2.6 Billion. http://csdd.tufts.edu/news/complete_story/pr_tufts_csdd_2014_cost_study.
2. E. Vela, *Viruses* **4**, 1802 (2012).
3. R. M. Friedman, *Br. J. Clin. Pharmacol.* **65**, 158 (2008).
4. T. K. Warren et al., *Nature* **508**, 402 (2014).
5. Y. Furuta et al., *Antiviral Res.* **100**, 446 (2013).
6. D. F. Florescu, M. A. Keck, *Expert Rev. Anti Infect. Ther.* **12**, 1171 (2014).
7. K. Lin, P. Gallay, *Antiviral Res.* **99**, 68 (2013).
8. J. Chang, T. M. Block, J. T. Guo, *Antiviral Res.* **99**, 251 (2013).
9. G. Neveu et al., *PLoS Pathog.* **8**, e1002845 (2012).
10. J. Dyall et al., *Antimicrob. Agents Chemother.* **58**, 4885 (2014).
11. M. Garcia et al., *Sci. Transl. Med.* **4**, 123ra24 (2012).
12. J. F. Rossignol, *Antiviral Res.* **110**, 94 (2014).
13. J. M. Rolain, P. Colson, D. Raoult, *Int. J. Antimicrob. Agents* **30**, 297 (2007).
14. S. Pollock et al., *Proc. Natl. Acad. Sci. U.S.A.* **107**, 17176 (2010).
15. A. A. Haqqani, J. C. Tilton, *Antiviral Res.* **98**, 158 (2013).

10.1126/science.aaa3778

DEVELOPMENTAL BIOLOGY

A scar is born: Origins of fibrotic skin tissue

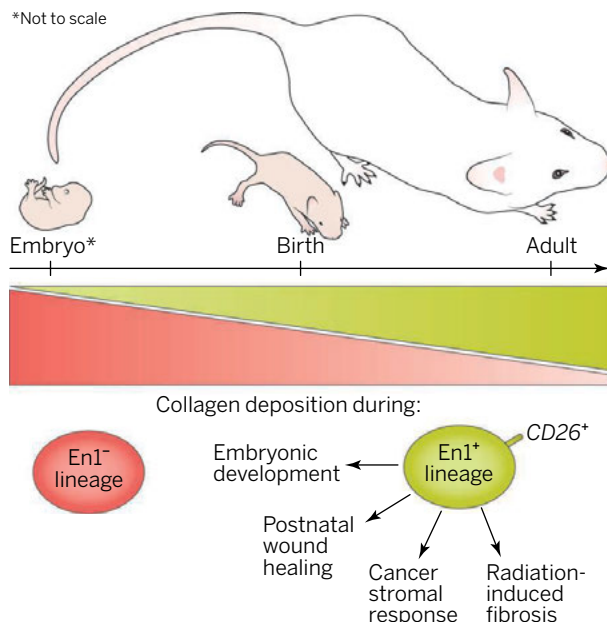
A fibroblast lineage is characterized by an inherent ability to form scar tissue in skin

By Rachel Sennett^{1,2} and Michael Rendl^{1,2,3}

Tissues rely on fibroblasts to produce and distribute extracellular matrix (ECM) proteins that provide crucial structure and organization for other resident cells. Although their presence is imperative to normal tissue morphogenesis and maintenance, these mesenchymal cells are frequently overlooked as “merely” ubiquitous supportive cells or uniformly vilified because of their role in aberrant connective tissue deposition that can occur during wound healing or reactive fibrosis. Consequently, the study by Rinkevich *et al.* on page 302 of this issue (1), teasing apart the embryonic origins, molecular profiles, and functional capacities of discrete fibroblast lineages within adult skin, turns a thought-provoking spotlight on these unassuming cells and paves the way for future studies with potentially important clinical implications.

Historically, skin fibroblast heterogeneity has been solely described in terms of localization within the skin; papillary fibroblasts sit close to the epidermis, the outer epithelial layer of skin, as opposed to reticular fibroblasts residing deeper in the dermis, both distinct from hair follicle-associated mesenchymal cells (2–4). Each region has largely been defined by morphology and/or localization of specific protein markers. By a relatively early stage of development, postnatal skin fibroblasts have already acquired a positional identity that they maintain after transplantation (5). In a break from tradition, the two main fibroblast populations identified by Rinkevich *et al.* are initially defined on the basis of their embryonic ancestry and are peppered throughout the entire dermis.

The authors found these cells by taking an inclusive inventory of mainly connective tissue cells in a preparation of digested dermis from mice, with a twist: All cells originating from *Engrailed1* (*En1*)-expressing progenitors had been permanently labeled by recombination-mediated activation of a green



Scar potential. A specific fibroblast lineage in dorsal skin increasingly populates skin with age and is responsible for extracellular matrix production in multiple developmental and pathophysiological scenarios.

fluorescent protein (GFP) reporter. *En1* is a homeobox transcription factor transiently expressed by cells of the central dermomyotome, a derivative of embryonic mesodermal segments or somites along the head-to-tail axis, and their progeny are known to contribute to the dorsal dermis in addition to other organs (6). Flow cytometry enabled Rinkevich *et al.* to account for and disregard hematopoietic, endothelial, and epithelial cells from their dermal preparations using a negative gating strategy also famously utilized in studies of hematopoietic stem cells (7) but not generally used for studies of heterogeneous skin cell populations. By weeding out cells that are not fibroblasts, the authors avoided preselecting for any fibroblast subset. Using single-cell and population-level gene analysis of freshly isolated cells, they determined that of the dermal cells remaining, both GFP-positive and -negative fractions are enriched for fibroblasts according to canonical marker expression.

Despite fundamental similarities between the two populations, the *En1*-lineage fate-mapped cells are distinguished by their unique expression of select genes and their proclivity to produce and deposit extra-cellular collagens during normal

skin development. More remarkably, when the authors challenged their two fibroblast lineages by engineering situations that call for ECM expansion, including wound healing (8), a melanoma-associated stromal response (9), or radiation-induced fibrosis (10), they observed collagen production exclusively from *En1*-derived cells. It therefore appears that this discrete lineage of fibroblasts carries fibrogenic potential, which the authors confirmed when they genetically ablated these cells and observed a significant decrease in connective tissue deposition during wound healing and tumor response.

Concurrently with investigating heterogeneity between dorsal skin fibro-

blasts, Rinkevich *et al.* explored separate lineages from oral and cranial skin that appear to function similarly in that they are primarily responsible for ECM deposition in their respective regions. Isolation and genome-wide expression analyses revealed distinctions among scar-forming oral, cranial, ventral, and dorsal fibroblasts that were mirrored by functional studies. For example, in local wound-healing assays, the authors observed that fibrogenic cells within the oral cavity respond by patterning connective tissue with appreciably less collagen than scars observed in dorsal skin. In cross-transplantation assays, in which dorsal fibroblasts work to heal oral wounds and vice versa, the authors noted that donor cells manufacture scars that are structurally faithful to their original location. These results are reminiscent of studies describing the “positional memory” of fibroblasts native to distinct adult and fetal tissues with defined gene expression profiles and functional capacity (11).

Although the findings of Rinkevich *et al.* are intriguing, perhaps equally exciting are the areas of future research they suggest. First, because ~70% of adult dermal fibroblasts are *En1*-derived, it is tempting

¹Black Family Stem Cell Institute, Icahn School of Medicine at Mount Sinai, New York, NY 10029, USA. ²Department of Developmental and Regenerative Biology, Icahn School of Medicine at Mount Sinai, New York, NY 10029, USA. ³Department of Dermatology, Icahn School of Medicine at Mount Sinai, New York, NY 10029, USA. E-mail: michael.rendl@mssm.edu

to speculate that such a broadly represented population contains further subsets of specialized fibroblasts. Furthermore, it is not entirely clear how this large population originates from a very small pool of precursors in skin at early embryonic time points, nor where other fibroblast-type, mesenchymal cell subsets fit into their lineage partition, such as hair follicle-associated dermal papilla and sheath cells and vascular smooth muscle cells. In addition, the results of this study focus primarily on the fibrogenic activity of En1-lineage-positive cells, leaving us to wonder about the origins and purpose of the lineage-negative cells that constitute at least 30% of adult skin fibroblasts.

Finally, the authors used a cell surface marker screen to identify *CD26/Dpp4* as a unique label for En1 fate-mapped fibrogenic fibroblasts in adult skin. Subsequent experiments revealed that prospectively isolated adult *CD26⁺* mesenchymal cells primarily contributed ECM components during wound-healing and tumor response assays. More intriguingly, the authors observed a slight but significant difference in fibrogenic gene expression between *CD26⁺* and *CD26⁻* fibroblasts that was greatly exacerbated by a wounding assay stimulus. Thus, although fibroblasts from separate lineages are intrinsically similar at baseline, they are unique in their individual transcriptional and functional responses to signals from within the greater milieu of the skin.

Not only is *CD26/Dpp4* useful for isolating or identifying fibrogenic cells in situ, but the discovery is also clinically relevant. *Dpp4* signaling itself appears to coordinate fibrogenic activity, and the authors could mitigate scar size during healing by applying a specific *Dpp4* inhibitor to wound sites. This discovery has far-reaching implications for drug development, provided the observation proves relevant to wound healing in human skin as well. Furthermore, the utility of *Dpp4* as a marker or druggable target might also be applicable to studying or treating fibrosis in organs outside of the skin. ■

REFERENCES

1. Y. Rinkevich *et al.*, *Science* **348**, aaa2151 (2015).
2. R. R. Driskell, F. M. Watt, *Trends Cell Biol.* **25**, 92 (2015).
3. R. Sennett, M. Rendi, *Semin. Cell Dev. Biol.* **23**, 917 (2012).
4. J. M. Sorrell, A. I. Caplan, *J. Cell Sci.* **117**, 667 (2004).
5. R. R. Driskell *et al.*, *Nature* **504**, 277 (2013).
6. R. Atit *et al.*, *Dev. Biol.* **296**, 164 (2006).
7. G. J. Spangrude *et al.*, *Science* **241**, 58 (1988).
8. S. Werner *et al.*, *J. Invest. Dermatol.* **127**, 998 (2007).
9. S. Madar *et al.*, *Trends Mol. Med.* **19**, 447 (2013).
10. B. O'Sullivan, W. Levin, *Semin. Radiat. Oncol.* **13**, 274 (2003).
11. H. Y. Chang *et al.*, *Proc. Natl. Acad. Sci. U.S.A.* **99**, 12877 (2002).

ACKNOWLEDGMENTS

R. S. was supported by NIH fellowship F30AR065847; M. R. by NIH grants R01AR059143; R01AR063151 and NYSM (C029574).

10.1126/science.aab0120

NEUROSCIENCE

Systemically treating spinal cord injury

A drug that crosses the blood-brain barrier has therapeutic potential for central nervous system trauma

By Amanda P. Tran and Jerry Silver

Spinal cord injury is a debilitating condition. Axons of nerve cells are severed, resulting in a range of deficits, including the loss of voluntary movements and sensation. Failure of axonal regeneration after such an injury may be partly explained by a decreased intrinsic capacity for neuron growth, especially at the lesion site (1). On page 347 in this issue, Ruschel *et al.* (2) show that this inhibition can be overcome with a small molecule that can be injected into the body cavity, cross the blood-brain barrier, and reach the central nervous system. The drug, epothilone B, stabilizes microtubules in extending axons, thereby promoting spinal cord regeneration.

Upon approaching the glial scar at the lesion site of the spinal cord, the tips of regenerating axons form swollen dystrophic growth cones (3). These were first described as “sterile clubs” by the neuroscientist and Nobel laureate Ramón y Cajal, who also believed that they persisted only briefly in a quiescent state before the axon “died back” to a sustaining collateral (now defined as a branch off the main axon that feeds back onto the neuron’s cell body) (4). By contrast, Ruschel *et al.* describe how dystrophic growth cones remain in the injured human spinal cord for a remarkable 42 years after injury. Advances in *in vivo* imaging have also revealed that, for a time, dystrophic growth cones are dynamic and can regenerate in a more accommodating environment (5). Moreover, dystrophic growth cones eventually form synaptic-like relationships with oligodendrocyte precursor cells in the lesion core, enabling them to persist for long periods (6, 7).

Electron micrographs of adult rats with spinal cord injury illustrated that dystrophic growth cones are bloated with disorganized microtubules arranged in nonparallel networks (8). To better understand the internal machinery of dystrophic growth cones and determine whether they are malleable, earlier studies assessed the effects of the anticancer drug paclitaxel (Taxol). Paclitaxel belongs to the taxane family of drugs that targets tubulin. It

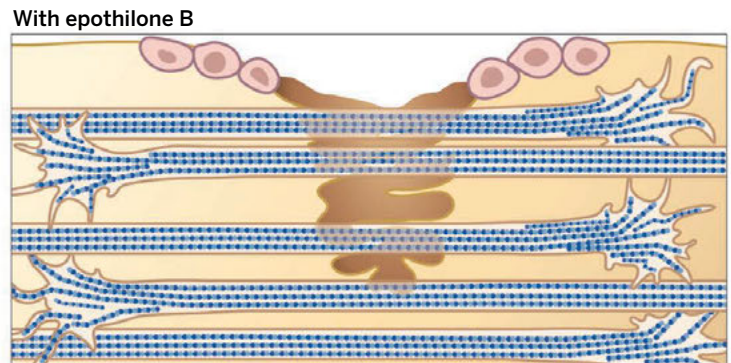
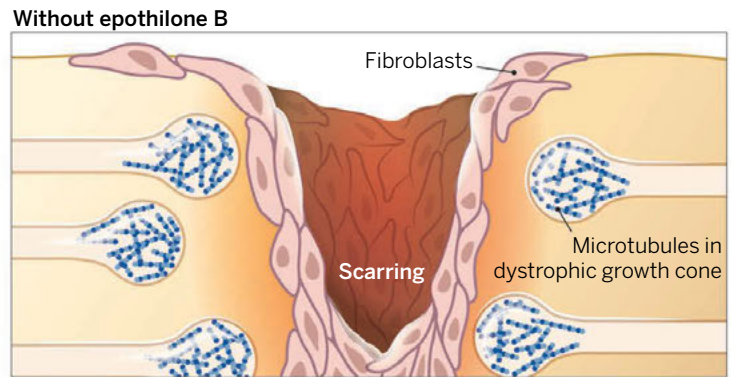
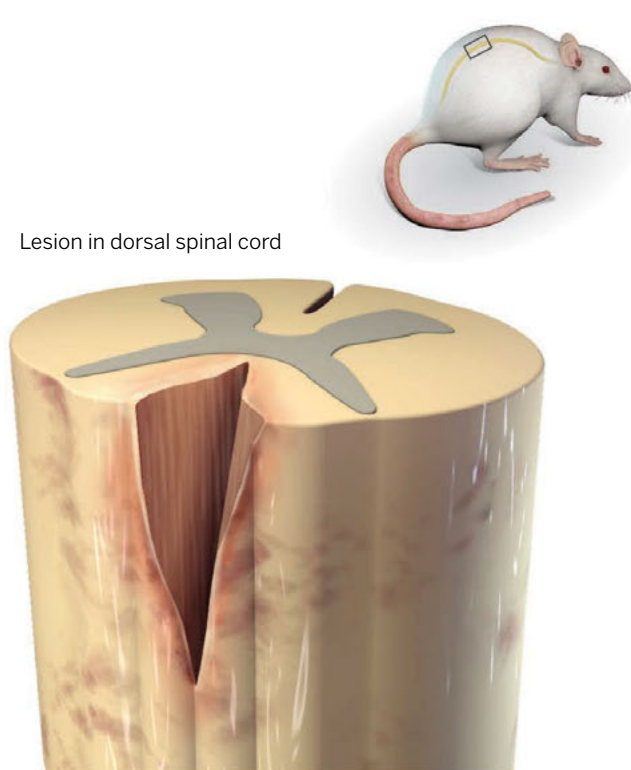
stabilizes microtubule polymers and protects them from disassembly. Suppression of microtubule dynamics thus interferes with cellular processes such as cell division and cell motility. Indeed, it was shown that caged Taxol (which could be activated in a restricted area) specifically stabilized the dystrophic growth cone microtubule cytoskeleton in cultured rat neurons, and that this was sufficient for axon forma-

“...there are currently no drugs approved...to treat this traumatic injury that allow for functional recovery.”

tion (9). This effect was reversed with nocodazole, a microtubule-destabilizing drug (8, 9). Intrathecal delivery (injection into the spinal fluid) of Taxol following a dorsal hemisection of the rat spinal cord also promoted microtubule stabilization, allowing increased axonal penetration through the glial scar (10). Taxol additionally decreased the ability of transforming growth factor- β 1 to adversely affect rearrangement of the cytoskeleton in astrocytes, which reduced scarring induced by spinal cord injury (10).

Using a more clinically relevant microtubule stabilization strategy as a putative spinal cord injury therapy, Ruschel *et al.* tested epothilone B in different rat models of spinal cord injury. Epothilone B also targets tubulin, but is a member of a different family of drugs. Unlike Taxol, it penetrates the blood-brain barrier, as seen through mass spectrometry analysis of rat spinal cord tissue after intraperitoneal delivery (injection into the body cavity). Ruschel *et al.* found that by stabilizing microtubules, epothilone B enhanced axon regeneration and ultimately improved sensorimotor function in an injured rat, boosting intrinsic axonal growth while reducing axon-inhibitory scarring after injury.

Department of Neurosciences, Case Western Reserve University, Cleveland, OH 44106, USA. E-mail: jxs10@case.edu



Dual acting drug. After spinal cord injury, dystrophic growth cones fill with disorganized microtubules and axons cannot extend. Fibroblasts migrate to the lesion and contribute to an environment that inhibits axon outgrowth. Systematically delivered epothilone B, which crosses the blood-brain barrier, stabilizes neuron microtubules and promotes axon extension through the injured site. It also hampers fibroblast migration and scar formation.

Fibroblasts proliferate after spinal cord injury and contribute to scarring (11). Ruschel *et al.* observed that epothilone B attenuated fibrotic scar formation in vivo and propose that the effect may be due to the drug's ability to decrease fibroblast migration. Fibroblasts surrounding the edge of the dorsal hemisection lesion displayed a rounder shape and an increase in stabilized tubulin when exposed to the drug. Why is the drug's effect on fibroblasts seemingly opposite from its effect on neurons? The authors propose the difference may be due to epothilone B's interactions with tau, a microtubule-associating protein enriched in neurons.

Even more impressive is the ability of epothilone B to drive axon outgrowth (in vitro) across classically inhibitory substrates such as Nogo-A, chondroitin sulfate proteoglycans, and semaphorin 3A (an effect that was abolished with nocodazole). Injection of epothilone B into the rat body cavity after dorsal column transection transformed dystrophic growth cones into regenerating axons that could more readily penetrate the scar compared to injured animals injected with a control. After spinal contusion injury, epothilone B treatment increased sprouting of neurons containing the neurotransmitter serotonin. Interestingly, the addition of a serotonin antagonist abrogated gains in sensorimotor function,

further substantiating the importance of this neuronal subtype in functional recovery after spinal cord injury (12). How serotonergic neurons respond to different treatments, including microtubule stabilization, and how they robustly sprout after injury remain pressing questions.

The value of epothilone B treatment after spinal cord injury lies in its ability to modulate both the inhibitory scar environment and the regenerating potential of neurons in a noninvasive manner (see the figure). The dual effects point to the potential of combinatorial strategies to target more than one underlying problem of a given condition, such as spinal cord injury. Moreover, systemically delivered drugs represent the next frontier of research in therapies for injuries of the central nervous system.

Aside from drugs that manage symptoms caused by spinal cord injury, there are currently no drugs approved by the U.S. Food and Drug Administration to treat this traumatic injury that allow for functional recovery. The systemic delivery of a drug such as epothilone B could therefore be a turning point in treatment. Additionally, one could combine this drug with intravenous delivery of synthetic platelets to stanch bleeding (13), and with an immune-modulating therapy to allow for neuroprotection, as bone marrow-derived activated macrophages

have been shown to cross the blood-brain barrier and inhibit axon regeneration (14). This systemic "cocktail" could further include a drug that enables neuronal growth cones to bypass inhibitory components of the extracellular matrix (15). In this way, the differing molecular challenges of recovering from spinal cord injury may be overcome, without the risk of exposing the spinal cord, to allow for meaningful regeneration and ultimately functional recovery from a devastating condition. ■

REFERENCES

1. J. M. Cregg *et al.*, *Exp. Neurol.* **253**, 197 (2014).
2. J. Ruschel *et al.*, *Science* **348**, 347 (2015).
3. C. E. Hill, M. S. Beattie, J. C. Bresnahan, *Exp. Neurol.* **171**, 153 (2001).
4. R. y Cajal, *Degeneration and Regeneration of the Nervous System*, R. M. May, Transl. (Oxford Univ. Press, London, 1928).
5. V. J. Tom, M. P. Steinmetz, J. H. Miller, C. M. Doller, J. Silver, *J. Neurosci.* **24**, 6531 (2004).
6. A. R. Filous *et al.*, *J. Neurosci.* **34**, 16369 (2014).
7. A. Di Maio *et al.*, *J. Neurosci.* **31**, 4569 (2011).
8. A. Ertürk, F. Hellal, J. Enes, F. Bradke, *J. Neurosci.* **27**, 9169 (2007).
9. H. Witte, D. Neukirchen, F. Bradke, *J. Cell Biol.* **180**, 619 (2008).
10. F. Hellal *et al.*, *Science* **331**, 928 (2011).
11. C. Göritz *et al.*, *Science* **333**, 238 (2011).
12. R. van den Brand *et al.*, *Science* **336**, 1182 (2012).
13. J. P. Bertram *et al.*, *Sci. Transl. Med.* **1**, 11ra22 (2009).
14. S. A. Buschet *et al.*, *J. Neurosci.* **31**, 944 (2011).
15. B. T. Lang *et al.*, *Nature* **518**, 404 (2015).

10.1126/science.aab1615

Nanoplasmonic sensing and detection

Enhanced optical fields in nanoplasmonic systems provide efficient sensing and detection

By Mark I. Stockman

Measuring minute amounts of chemical and biological objects in the environment and in living organisms is one of the most common and important tasks in chemistry, biology, medicine, environmental monitoring, transportation, homeland security, and defense. Although the existing methods of sensing and detection are numerous and powerful, they are not without shortcomings: insufficient sensitivity; long detection times; necessity for enzymatic, fluorescent, or radioactive labeling; high costs, and so on. Optical spectroscopic methods have the advantage of being fast, noncontact, and relatively inexpensive, but they are not necessarily sensitive enough.

Nanoplasmonics deals with optical phenomena localized at surfaces and interfaces of metals that are due to light-induced electronic excitations called surface plasmons (SPs). For a metal nanoparticle embedded in a dielectric, the SPs are oscillations of electric field and polarization localized in space. These are localized surface plasmons (LSPs), whose excitation frequencies depend mainly on the dielectric properties of the constituents and weakly depend on the system size. For extended systems, the SPs are electromagnetic waves, the so-called surface plasmon polaritons (SPPs), bound to the surfaces and interfaces and propagating along them (1, 2).

The SPs are oscillations of dielectric polarization, which create opposite surface charges at the nanoscale, whose attraction supplies the restoring force necessary for any oscillations. Objects to be detected (for example, analyte) bind to the surface carrying SPs. This binding can be made chemically and immunologically specific by using corresponding antibodies linked to the surface. The result is a change of the permittivity of the dielectric adjacent to this surface and, thus, an increase in the dielectric screening that then reduces the restoring force for plasmonic oscillations and, hence, reduction of the LSP resonant frequency and the SPP propagation velocity. High sensitivity of the SP sensing is due to the fact that

SPs are tightly localized at the surface and thus highly sensitive to its dielectric environment. The proximity of the object to be detected to the surface carrying SPs results in a shift in surface plasmon resonance peak—detectable with both high selectivity and high signal-to-noise ratio.

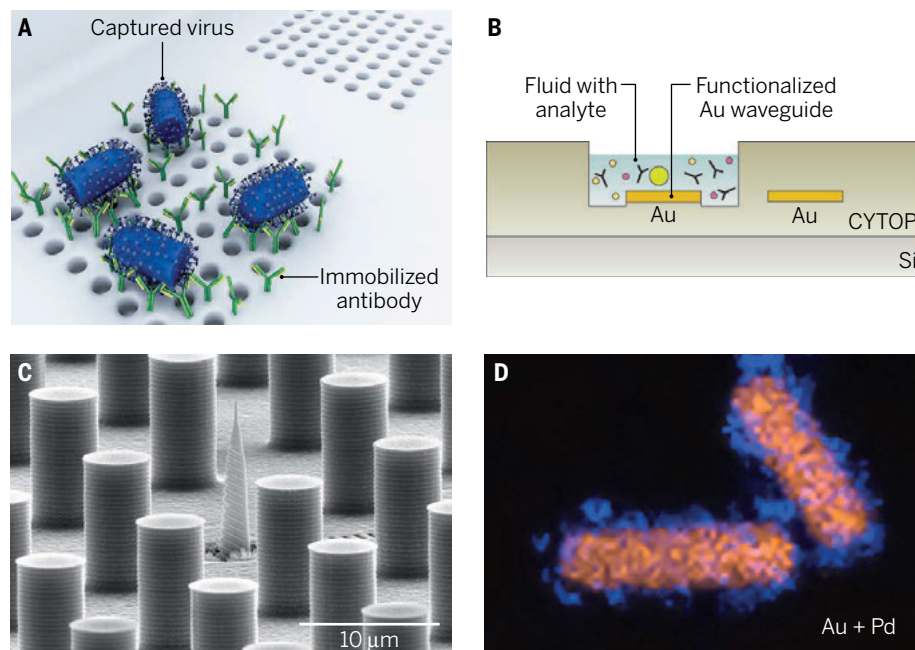
In biomedical research and applications, SPPs have been used for more than two decades (3, 4). However, a problem is that the SPPs on flat surfaces propagate too slowly to be directly excited by laser light. To resolve this problem, most SPP sensors are based on the so-called Kretschmann geometry (5), which requires precise adjustment of the incidence angle of the probing radiation.

The observation of extraordinary transmission through a periodic array of nanoholes (6) is a foundation of a novel plasmonic detection method (7) (see the figure, panel A). External radiation is incident normally on a periodic array of nanoholes in a plas-

monic metal (gold) nanofilm and excites SPPs when the period is a multiple of the SPP wavelength; these SPPs carry optical energy through the holes with a high efficiency. The surface of the holey array is functionalized by antibodies selectively binding to components (antigens) of the Ebola virus. The model virus in biologically relevant concentrations is delivered by microfluidics to the surface and binds to it, decreasing the SPP velocity. The measured resonant frequency shift is very pronounced, thus demonstrating detection of this highly contagious pathogen. Due to the absence of the moving parts, stability, and low weight, the corresponding device can be made handheld for field use.

In another example, detection of the Dengue fever antibodies (8) uses a SPP interferometer (see the figure, panel B). Although interferometric SPP sensing is already known (4), this approach represented a first study on real patients suffering from this

Capture and detection



Nanoplasmonic sensing and detection. Four nanoplasmonic detection experiments are presented. (A) Detection of Ebola-antigen-carrying virus [adapted from (7)]. (B) Detection of Dengue fever-specific antibodies from three actual patients [adapted from (8)]. (C) Detection of proteins and SERS identification of proteins in record-low femtomolar (10^{-15} mol/l) concentrations using adiabatic compression of surface plasmon polaritons and superhydrophobic delivery [adapted from (10)]. (D) Detection of hydrogen in the air in cycles of 10, 20, and 30 volume percent H_2 , using gold nanorod-palladium nanospheres sensor-assembled employing DNA-directed assembly [adapted from (12)].

Center for Nano-Optics (CeNO) and Department of Physics and Astronomy, Georgia State University, 29 Peachtree Center Avenue, Atlanta, GA 30302, USA. E-mail: mstockman@gsu.edu

highly contagious and potentially deadly disease. The detection of the marker of the infection (antibodies to the virus in the blood) is so reliable that the detection efficiency is an order of magnitude better than for a “gold-standard” enzyme-linked immunosorbent assay (ELISA) method that is widely used in research and clinic.

One of the serious limitations of ultrasensitive detection comes not from plasmonics but from kinetics of the binding to the surfaces: The concentration of analyte should be on the order of or greater than ~5 to 20 fmol/l (3, 9) for immunological reactions, which tends to make femtomolar to attomolar sensing and detection impossible. A novel

“...plasmonics provides the fundamental basis and practical device designs that allow for the rapid sensing and detection of a wide range of important chemical and biological objects...”

approach (see the figure, panel C) overcomes this kinetic barrier and allows precise nanofocusing of the analyte at the active sensing center (10). This is achieved by using superhydrophobic coating of the shown micropillars. Surface-enhanced Raman scattering (SERS) detection is performed using the effect of adiabatic concentration of SPPs (11): Light is converted to SPPs by the grating in the metal nanocone shown in the center of this panel. The SPPs propagate to the tip, concentrating and creating a hot spot of optical near-field at the tip, exciting SERS in the analyte delivered to the tip due to superhydrophobicity. The analyte, enzyme lysozyme, was delivered in a concentration of 1 fmol/l in a 160-nl drop, containing ~100 molecules overall. The subsequently detected Raman signature spectrum of lysozyme demonstrates a highly promising approach for ultrasensitive detection with chemical identification.

One of the most important issues in clean energy is hydrogen technology, where a critical and yet unsolved problem is rapid and sensitive enough detection of hydrogen leaks. A single nanoparticle sensing for such detection (12) (see the figure, panel D) uses a gold nanorod covered with palladium nanospheres. Palladium is known to absorb hydrogen from air, which changes its dielectric properties and shifts the frequency of the LSP resonance of the nanorod. Such measurable shifts allow one to reliably and reversibly

detect hydrogen in the air in concentrations relevant for hydrogen energy applications.

Plasmonic sensing of single proteins has been done with a hybrid photonic-plasmonic sensor consisting of a silica microsphere covered by a gold nanoshell (13). Here, the attachment of a single protein molecule to the nanoshell affects its plasmonic response and shifts the frequency of a whispering-gallery mode of the microsphere. More sensitive than the previous examples, such a shift affords the detection of single protein molecules.

A fundamentally novel principle, active plasmonic nanosensing, has recently been developed (14) based on spaser (plasmonic nanolaser) (15) as a metal nanoparticle surrounded by gain medium to generate coherent and intense local optical fields. The detection device consists of a nanoslab of semiconductor (CdS) separated by MgF_2 nanofilm from a silver surface. Optical pumping induces spasing on a mode localized mostly between the CdS and the silver surface. Exposure of such a spaser to 2 to 8 parts per billion concentration of vapor of explosive precursor dinitrotoluene causes an appreciable and reversible increase of the generated intensity—corresponding to one of the highest sensitivities of explosives sensors yet demonstrated. The examples discussed here demonstrate that plasmonics provides the fundamental basis and practical device designs that allow for the rapid sensing and detection of a wide range of important chemical and biological objects, such as hydrogen molecules, explosives vapors, protein molecules, and pathogenic viruses, and it can do so with unprecedented sensitivity and robustness. ■

REFERENCES AND NOTES

1. L. Novotny, B. Hecht, *Principles of Nano-Optics* (Cambridge Univ. Press, Cambridge, New York, 2012).
2. M. I. Stockman, *Opt. Express* **19**, 22029 (2011).
3. M. Malmqvist, *J. Mol. Recognit.* **7**, 1 (1994).
4. X. D. Hoa, A. G. Kirk, M. Tabrizian, *Biosens. Bioelectron.* **23**, 151 (2007).
5. M. I. Stockman, *Phys. Today* **64**, 39 (2011).
6. T. W. Ebbesen, H. J. Lezec, H. F. Ghaemi, T. Thio, P. A. Wolff, *Nature* **391**, 667 (1998).
7. A. A. Yanik *et al.*, *Nano Lett.* **10**, 4962 (2010).
8. W. R. Wong, O. Krupin, S. D. Sekaran, F. R. Mahamd Adikan, P. Berini, *Anal. Chem.* **86**, 1735 (2014).
9. K. Saha, F. Bender, E. Gizeli, *Anal. Chem.* **75**, 835 (2003).
10. F. De Angelis *et al.*, *Nat. Photonics* **5**, 682 (2011).
11. M. I. Stockman, *Phys. Rev. Lett.* **93**, 137404 (2004).
12. N. Li *et al.*, *Light-Sci. Appl.* **3**, e226 (2014).
13. V. R. Dantham *et al.*, *Nano Lett.* **13**, 3347 (2013).
14. R.-M. Ma, S. Ota, Y. Li, S. Yang, X. Zhang, *Nat. Nano* **9**, 600 (2014).
15. D. J. Bergman, M. I. Stockman, *Phys. Rev. Lett.* **90**, 027402 (2003).

ACKNOWLEDGMENTS

Funded by Grant No. DE-SC0007043 from the Materials Sciences and Engineering Division of the Office of the Basic Energy Sciences, Office of Science, U.S. Department of Energy.

STRUCTURAL BIOLOGY

Mitoribosome oddities

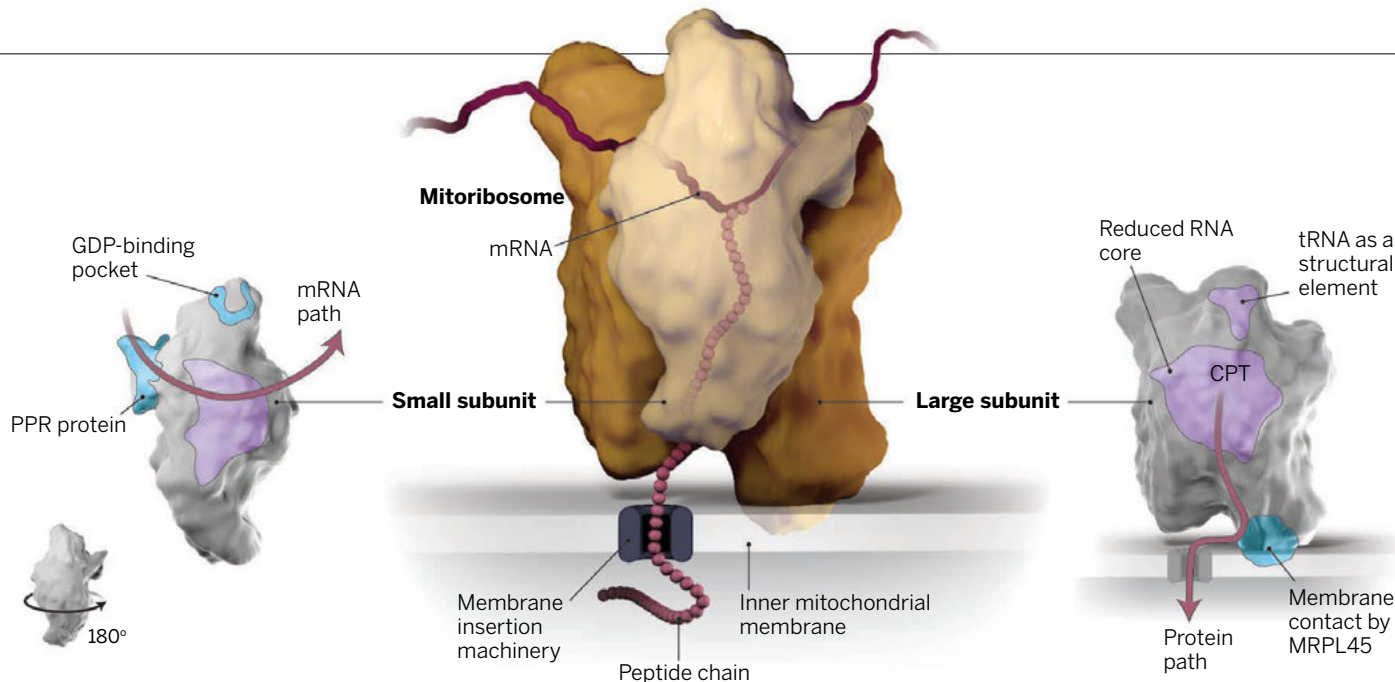
The mitochondrial ribosome has evolved structural differences from its cytosolic counterpart

By **Roland Beckmann¹**
and **Johannes M. Herrmann²**

Eukaryotic cells contain two separate translation machineries for protein synthesis—one in the cytosol and one in mitochondria. This situation is attributable to the evolutionary history of eukaryotic cells, which originate from a merger of two formerly independent cells—the host cell and the bacterial endosymbiont—with each contributing a full-fledged protein synthesis system. However, during the past 1.5 billion years, the two translation machineries have evolved very differently. That of the host cell, which acts in the cytosol, synthesizes almost all cellular proteins, including most mitochondrial proteins. By contrast, in mitochondria—the descendants of the bacterial endosymbionts—ribosomes (mitoribosomes) are now highly specialized for the synthesis of a very small number (13 in humans) of membrane proteins that function in energy production. It has been assumed that mitoribosomes are still similar to those of bacteria. Now, advances in high-resolution cryo-electron microscopy have allowed fascinating insights into the molecular structure of mitoribosomes, as reported by Greber *et al.* (1) on page 303 of this issue and by Amunts *et al.* (2). It is clear that the mitoribosome differs dramatically from the “canonical” cytosolic ribosome of bacteria and eukaryotes (see the figure).

Ribosomes are composed of RNAs (so-called rRNAs) and around 70 to 100 different proteins (depending on the species). They are ribozymes, meaning that the enzymatic activity is exhibited by a catalytic RNA rather than by a protein. This is also true for mitoribosomes; however, in animals the RNA content is considerably smaller than observed for cytosolic ribosomes and is restricted to the catalytic core of the particle (3). Instead, all mitoribosomes exhibit greatly increased protein content: In mammalian cells, they contain 36 proteins that do not have homologs in bacteria and that

10.1126/science.aaa6805



The mammalian mitochondrial ribosome. High-resolution cryo-electron microscopy (at 3.3 to 3.8 Å) reveals structural differences between the mammalian mitoribosome and the canonical mammalian and bacterial ribosomes in the cytosol. CPT, central protuberance.

cover almost the entire surface of the mitoribosome. In some instances, these proteins replace rRNA structures that were lost during evolution, but perhaps most of them serve to stabilize the RNA-poor structure and/or to protect the mitoribosome from oxidative damage.

Remodeling in the mitoribosome is particularly extreme in a part of the large subunit referred to as the central protuberance. In all ribosomes analyzed so far, this critical region is formed by a small structural rRNA molecule called the 5S rRNA. This element is absent in mammalian mitoribosomes, which contain, instead, a copy of the mitochondrial valine-encoding transfer RNA (tRNA) (4, 5). tRNAs are normally soluble adaptors that deliver amino acids for protein synthesis to the ribosome. Apparently, during mitochondrial evolution, one of these tRNAs gained a new function as a structural building block of the ribosome.

Ribosomes consist of two subcomplexes, the small and large subunits. The messenger RNA (mRNA), which contains genetic information, is threaded through a cavity at the interface of the two subunits and is translated into a protein sequence in repetitive reaction cycles that are driven by guanosine triphosphate (GTP)-hydrolyzing elongation

factors. The structures of the mammalian mitoribosome (human and porcine), as observed in the electron microscopy reconstructions of Amunts *et al.* and Greber *et al.*, respectively, suggest that the mechanical movements of the two subunits toward each other differ substantially from those in a “canonical” ribosome (1, 2). Moreover, a mitochondrion-specific intrinsic GTP-hydrolyzing protein, the function of which is unknown, is built into the mitoribosome at the subunit interface. Likewise unknown is the function of a pentatricopeptide repeat (PPR) protein at the mRNA entry site that presumably serves in mRNA binding. It is unknown how the mitoribosome recognizes mRNAs, and this newly identified PPR protein might represent a key element in this process.

Owing to their extreme specialization in the synthesis of only a few hydrophobic membrane proteins, mitoribosomes are tethered to the matrix side of the mitochondrial inner membrane (6). Membrane binding is achieved by mitochondrial ribosomal protein L45 [MRPL45; called Mba1 in yeast] (4, 5), which is located near the exit tunnel where newly synthesized proteins emerge. Proteins are guided to oxidase assembly protein 1 (Oxa1), a protein of the inner membrane (7). In fungi, mitoribosomes are even more tightly bound to the membrane by a second membrane tether that is formed by an extension of rRNA (8). It has been known for many years that mitoribosomes behave like membrane proteins in biochemical fractionation experiments. However, only now have the electron microscopy-derived structures allowed the identification of the molecular elements that form these unusual membrane contacts.

The well-resolved structures of the mitoribosome are certainly milestones in the

field. In the past, high-resolution structures of proteins were typically solved a considerable time after their detailed biochemical characterization. This is not the case here. Despite much effort, scientists failed to establish assays to monitor mitochondrial protein synthesis *in vitro*, although the analysis of cytosolic translation has been established for more than half a century (9). In the case of mitoribosomes, the electron microscopy structures precede the detailed biochemical characterization and will be of tremendous value to guide biochemists in understanding how mitoribosomes function. This will be particularly interesting with respect to their unique way of regulating the initiation of translation as well as to their adaptation to the synthesis of membrane proteins exclusively.

It is obvious that the mitoribosome is very different from cytosolic ribosomes. However, and perhaps even more puzzling, there are also dramatic differences between the structures of mitoribosomes of different species (10). Apparently, evolutionary tinkering has remodeled the bacterial ribosome of the endosymbiont in divergent ways to form surprisingly different ribosomes in present-day mitochondria. ■

REFERENCES

1. B. J. Greber *et al.*, *Science* **348**, 303 (2015).
2. A. Amunts, A. Brown, J. Toots, S. H. W. Scheres, V. Ramakrishnan, *Science* **348**, 95 (2015).
3. M. R. Sharma *et al.*, *Cell* **115**, 97 (2003).
4. B. J. Greber *et al.*, *Nature* **515**, 283 (2014).
5. A. Brown *et al.*, *Science* **346**, 718 (2014).
6. M. Liu, L. Spemull, *J. Biol. Chem.* **275**, 29400 (2000).
7. M. Ott *et al.*, *EMBO J.* **25**, 1603 (2006).
8. S. Pfeffer, M. W. Woellhaf, J. M. Herrmann, F. Förster, *Nat. Commun.* **6**, 6019 (2015).
9. R. Schweet, H. Lamfrom, E. Allen, *Proc. Natl. Acad. Sci. U.S.A.* **44**, 1029 (1958).
10. A. Amunts *et al.*, *Science* **343**, 1485 (2014).

10.1126/science.aab1054

¹Gene Center, University of Munich, 81377 Munich, Germany; ²Cell Biology, University of Kaiserslautern, 67663 Kaiserslautern, Germany.
E-mail: hannes.herrmann@biologie.uni-kl.de

OCEANOGRAPHY

Escape by dilution

Dissolved organic matter in much of the deep ocean is too dilute to be consumed by microbes

By Jack J. Middelburg

Earth's oceans contain as much carbon in the form of dissolved organic matter (DOM) as does the biosphere, and more than 200 times that of living marine biomass. Most of the DOM is in the deep sea below 1000 m. Radiocarbon data show that the bulk of the DOM is thousands of years old (1). This long residence of DOM in the deep ocean is intriguing: Prokaryotes (bacteria and archaea) are abundant and active in the deep ocean, and many of them require DOM for energy and carbon. Moreover, molecular biology data show high metabolic diversity in the deep ocean (2). Why does some DOM escape degradation in the deep sea? Nutrient limitation of consumer biomass may explain underutilization of resources in nutrient-low surface waters (3), but this does not apply to the nutrient-rich deep sea. On page 331 of this issue, Arrieta *et al.* (4) show that DOM is too dilute to be consumed.

The ruling paradigm is that deep-sea DOM accumulates because it is difficult for microbes to break down (it is recalcitrant) (1, 5). This low reactivity of DOM is thought to relate to its chemical composition and degradation history. However, DOM in the deep sea is largely unidentified, and chemical structure information thus provides little guidance as to whether DOM compounds are inherently recalcitrant.

Arrieta *et al.* challenge the commonly accepted paradigm. Instead, they revisit Jannasch's dilution hypothesis (6), which states that the growth of microbes (and hence DOM consumption) ceases when concentrations fall below a threshold value (see the figure). They provide direct experimental proof that an increase in DOM concentration results in microbial growth under conditions similar to those in the deep sea in terms of substrate and temperature (although not pressure). No response would be expected if deep-sea DOM were intrinsically resistant to consumption. Moreover, using Fourier-transform ion cyclotron resonance mass spectrometry, the authors show that marine DOM contains thousands of different

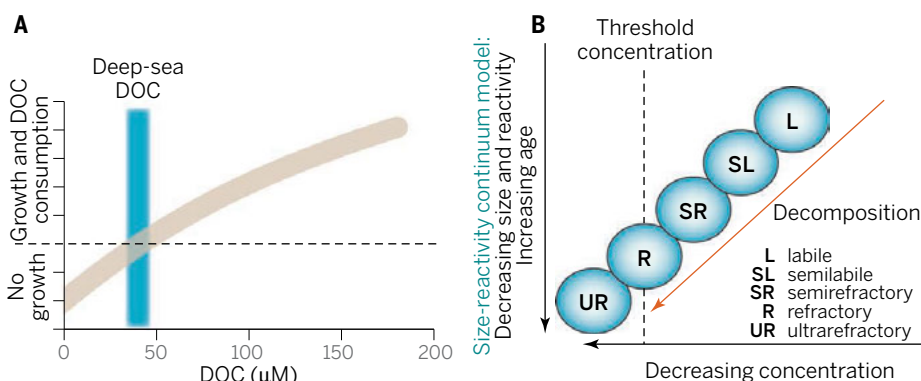
molecules, many of which were consumed during incubation.

If dilution rather than the intrinsically recalcitrant nature of compounds limits DOM utilization, one would expect DOM to never be depleted completely and deep-sea DOM concentrations to be near the threshold for consumption. This is indeed what is observed (see the figure, panel A) (5). Moreover, addition of dissolved organics to the DOM pool should stimulate consumption.

lular size and reactivity and increases in radiocarbon age and chemical complexity. In contrast, the dilution hypothesis is neutral with regard to the quality of organic matter. How can we reconcile these two apparently conflicting views of DOM dynamics?

Organic matter degradation involves not only a decline in concentration but also a decrease in reactivity (9) because of the preferential consumption of labile organic matter (see the figure, panel B). During the initial stages of degradation, DOM concentrations are far above the threshold, and changes in reactivity, size, and composition of organic matter upon degradation are clear. Steady degradation of DOM eventually results in concentrations near the threshold level in the deep sea, and DOM consumption rates decrease. Arrieta *et al.* show that deep-sea DOM is consumed when

Carbon consumption in the deep ocean



Too dilute to be consumed. (A) DOM concentrations in the deep sea are near the threshold below which no microbial growth occurs. Arrieta *et al.* report active DOM degradation by microbes at concentrations above the threshold. (B) Degradation of DOM results both in a decrease in size and reactivity and a decrease in concentration down to the threshold level identified by Arrieta *et al.* (4). Below the threshold, degradation of DOM is limited, but aging may continue.

Thus, addition of newly produced DOM in the sunlit layer may elevate compound concentration levels above the threshold, causing degradation of "aged" organic matter brought to the surface by upwelling. This priming may, combined with ultraviolet-induced photolysis, cause eventual removal of DOM from the ocean.

Arrieta *et al.*'s results also put an upper limit on the efficiency of the microbial carbon pump—that is, the microbial conversion of labile into more refractory DOM that remains in the ocean for long periods of time (7). Large increases and decreases of the deep-sea DOM reservoir have been proposed for the Precambrian and Eocene (8). This will not be a feasible mechanism if the dilution hypothesis is correct.

The well-established and widely accepted reactivity-size continuum model (5) links degradation of DOM to decreases in mo-

concentrated, which suggests that the reactivity of DOM compounds is concentration-dependent. This complicates attribution of DOM survival to either quantity or quality of DOM. It also adds to the emerging picture that organic matter degradation kinetics are not merely an inherent property of the compounds, but rather depend on the context (such as oxygen availability, time frame, and concentration). ■

REFERENCES

1. D. A. Hansell, *Annu. Rev. Mar. Sci.* **5**, 421 (2013).
2. E. B. Kujawinski, *Annu. Rev. Mar. Sci.* **3**, 567 (2011).
3. T. F. Thingstad *et al.*, *Limnol. Oceanogr.* **42**, 398 (1997).
4. J. M. Arrieta *et al.*, *Science* **348**, 331 (2015).
5. R. Benner, R. W. M. Amon, *Annu. Rev. Mar. Sci.* **7**, 185 (2015).
6. H. W. Jannasch, *Limnol. Oceanogr.* **12**, 264 (1967).
7. N. Jiao *et al.*, *Nat. Rev. Microbiol.* **8**, 593 (2010).
8. A. Ridgwell, *Proc. Natl. Acad. Sci. U.S.A.* **108**, 16485 (2011).
9. J. J. Middelburg, F. J. R. Meysman, *Science* **316**, 1294 (2007).

Department of Earth Sciences, Faculty of Geosciences, Utrecht University, P.O. Box 80021, 3508 TA Utrecht, Netherlands.
E-mail: j.b.m.middelburg@uu.nl

Improve customs systems to monitor global wildlife trade

Widely used trade codes lack taxonomic granularity

By Hon-Ki Chan,* Huarong Zhang, Feng Yang, Gunter Fischer

The volume of international trade in wildlife commodities is immense and, in many cases, is rising (1). Although there are already wildlife trade data sources [e.g., the Convention on International Trade in Endangered Species of Wild Fauna and Flora (CITES) Trade Database and the U.S. Fish and Wildlife Service Law Enforcement Management Information System (LEMIS)], coverage of traded species or countries involved is not comprehensive. This can undermine supply-chain monitoring and fast aggregation of data to inform policy-making (2). We discuss whether widely used, but limited, international customs codes and governance might evolve to address these gaps.

The Harmonized System (HS) administered by the World Customs Organization (WCO) accounts for more than 98% of global trade volume and is arguably the most comprehensive data set available for global commodity trade. Each commodity type is assigned a universal six-digit code, and individual member nations of WCO can assign two or more additional digits as domestic codes for tariff purposes (e.g., HS designated 0106.20 for “live reptile”; Hong Kong domestic HS designated 0106.20.10 for “live snakes”). Although not designed for global commodity tracking (3), the HS has been providing trade flow information to researchers and agencies, because external trade data for wildlife is usually limited (4, 5).

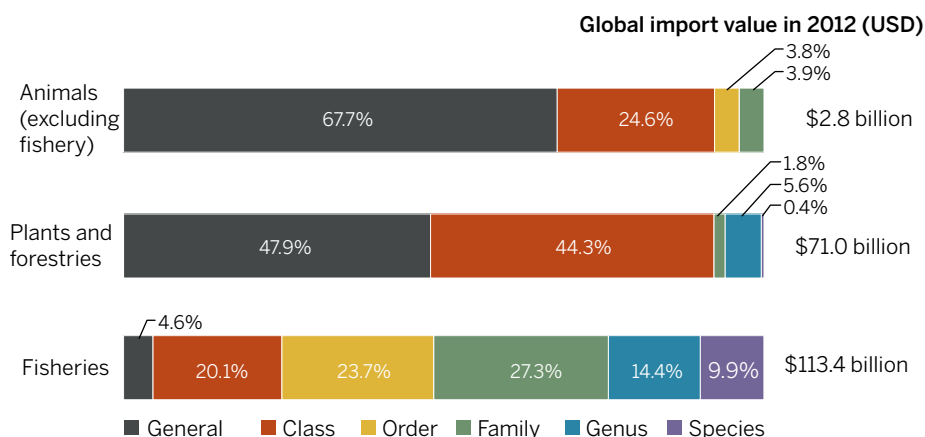
However, a considerable proportion of wildlife commodities eludes monitoring via HS because they are classified into broad categories that cannot be disaggregated into smaller and well-defined taxonomic units (6). To assess the trade volume of such categories in the current HS classification (2012 edition), we analyzed the global commodities trade statistics of 2012 (7). There were 308 HS subheadings composed of wild animals, fisheries commodities, and plant and forestry products. We classified the taxonomic level of each subheading into class, order,

family, genus, and species. Descriptions that were not in taxonomic terms or that covered more than one class were designated as “general.” Subheadings composed of largely domestic or captive-bred animals (e.g., bovine, poultry, and farmed fur) were excluded from analysis. Aquaculture fishery commodities were not excluded because they were indistinguishable from wild-caught fish in HS statistics (table S1).

the current 86 wood types and will cover all wood species produced in the tropics. This amendment reflects the growth of the forestry sector and the increasing species diversity involved in international trade. Improving taxonomic information is crucial for estimating forest consumption rates, as well as energy and carbon balance (9). The statistics of fisheries being better than other sectors is partially due to multilateral fishery management agreements that coerce fishers into systemically reporting their catch. Trade organizations and governance bodies such as the International Tropical Timber Organization (ITTO) should deepen their role in enhancing industry reporting standards.

The insufficient specificity of wildlife commodities in the HS stems from commodities listing requirements. To warrant a

Lack of trade code granularity limits ability to monitor wildlife



Proportion of classification levels for animal, fisheries, and plant commodities. “General” stands for classification that is not in taxonomic terms or covers more than one class. Data are based on the HS global import values in 2012 (7). USD, U.S. dollars. See the supplementary materials.

Global import of wildlife products reported to the HS amounted to U.S.\$187.3 billion, with fishery commodities accounting for \$113.4 billion (60.6%), \$71.1 billion (38.0%) for plant and forestry products, and \$2.8 billion (1.5%) for nonfishery animal products. About 22% of total global imports of wildlife commodities were classified into general categories. Animal commodities were the least resolved, with 67.7% concealed in general categories. This was substantially higher than plant and forestry products (47.9%) and fishery commodities (4.6%) (see the chart). The high specificity of fishery statistics implies much room for improvement for both animal and forestry trade sectors.

Timber trade statistics are particularly poor (8), despite huge trade volume. In the upcoming 2017 update of HS, the “tropical wood” product will no longer be limited to

HS subheading, annual global trade should exceed \$50 million. Some wild populations may be threatened even when traded well below the HS threshold. Although this threshold criterion is exempted for commodities of environmental and social concern, there is no clear or agreed-upon scientific basis for determining the exemption (e.g., the International Union for Conservation of Nature and Natural Resources Red List status). Many wildlife commodities that marginally fit the exemption criteria are thus either not listed owing to their low values or delisted when trade volumes dip to low levels. For instance, there is a glaring absence of major taxonomic groups such as amphibians and live corals; no codes are reserved for many frequently traded CITES species used in traditional medicine, such as orchids, seahorses, and turtles.

Kadoorie Farm and Botanic Garden, Tai Po, Hong Kong.
*E-mail: honkichan@gmail.com

Although countries may list specific commodities on their national customs tariff codes, traceability suffers when they are exported to countries that do not have specific customs codes. Patterns of species trade and consumption vary between regions and cultures. Unlike staple commodities, most wildlife products are traded between a few countries, limiting incentives for collaborative monitoring. There is increasing necessity to enhance the specificity of the HS to strengthen enforcement and monitoring to help meet broader conservation targets—for example, Aichi Biodiversity Targets (5, 9). CITES Parties in 2013 directed the standing committee to liaise with the WCO with regard to inclusion of CITES-listed species in the HS to enhance enforcement and safeguard endangered species (10).

The HS is reviewed every 5 years. With only six digits to classify the large variety of goods, vacant codes have been quickly depleted, especially for the fisheries chapter. Although unambiguous products—such as chemicals or machineries with distinct functions—are easier to accept into the HS, national customs' capability to verify compliance with HS reporting for wildlife commodities varies greatly. Developed countries have better expertise and technologies in handling wildlife trade—for example, wildlife forensics genetics techniques. However, three-quarters of the 179 WCO member states are developing countries that do not have similar capabilities. Developing countries have less incentive to accept new HS codes because they may further burden their limited customs resources.

In this setting, proposals to create HS codes for specific wildlife commodities may struggle to secure two-thirds majority votes as required by the HS Convention. Constraints of the HS prompted the idea of a new Taxonomic Serial Number (TSN) system complementary to the HS framework (6). This would require species information to be declared as TSN assigned by the Integrated Taxonomic Information System (ITIS). This is an ideal system that can accurately account for huge varieties of wildlife. However, the technical complexity (e.g., nomenclatural variability and disputability) and the resources required currently make it difficult to apply TSN extensively (11). HS, on the contrary, has a fixed list of defined taxonomic entities for consistency to avoid legal loopholes and has active customs enforcement worldwide due to its important role in tariff management. There is, therefore, a strategic necessity to remain reliant on and continue to strengthen the HS framework.

The Organization for Economic Cooperation and Development contends that if the national customs tariff code can be stan-

"We suggest that the WCO should...modify the... universal HS codes...from 6 to 10 digits..."

dardized across countries, trade data will be of increased value for consumption-side monitoring (12). Standardization could be achieved by nonbinding WCO Council recommendations to member states. However, only a small subset of commodities could be standardized by recommendations. Broader HS reform would be needed to standardize commodities worldwide.

We suggest that the WCO should consider the HS a scalable system and take initiative to modify the HS Convention. The universal HS codes could be extended from 6 to 10 digits, with potential for accommodating thousands of commodities per subheading. Trade value threshold for listing of commodities should not be applied at the 10-digit level to allow a more inclusive listing. Developing countries, having low customs capacity, can maintain the current 6-digit (or less) classification as "partial application" permissible in the HS Convention (13). The universal 10-digit HS would apply only to developed countries or countries with capable customs administration to ensure data reliability. Given differences in purpose and implementing countries, the two levels of HS should have separate review committees and negotiation processes; relevant nongovernmental organizations (NGOs) should be engaged as observers in the amendment process.

We do not intend to impose a strictly taxonomic scheme. The HS will ultimately need to be developed suitably for the industry and customs and to rely on competent agencies such as the Food and Agriculture Organization (FAO) of the United Nations and ITTO to steer it. Although the cost to overhaul the HS could be high, reduced resources needed for case-by-case trade investigations, combined with benefits gained in safeguarding wildlife, may offset administrative costs in the long run.

We believe expanding the code space can enhance the function of the HS. The Wildlife Trafficking Response, Assessment, and Priority Setting (Wildlife TRAPS) project—which engages private logistics companies, NGOs, and the WCO—recently identified the transport sector as the weakest link in combating wildlife trafficking (14). Because the HS forms the basis for goods declaration in national customs law, improving specificity of the HS will raise awareness among traders and the transport industry and make

them more liable for accurate reporting of wildlife commodities.

Traders already work with various national tariff schedules that have 8 to 10 digits. Standardizing these codes across countries should reduce confusion at the operational level. The destinations of most wildlife commodities are usually developed countries with better customs facilities to serve as gatekeepers. If these countries adopt a 10-digit HS, the statistics would be representative of global trade.

Standardization of national tariff codes across countries could simplify international trade procedures in accordance with the World Trade Organization (WTO) Trade Facilitation Agreement that will soon enter into force. National-level customs could target shipments with a risk of trafficking more effectively. At the regional level, standardized code allows direct cross-verification of trade data between customs officials to detect potential fraud, mutually assisting enforcement of those that have different expertise. At the global level, consumption of wildlife commodities could be evaluated to address sustainability.

Although the HS has the potential to better monitor global wildlife trade and support enforcement of biodiversity conservation treaties, it is limited by the fundamental constraint of the code space and amendment process. The HS Convention should be reformed to extend the universal HS code to 10 digits. Developed countries should take the lead in improving customs data specificity. ■

REFERENCES AND NOTES

1. TRAFFIC, *What's Driving the Wildlife Trade? A Review of Expert Opinion on Economic and Social Drivers of the Wildlife Trade and Trade Control Efforts in Cambodia, Indonesia, Lao PDR, and Vietnam* (World Bank, Washington, DC, 2008).
2. D. O'Rourke, *Science* **344**, 1124 (2014).
3. I. Bannon, P. Collier, *Natural Resources and Violent Conflict: Options and Actions* (The World Bank, 2003).
4. B. Gratwicke et al., *Front. Ecol. Environ.* **8**, 438 (2010).
5. S. C. Clarke, *Fish Fish.* **5**, 53 (2004).
6. H. Gerson et al., *Conserv. Biol.* **22**, 1651 (2008).
7. U.N. Comtrade Database, comtrade.un.org.
8. A. Goetzl, *ITTO Trop. Forest Update* **15**, 8 (2005).
9. FAO, "Supporting material to the FAO revised proposal for the harmonized system 2017 edition" FAO, Rome, (2012), pp. 1–99.
10. CITES Decision, 16.62, Rev. CoP16 (2013); www.cites.org/sites/default/files/eng/dec/valid16/E16-Dec.pdf (2013).
11. G. Frago, S. Ferriss, *Conserv. Biol.* **22**, 1648 (2008).
12. Organisation for Economic Co-operation and Development (OECD), "Illegal trade in environmentally sensitive goods" (OECD Trade Policy Studies, OECD Publishing, Paris, 2012).
13. WCO Harmonized System Convention, www.wcoomd.org/en/topics/nomenclature/instrument-and-tools/hs_convention.aspx.
14. WCO, *Wildlife trafficking: Targeting solutions in the transport sector* (2015); www.wcoomd.org/en/media/newsroom/2015/february/wildlife-trafficking-targeting-solutions-in-the-transport-sector.aspx.

ACKNOWLEDGMENTS

The authors thank anonymous reviewers and two experts from the World Trade Organization for comments and suggestions.

SUPPLEMENTARY MATERIALS

www.sciencemag.org/content/348/6232/291/suppl/DC1

10.1126/science.aaa3141

BOOKS *et al.*

Beef is readied for distribution in Chicago's Union Stock Yards at the turn of the 20th century.

ANIMAL DISEASE CONTROL

The fever on the farm

Lessons from America's early efforts to control livestock diseases

By Delia Grace

The riots were in their 13th year. Two federal officials had recently been shot, and one of them had died from his injuries, but the local grand jury, drawn from an aggrieved and angry community, refused to indict the shooter. The year was 1922, and farming communities across the United States were vigorously resisting new regulations imposed by the Bureau of Animal Industry (BAI) that were intended to eradicate a parasitic infection known as Texas fever in domestic cattle.

Arresting Contagion is at once a biography (even a hagiography) of the BAI and a penetrating glimpse into the behavioral economics that defined early animal disease control efforts in the United States. The book begins in the late 19th century, a time of enormous innovation in agriculture and infrastructure. Animals were bred and killed on an unprecedented scale and transported over

vast distances, both domestically and internationally. This created enormous opportunities for diseases—including Texas fever, contagious bovine pleuropneumonia (lung plague), bovine tuberculosis, pork measles, and hog cholera—to emerge and spread. The book focuses on how some of these devastating livestock diseases were progressively controlled—a story that is complete with setbacks and victories, heroes and villains.

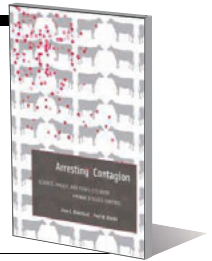
From 1904 to 1915, James Dorsey, who falls firmly into the villain category, did a good trade in cheap cattle that had failed a tuberculin test, passing them off as healthy animals to unsuspecting farmers. This practice created at least 10,000 foci of tuberculosis among dairy herds across the United States and likely contributed to tens of thousands of cases of human tuberculosis (1). Compared to “TB James,” Typhoid Mary was an amateur.

A pleasant contrast to Dorsey can be found in Daniel E. Salmon, who became the first person to be awarded a veterinary degree in the United States in 1876 and was appointed the first chief of the BAI in 1884. Within eight years of his appointment, lung plague had been eradicated in the United States. Under his leadership, veterinary scientists showed medical researchers the way by demonstrating that insect vectors could transmit disease, developing the first killed vaccine, and identifying the human hookworm parasite. *Salmonella* bacteria, discovered by his research group in 1885, were named after him in 1900.

In their book, Olmstead and Rhode probe the motives that drive individuals to comply with, or reject, efforts to mitigate animal

Arresting Contagion
Science, Policy, and Conflicts
over Animal Disease Control
Alan L. Olmstead and Paul
W. Rhode

Harvard University Press,
2015. 477 pp.



disease transmission. These motives are both fascinating and, more often than not, uncomfortably predictable. For example, many men who made money moving cattle refused to believe in contagions altogether. In the early 1880s, Chicago stockyard owners argued that their animals were in perfect health and that it would be financial suicide for them to sell unwholesome meat. Yet, inspections conducted in September 1886 revealed an industry plagued by filth and disease, a condition that persisted until federal legislation was established and regular, mandatory inspections were instituted. The authors make a strong case that disease is too important to leave to market forces and that the government has an essential role in controlling zoonotic disease.

In addition to regulation, the authors emphasize the need to incentivize farmers and merchants to comply with health and safety regulations. For example, in the 1920s, after their own cattle had been cleansed of Texas fever, farmers started to demand vociferously that disease control be mandated for still-infected cattle populations, which were now a major threat for disease reintroduction. Compensation for culled animals and the (limited) legal provisions that entitle farmers to recover damages from disease are also well addressed in the book.

Written by two economists, the book features a number of terms that may not be familiar to readers from health backgrounds, such as “externalities,” “rent-seeking,” and “public choice theory.” There are also occasional infelicities of phrasing: Cattle herds are ravished (rather than ravaged) by disease, and scientists attain notoriety (rather than fame) from their discoveries. Apart from these quibbles, the book is comprehensive, is well written, and contains a substantial amount of original research. This, along with extensive notes and references, will make it useful to those who are grappling with the recent resurgence in zoonotic diseases brought about by the rapid expansion of the livestock sector in developing countries and elsewhere.

REFERENCES

1. National Archives and Records Administration, Records of the Bureau of Animal Industry, Chief of the Bureau to Fitts, 9 July 1920.

10.1126/science.aaa7672

The reviewer is at the International Livestock Research Institute, Nairobi 00100, Kenya. E-mail: d.grace@cgiar.org

The evolution of evolution

Looking back at the theories that shaped modern evolutionary biology

By Jim Endersby

The question of how species evolved was debated long before the time of Charles Darwin, as Niles Eldredge shows in a meticulously researched history of evolutionary theories that will likely be unfamiliar to most readers. It is generally acknowledged that although Jean-Baptiste Lamarck had a few evolutionary notions (something about giraffes stretching their necks through their own efforts), they were wrong and can safely be ignored. However, as Eldredge demonstrates, this caricature of Lamarck's thinking obscures the context of Darwin's ideas. Nor was Lamarck the only person to speculate about evolution. In the early 1800s, the geologist Giambattista Brocchi offered an alternative to Lamarck's, one that briefly persuaded Darwin. Eldredge recovers Brocchi's largely lost contribution and links it to much more recent ideas in evolutionary thinking.

The key difference between Lamarck's and Brocchi's ideas about evolution lies in how they conceived of the nature of species. For Lamarck, life was continual progress from a simple progenitor up through stages of increasing complexity; each group of organisms traveled on its own evolutionary pathway and was constantly transforming. What naturalists call "species" are, according to Lamarck, arbitrary snapshots of something that is already on its way to becoming something else. That sounds, as Eldredge notes, very like conventional Darwinism. Following this line of thought, one could surmise that the species we observe, name, and classify only look like stable entities because the fossil record is incomplete.

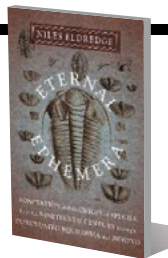
By contrast, Brocchi saw species almost as individuals, things that were born and died, to be replaced by new species. This perspective is supported by the fact that speciation is more common among geographically isolated populations than it is within lineages that persist at a single location. In this case, the fossil record is perceived to be an accurate reflection of species that come and go because of speciation and extinction but do not change much in between. If you think that sounds a lot like the theory of punctu-

Eternal Ephemera

Adaptation and the Origin of Species from the Nineteenth Century Through Punctuated Equilibria and Beyond

Niles Eldredge

Columbia University Press, 2015. 398 pp.



ated equilibria (which Eldredge developed with the late Stephen Jay Gould), that is not surprising, because so does Eldredge.

Eldredge's research into 19th-century history is meticulous; he has clearly spent many hours in the archive, tracing the development (and loss) of the Brocchian strand in Darwin's thinking. However, historians may feel (to paraphrase an old joke about statistics) that he uses history as a drunk uses a lamppost, for support rather than illumination. At one point, he announces bluntly, "I still think I am right" about punctuated equilibria and is pleased to see that Darwin once shared his opinion. Yet surely Darwin's opinion adds nothing to Eldredge's credibility, and the author's determination to juxtapose current evolutionary debates with historical theories leaves him puzzled by some of what he finds in the past.



Lamarck famously speculated that early giraffes stretched their necks to reach higher vegetation and that their offspring inherited the resulting long necks.

Why, Eldredge ponders, did Darwin not stick with his earlier, Brocchian approach? A fuller understanding of Darwin's times might explain the puzzle. As Eldredge notes, fossils "become progressively more and more like modern species" as one gets closer to the present. To the Victorians, that looked like a record of progress: slow and gradual improvement without revolutionary upheaval. This would have been an attractive model to gentlemen like Darwin—property men who feared radical change. It is always hard to judge something as nebulous as the spirit of an age and even harder to know what weight (if any) to give it when offering a historical explanation. But Darwin's gradualism is such a perfect fit for his times that it would be surprising if he had managed to formulate a radically different view (and even more surprising if he had persuaded his contemporaries to accept it).

Eldredge ignores everything between *The Origin of Species* (1859) and the development of the modern evolutionary synthesis of natural selection and population genetics in the 1930s. He dismisses the early-20th-century "eclipse" of Darwinism (the period when natural selection was considered inadequate to explain evolution) as "of little lasting interest," but in fact it was concerned with precisely the same questions he explores. As one late-19th-century wit put it, natural selection explained the survival of the fittest but not the arrival of the fittest. How, then, did speciation occur? The answers proposed during this time may not have been right, but they shaped biology during the early 20th century. For example, although Eldredge dismisses Hugo de Vries's mutation theory, which tried to explain speciation as the product of rapid genetic change during "mutation periods," as "egregious," it was the inspiration behind both Thomas Morgan's work at Columbia and the founding of the Cold Spring Harbor laboratory. De Vries turned out to be wrong in key respects, but it's unfair to say that he and his contemporaries are of "little lasting interest."

At times, it seems that history is not central to Eldredge's concerns, and he is aware that people will therefore ask what it is doing in the book. His reply is that the close parallels he sees between early-19th- and mid-20th-century evolution look a little like convergent evolution: two unrelated lineages converging on similar solutions to the problem of survival. He believes that this is the "best single set of phenomena" you can use to prove that evolution is true. Whether or not that is true of evolutionary theory, it seems like a weak historical argument. It will be fascinating to see whether biologists find Eldredge's analogy more persuasive.

10.1126/science.aaa5821

The reviewer is in the School of History, Art History, and Philosophy, University of Sussex, Brighton BN1 9RH, UK. E-mail: j.j.endersby@sussex.ac.uk

LETTERS

Edited by Jennifer Sills

Shaping the future of synthetic biology

OVER THE PAST few years, a debate has been taking place within the Convention on Biological Diversity regarding the risks and benefits of organisms, components, and products arising from synthetic biology techniques to the conservation and sustainable use of biodiversity. If synthetic biology were recognized as a new and emerging issue, the Convention would be able to develop rules governing its use. The voices and expertise of the scientific community have been mostly silent in this debate. In October 2014, about 20 of the 168 countries that are signatories to the Convention determined that there was insufficient information to make this designation and established an online forum and expert working group to collect more information in order to make a final recommendation to the Conference of the Parties by December 2016 (1). The United States is not a signatory to the Convention and therefore has limited influence on the process and final decisions. Although the United States will not be bound by the Convention, any researcher or company planning on developing or deploying synthetic biology in the other 168 countries that are signatories will be affected. It is therefore critical that the scientific community become actively engaged in this process.

There is an open call for information related to synthetic biology to be submitted by 30 April (2). Issues being considered include (i) how to address the relationship between synthetic biology and biological diversity; (ii) similarities and differences between living modified organisms (as defined in the Cartagena Protocol) and organisms, components, and products of synthetic biology techniques; (iii) operational definition of synthetic biology, comprising inclusion and exclusion criteria; (iv) potential benefits and risks of organisms, components, and products arising from synthetic biology techniques to the conservation and sustainable use of biodiversity and related human health and socioeconomic impacts relevant to the mandate of the Convention and its Protocols; and (v) best practices on risk assessment and monitoring regimes currently used by Parties to the Convention and other governments.

There will also be an online forum of experts discussing these issues, beginning on 27 April. If members of the scientific community cannot participate fully as designated experts, they can submit information through the Woodrow Wilson Center, which is a member of the expert online forum.

Todd Kuiken

Science and Technology Innovation Program,
Woodrow Wilson Center, Washington, DC 20004,
USA. E-mail: todd.kuiken@wilsoncenter.org

REFERENCES

1. Convention on Biological Diversity, Biosafety Clearing-House, Tentative calendar of activities related to synthetic biology (<https://bch.cbd.int/synbio/calendar>).
2. Submission of Information on Synthetic Biology (www.cbd.int/doc/notifications/2015/ntf-2015-013-synthetic-biology-en.pdf?;=download).

Combating the next lethal epidemic

OVER THE PAST 40 years, we have seen a consistent pattern of war and conflict leading to the collapse of public health systems and the subsequent reemergence of deadly tropical infections. Outbreaks have undermined the health and livelihoods of individuals, the economic growth of communities, security, and ultimately the development potential of nations.

We may now be witnessing the

beginnings of a similar pattern in the Middle East and North Africa (MENA) region. Outbreaks of a disfiguring skin form of leishmaniasis have affected tens of thousands of people in Syria, including Syrian refugees fleeing to neighboring Jordan, Lebanon, and Iraq (1). Polio, measles, rabies, and tuberculosis have also reemerged in Syria (2). Meanwhile, cutaneous leishmaniasis has reached epidemic proportions in parts of Afghanistan, dengue fever cases are mounting in Egypt, and helminth infections remain widespread in Yemen (3). Another concerning trend has been the absence of animal control across borders, which could lead to diseases of livestock such as brucellosis and zoonotic infections transmitted from animals to humans (4).

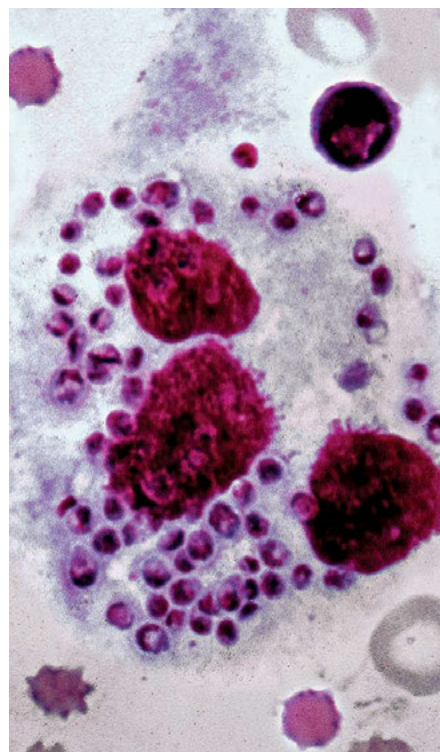
Islamic State of Iraq and the Levant (ISIL) hostilities in Syria and Iraq, and ongoing fighting in Afghanistan and parts of Pakistan place a region that comprises almost 1 million square miles and nearly 270 million people at great risk for serious epidemic infections. Neighboring countries will also be at risk.

Now is the time for coordinated local, national, regional, and global action to prepare for the emergence of disease epidemics in this volatile region. UNICEF has set a 2015 goal of vaccinating 16.3 million children against polio in countries hosting Syrian refugees (5). There is urgency to expand the core capacities for health emergency preparedness in the region through the Global Health Security Agenda (GHS) (6), including the development of new countermeasures and especially vaccines.

Many of the vaccines urgently needed for the MENA region will include those that target diseases of enormous public health importance and yet offer minimal commercial potential. Even with the Developing Country Vaccine Manufacturers Network (DCVMN) (7), the MENA region is relatively dependent on importing vaccines or providing vial fill and finish facilities for imported bulk vaccine materials. This situation has created vulnerabilities to diseases of regional importance.

Policy must be shaped to link nascent vaccine capabilities in the MENA region with one or more nonprofit organizations established to develop new biotechnology products for neglected diseases (product development partnerships), including our Sabin Vaccine Institute and Texas Children's Hospital Center for Vaccine Development based in Houston. The United States can assist through a program of vaccine science diplomacy in selected countries where there is a baseline of scientific strengths, together with political will and interests (8).

The international public health



Colored microscopy of leishmaniasis.

OUTSIDE THE TOWER

More than a science camp

Daniel, a smart and even-tempered boy of 15, lives in a humble neighborhood in the metropolitan area of Buenos Aires without access to Internet or even a phone in his home. He has just completed a hands-on activity in which he retraced the steps leading Lavoisier to the discovery of oxygen. He looks at me amazed, and exclaims, "I understood things differently! I felt like there was a strong wind inside my head!" Iván, a shy but brilliant 17-year-old, goes to one of the best public schools of Argentina and participates regularly in a range of science-related activities. He turns to me after taking part in a spirited stem cell debate and marvels, "I had the chance to hear good arguments for ideas that contradict my own. I've never had that opportunity before." Despite Daniel and Iván's disparate experiences, the pleasure they felt when they found answers on their

Outside the Tower is an occasional feature highlighting science advocacy projects led by scientists and citizen scientists. How do you advocate for science? Tell us at submit2science.org.



Campers at Expedición Ciencia perform astronomical observations.

own was the same.

Daniel, Iván, and another 38 boys and girls from Argentina and other Latin American countries were attending a science camp held every February by "Expedición Ciencia," a nongovernmental organization of scientists, educators, and students devoted to promoting science education for children in middle and high school (1). When I was 16 years old, this science camp changed my life. There, I learned how to think scientifically, realized I wanted to pursue a scientific career, and above all forged unconditional friendships. Today, as a passionate Ph.D. student in immunology, I actively participate in this NGO by helping to organize the camp and serving as a junior counselor.

At Expedición Ciencia, we challenge 14- to 17-year-olds to ask questions about nature as if they were the first ones in

history to do so. Through observation and experiments, they follow the crucial steps that lead to scientific breakthroughs and learn the scientific method firsthand. But something else happens in the meantime: They become very close friends, breaking down social barriers and establishing relationships that persist through time and distance.

Science not only allows us to see and comprehend the world; it's also a bridge between people coming from different backgrounds who share the same curiosity and passion to understand the beautiful world that surrounds us.

Luciano Gastón Morosi

Instituto de Biología y Medicina Experimental (IBYME-CONICET), C1428ADN Buenos Aires, Argentina. E-mail: luciano.morosi@gmail.com

REFERENCE

1. www.expedicionciencia.org.ar

community was largely blindsided by the 2014 Ebola outbreak in West Africa. A similar situation could arise in the MENA region, but could be averted through innovative and sustained programs of vaccine science diplomacy and global health security.

Peter J. Hotez

U.S. Science Envoy Program, Department of State and White House, Washington, DC 20520, USA; Sabin Vaccine Institute and Texas Children's Hospital Center for Vaccine Development, National School of Tropical Medicine, Baylor College of Medicine, Houston, TX 77030, USA; Department of Biology, Baylor University, Waco, TX 76706, USA; James A. Baker III Institute of Public Policy, Rice University, Houston, TX 77005, USA. E-mail: hotez@bcm.edu

REFERENCES AND NOTES

1. N. Salam, W. M. Al-Shaqha, A. Azzi, *PLOS Negl. Trop. Dis.* **8**, e3208 (2014).
2. S. Cousins, *Lancet* **385**, 931 (2015).
3. P. J. Hotez, L. Savioli, A. Fenwick, *PLOS Negl. Trop. Dis.* **6**, e1475 (2012).
4. M. Gwida et al., *Croat. Med. J.* **51**, 289 (2010).
5. UNICEF, Humanitarian Action for Children, Syrian Refugees (www.unicef.org/appeals/syrianrefugees.html).

6. GlobalHealth.gov, Global Health Topics, The Global Health Security Agenda (www.globalhealth.gov/global-health-topics/global-health-security/ghsagenda.html).
7. DCMN (www.dcmn.org).
8. P. J. Hotez, *PLOS Negl. Trop. Dis.* **8**, e2808 (2014).
9. The views presented herein are those of the author and not necessarily those of the U.S. Department of State, White House, or U.S. Government.

TECHNICAL COMMENT ABSTRACTS

Comment on "Local reorganization of xanthophores fine-tunes and colors the striped pattern of zebrafish"

Masakatsu Watanabe and Shigeru Kondo

Mahalwar et al. (Reports, 12 September 2014, p. 1362) observed the onset of pigment pattern formation in zebrafish. They concluded that their data do not support our Turing mechanism-based model and presented an essentially different mechanism. Here, we clarify their misunderstanding that may have caused their conclusion and explain past experimental data that do not

support their proposed mechanism.

Full text at <http://dx.doi.org/10.1126/science.1261947>

Response to Comment on "Local reorganization of xanthophores fine-tunes and colors the striped pattern of zebrafish"

Ajeet Pratap Singh, Hans-Georg Frohnhöfer, Uwe Irion, Christiane Nüsslein-Volhard

Watanabe and Kondo question our conclusion that the current Turing-type model of color patterning in zebrafish requires modification. In addition to xanthophores and melanophores, iridophores are essential for stripe formation in the body, although not in the fins. A model of predictive value should accommodate the in vivo dynamics and interactions of all three chromatophore types in body stripe formation.

Full text at <http://dx.doi.org/10.1126/science.aaa2804>

TECHNICAL COMMENT

FISH PIGMENTATION

Comment on “Local reorganization of xanthophores fine-tunes and colors the striped pattern of zebrafish”

Masakatsu Watanabe and Shigeru Kondo*

Mahalwar *et al.* (Reports, 12 September 2014, p. 1362) observed the onset of pigment pattern formation in zebrafish. They concluded that their data do not support our Turing mechanism-based model and presented an essentially different mechanism. Here, we clarify their misunderstanding that may have caused their conclusion and explain past experimental data that do not support their proposed mechanism.

Recent observations regarding the cell behaviors of zebrafish pigment from the Singh and Nüsslein-Volhard research group concluded that the current model based on the Turing mechanism cannot explain stripe development (1, 2). Rather, they presented an essentially different model, in which the stripes

depend on a prepattern specified by iridophores. This conclusion reflects a misunderstanding of the current Turing-based model and its predictions (3). In fact, the reported observations do not contradict the current Turing model. Here, we clarify these issues and discuss the validity of the two models with respect to experimental observations.

First, they claim that the current Turing-based model cannot apply to zebrafish because the model assumes random initial conditions (1).

This claim might result from misunderstanding of the model. We selected different initial conditions depending on the phenomenon to be simulated. When we simulated zebrafish stripe formation (4), we selected a single horizontal stripe, analogous to the early pattern of iridophores (1, 2, 5, 6), as an initial nonrandom condition. In case of regeneration that gives rise to labyrinthine patterns, we selected random initial conditions (7). It is a merit of the Turing model that it can explain both development and regeneration.

Second, they rarely observed cell migration during pattern formation and used this to argue against the Turing-based model (1). Because we and others observed the migration of pigment cells and their precursors, we wonder if this conflict might be from a difference in some experimental conditions (8–11). More fundamentally, however, migration is not a crucial requirement of our Turing-based model. The core element of the model is an interaction network having properties of short-range activation and long-range inhibition (12). In principle, any cellular behavior might be accommodated. Following this idea, we have never presented any detailed simulation in which a specific cellular behavior is included. The arrows in our model represent rough relationships (inhibition or enhancement) between the pigment cells (13). In our previous papers (4), we suggested that the differentiation, death, and repulsive migration are the possible behaviors of actual cell-cell interactions (4, 14). Because pigment pattern arises in many different

Graduate School of Frontier Biosciences, Osaka University, 1-3 Yamadaoka, Suita, Osaka, 565-0871, Japan.

*Corresponding author. E-mail: skondo@fbs.osaka-u.ac.jp

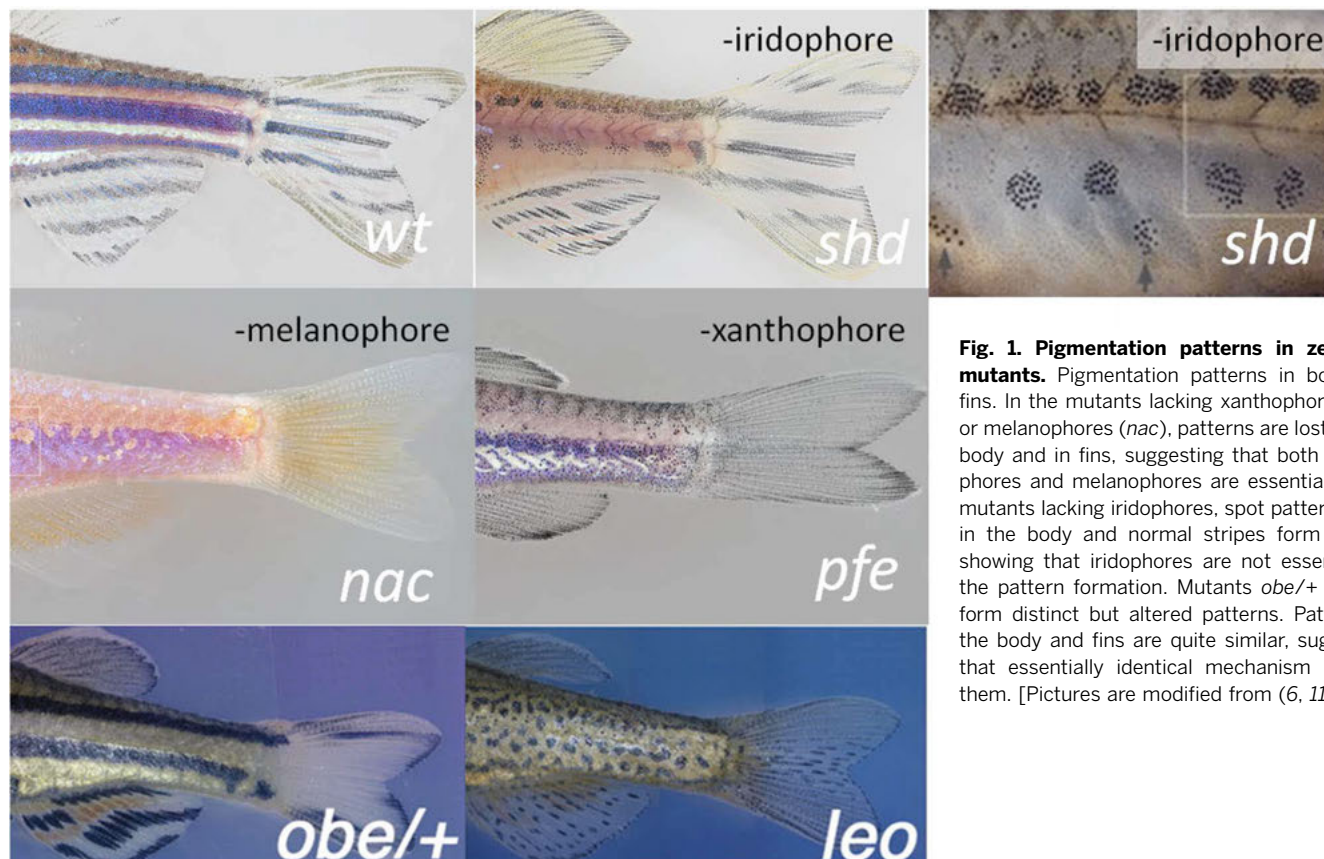


Fig. 1. Pigmentation patterns in zebrafish mutants. Pigmentation patterns in body and fins. In the mutants lacking xanthophores (*pfe*) or melanophores (*nac*), patterns are lost both in body and in fins, suggesting that both xanthophores and melanophores are essential. In the mutants lacking iridophores, spot pattern forms in the body and normal stripes form in fins, showing that iridophores are not essential for the pattern formation. Mutants *obe/+* and *leo* form distinct but altered patterns. Patterns in the body and fins are quite similar, suggesting that essentially identical mechanism underlie them. [Pictures are modified from (6, 11)]

situations—in body, in fins, and in the process of regeneration—it seems natural that there is some difference in the actual cellular event. As long as the specific property is kept, the system can act as Turing mechanism (12).

The most important argument of theirs is that our current model does not contain iridophores (1, 2). Zebrafish have stripes on both the body and the fins. The fin stripes are continuous with those on the body, and the width of the stripes is almost identical (Fig. 1, wt). In some mutants (leo and obe), the pattern in the body and the fins change in the same way (11). Therefore, it is highly probable that the same mechanism underlies body and fin stripe development. In the mutants without melanophores or xanthophores, patterns are lost in both the body and the fins. However, in the iridophore-free mutants (Fig. 1, shd), normal stripes form in the fins and spot pattern forms in the body (5, 6), demonstrating that iridophores are not absolutely essential. This is not explicitly stated by them but is the reason that our current model consists of only melanophores and xanthophores. Although iridophores need to be added to explain the body patterning, it is unlikely that the major role of melanophores and xanthophores is drastically changed. (It is theoretically easy to construct a Turing mechanism with three elements.) As described below,

past experiments revealed the major contribution of melanophores and xanthophores in the body trunk patterns.

They claim that the early iridophore distribution functions as a “prepattern” to establish all four to five adult stripes and that later cell-cell interactions merely sharpen stripe boundaries (1, 2). However, transition of the patterns from juvenile to adult in some mutants indicates that cell-cell interactions can change the initial pattern (Fig. 2, leo, Tg-2, and Tg3). For example, *leopard* mutants develop normal iridophore prepatterns but gradually change to widely distributed adult spots.

The *leopard* gene mediates interactions between melanophores and xanthophores (11) and encodes the gap junction protein connexin41.8 (15). We constructed a series of *leopard* genes with varying activity to “tune” the melanophore-xanthophore interaction and successfully generated a variety of patterns (for example, spots, rings, and labyrinth) in transgenic zebrafish without changing the juvenile iridophores pattern (15). It is notable that all these patterns are common outcomes of the Turing mechanism but cannot be made by the prepattern mechanism. This “tuning” of the *leopard* gene also produced

various stripe patterns with altered numbers, widths, and positions, demonstrating that these parameters are determined by the interaction between melanophores and xanthophores. One particular property of the juvenile pattern that cannot be changed by later rearrangement is the directionality of the stripes. When all the pigment cells are ablated artificially, zebrafish regenerate a labyrinthine pattern, or stripes without directionality, suggesting that the directionality of adult stripes is derived from the juvenile pattern (7, 9).

Numerous other reports using cell transplantation, laser ablation, and other genetic approaches emphasize the contribution of melanophore-xanthophore interactions to adult patterns (9, 11, 14). The interaction network deduced from these studies shows that the interaction network satisfies the property of short-range activation and long-range inhibition, which is an essential requirement for Turing pattern formation (13).

Furthermore, we and others have shown the dynamic rearrangement of pigment patterns following laser or genetic ablation. These experiments demonstrate pattern autonomy that is specific to the Turing mechanism, which is the definitive reason we use the Turing model as the working hypothesis. Because of this dynamic property, Turing-based models can generate many kinds of patterns and can be applied to both development and regeneration of the pattern (4). This merit is important because if the Turing mechanism generally underlies these processes, we do not need to find new mechanisms for other pigmentation patterns. Although our current knowledge of the detailed cellular and molecular mechanism is far from complete (e.g., the unknown role of iridophores in the body), experimental analyses over the past 15 years support the Turing mechanism.

REFERENCES

1. P. Mahalwar, B. Walderich, A. P. Singh, C. Nüsslein-Volhard, *Science* **345**, 1362–1364 (2014).
2. A. P. Singh, U. Schach, C. Nüsslein-Volhard, *Nat. Cell Biol.* **16**, 607–614 (2014).
3. A. Turing, *Philos. Trans. R. Soc. Lond. B Biol. Sci.* **237**, 37–72 (1952).
4. A. Nakamasu, G. Takahashi, A. Kanbe, S. Kondo, *Proc. Natl. Acad. Sci. U.S.A.* **106**, 8429–8434 (2009).
5. L. B. Patterson, D. M. Parichy, *PLOS Genet.* **9**, e1003561 (2013).
6. H. G. Frohnhöfer, J. Krauss, H. M. Maischein, C. Nüsslein-Volhard, *Development* **140**, 2997–3007 (2013).
7. M. Yamaguchi, E. Yoshimoto, S. Kondo, *Proc. Natl. Acad. Sci. U.S.A.* **104**, 4790–4793 (2007).
8. E. H. Budi, L. B. Patterson, D. M. Parichy, *PLOS Genet.* **7**, e1002044 (2011).
9. D. M. Parichy, J. M. Turner, *Development* **130**, 817–833 (2003).
10. G. Takahashi, S. Kondo, *Pigment Cell Melanoma Res.* **21**, 677–686 (2008).
11. F. Maderspacher, C. Nüsslein-Volhard, *Development* **130**, 3447–3457 (2003).
12. H. Meinhardt, A. Gierer, *BioEssays* **22**, 753–760 (2000).
13. S. Kondo, T. Miura, *Science* **329**, 1616–1620 (2010).
14. M. Inaba, H. Yamanaka, S. Kondo, *Science* **335**, 677 (2012).
15. M. Watanabe, S. Kondo, *Pigment Cell Melanoma Res.* **25**, 326–330 (2012).

1 October 2014; accepted 18 February 2015
10.1126/science.1261947

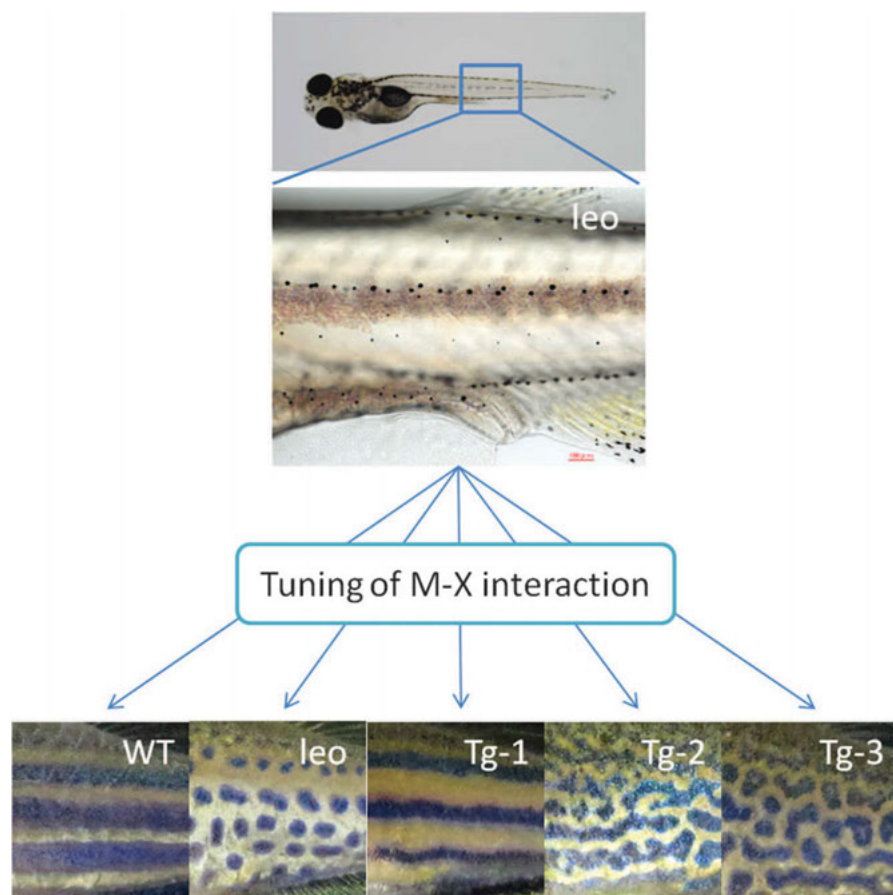
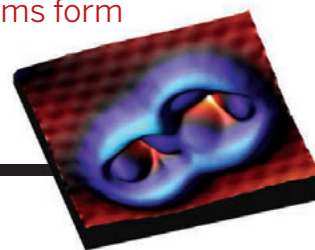


Fig. 2. Tuning of melano-xantho interactions generates a series of patterns without changing the activity of iridophores. Juvenile zebrafish of all *leopard* variants show almost identical juvenile pattern. However, depending on the activity of melano-xantho interactions, they form different adult patterns. In most cases, the juvenile pattern disappears. [Pictures are modified from (15)]

RESEARCH

Copper and iron atoms form toroidal structures

Emmrich et al., p. 308



IN SCIENCE JOURNALS

Edited by Caroline Ash



Yanomami microbiota contain antibiotic resistance genes

MICROBIAL ECOLOGY

Microbiome of uncontacted Amerindians

Surprisingly, the previously unexplored microbiome of Amerindians contains antibiotic resistance genes. Clemente *et al.* characterized the fecal, oral, and skin bacterial microbiome of people in a Yanomami Amerindian village with no known previous contact with Western peoples for the past 11,000 years. Their microbiota are the most diverse yet reported for humans. These data offer a rare opportunity to understand what latent antibiotic resistance might have been present in the human holobiont before antibiotic use. — PLY

Sci. Adv. 10.1126/sciadv.1500183 (2015).

SUPERCONDUCTIVITY

Massive electrons signify correlations

Thirty years on, and the mechanism of superconductivity in copper-oxide superconductors remains a mystery. Knowledge of their normal nonsuperconducting state is also incomplete; however, we do know that the more robust the superconductivity, the higher the magnetic fields required to suppress it. Ramshaw *et al.* studied samples of three different compositions of the copper-oxide $\text{YBa}_2\text{Cu}_3\text{O}_{6+x}$ in magnetic fields exceeding 90 T. They found that as the oxygen content increased toward the point of the maximum transition temperature, the conducting electrons became heavier and heavier. This mass enhancement reflected an increase in electronic

correlations, which in turn may be a signature of a quantum critical point. — JS

Science, this issue p. 317

BIOGEOCHEMISTRY

Dilution solves the recalcitrance question

The deep ocean is full of dissolved organic carbon, some of which has remained unchanged for thousands of years. What makes these compounds so resistant to microbial degradation? Perhaps their chemical structures make them intrinsically difficult to metabolize? In contrast, Arrieta *et al.* show that they are simply too dilute to be viable sources of energy for microorganisms (see the Perspective by Middleburg). Further experiments show that if these seemingly recalcitrant

organic molecules are concentrated, the ambient microbes can consume them. — HJS

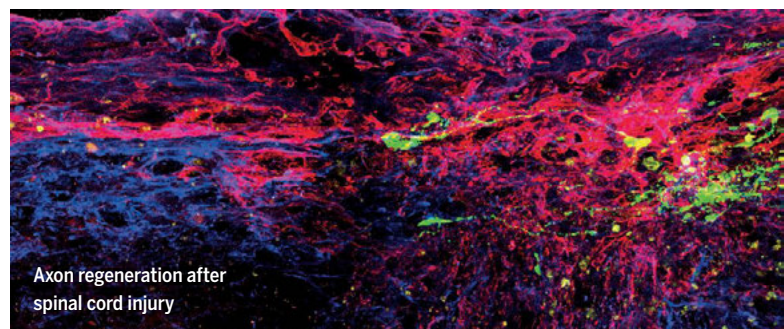
Science, this issue p. 331; see also p. 290

AXONAL REGENERATION

Progress toward fixing a broken back?

Axon regeneration after a spinal cord injury requires

interference with neuronal mechanisms to promote axon extension and early suppression of scar formation. Microtubule stabilization could provide, in principle, a basis for such intervention. Ruschel *et al.* used animal models of spinal cord injury, time-lapse imaging in vivo, primary neuronal cultures, and behavioral studies to tackle this challenge (see the Perspective by Tran and



Axon regeneration after spinal cord injury

Silver). They showed that epothilone B, a U.S. Food and Drug Administration–approved microtubule-stabilizing drug that can cross the blood-brain barrier, does promote functional axon regeneration, even after injury. — SMH

Science, this issue p. 347;
see also p. 285

STRUCTURAL BIOLOGY

Resolving whole mitoribosomes

Mitochondria probably evolved from a prokaryotic cell living within a proto-eukaryotic cell. Consequently, mitochondria have lost much of their genomic DNA, except for a few genes that require highly divergent mitoribosomes for protein translation. Greber *et al.* and Amunts *et al.* have used cryo–electron microscopy to uncover the structure of this complex (see the Perspective by Beckmann and Hermann) and reveal an unusual mRNA binding channel. The structure supplies clues for how aminoglycoside antibiotics might inhibit mitoribosomes and how mutations in mitoribosomes might cause human disease. — GR

Science, this issue p. 303, p. 288;
see also A. Amunts *et al.*,
Science, 3 April, p. 95

SOCIAL EVOLUTION

Gaze into my eyes

Humans bond emotionally as we gaze into each other's eyes—a process mediated by the hormone oxytocin. Nagasawa *et al.* show that such gaze-mediated bonding also exists between us and our closest

animal companions, dogs (see the Perspective by MacLean and Hare). They found that mutual gazing increased oxytocin levels, and sniffing oxytocin increased gazing in dogs, an effect that transferred to their owners. Wolves, who rarely engage in eye contact with their human handlers, seem resistant to this effect. — SNV

Science, this issue p. 333;
see also p. 280

STEM CELLS

Stem cells can sort mitochondria by age

The renewal of tissues in aging organisms requires stem cells, which have the unusual ability to divide asymmetrically into one daughter cell that retains stem cell properties and another that differentiates into a particular tissue type. Katajisto *et al.* used photoactivated marker proteins to monitor the age of cell organelles in stemlike cells from human breast tissue and their distribution into daughter cells. Most organelles were evenly distributed, but daughter cells that maintained stem-cell properties received more newly produced mitochondria and fewer old ones. — LBR

Science, this issue p. 340

CANCER

Will the real mutation please stand up?

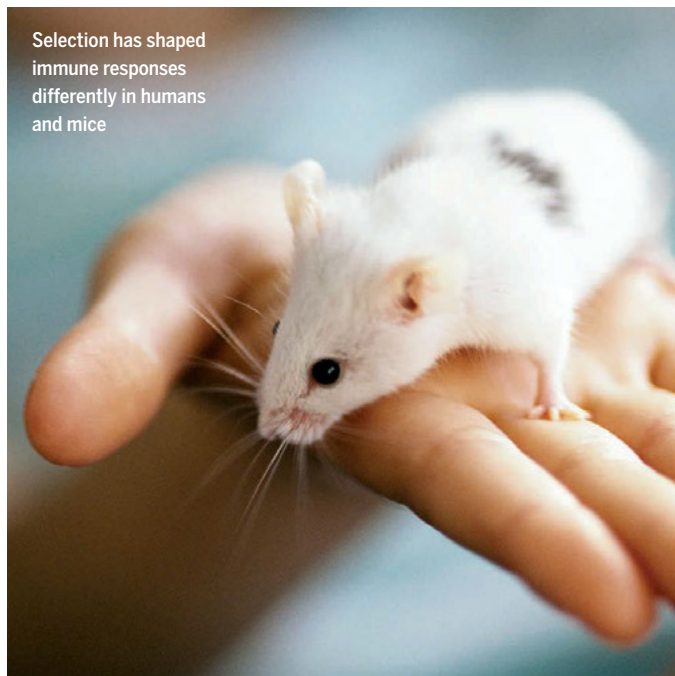
When a patient is diagnosed with cancer, tumor samples are analyzed to search for mutations that might guide targeted treatment of the disease. Jones *et al.* characterized samples from more than 800 patients with 15 different cancer types. For accuracy, this approach requires a matched sample of normal DNA from the same patient. By doing this, mutations present in the patient's normal tissues can be excluded as therapeutic targets, and therapeutically useful new mutations in the tumor are revealed. — YN

Sci. Transl. Med. **7**, 283ra53 (2015).

IN OTHER JOURNALS

Edited by **Sacha Vignieri**
and **Jesse Smith**

Selection has shaped immune responses differently in humans and mice



IMMUNOGENETICS

Of mice and men

Species undergo different selective forces, and those that drive immunity are of special interest because they may affect studies of human health. Webb *et al.* investigated the differences between human and mouse for 456 protein-coding gene families involved in innate immunity. Of these, 2 genes in humans and 35 genes in mice exhibited signatures of positive selection. Examining the evolutionary distance between mice and humans, they further identified many genes likely to be under positive selection in the primate and murid lineages. These changes, for the most part, appear to have been fixed within humans and mice, respectively, demonstrating the different evolutionary trajectories that immune genes have taken during evolution. — LMZ

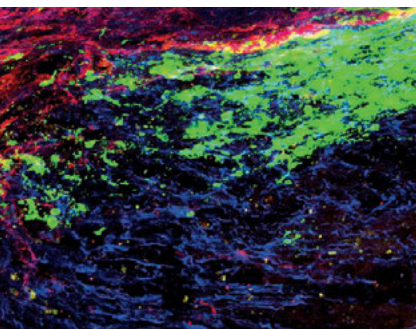
Mol. Biol. Evol. 10.1093/molbev/msv051 (2015).

PROTEIN FOLDING

Interfering in an aggregation pathway

Most dementia cases are caused by neurodegenerative Alzheimer's disease. Plaques composed of fibrils of a 42-residue amyloid- β peptide (A β 42) are characteristic of this disease. There is evidence that neurotoxicity is caused by A β 42 oligomers rather than the fibrils, but fibrils catalyze the

formation of oligomers. Cohen *et al.* show that the human chaperone domain Briochos binds to the surface of A β 42 fibrils and prevents them from catalyzing oligomer formation. In electrophysiology experiments in mouse brain slices, Briochos prevented the inhibition of neural oscillations caused by A β 42 aggregation. In this case, a chaperone acts not by promoting folding or preventing misfolding but by targeting a





SPECIATION

Not a panacea

Emerging genetic technologies, such as single-nucleotide anonymous markers (SNPs), have provided incredible insight about speciation. Mason and Taylor used hundreds of thousands of SNPs in conjunction with gene expression and niche modeling to define patterns of speciation in the Holarctic redpoll species flock, which consists of three morphologically distinct species in the genus *Acanthis*. Despite the large number of loci, they found almost no genetic divergence among the three species, although they did reveal differences in gene expression and slight differences in niche use. They suggest that speciation in this group may be on-going, perhaps driven by small ecological shifts, and argue that even high-powered genetic techniques may not be able to uncover a species' whole story. — SNV

Mol. Ecol. 10.1111/mec.13140 (2015).

Though morphologically distinct, the three species of Holarctic redpolls, including this hoary redpoll, display almost no genetic divergence

nucleation step in the aggregation pathway. — VV

Nat. Struct. Mol. Biol. 10.1038/nsmb.2971 (2015).

PHYSICS

Shocking aluminum into a warm dense state

In some extreme environments (such as the interior of Saturn, for example), matter is a dense soup of strongly interacting particles: "warm dense matter" by name. Scientists can create this regime in the laboratory by hitting a material with powerful laser beams, causing shock

waves that lead to melting. Fletcher *et al.* monitored the properties of a thin sample of aluminum as it transformed from a solid into warm dense matter, its density more than doubling in the process. Using x-ray scattering and comparing their results to model calculations, they found that short-range repulsive interactions between ions played a major role in the transition. — JS

Nat. Photon. 10.1038/nphoton.2015.41 (2015).

EDUCATION

Out with tradition and in with inquiry

Replacing traditional chemistry labs with inquiry-based laboratories that mimic a research project is no easy feat. Hartings *et al.* describe the creation and assessment of two, two-semester-long, student-driven, faculty-assisted laboratory curricula. What makes this approach unique is that the students control the research direction. Research done in the first semester is considered to be a control experiment forming the basis for the second

semester, which is then dictated by the expertise and interest of the researchers. The research trajectory continues as the second-semester experiments from one year become the control experiments for the next year. This allows the research project to continually evolve according to student decisions, making it a research project that truly belongs to students. — MM

J. Chem. Educ. 10.1021/ed500793q (2015).

CELL BIOLOGY

Keeping the cell nucleus pumped up

The nucleus is the most prominent organelle inside eukaryotic cells. It is often roughly spherical in shape and houses the genomic DNA. Nuclear Lamins are important for maintaining nuclear shape, and deformed nuclei are often associated with premature aging diseases. Verboon *et al.* find that the fruit fly gene *washout* (*wash*), involved in maintaining endosome shape in the cytoplasm, is also required to maintain the smooth spherical shape of the nucleus. Wash protein interacts with Lamin and is associated

with heterochromatin in the nucleus. It also helps organize chromosomes and subnuclear domains, such as the nucleolus and cajal bodies. — GR

Curr. Biol. 25, 804 (2015).

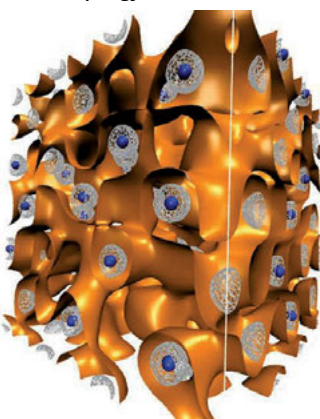
ANTIBIOTIC RESISTANCE

Challenging antimicrobial growth trends

Antimicrobial use in animal production could exceed 100,000 tons a year by 2030. Chronic use of growth-promoting antimicrobials in farming has selected for resistant bacteria that have spread into humans. Facing the reluctance of the food and veterinary industries to report on antimicrobial sales, Van Boeckel *et al.* used statistical models to map and project global antimicrobial consumption. By far the biggest current and future consumer is China, followed by the United States, but Brazil, India, and Mexico also are or soon will be major users, along with other transitional countries seeking to intensify animal production for their increasingly affluent societies who are demanding more meat to eat. — CA

Proc. Natl. Acad. Sci. U.S.A. 10.1073/pnas.1503141112 (2015).

Simulation of warm dense matter topology



ALSO IN SCIENCE JOURNALS

Edited by Caroline Ash

PLANT ECOLOGY

Biodiversity protects grassland stability

How biodiversity interacts with ecosystem stability and productivity is key to understanding the impacts of environmental changes on ecosystem functions. In a series of decade-long experiments in temperate grassland, Hautier *et al.* manipulated nitrogen, water, carbon dioxide, herbivory, and fire. In all cases, plant species diversity was important for preserving ecosystem function during environmental change. Hence, the preservation and restoration of biodiversity buffer ecosystems against anthropogenic assault. — AMS

Science, this issue p. 336

VERTEBRATE EVOLUTION

Similar shapes inhabit the sea

Over biological history, several different groups of vertebrate tetrapods have reinvaded the marine environment. Although these groups are widely distributed among reptiles, mammals, amphibians, and birds, the shapes they have evolved are remarkably similar. Kelley and Pyenson review the literature on marine vertebrate groups over time and describe the innovations that facilitated the evolution of these marine forms, the environmental conditions that selected for such convergence of form, and the threats they face from future environment change. — SNV

Science, this issue p. 301

SKIN FIBROSIS

Fibroblasts in fibrosis

Excess fibrous connective tissue, similar to scarring, forms during the repair of injuries. Fibroblasts are known to be involved, but their role is poorly characterized. Rinkevich *et al.*

identify two lineages of dermal fibroblasts in the dorsal skin of mice (see the Perspective by Sennett and Rendl). A fibrogenic lineage, defined by embryonic expression of *Engrailed-1*, plays a central role in dermal development, wound healing, radiation-induced fibrosis, and cancer stroma formation. Targeted inhibition of this lineage results in reduced melanoma growth and scar formation, with no effect on the structural integrity of the healed skin, thus indicating therapeutic approaches for treating fibrotic disease. — BAP

Science, this issue p. 302;
see also p. 284

ACTIVE GALAXIES

The polarized mark of magnetic fields

Powerful twin jets of plasma often reach more than tens of thousands of light-years from their base in an active galactic nucleus (AGN). Astronomers are still at work investigating what can corral the jets so tightly and propel them so far. Martí-Vidal *et al.* may have found the answer hiding in polarized light signals that show evidence of a phenomenon called Faraday rotation. This measure can indicate the strength of the magnetic field present, which for the AGN PKS 1830-211 is as strong as a few Gauss. The knowledge that magnetic fields have a driving role brings us closer to understanding this phenomenon. — MMM

Science, this issue p. 311

GALAXY EVOLUTION

Eat your heart out, old galaxies

Most galaxies exceeding 100 billion solar masses are dense spheroids that exhibit no star-forming activity in the present day. Nevertheless, galaxies of the same size were

actively forming stars when the universe was only a few billion years old. Tacchella *et al.* used integral-field spectroscopy and high-resolution imaging to map the distributions of star formation rates and stellar mass densities within ancient galaxies. Star formation apparently quenched first in the center, while remaining lively in the galactic outskirts, with quenching taking a few billion years to proceed outward. — MMM

Science, this issue p. 314

LUNAR FORMATION

Traces of collisions within collisions

The Moon is widely accepted to have been created by the collision of a Mars-sized body with Earth. However, information about exactly when this event occurred is still welcome. To find out more, Bottke *et al.* compared models and the meteorite record with estimates of impact heating. When ejecta was thrown off during the main collision, high-velocity kilometer-sized fragments hit and heated main-belt asteroids. Evidence of such collisions emerges when pieces of those asteroids turn up as meteorites on Earth. The model and empirical record converge on 4.48 billion years ago, confirming previous estimates reached by different approaches. — MMM

Science, this issue p. 321

CLIMATE WARMING

Smaller differences and greater extremes

Has recent rapid warming in the Arctic affected weather elsewhere in the world? Coumou *et al.* find that some key measures of atmospheric circulation in the Northern Hemisphere have weakened during the summer. This change has been caused by the reduction of the temperature difference between

mid-latitudes and the North Pole. As summertime circulation has decreased in intensity, episodes of hot weather have become more persistent because there are fewer storms to bring cooler conditions. — HJS

Science, this issue p. 324

CLIMATE WARMING

Disappearing faster around the edges

The floating ice shelves around Antarctica, which buttress ice streams from the continent and slow their discharge into the sea, are thinning at faster rates. Paolo *et al.* present satellite data showing that ice shelves in many regions around the edge of the continent are losing mass. This result increases concern about how fast sea level might rise as climate continues to warm. If warming continues to cause ice shelves to thin, as they have for the past couple of decades, their disappearance may allow land-based ice to collapse and melt. — HJS

Science, this issue p. 327

INFECTIOUS DISEASE

Toward broad-spectrum antiviral drugs

For many emerging viruses such as Ebola and dengue, no licensed drug treatments exist. In a Perspective, Bekerman and Einav argue that broad-spectrum antiviral drugs could play a key role in treating infections caused by these and other viruses. These drugs can either target the virus or the host cell. Drugs licensed for treating other diseases, including several cancer drugs, are also showing promise as possible antiviral treatments. If challenges such as toxicity and drug resistance can be addressed, broad-spectrum antiviral drugs will be a useful complement to existing narrow-spectrum approaches. — JFU

Science, this issue p. 282

SURFACE STRUCTURE

Metal clusters really close-up

Atomic force microscopy (AFM) can be used to reveal subatomic structures. By this means, Emmrich *et al.* found that individual copper and iron atoms formed toroidal structures on a copper surface. These shapes arise from the electrostatic attractions in the center of the atoms and Pauli repulsions at their edges. Individual atoms within clusters have underlying surface symmetry and can bind to different surface sites as clusters form. — PDS

Science, this issue p. 308

PROTEIN STRUCTURE

Engineering super- enzyme function

Understanding how protein domains and subunits operate is critical for engineering novel functions into proteins. Arslan *et al.* introduced intramolecular crosslinks between two domains of the *Escherichia coli* helicase Rep, which unwinds DNA. By inserting linkers of different lengths, the domains can be held either “open” or “closed.” The closed conformation activates the helicase, but it can also generate super-helicases capable of unzipping long stretches of DNA at high speed and with considerable force. Comstock

et al. used optical tweezers and fluorescence microscopy to simultaneously measure the structure and function of the bacterial helicase UvrD. They monitored its DNA winding and unwinding activity and its shape during these activities. The motor domain also has a “closed” conformation during DNA unwinding and switches to a reversed “open” conformation during the zipping-up interaction. — GR

Science, this issue p. 344 and p. 352

PHYSIOLOGY

Red cells need leucine for hemoglobin

Inhibitors of the protein complex mTORC1 are used clinically, but they can cause anemia. Low availability of the amino acid leucine inhibits mTORC1 activity, which suppresses protein synthesis by blocking mRNA translation. The globin proteins in hemoglobin have a particularly high percentage of leucine residues. Chung *et al.* (see also the Focus by Nathan) found that hemoglobin production by developing red blood cells was decreased by deficiency or inhibition of LAT3, a transporter that enables cells to take up leucine. Specifically, inadequate leucine uptake prevented the translation of globin-encoding transcripts. — WW

Sci. Signal. **8**, ra34 and fs9 (2015).

REVIEW SUMMARY

VERTEBRATE EVOLUTION

Evolutionary innovation and ecology in marine tetrapods from the Triassic to the Anthropocene

Neil P. Kelley^{1,2*} and Nicholas D. Pyenson^{1,3}

BACKGROUND: More than 30 different lineages of amphibians, reptiles, birds, and mammals have independently invaded oceans ecosystems. Prominent examples include ichthyosaurs and mosasaurs during the Mesozoic (252 to 66 million years ago) and penguins and sea otters during the Cenozoic (66 million years ago to the present). In today's oceans, marine tetrapods are ecologically important consumers with trophic influence disproportionate to their abundance. They have occupied apex roles in ocean food webs for more than 250 million years, through major changes in ocean and climate, and through mass ex-

tinctions. Major paleontological discoveries in the past 40 years have clarified the early land-sea transitions for some marine tetrapods (e.g., whales, sea cows), although the terrestrial origins of many lineages remain obscure. Incipient invasions appear frequently in marine tetrapod history, but such early transitions account for only a small proportion of the total fossil record of successful marine lineages, which in some cases persist for hundreds of millions of years.

ADVANCES: Marine tetrapods provide ideal models for testing macroevolutionary hypotheses because the repeated transitions between

land and sea have driven innovation, convergence, and diversification against a backdrop of changing marine ecosystems and mass extinctions. Recent investigations across a broad range of scales—from molecules to food webs—have clarified the phylogenetic scope, timing, and ecological consequences of these repeated innovations. Studies of the physiology and functional morphology of living species have illuminated the constraints and tradeoffs that

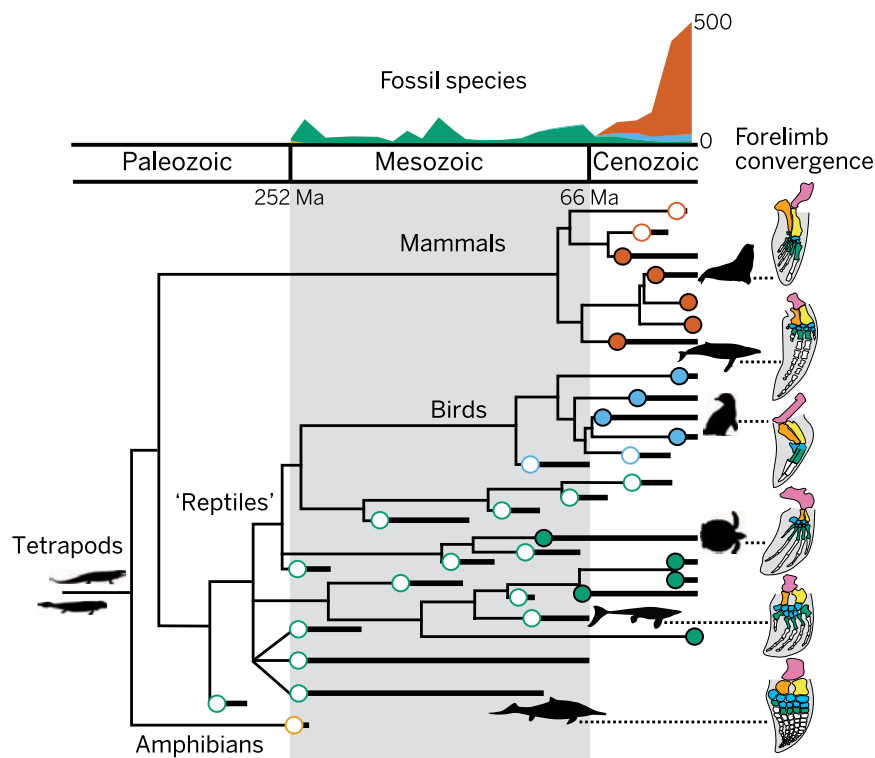
ON OUR WEB SITE

Read the full article at <http://dx.doi.org/10.1126/science.aaa3716>

shape the pathway of initial marine invasions. Comparative studies on muscle myoglobin concentration or the evolution of sex determination mechanisms, for example, have revealed

rampant convergence for these adaptive traits in the marine realm. Exceptionally preserved fossils have also revealed insights into reproductive biology, soft tissue structures, and trophic interactions. Fossils provide critical baselines for understanding historical changes in marine communities and diversity through time, and these baselines remain vital for evaluating the ongoing and severe anthropogenic disturbance to marine tetrapod populations and marine ecosystems as a whole.

OUTLOOK: Technological advances in remote sensing and biologging will continue to provide crucial insights into the macroecology of marine tetrapods below the water's edge. Field data, when combined with extensive vouchers represented in museum collections, provide the basis for integrative models of the function and ecology of these logistically challenging organisms. Placed in a phylogenetic comparative framework, these data can enable tests of hypotheses about macroevolutionary patterns. Although perpetually incomplete, new fossil discoveries continue to improve our understanding of the early land-sea transitions in lineages and reveal past ecologies that could not have otherwise been predicted. Emerging imaging, molecular, and isotopic techniques provide an opportunity to expand the investigational scope for studying extinct taxa and to inform our understanding of how living species evolved. Lastly, resolving the full evolutionary scope of marine tetrapod history provides context for the origins of modern ecological patterns and interactions, which are fundamentally being altered by human activities. ■



A unified view of marine tetrapod evolution. Circles mark initial invasions of marine tetrapod groups. Extinct and extant lineages are denoted by open and solid circles, respectively (yellow, amphibians; green, nonavian reptiles; blue, birds; red, mammals). Top curve summarizes marine tetrapod fossil richness through time. Schematic limb drawings demonstrate convergent hydrodynamic forelimbs in marine tetrapods (top to bottom): sea lion, whale, penguin, sea turtle, mosasaur, ichthyosaur. Ma, millions of years ago.

¹Department of Paleobiology, National Museum of Natural History, Smithsonian Institution, Washington, DC 20013, USA.

²Department of Earth and Environmental Sciences, Vanderbilt University, Nashville, TN 37240, USA.

³Departments of Mammalogy and Paleontology, Burke Museum of Natural History and Culture, Seattle, WA 98195, USA.

*Corresponding author. E-mail: kelleyp@si.edu

Cite this article as N. P. Kelley, N. D. Pyenson, *Science* 348, aaa3716 (2015). DOI:10.1126/science.aaa3716

REVIEW

VERTEBRATE EVOLUTION

Evolutionary innovation and ecology in marine tetrapods from the Triassic to the Anthropocene

Neil P. Kelley^{1,2*} and Nicholas D. Pyenson^{1,3}

Many top consumers in today's oceans are marine tetrapods, a collection of lineages independently derived from terrestrial ancestors. The fossil record illuminates their transitions from land to sea, yet these initial invasions account for a small proportion of their evolutionary history. We review the history of marine invasions that drove major changes in anatomy, physiology, and ecology over more than 250 million years. Many innovations evolved convergently in multiple clades, whereas others are unique to individual lineages. The evolutionary arcs of these ecologically important clades are framed against the backdrop of mass extinctions and regime shifts in ocean ecosystems. Past and present human disruptions to marine tetrapods, with cascading impacts on marine ecosystems, underscore the need to link macroecology with evolutionary change.

More than 30 lineages of tetrapods (amphibians, reptiles, birds, and mammals) independently invaded marine ecosystems during the Phanerozoic (Fig. 1). Such repeated transitions from terrestrial or freshwater to marine habitats are generally uncommon in other clades (1). Reconfigurations in morphology, physiology, life history, and sensory systems characterize each transition. For example, differential constraints on movement between these realms—gravity on land versus drag in water—led to similar locomotory adaptations in marine tetrapods (2) (Fig. 2).

Sequences of fossil cetaceans (3) and sirenians (4) from Eocene rocks provide the best examples of major morphological transformations following marine invasions. Both groups show pelvic decoupling from the vertebral column and subsequent reduction of the pelvis and hindlimbs; later specializations included forelimb streamlining, tail propulsion, and posterior migration of the nostrils. Unfortunately, the early histories of most other marine tetrapod lineages remain obscure. For example, the freshwater carnivorous *Puijila darwini* provides clues about the origins of pinnipeds (5), but it is geologically younger than other marine stem pinnipeds (6) and is thus not likely a direct ancestor of modern pinnipeds. Likewise, semi-aquatic Permian reptiles, initially proposed to represent plesiosaur ancestors (7), are not closely related to plesiosaurs in recent analyses (8); the Early Cretaceous turtle *Santanachelys* (9) was once viewed as a stem predecessor to mod-

ern sea turtles, but this position is no longer supported (10). Thus, origins of several important marine tetrapod groups remain essentially unknown, with the oldest known fossil representatives exhibiting derived morphologies without obvious terrestrial antecedents. Prominent examples include penguins (11) and ichthyosaurs (12), although the recently described basal ichthyosauriform *Cartorhynchus* may clarify the origins of the latter (13).

The history of terrestrial-marine transitions reveals links between Earth system changes and marine tetrapod invasions, modulated by ecology and physiology. Marine transgressions and warming episodes coincided with Mesozoic and Early Cenozoic marine tetrapod invasions (3, 4, 14–18). Modern marginal marine tetrapods are concentrated in low-latitude mangroves, estuaries, and archipelagos (19). The paleoenvironmental context of marginal marine tetrapod fossils (7, 20) likewise indicates that warm, shallow marginal marine habitats provide favorable settings for terrestrial-marine transitions, especially in ectotherms. Conversely, mid-Cenozoic cooling and increases in marine productivity—particularly in the North Pacific and Southern Ocean—coincided with bird and mammal invasions (21, 22), and these regions remain hotspots of marine mammal diversity (23). However, such relationships are not always rigid throughout the history of a clade: Cetaceans evolved in shallow equatorial seas (18) but now thrive in high-latitude oceans; the origin of penguins preceded Southern Hemisphere cooling by several million years (24).

Studies of living marginal marine species illuminate ecological (25, 26), functional (2, 27–29), and physiological (30–32) pathways that facilitate transitions. A common theme is the high degree of plasticity in ecologically marginal taxa (26, 28, 31). Isotopic investigations of fossils suggest similar

patterns, demonstrating mixed habitat and resource use (33). Repeated independent invasions among some clades suggest that certain ecologies and/or body plans may predispose groups to marine transitions. Independent adaptation to marine lifestyles among close relatives simultaneously or in close succession would complicate efforts to decipher and enumerate transitions in the fossil record (34, 35).

Convergent evolution from molecules to morphology

Marine tetrapods provide canonical illustrations of evolutionary convergence (Fig. 2) (36), widely regarded as repeated solutions to problems imposed by physical contrasts between land and water. Simple visual comparisons, however, cannot fully decipher the processes that shape evolutionary convergence. Apparent similarities can mask differences in functional performance (37), and mechanical convergence can be achieved with alternative morphological solutions, often constrained by phylogeny (38). Thus, the dorsoventral caudal propulsion of cetaceans derives from the bounding locomotory mode of terrestrial mammalian ancestors (2), while the lateral caudal propulsion of ichthyosaurs evolved from the locomotion of lizard-like predecessors (39).

Quantitative functional morphology provides a means to quantify and compare performance and functional trade-offs, particularly in species that spend time both on land and in the water, such as snakes (29) and pinnipeds (40). Functional trade-offs can ultimately drive specialization and steer evolutionary convergence, as with repeated loss of flight among seabirds specialized for aquatic locomotion (41). In vivo studies of feeding performance provide similar insight into functional trade-offs and specialization (42–44), which shaped convergence in marine tetrapod feeding systems (45).

Increased bone density evolved repeatedly in coastal marine tetrapods for stability and buoyancy regulation (46–51). Conversely, decreased bone density has evolved among many pelagic groups, reducing the costs of sustained swimming, or as a consequence of increased growth rates (50). Some lineages, such as cetaceans (48, 49), ichthyosaurs (13, 49), and sauropterygians (51), transitioned through these contrasting phases sequentially, with increased bone density during early evolution followed by reduced bone density after open marine adaptation. The evolution of insulating structures in marine mammals follows a similar progression, with thick fur in coastal invaders replaced by thick insulating fat for energy storage and streamlining in more oceanic marine mammals (52). Fossil anatomy reveals the evolution of countercurrent heat exchange in penguins (53), convergent with similar systems in marine mammals.

The scope of recent studies of convergent evolution extends beyond morphology to include molecular physiology (54), metabolism and thermoregulation (55, 56), and life history (56, 57). Genomic investigations have revealed convergent genetic origins of important innovations, such as

¹Department of Paleobiology, National Museum of Natural History, Smithsonian Institution, Washington, DC 20013, USA.

²Department of Earth and Environmental Sciences, Vanderbilt University, Nashville, TN 37240, USA. ³Departments of Mammalogy and Paleontology, Burke Museum of Natural History and Culture, Seattle, WA 98195, USA.

*Corresponding author. E-mail: kelleynp@si.edu

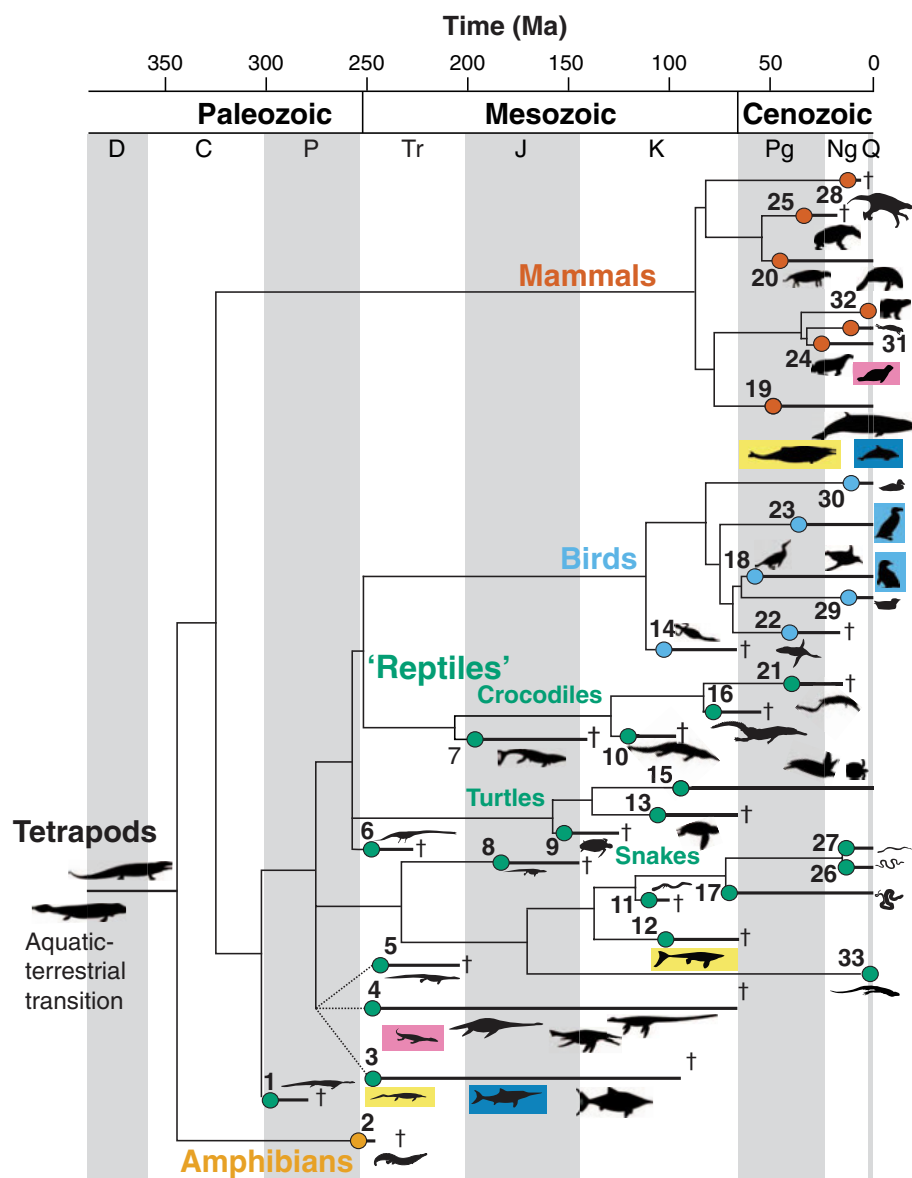


Fig. 1. Temporal and phylogenetic distribution of marine tetrapod groups. Circles indicate first appearance datum (FAD) for each lineage based on fossils, or divergence estimates for groups lacking a fossil record (136); daggers denote extinctions. Marine tetrapod taxa are numbered in order of appearance in the fossil record: (1) Mesosauria, (2) Trematosauria, (3) Ichthyosauromorpha, (4) Sauropterygia, (5) Thalattosauriformes, (6) Tanystropheidae, (7) Thalattosuchia, (8) Pleurosauridae, (9) Plesiochelyidae, (10) Pholidosauridae, (11) Simiolophiidae, (12) Mosasauridae, (13) Protostegidae, (14) Hesperornithiformes, (15) Chelonioidea, (16) Dyrosauridae, (17) Acrochordoidea, (18) Sphenisciformes, (19) Cetacea, (20) Sirenia, (21) Gryposuchinae, (22) Pliopteridae, (23) Alcidae, (24) Pinnipedimorpha, (25) Desmostylia, (26) Laticaudini, (27) Hydrophiini, (28) *Thalassocnus*, (29) *Pelecanoides*, (30) *Tachyeres*, (31) *Enhydra*, (32) *Ursus maritimus*, (33) *Amblyrhynchus*. Colored boxes match convergent taxa shown in Fig. 2. A to D, Ma, millions of years ago. (Silhouettes from phylopic.org; see supplementary materials for usage and attribution details.)

sex determination mechanisms (58), myoglobin adaptations facilitating deep diving (54), and echolocation (59). Stable isotopes from fossils elucidate parallel histories of habitat shift in early cetaceans and sirenians (33) and convergent evolution of endothermy in Mesozoic marine reptiles (53). Recent breakthroughs in fossil pigment reconstruction have resolved structural and pigment adaptations in fossil seabird feathers (60) and have revealed widespread dark coloration in

fossil marine reptiles, possibly for temperature regulation or ultraviolet light protection (55).

Exceptionally preserved fossils (57, 61, 62) document convergent reproductive adaptations in marine reptiles. Recently discovered early ichthyosaur fossils (62) extend the history of viviparity in this group back to the Early Triassic and indicate that viviparity evolved in terrestrial fore-runners as an enabling factor for, rather than an adaptive response to, aquatic life. Fossils sug-

gest that some marine reptiles converged upon K-selected life histories observed among marine mammals (57). Aquatic birth evolved early in cetacean and sirenian evolution, but these transitions are so far only partly constrained by fossils (63).

Causes and consequences of convergence, innovation, and radiation

In addition to external drivers, convergent evolution is shaped by the underlying genetic and developmental pathways that give rise to convergent structures. Thus, repeated evolution of hydrodynamic limbs (Fig. 2E) (64) and axial modifications (65) likely exploited parallel developmental mechanisms. Such shared pathways may extend to the level of gene regulation linking genomic and phenotypic convergence and innovation. Recent work on marine mammal genomic convergence has questioned the prevalence of such linkages (66); however, more work is needed to evaluate potential scaling of convergence from gene to phenotype.

Innovations facilitate and constrain downstream evolution, as illustrated in the discrete pathways from drag-based to lift-based swimming in limb- and tail-propelled aquatic mammals (2). Likewise, independent innovation of aquatic birth in multiple marine reptile and marine mammal lineages removed the constraints of terrestrial locomotion, enabling limb and skeletal modification to increase swimming performance, as well as gigantism in some clades. Convergent evolutionary pathways [e.g., the emergence of tail-driven locomotion in ichthyosaurs, mosasaurs, and whales (Fig. 2A)] might follow similar tempos across groups (67), but this hypothesis awaits further testing.

Particularly diverse clades have frequently been characterized as adaptive radiations facilitated by new ecological opportunities after marine invasions (68). However, external factors may be equally important in shaping and pacing these radiations (69). Although diverse clades are often ecologically and morphologically disparate, as predicted under adaptive radiation models (70), diversity and disparity are not tightly coupled in other radiations (71).

Diversification can be triggered by innovations that occur well after initial invasions. For example, echolocation and baleen—two key innovations that evolved tens of millions of years after whales first entered the oceans—mark the emergence of crown cetaceans (72), the most species-rich marine tetrapod clade. Hydrophiine sea snakes, which entered marine environments in the last 6 million years and now comprise at least 60 species (71, 73), provide a key example of a marine tetrapod group in the midst of major radiation. Even within this group, diversity is heterogeneously distributed within subclades and linked to specific intraclade innovations, rather than simply reflecting rapid niche expansion after initial marine invasion (71).

Iterative evolution and ecological turnover

Marine tetrapods first diversified during the restructuring of marine ecosystems that followed

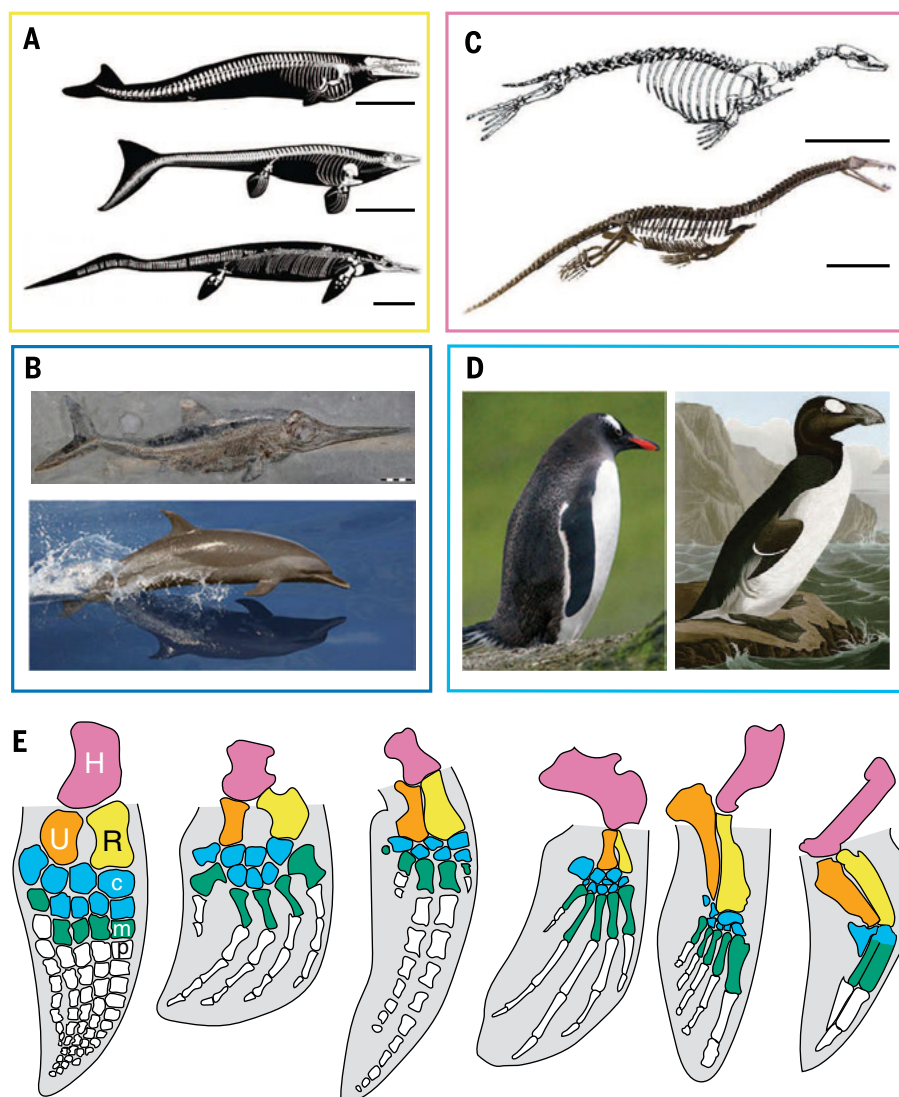


Fig. 2. Convergent morphology in marine tetrapods. Similar anatomy evolved among lineages that independently adopted marine lifestyles. From top to bottom: (A) early whale *Dorudon*, mosasaur *Platecarpus*, ichthyosaur *Cymbospondylus* (scale bars, 1 m); (B) ichthyosaur *Stenopterygius*, dolphin *Stenella*; (C) early seal *Acrophoca*, sauropterygian *Nothosaurus* (scale bars, 50 cm); (D) penguin *Pygoscelis* (left), great auk *Pinguinus* (right). (E) Forelimbs of select marine tetrapods (from left to right: ichthyosaur, mosasaur, whale, sea turtle, sea lion, penguin) showing anatomical convergence reflecting limb streamlining [adapted from (36, 64)]. Colors identify homologous elements labeled on ichthyosaur: H, humerus (pink); R, radius (yellow); U, ulna (orange); c, carpals (blue); m, metacarpals (green); p, phalanges (white). Phylogeny and contrasting locomotory patterns account for finer scale differences, such as proportionally longer humeri in forelimb-driven swimmers (sea turtle, sea lion, penguin) relative to tail-driven swimmers (ichthyosaur, mosasaur, whale). See supplementary materials for image sources.

the end-Permian mass extinction, and the rise of the so-called “Modern Fauna” (74). Their appearance has been characterized as a final step in the bottom-up reassembly of marine ecosystems after a delayed recovery (75, 76). However, the early appearance of predatory marine tetrapods in the Triassic has recently been cited as evidence that recovery was not delayed after all (77). Although later Mesozoic and Cenozoic invasions replaced these early groups, marine tetrapods have remained a persistent fixture of marine ecosystems since the Triassic. Some replacements coincided with mass extinctions (Fig. 1) (78);

others were staggered across intervals of gradual faunal change (78, 79).

Persistent biological processes such as competition (“Red Queen”) and stochastic environmental factors (“Court Jester”) (80) may regulate marine tetrapod community structure and diversity at different time scales (81). Pelagic habitats are typically dominated by one or two cosmopolitan marine tetrapod clades with long histories [e.g., ichthyosaurs from the Triassic to Cretaceous (78), plesiosaurs from the Jurassic to the Cretaceous–Paleogene (K–Pg) boundary (78), cetaceans since the Eocene (3)]. Near-shore communities often

host more lineages with higher endemism and frequent turnover (16, 82–84). Specific spatial and temporal successions hint at competitive interactions, as among flightless seabirds and marine mammals competing for shore space (22), replacement of herbivorous desmostylians by sirenians in the North Pacific (82), and replacement of phocids by otariids in South America (83).

These episodes of replacement between lineages are mirrored by iterative patterns within lineages. For example, evolution of herbivory and durophagy (feeding on hard-shelled prey) drove repeated convergent feeding morphologies in living and fossil sea turtles (85). Similarly, independent invasions of freshwater ecosystems by different odontocete lineages gave rise to a convergent “river dolphin” morphotype (86). Ecological interactions among sympatric relatives also drive iterative evolution. Multispecies fossil sirenian assemblages show parallel patterns of ecomorphological partitioning (82), contrasting with the relictual and disjunct distribution of living species. Sympatric or parapatric ecomorphs observed in widely distributed odontocetes (87, 88) have arisen through niche differentiation and onshore-offshore partitioning. Cryptic speciation and iteration is common among sea snakes, with repeated parallel evolution of morphotypes (71). Iterative evolution and resource partitioning may account for contrasting morphotypes in co-occurring fossil taxa (82, 89) and repeated evolution of certain morphotypes, such as polyphyletic “pliosaurus” (90).

Marine tetrapods themselves constituted an important trophic resource for other species in Mesozoic ecosystems beginning in the Triassic (76). Intriguingly, although hypercarnivory evolved repeatedly among Cenozoic marine mammals (91, 92), many lineages later specialized on resources at lower trophic levels. Hypercarnivorous species that regularly consume other tetrapods are comparatively rare in modern oceans, represented only by killer whales, leopard seals, and marginal marine crocodiles, all generalist predators that also feed regularly at lower trophic levels (42, 88). The comparative rarity of hypercarnivorous marine tetrapods in modern oceans may reflect different structuring of Mesozoic, Early Cenozoic, and modern marine food webs.

Contrasting Mesozoic and Cenozoic patterns of fossil richness

Patterns in raw marine tetrapod fossil species richness (Fig. 3) resemble those observed in the marine invertebrate record (93–95). Fluctuating Mesozoic diversity reflects repeated extinctions of incumbent clades (Fig. 1) followed by diversification of new groups (78) as well as geologic biases on the marine tetrapod fossil record (14). Contrasting patterns between coastal and pelagic Mesozoic marine tetrapod groups (14, 15) point to “common-cause” dynamics, whereby geologic processes that affect marine diversity also control sedimentary rock accumulation (95). The pronounced drop in richness at the K–Pg boundary corresponds to the simultaneous extinction of mosasaurs, plesiosaurs, and other lineages (Figs. 1 and 3).

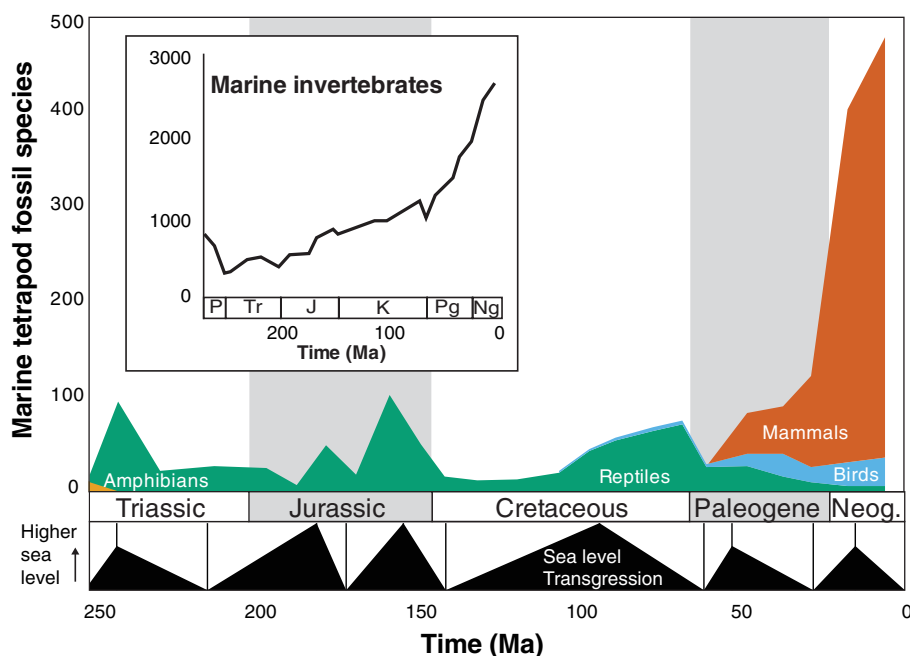


Fig. 3. Marine tetrapod fossil richness. Raw marine tetrapod fossil occurrence binned at intervals of ~10 million years [from (81)] and marine invertebrate genera [from (94)]. Both groups show episodic variation in fossil richness during the Mesozoic ending with abrupt drop at the K-Pg mass extinction, followed by continually increasing richness during the Cenozoic. Partial correspondence with marine transgression/regression [second order, cycles of ~10 to 100 million years, from (134)] suggests influence of sea level on shallow marine diversity and/or rock record bias, particularly in the Mesozoic.

After the K-Pg mass extinction, Early Cenozoic diversification of cetaceans (3), sirenians (96), and penguins (24, 97) brought Paleogene marine tetrapod richness back to peak Mesozoic levels. The emergence of crown cetaceans (72) and the invasion of pinnipeds (21), along with other groups, coincide with a marked increase in fossil richness to even higher levels. The apparent Cenozoic marine tetrapod diversity increase, like marine invertebrate richness (94), may be inflated by preservation biases (e.g., “pull of the recent”). However, recent investigations of fossil invertebrates (93) and marine mammals (98, 99) propose that increasing Cenozoic richness largely reflects a real biological signal. Fossil bias has been evaluated for some marine tetrapod groups (14, 98), but integrated comparisons of biases across the Mesozoic and Cenozoic are still needed.

Changes in ocean productivity regimes (100) and ecological escalation (101) may help to explain the differing trajectories of Cenozoic and Mesozoic marine tetrapod diversification. Exceptional diversification rates of eutherian mammals (102) might also account for increasing Cenozoic diversity, given the repeated marine invasions of placental mammals during the Cenozoic. However, other groups with elevated diversification rates, including Neoaves and squamates, also invaded marine ecosystems with varying degrees of success, indicating that phylogenetic differences alone cannot account for these differences.

Increasing marine tetrapod diversity since the Mesozoic also tracks increasing marine resources and expanding niches. Clear evidence of herbivory is unknown among marine reptiles until herbiv-

orous sea turtles evolved, coincident with the first seagrasses in the Cretaceous (85), which is consistent with “delayed herbivory” in other marine clades (103). Likewise, there is no evidence for pelagic suspension-feeding marine tetrapods in the Mesozoic (104) and little evidence for deep-diving mesopelagic feeders until the Jurassic (37). These absent ecologies suggest that Early Mesozoic marine food webs were less complex than modern equivalents.

Shifted baselines and marine tetrapod macroecology since the Pleistocene

Marine tetrapod and hominid ecological interactions began at least by the Late Pleistocene, with evidence for Neandertal (*Homo neanderthalensis*) exploitation of marine mammals in Gibraltar, Spain (105). Humans have continued to directly and indirectly interact with marine ecosystems ever since this time (106). Although these impacts have lagged behind profound human perturbations to terrestrial ecosystems, technological innovation has escalated their rate and magnitude in recent centuries (107).

The extinction of Steller’s sea cow (*Hydrodamalis gigas*) marks the first well-documented marine mammal species extinction in historic times (108). Hunting brought some cetacean species perilously close to extinction (109) and exterminated at least two pinniped species (110, 111). Historically, several marine mammal species were thought extinct until refugial populations were rediscovered (112, 113). Seabirds have been similarly vulnerable to human hunting, with historic and prehistoric extinctions of large flightless

seabirds (114–116) and others critically endangered (117). Many living marine reptiles also risk extinction—including six of seven sea turtle species—largely because of human exploitation and habitat alteration (117). The conservation status of many marine tetrapod species is poorly known because of the difficulties of studying wild marine populations.

The only cetacean extinction at human hands, the Yangtze River dolphin (*Lipotes*), was largely caused by habitat degradation (118). Before the end of this decade, another cetacean, the vaquita (*Phocoena sinus*), may be driven extinct through by-catch in small-scale fisheries in the Gulf of California (119). Such indirect impacts are a growing concern, with recent attention turning to ship collisions (120), shipping noise (121), military sonar (122), microplastics (123), and human-borne pathogens (124), among other emerging threats (107).

Anthropogenic climate change is already driving changes in marine tetrapod populations, particularly in polar ecosystems (125). Shrinking sea ice and changing ocean thermal gradients are also driving range shifts, most strikingly documented by repeated recent dispersal from the Pacific into the Atlantic by gray whales (*Eschrichtius*) via an ice-free northwest passage (126), potentially anticipating a recolonization of the Atlantic following extirpation four centuries ago (127). Global warming may have major impacts on ectothermic marine reptiles, potentially altering range limits, activity levels (128), and even the sex ratio in species with temperature-dependent reproduction (129). Potential feedbacks between anthropogenic warming and complex climate dynamics such as El Niño—known to trigger marine tetrapod population collapses (130)—suggest that impacts of climate change on marine tetrapods may be abrupt, episodic, and difficult to predict (100).

Anthropogenic declines in marine mammal populations also have downstream effects on marine food webs (131) via trophic cascades, for example, with killer whale–sea otter–mysticete interactions off southeast Alaska (132) and mysticete–seal–penguin interactions in the Southern Ocean (133). Emerging technologies such as animal-borne recording devices (used in biologging) promise to reveal new details about marine tetrapod ecology (134) and the state of the oceans themselves, such as information about ocean currents provided by biologged data (135).

Conclusions

Despite their status as conservation icons, major questions remain concerning marine tetrapod macroecology, morphology, and even alpha taxonomy. New discoveries and new techniques are helping to frame and test hypotheses about marine tetrapod evolution. Realizing the full potential of these advances requires integrating data sets from disparate disciplines to address unifying questions in ecology, evolutionary biology, and Earth systems history. Marine tetrapods have been ecologically influential members of ocean food webs since the end-Permian mass extinction, persisting through later mass extinctions, anoxic

events, and ocean restructuring. The ecological importance of marine tetrapods in modern food webs raises questions about their role during major episodes of change and their sensitivity to bottom-up perturbations in the past. Evaluating the place of tetrapods in contemporary ocean ecosystems also requires accounting for shifts from baseline abundances driven by human activities. Understanding the full history of marine tetrapods provides necessary context for constraining the scope of potential future shifts in marine ecosystems.

REFERENCES AND NOTES

- G. J. Vermeij, R. Dudley, Why are there so few evolutionary transitions between aquatic and terrestrial ecosystems? *Biol. J. Linn. Soc. London* **70**, 541–554 (2000). doi: [10.1111/j.1095-8312.2000.tb00216.x](#)
- F. E. Fish, Transitions from drag-based to lift-based propulsion in mammalian swimming. *Am. Zool.* **36**, 628–641 (1996).
- M. D. Uhen, The origin(s) of whales. *Annu. Rev. Earth Sci.* **38**, 189–219 (2010). doi: [10.1146/annurev-earth-040809-152453](#)
- D. P. Domning, The earliest known fully quadrupedal sirenian. *Nature* **413**, 625–627 (2001). doi: [10.1038/35098072](#); pmid: [11675784](#)
- N. Rychczynski, M. R. Dawson, R. H. Tedford, A semi-aquatic Arctic mammalian carnivore from the Miocene epoch and origin of Pinnipedia. *Nature* **458**, 1021–1024 (2009). doi: [10.1038/nature07985](#); pmid: [19396145](#)
- A. Berta, C. E. Ray, A. R. Wyss, Skeleton of the oldest known pinniped, *Enaliarctos maelsi*. *Science* **244**, 60–62 (1989). doi: [10.1126/science.244.4900.60](#); pmid: [17818847](#)
- R. L. Carroll, Plesiosaur ancestors from the Upper Permian of Madagascar. *Philos. Trans. R. Soc. London Ser. B* **293**, 315–383 (1981). doi: [10.1098/rstb.1981.0079](#)
- J. M. Neenan, N. Klein, T. M. Scheyer, European origin of placodont marine reptiles and the evolution of crushing dentition in Placodontia. *Nat. Commun.* **4**, 1621 (2013). doi: [10.1038/ncomms2633](#)
- R. Hirayama, Oldest known sea turtle. *Nature* **392**, 705–708 (1998). doi: [10.1038/33669](#)
- W. G. Joyce, J. F. Parham, T. R. Lyson, R. C. Warnock, P. C. Donoghue, A divergence dating analysis of turtles using fossil calibrations: An example of best practices. *J. Paleontol.* **87**, 612–634 (2013). doi: [10.1666/12-149](#)
- D. T. Ksepka, S. Bertelli, N. P. Giannini, The phylogeny of the living and fossil Sphenisciformes (penguins). *Cladistics* **22**, 412–441 (2006). doi: [10.1111/j.1096-0031.2006.00116.x](#)
- M. W. Maisch, Phylogeny, systematics, and origin of the Ichthyosauria—the state of the art. *Palaeodiversity* **3**, 151–214 (2010).
- R. Motani *et al.*, A basal ichthyosauriform with a short snout from the Lower Triassic of China. *Nature* **517**, 485–488 (2015). doi: [10.1038/nature13866](#)
- R. B. Benson, R. J. Butler, Uncovering the diversification history of marine tetrapods: Ecology influences the effect of geological sampling biases. *Geol. Soc. London Spec. Publ.* **358**, 191–208 (2011). doi: [10.1144/SP358.13](#)
- N. P. Kelley, R. Motani, D. Y. Jiang, O. Rieppel, L. Schmitz, Selective extinction of Triassic marine reptiles during long-term sea-level changes illuminated by seawater strontium isotopes. *Palaeogeogr. Palaeoclimatol. Palaeoecol.* **400**, 9–16 (2014). doi: [10.1016/j.palaeo.2012.07.026](#)
- J. E. Martin, R. Amiot, C. Lécuyer, M. J. Benton, Sea surface temperature contributes to marine crocodylomorph evolution. *Nat. Commun.* **5**, 4658 (2014). doi: [10.1038/ncomms5658](#)
- N. Bardet, A. Houssaye, J. C. Rage, X. Pereda Suberbiola, The Cenomanian-Turonian (Late Cretaceous) radiation of marine squamates (Reptilia): The role of the Mediterranean Tethys. *Bull. Soc. Geol. Fr.* **179**, 605–622 (2008). doi: [10.2113/gssgfbull.179.6.605](#)
- P. D. Gingerich, N. A. Wells, D. E. Russell, S. M. Shah, Origin of whales in epicontinental remnant seas: New evidence from the early Eocene of Pakistan. *Science* **220**, 403–406 (1983). doi: [10.1126/science.220.4595.403](#); pmid: [17831411](#)
- J. C. Murphy, Marine invasions by non-sea snakes, with thoughts on terrestrial-aquatic-marine transitions. *Integr. Comp. Biol.* **52**, 217–226 (2012). doi: [10.1093/icb/ics060](#); pmid: [22576813](#)
- G. Piñeiro, A. Ramos, C. Goso, F. Scarabino, M. Laurin, Unusual environmental conditions preserve a Permian mesosaur-bearing Konservat-Lagerstätte from Uruguay. *Acta Palaeontol. Pol.* **57**, 299–318 (2011). doi: [10.4202/app.2010.0113](#)
- T. A. Deméré, A. Berta, P. J. Adam, Pinnipedimorph evolutionary biogeography. *Bull. Am. Mus. Nat. Hist.* **279**, 32–76 (2003). doi: [10.1206/0003-0090\(2003\)279<0032:C>2.0.CO;2](#)
- T. Ando, R. E. Fordyce, Evolutionary drivers for flightless, wing-propelled divers in the Northern and Southern Hemispheres. *Palaeogeogr. Palaeoclimatol. Palaeoecol.* **400**, 50–61 (2014). doi: [10.1016/j.palaeo.2013.08.002](#)
- D. P. Tittensor *et al.*, Global patterns and predictors of marine biodiversity across taxa. *Nature* **466**, 1098–1101 (2010). doi: [10.1038/nature09329](#); pmid: [20668450](#)
- J. A. Clarke *et al.*, Paleogene equatorial penguins challenge the proposed relationship between biogeography, diversity, and Cenozoic climate change. *Proc. Natl. Acad. Sci. U.S.A.* **104**, 11545–11550 (2007). doi: [10.1073/pnas.0611099104](#); pmid: [17601778](#)
- W. A. Buttemer, W. R. Dawson, Temporal pattern of foraging and microhabitat use by Galapagos marine iguanas, *Amblyrhynchus cristatus*. *Oecologia* **96**, 56–64 (1993). doi: [10.1007/BF00318031](#)
- D. H. Monson, J. A. Estes, J. L. Bodkin, D. B. Siniff, Life history plasticity and population regulation in sea otters. *Oikos* **90**, 457–468 (2000). doi: [10.1034/j.1600-0706.2000.900304.x](#)
- T. M. Williams, The evolution of cost efficient swimming in marine mammals: Limits to energetic optimization. *Philos. Trans. R. Soc. London Ser. B* **354**, 193–201 (1999). doi: [10.1098/rstb.1999.0371](#)
- F. Aubret, X. Bonnet, R. Shine, The role of adaptive plasticity in a major evolutionary transition: Early aquatic experience affects locomotor performance of terrestrial snakes. *Funct. Ecol.* **21**, 1154–1161 (2007). doi: [10.1111/j.1365-2435.2007.01310.x](#)
- F. Aubret, R. Shine, The origin of evolutionary innovations: Locomotor consequences of tail shape in aquatic snakes. *Funct. Ecol.* **22**, 317–322 (2008). doi: [10.1111/j.1365-2435.2007.01359.x](#)
- D. P. Costa, G. L. Kooyman, Contribution of specific dynamic action to heat balance and thermoregulation in the sea otter *Enhydra lutris*. *Physiol. Zool.* **57**, 199–203 (1984).
- R. L. Cramp, E. A. Meyer, N. Sparks, C. E. Franklin, Functional and morphological plasticity of crocodile (*Crocodylus porosus*) salt glands. *J. Exp. Biol.* **211**, 1482–1489 (2008). doi: [10.1242/jeb.015636](#); pmid: [18424682](#)
- F. Brischoux, Y. V. Kornilev, Hypermnatremia in dice snakes (*Natrix tessellata*) from a coastal population: Implications for osmoregulation in marine snake prototypes. *PLOS ONE* **9**, e92617 (2014). doi: [10.1371/journal.pone.0092617](#)
- M. T. Clementz, A. Goswami, P. D. Gingerich, P. L. Koch, Isotopic records from early whales and sea cows: Contrasting patterns of ecological transition. *J. Vertebr. Paleontol.* **26**, 355–370 (2006). doi: [10.1671/0272-4634\(2006\)26\[355:IRFEWA\]2.0.CO;2](#)
- M. W. Caldwell, A challenge to categories: “What, if anything, is a mosasaur?” *Bull. Soc. Geol. Fr.* **183**, 7–34 (2012). doi: [10.2113/gssgfbull.183.1.7](#)
- X. H. Chen, R. Motani, L. Cheng, D. Y. Jiang, O. Rieppel, The enigmatic marine reptile Nanchangosaurus from the Lower Triassic of Hubei, China and the phylogenetic affinities of Hupehsuchia. *PLOS ONE* **9**, e102361 (2014). doi: [10.1371/journal.pone.0102361](#)
- A. B. Howell, *Aquatic Mammals: Their Adaptations to Life in the Water* (Charles C. Thomas, Baltimore, MD, 1930).
- R. Motani *et al.*, Absence of suction feeding ichthyosaurs and its implications for Triassic mesopelagic paleoecology. *PLOS ONE* **8**, e66075 (2013). doi: [10.1371/journal.pone.0066075](#)
- P. C. Wainwright, M. E. Alfaro, D. I. Bolnick, C. D. Hulsey, Many-to-one mapping of form to function: A general principle in organismal design? *Integr. Comp. Biol.* **45**, 256–262 (2005). doi: [10.1093/icb/45.2.256](#); pmid: [21676769](#)
- R. Motani, H. You, C. McGowan, Eel-like swimming in the earliest ichthyosaurs. *Nature* **382**, 347–348 (1996). doi: [10.1038/382347a0](#)
- J. N. Garrett, F. E. Fish, Kinematics of terrestrial locomotion in harbor seals and gray seals: Importance of spinal flexion by amphibious phocids. *Mar. Mamm. Sci.* **10**, 1111/mms.12170 (2014). doi: [10.1111/mms.12170](#)
- K. H. Elliott *et al.*, High flight costs, but low dive costs, in auks support the biomechanical hypothesis for flightlessness in penguins. *Proc. Natl. Acad. Sci. U.S.A.* **110**, 9380–9384 (2013). doi: [10.1073/pnas.1304838110](#); pmid: [23690614](#)
- D. P. Hocking, A. R. Evans, E. M. Fitzgerald, Leopard seals (*Hydrurga leptonyx*) use suction and filter feeding when hunting small prey underwater. *Polar Biol.* **36**, 211–222 (2013). doi: [10.1007/s00300-012-1253-9](#)
- E. A. Kane, C. D. Marshall, Comparative feeding kinematics and performance of odontocetes: Belugas, Pacific white-sided dolphins and long-finned pilot whales. *J. Exp. Biol.* **212**, 3939–3950 (2009). doi: [10.1242/jeb.034686](#); pmid: [19946072](#)
- J. A. Goldbogen, N. D. Pyenson, R. E. Shadwick, Big gulps require high drag for fin whale lunge feeding. *Mar. Ecol. Prog. Ser.* **349**, 289–301 (2007). doi: [10.3354/meps07066](#)
- N. P. Kelley, R. Motani, Trophic convergence drives morphological convergence in marine tetrapods. *Biol. Lett.* **11**, 20140709 (2015). doi: [10.1098/rsbl.2014.0709](#); pmid: [25631228](#)
- A. Houssaye, “Pachyostosis” in aquatic amniotes: A review. *Integr. Zool.* **4**, 325–340 (2009). doi: [10.1111/j.1749-4877.2009.00146.x](#); pmid: [21392306](#)
- E. Amson, C. de Muizon, M. Laurin, C. Argot, V. de Buffrénil, Gradual adaptation of bone structure to aquatic lifestyle in extinct sloths from Peru. *Proc. R. Soc. B* **281**, 20140192 (2014). doi: [10.1098/rspb.2014.0192](#); pmid: [24621950](#)
- N. M. Gray, K. Kainec, S. Madar, L. Tomko, S. Wolfe, Sink or swim? Bone density as a mechanism for buoyancy control in early cetaceans. *Anat. Rec.* **290**, 638–653 (2007). doi: [10.1002/ar.20533](#); pmid: [17516430](#)
- A. Houssaye, P. Tafforeau, C. de Muizon, P. D. Gingerich, Transition of Eocene whales from land to sea: Evidence from bone microstructure. *PLOS ONE* **10**, e0118409 (2015). doi: [10.1371/journal.pone.0118409](#)
- A. Houssaye, T. M. Scheyer, C. Kolb, V. Fischer, P. M. Sander, A new look at ichthyosaur long bone microanatomy and histology: Implications for their adaptation to an aquatic life. *PLOS ONE* **9**, e95637 (2014). doi: [10.1371/journal.pone.0095637](#)
- A. Krah, N. Klein, P. M. Sander, Evolutionary implications of the divergent long bone histologies of *Nothosaurus* and *Pistosaurus* (Sauropterygia, Triassic). *BMC Evol. Biol.* **13**, 123 (2013). doi: [10.1186/1471-2148-13-123](#); pmid: [23773234](#)
- H. E. Liwanag, A. Berta, D. P. Costa, S. M. Budge, T. M. Williams, Morphological and thermal properties of mammalian insulation: The evolutionary transition to blubber in pinnipeds. *Biol. J. Linn. Soc.* **107**, 774–787 (2012). doi: [10.1111/j.1095-8312.2012.01992.x](#)
- D. B. Thomas, D. T. Ksepka, R. E. Fordyce, Penguin heat-retention structures evolved in a greenhouse Earth. *Biol. Lett.* **7**, 461–464 (2011). doi: [10.1098/rsbl.2010.0993](#); pmid: [21177693](#)
- S. Mirceta *et al.*, Evolution of mammalian diving capacity traced by myoglobin net surface charge. *Science* **340**, 1234192 (2013). doi: [10.1126/science.1234192](#); pmid: [23766330](#)
- A. Bernard *et al.*, Regulation of body temperature by some Mesozoic marine reptiles. *Science* **328**, 1379–1382 (2010). doi: [10.1126/science.1187443](#); pmid: [20538946](#)
- J. Lindgren *et al.*, Skin pigmentation provides evidence of convergent melanism in extinct marine reptiles. *Nature* **506**, 484–488 (2014). doi: [10.1038/nature12899](#); pmid: [24402224](#)
- F. R. O’Keefe, L. M. Chiappe, Viviparity and K-selected life history in a Mesozoic marine plesiosaur (Reptilia, Sauropterygia). *Science* **333**, 870–873 (2011). doi: [10.1126/science.1205689](#); pmid: [21836013](#)
- C. L. Organ, D. E. Janes, A. Meade, M. Pagel, Genotypic sex determination enabled adaptive radiations of extinct marine reptiles. *Nature* **461**, 389–392 (2009). doi: [10.1038/nature08350](#); pmid: [19759619](#)
- J. Parker *et al.*, Genome-wide signatures of convergent evolution in echolocating mammals. *Nature* **502**, 228–231 (2013). doi: [10.1038/nature12511](#); pmid: [24005325](#)
- J. A. Clarke *et al.*, Fossil evidence for evolution of the shape and color of penguin feathers. *Science* **330**, 954–957 (2010). doi: [10.1126/science.1193604](#); pmid: [20929737](#)
- P. M. Sander, Reproduction in early amniotes. *Science* **337**, 806–808 (2012). doi: [10.1126/science.1224301](#); pmid: [22904001](#)
- R. Motani, D. Y. Jiang, A. Tintori, O. Rieppel, G. B. Chen, Terrestrial origin of viviparity in Mesozoic marine reptiles indicated by early Triassic embryonic fossils. *PLOS ONE* **9**, e88640 (2014). doi: [10.1371/journal.pone.0088640](#)

63. P. D. Gingerich, W. von Koenigswald, W. J. Sanders, B. H. Smith, I. S. Zalmout, New protodontid whale from the middle Eocene of Pakistan: Birth on land, precocial development, and sexual dimorphism. *PLOS ONE* **4**, e4366 (2009). doi: [10.1371/journal.pone.0004366](https://doi.org/10.1371/journal.pone.0004366)
64. M. W. Caldwell, From fins to limbs to fins: Limb evolution in fossil marine reptiles. *Am. J. Med. Genet.* **112**, 236–249 (2002). doi: [10.1002/ajmg.10773](https://doi.org/10.1002/ajmg.10773); pmid: [12357467](https://pubmed.ncbi.nlm.nih.gov/12357467/)
65. J. Müller et al., Homeotic effects, somitogenesis and the evolution of vertebral numbers in recent and fossil amniotes. *Proc. Natl. Acad. Sci. U.S.A.* **107**, 2118–2123 (2010). doi: [10.1073/pnas.0912622107](https://doi.org/10.1073/pnas.0912622107); pmid: [20080660](https://pubmed.ncbi.nlm.nih.gov/20080660/)
66. A. D. Foote et al., Convergent evolution of the genomes of marine mammals. *Nat. Genet.* **47**, 272–275 (2015). doi: [10.1038/ng.3198](https://doi.org/10.1038/ng.3198); pmid: [25621460](https://pubmed.ncbi.nlm.nih.gov/25621460/)
67. J. Lindgren, M. W. Caldwell, T. Konishi, L. M. Chiappe, Convergent evolution in aquatic tetrapods: Insights from an exceptional fossil mosasaur. *PLOS ONE* **5**, e11998 (2010). doi: [10.1371/journal.pone.0011998](https://doi.org/10.1371/journal.pone.0011998)
68. J. H. Lipps, E. Mitchell, Trophic model for the adaptive radiations and extinctions of pelagic marine mammals. *Paleobiology* **2**, 147–155 (1976).
69. M. E. Steeman et al., Radiation of extant cetaceans driven by restructuring of the oceans. *Syst. Biol.* **58**, 573–585 (2009). doi: [10.1093/sysbio/syp060](https://doi.org/10.1093/sysbio/syp060); pmid: [20525610](https://pubmed.ncbi.nlm.nih.gov/20525610/)
70. G. J. Slater, S. A. Price, F. Santini, M. E. Alfaro, Diversity versus disparity and the radiation of modern cetaceans. *Proc. R. Soc. B* **277**, 3097–3104 (2010). doi: [10.1098/rspb.2010.0408](https://doi.org/10.1098/rspb.2010.0408); pmid: [20484243](https://pubmed.ncbi.nlm.nih.gov/20484243/)
71. K. L. Sanders, M. S. Mumpuni, M. S. Y. Lee, Uncoupling ecological innovation and speciation in sea snakes (Elapidae, Hydrophiinae, Hydrophiini). *J. Evol. Biol.* **23**, 2685–2693 (2010). doi: [10.1111/j.1420-9101.2010.02131.x](https://doi.org/10.1111/j.1420-9101.2010.02131.x); pmid: [21077974](https://pubmed.ncbi.nlm.nih.gov/21077974/)
72. J. Gatesy et al., A phylogenetic blueprint for a modern whale. *Mol. Phylogenet. Evol.* **66**, 479–506 (2013). doi: [10.1016/j.ympev.2012.10.012](https://doi.org/10.1016/j.ympev.2012.10.012); pmid: [23103570](https://pubmed.ncbi.nlm.nih.gov/23103570/)
73. K. L. Sanders et al., Multiculus phylogeny and recent rapid radiation of the viviparous sea snakes (Elapidae: Hydrophiinae). *Mol. Phylogenet. Evol.* **66**, 575–591 (2013). doi: [10.1016/j.ympev.2012.09.021](https://doi.org/10.1016/j.ympev.2012.09.021); pmid: [23026811](https://pubmed.ncbi.nlm.nih.gov/23026811/)
74. J. J. Sepkoski Jr., A kinetic model of Phanerozoic taxonomic diversity. III. Post-Paleozoic families and mass extinctions. *Paleobiology* **10**, 246–267 (1984).
75. Z. Q. Chen, M. J. Benton, The timing and pattern of biotic recovery following the end-Permian mass extinction. *Nat. Geosci.* **5**, 375–383 (2012). doi: [10.1038/ngeo1475](https://doi.org/10.1038/ngeo1475)
76. N. B. Fröbisch, J. Fröbisch, P. M. Sander, L. Schmitz, O. Rieppel, Macro predatory ichthyosaur from the Middle Triassic and the origin of modern trophic networks. *Proc. Natl. Acad. Sci. U.S.A.* **110**, 1393–1397 (2013). doi: [10.1073/pnas.1216750110](https://doi.org/10.1073/pnas.1216750110); pmid: [23297200](https://pubmed.ncbi.nlm.nih.gov/23297200/)
77. T. M. Scheyer, C. Romano, J. Jenks, H. Bucher, Early Triassic marine biotic recovery: the predators' perspective. *PLOS ONE* **9**, e88987 (2014). doi: [10.1371/journal.pone.0088987](https://doi.org/10.1371/journal.pone.0088987)
78. N. Bardet, Extinction events among Mesozoic marine reptiles. *Hist. Biol.* **7**, 313–324 (1994). doi: [10.1080/10292389409380462](https://doi.org/10.1080/10292389409380462)
79. R. B. Benson, P. S. Druckenmiller, Faunal turnover of marine tetrapods during the Jurassic-Cretaceous transition. *Biol. Rev. Camb. Philos. Soc.* **89**, 1–23 (2014). doi: [10.1111/brv.12038](https://doi.org/10.1111/brv.12038); pmid: [23581455](https://pubmed.ncbi.nlm.nih.gov/23581455/)
80. M. J. Benton, The Red Queen and the Court Jester: Species diversity and the role of biotic and abiotic factors through time. *Science* **323**, 728–732 (2009). doi: [10.1126/science.1157719](https://doi.org/10.1126/science.1157719); pmid: [19197051](https://pubmed.ncbi.nlm.nih.gov/19197051/)
81. N. D. Pyenson, N. P. Kelley, J. F. Parham, Marine tetrapod macroevolution: Physical and biological drivers on 250 Ma of invasions and evolution in ocean ecosystems. *Palaeogeogr. Palaeoclimatol. Palaeoecol.* **400**, 1–8 (2014). doi: [10.1016/j.palaeo.2014.02.018](https://doi.org/10.1016/j.palaeo.2014.02.018)
82. J. Velez-Juarbe, D. P. Domning, N. D. Pyenson, Iterative evolution of sympatric seaweed (Dugongidae, Sirenia) assemblages during the past ~26 million years. *PLOS ONE* **7**, e31304 (2012). doi: [10.1371/journal.pone.0031304](https://doi.org/10.1371/journal.pone.0031304)
83. A. M. Valenzuela-Toro, C. S. Gutstein, R. M. Varas-Malca, M. E. Suarez, N. D. Pyenson, Pinniped turnover in the South Pacific Ocean: New evidence from the Plio-Pleistocene of the Atacama Desert, Chile. *J. Vertebr. Paleontol.* **33**, 216–223 (2013). doi: [10.1080/02724634.2012.710282](https://doi.org/10.1080/02724634.2012.710282)
84. D. P. Domning, An ecological model for late Tertiary sirenian evolution in the North Pacific Ocean. *Syst. Biol.* **25**, 352–362 (1976).
85. J. F. Parham, N. D. Pyenson, New sea turtle from the Miocene of Peru and the iterative evolution of feeding ecomorphologies since the Cretaceous. *J. Paleontol.* **84**, 231–247 (2010). doi: [10.1666/09-077R.1](https://doi.org/10.1666/09-077R.1)
86. H. Hamilton, S. Caballero, A. G. Collins, R. L. Brownell Jr., Evolution of river dolphins. *Proc. R. Soc. B* **268**, 549–556 (2001). doi: [10.1098/rspb.2000.1385](https://doi.org/10.1098/rspb.2000.1385); pmid: [11296868](https://pubmed.ncbi.nlm.nih.gov/11296868/)
87. A. E. Moura et al., Recent diversification of a marine genus (*Tursiops* spp.) tracks habitat preference and environmental change. *Syst. Biol.* **62**, 865–877 (2013). doi: [10.1093/sysbio/syt051](https://doi.org/10.1093/sysbio/syt051); pmid: [23929779](https://pubmed.ncbi.nlm.nih.gov/23929779/)
88. P. J. de Bruyn, C. A. Tosh, A. Terauds, Killer whale ecotypes: Is there a global model? *Biol. Rev. Camb. Philos. Soc.* **88**, 62–80 (2013). doi: [10.1111/j.1469-185X.2012.00239.x](https://doi.org/10.1111/j.1469-185X.2012.00239.x); pmid: [22882545](https://pubmed.ncbi.nlm.nih.gov/22882545/)
89. J. E. Martin, V. Fischer, P. Vincent, G. Suan, A longirostre *Temnodontosaurus* (Ichthyosauria) with comments on Early Jurassic ichthyosaur niche partitioning and disparity. *Palaeontology* **55**, 995–1005 (2012). doi: [10.1111/j.1475-4983.2012.01159.x](https://doi.org/10.1111/j.1475-4983.2012.01159.x)
90. F. R. O'Keefe, The evolution of plesiosaur and plesiosaur morphotypes in the Plesiosauroidea (Reptilia: Sauropterygia). *Paleobiology* **28**, 101–112 (2002). doi: [10.1666/0094-8373\(2002\)028<0101:TEOPAP>2.0.CO;2](https://doi.org/10.1666/0094-8373(2002)028<0101:TEOPAP>2.0.CO;2)
91. E. M. Fitzgerald, Archaeocete-like jaws in a baleen whale. *Biol. Lett.* **8**, 94–96 (2012). doi: [10.1098/rsbl.2011.0690](https://doi.org/10.1098/rsbl.2011.0690); pmid: [21849306](https://pubmed.ncbi.nlm.nih.gov/21849306/)
92. O. Lambert et al., The giant bite of a new raptorial sperm whale from the Miocene epoch of Peru. *Nature* **466**, 105–108 (2010). doi: [10.1038/nature09067](https://doi.org/10.1038/nature09067); pmid: [20596020](https://pubmed.ncbi.nlm.nih.gov/20596020/)
93. D. Jablonski, K. Roy, J. W. Valentine, R. M. Price, P. S. Anderson, The impact of the pull of the recent on the history of marine diversity. *Science* **300**, 1133–1135 (2003). doi: [10.1126/science.1083246](https://doi.org/10.1126/science.1083246); pmid: [12750517](https://pubmed.ncbi.nlm.nih.gov/12750517/)
94. J. Alroy et al., Phanerozoic trends in the global diversity of marine invertebrates. *Science* **321**, 97–100 (2008). doi: [10.1126/science.1156963](https://doi.org/10.1126/science.1156963); pmid: [18599780](https://pubmed.ncbi.nlm.nih.gov/18599780/)
95. A. B. Smith, G. T. Lloyd, A. J. McGowan, Phanerozoic marine diversity: Rock record modelling provides an independent test of large-scale trends. *Proc. R. Soc. B* **279**, 4489–4495 (2012). doi: [10.1098/rspb.2012.1793](https://doi.org/10.1098/rspb.2012.1793); pmid: [22951734](https://pubmed.ncbi.nlm.nih.gov/22951734/)
96. J. Velez-Juarbe, Ghost of seagrasses past: Using sirenians as a proxy for historical distribution of seagrasses. *Palaeogeogr. Palaeoclimatol. Palaeoecol.* **400**, 41–49 (2014). doi: [10.1016/j.palaeo.2013.05.012](https://doi.org/10.1016/j.palaeo.2013.05.012)
97. D. T. Ksepka, J. A. Clarke, The basal penguin (Aves: Sphenisciformes) *Perudyptes devriesi* and a phylogenetic evaluation of the penguin fossil record. *Bull. Am. Mus. Nat. Hist.* **337**, 1–77 (2010). doi: [10.1206/653.1](https://doi.org/10.1206/653.1)
98. M. D. Uhen, N. D. Pyenson, Diversity estimates, biases, and historiographic effects: Resolving cetacean diversity in the Tertiary. *Palaeontol. Electronica* **10**, 11–22 (2007).
99. F. G. Marx, M. D. Uhen, Climate, critters, and cetaceans: Cenozoic drivers of the evolution of modern whales. *Science* **327**, 993–996 (2010). doi: [10.1126/science.1185581](https://doi.org/10.1126/science.1185581); pmid: [20167785](https://pubmed.ncbi.nlm.nih.gov/20167785/)
100. R. D. Norris, S. K. Turner, P. M. Hull, A. Ridgwell, Marine ecosystem responses to Cenozoic global change. *Science* **341**, 492–498 (2013). doi: [10.1126/science.1240543](https://doi.org/10.1126/science.1240543); pmid: [23908226](https://pubmed.ncbi.nlm.nih.gov/23908226/)
101. G. J. Vermeij, On escalation. *Annu. Rev. Earth Sci.* **41**, 1–19 (2013). doi: [10.1146/annurev-earth-050212-124123](https://doi.org/10.1146/annurev-earth-050212-124123)
102. M. E. Alfaro et al., Nine exceptional radiations plus high turnover explain species diversity in jawed vertebrates. *Proc. Natl. Acad. Sci. U.S.A.* **106**, 13410–13414 (2009). doi: [10.1073/pnas.0811087106](https://doi.org/10.1073/pnas.0811087106); pmid: [19633192](https://pubmed.ncbi.nlm.nih.gov/19633192/)
103. G. J. Vermeij, D. R. Lindberg, Delayed herbivory and the assembly of marine benthic ecosystems. *Paleobiology* **26**, 419–430 (2000). doi: [10.1666/0094-8373\(2000\)026<0419:DHATAO>2.0.CO;2](https://doi.org/10.1666/0094-8373(2000)026<0419:DHATAO>2.0.CO;2)
104. R. Collin, C. M. Janis, in *Ancient Marine Reptiles*, J. M. Callaway, E. L. Nicholls, Eds. (Academic Press, San Diego, CA, 1997), pp. 451–466.
105. C. B. Stringer et al., Neanderthal exploitation of marine mammals in Gibraltar. *Proc. Natl. Acad. Sci. U.S.A.* **105**, 14319–14324 (2008). doi: [10.1073/pnas.0805471105](https://doi.org/10.1073/pnas.0805471105); pmid: [18809913](https://pubmed.ncbi.nlm.nih.gov/18809913/)
106. T. C. Rick, J. Erlandson, Eds., *Human Impacts on Ancient Marine Ecosystems: A Global Perspective* (Univ. of California Press, Berkeley, 2008).
107. D. J. McCauley et al., Marine defaunation: Animal loss in the global ocean. *Science* **347**, 1255641 (2015). doi: [10.1126/science.1255641](https://doi.org/10.1126/science.1255641); pmid: [25593191](https://pubmed.ncbi.nlm.nih.gov/25593191/)
108. S. T. Turvey, C. L. Risley, Modelling the extinction of Steller's sea cow. *Biol. Lett.* **2**, 94–97 (2006). doi: [10.1098/rsbl.2005.0415](https://doi.org/10.1098/rsbl.2005.0415); pmid: [17148336](https://pubmed.ncbi.nlm.nih.gov/17148336/)
109. R. R. Reeves, T. D. Smith, in *Whales, Whaling, and Ocean Ecosystems*, J. A. Estes et al., Eds. (Univ. of California Press, Berkeley, 2006), pp. 82–101.
110. L. R. Gerber, R. Hilborn, Catastrophic events and recovery from low densities in populations of otariids: Implications for risk of extinction. *Mammal Rev.* **31**, 131–150 (2001). doi: [10.1046/j.1365-2907.2001.00081.x](https://doi.org/10.1046/j.1365-2907.2001.00081.x)
111. D. M. Scheel et al., Biogeography and taxonomy of extinct and endangered monk seals illuminated by ancient DNA and skull morphology. *ZooKeys* **409**, 1–33 (2014). doi: [10.3897/zookeys.409.6244](https://doi.org/10.3897/zookeys.409.6244); pmid: [24899841](https://pubmed.ncbi.nlm.nih.gov/24899841/)
112. C. L. Hubbs, K. S. Norris, in *Antarctic Pinnipedia*, W. H. Burt, Ed. (American Geophysical Union, Washington, DC, 1971), pp. 35–52.
113. M. L. Bonnell, R. K. Selander, Elephant seals: Genetic variation and near extinction. *Science* **184**, 908–909 (1974). doi: [10.1126/science.184.4139.908](https://doi.org/10.1126/science.184.4139.908); pmid: [4825892](https://pubmed.ncbi.nlm.nih.gov/4825892/)
114. G. J. Vermeij, Biogeography of recently extinct marine species: Implications for conservation. *Conserv. Biol.* **7**, 391–397 (1993). doi: [10.1046/j.1523-1739.1993.07020391.x](https://doi.org/10.1046/j.1523-1739.1993.07020391.x)
115. S. Boessenkool et al., Relict or colonizer? Extinction and range expansion of penguins in southern New Zealand. *Proc. R. Soc. B* **276**, 815–821 (2009). doi: [10.1098/rspb.2008.1246](https://doi.org/10.1098/rspb.2008.1246); pmid: [19019791](https://pubmed.ncbi.nlm.nih.gov/19019791/)
116. T. L. Jones et al., The protracted Holocene extinction of California's flightless sea duck (*Chendytes lawi*) and its implications for the Pleistocene overkill hypothesis. *Proc. Natl. Acad. Sci. U.S.A.* **105**, 4105–4108 (2008). doi: [10.1073/pnas.0711140105](https://doi.org/10.1073/pnas.0711140105); pmid: [18334640](https://pubmed.ncbi.nlm.nih.gov/18334640/)
117. IUCN Red List of Species, version 2014.3; www.iucnredlist.org.
118. N. D. Pyenson, Requiem for *Lipotes*: An evolutionary perspective on marine mammal extinction. *Mar. Mamm. Sci.* **25**, 714–724 (2009). doi: [10.1111/j.1748-7692.2008.00266.x](https://doi.org/10.1111/j.1748-7692.2008.00266.x)
119. T. Gerrodette, L. Rojas-Bracho, Estimating the success of protected areas for the vaquita, *Phocoena sinus*. *Mar. Mamm. Sci.* **27**, E101–E125 (2011). doi: [10.1111/j.1748-7692.2010.00449.x](https://doi.org/10.1111/j.1748-7692.2010.00449.x)
120. F. Ritter, Collisions of sailing vessels with cetaceans worldwide: First insights into a seemingly growing problem. *J. Cetacean Res. Manage.* **12**, 119–128 (2012).
121. R. M. Rolland et al., Evidence that ship noise increases stress in right whales. *Proc. R. Soc. B* **279**, 2363–2368 (2012). doi: [10.1098/rspb.2011.2429](https://doi.org/10.1098/rspb.2011.2429); pmid: [22319129](https://pubmed.ncbi.nlm.nih.gov/22319129/)
122. P. L. Tyack et al., Beaked whales respond to simulated and actual navy sonar. *PLOS ONE* **6**, e17009 (2011). doi: [10.1371/journal.pone.0017009](https://doi.org/10.1371/journal.pone.0017009)
123. M. C. Fossi et al., Large filter feeding marine organisms as indicators of microplastic in the pelagic environment: The case studies of the Mediterranean basking shark (*Cetorhinus maximus*) and fin whale (*Balaenoptera physalus*). *Mar. Environ. Res.* **100**, 17–24 (2014). doi: [10.1016/j.marenvres.2014.02.002](https://doi.org/10.1016/j.marenvres.2014.02.002); pmid: [24612776](https://pubmed.ncbi.nlm.nih.gov/24612776/)
124. F. Mazzillo, K. Shapiro, M. W. Silver, A new pathogen transmission mechanism in the ocean: The case of sea otter exposure to the land-parasite *Toxoplasma gondii*. *PLOS ONE* **8**, e82477 (2013). doi: [10.1371/journal.pone.0082477](https://doi.org/10.1371/journal.pone.0082477)
125. O. Schofield et al., How do polar marine ecosystems respond to rapid climate change? *Science* **328**, 1520–1523 (2010). doi: [10.1126/science.1185779](https://doi.org/10.1126/science.1185779); pmid: [20558708](https://pubmed.ncbi.nlm.nih.gov/20558708/)
126. S. E. Alter et al., Climate impacts on transoceanic dispersal and habitat in gray whales from the Pleistocene to 2100. *Molec. Ecol.* **24**, 1510–1522 (2015). doi: [10.1111/mec.13121](https://doi.org/10.1111/mec.13121)
127. S. E. Noakes, N. D. Pyenson, G. McFall, Late Pleistocene gray whales (*Eschrichtius robustus*) offshore Georgia, USA, and the antiquity of gray whale migration in the North Atlantic Ocean. *Palaeogeogr. Palaeoclimatol. Palaeoecol.* **392**, 502–509 (2013). doi: [10.1016/j.palaeo.2013.10.005](https://doi.org/10.1016/j.palaeo.2013.10.005)
128. H. Heatwole, A. Grech, J. F. Monahan, S. King, H. Marsh, Thermal biology of sea snakes and sea kraits. *Integr. Comp. Biol.* **52**, 257–273 (2012). doi: [10.1093/icb/ics080](https://doi.org/10.1093/icb/ics080); pmid: [22669175](https://pubmed.ncbi.nlm.nih.gov/22669175/)
129. L. I. Wright et al., Turtle mating patterns buffer against disruptive effects of climate change. *Proc. R. Soc. B* **279**, 2122–2127 (2012). doi: [10.1098/rspb.2011.2285](https://doi.org/10.1098/rspb.2011.2285); pmid: [22279164](https://pubmed.ncbi.nlm.nih.gov/22279164/)
130. P. C. Fiedler, Environmental change in the eastern tropical Pacific Ocean: Review of ENSO and decadal variability. *Mar. Ecol. Prog. Ser.* **244**, 265–283 (2002). doi: [10.3354/meps244265](https://doi.org/10.3354/meps244265)

131. J. A. Estes *et al.*, Trophic downgrading of planet Earth. *Science* **333**, 301–306 (2011). doi: [10.1126/science.1205106](https://doi.org/10.1126/science.1205106); pmid: [21764740](https://pubmed.ncbi.nlm.nih.gov/21764740/)
132. J. A. Estes, M. T. Tinker, T. M. Williams, D. F. Doak, Killer whale predation on sea otters linking oceanic and nearshore ecosystems. *Science* **282**, 473–476 (1998). doi: [10.1126/science.282.5388.473](https://doi.org/10.1126/science.282.5388.473); pmid: [9774274](https://pubmed.ncbi.nlm.nih.gov/9774274/)
133. D. G. Ainley, G. Ballard, K. M. Dugger, Competition among penguins and cetaceans reveals trophic cascades in the western Ross Sea, Antarctica. *Ecology* **87**, 2080–2093 (2006). doi: [10.1890/0012-9658\(2006\)87\[2080:CAPACR\]2.0.CO;2](https://doi.org/10.1890/0012-9658(2006)87[2080:CAPACR]2.0.CO;2); pmid: [16937647](https://pubmed.ncbi.nlm.nih.gov/16937647/)
134. B. A. Block *et al.*, Tracking apex marine predator movements in a dynamic ocean. *Nature* **475**, 86–90 (2011). doi: [10.1038/nature10082](https://doi.org/10.1038/nature10082); pmid: [21697831](https://pubmed.ncbi.nlm.nih.gov/21697831/)
135. K. I. Ohshima *et al.*, Antarctic Bottom Water production by intense sea-ice formation in the Cape Darnley polynya. *Nat. Geosci.* **6**, 235–240 (2013). doi: [10.1038/ngeo1738](https://doi.org/10.1038/ngeo1738)
136. See supplementary materials on Science Online.
137. TSCreator, version 6.4; <https://engineering.purdue.edu/Stratigraphy/tcreator/index/index.php>.
138. J. Vélaz-Juarbe, C. A. Brochu, H. Santos, A gharial from the Oligocene of Puerto Rico: Transoceanic dispersal in the history of a non-marine reptile. *Proc. R. Soc. B* **274**, 1245–1254 (2007). doi: [10.1098/rspb.2006.0455](https://doi.org/10.1098/rspb.2006.0455); pmid: [17341454](https://pubmed.ncbi.nlm.nih.gov/17341454/)
139. T. H. Worthy, A. J. D. Tennyson, C. Jones, J. A. McNamara, B. J. Douglas, Miocene waterfowl and other birds from Central Otago, New Zealand. *J. Syst. Palaeontol.* **5**, 1–39 (2007). doi: [10.1017/S1477201906001957](https://doi.org/10.1017/S1477201906001957)
140. T. L. Fulton, B. Letts, B. Shapiro, Multiple losses of flight and recent speciation in steamer ducks. *Proc. R. Soc. B* **279**, 2339–2346 (2012). doi: [10.1098/rspb.2011.2599](https://doi.org/10.1098/rspb.2011.2599); pmid: [22319122](https://pubmed.ncbi.nlm.nih.gov/22319122/)
141. T. L. Fulton, C. Strobeck, Multiple fossil calibrations, nuclear loci and mitochondrial genomes provide new insight into biogeography and divergence timing for true seals (Phocidae, Pinnipedia). *J. Biogeogr.* **37**, 814–829 (2010). doi: [10.1111/j.1365-2699.2010.02271.x](https://doi.org/10.1111/j.1365-2699.2010.02271.x)
142. F. Hailer *et al.*, Nuclear genomic sequences reveal that polar bears are an old and distinct bear lineage. *Science* **336**, 344–347 (2012). doi: [10.1126/science.1216424](https://doi.org/10.1126/science.1216424); pmid: [22517859](https://pubmed.ncbi.nlm.nih.gov/22517859/)
143. K. Rassmann, D. Tautz, F. C. Trillmich, C. Gliddon, The microevolution of the Galápagos marine iguana *Amblyrhynchus cristatus* assessed by nuclear and mitochondrial genetic analyses. *Mol. Ecol.* **6**, 437–452 (1997). doi: [10.1046/j.1365-294X.1997.00209.x](https://doi.org/10.1046/j.1365-294X.1997.00209.x)
144. TimeTree, www.timetree.org.
145. S. B. Hedges, J. Dudley, S. Kumar, TimeTree: A public knowledge-base of divergence times among organisms. *Bioinformatics* **22**, 2971–2972 (2006). doi: [10.1093/bioinformatics/btl505](https://doi.org/10.1093/bioinformatics/btl505); pmid: [17021158](https://pubmed.ncbi.nlm.nih.gov/17021158/)
146. Fossil Calibration Database, <http://fossilcalibrations.org>.
147. F. Gradstein, J. Ogg, M. Schmitz, G. Ogg, *The Geologic Time Scale 2012* (Elsevier, Amsterdam, 2012).

ACKNOWLEDGMENTS

We thank D. Erwin, J. Jackson, M. Carrano, J. Goldbogen, J. Parham, J. Velez-Juarbe, and J. Oster for helpful comments on previous versions of this paper, and three anonymous reviewers for helpful suggestions. D. Johnston provided the penguin photograph for Fig. 2. Supported by a Smithsonian Institution Peter Buck Postdoctoral Fellowship (N.P.K.), a Smithsonian Institution National Museum of Natural History Small Grant Award and the Remington Kellogg Fund (N.D.P.), and the Basis Foundation (N.D.P. and N.P.K.).

SUPPLEMENTARY MATERIALS

www.sciencemag.org/content/348/6232/aaa3716/suppl/DC1

Materials and Methods
References (137–147)

10.1126/science.aaa3716

RESEARCH ARTICLE SUMMARY

SKIN FIBROSIS

Identification and isolation of a dermal lineage with intrinsic fibrogenic potential

Yuval Rinkevich,* Graham G. Walmsley, Michael S. Hu, Zeshaan N. Maan, Aaron M. Newman, Micha Drukker, Michael Januszyk, Geoffrey W. Krampitz, Geoffrey C. Gurtner, H. Peter Lorenz, Irving L. Weissman,* Michael T. Longaker*

INTRODUCTION: Fibroblasts are the predominant cell type that synthesizes and remodels the extracellular matrix in organs during both embryonic and adult life and are central to the fibrotic response across a range of pathologic states. Morphologically, they are most commonly defined as elongated, spindle-shaped cells that readily adhere to and migrate over tissue culture substrates. However, fibroblasts exhibit a variety of shapes and sizes, depending on the physiologic or pathologic state of the host tissue, and represent a heterogeneous population of cells with diverse features that remain largely undefined. In cutaneous tissues, fibroblasts display considerable functional variation during wound repair, depending on developmental time, and between anatomic sites. For example, wounds in the oral cavity remodel with

minimal scar formation, whereas scar tissue deposition within cutaneous wounds is substantial. The mechanisms underlying this diversity of regenerative responses in cutaneous tissues have remained largely underexplored.

RATIONALE: The effective development of treatments for fibrosis depends on a mechanistic understanding of its pathogenesis. The identification and characterization of distinct lineages of fibroblasts, based on functional role, hold potential value for developing therapeutic approaches to fibrosis. We employed a nonselective depletion-based fluorescence-activated cell sorting strategy to isolate fibroblasts from a murine model that labels a particular lineage of cells based on the gene expression of *Engrailed-1* (*En1*) in its embryonic progenitors. Using this

reporter mouse, we reveal the presence of at least two functionally distinct embryonic fibroblast lineages in murine dorsal skin and characterize a single lineage that plays a primary role in connective tissue formation.

RESULTS: Genetic lineage tracing and transplantation assays demonstrate that a single somitic-derived fibroblast lineage that is defined by embryonic expression of *En1* is responsible for the bulk of connective tissue deposition during embryonic development,

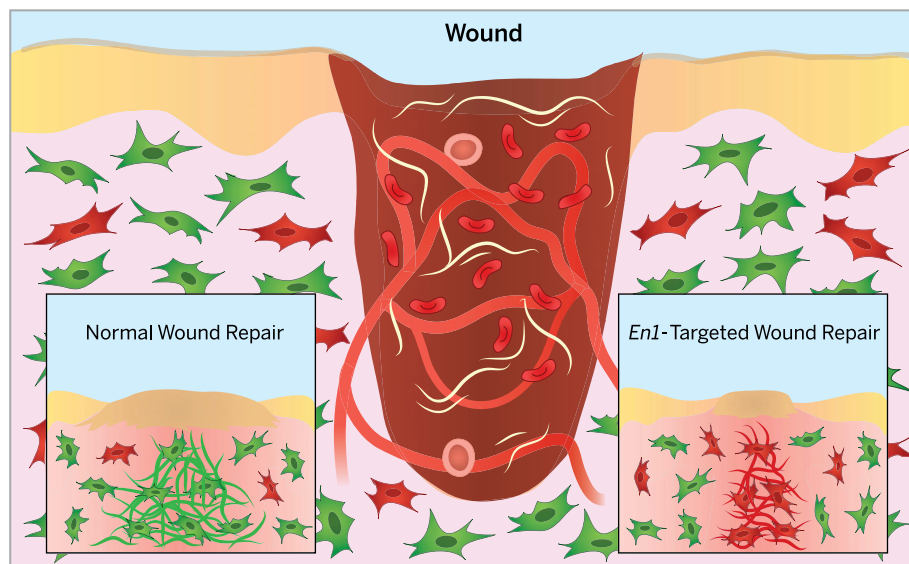
ON OUR WEB SITE

Read the full article at <http://dx.doi.org/10.1126/science.aaa2151>

cutaneous wound healing, radiation fibrosis, and cancer stroma formation. Reciprocal transplantation of distinct fibroblast lineages between the dorsal back

and oral cavity induces ectopic dermal architectures that mimic their place of origin rather than their site of transplantation. Lineage-specific cell ablation using transgenic-mediated expression of the simian diphtheria toxin receptor in conjunction with localized administration of diphtheria toxin leads to diminished connective tissue deposition in wounds and significantly reduces melanoma growth in the dorsal skin of mice. Tensile strength testing reveals that, although scar formation is significantly reduced in wounds treated with diphtheria toxin to ablate the *En1* lineage, as compared with control wounds, tensile strength in lineage-ablated wounds is not significantly affected. Using flow cytometry and in silico approaches, we identify CD26/dipeptidyl peptidase-4 (DPP4) as a surface marker that allows for the isolation of this fibrogenic, scar-forming lineage. Small molecule-based inhibition of CD26/DPP4 enzymatic activity in the wound bed of wild-type mice during wound healing results in diminished cutaneous scarring after excisional wounding.

CONCLUSION: We have identified multiple lineages of fibroblasts in the dorsal skin. Among these, we have characterized a single lineage responsible for the fibrotic response to injury in the dorsal skin of mice and demonstrated that targeted inhibition of this lineage results in reduced scar formation with no effect on the structural integrity of the healed skin. Furthermore, these studies demonstrate that intra- and intersite diversity of dermal architectures are set embryonically and are maintained postnatally by distinct lineages of fibroblasts in different anatomic locations. These results hold promise for the development of therapeutic approaches to fibrotic disease, wound healing, and cancer progression in humans. ■



Schematic showing reduced scarring with targeted ablation/inhibition of *En1* fibroblasts.

Fibroblasts derived from embryonic precursors expressing *En1* are responsible for most connective tissue deposition in skin fibrosis. Targeted ablation/inhibition of this lineage leads to a reduction in fibrosis during wound repair and tumor stroma formation. These findings may lead to the elimination of scarring and other types of fibrotic tissue disease. Green cells, *En1*-positive fibroblasts; red cells, *En1*-negative fibroblasts.

The list of author affiliations is available in the full article online.

*Corresponding author. E-mail: ryuval@stanford.edu (Y.R.); irv@stanford.edu (I.L.W.); longaker@stanford.edu (M.T.L.)
Cite this article as Y. Rinkevich et al., *Science* **348**, aaa2151 (2014). DOI: 10.1126/science.aaa2151

RESEARCH ARTICLE

SKIN FIBROSIS

Identification and isolation of a dermal lineage with intrinsic fibrogenic potential

Yuval Rinkevich,^{1,*†} Graham G. Walmsley,^{1,2†} Michael S. Hu,^{1,2§} Zeshaan N. Maan,^{2§} Aaron M. Newman,¹ Micha Drukker,¹ Michael Januszyk,² Geoffrey W. Krampitz,¹ Geoffrey C. Gurtner,² H. Peter Lorenz,² Irving L. Weissman,^{1,3*} Michael T. Longaker^{1,2*}

Dermal fibroblasts represent a heterogeneous population of cells with diverse features that remain largely undefined. We reveal the presence of at least two fibroblast lineages in murine dorsal skin. Lineage tracing and transplantation assays demonstrate that a single fibroblast lineage is responsible for the bulk of connective tissue deposition during embryonic development, cutaneous wound healing, radiation fibrosis, and cancer stroma formation. Lineage-specific cell ablation leads to diminished connective tissue deposition in wounds and reduces melanoma growth. Using flow cytometry, we identify CD26/DPP4 as a surface marker that allows isolation of this lineage. Small molecule–based inhibition of CD26/DPP4 enzymatic activity during wound healing results in diminished cutaneous scarring. Identification and isolation of these lineages hold promise for translational medicine aimed at in vivo modulation of fibrogenic behavior.

Fibroblasts are the predominant cell type that synthesizes and remodels the extracellular matrix (ECM) in both embryonic and adult organs (1) and are the principal cell type responsible for tissue and organ fibrosis, cutaneous scarring, atherosclerosis, systemic sclerosis, and formation of atheromatous plaques after blood vessel injury (2–5). Numerous studies have investigated the contribution of fibroblasts to the progression of carcinoma (6–9), but, as in the case of wound healing, the identity and embryonic origin of the fibroblasts that contribute to tumor stroma have not been adequately defined. Identifying and prospectively isolating the fibroblast lineage(s) endowed with fibrogenic potential in vivo is an essential step toward effectively manipulating their response to injury across a wide range of acute and chronic disease states.

Here, we identify an embryonic lineage within the dorsal dermis that possesses many of the functional attributes commonly associated with the term “fibroblast.” Despite the presence of other fibroblast lineages in the dorsal dermis, the *Engrailed-1* lineage is the primary contrib-

utor to connective tissue secretion and organization during embryonic development, cutaneous wounding, radiation fibrosis, and cancer stroma formation. By identifying and prospectively isolating defined embryonic lineages from skin and oral dermis, we find that fibrogenic properties are cell intrinsic, reflecting inherent functional diversity that exists in cutaneous tissues from different anatomical sites. These findings demonstrate that distinct fibroblast lineages represent unique cell types and take us one step closer to effectively modulating their fibrogenic behavior in vivo.

Results

Multiple lineages of fibroblasts in the dorsal skin

Engrailed-1^{Cre} (*En1^{Cre}*) transgenic mice were crossed with *ROSA26^{mTmG}* (*R26^{mTmG}*) reporter mice (10) to trace the lineage of a population of *En1*-lineage–positive fibroblasts (EPFs), defined in vivo by the expression of green fluorescent protein (GFP), which migrates during embryonic development from the somites into the dorsal trunk dermis (11) (Fig. 1A). To be sure that *Engrailed-1* defines a single embryonic lineage and is not expressed into adulthood, we analyzed its protein and mRNA expression at P1 and P30 in dorsal skin and wounded skin and found absence of expression at these stages (figs. S1, A and B).

Fibroblasts were isolated from the dorsal skin of *En1^{Cre};R26^{mTmG}* mice using a fluorescence-activated cell sorting (FACS)–based isolation strategy that allowed for the exclusion of non-mesenchymal lineages (see Materials and Meth-

ods) via a lineage negative gate (*Lin*[−]). We employed this approach in lieu of a positive selection strategy to be as inclusive as possible and avoid preselection or enrichment of a subpopulation of fibroblasts expressing specific surface markers. This protocol enabled the isolation of uncultured EPFs (defined as GFP⁺RFP[−]*Lin*[−]) and *En1*-lineage–negative fibroblasts (ENFs) (defined as GFP[−]RFP⁺*Lin*[−]).

To confirm the validity of our protocol, we performed microfluidic single-cell gene expression analysis of 96 gene targets (table S1) on FACS-isolated EPFs, ENFs, and unfractionated skin cells (as internal controls) from adult (P56) mice. Partitional clustering independently revealed the existence of three transcriptionally distinct cell clusters in dermal tissues, two of which were well represented among labeled cells (termed here as EPFs, ENFs) and one of which was not (Fig. 1B). Compared with the third cluster, the first two were defined by increased expression of “fibroblast” genes such as *Pdgfra*, *Vim*, *P4hb*, *Col1a1*, *Col3a1*, and *Fbn1*, as well as decreased expression of *CDH1*, *Epcam*, and *Pecam1* (Fig. 1C). Population-level quantitative real-time polymerase chain reaction (qRT-PCR) analysis of FACS-isolated EPFs, ENFs, and unfractionated skin lysate reinforced these findings, demonstrating that genes associated with nonfibroblast cells (adipocyte, endothelial, neuronal, hematopoietic, muscle, and epidermal) were minimally or not expressed by EPFs and ENFs (Fig. 1D).

Microarray analysis of FACS-isolated uncultured EPFs and ENFs from adult (P56) mice demonstrated that EPFs and ENFs shared a high degree of transcriptome-wide similarity ($R^2 = 0.97$) (Fig. 2A) and similar expression of fibroblast-related genes—such as vimentin, decorin, and S100A4 (Fig. 2B, left)—and remodeling genes of the ECM (Fig. 2B, right). However, key differences in transcript expression were present, including differential expression of *HOXC10*, *Slit2*, *Foxp1*, leptin receptor (*Lepr*), myosin light chain kinase (*Mylk*), and actin alpha 1 (*Acta1*), among many others (Fig. 2C).

Flow cytometry revealed the existence of two separate population dynamics in vivo. At embryonic day 10.5 (E10.5), EPFs represented less than 1% of total dermal fibroblasts, which at this stage of development were dominated by ENFs (95.5% of dermal fibroblasts). With time, EPFs increased from 22.2% of total dermal fibroblasts at E16.5, to 42.9% at P1, and to 75.3% of total dermal fibroblasts at P30 (Fig. 2D), with similar percentages of EPFs/ENFs at subsequent postnatal stages (P56).

EPFs and ENFs, sorted from embryonic (E16.5) and adult (P30) mice, and cultured in vitro, displayed similar spindle-shaped morphology characteristic of fibroblasts (Fig. 2E). The cells were highly motile, stained positive for markers classically associated with fibroblasts, such as fibroblast-specific protein 1 (FSP-1) and vimentin, as well as expressing components of the ECM, including type I collagen and fibronectin (Fig. 2F), and were negative for epithelial (keratin 5/14), neural (neurofilament NF-H), adipocytic (adiponectin),

¹Institute for Stem Cell Biology and Regenerative Medicine, Departments of Pathology and Developmental Biology, Stanford University School of Medicine, Stanford, CA 94305, USA. ²Hagey Laboratory for Pediatric Regenerative Medicine, Department of Surgery, Plastic and Reconstructive Surgery, Stanford University School of Medicine, Stanford, CA 94305, USA. ³Ludwig Center for Cancer Stem Cell Biology and Medicine, Stanford University School of Medicine, Stanford, CA 94305, USA.

*Corresponding author. E-mail: ryuval@stanford.edu (Y.R.); irv@stanford.edu (I.L.W.); longaker@stanford.edu (M.T.L.) †These authors contributed equally to this work. §These authors contributed equally to this work.

endothelial (CD31), and hematopoietic (CD45) markers (fig. 3I,C).

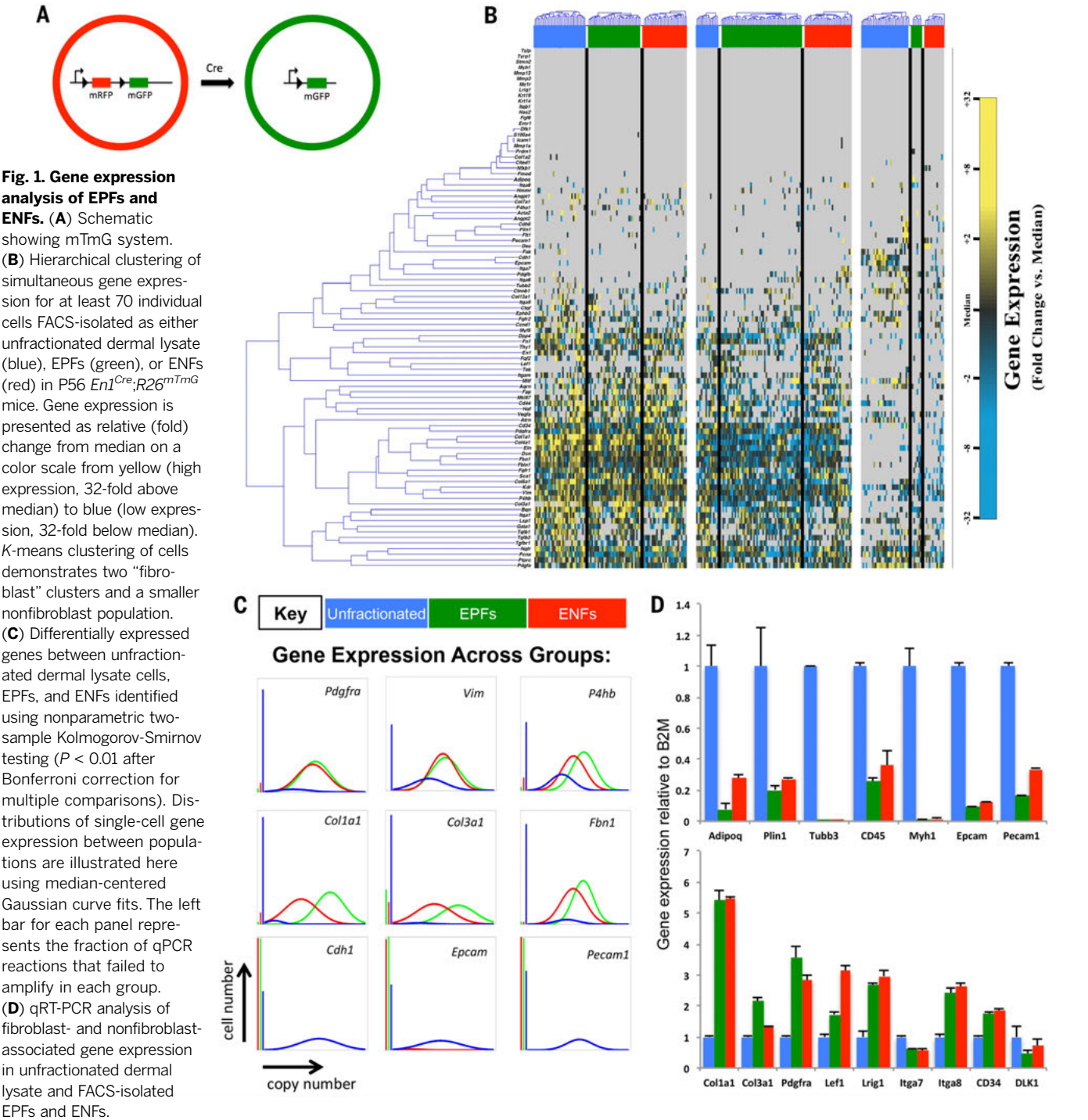
Fibrogenic potential of dermal fibroblasts is lineage-restricted

Next, we performed lineage-tracing analysis using *En1^{Cre};R26^{mTmG}* mice. Upon histologic analysis of dorsal skin from *En1^{Cre};R26^{mTmG}* mice, we observed labeling of dermal ECM with the fluorescent protein expressed on the surface of the cell responsible for depositing those ECM

components (Fig. 3, A to C). At E10.5, ENFs comprised the entirety of the developing dermis, and RFP signal labeled all cells and dermal ECM (Fig. 3B, top panel). At E12.5, EPFs were observed localizing to the papillary dermis only (Fig. 3B, second panel). Subsequently, at E16.5, EPFs appeared to migrate to the lower reticular dermis (Fig. 3B, third panel), complete their migration at P1, and maintain a presence there throughout postnatal stages of development (Fig. 3B, bottom panel, and Fig. 3C). Consequently, the majority of

the deposited connective tissue within the underlying dermis, the stroma associated with dermal pegs, the stroma surrounding hair follicles, and dermal papillae (Fig. 3, B and C) was GFP-positive and hence EPF-derived.

To confirm that the observed ECM fluorescence correlated with the deposition of ECM components, dorsal dermis from adult (P30) *En1^{Cre};R26^{mTmG}* mice was stained for the predominant collagens (types I and III) in cutaneous dermis (12), which displayed an overlapping



pattern with GFP fluorescence (Fig. 3D, top and middle panel). In contrast, keratin 14, a marker for basal keratinocytes and hair follicle epithelium, displayed a nonoverlapping pattern with GFP fluorescence (Fig. 3D, bottom panel). These results indicate that, while at least two separate embryonic lineages of fibroblasts exist within the dorsal dermis, only EPFs function in vivo as effectors of connective tissue secretion and formation.

Analysis of wounded and unwounded dorsal dermis in uncrossed *R26^{mTmG}* mice demonstrated the presence of RFP in all connective tissue fibers within the dermis (fig. S1D) in a pattern identical to that of GFP in the dorsal dermis of *En1^{Cre};R26^{mTmG}* mice (Fig. 3, C and E), ensuring that our findings were not a result of difference in emission intensities between membrane-bound GFP and RFP in connective tissue stroma.

As expected, dorsal cutaneous wounds in *Tie2^{Cre};R26^{mTmG}* (endothelial and hematopoietic lineages) and *K14^{Cre};R26^{mTmG}* (epithelial lineage) mice were completely negative for GFP-labeled connective tissue (fig. S1E, top two panels). These results demonstrate that ECM deposition in the dorsal skin is a property unique to EPFs, with absence of any contributions from hematopoietic, endothelial, or epithelial cell lineages.

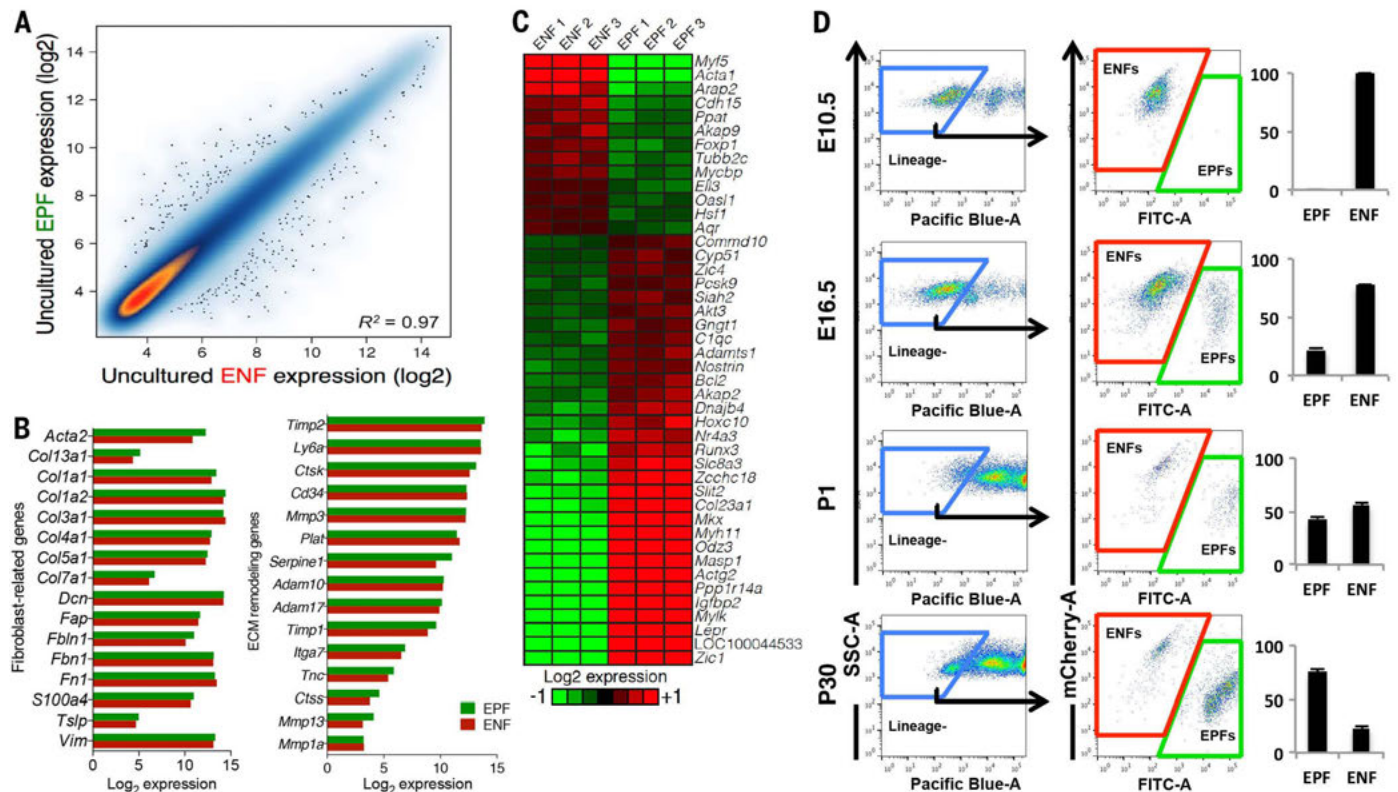


Fig. 2. EPFs and ENFs are two distinct lineages of fibroblasts. (A) Scatter plot depicting transcriptome-wide expression differences between uncultured FACS-isolated EPF and ENF populations from P56 *En1^{Cre};R26^{mTmG}* mice. For each population ($n = 3$), the median expression of each gene is plotted. Within the scatter plot, gene density is represented as a heat map, with orange regions containing larger numbers of genes than blue regions. Outliers are shown as individual points. (B) Similar expression of known fibroblast markers and fibroblast-related genes (left) and ECM remodeling genes (right) compared between uncultured FACS-isolated EPF and ENF populations by microarray analysis. (C) Expression of top differentially regulated genes between uncultured FACS-isolated EPF and ENF populations by microarray analysis. Genes were filtered for Q value of <0.3 (30% false discovery rate) and a fold change of at least 1.5x. (D) FACS analysis showing abundance of EPFs and ENFs FACS-isolated from the dorsal dermis of E10.5 (top), E16.5 (one down from top), P1 (one up from bottom), and P30 (bottom) *En1^{Cre};R26^{mTmG}* mice reveals a shift in population dynamics during dermal development from ENF-dominated dermis at E10.5 to EPF-dominated dermis at P1 and subsequent postnatal stages ($n = 5$ mice). (E) Fluorescent imaging of EPFs and ENFs cultured after FACS-sorting from the dorsal dermis of E16.5 and P30 *En1^{Cre};R26^{mTmG}* mice. The relative abundance of EPFs and ENFs defined in the FACS analyses was consistent with the relative abundance seen after tissue culture plating at each time point. Scale bar, 100 μ m. (F) Immunostaining of FACS-isolated EPFs and ENFs from P30 *En1^{Cre};R26^{mTmG}* mice in vitro revealed that traditional fibroblast markers (vimentin and FSP-1) and secreted ECM components (col type I and fibronectin) are expressed similarly across both populations. Scale bar, 200 μ m.

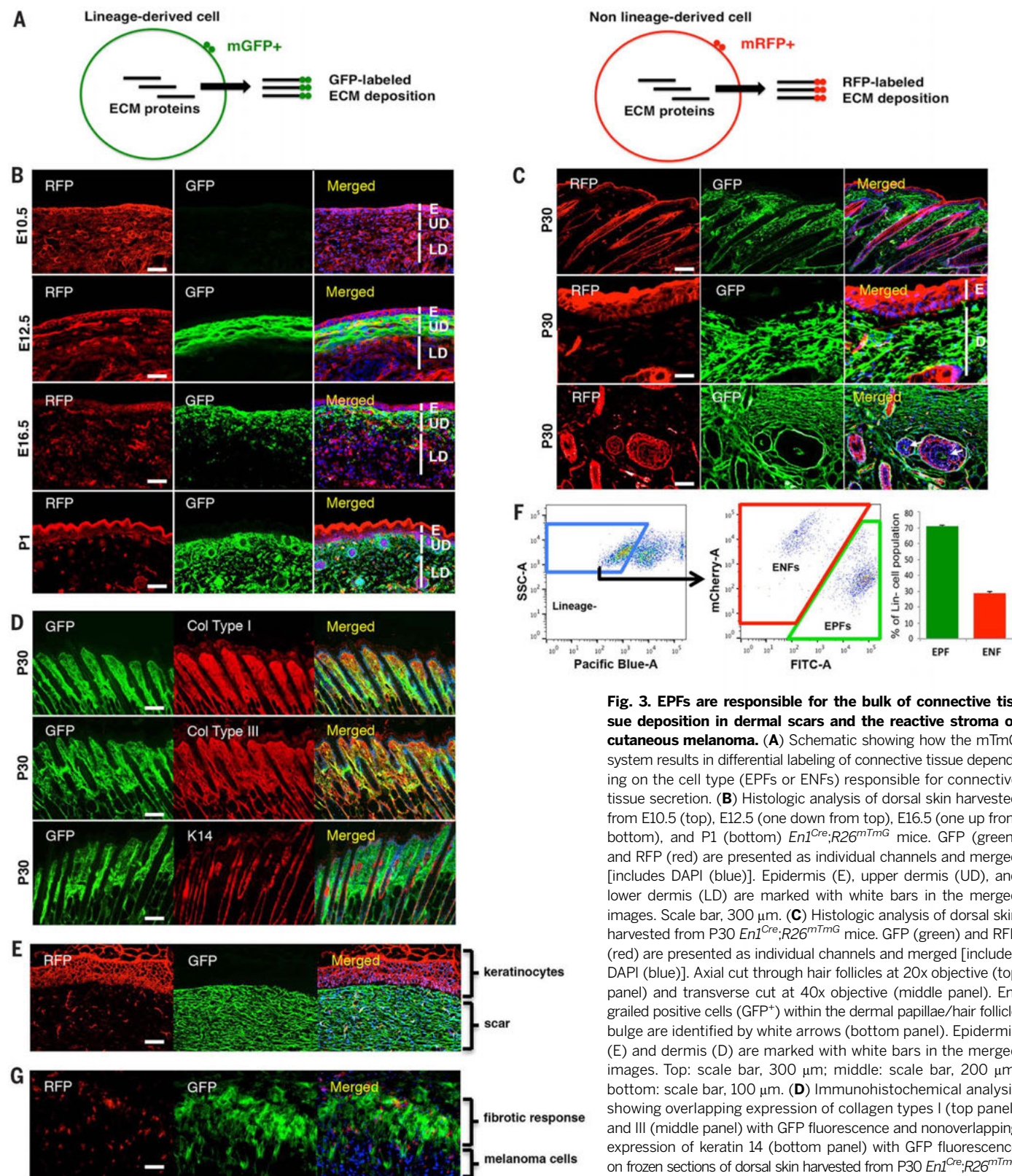


Fig. 3. EPFs are responsible for the bulk of connective tissue deposition in dermal scars and the reactive stroma of cutaneous melanoma.

(A) Schematic showing how the mTmG system results in differential labeling of connective tissue depending on the cell type (EPFs or ENFs) responsible for connective tissue secretion. (B) Histologic analysis of dorsal skin harvested from E10.5 (top), E12.5 (one down from top), E16.5 (one up from bottom), and P1 (bottom) *En1^{Cre};R26^{mTmG}* mice. GFP (green) and RFP (red) are presented as individual channels and merged [includes DAPI (blue)]. Epidermis (E), upper dermis (UD), and lower dermis (LD) are marked with white bars in the merged images. Scale bar, 300 μ m. (C) Histologic analysis of dorsal skin harvested from P30 *En1^{Cre};R26^{mTmG}* mice. GFP (green) and RFP (red) are presented as individual channels and merged [includes DAPI (blue)]. Axial cut through hair follicles at 20x objective (top panel) and transverse cut at 40x objective (middle panel). Engrafted positive cells (GFP⁺) within the dermal papillae/hair follicle bulge are identified by white arrows (bottom panel). Epidermis (E) and dermis (D) are marked with white bars in the merged images. Top: scale bar, 300 μ m; middle: scale bar, 200 μ m; bottom: scale bar, 100 μ m. (D) Immunohistochemical analysis showing overlapping expression of collagen types I (top panel) and III (middle panel) with GFP fluorescence and nonoverlapping expression of keratin 14 (bottom panel) with GFP fluorescence on frozen sections of dorsal skin harvested from P30 *En1^{Cre};R26^{mTmG}* mice. Scale bar, 300 μ m. (E) Histologic analysis of wounded

dorsal skin from *En1^{Cre};R26^{mTmG}* mice at 12 to 14 days after wounding showing GFP-labeled ECM deposition and RFP-labeled fibroblasts, epidermis, and vasculature. Scale bar, 200 μ m. (F) FACS analysis (left panel) and bar graphs (right panel) showing abundance of EPFs and ENFs in wounds of P30 *En1^{Cre};R26^{mTmG}* mice. (G) Histologic analysis of transplanted melanoma cells showing their associated stroma (primarily GFP⁺) and vasculature (primarily RFP⁺) in the dorsal backs of *En1^{Cre};R26^{mTmG}* mice at 30 days after transplantation. Scale bar, 100 μ m.

We analyzed the dermis of *FVB-Tg(CAG-luc, GFP)/L2G85Chco/J(L2G)* mice, which express cytoplasmic enhanced GFP (eGFP) constitutively in all cells (13) and found that in marked contrast to the *R26^{mTmG}* system, GFP fluorescence within the dorsal dermis of adult *L2G* mice was localized to dermal cells, epidermis, and hair follicle epithelium (fig. S1E, third panel), but did not label the dermal ECM to the degree seen in *En1^{Cre};R26^{mTmG}* mice (Fig. 3C). Furthermore, GFP fluorescence highlighted individual stromal and vascular cells within scar tissue from 6-mm excisional wounds induced on the dorsal backs of adult *L2G* mice at 12 to 14 days after wounding but did not label deposited connective tissue and ECM components (fig. S1E, bottom panel).

Given the important role of EPFs in connective tissue secretion during embryonic and postnatal development, we next assessed the relative contributions of EPFs and ENFs to scar formation after cutaneous wounding in the dorsal skin of adult (P30) *En1^{Cre};R26^{mTmG}*. The majority of the deposited scar tissue was GFP-positive and hence EPF-derived (Fig. 3E). Moreover, collagen type I protein expression within the scar site displayed an overlapping pattern with GFP fluorescence, implicating EPFs as the primary secretors of collagen in the healing wound (fig. S1F). We repeated this analysis using a humanized model of wound healing, which proceeds through granulation tissue formation and re-epithelialization, with minimal contraction. Tissues harvested at 14 days after wounding showed abundant EPF-derived collagen filaments and connective tissue (fig. S1G), indicating that regardless of the primary mechanisms underlying wound closure, and despite the presence of ENFs in the healed dermis (Fig. 3F), EPFs are responsible for the bulk of ECM deposition after injury of the dorsal skin in adult mice.

To assess the possibility of a migratory cell lineage contributing to ECM deposition, including the migratory capacity of EPFs, we performed parabiosis between *En1^{Cre};R26^{mTmG}* and background strain (*B6*) mice. After 2 months, excisional skin wounds were induced on the dorsum of the *B6* strain mice. After 14 days, wounds were harvested and analyzed for GFP/RFP fluorescence. We found only scattered donor-derived RFP⁺ cells in the wound site, with a complete absence of both RFP⁺ ECM and GFP⁺ cells (fig. S1H). The absence of GFP⁺ cells and RFP signal from wound connective tissue/ECM indicates that EPFs are not capable of migrating through the circulation to wound sites and that migratory RFP⁺ cells were not directly contributing to scar formation/connective tissue deposition. To further rule out a connection between the EPF lineage and a migratory/circulatory hematopoietic niche, we harvested bone marrow from adult *En1^{Cre};R26^{mTmG}* mice and found a complete absence of GFP signal within the marrow (fig. S1I).

Fibrosis can also occur in a slowly developing reactive process, such as the stromal response to radiation (14) or carcinoma, particularly ma-

lignant melanoma (15). B16 mouse melanoma cells were transplanted to the dorsum of *En1^{Cre};R26^{mTmG}* mice, and after 30 days, tumors were harvested for histology. Consistent with previous reports (16, 17), we found multiple host-derived cells within the melanoma tumor, including various hematopoietic cell types, blood vessels, and fibroblasts surrounded by connective tissue stroma. The stroma of the melanoma was predominantly EPF-derived (GFP⁺) (Fig. 3G). To be sure that *Engrailed-1* was not expressed in response to tumor cells, we stained tumor stroma sections for *Cre* and found no expression (fig. S1J). As a positive control, *Cre* was expressed in E11.5 *En1^{Cre};R26^{mTmG}* dorsal skin sections, as expected (fig. S1J).

We next explored the contribution of EPFs versus ENFs to connective tissue deposition during radiation-induced fibrosis of the skin. Irradiated skin was harvested on day 14 and showed gross signs of radiation-induced fibrosis, including erythema and leathery skin. Histologic analysis revealed a significant fibrotic response with primarily EPF-derived ECM and an absence of ENF-derived ECM (fig. S1K). All blood vessels and hematopoietic infiltrates within the fibrotic tissue were RFP-positive, as expected. These data further demarcate EPFs as the primary lineage contributing to connective tissue deposition during embryonic development, postnatal wound healing, cancer stroma formation, and radiation fibrosis of the skin.

Fibrogenic potential of dermal fibroblasts is cell-intrinsic

To investigate whether differences in wound repair between oral and cutaneous dermis (18) are a consequence of cell-intrinsic versus environmental properties, we analyzed the contribution of the embryonic neural crest to the cranial and oral dermis, using the *Wnt1^{Cre}* transgenic mouse, which permanently labels early migratory neural crest populations at all axial levels (19–21). The oral dermis from *Wnt1^{Cre};R26^{mTmG}* was harvested, and *Wnt1* lineage-positive fibroblasts (WPFs), defined *in vivo* by their GFP positivity (and GFP⁺RFP⁺Lin[−] by flow cytometry), were present within oral dermis and exhibited a significant contribution to connective tissue secretion and organization, as seen by GFP signal that labeled the dermal ECM (Fig. 4A).

However, a population of *Wnt1* lineage-negative fibroblasts (WNFs, defined as GFP[−]RFP⁺Lin[−] by flow cytometry) was also present within the oral dermis, as seen by histology and FACS analyses (Fig. 4, A and B). FACS-isolated WPFs and WNFs both exhibited spindle-shaped morphologies and were highly motile (Fig. 4C). These results indicate that, similarly to cutaneous sites, at least two separate lineages of fibroblasts coexist within the oral dermis (WPFs defined as GFP⁺RFP⁺Lin[−] and WNFs defined as GFP[−]RFP⁺Lin[−]), out of which only WPFs are the primary contributing lineage to ECM deposition *in vivo*.

Given the role of WPFs in connective tissue secretion and organization of the oral dermis during postnatal development (Fig. 4A), we hy-

pothesized that WPFs contribute significantly to connective tissue deposition within the oral cavity after wounding. Full thickness wounds in the buccal mucosa of adult (P30) *Wnt1^{Cre};R26^{mTmG}* mice displayed a beehive pattern of collagen deposition within the dermis and a characteristic epidermal hyperproliferation of keratinocytes (Fig. 4D). The majority of the deposited scar tissue was GFP-positive and hence WPF-derived (Fig. 4D). The architecture of these oral scars differed significantly from the dense plugs of connective tissue seen in cutaneous dorsal scars (Fig. 3E). Consistent with this difference in scar architecture, collagen content was significantly diminished within oral wounds in comparison with dorsal skin wounds (Fig. 4E), as seen by decreased blue (collagen) staining with Masson's trichrome.

To begin investigating the intrasite and intersite diversity in fibroblast heterogeneity, we compared the transcriptional programs of EPFs isolated from dorsal and ventral dermal sites of adult (P30) mice to those of WPFs from cranial and oral dermal sites of adult (P30) mice, using gene expression microarray analysis. Unsupervised clustering using AutoSOME (22) revealed groups of coordinately expressed genes underlying similarities and differences among the fibroblast populations (Fig. 4F), with the most notable differences identified between EPFs and WPFs (fig. S2A). Indeed, although each of the four populations (dorsal, ventral, cranial, and oral cavity) is readily distinguishable by transcriptome-wide expression analysis ($P < 0.05$; AutoSOME clustering), EPFs and WPFs exhibit the highest degree of difference in global expression signatures (Fig. 4G), consistent with their separate somitic and neural crest origins.

To directly assess whether site-specific differences in dermal architecture reflect cell-intrinsic properties of distinct fibroblast lineages (*Wnt1* neural crest derived versus *Engrailed-1* somitic derived) or are an outcome of distinct anatomic microenvironments, we initiated reciprocal transplantation experiments. Ten days after transplantation, both sites (oral cavity and dorsal back) revealed ectopic deposition of connective tissue that was donor-cell derived (GFP⁺). However, the EPF-derived scar tissue deposited within the oral cavity was significantly different from host-derived ECM, with dense and elongated collagen fibrils, minimal infiltrate of vasculature or hematopoietic cells, and exhibited classic dorsal scar phenotypes (Fig. 4H). Although similar cell numbers were transplanted in both experiments (1×10^5), WPFs transplanted into the dorsal back exhibited considerably reduced scarring in comparison with EPFs transplanted into the oral cavity, as seen by GFP fluorescence and collagen type I staining (Fig. 4H, bottom panels). Instead of forming a dense plug of scar tissue, as seen by EPFs transplanted into the oral cavity, WPFs were dispersed around hair follicles, where they secreted a beehive pattern of collagen deposition (Fig. 4H, bottom panels), mimicking a minimal oral cavity scar (Fig. 4, D and E). We found no significant difference at 10 days after transplantation, in either cell proliferation or cell survival parameters between

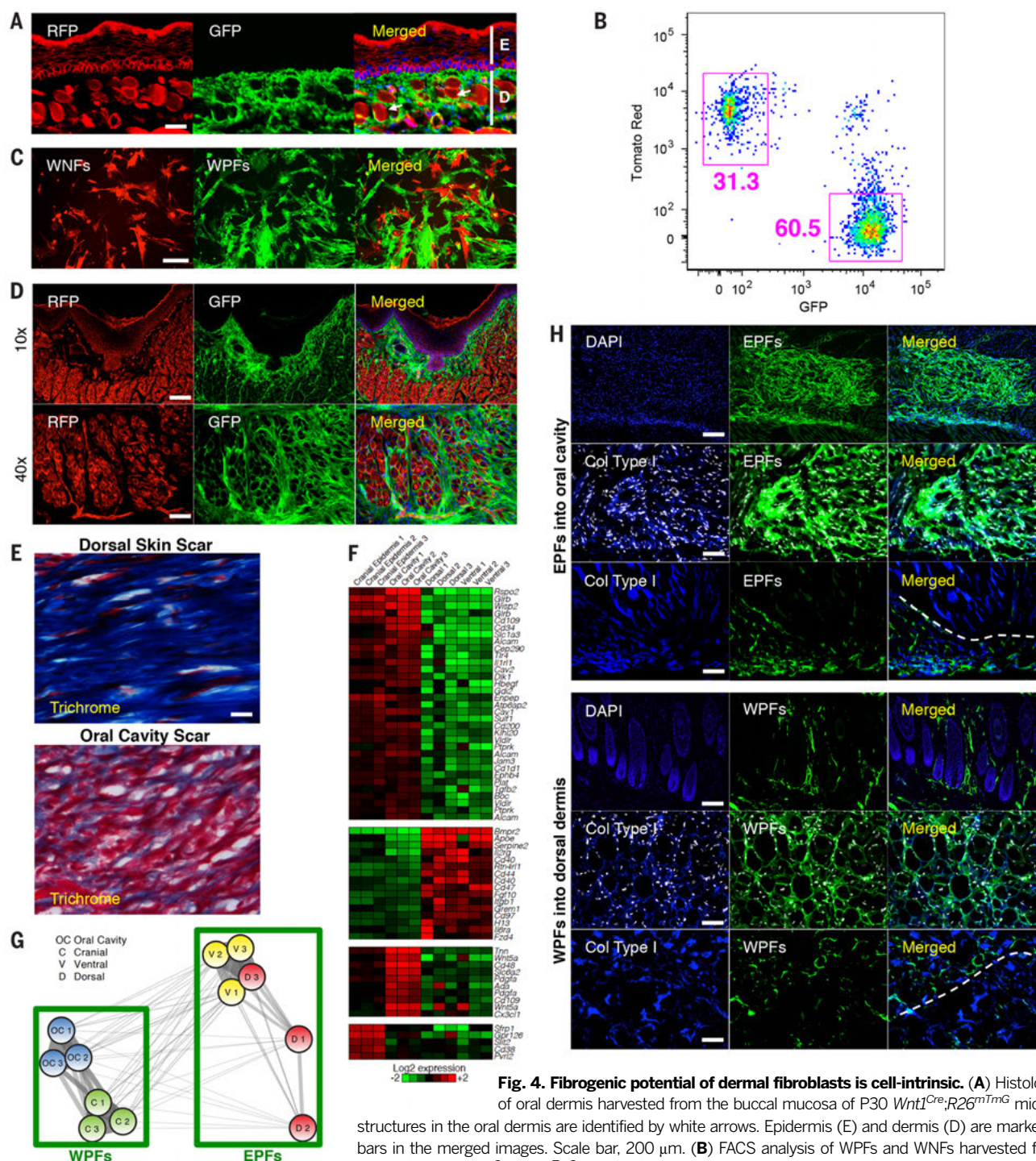


Fig. 4. Fibrogenic potential of dermal fibroblasts is cell-intrinsic. (A) Histologic analysis of oral dermis harvested from the buccal mucosa of P30 *Wnt1^{Cre};R26^{mTmG}* mice. Glandular structures in the oral dermis are identified by white arrows. Epidermis (E) and dermis (D) are marked with white bars in the merged images. Scale bar, 200 μ m. (B) FACS analysis of WPFs and WNFs harvested from the oral dermis of P30 *Wnt1^{Cre};R26^{mTmG}* mice showing the relative percentage of each population within the oral dermis.

(C) Cultured WPFs and WNFs portray characteristic fibroblast morphologies. Scale bar, 100 μ m. (D) Histologic analysis of wounded oral dermis from *Wnt1^{Cre};R26^{mTmG}* mice at 12 to 14 days after wounding showing GFP-labeled scar tissue, as well as RFP-labeled epidermis, vasculature, and adipose tissue in 10x (top) and 40x (bottom) magnification. Top: scale bar, 400 μ m; bottom: scale bar, 100 μ m. (E) Trichrome staining of oral cavity and dorsal scars at 14 days after wounding. Scale bar, 50 μ m. (F) Heat map showing four representative clusters of differentially expressed genes from cultured WPFs (cranial dermis and oral dermis) and EPFs (dorsal dermis and ventral dermis). Although all probe sets were analyzed by the AutoSOME unsupervised clustering algorithm (22), for clarity, only surface markers are shown here. Detailed cluster results are provided in fig. S2A. (G) Fuzzy cluster network showing transcriptome-wide differences between oral cavity (WPFs), cranial (WPFs), dorsal (EPFs), and ventral (EPFs) fibroblast populations. Each node represents a microarray data set, and edges between nodes depict the pairwise similarity between fibroblasts as determined using AutoSOME (22), ranging from low similarity (thin and translucent) to high similarity (thick, with higher opacity). (H) Histologic analysis (GFP fluorescence and collagen type I staining) of EPFs from dorsal back of P30 *En1^{Cre};R26^{mTmG}* mice transplanted into the oral cavity of *RAG-2^{-/-}* double-knockout mice (top panels) and WPFs from the oral cavity of P30 *Wnt1^{Cre};R26^{mTmG}* mice transplanted into the dorsal back of *RAG-2^{-/-}* double-knockout mice (bottom panels). White dotted lines separate transplanted cells expressing collagen and native cells expressing collagen. 1st and 4th rows: scale bar, 300 μ m; 2nd and 5th rows: scale bar, 100 μ m; 3rd and 6th rows: scale bar, 200 μ m.

EPFs transplanted into the oral cavity and WPFs transplanted into the dorsal dermis ($n = 5$) (fig. S2, B and C). These data indicate that WPFs and EPFs are functionally distinct populations in terms of their migratory and secretory programs.

Cycles of growth and rest phase of hair follicles within the dorsal skin cause cyclic change in dermal thickness (23). To investigate whether these changes may affect the ECM deposition of implanted cells, we transplanted WPFs (1×10^5) to the dorsal back skin of mice at 4 and 7 weeks of age, representing anagen and telogen phases of the hair follicle cycle, respectively. We found no difference in collagen distribution pattern in relation to hair follicle cycle ($n = 5$) (fig. S2D). These data indicate that site-specific differences in dermal architecture between oral and cutaneous dermis are predominantly outcomes of lineage-intrinsic properties that are unaffected by new host tissue, regardless of anatomic location, dermal age, or hair follicle cycle.

DTR-based ablation of EPFs reduces cutaneous scarring during wound healing

Given the role of EPFs as the primary lineage responsible for cutaneous scar deposition, we next investigated whether ablation of the lineage could lead to a reduction in scarring.

We crossed $R26^{tm1(HBEGF)Aval}$ mice, which express simian diphtheria toxin receptor (DTR) in a Cre-dependent manner, with $En1^{Cre};R26^{mTmG}$ mice. The resulting triple-positive offspring ($En1^{Cre};R26^{mTmG};R26^{tm1(HBEGF)Aval}$), expressing both GFP and DTR in EPFs only, were dorsally wounded and were treated with either 200-ng diphtheria toxin (DT) in phosphate-buffered saline (PBS) or PBS alone (control).

Wound size in DT-treated mice increased from day 0 to day 3 of wounding (Fig. 5A), implicating EPFs as the predominant lineage from which contractile, scar-forming myofibroblasts are derived. Complete healing of DT-treated wounds required 20 days, an additional 6 days over that of control wounds (14 days) and reported splinted excisional wound healing rates (24) in mice (Fig. 5B). Endpoint analyses were therefore conducted on fully healed DT-treated and control wounds harvested at 21 days and 15 days after wounding, respectively.

Scar size, measured as a percentage of initial wound size, was not significantly different in DT-treated as compared with control wounds ($P = 0.3192$) (Fig. 5C). However, histologic analysis revealed greatly reduced GFP-labeled connective tissue deposition in DT-treated as compared with PBS-treated controls (Fig. 5D). Moreover, the overall pattern and density of collagen deposition differed markedly between DT-treated and control wounds. Masson's trichrome staining revealed greater cellularity and reduced collagen density, evidenced by a higher ratio of red to blue staining, in treated as compared with control wounds (Fig. 5E). The change in collagen deposition did not influence the tensile strength of the healed wounds (Fig. 5F) or result in regeneration of adipocytes or hair follicles in the healed dermis

(Fig. 5, G and H). Taken together, these data confirm an important functional role for EPFs both in terms of wound closure and connective tissue deposition during wound healing.

DTR-based ablation of EPFs reduces melanoma growth

Given our finding that EPFs are the primary fibroblast lineage responsible for dermal fibrosis seen in cutaneous melanoma, we next assessed the effects of ablating EPFs before melanoma growth. Tumors were allowed to grow in DT-treated ($n = 10$) and control ($n = 10$) mice until euthanasia was dictated by protocol parameters for a single mouse, at which point all mice were killed for endpoint analyses. Tumor burden (as measured by total tumor weight at day 22) was significantly higher ($P = 0.0166$) in control melanomas than in DT-treated melanomas (Fig. 5I). Histologic analysis of GFP/RFP fluorescence revealed reduced deposition of EPF-derived (GFP⁺) connective tissue in DT-treated as compared with control melanomas (Fig. 5J). As expected, deposition patterns in the control-treated melanomas of $En1^{Cre};R26^{mTmG};R26^{tm1(HBEGF)Aval}$ mice (Fig. 5J) closely resembled those seen in $En1^{Cre};R26^{mTmG}$ mice transplanted with melanoma (Fig. 3G).

Surface profiling and prospective isolation of EPFs

Having identified EPFs as a fibrogenic lineage in the dorsal dermis and established their functional importance through DTR-based ablation, we endeavored to prospectively isolate EPFs from the dermis of wild-type mice using flow cytometry methods. As before, a FACS-based fibroblast purification strategy using a lineage-negative gate (Lin⁻) was employed to isolate EPF and ENF populations for all experiments discussed here. Adult mice aged 8 weeks were used.

Both surface markers currently proposed for fibroblast isolations—including CD44, CD90 (Thy1), biglycan, CD73 (fig. S2E)—and 35 additional surface molecules that were identified based on a whole-transcriptome microarray data of uncultured EPFs and ENFs (fig. S3) were expressed on both EPFs and ENFs, precluding them as discriminatory surface molecules. We employed a cell surface marker screen composed of 176 monoclonal antibodies to assess the presence and relative abundance of each surface molecule on EPFs and ENFs. FACS analysis revealed that most of the 176 surface molecules in the screen were either marginally expressed on both populations or were present on both populations to similar degrees (table S2). For example, CD13 was expressed on both EPFs (35.2%) and ENFs (28.7%). CD34, a transmembrane glycoprotein thought to be involved in the modulation of signal transduction and cell adhesion (25), was broadly expressed on EPFs (75.6%) and ENFs (50.5%). CD47, a surface molecule known to interact with macrophages and inhibit apoptosis (26), was expressed on a greater percentage of EPFs (65.5%) than ENFs (24.1%). Thus, although these molecules cannot be used to uniquely identify or substantially enrich for EPFs over ENFs,

their presence on large fractions of EPFs indicates that they may hold functional importance. The commonly cited fibroblast marker Thy1 (CD90) was expressed broadly within both EPF and ENF populations and therefore was ineffective as a discriminatory lineage marker, consistent with our whole-genome and flow cytometry analysis (table S2).

From the list of 176 surface molecules, we identified several markers that were highly expressed on EPFs and marginally on ENFs (CD26, LY-51, CD54, and CD61) (table S2). FACS analysis of primary noncultured EPFs and ENFs isolated from $En1^{Cre};R26^{mTmG}$ mice identified CD26 as the surface marker offering the highest-fold enrichment of EPFs over ENFs (nearly 15-fold) (fig. S4A) and labeled a large percentage of EPFs (94%) (Fig. 6A). The fold enrichment and purity of EPFs achieved with CD26 significantly surpassed those of the classic fibroblast markers previously described, such as CD73, CD90, and biglycan, which either did not enrich for EPFs (CD90 and biglycan) or were limited to a maximum enrichment of 3.5-fold (CD73) (fig. S2E). WPFs were found to express CD26 at levels similar to EPFs (fig. S4B).

To further confirm the presence and specificity of these markers on EPFs in situ, we performed immunohistochemical analyses on dorsal dermis from P30 $En1^{Cre};R26^{mTmG}$ mice. Consistent with FACS analyses, high CD26 immunopositivity was observed in regions of upper dermis between hair follicles, but not on the follicles themselves, and displayed an overlapping pattern with GFP but not RFP fluorescence (Fig. 6B). Furthermore, although CD26 has been reported to be a specific marker for upper dermis during fetal development (27), it appears that CD26 is also expressed in the lower reticular dermis during adult stages (Fig. 6B).

To functionally corroborate that possibility, CD26⁺Lin⁻ and CD26⁺Lin⁻ fibroblast populations from uncrossed $R26^{mTmG}$ transgenic mice, representing EPFs and ENFs, respectively, were FACS-sorted and transplanted via intradermal injection into the dorsal backs of immunodeficient $RAG-2^{-/-}$ double-knockout mice. Intradermal injection induces an initial inflammatory response followed by fibrosis (scarring) and was therefore chosen as an in vivo assay for ECM deposition.

Histologic analysis of grafted cells at 10 days after transplant revealed a dermal architecture with abundant deposition of RFP-labeled ECM in the CD26-positive grafts that was nearly absent in the CD26-negative grafts (Fig. 6C). Despite approximately equal numbers of total RFP⁺ cells, the increased and more diffuse pattern of RFP-labeled ECM is evident in skin transplanted with CD26-positive as compared with CD26-negative fibroblasts (Fig. 6C). RFP signal was found to be significantly higher in CD26-positive as compared with CD26-negative grafts (Fig. 6C). qRT-PCR analysis of RFP-positive cells FACS-sorted 10 days after transplant from CD26⁺Lin⁻ and CD26⁺Lin⁻ grafts revealed 5.32-fold greater expression of collagen type I (collagen type in cutaneous scars) and 7.11-fold greater expression of alpha-smooth-muscle

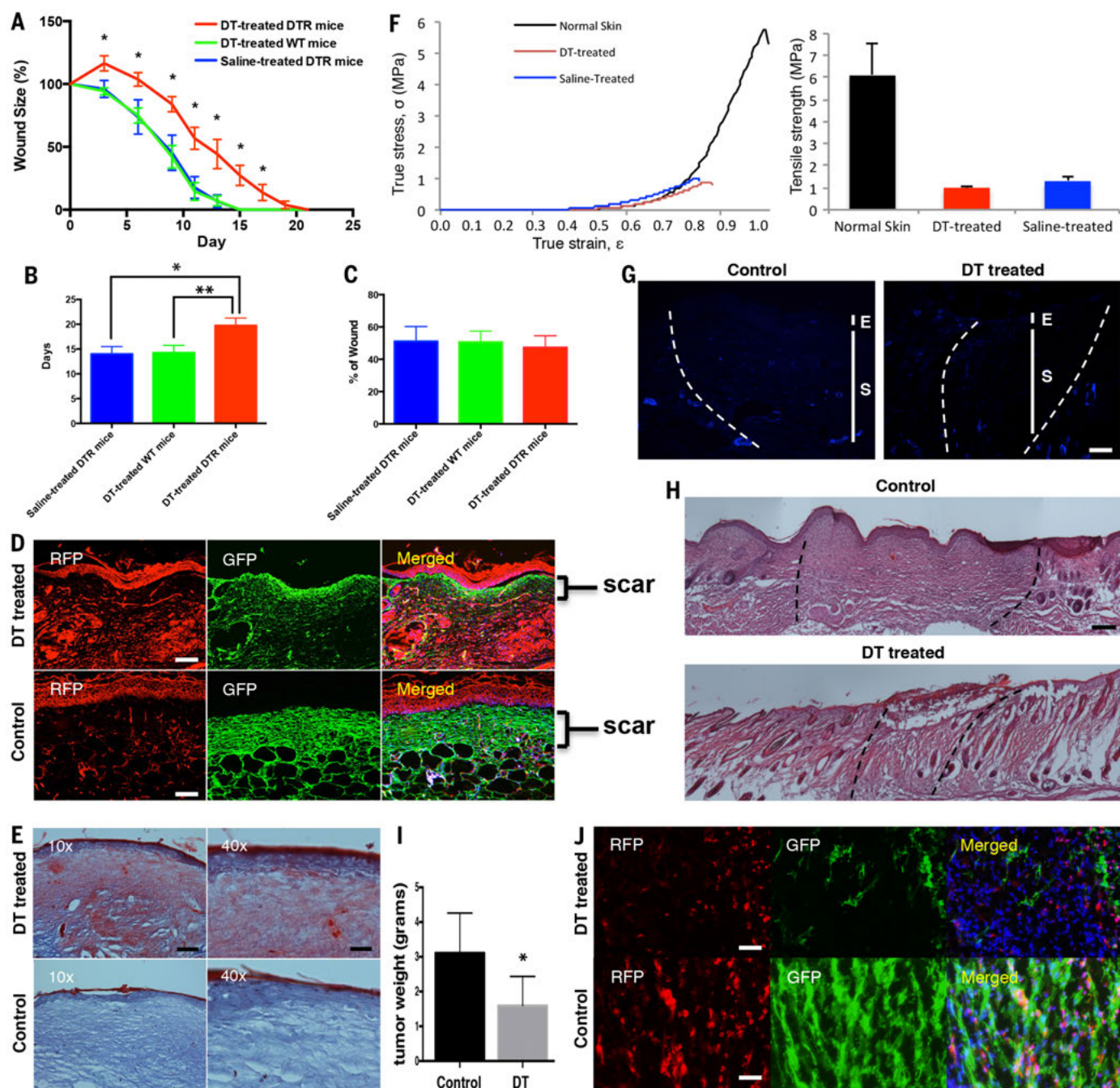


Fig. 5. DTR-based ablation of EPFs results in decreased connective tissue deposition (scar) after cutaneous wounding and reduced melanoma tumor size. (A) Wound healing curve plotted as a percentage of day 0 wound size versus days since wounding. DT-treated wounds ($n = 10$) (red) show significantly ($P < 0.01$) slower healing as compared with control wounds ($n = 10$) (green and blue). (B) Time to complete healing in DT-treated wounds ($n = 10$) (red) compared with control wounds ($n = 10$) (green and blue). (C) Scar size (area) measured as a percentage of the original wound area in DT-treated wounds ($n = 10$) (red) compared with control wounds ($n = 10$) (green and blue) showing no significant difference in scar. (D) Histologic analysis of GFP and RFP fluorescence in DT-treated wounds and control wounds. GFP (green) and RFP (red) are presented as individual channels and merged [includes DAPI (blue)]. Scale bar, 200 μm . (E) Trichrome staining of DT-treated wounds and control wounds showing reduced collagen deposition in DT-treated (higher ratio of red:blue staining) as compared with control wounds (lower ratio of red:blue staining). Left: scale bar, 400 μm ; right: scale bar, 100 μm . (F) Rep-

representative stress-strain profile (left) and ultimate tensile strength (right) of *En1^{Cre};R26^{mTmG};R26^{tm1(HBEGF)Awai}* normal skin and fully healed wounds treated with DT and saline on days 21 and 15. (G) Immunofluorescent staining for adipocytes with FABP4 antibody showing that DT-treated wounds did not regenerate adipocytes compared with control wounds. Epidermis (E) and scar (S) are marked with white bars. In the control image, the healed wound is to the right of the white dotted line, and in the DT-treated image, the healed wound is in between the white dotted lines. Scale bar, 200 μm . (H) Hematoxylin and eosin (H&E) staining to visualize hair follicles showing that DT-treated wounds did not regenerate any hair follicles compared with control wounds. The healed wound is in between the black dotted lines. Scale bar, 500 μm . (I) Bar graph showing a significant ($P = 0.0413$) reduction in the weight of melanoma tumors at day 22 in DT-treated ($n = 7$) mice versus control ($n = 7$) tumors. (J) Histologic analysis of GFP and RFP fluorescence in DT-treated and control melanomas showing reduced EPF-derived connective tissue deposition in DT-treated as compared with control melanomas. Scale bar, 100 μm .

actin (a marker of fibroblast activation) in CD26-positive grafts than in CD26-negative grafts (Fig. 6D, left). At baseline, this difference is markedly

reduced, suggesting that, although CD26⁺ EPFs and CD26⁻ ENFs have similar expression of ECM genes, their ability to respond to stimuli

and up-regulate the expressions of ECM and contractile genes is one major molecular difference between these populations (Fig. 6D, right).

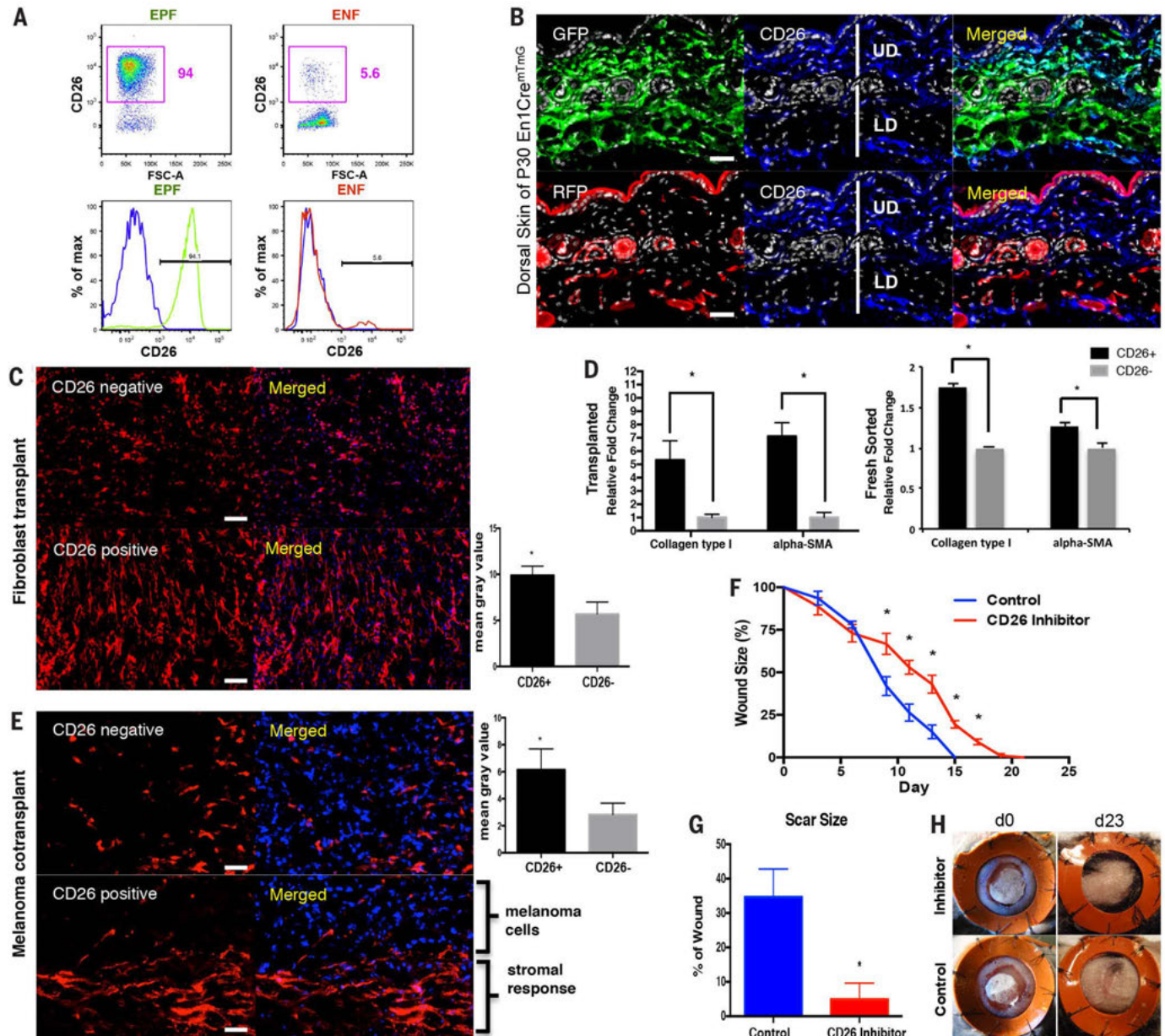


Fig. 6. CD26 allows enrichment of EPFs over ENFs, and its inhibition results in decreased connective tissue deposition (scar) after cutaneous wounding. (A) FACS analysis of CD26 expression on the surface of FACS-isolated EPFs and ENFs. (B) Immunohistochemical analysis of CD26 expression in the dorsal skin of *En1Cre^{mTmG}* mice. White lines are marked on one of the images to denote upper (UD) and lower (LD) dermis. Scale bar, 200 μ m. (C) Histologic analysis of FACS-isolated CD26^{Lin} and CD26^{+Lin} populations from the dorsal skin of *R26^{mTmG}* mice transplanted via intradermal injection into the dorsal backs of *RAG-2^{-/-}* double-knockout mice. Bar graph shows quantification of RFP fluorescence in CD26^{Lin} (black) and CD26^{+Lin} (gray) grafts. Scale bar, 100 μ m. (D) qRT-PCR analysis of collagen type I ($P = 0.00957$) and α -smooth-muscle actin ($P = 0.0151$) from FACS-isolated CD26^{Lin} and CD26^{+Lin} cells. Right panel represents analysis of fibroblasts isolated from naïve dermis; left panel represents analysis of fibroblasts isolated from wounded dermis at 10 days after transplant from CD26^{Lin} ($n = 3$) and

CD26^{+Lin} ($n = 3$) grafts [for graft histology, see (C)]. (E) Histologic analysis of FACS-isolated CD26^{Lin} and CD26^{+Lin} populations from the dorsal skin of *R26^{mTmG}* mice cotransplanted with B16 F10 mouse melanoma cells via intradermal injection into dorsal backs of *RAG-2^{-/-}* double-knockout mice. Bar graph shows quantification of RFP fluorescence in CD26^{Lin} (black) and CD26^{+Lin} (gray) melanomas grafts. Scale bar, 100 μ m. (F) Wound healing curve plotted as a percentage of day 0 wound size versus days since wounding. CD26 inhibitor (diprotin A)-treated wounds ($n = 10$) (red) show significantly ($P < 0.01$) slower healing as compared with control wounds ($n = 10$) (blue). (G) Scar size (area) measured as a percentage of the original wound area in CD26 inhibitor (diprotin A)-treated (red) and control (black) wounds showing significantly reduced ($P = 0.0003$) scar size in CD26 inhibitor-treated wounds ($n = 10$) as compared with control wounds ($n = 10$) (blue). (H) Representative photographic images of wounds at day 0 and day 23 after wounding (complete healing and scar formation) in both control and CD26 inhibitor (diprotin A)-treated wounds.

Together, these findings functionally corroborate CD26 as a marker for a distinct fibrogenic lineage in the dorsum of mice.

Given the fibrogenic contributions of EPFs to melanoma progression in the dorsal backs of *Enl^{Cre};R26^{mTmG}* mice (Fig. 3G), we investigated the contribution of the CD26⁺Lin⁻ versus CD26⁻Lin⁻ fibroblasts to the stromal compartment of melanomas. Primary fibroblasts were sorted from the dorsal dermis of uncrossed *R26^{mTmG}* reporter mice based on their membrane expression of CD26 and cotransplanted with B16 F10 mouse melanoma cells by intradermal injection into the dorsal skin of *RAG-2^{-/-}* double-knockout mice. After 30 days, histologic analysis of the transplanted tumors revealed a dermal fibrotic phenotype with increased deposition of RFP-labeled ECM in melanomas cotransplanted with CD26⁺Lin⁻ fibroblasts in comparison with melanomas cotransplanted with CD26⁻Lin⁻ fibroblasts (Fig. 6E). These data functionally corroborate CD26 as a surface marker for a fibroblast lineage responsible for ECM deposition after cutaneous injury and melanoma stroma formation.

Inhibition of CD26 reduces cutaneous scarring during wound healing

CD26, also known as dipeptidyl peptidase-4 (DPP4), is a cell-surface serine exopeptidase that cleaves X-proline dipeptides from the N terminus of polypeptides (28). Given the selective expression of CD26 on the surface of scar-forming EPFs, we next assessed the effects of inhibiting CD26 on scar formation during wound healing using a small molecule (diprotin A), which acts as a selective allosteric inhibitor of CD26 peptidase activity through its function as a slowly hydrolyzed substrate for CD26 (29).

The rates of healing between treated and control wounds during the initial days of wound healing remained approximately equal. However, a significant difference in wound size of ~30% developed by day 9 after wounding, with larger and less healed wounds in CD26-inhibitor-treated cohorts in comparison with controls (Fig. 6F). This difference persisted through the remaining days of wound healing. Ultimately, complete healing of CD26-inhibitor-treated wounds took 5 days longer ($P < 0.01$) than control wounds (Fig. 6F). Most important, although the rate of healing was decreased in inhibitor-treated versus control wounds, treated wounds showed significantly reduced final scar size ($P < 0.001$) after wound healing had reached completion as a percentage of the original wound size in comparison with control wounds (Fig. 6, G and H).

Discussion

Fibroblast functional properties: Intrinsic or extrinsic?

A critical question concerning fibroblast biology is whether their specific functional properties are cell-intrinsic or cell-extrinsic. Our reciprocal transplantation experiments showed that differences in dermal architecture and wound healing outcomes between oral versus dorsal dermis are

independent of the local microenvironment and can be mimicked by transplantations of distinct fibroblast lineages, indicating that cell-intrinsic properties rather than environmental differences are the primary effecting mechanisms underlying intersite diversity.

A recent study also lends support to this notion. Driskell *et al.* identified a distinct lineage of fibroblasts involved in forming the embryonic dermal architecture (27). Our data, along with that of Driskell *et al.*, begin to define fibroblast lineages that have different roles in skin development, homeostasis, and response to acute or chronic injury. The analysis of the Driskell *et al.* report and our data implies that embryonic lineages of fibroblasts represent de facto operational hierarchies that underlie the diversities of regenerative programs and outcomes between anatomic sites.

Our data describing the fibroblast lineages (*Enl* and *Wnt1*) responsible for scar deposition after wounding of dorsal skin and oral mucosa also address a long-standing question: Where do the dermal fibroblasts that deposit scar tissue after wounding come from? In the internal organs, some have shown that wound fibroblasts are derived from circulating fibroblast-like cells (30, 31) and that dermal architectures may be additionally supported by nonmesenchyme lineages (32), as in kidney fibrosis. Our data indicate that within cutaneous tissues, a distinct and local lineage of resident fibroblasts is responsible for the fibrosis seen during wound healing, with an absence of ECM contributions from other mesenchyme or nonmesenchyme lineages. Our data also indicate that local fibroblasts, not circulating cells, are responsible for the connective tissue seen in the fibrosis formed in response to both radiation and carcinoma.

Targeting the fibroblast culprit behind cutaneous scarring

On the basis of CD26/DPP4 expression, we have prospectively isolated the lineage of cells that is responsible for the bulk of fibrosis, including the cells involved in tumor stroma. Our mouse data are consistent with reports on expression of CD26/DPP4 and its related serine protease FAP α (fibroblast activation protein- α) on stromal subsets of human cancers (33, 34). Depletions of FAP α -expressing stromal subsets from human cancers were recently shown to inhibit antitumor immunity and suppress tumor growth (34), and a similar anti-immunogenic mechanism could, in part, explain the CD26 depletion phenotypes of our tumor growth assays and slower rate of healing in wound-healing models.

Driskell *et al.* (27) have recently reported CD26 to be a marker of the upper dermis during fetal development. Our data demonstrate that CD26 is expressed in both upper and lower dermis at adult stages of development (Fig. 6B). The Driskell *et al.* report initially employs Pdgfra-GFP transgenic mice (using FACS isolation of Pdgfra surface expression) to verify and prospectively isolate dermal fibroblasts from the back-skin. Yet, our flow cytometry analysis on adult

dermis indicates that 35% and 87% of EPFs and ENFs, respectively, do not express Pdgfra surface protein (fig. S4C). Therefore, a significant fraction of the dermal fibroblasts assessed in our study are in fact absent from the analysis of the Driskell *et al.* report.

Given that CD26/DPP4 inhibitors such as sitagliptin (Merck) and vildagliptin (Novartis) have been approved by the FDA for the treatment for type 2 diabetes (35), it is possible that blood concentrations of orally administered gliptins may be sufficient to affect wound healing and fibrosis in patients. If not, clinical trials to test topical delivery of a CD26/DPP4 inhibitor in a dermal hydrogel or other local carrier would be an appropriate next step toward clinical implementation.

Materials and Methods

Mice

Mice were bred and maintained at the Stanford University Research Animal Facility in accordance with Stanford University guidelines. All the animals were housed in sterile micro-insulators and given water and rodent chow ad libitum. *Enl^{Cre}*, *Wnt1^{Cre}*, *Sox9^{Cre}*, *Tie2^{Cre}*, *K5^{Cre}*, *K14^{Cre}*, *RAG-2^{-/-}*, *FVB*, *R26^{tm1(HBEGF)Awa1}*, and *CAG-luc-eGFP L2G85* strains were obtained from Jackson laboratories. The *ROSA26^{mTmG}* (*R26^{mTmG}*) reporter mice, which harbor a double-fluorescent reporter that permanently replaces the expression of membrane-bound tomato red fluorescent protein (RFP) with membrane-bound GFP after recombination (10), were a gift from L. Luo (Stanford University). *Enl^{Cre}* transgenic mice were crossed with *R26^{mTmG}* reporter mice (Fig. 1A). *Enl^{Cre}*; *R26^{mTmG}* offspring were used to trace *Enl*-lineage-positive fibroblasts (EPFs), defined in vivo by their GFP positivity, into the dorsal dermis.

Harvesting dermal fibroblasts

Mice were killed, and the dorsal fur was clipped; a hair-removal product was then applied topically to the dorsum for 1 to 5 min, followed by rinsing of the shaved skin with PBS. To preserve cell viability (36), dorsal skin was harvested immediately using dissecting scissors by separation along fascial planes and rinsed in betadine followed by 5x PBS washes on ice. Subcutaneous fat was then trimmed and cleaned from the dermis using a scalpel. Tissue was then incubated in 0.12 mg/mL Elastase (Abcam) in Dulbecco's modified Eagle's medium (DMEM) at 37°C for 25 min to allow for dermal-epidermal separation. Epidermis was then discarded, and dermis was mechanically diced with razor blades and dissecting scissors until samples reached uniform consistency. Oral mucosa was harvested using 3-mm biopsy punches and dissecting scissors along the buccal mucosa bilaterally and then processed identically to dorsal skin from this stage onward. After mechanical dissociation, samples were incubated in 20 mL Collagenase IV (Gibco) at a concentration of 4 mg/mL in DMEM [no fetal bovine serum (FBS)] on a water-bath shaker at 37°C for 1 hour. Samples were then passed through a 10-mL syringe (no needle)

5x and then through an 18.5 gauge syringe 5x, using “back loading” to load the syringe. Samples were placed back onto the shaker at 37°C for 1 hour. Enzymatic digestion was stopped by addition of 10% FBS DMEM, at which time the sample was centrifuged at 1250 revolutions per minute (rpm) for 5 min at 4°C to pellet cells. Supernatant was removed, with care taken to first remove the top layer of adipocytes before the remaining supernatant. Cells were resuspended in 10% FBS DMEM and passed through a 100- μ m filter using centrifugation. The filtered suspension was further centrifuged at 1250 rpm for 5 min at 4°C. The supernatant was removed and the pellet was resuspended in 10% FBS DMEM and passed through a 70- μ m filter. The filtered suspension was centrifuged again at 1250 rpm for 5 min, supernatant was removed, and the pellet was resuspended in ammonium-chloride-potassium (ACK) lysing buffer for 10 min at room temperature to facilitate lysis of red blood cells. ACK suspension was then diluted with equal volume FACS buffer and passed through a 40- μ m filter. The filtered suspension was centrifuged at 1250 rpm for 5 min at 4°C, supernatant was removed, and the pellet was resuspended in FACS buffer containing deoxyribonuclease (DNase) (10 μ g/ml). The cell suspension was then stained with PacBlue-conjugated CD31, CD45, Tie2, Ter119, and EpCAM for 20 min on ice and washed three times with FACS buffer and centrifuged. Cells were then resuspended in FACS buffer containing DNase (10 μ g/ml) and 4',6-diamidino-2-phenylindole (DAPI) (1X). FACS sorting (FACSARIA III) for DAPI-negative, CD31-negative, CD45-negative, Tie2-negative, Ter119-negative, and EpCAM-negative cells (for hematopoietic, endothelial, and epithelial cells) was then performed to isolate dermal fibroblasts. Positivity for GFP or RFP allowed for the separation of EPFs from ENFs and WPFs from WNFs.

FACS analysis of dermal fibroblasts

All flow cytometry analysis on dermal fibroblasts described in this manuscript was performed on dissociated primary dermal fibroblasts after lineage-negative gating of hematopoietic, endothelial, and epithelial cell lineages, using CD31, CD45, Tie2, Ter119, and EpCAM (CD326). The following antibodies were used to interrogate surface marker expression on EPFs and ENFs: CD44, CD73, CD90.1, CD90.2, CD105, biglycan, CD9, CD26, CD29, CD207, CD184, CD63, CD117, CD41, CD83, CD49e, CD49d, CD71, CD98, CD157, CD19, CD16/32, CD140a, CD172a, CD61, Ly-51, CD23, CD115, CD200, CD47, CD51, H2-Kb, and CD183 (BioLegend, eBioscience, Abcam). Cells were stained with a single anaphase-promoting complex conjugated antibody (above) during the harvest protocol along with PacBlue-conjugated CD31, CD45, Tie2, Ter119, and EpCAM antibodies. Cells were resuspended in FACS buffer and DAPI before FACS analysis.

Immunostaining of cultured fibroblasts

Fibroblasts (FACS-isolated as described previously from *Enl^{Cre};R26^{mTmG}* mice) were plated into 8-well culture slides for 2 days (BD Biosciences) and

then fixed in 4% paraformaldehyde at 4°C for 10 min and stained with the following primary antibodies: FSP-1 (Abcam), vimentin (Abcam), α -SMA (Abcam), type IV collagen (Abcam), type III collagen (Abcam), type I collagen (Abcam), fibronectin (Abcam), and Thy1.1 (Abcam). Alexa Fluor 647-conjugated antirabbit, antigoat, or antirat antibodies (Invitrogen) were used as secondary and incubated for 1 hour. Fluorescent and bright-field images were taken with a Leica DM4000B microscope (Leica Microsystems) and RETIGA 2000R camera (QImaging Scientific Cameras).

Dorsal wounding

Four-week-old male *Enl^{Cre};R26^{mTmG}* and *R26^{mTmG}* mice were used for cutaneous wound healing experiments. Both unsplinted and splinted excisional dorsal wounding was performed on *Enl^{Cre};R26^{mTmG}* and *R26^{mTmG}* mice in accordance with well-established protocols. In brief, induction of anesthesia was performed under 2.5% isoflurane/oxygen mixture at 2 l per minute followed by maintenance anesthesia at 1 l per minute. Dorsal fur was clipped, hair-removal product was applied topically to dorsal skin for 1 to 5 min or until depilation was achieved, and skin was prepped with povidone-iodine and alcohol. Two 6-mm full-thickness circular wounds were placed through the panniculus carnosus on the dorsum of each animal at the same level, ~6 mm below the ears and 4 mm lateral to the midline. Unsplinted wounds were dressed with sterile Tegaderm (3M) at this stage. For splinted wounds, two circular silicone 12-mm diameter stents (Invitrogen) were placed around the perimeter of each wound and secured in place with glue and 8 simple interrupted Ethilon 6-0 sutures (Ethicon). Dressings were changed every other day under anesthesia until full wound closure.

Oral wounding

Four-week-old male *Wnt1^{Cre};R26^{mTmG}* mice were used for oral wound healing experiments. In brief, mice were anesthetized with isoflurane/oxygen mixture as previously described. Full thickness wounds were excised on both sides of the buccal mucosa using a 1.5-mm biopsy punch. Wounds were harvested 14 days after surgery.

Melanoma transplantation

Depilation of the dorsal backs of 5-week-old male *Enl^{Cre};R26^{mTmG}* mice was performed as described previously in the section “Dorsal wounding.” The B16-F10 mouse melanoma cell line (ATCC) was passaged twice in culture and injected interdermally into the dorsal skin of each mouse (5.0×10^4 cells per injection). After 30 days, a palpable tumor had formed and was harvested at that stage for histology.

Model of radiation-induced fibrosis (skin)

All irradiation was performed using a Kimtron Polaris SC-500 Series II x-ray machine (Kimtron, Inc., Oxford, Connecticut, USA; 225 kV, 13.3 mA, 0.5 mm Cu, 1 Gy/min) according to Stanford University Administrative Panel on Laboratory

Animal Care (APLAC) protocol #9981. Mice were anesthetized with a 50% concentration (1:1 dilution with 0.9% NaCl) of anesthetic cocktail consisting of ketamine hydrochloride (80 mg/kg), xylazine (2.5 mg/kg), and acepromazine (2.5 mg/kg). The dorsal backs of mice were prepared by removing fur by clipping and light application of depilatory cream. Mice were placed onto customized individual lead jigs allowing dorsal cutaneous exposure to a circumferential region 2 cm in diameter. The dorsum of each mouse was irradiated with 2 doses of 40 Gy spaced 7 days apart. Mice were killed on day 14 after the first dose when signs of acute skin reactions (erythema and moist desquamation) were present.

Reciprocal transplantation into cutaneous and oral wounds

Dermal fibroblasts were harvested for FACS, as previously described, from the oral dermis of *Wnt1^{Cre};R26^{mTmG}* mice and the dorsal dermis of *Enl^{Cre};R26^{mTmG}* mice at 4 weeks of age. Harvested cells were stained with DAPI, as well as PacBlue-conjugated CD31 (1:100), CD45 (1:200), and Ter-119 (1:200), and sorted for viable GFP⁺/CD31⁺/CD45⁺/Ter-119⁺ populations from each anatomical site. FACS-isolated cells from the dorsal dermis of *Enl^{Cre};R26^{mTmG}* mice were transplanted into the buccal mucosa (described previously) of recipient *RAG-2^{-/-}* double-knockout mice (1.0×10^5 cells per site). FACS-isolated cells from the oral dermis of *Wnt1^{Cre};R26^{mTmG}* mice were transplanted into the dorsal dermis of recipient *RAG-2^{-/-}* double-knockout mice (1.0×10^5 cells per site). All tissues were harvested for analysis at 10 days after transplantation.

Histology and tissue analysis

For fixation, tissues were placed in 2% paraformaldehyde for 12 to 16 hours at 4°C. Samples were prepared for embedding by soaking in 30% sucrose in PBS at 4°C for 24 hours. Samples were removed from the sucrose solution, and tissue blocks were prepared by embedding in Tissue Tek O.C.T. (Sakura Finetek) under dry ice to freeze the samples within the compound. Frozen blocks were mounted on a MicroM HM550 cryostat (MICROM International GmbH), and 5- to 8- μ m-thick sections were transferred to Superfrost/Plus adhesive slides (Fisher brand).

Immunohistochemistry

For hematoxylin and eosin staining and Masson's trichrome staining, standardized protocols were used with no modifications. Immunostaining on frozen sections was performed using the following primary antibodies: type I collagen, type III collagen (Abcam), type IV collagen (Abcam), keratin-14 (Abcam), CD26 (eBioscience), CD29 (eBioscience), biglycan (Abcam), and FABP4 (Abcam). Briefly, slides were fixed in cold acetone (-20°C), and then blocked for 30 min in 10% bovine serum albumin with 5% horse serum followed by incubation with primary antibody for 12 to 16 hours. Slides were then incubated for 1 hour with Alexa Fluor 647-conjugated antirabbit, antigoat, or antirat secondary antibodies (Invitrogen).

Fluorescent and bright-field images were taken with a Leica DM4000B microscope (Leica Microsystems) and RETIGA 2000R camera (QImaging Scientific Cameras).

TUNEL staining

Terminal deoxynucleotidyl transferase-mediated deoxyuridine triphosphate nick end labeling (TUNEL) staining was performed using DeadEnd Fluorometric TUNEL System (Promega, Madison, Wisconsin) according to the manufacturer's protocol. Analysis was performed by counting positive cells per high-power field.

Microarray analysis

Dermal fibroblasts were harvested for FACS from the oral dermis and cranial dermis of *Wnt1^{Cre};R26^{mTmG}* mice and from ventral and dorsal dermis of *En1^{Cre};R26^{mTmG}* mice, as previously described. For all microarray analysis, EPFs and ENFs were harvested from back-skin of adult (P56) mice. Positivity for GFP or RFP allowed for the separation of EPFs from ENFs and WPFs from WNFs. RNA was precipitated via chloroform-phenol extraction. Samples were processed for cleanup and concentration using RNeasy MinElute cleanup kit (cat. 74204, QIAGEN). RNA yield was typically 0.5 to 1 µg RNA/sorted subpopulations. RNA samples from all sorted populations were converted to cDNA using SuperScript III first-strand synthesis system for RT-PCR (cat. 18080-051, Invitrogen) and hybridized to Affymetrix Mouse Genome 430 2.0 arrays. Microarrays were normalized by robust multiplex average and quantile normalization in R. Cluster analysis was performed with AutoSOME (22), using the following settings for gene expression clustering: *P*-value threshold of 0.05, 100 ensemble iterations, unit variance normalization of arrays, median centering of genes, and sum of squares = 1 normalization for both genes and arrays. The following settings were used for AutoSOME fuzzy clustering: *P*-value threshold of 0.05, 500 ensemble iterations, unit variance normalization of arrays, and uncentered correlation for distance matrix construction. The fuzzy cluster network (Fig. 3F) was rendered with Cytoscape 2.8.3 (37).

Cell surface marker screening

Dermal fibroblasts were harvested as described previously from adult (P56) *En1^{Cre};R26^{mTmG}* transgenic mice. Cells were analyzed using BD Lyoplate Mouse Cell Surface Marker Screening Panel (BD Biosciences, cat. 562208) containing 176 purified monoclonal antibodies and corresponding isotype controls. Manufacturer's staining protocol was followed with slight modifications. Cells isolated from the dorsal dermis of *En1^{Cre};R26^{mTmG}* mice were plated into U-bottom 96-well plates at a density of 2.5 to 5 × 10⁵ cells per well in FACS buffer. Primary antibody incubation was done in 100-µl volume for 30 min on ice. Next, cells were incubated with biotinylated secondary antibodies (goat antimouse 1:400, goat antirat 1:400, goat antisyrrian hamster 1:400, goat anti-Armenian hamster 1:800) in 100-µl volume for

30 min on ice. Tertiary incubation with Alexa Fluor 647 Streptavidin (1:4000)—as well as PacBlue-conjugated CD31 (1:100), CD45 (1:200)—and Ter-119 (1:200), was carried out in 100-µl volume for 30 min on ice. Analysis was performed using flow cytometer BD LSR Fortessa with High Throughput Sampler.

Intradermal transplantation of CD26⁺ and CD26⁻ fibroblasts

CD26⁺Lin⁻ and CD26⁻Lin⁻ dermal fibroblasts from the dorsal skin of uncrossed *R26^{mTmG}* mice (at 6 to 8 weeks of age) were harvested as previously described, and 2.0 × 10⁵ cells from each of these populations were transplanted via intradermal injection (in 100 µl PBS) into the dorsal backs of *RAG-2^{-/-}* double-knockout mice. Grafts containing FACS-sorted cells alone were harvested after 10 days and processed for histology.

Intradermal cotransplantation of CD26⁺ and CD26⁻ fibroblasts with B16 mouse melanoma

CD26⁺Lin⁻ and CD26⁻Lin⁻ dermal fibroblasts from the dorsal skin of uncrossed *R26^{mTmG}* mice (at 6 to 8 weeks of age) were harvested, as previously described, and 2.0 × 10⁵ cells from each of these populations were cotransplanted intradermally along with 5.0 × 10⁴ B16-F10 mouse melanoma cells (ATCC) into the dorsal backs of *RAG-2^{-/-}* double-knockout mice. Grafts were harvested 30 days after transplantation and processed for histology.

Fluorescence quantification

Randomly chosen sections (*n* = 25) from both CD26⁺Lin⁻ and CD26⁻Lin⁻ intradermal fibroblast grafts and melanoma cotransplant grafts were analyzed using ImageJ software. The “mean gray value” (sum of the gray values of all the pixels in the selection divided by the number of pixels) for the entire image was calculated for images taken in the RFP channel only. The mean gray value measuring total RFP signal for a given image was then normalized to the number of RFP-positive cells in that image. All data are quantified by a blinded observer from digital photographs analyzed using ImageJ and Adobe Photoshop CS6 (Adobe Systems, San Jose, California).

qRT-PCR analysis of CD26⁺ and CD26⁻ fibroblasts transplanted into dorsal wounds

CD26⁺ (*n* = 3) and CD26⁻ (*n* = 3) grafts were harvested at 7 days after transplant (10 days after wounding), digested using Liberase (1 mg/mL in DMEM). Cells harvested from each graft were then FACS-sorted for viability (DAPI) and RFP positivity directly into TRIZOL. Reverse transcription was performed with 1 µg RNA using Taqman Reverse Transcription Reagents (Applied Biosystems), and qRT-PCR was carried out using Applied Biosystems Prism 7900HT Sequence Detection System and SYBR Green PCR Master Mix (Applied Biosystems). Expression of collagen type I and alpha-smooth muscle actin (alpha-SMA) mRNA was measured. mRNA amounts were cal-

culated relative to the amount of β-actin mRNA in the same samples. For primers, see table S1.

qRT-PCR analysis of Cre expression

Fibroblasts were FACS-isolated using the fibroblast isolation methodology discussed previously from the dorsal skin of P1 *R26^{mTmG}* (*n* = 3) skin, E11.5 *En1^{Cre}* (*n* = 3) skin, *R26^{mTmG}* (*n* = 3) skin, P1 *En1^{Cre};R26^{mTmG}* (*n* = 3) skin, P30 *En1^{Cre};R26^{mTmG}* (*n* = 3) skin, and dorsal wounds on P30 *En1^{Cre};R26^{mTmG}* (*n* = 3) mice. Fibroblasts were sorted directly into TRIZOL. Reverse transcription was performed with 1 µg RNA using Taqman Reverse Transcription Reagents (Applied Biosystems), and qRT-PCR was carried out using Applied Biosystems Prism 7900HT Sequence Detection System and SYBR Green PCR Master Mix (Applied Biosystems). mRNA amounts were calculated relative to the amount of β-actin mRNA in the same samples. For primers, see table S1.

Microfluidic single-cell gene expression analysis

Gene lists defining fibroblast and nonfibroblast markers were collected from a literature search (38, 39). Single-cell reverse transcription and low cycle pre-amplification were performed as previously described (24, 40). Briefly, dermal lysate cell suspensions were sorted from *En1^{Cre};R26^{mTmG}* transgenic mice (at 6 to 8 weeks of age) as single cells into each well of a 96-well plate using a Becton Dickinson FACS Aria flow cytometer (Franklin Lakes, NJ) into 6 µl of lysis buffer and SUPERase-In RNase inhibitor (Applied Biosystems, Foster City, CA) (*n* = 6 cell lines). Live/dead gating was performed based on DAPI exclusion. EPFs and ENFs were defined as previously described. Live, single cells were also sorted as unfractionated dermis. Reverse transcription and low-cycle pre-amplification were performed using Cells Direct (Invitrogen) with Taqman assay primer sets (Applied Biosystems) as per the manufacturer's specifications. Exon-spanning primers were used where possible to avoid amplification of genomic background. cDNA was loaded onto 96.96 Dynamic Arrays (Fluidigm, South San Francisco, California) for qPCR amplification using Universal PCR Master Mix (Applied Biosystems) with a uniquely compiled Taqman assay primer set (table S1), as previously described (41).

Statistical analysis of single-cell data

Analysis of single-cell data was performed, as described previously (42). Briefly, data from all samples were normalized relative to the pooled median expression for each gene and converted to base 2 logarithms. Absolute bounds (±5 cycle thresholds from the median or 32-fold increases/decreases in expression) were set, and nonexpressers were assigned to this floor. Clustergrams were then generated using hierarchical clustering (with a “complete” linkage function and Euclidean distance metric) to facilitate data visualization (MATLAB R2011b, MathWorks, Natick, Massachusetts).

To detect overlapping patterns within the single-cell transcriptional data, *k*-means clustering was

employed using a standard Euclidean distance metric. Accordingly, each cell was assigned membership to a specific cluster as dictated by similarities in expression profiles (minimizing the within-cluster sum of square distances) in MATLAB. Optimally partitioned clusters were then subgrouped using hierarchical clustering to facilitate visualization of data patterning (41, 42). Non-parametric, two-sample Kolmogorov-Smirnov (K-S) tests were used to identify those genes with expression patterns that differed significantly between population clusters and/or groups, following Bonferroni correction for multiple samples using a strict cutoff of $P < 0.05$. For subgroup comparisons, the empirical distribution of cells from each cluster was evaluated against that of the remaining cells in the experiment. Ingenuity Pathway Analysis (IPA, Ingenuity Systems, Redwood City, California) was used to construct transcriptome networks based on genes that were significantly increased within clusters (including both direct and indirect relationships).

Small molecule-based CD26 inhibition during wound healing using diproton A

Background strain (B6) mice aged 4 to 6 weeks were dorsally wounded, and pullulan-collagen scaffolds seeded with either 500 ng diproton A + carrier or carrier alone were loaded onto the wound site at the time of wounding. On days 3 and 6 after wounding, new scaffolds seeded as on day 0 were loaded onto the wound site. Wound healing was then allowed to proceed unperturbed until completion. Photographic images taken every 2 or 3 days documented wound and scar size until healing reached completion.

DTR-based ablation of EPFs (GFP⁺) during cutaneous wounding

En1^{Cre};R26^{mTmG};R26^{tm1(HBEGF)Awa1} mice were dorsally wounded (splinted 6 mm excisional) and pullulan-collagen dermal hydrogels seeded with either 200 ng DT in PBS or PBS alone (control) were transplanted onto the wound sites at the time of wounding (day 0). On days 3 and 6 after wounding, new hydrogels seeded as on day 0 were transplanted onto the wound sites. Photographic images taken every 2 days documented wound and scar size until healing reached completion, at which point wounds were harvested for histologic analysis of GFP/RFP fluorescence and connective tissue deposition by Masson's trichrome.

Quantification of scar size

Gross scar size is determined by quantifying the area of the scar relative to the inner ring of the silicone splint on the day all wounds have completely healed. Scar size is represented as a percentage of the original wound at baseline (day 0). All data are quantified by a blinded observer from digital photographs analyzed using Adobe Photoshop CS6 (Adobe Systems, San Jose, California).

Quantification of the rate of wound healing

Rate of wound healing is determined by quantifying the area of the wound relative to the inner

ring of the silicone splint at baseline (day 0), 3 days after each application of hydrogel, and every 2 days. Wound size is then calculated as a percent of the original wound at baseline. All data are quantified by a blinded observer from digital photographs analyzed using Adobe Photoshop CS6 (Adobe Systems).

Tensile strength testing

Tensile strength tests for fully healed wounds on *En1^{Cre};R26^{mTmG};R26^{tm1(HBEGF)Awa1}* mice treated with or without DT via pullulan-collagen hydrogel on days 0, 3, and 6 was performed on day 22 and day 16, respectively. Tests were performed with a microtester (model 5848, Instron, Norwood, Massachusetts) equipped with a 100 N load cell. The tissue specimens were attached to custom grips with double-sided tape, giving a final gauge length of 10 mm. The region between the grips (gauge region) was stretched until a break in the skin was detected by a decrease in stress with increasing strain. Analysis was performed as previously described (43). True strain was calculated as the change in length divided by the gauge length, and true stress was calculated as the force divided by the original cross-sectional area. The tensile strength was determined as the greatest true stress achieved. The modulus was determined via least squares regression as the slope of the linear region of the true stress-true strain curve ($R^2 \geq 0.99$).

DTR-based ablation of EPFs (GFP⁺) before melanoma transplantation

En1^{Cre};R26^{mTmG};R26^{tm1(HBEGF)Awa1} mice were injected (4x) intradermally with either 100 ng DT in 25 μ l PBS ($n = 7$) or 25 μ l PBS alone ($n = 7$) in four evenly spaced locations along the circumference, 6 mm in diameter. Twenty-four hours later, 5.0×10^5 B16 mouse melanoma cells were transplanted intradermally into the middle of the marked circle on the dorsum of these mice. Tumors were allowed to grow in DT-treated ($n = 7$) and control mice ($n = 7$) until killing was dictated by protocol parameters (tumor size > 2 cm) for one mouse, at which point all mice were killed and tumors were harvested for analysis.

REFERENCES AND NOTES

1. J. M. Sorrell, A. I. Caplan, Fibroblasts: a diverse population at the center of it all. *Int. Rev. Cell Mol. Biol.* **276**, 161–214 (2009). doi: [10.1016/S1937-6448\(09\)76004-6](https://doi.org/10.1016/S1937-6448(09)76004-6); pmid: [19584013](https://pubmed.ncbi.nlm.nih.gov/19584013/)
2. T. A. Wynn, Cellular and molecular mechanisms of fibrosis. *J. Pathol.* **214**, 199–210 (2008). doi: [10.1002/path.2277](https://doi.org/10.1002/path.2277); pmid: [18161745](https://pubmed.ncbi.nlm.nih.gov/18161745/)
3. D. W. Powell et al., Myofibroblasts. I. Paracrine cells important in health and disease. *Am. J. Physiol.* **277**, C1–C9 (1999). doi: [10.1111/j.1469-7793.1999.001af.x](https://doi.org/10.1111/j.1469-7793.1999.001af.x); pmid: [10409103](https://pubmed.ncbi.nlm.nih.gov/10409103/)
4. M. S. Wilson, T. A. Wynn, Pulmonary fibrosis: Pathogenesis, etiology and regulation. *Mucosal Immunol.* **2**, 103–121 (2009). doi: [10.1038/mi.2008.85](https://doi.org/10.1038/mi.2008.85); pmid: [19129758](https://pubmed.ncbi.nlm.nih.gov/19129758/)
5. B. Hinz et al., The myofibroblast: One function, multiple origins. *Am. J. Pathol.* **170**, 1807–1816 (2007). doi: [10.2353/ajpath.2007.070112](https://doi.org/10.2353/ajpath.2007.070112); pmid: [17525249](https://pubmed.ncbi.nlm.nih.gov/17525249/)
6. N. Dumont et al., Breast fibroblasts modulate early dissemination, tumorigenesis, and metastasis through alteration of extracellular matrix characteristics. *Neoplasia* **15**, 249–262 (2013). pmid: [23479504](https://pubmed.ncbi.nlm.nih.gov/23479504/)
7. C. Servais, N. Erez, From sentinel cells to inflammatory culprits: Cancer-associated fibroblasts in tumour-related

- inflammation. *J. Pathol.* **229**, 198–207 (2013). doi: [10.1002/path.4103](https://doi.org/10.1002/path.4103); pmid: [22996812](https://pubmed.ncbi.nlm.nih.gov/22996812/)
8. M. Tripathi, S. Bille, N. A. Bhowmick, Understanding the role of stromal fibroblasts in cancer progression. *Cell Adhes. Migr.* **6**, 231–235 (2012). doi: [10.4161/cam.20419](https://doi.org/10.4161/cam.20419); pmid: [22568983](https://pubmed.ncbi.nlm.nih.gov/22568983/)
 9. A. Orimo, R. A. Weinberg, Stromal fibroblasts in cancer: A novel tumor-promoting cell type. *Cell Cycle* **5**, 1597–1601 (2006). doi: [10.4161/cc.5.15.3112](https://doi.org/10.4161/cc.5.15.3112); pmid: [16880743](https://pubmed.ncbi.nlm.nih.gov/16880743/)
 10. M. D. Muzumdar, B. Tasic, K. Miyamichi, L. Li, L. Luo, A global double-fluorescent Cre reporter mouse. *Genesis* **45**, 593–605 (2007). doi: [10.1002/dvg.20335](https://doi.org/10.1002/dvg.20335); pmid: [17868096](https://pubmed.ncbi.nlm.nih.gov/17868096/)
 11. R. Atit et al., Beta-catenin activation is necessary and sufficient to specify the dorsal dermal fate in the mouse. *Dev. Biol.* **296**, 164–176 (2006). doi: [10.1016/j.ydbio.2006.04.449](https://doi.org/10.1016/j.ydbio.2006.04.449); pmid: [16730693](https://pubmed.ncbi.nlm.nih.gov/16730693/)
 12. L. Weber, E. Kirsch, P. Müller, T. Krieg, Collagen type distribution and macromolecular organization of connective tissue in different layers of human skin. *J. Invest. Dermatol.* **82**, 156–160 (1984). doi: [10.1111/1523-1747.ep12259720](https://doi.org/10.1111/1523-1747.ep12259720); pmid: [6693779](https://pubmed.ncbi.nlm.nih.gov/6693779/)
 13. Y. A. Cao et al., Shifting foci of hematopoiesis during reconstitution from single stem cells. *Proc. Natl. Acad. Sci. U.S.A.* **101**, 221–226 (2004). doi: [10.1073/pnas.2637010100](https://doi.org/10.1073/pnas.2637010100); pmid: [14688412](https://pubmed.ncbi.nlm.nih.gov/14688412/)
 14. P. Gottlöhner et al., Interferon-gamma in 5 patients with cutaneous radiation syndrome after radiation therapy. *Int. J. Radiat. Oncol. Biol. Phys.* **50**, 159–166 (2001). doi: [10.1016/S0360-3016\(00\)01542-X](https://doi.org/10.1016/S0360-3016(00)01542-X); pmid: [11316559](https://pubmed.ncbi.nlm.nih.gov/11316559/)
 15. A. L. Labrousse, C. Ntai, W. Hornebeck, P. Bernard, Stromal reaction in cutaneous melanoma. *Crit. Rev. Oncol. Hematol.* **49**, 269–275 (2004). doi: [10.1016/j.critrevonc.2003.10.007](https://doi.org/10.1016/j.critrevonc.2003.10.007); pmid: [15036266](https://pubmed.ncbi.nlm.nih.gov/15036266/)
 16. K. Moore, M. Moore, Intra-tumour host cells of transplanted rat neoplasms of different immunogenicity. *Int. J. Cancer* **19**, 803–813 (1977). doi: [10.1002/ijc.2910190610](https://doi.org/10.1002/ijc.2910190610); pmid: [326682](https://pubmed.ncbi.nlm.nih.gov/326682/)
 17. T. Udagawa, M. Puder, M. Wood, B. C. Schaefer, R. J. D'Amato, Analysis of tumor-associated stromal cells using SCID GFP transgenic mice: Contribution of local and bone marrow-derived host cells. *FASEB J.* **20**, 95–102 (2006). doi: [10.1096/fj.04-3669com](https://doi.org/10.1096/fj.04-3669com); pmid: [16394272](https://pubmed.ncbi.nlm.nih.gov/16394272/)
 18. A. M. Szpadarska, J. D. Zuckerman, L. A. DiPietro, Differential injury responses in oral mucosal and cutaneous wounds. *J. Dent. Res.* **82**, 621–626 (2003). doi: [10.1177/154405910308200810](https://doi.org/10.1177/154405910308200810); pmid: [12885847](https://pubmed.ncbi.nlm.nih.gov/12885847/)
 19. K. Janabodin et al., Isolation and characterization of neural crest-derived stem cells from dental pulp of neonatal mice. *PLOS ONE* **6**, e27526 (2011). doi: [10.1371/journal.pone.0027526](https://doi.org/10.1371/journal.pone.0027526); pmid: [22087335](https://pubmed.ncbi.nlm.nih.gov/22087335/)
 20. D. H. Nichols, L. L. Bruce, Migratory routes and fates of cells transcribing the Wnt-1 gene in the murine hindbrain. *Dev. Dyn.* **235**, 285–300 (2006). doi: [10.1002/dvdy.20611](https://doi.org/10.1002/dvdy.20611); pmid: [16273520](https://pubmed.ncbi.nlm.nih.gov/16273520/)
 21. T. Yoshida, P. Vivatbutsi, G. Morris-Kay, Y. Suga, S. Iseki, Cell lineage in mammalian craniofacial mesenchyme. *Mech. Dev.* **125**, 797–808 (2008). doi: [10.1016/j.jmd.2008.06.007](https://doi.org/10.1016/j.jmd.2008.06.007); pmid: [18617001](https://pubmed.ncbi.nlm.nih.gov/18617001/)
 22. A. M. Newman, J. B. Cooper, AutoSOME: A clustering method for identifying gene expression modules without prior knowledge of cluster number. *BMC Bioinformatics* **11**, 117 (2010). doi: [10.1186/1471-2105-11-117](https://doi.org/10.1186/1471-2105-11-117); pmid: [20202218](https://pubmed.ncbi.nlm.nih.gov/20202218/)
 23. L. S. Hansen, J. E. Coggie, J. Wells, M. W. Charles, The influence of the hair cycle on the thickness of mouse skin. *Anat. Rec.* **210**, 569–573 (1984). doi: [10.1002/ar.1092100404](https://doi.org/10.1002/ar.1092100404); pmid: [6524697](https://pubmed.ncbi.nlm.nih.gov/6524697/)
 24. R. D. Galiano, J. Michaels 5th, M. Dobryansky, J. P. Levine, G. C. Gurtner, Quantitative and reproducible murine model of excisional wound healing. *Wound Repair Regen.* **12**, 485–492 (2004). doi: [10.1111/j.1067-1927.2004.12404.x](https://doi.org/10.1111/j.1067-1927.2004.12404.x); pmid: [15260814](https://pubmed.ncbi.nlm.nih.gov/15260814/)
 25. J. S. Nielsen, K. M. McNagny, Novel functions of the CD34 family. *J. Cell Sci.* **121**, 3683–3692 (2008). doi: [10.1242/jcs.037507](https://doi.org/10.1242/jcs.037507); pmid: [18987355](https://pubmed.ncbi.nlm.nih.gov/18987355/)
 26. S. B. Willingham et al., The CD47-signal regulatory protein alpha (SIRP α) interaction is a therapeutic target for human solid tumors. *Proc. Natl. Acad. Sci. U.S.A.* **109**, 6662–6667 (2012). doi: [10.1073/pnas.112623109](https://doi.org/10.1073/pnas.112623109); pmid: [22451913](https://pubmed.ncbi.nlm.nih.gov/22451913/)
 27. R. R. Driskell et al., Distinct fibroblast lineages determine dermal architecture in skin development and repair. *Nature* **504**, 277–281 (2013). doi: [10.1038/nature12783](https://doi.org/10.1038/nature12783); pmid: [24336287](https://pubmed.ncbi.nlm.nih.gov/24336287/)
 28. E. N. Arwert et al., Upregulation of CD26 expression in epithelial cells and stromal cells during wound-induced skin tumour formation. *Oncogene* **31**, 992–1000 (2012). doi: [10.1038/ncr.2011.298](https://doi.org/10.1038/ncr.2011.298); pmid: [21765471](https://pubmed.ncbi.nlm.nih.gov/21765471/)

29. H. Hiramatsu *et al.*, The crystal structure of human dipeptidyl peptidase IV (DPP-IV) complex with diprotin A. *Biol. Chem.* **385**, 561–564 (2004). doi: [10.1515/BC.2004.068](https://doi.org/10.1515/BC.2004.068); pmid: [15255191](https://pubmed.ncbi.nlm.nih.gov/15255191/)
 30. T. E. Quan, S. Cowper, S. P. Wu, L. K. Bockenstedt, R. Bucala, Circulating fibrocytes: Collagen-secreting cells of the peripheral blood. *Int. J. Biochem. Cell Biol.* **36**, 598–606 (2004). doi: [10.1016/j.biocel.2003.10.005](https://doi.org/10.1016/j.biocel.2003.10.005); pmid: [15010326](https://pubmed.ncbi.nlm.nih.gov/15010326/)
 31. M. Schmidt, G. Sun, M. A. Stacey, L. Mori, S. Mattoli, Identification of circulating fibrocytes as precursors of bronchial myofibroblasts in asthma. *J. Immunol.* **171**, 380–389 (2003). doi: [10.4049/jimmunol.171.1.380](https://doi.org/10.4049/jimmunol.171.1.380); pmid: [12817021](https://pubmed.ncbi.nlm.nih.gov/12817021/)
 32. V. S. LeBleu *et al.*, Origin and function of myofibroblasts in kidney fibrosis. *Nat. Med.* **19**, 1047–1053 (2013). doi: [10.1038/nm.3218](https://doi.org/10.1038/nm.3218); pmid: [23817022](https://pubmed.ncbi.nlm.nih.gov/23817022/)
 33. A. J. Atherton *et al.*, Dipeptidyl peptidase IV expression identifies a functional sub-population of breast fibroblasts. *Int. J. Cancer* **50**, 15–19 (1992). doi: [10.1002/ijc.2910500105](https://doi.org/10.1002/ijc.2910500105); pmid: [1345821](https://pubmed.ncbi.nlm.nih.gov/1345821/)
 34. M. Kraman *et al.*, Suppression of antitumor immunity by stromal cells expressing fibroblast activation protein- α . *Science* **330**, 827–830 (2010). doi: [10.1126/science.1195300](https://doi.org/10.1126/science.1195300); pmid: [21051638](https://pubmed.ncbi.nlm.nih.gov/21051638/)
 35. B. Åhrén, DPP-4 inhibitors. *Best Pract. Res. Clin. Endocrinol. Metab.* **21**, 517–533 (2007). doi: [10.1016/j.beem.2007.07.005](https://doi.org/10.1016/j.beem.2007.07.005); pmid: [18054733](https://pubmed.ncbi.nlm.nih.gov/18054733/)
 36. S. Parrinello *et al.*, Oxygen sensitivity severely limits the replicative lifespan of murine fibroblasts. *Nat. Cell Biol.* **5**, 741–747 (2003). doi: [10.1038/ncb1024](https://doi.org/10.1038/ncb1024); pmid: [12855956](https://pubmed.ncbi.nlm.nih.gov/12855956/)
 37. P. Shannon *et al.*, Cytoscape: A software environment for integrated models of biomolecular interaction networks. *Genome Res.* **13**, 2498–2504 (2003). doi: [10.1101/gr.1239303](https://doi.org/10.1101/gr.1239303); pmid: [14597658](https://pubmed.ncbi.nlm.nih.gov/14597658/)
 38. M. Rendl, L. Lewis, E. Fuchs, Molecular dissection of mesenchymal-epithelial interactions in the hair follicle. *PLOS Biol.* **3**, e331 (2005). doi: [10.1371/journal.pbio.0030331](https://doi.org/10.1371/journal.pbio.0030331); pmid: [16162033](https://pubmed.ncbi.nlm.nih.gov/16162033/)
 39. A. W. Joe *et al.*, Muscle injury activates resident fibro/adipogenic progenitors that facilitate myogenesis. *Nat. Cell Biol.* **12**, 153–163 (2010). doi: [10.1038/ncb2015](https://doi.org/10.1038/ncb2015); pmid: [20081841](https://pubmed.ncbi.nlm.nih.gov/20081841/)
 40. B. Levi *et al.*, CD105 protein depletion enhances human adipose-derived stromal cell osteogenesis through reduction of transforming growth factor β 1 (TGF- β 1) signaling. *J. Biol. Chem.* **286**, 39497–39509 (2011). doi: [10.1074/jbc.M111.256529](https://doi.org/10.1074/jbc.M111.256529); pmid: [21949130](https://pubmed.ncbi.nlm.nih.gov/21949130/)
 41. M. Januszzyk *et al.*, Diabetes irreversibly depletes bone marrow-derived mesenchymal progenitor cell subpopulations. *Diabetes* **63**, 3047–3056 (2014). doi: [10.2337/db13-1366](https://doi.org/10.2337/db13-1366); pmid: [24740572](https://pubmed.ncbi.nlm.nih.gov/24740572/)
 42. J. P. Glotzbach *et al.*, An information theoretic, microfluidic-based single cell analysis permits identification of subpopulations among putatively homogeneous stem cells. *PLOS ONE* **6**, e21211 (2011). doi: [10.1371/journal.pone.0021211](https://doi.org/10.1371/journal.pone.0021211); pmid: [21731674](https://pubmed.ncbi.nlm.nih.gov/21731674/)
 43. K. C. Rustad *et al.*, Enhancement of mesenchymal stem cell angiogenic capacity and stemness by a biomimetic hydrogel scaffold. *Biomaterials* **33**, 80–90 (2012). doi: [10.1016/j.biomaterials.2011.09.041](https://doi.org/10.1016/j.biomaterials.2011.09.041); pmid: [21963148](https://pubmed.ncbi.nlm.nih.gov/21963148/)
- ACKNOWLEDGMENTS**
- We thank D. T. Montoro and S. D. Morrison for their early contribution to developing the live fibroblast harvest protocol. This work was supported in part by NIH grant R01 GM087609 (to H.P.L.), a gift from Ingrid Lai and Bill Shu in honor of Anthony Shu (to H.P.L.), the California Institute of Regenerative Medicine (RC1 00354 to I.L.W.), the Smith Family Trust (to I.L.W.), the Hagey Laboratory for Pediatric Regenerative Medicine and The Oak Foundation (to M.T.L., H.P.L., and G.C.G.), NIH grants U01 HL099776 (to M.T.L.) and U01 HL099999 (to I.L.W.), the Virginia and D. K. Ludwig Fund for Cancer Research (to I.L.W.), and the Gunn/Oliver fund (to M.T.L. and I.L.W.). G.G.W. was supported by the Stanford School of Medicine, the Stanford Medical Scientist Training Program, and National Institute of General Medical Sciences training grant GM07365. Y.R. was supported by the Human Frontier Science Program (HFSP) Long Term Fellowship, the Machiah Foundation Fellowship, and the Siebel Scholarship. M.S.H. was supported by the California Institute for Regenerative Medicine Clinical Fellow training grant TG2-01159. Z.N.M. was supported by the Plastic Surgery Foundation Research Fellowship grant 114288 and the Translational Research and Applied Medicine program pilot grant. Microarray data are available at the Gene Expression Omnibus (GEO) at www.ncbi.nlm.nih.gov/geo/, under accession number GSE65402. Author contributions: Y.R. and G.G.W. conceived, designed, and oversaw the experiments, with suggestions from I.L.W. and M.T.L. Y.R., G.G.W., M.S.H., and Z.N.M. performed the experiments and analyzed the data. A.M.N. and M.J. assisted with collection and analysis of data. M.D. assisted with microarray preparations, and A.M.N. analyzed the microarray data. Y.R., G.G.W., M.S.H., and Z.N.M. wrote the manuscript, with helpful suggestions from G.C.G., H.P.L., I.L.W., and M.T.L. The authors have no competing interests.
- SUPPLEMENTARY MATERIALS**
- www.sciencemag.org/content/348/6232/aaa2151/suppl/DC1
Figs. S1 to S4
Tables S1 and S2
References
- 2 November 2014; accepted 12 February 2015
[10.1126/science.aaa2151](https://doi.org/10.1126/science.aaa2151)

RESEARCH ARTICLE

RIBOSOME

The complete structure of the 55S mammalian mitochondrial ribosome

Basil J. Greber,^{1*} Philipp Bieri,^{1*} Marc Leibundgut,^{1*} Alexander Leitner,²
Ruedi Aebersold,^{2,3} Daniel Boehringer,¹ Nenad Ban^{1†}

Mammalian mitochondrial ribosomes (mitoribosomes) synthesize mitochondrially encoded membrane proteins that are critical for mitochondrial function. Here we present the complete atomic structure of the porcine 55S mitoribosome at 3.8 angstrom resolution by cryo-electron microscopy and chemical cross-linking/mass spectrometry. The structure of the 28S subunit in the complex was resolved at 3.6 angstrom resolution by focused alignment, which allowed building of a detailed atomic structure including all of its 15 mitoribosomal-specific proteins. The structure reveals the intersubunit contacts in the 55S mitoribosome, the molecular architecture of the mitoribosomal messenger RNA (mRNA) binding channel and its interaction with transfer RNAs, and provides insight into the highly specialized mechanism of mRNA recruitment to the 28S subunit. Furthermore, the structure contributes to a mechanistic understanding of aminoglycoside ototoxicity.

Mitochondria are eukaryotic cellular organelles specialized for energy conversion and adenosine triphosphate (ATP) production. Because they originated by endosymbiosis from α -proteobacteria (1),

they still contain the machinery required to express the genetic information encoded on their highly reduced genome, including mitochondrial ribosomes (mitoribosomes). Mammalian 55S mitoribosomes, composed of the 28S small and

39S large mitoribosomal subunits (2), have diverged markedly from their bacterial predecessors by extensive shortening of their ribosomal RNAs (rRNAs) and the acquisition of numerous mitochondrial-specific ribosomal proteins (3–6). The initiation of mammalian mitochondrial translation, which involves recruitment of leaderless mRNAs to the 28S subunit and start-codon selection in the absence of Shine-Dalgarno sequences (7, 8), is poorly understood.

Mitoribosomes are of high medical interest because aminoglycosides, which are used as antibiotics targeting bacterial ribosomes (9), can also inhibit mitoribosomes, causing severe side effects, such as hearing loss (ototoxicity) (10, 11) in up to 10 to 20% of patients (10). Furthermore, mitoribosomal mutations play a role in congenital disorders (11, 12), and up-regulation of mitochondrial translation appears to be associated with the development of cancer (13).

Structures of the porcine (14) and human (15) mitoribosomal 39S subunits at 3.4 Å resolution provided detailed insight into their architecture

¹Department of Biology, Institute of Molecular Biology and Biophysics, Otto-Stern-Weg 5, ETH Zurich, CH-8093 Zurich, Switzerland. ²Department of Biology, Institute of Molecular Systems Biology, Auguste-Piccard-Hof 1, ETH Zurich, CH-8093 Zurich, Switzerland. ³Faculty of Science, University of Zurich, CH-8057 Zurich, Switzerland.

*These authors contributed equally to this work. †Corresponding author. E-mail: ban@mol.biol.ethz.ch

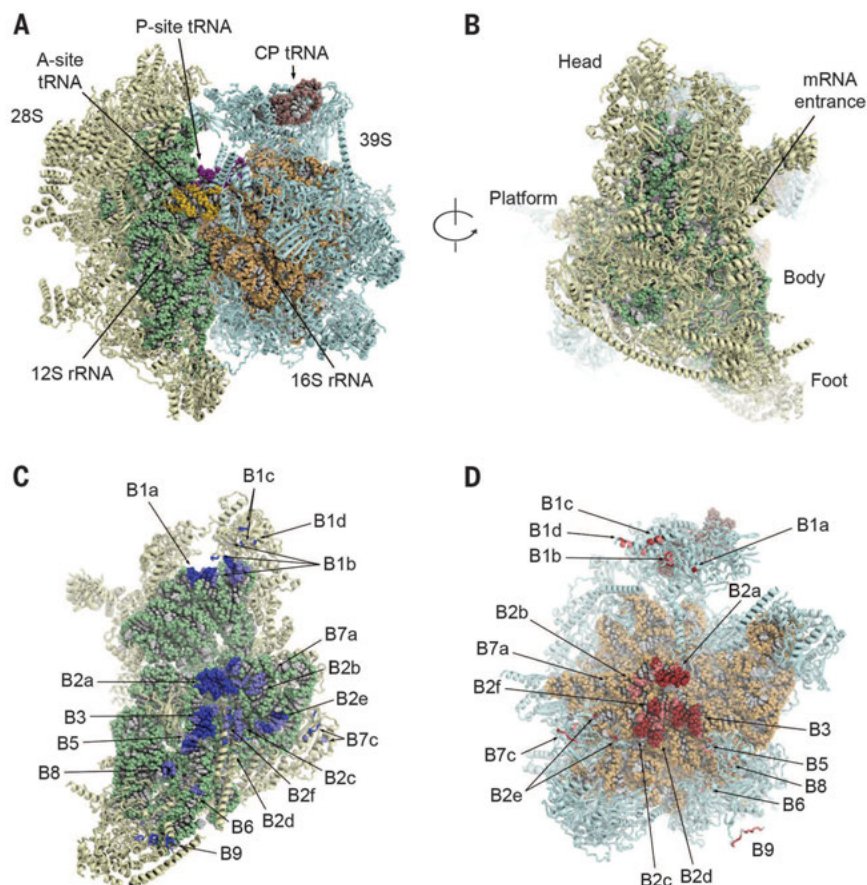


Fig. 1. Overall structure of the 55S mitoribosome. (A and B) Structure of the 55S mitoribosome. 39S subunit proteins blue, 16S rRNA orange, CP tRNA brown, 28S subunit proteins pale yellow, 12S rRNA light green, P-site tRNA purple, A-site tRNA yellow. (C and D) Intersubunit bridges in the 55S mitoribosome. Contact surfaces (distance <4 Å) and surfaces in close proximity (<6 Å) are colored in blue and pale blue (C) or red and pale red (D), respectively, and labeled with the bridge number.

and function, including the architectural replacement of the 5S rRNA by a transfer RNA (tRNA) molecule. However, structural information on the mammalian 28S small mitoribosomal subunit is currently limited to fitting of homology models into lower-resolution reconstructions (16). Here we present the complete structure of the porcine 28S small mitoribosomal subunit at 3.6 Å resolution and an atomic model of the entire 55S mitoribosome in complex with mRNA and tRNAs based on a 3.8 Å cryo-electron microscopic (cryo-EM) reconstruction.

Structure of the mammalian 55S mitoribosome

To determine the structure of the 55S mitoribosome, we used a previously collected cryo-EM data set (14). We first calculated a map of the 28S subunit at 3.6 Å resolution by focused classification and alignment (fig. S1, A and B), which allowed us to build a structure for >99% of the 12S rRNA nucleotides and all 30 proteins of the 28S mitoribosomal subunit (figs. S1, B to H, and S2, A to C, and tables S1 to S3). Two proteins, mS27 and mS39, were modeled as polyserines

(table S3) because of lower local resolution (fig. S1, C and D). This structure was then combined with our previously determined structure of the 39S mitoribosomal subunit at 3.4 Å resolution (14) to build, refine, and validate a complete atomic model of the 55S mitoribosome (Fig. 1, A and B; fig. S2, D to F; and tables S2 to S4) based on a 3.8 Å cryo-EM map (fig. S3 and supplementary text).

The mammalian 55S mitoribosome has a strikingly different appearance from the bacterial 70S ribosome (5, 17). The reduced rRNA is limited to the innermost core of the ribosome, whereas numerous proteins cover the surface of the ribosome almost entirely and extend far away from the core.

The structure reveals that in mitochondria, the subunits interact less extensively than in bacteria (Fig. 1, C and D, fig. S4, and table S5; for nomenclature see the materials and methods) and that many bridges are formed by mitochondrial-specific protein elements (fig. S4, G to L, table S5, and supplementary text). The reduction of peripheral contacts in the mitoribosome may lead to increased conformational flexibility of the mito-

ribosomal subunits, including tilting of the subunits relative to each other (figs. S3, E to G, and S5; and supplementary text).

Interactions of tRNAs with the 55S mitoribosome

The binding sites for the A-site and P-site tRNAs at the subunit interface lack many ribosomal elements that are present in cytosolic ribosomes (14, 15, 17), which are compensated for by unique structural features of the mammalian mitoribosome (table S6). The 39S subunit interactions with the highly variable mitochondrial tRNA elbows, which could not be modeled because the mitoribosomes in our sample contain a mixture of all mitochondrial tRNAs, have been weakened by the loss of ribosomal protein uL5 in the P site and bL25 and the A-site finger (rRNA helix H38) in the A site (Fig. 2, A and B) (14, 15). Additionally, uS13, which binds to the anticodon stem loops (ASLs) in bacterial ribosomes (18), has been lost from the 28S subunit (Fig. 2, A and C). A unique structural element of the mammalian mitoribosome, the P-site finger (5, 14), compensates for some of these missing interactions,

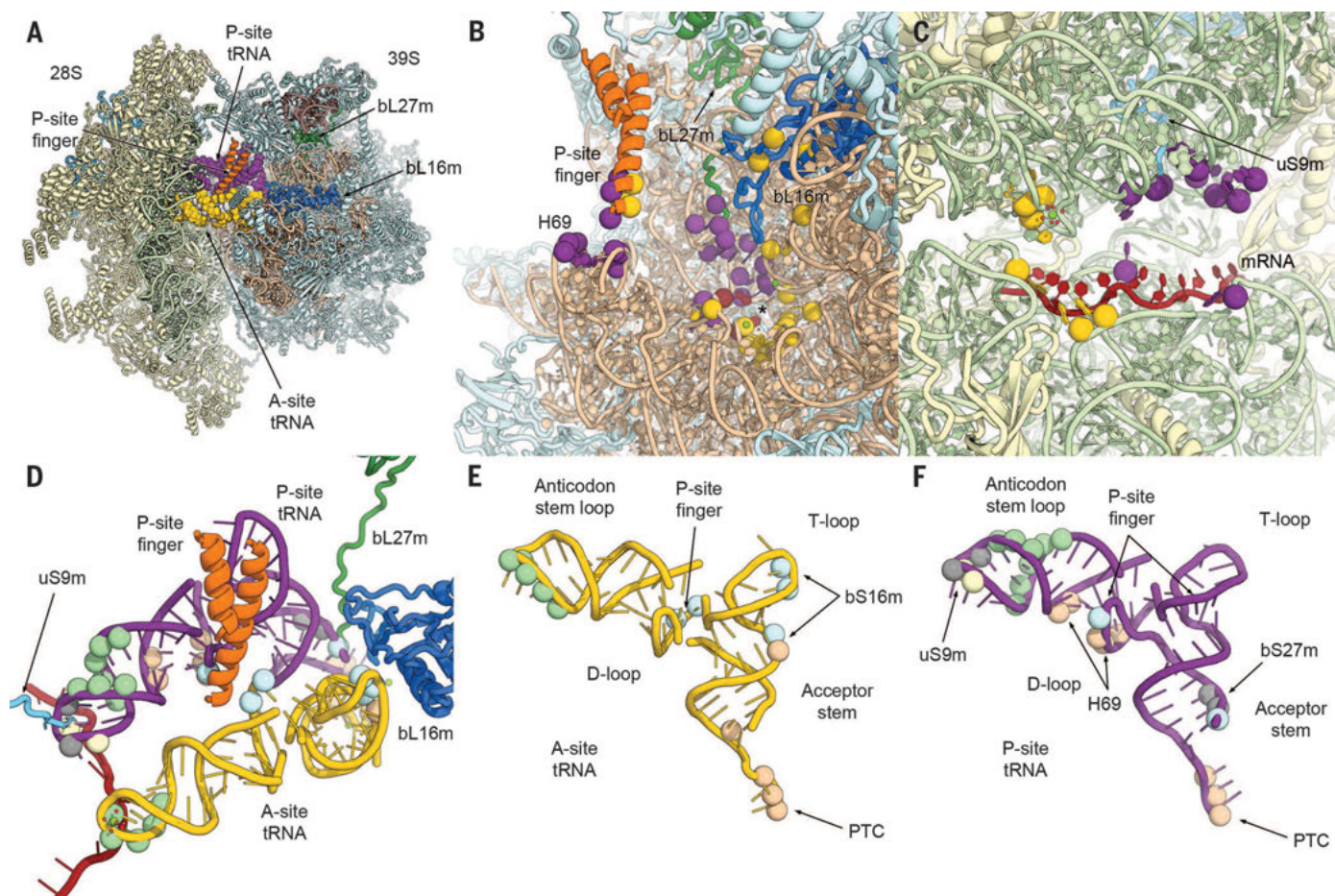


Fig. 2. Interactions of tRNAs in the 55S mitoribosome. (A) Overview of the 55S mitoribosome. Colors as in Fig. 1 but with proteins approaching the A- and P-site tRNAs highlighted (bL16m blue, bL27m green, P-site finger orange, uS9m cyan). (B and C) View of the 39S (B) and 28S (C) tRNA binding sites (A- and P-site tRNA contacts yellow and purple; peptidyl transferase center indicated by asterisk). (D) tRNA-protein interactions in the 55S mitoribosome (contacts to 16S rRNA brown, 12S rRNA light green, 39S proteins cyan, 28S proteins pale yellow, residues contacting both rRNA and proteins gray). (E and F) A- and P-site tRNAs displayed as in (D), with major tRNA domains labeled and interacting mitoribosomal components indicated.

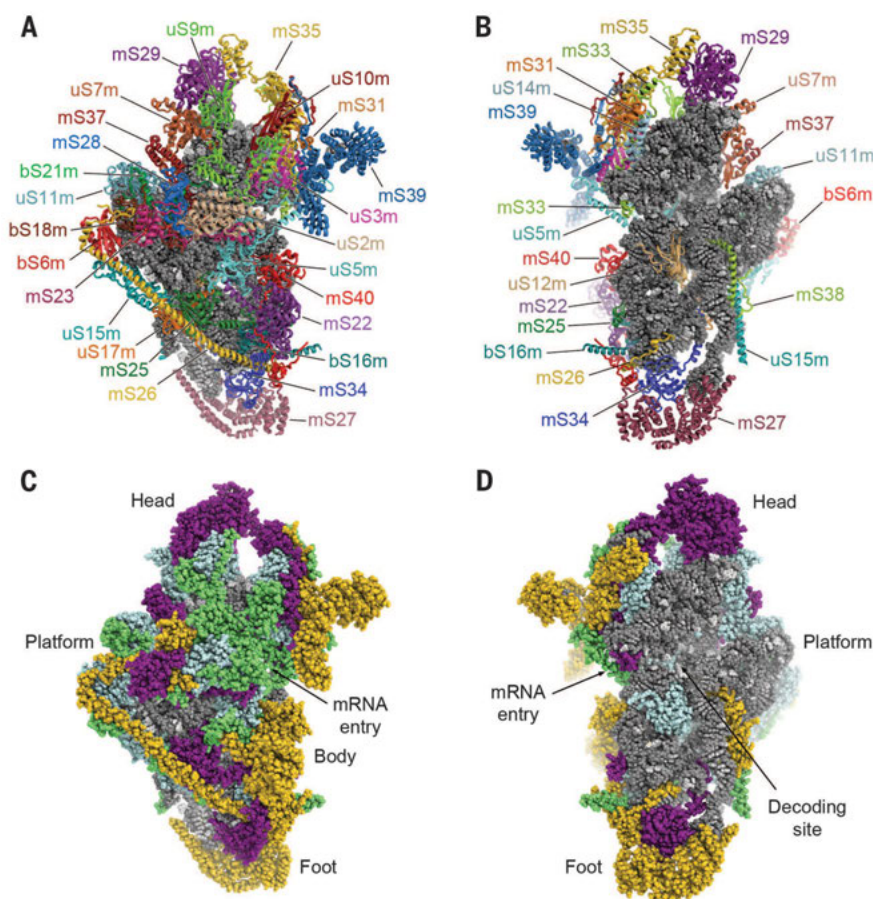


Fig. 3. Overall structure of the 28S subunit. (A and B) Locations of proteins in the 28S subunit [(A), solvent side; (B), subunit interface side]. (C and D) 28S subunit [oriented as in (A) and (B)], with ribosomal proteins colored according to conservation (gray: 12S rRNA; cyan: proteins conserved in bacteria, mitoribosomal extensions green; purple: proteins shared between fungal and mammalian mitoribosomes; yellow: proteins not present in fungal mitoribosomes).

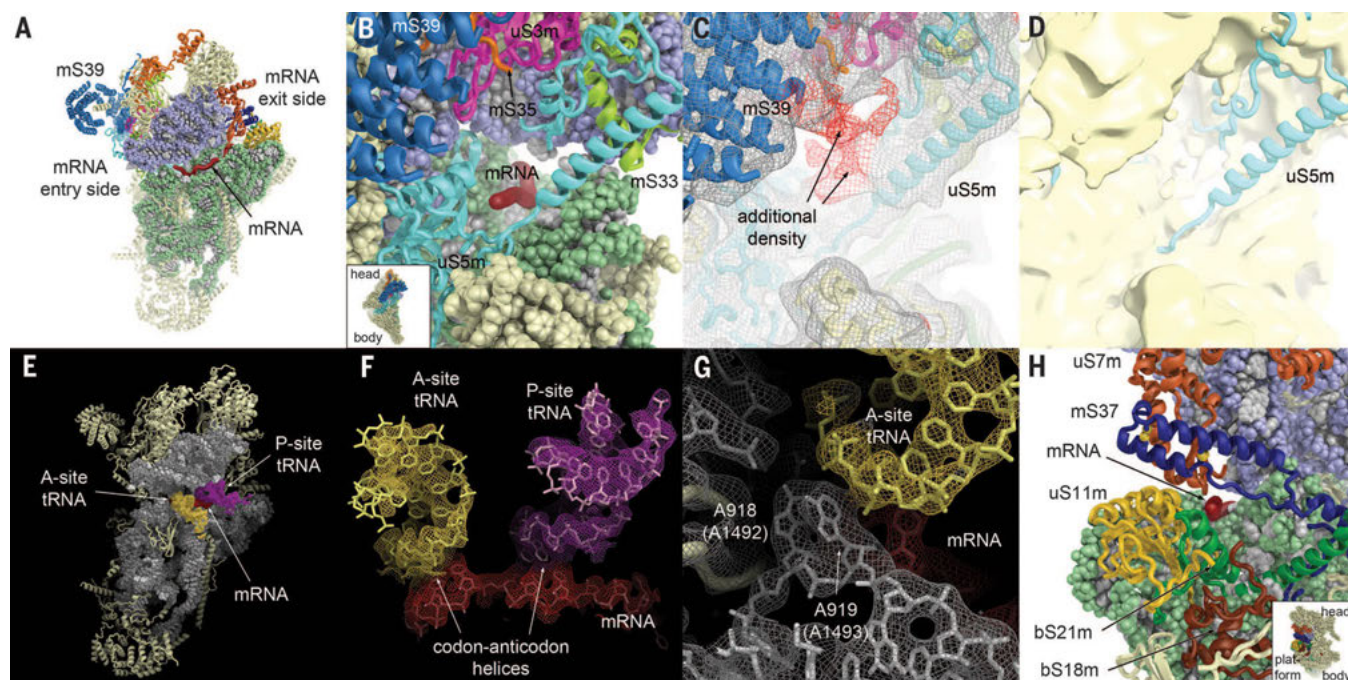


Fig. 4. The mRNA binding channel of the 28S subunit. (A) Subunit interface view of the 28S subunit (proteins surrounding the mRNA entry and exit sites are colored). (B) uS5m (cyan) forms a latch across the entrance of the mRNA channel (mRNA dark red). (C) Additional density (red) is visible near the mRNA entry path in a particle subclass with a well-ordered mRNA gate. (D) The mRNA entry site of the 28S without bound mRNA and tRNAs (yellow surface) lacks density for the uS5m latch (cyan). (E) Density for mRNA (red) and tRNAs (P site purple, A site yellow). (F) Close-up view of the mRNA and tRNA density. (G) Conservation of the decoding center with flipped-out A918 and A919. (H) The exit of the mRNA channel [colors as in (A), with disulfide bridges in mS37 shown as yellow spheres].

as it extends from the central protuberance (CP) of the 39S subunit and is inserted between the A- and P-site tRNAs. The P-site finger seems to play a critical role in the positioning of both tRNAs in the active site, as it binds to the D-stem junction and the T stem of the P-site tRNA and the D stem of the A-site tRNA (Fig. 2, D to F).

Structure of the 28S subunit

The structure of the 28S subunit reveals the folds and locations of its 30 ribosomal proteins, 15 of which are specific to mitoribosomes (Fig. 3, A and B, and fig. S6A), in agreement with our cross-linking/mass spectrometry data (fig. S6, B to D, and table S1).

The 12S rRNA in the 28S subunit is shortened as compared to the bacterial 16S rRNA, due to the absence of a number of large rRNA helices (fig. S7). At the 28S subunit head, the rRNA of the beak is almost entirely missing (fig. S7, A to D), whereas the loss of bacterial h12 near the center of the small subunit body has resulted in the formation of a channel through the 28S subunit (fig. S7F), which widens into a large cavity below mS22 on the solvent side of the subunit (fig. S7G). The distal end of rRNA helix h44 at the subunit interface is partially unwound to position its tip similarly to the tip of h44 in bacteria and in proximity to mS27, even though the mitoribosomal h44 is 18 nucleotides shorter. This unwound segment no longer recognizably forms an A-form RNA helix and appears flexible in our cryo-EM maps (fig. S2B).

Three homologs of bS18, previously termed MRPS18A, -B, and -C (19, 20), localize to three distinct sites in the mammalian mitoribosome (fig. S8, A and B), contrary to the initial assumption that all of them occupy a single site in a mutually exclusive fashion (16, 19). bS18m (MRPS18C) binds to the same site as bacterial bS18, mS40 (MRPS18B) binds to a novel location of the 28S subunit (fig. S8A), and mL66 (MRPS18A) binds to the 39S subunit (14, 15). All three mitochondrial bS18 homologs are zinc-binding proteins, but one of the zinc-coordinating residues is missing in bS18m (MRPS18C) and mL66 (MRPS18A) and is instead provided in trans by uL10m and bS6m, respectively (fig. S8, C to G). These unusual interactions where two protein chains coordinate the same zinc ion may have evolved to stabilize the folds of rapidly evolving mitoribosomal proteins and their quaternary interactions.

The mRNA channel

The structure of the 28S subunit reveals the molecular details of the highly remodeled entry and exit regions of the mitoribosomal mRNA channel (Fig. 4A). The mRNA entry site is surrounded by proteins uS3m, uS5m, mS33, and mS35. An extension of uS5m lines a part of the mRNA entry path and connects the 28S subunit body to the head (Fig. 4B), thus forming a latch across the mRNA channel entrance. Therefore, during translation initiation, the mRNA may need to be threaded through the opening defined by the 12S rRNA and uS5m, unless the uS5m latch dissociates (Fig. 4B). A dynamic role of this protein

in mRNA binding is supported by a comparison of two reconstructions of particle subclasses, one with and one without bound mRNA and tRNAs (fig. S1A), indicating that although the contact points of the latch to the 28S body and head re-

main intact, the helical part of the extension of uS5m that encircles the mRNA entry path is disordered in the complex devoid of tRNAs but ordered in the complex containing mRNA and tRNAs (Fig. 4, C and D).

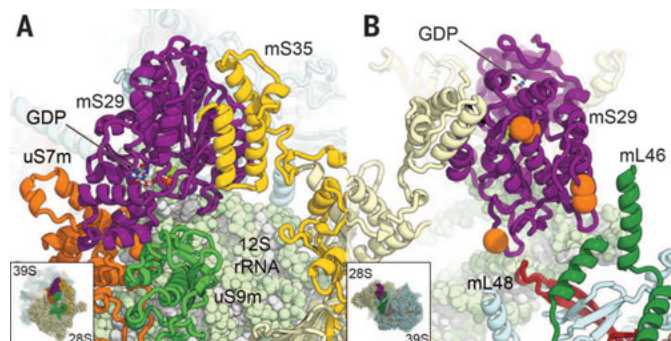


Fig. 5. The guanine nucleotide-binding protein mS29. (A) Position of mS29 (purple, GDP white) in the head domain of the 28S subunit. (B) Putative mS29 phosphorylation sites (orange spheres) near subunit bridges B1b and B1c (mL46 green, mL48 dark red).

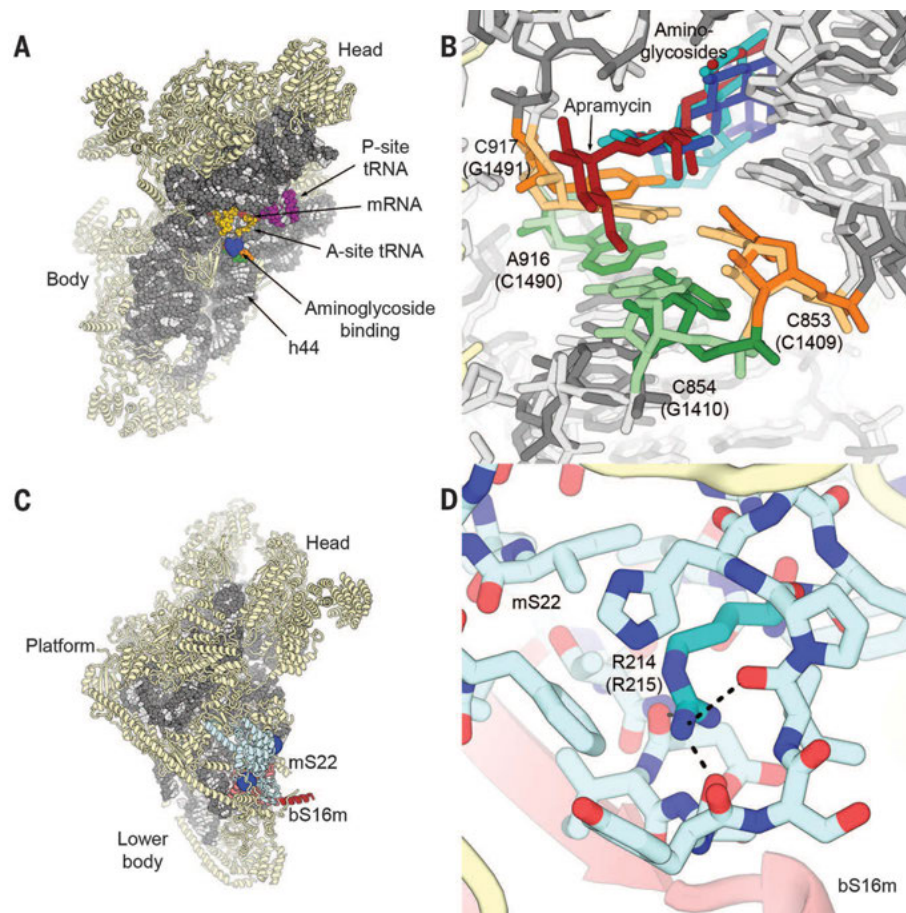


Fig. 6. Aminoglycoside binding to the 28S subunit and mapping of mitoribosomal protein mutations. (A) 28S subunit, with the aminoglycoside binding region near the A site in blue (A- and P-site tRNA fragments gold and purple, respectively). (B) Superposition of the structures of paromomycin (cyan), gentamycin (blue), and apramycin (red) bound to the bacterial 30S subunit (18, 33, 36). Positions of relevant sequence differences between mammalian mitoribosomes and bacterial ribosomes (lighter colors) (18) are shown in orange and green. (C) Location of human mutations in mS22 (light blue, affected residues as blue spheres) and bS16m (red, helix truncated by a nonsense mutation dark red). (D) Location and environment of mS22 residue R214 (R215H mutation in humans).

The pentatricopeptide repeat (PPR)-containing protein mS39 is located close to the mRNA channel entry (Fig. 4, A and B) and forms part of the structure previously termed the mRNA gate (5). The remaining difference density, possibly attributable to mRNA, extends toward the PPR domain of mS39 (Fig. 4C). Consistent with the described role of PPR repeats in single-stranded RNA binding (21), mS39 may therefore bind and guide mitochondrial mRNAs into the mitoribosomal mRNA channel.

Near the decoding center, where mRNA codon-tRNA anticodon base pairing is monitored to select cognate tRNAs (22), density for the mRNA and the well-ordered ASLs of the bound A- and P-site tRNAs can be directly visualized in our cryo-EM map (Fig. 4, E and F). The conformation of the mRNA in this region is similar to that of bacterial ribosomes (fig. S9). Even though the density in our cryo-EM map is an average of all mRNA and tRNA species, the location of base pairs formed between the tRNAs and the mRNA can be directly observed (Fig. 4F). Our structure indicates that the mechanism of decoding of the 28S subunit is highly conserved, including the interactions of the flipped-out bases A918 and A919, as well as the interactions of base G256 [corresponding to bacterial nucleotides A1492, A1493, and G530, respectively (22)] with the minor groove of the codon-anticodon helix (Fig. 4G).

The recognition of leaderless mitochondrial mRNAs (7) by the 28S subunit during initiation does not rely on base pairing with rRNA (23). Consequently, the exit region of the mitoribosomal mRNA channel has very different features from those of bacteria, and the 12S rRNA lacks the anti-Shine-Dalgarno sequence. The exit of the mitoribosomal mRNA channel is encircled by the conserved proteins uS7m, uS11m, bS18m, and bS21m and the mitochondrial-specific protein mS37 (Fig. 4H). It has been suggested that respiratory chain failure prevents the formation of two conserved regulatory disulfide bridges in Mrp10, the yeast homolog of mS37 (Fig. 4H), leading to degradation of the protein and mitochondrial translation shutdown (24). This suggests that impaired assembly of the mRNA exit channel may play a role in this process.

The guanine nucleotide-binding protein of the 28S subunit

Mammalian mitoribosomes bind guanine nucleotides with high affinity (25). The protein that confers this activity has been identified as mS29 (also termed DAP3 for death-associated protein 3) (26, 27). Our structure reveals that mS29 forms part of the small subunit head (Figs. 3A and 5A) and interacts with the 12S rRNA, uS7m, uS9m, and mS35 (Fig. 5A), burying a large surface area of approximately 3400 Å², in addition to its involvement in intersubunit bridge formation with the 39S subunit (fig. S4G). The topology of the β sheet in the nucleotide-binding domain (NBD) and the presence of a C-terminal α -helical bundle (fig. S10A) indicate that mS29 is structurally related to members of the AAA+ ATPase family (28). In the mS29 nucleotide-binding pocket, one

of two conserved acidic residues in the Walker B motif is replaced by a glycine (fig. S10C) (28). This is typical for the NACHT NTPase subfamily of STAND ATPases, which perform a variety of functions, including the regulation of apoptosis in metazoans (29), and where a preference for guanine over adenine nucleotides also occurs (29).

In comparison to the AAA+ ATPase core, mS29 contains two sequence insertions that participate in rRNA binding and intersubunit bridge formation, and additionally its N terminus forms a compact $\alpha_2\beta_2$ domain that covers the nucleotide-binding pocket (fig. S10B). Our density indicates that a nucleotide, likely guanosine diphosphate (GDP), is bound to mS29 in our sample (fig. S10D). Because of the close proximity of the mS29 nucleotide-binding pocket to the rRNA-binding interface (fig. S10C), the presence of a γ phosphate in GTP-bound mS29 might induce conformational rearrangements of rRNA-binding residues that interfere with the binding of mS29 to the 28S subunit.

mS29 has been shown to be phosphorylated in vivo (30). Because the proposed phosphorylation sites map to the region involved in the formation of intersubunit bridges B1b-B1d (Fig. 5B), mS29 phosphorylation may affect intersubunit bridge formation, which might provide a means of regulating the activity of the mammalian mitoribosome.

Insights into antibiotic binding and human pathologies

Aminoglycosides target the bacterial 30S subunit by binding to a pocket in rRNA helix 44 near the ribosomal A site and the decoding center (9, 31, 32) (Fig. 6A). Overlaying our structure of the 28S subunit with structures of the bacterial 30S subunit in complex with the aminoglycosides paromomycin (18) and gentamicin (33) reveals that one end of the binding pocket of these aminoglycosides is widened in the 28S subunit because of the presence of the A916-C854 and C917-C853 mismatches (Fig. 6B), in agreement with sequence analysis (34). In spite of these structural differences, some aminoglycosides can still bind to the decoding site of the small subunit of the mitoribosome, which can lead to hearing loss (ototoxicity), particularly in patients with the A916G or C854U mutation in the 12S rRNA [A1555G and C1494T in the human mitochondrial genome (34)], which occurs in roughly 0.2 to 0.3% of the general population (35). These mutations revert the A916-C854 mismatch found in wild-type mitoribosomes to a bacterial-like state with a Watson-Crick base pair at this position. The aminoglycoside apramycin binds to the 30S subunit in the same region but exhibits lower toxicity toward mitochondrial translation even in the presence of sensitizing mutations (36). Apramycin is embedded less deeply in the rRNA than are other aminoglycosides (36), probably making its binding more dependent on the stacking interaction of its bicyclic ring system with the bacterial G1491-C1409 base pair, which is replaced by the C917-C853 mismatch in the mitoribosomal 12S rRNA (Fig. 6B).

Several mutations in mitoribosomal proteins have been identified in human pathologies. A nonsense mutation in bS16m (MRPS16) that leads to death soon after birth (37) and two point mutations in mS22 (MRPS22) (38, 39) affect the lower body domain of the 28S subunit (Fig. 6, C and D), where they may impair its assembly (40).

The atomic structures presented here pave the way to a mechanistic understanding of human mitochondrial translation and associated pathologies and will also facilitate the rational design of antimicrobials and compounds that block cancer cell proliferation.

REFERENCES AND NOTES

- L. Sagan, *J. Theor. Biol.* **14**, 225–274 (1967).
- T. W. O'Brien, *J. Biol. Chem.* **246**, 3409–3417 (1971).
- E. C. Koc et al., *Front. Physiol.* **4**, 183 (2013).
- E. Desmond, C. Brochier-Armanet, P. Porterre, S. Gribaldo, *Res. Microbiol.* **162**, 53–70 (2011).
- M. R. Sharma et al., *Cell* **115**, 97–108 (2003).
- B. J. Greber et al., *Nature* **505**, 515–519 (2014).
- J. Montoya, D. Ojala, G. Attardi, *Nature* **290**, 465–470 (1981).
- C. N. Jones, K. A. Wilkinson, K. T. Hung, K. M. Weeks, L. L. Spremulli, *RNA* **14**, 862–871 (2008).
- D. N. Wilson, *Nat. Rev. Microbiol.* **12**, 35–48 (2014).
- J. Xie, A. E. Talaska, J. Schacht, *Hear. Res.* **281**, 28–37 (2011).
- A. Rötig, *Biochim. Biophys. Acta* **1807**, 1198–1205 (2011).
- S. B. Vafai, V. K. Mootha, *Nature* **491**, 374–383 (2012).
- F. Sotgia et al., *Cell Cycle* **11**, 4390–4401 (2012).
- B. J. Greber et al., *Nature* **515**, 283–286 (2014).
- A. Brown et al., *Science* **346**, 718–722 (2014).
- P. S. Kaushal et al., *Proc. Natl. Acad. Sci. U.S.A.* **20**, 7284–7289 (2014).
- M. M. Yusupov et al., *Science* **292**, 883–896 (2001).
- R. M. Voorhees, A. Weixlbaumer, D. Loakes, A. C. Kelley, V. Ramakrishnan, *Nat. Struct. Mol. Biol.* **16**, 528–533 (2009).
- E. Cavdar Koc, W. Burkhart, K. Blackburn, A. Moseley, L. L. Spremulli, *J. Biol. Chem.* **276**, 19363–19374 (2001).
- T. Suzuki et al., *J. Biol. Chem.* **276**, 33181–33195 (2001).
- A. Filipovska, O. Rackham, *RNA Biol.* **10**, 1426–1432 (2013).
- J. M. Ogle et al., *Science* **292**, 897–902 (2001).
- J. Shine, L. Dalgarno, *Proc. Natl. Acad. Sci. U.S.A.* **71**, 1342–1346 (1974).
- S. Longen, M. W. Woellhaf, C. Petrunzaro, J. Riemer, J. M. Herrmann, *Dev. Cell* **28**, 30–42 (2014).
- N. D. Denslow, J. C. Anders, T. W. O'Brien, *J. Biol. Chem.* **266**, 9586–9590 (1991).
- E. C. Koc et al., *FEBS Lett.* **492**, 166–170 (2001).
- T. Miyazaki, J. C. Reed, *Nat. Immunol.* **2**, 493–500 (2001).
- J. P. Erzberger, J. M. Berger, *Annu. Rev. Biophys. Biomol. Struct.* **35**, 93–114 (2006).
- D. D. Leipe, E. V. Koonin, L. Aravind, *J. Mol. Biol.* **343**, 1–28 (2004).
- J. L. Miller, H. Koc, E. C. Koc, *Protein Sci.* **17**, 251–260 (2008).
- A. P. Carter et al., *Nature* **407**, 340–348 (2000).
- D. Moazed, H. F. Noller, *Nature* **327**, 389–394 (1987).
- M. A. Borovinskaya et al., *Nat. Struct. Mol. Biol.* **14**, 727–732 (2007).
- T. R. Prezant et al., *Nat. Genet.* **4**, 289–294 (1993).
- M. Bitner-Glindzic et al., *N. Engl. J. Med.* **360**, 640–642 (2009).
- T. Matti et al., *Proc. Natl. Acad. Sci. U.S.A.* **109**, 10984–10989 (2012).
- C. Miller et al., *Ann. Neurol.* **56**, 734–738 (2004).
- P. Smits et al., *Eur. J. Hum. Genet.* **19**, 394–399 (2011).
- A. Saada et al., *J. Med. Genet.* **44**, 784–786 (2007).
- M. Ermdadul Haque, D. Grasso, C. Miller, L. L. Spremulli, A. Saada, *Mitochondrion* **8**, 254–261 (2008).

ACKNOWLEDGMENTS

EM data were collected at the ScopeM facility of ETH Zurich. We thank P. Tittmann (ScopeM) for support and J. Erzberger for discussions. This work was supported by the Swiss National

Science Foundation (SNSF), the National Center of Excellence in Research (NCCR) Structural Biology and RNA & Disease programs of the SNSF, European Research Council grant 250071 under the European Community's Seventh Framework Programme (to N.B.), the Commission of the European Communities through the PROSPECTS consortium (European Union FP7 projects 201648 and 233226) (R.A.), and the European Research Council (grant ERC-2008-AdG 233226) (R.A.). The 3.6 Å cryo-EM map of the 28S mitoribosomal subunit and the 3.8 Å cryo-EM map of the 55S mitoribosome have been deposited at the Electron Microscopy Data Bank (EMDB) with accession codes EMD-2913

and EMD-2914. Coordinates of the refined 28S subunit and the 55S mitoribosome in the canonical state have been deposited in the Protein Data Bank (PDB) with PDB codes 5AJ3 (28S) and 5AJ4 (55S). A PyMol script for display of the 55S mitoribosome is available from the Ban Lab website (www.mol.biol.ethz.ch/groups/ban_group/). ETH Zurich has filed a patent application to use the coordinates of the porcine mitoribosome structure for development of compounds that can (i) specifically interfere with mitochondrial translation by binding to mitoribosomes or (ii) specifically inhibit translation in pathogenic organisms without interfering with mitoribosomes.

SUPPLEMENTARY MATERIALS

www.sciencemag.org/content/348/6232/303/suppl/DC1
Materials and Methods
Supplementary Text
Figs. S1 to S10
Tables S1 to S7
References (41–67)
Data Table S1

27 November 2014; accepted 6 March 2015
10.1126/science.aaa3872

REPORTS

SURFACE STRUCTURE

Subatomic resolution force microscopy reveals internal structure and adsorption sites of small iron clusters

Matthias Emmrich,¹ Ferdinand Huber,¹ Florian Pielmeier,¹ Joachim Welker,¹ Thomas Hofmann,¹ Maximilian Schneiderbauer,¹ Daniel Meuer,¹ Svitlana Polesya,² Sergiy Mankovsky,² Diemo Ködderitzsch,² Hubert Ebert,² Franz J. Giessibl^{1*}

Clusters built from individual iron atoms adsorbed on surfaces (adatoms) were investigated by atomic force microscopy (AFM) with subatomic resolution. Single copper and iron adatoms appeared as toroidal structures and multiatom clusters as connected structures, showing each individual atom as a torus. For single adatoms, the toroidal shape of the AFM image depends on the bonding symmetry of the adatom to the underlying structure [twofold for copper on copper(110) and threefold for iron on copper(111)]. Density functional theory calculations support the experimental data. The findings correct our previous work, in which multiple minima in the AFM signal were interpreted as a reflection of the orientation of a single front atom, and suggest that dual and triple minima in the force signal are caused by dimer and trimer tips, respectively.

The observation of “subatomic features” by atomic force microscopy (AFM) (1) in experiments where the front atom of the tip was imaged by the highly localized dangling bonds of the Si(111)-(7×7) surface atoms (2) raised discussions within the community (3). Similar observations were reported later for Si adatoms imaging Si tips (4), CoSm tips (5), and even in scanning tunneling microscopy (STM) (6). The initial results were obtained at room temperature, where the atomic configuration of the tip changes frequently. The stability offered at liquid helium temperatures allowed to resolve small features in tip images spaced by merely 77 pm (0.77 Å) (7). Again, the front atom of the tungsten tip was imaged by a sample consisting of light and small atoms (carbon in graphite) (7). Later, we used CO molecules to establish the COFI technique (carbon monoxide front atom identification) (8, 9), building on expertise with CO imaging when measuring the forces that act

during atomic manipulation (10). The adsorption geometry of CO molecules on Cu(111) surfaces is critical for the effectiveness of COFI: CO adsorbs perpendicular to Cu(111), with the C atom sitting on top of a Cu surface atom (11).

However, the purpose of microscopy is to image a sample, not to inspect the tip, so it was important to design well-defined tips with front atoms much smaller than typical metals. Gross *et al.* created such a sharp and well-defined tip by adsorbing a CO molecule to the metal tip, demonstrating submolecular (12) resolution on pentacene (13) and other molecules by AFM with a resolution that exceeds STM. The CO molecule attaches to the tip with the carbon atom, and the front atom of the tip is an oxygen atom. Tip functionalization by adsorbing a CO molecule on a metal tip had been introduced in STM before (14), but the dramatic increase in AFM resolution on organic matter was not foreseen and is used widely now—for example, to determine bond order (15) and chemical reaction products (16). The use of CO-terminated metal tips enabled reversing the experiment (8) and imaging single atoms in various bonding configurations to check whether subatomic resolution (12)

is possible on a sample. Here, we first analyze the imaging of single adatoms and then expand to image small clusters.

The contrast for CO tips at small distances arises from Pauli repulsion forces that increase with charge density (17), similar to the interaction of closed-shell atoms with molecules (18). Pauli repulsion allows for a descriptive interpretation where the AFM image represents the charge density that is maximal on top of atoms—in contrast to STM, which maps the charge density at the Fermi level. However, the CO molecule bonded to the metal tip easily bends laterally (13, 19), and artifacts such as lateral distortions, apparent bond lengthening, bond sharpening, and cusplike maxima within aromatic rings must be anticipated [see figure 1 in (15)]. Thus, we first checked the imaging characteristics of CO tips for adatoms using silicon, with its well-known structure.

A CO-terminated tip created AFM images of the Si(111)-(7×7) reconstruction (Fig. 1A) that clearly display the 12 adatoms and even the 6 rest atoms in each unit cell. Adatoms and rest atoms hybridize into four 3sp³ orbitals, where the orbitals normal to the surface appear as roughly Gaussian protrusions. The calculated charge density of Si(111)-(7×7) (Fig. 1B) is similar to the experimental image in Fig. 1A. Figure 1B shows the charge density of the protruding 3sp³ orbitals, and Fig. 1C (experimental) and Fig. 1D (calculated) focus on a single Si adatom. The density calculations of Fig. 1 use Slater-type orbitals (STO) (20), with details for Si in (4) and in (9) for the following metallic adatoms.

Figure 1E is an AFM image of a single Cu adatom on a Cu(111) surface. Surprisingly, the Cu adatom does not appear as a single protrusion like the Si adatom in Fig. 1C but shows a toroidal structure. We postulate that the origin of this toroidal shape is in the electronic configuration of the adatom. Figure S1 (21) shows the contrast development for the Cu adatom with distance: For larger distances, the adatom appears attractive (fig. S1A); for an intermediate distance, a repulsive ring appears (fig. S1B); finally, for very close distances, artifacts from CO bending (which have also been seen when imaging organic molecules) appear in which the repulsive ring becomes sharper (fig. S1C) and a repulsive center cusp starts to emerge (fig. S1D). The electronic configuration of a neutral Cu atom is [Ar]3d¹⁰4s¹. Fully occupied subshells as well as the 4s electron of a free Cu atom yield a spherically symmetric charge density. However, the Smoluchowski effect (22) leads to a positive charge of protruding

¹Institute of Experimental and Applied Physics, Department of Physics, University of Regensburg, 93053 Regensburg, Germany. ²Department Chemie, Ludwig-Maximilians-Universität München, Butenandtstrasse 11, 81377 München, Germany.
*Corresponding author. E-mail: franz.giessibl@ur.de

Science Foundation (SNSF), the National Center of Excellence in Research (NCCR) Structural Biology and RNA & Disease programs of the SNSF, European Research Council grant 250071 under the European Community's Seventh Framework Programme (to N.B.), the Commission of the European Communities through the PROSPECTS consortium (European Union FP7 projects 201648 and 233226) (R.A.), and the European Research Council (grant ERC-2008-AdG 233226) (R.A.). The 3.6 Å cryo-EM map of the 28S mitoribosomal subunit and the 3.8 Å cryo-EM map of the 55S mitoribosome have been deposited at the Electron Microscopy Data Bank (EMDB) with accession codes EMD-2913

and EMD-2914. Coordinates of the refined 28S subunit and the 55S mitoribosome in the canonical state have been deposited in the Protein Data Bank (PDB) with PDB codes 5AJ3 (28S) and 5AJ4 (55S). A PyMol script for display of the 55S mitoribosome is available from the Ban Lab website (www.mol.biol.ethz.ch/groups/ban_group/). ETH Zurich has filed a patent application to use the coordinates of the porcine mitoribosome structure for development of compounds that can (i) specifically interfere with mitochondrial translation by binding to mitoribosomes or (ii) specifically inhibit translation in pathogenic organisms without interfering with mitoribosomes.

SUPPLEMENTARY MATERIALS

www.sciencemag.org/content/348/6232/303/suppl/DC1
Materials and Methods
Supplementary Text
Figs. S1 to S10
Tables S1 to S7
References (41–67)
Data Table S1

27 November 2014; accepted 6 March 2015
10.1126/science.aaa3872

REPORTS

SURFACE STRUCTURE

Subatomic resolution force microscopy reveals internal structure and adsorption sites of small iron clusters

Matthias Emmrich,¹ Ferdinand Huber,¹ Florian Pielmeier,¹ Joachim Welker,¹ Thomas Hofmann,¹ Maximilian Schneiderbauer,¹ Daniel Meuer,¹ Svitlana Polesya,² Sergiy Mankovsky,² Diemo Ködderitzsch,² Hubert Ebert,² Franz J. Giessibl^{1*}

Clusters built from individual iron atoms adsorbed on surfaces (adatoms) were investigated by atomic force microscopy (AFM) with subatomic resolution. Single copper and iron adatoms appeared as toroidal structures and multiatom clusters as connected structures, showing each individual atom as a torus. For single adatoms, the toroidal shape of the AFM image depends on the bonding symmetry of the adatom to the underlying structure [twofold for copper on copper(110) and threefold for iron on copper(111)]. Density functional theory calculations support the experimental data. The findings correct our previous work, in which multiple minima in the AFM signal were interpreted as a reflection of the orientation of a single front atom, and suggest that dual and triple minima in the force signal are caused by dimer and trimer tips, respectively.

The observation of “subatomic features” by atomic force microscopy (AFM) (1) in experiments where the front atom of the tip was imaged by the highly localized dangling bonds of the Si(111)-(7×7) surface atoms (2) raised discussions within the community (3). Similar observations were reported later for Si adatoms imaging Si tips (4), CoSm tips (5), and even in scanning tunneling microscopy (STM) (6). The initial results were obtained at room temperature, where the atomic configuration of the tip changes frequently. The stability offered at liquid helium temperatures allowed to resolve small features in tip images spaced by merely 77 pm (0.77 Å) (7). Again, the front atom of the tungsten tip was imaged by a sample consisting of light and small atoms (carbon in graphite) (7). Later, we used CO molecules to establish the COFI technique (carbon monoxide front atom identification) (8, 9), building on expertise with CO imaging when measuring the forces that act

during atomic manipulation (10). The adsorption geometry of CO molecules on Cu(111) surfaces is critical for the effectiveness of COFI: CO adsorbs perpendicular to Cu(111), with the C atom sitting on top of a Cu surface atom (11).

However, the purpose of microscopy is to image a sample, not to inspect the tip, so it was important to design well-defined tips with front atoms much smaller than typical metals. Gross *et al.* created such a sharp and well-defined tip by adsorbing a CO molecule to the metal tip, demonstrating submolecular (12) resolution on pentacene (13) and other molecules by AFM with a resolution that exceeds STM. The CO molecule attaches to the tip with the carbon atom, and the front atom of the tip is an oxygen atom. Tip functionalization by adsorbing a CO molecule on a metal tip had been introduced in STM before (14), but the dramatic increase in AFM resolution on organic matter was not foreseen and is used widely now—for example, to determine bond order (15) and chemical reaction products (16). The use of CO-terminated metal tips enabled reversing the experiment (8) and imaging single atoms in various bonding configurations to check whether subatomic resolution (12)

is possible on a sample. Here, we first analyze the imaging of single adatoms and then expand to image small clusters.

The contrast for CO tips at small distances arises from Pauli repulsion forces that increase with charge density (17), similar to the interaction of closed-shell atoms with molecules (18). Pauli repulsion allows for a descriptive interpretation where the AFM image represents the charge density that is maximal on top of atoms—in contrast to STM, which maps the charge density at the Fermi level. However, the CO molecule bonded to the metal tip easily bends laterally (13, 19), and artifacts such as lateral distortions, apparent bond lengthening, bond sharpening, and cusplike maxima within aromatic rings must be anticipated [see figure 1 in (15)]. Thus, we first checked the imaging characteristics of CO tips for adatoms using silicon, with its well-known structure.

A CO-terminated tip created AFM images of the Si(111)-(7×7) reconstruction (Fig. 1A) that clearly display the 12 adatoms and even the 6 rest atoms in each unit cell. Adatoms and rest atoms hybridize into four 3sp³ orbitals, where the orbitals normal to the surface appear as roughly Gaussian protrusions. The calculated charge density of Si(111)-(7×7) (Fig. 1B) is similar to the experimental image in Fig. 1A. Figure 1B shows the charge density of the protruding 3sp³ orbitals, and Fig. 1C (experimental) and Fig. 1D (calculated) focus on a single Si adatom. The density calculations of Fig. 1 use Slater-type orbitals (STO) (20), with details for Si in (4) and in (9) for the following metallic adatoms.

Figure 1E is an AFM image of a single Cu adatom on a Cu(111) surface. Surprisingly, the Cu adatom does not appear as a single protrusion like the Si adatom in Fig. 1C but shows a toroidal structure. We postulate that the origin of this toroidal shape is in the electronic configuration of the adatom. Figure S1 (21) shows the contrast development for the Cu adatom with distance: For larger distances, the adatom appears attractive (fig. S1A); for an intermediate distance, a repulsive ring appears (fig. S1B); finally, for very close distances, artifacts from CO bending (which have also been seen when imaging organic molecules) appear in which the repulsive ring becomes sharper (fig. S1C) and a repulsive center cusp starts to emerge (fig. S1D). The electronic configuration of a neutral Cu atom is [Ar]3d¹⁰4s¹. Fully occupied subshells as well as the 4s electron of a free Cu atom yield a spherically symmetric charge density. However, the Smoluchowski effect (22) leads to a positive charge of protruding

¹Institute of Experimental and Applied Physics, Department of Physics, University of Regensburg, 93053 Regensburg, Germany. ²Department Chemie, Ludwig-Maximilians-Universität München, Butenandtstrasse 11, 81377 München, Germany.
*Corresponding author. E-mail: franz.giessibl@ur.de

surface features such as steps or adatoms, surrounded by a surplus in negative charge. Imaging the polar surface of Cu_2N with a CO-terminated tip has revealed that the CO-terminated tip forms a dipole with the negative end at the oxygen atom (23), in agreement with density functional theory (DFT) calculations (24, 25) and similar to CO adsorbed on several (111) metal surfaces (11).

Thus, the toroidal symmetry of the experimental image of a Cu adatom shown in Fig. 1E arose from electrostatic attraction at the center and Pauli repulsion at the circumference. The charge redistribution created by the Smoluchowski effect can be mapped on atomic states by a hybridization of $|4s\rangle$ into a $(|4s\rangle - |4p_z\rangle)/\sqrt{2}$ state. Figure 1F shows the calculated charge density of this state with STO orbitals, and the inset shows the charge gradient in the z direction using DFT. The calculation of the interaction of CO-terminated tips with adatoms and clusters is still too complex for the current status of DFT, so we use H and Xe atoms as tip models in DFT calculations. Given that the highest occupied states within bulk copper have a bonding energy of ~ 5 eV, perturbation theory yields an energetic lowering of the $|4s\rangle$ state when hybridizing into a $(|4s\rangle - |4p_z\rangle)/\sqrt{2}$ state. This process would also explain why a Cu adatom with its diameter of 255 pm has a much lower apparent height of ~ 100 pm in STM. We note that these toroidal symmetries have been observed before in the reverse situation, where a CO molecule adsorbed on Cu(111) probed the metallic tip atom [see figure 1D in (8); figure 1, c and h, in (9); and figure 1D in (10)].

Figure 1G shows a Cu adatom on a Cu(111) surface. The (110) surface has a twofold symmetry, and the toroidal image of the Cu adatom has two dips in it, according to the twofold symmetry of the substrate. It can be modeled in the STO-based charge density by a 2% mixing of a

$|4p_y\rangle$ orbital into the $(|4s\rangle - |4p_z\rangle)/\sqrt{2}$ state as calculated in Fig. 1H.

Figure 1I is an AFM image of an Fe adatom on Cu(111). A free Fe atom has an electronic configuration of $[\text{Ar}]3d^64s^2$. Similar to the Cu adatom, it shows an overall toroidal structure, and it is centered around a face-centered-cubic (fcc) site (see fig. S2). However, the torus has three bumps that point to the three next-nearest Cu atoms of the substrate. Figure 1J is an STO-type charge calculation with a $4s_{\text{Fe}}$ hybridization. Possibly, further hybridization with electrons from the unfilled 3d states occurs that could explain the three bumps on the torus-shaped image. The overall toroidal shape with a threefold symmetry of the Fe adatom interacting with a Xe tip is revealed by DFT using the Vienna Ab-initio Simulation Package (VASP) code (26) (inset of Fig. 1J and fig. S3). The possibility of detecting subatomic contrast has been discussed previously based on DFT calculations by Huang *et al.* (27) and Zotti *et al.* (28) for silicon and Wright and Solares (29) for tungsten. Figure 1K is an AFM image of an Fe atom on an Fe island. Its threefold symmetry is explained by the contribution of 3d states, as shown in Fig. 1L after the calculations published in figure S10 of (9).

Although atoms can be positioned with atomic precision by STM, their exact location is determined by the chemical bonds that develop. Because Cu(111) appears flat in STM under normal tunneling conditions, adsorption-site determination by STM is difficult. Brune *et al.* (30) used STM at low bias and high current to resolve the surface lattice and adsorption site of C on aluminum(111). Repp *et al.* (31) used STM and atomic manipulation (32) to determine that single Cu adatoms on a Cu(111) surface preferably adsorb at fcc sites, under the assumption that stripes of Cu adatoms also adsorb on fcc sites. Stroscio and Celotta (33) have identified fcc sites as the preferred ad-

sorption sites of Co atoms on Cu(111) by monitoring the fluctuations of the tunneling current during atomic manipulation. In the well-known quantum corral experiment, 48 Fe atoms were arranged in a circle on Cu(111) by atomic manipulation by STM (34). The adsorption site was not determined in the quantum corral, but evidence was found later that Fe adatoms preferentially adsorb on fcc sites (35).

Figure 2A shows an STM image of a dimer, Fig. 2E of a trimer, and Fig. 2I of a tetramer, recorded with a metal tip. In agreement with previous reports (36, 37), STM only reveals single roughly Gaussian peaks where the height depends on the number of atoms (see fig. S4). It has been observed before [figure 2 in (8)] that differential STM data or Laplace filtering of STM data recorded with CO-terminated tips partially reveals the highly resolved AFM data.

AFM with CO tips could directly image the Cu(111) surface lattice (38), so adsorption sites of Fe adatoms and clusters can be determined by centering a lattice overlay that registers with the Cu atom surface layer as in Fig. 2, C, G, and K. Although CO tip-bending artifacts lead to an apparent larger lateral size of clusters, the AFM images allow conclusions about the adsorption sites. Given that Fe monomers preferentially adsorb on fcc sites, one would assume that the two Fe atoms comprising a dimer also adsorb on fcc. However, the AFM image of the dimer in Fig. 2, B and C, does not share the symmetry of the surface. Although some of that asymmetry might be caused by a slight tilt in the CO tip molecule, DFT calculations in fig. S5 predict an asymmetric adsorption with adsorption sites near two next-nearest bridge sites, as displayed in Fig. 2D.

Trimers adsorb in three different geometries. The most prevalent adsorption symmetry is shown in Fig. 2, F and G. This trimer is centered on top

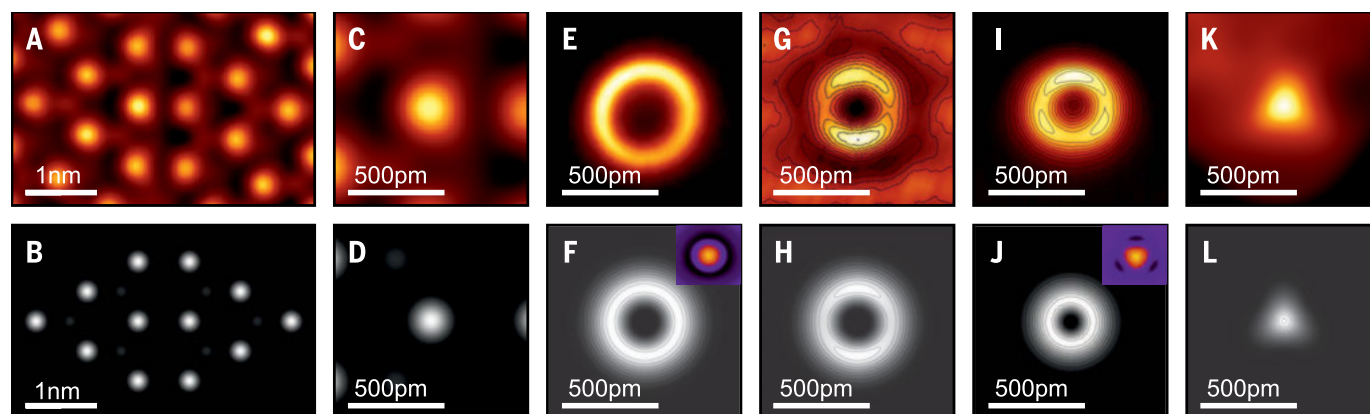


Fig. 1. Constant-height mode AFM images (top row) and simulations (bottom row) of silicon, copper, and iron surface atoms. (A) AFM image of the Si(111)-(7×7) reconstruction using a CO-terminated metal tip. The rest atoms are clearly visible. (B) Calculated valence charge density of Si(111)-(7×7) reconstruction, using Slater-type orbitals as discussed in (4). (C) Magnified view of a single adatom (center-faulted half). (D) Calculated charge density of that atom. (E) Experimental AFM image of a Cu adatom on Cu(111), showing a ringlike symmetry that is caused by a toroidal charge density of the adatoms. (F) Calculated charge density of the Cu adatom using a $4s_{\text{Cu}}$ hybrid state

(21). The inset shows the charge gradient calculated with DFT (see fig. S3D). (G) Experimental image of a Cu adatom on a Cu(110) surface. (H) Calculated charge density of the Cu adatom using a $4s_{\text{Cu}}$ hybrid state plus a $4p_y$ state (21). (I) Experimental AFM image of a Fe adatom on Cu(111), showing the Fe adatom as a torus with three local maxima. (J) Calculated charge density of the Fe adatom on Cu(111) using a $4s_{\text{Fe}}$ hybrid state. The inset shows the charge gradient calculated with DFT (see fig. S3E). (K) Experimental AFM image of an Fe adatom on an Fe island. (L) Simulated AFM image according to supplemental figure S10 in (9).

of a Cu atom, with the Fe atoms adsorbed near bridge sites pointing toward the nearest neighbors of the center atom. For this bonding geometry, two orientations exist, and they can be rotated by the AFM tip, as displayed in fig. S6. DFT confirms that the bridge-site adsorption geometry is energetically favorable over an fcc site geometry for trimers that are centered on top of a Cu atom (fig. S7). Experimentally, we also find a second type of trimer centered around a hexagonal close-packed (hcp) site (see fig. S8). DFT confirms that this trimer has an even lower adsorption energy (fig. S7A). Because of the symmetry of the surface lattice, a trimer centered on an hcp site with Fe atoms on fcc sites can only point in one orientation, with the three Fe atoms sitting on fcc sites. Experimentally, we only found hcp-centered trimers that show a triangle that pointed downward, as displayed in fig. S8. Unlike the bridge-site trimer, it was not possible to rotate or move the fcc-site trimer. A third type of trimer is depicted in fig. S9A. The Laplace-filtered version of it in fig. S9B shows that there is a mirror axis, but it is not possible to assign atomic positions from the data. Possibly, this orientation involves a dynamic state. The identity of these structures as trimers was verified by manipulating an additional Fe atom to them, yielding a stable tetramer, as displayed in Fig. 2J. For tetramers (Fig. 2J) and larger clusters discussed below, the iron atoms apparently adsorb on fcc sites.

Figure 3A shows AFM images of two large Fe clusters. The right cluster is composed of 16 atoms, with 15 atoms on the Cu(111) substrate and one atom on top. The left cluster is built from 12 atoms, with one atom on the top of the island. This top atom moved during imaging and appeared as a streak; it did not move in a consecutive fast scan of the same two clusters shown in fig. S13. Figure 3B is a Laplace-filtered version of Fig. 3A, and Fig. 3C includes a lattice overlay. The central parts of the clusters show that for large clusters, the Fe atoms are located on fcc sites. The edges of the clusters appear strongly distorted, similar to the distortions in edges of pentacene and other organic molecules (13, 15). Resolving the structure of small clusters should prove to be useful in many fields—for example, in nanomagnets, where the structure of Fe clusters influences their magnetic properties (37).

The initial goal of the present experiments was to achieve subatomic spatial resolution of AFM by reversing the experiment of (8), in which COFI images of tungsten tips similar to Fig. 2B were interpreted as single atom tips oriented in a [110] crystal direction, and COFI images similar to Fig. 2F were thought to originate from a single atom tip oriented in a [111] direction. We found that COFI images of Fe with its body-centered-cubic (bcc) structure are similar to COFI images of tungsten (also bcc) [see figure S4 in (39)]. It is easier to evaporate Fe on Cu(111) than W because of its lower melting point. Thus, we compared constant-height AFM images that use a CO tip to image Fe dimers and trimers with the constant-height COFI images of Fe tips with dual and triple minima in figs. S10 and S11, respectively. The similarity in force values, lateral extent,

and appearance is excellent, so we conclude that the interpretation of tips 2 and 3 as pointing in a [110] and [111] direction in (8) is incorrect. Rather, we conclude that tips 2 and 3 were dimer and trimer tips, respectively (40).

Constant-height AFM images of dimers showed two local minima separated by a repulsive barrier (fig. S10), and trimers showed a starlike structure (fig. S11). Figure S12 shows the square of a superposition of two (fig. S12A) and three (fig. S12B) $4sp_z$ states that were centered on two and three

Cu atoms. Qualitatively, this charge density calculated from the square of $4sp_z$ states is similar to the experimental constant-height images, which suggests that the $4sp_z$ states are important for bonding the clusters. The interplay of internal cluster bonding and bonding to the substrate allows manipulation for some clusters (fig. S6), and second-layer atoms on clusters (Fig. 3 and fig. S13) pose an interesting challenge for theory and experiment in catalysis and surface science in general.

Fig. 2. Dimers, trimers, and tetramers imaged by STM, AFM, and their calculated adsorption sites.

The first row shows constant-current STM data using a metal tip [(A), (E), and (I)] of an Fe dimer on Cu(111) (left column), Fe trimer (center column), and Fe tetramer (right column). The second row [(B), (F), and (J)] shows the AFM signal (frequency shift) recorded in constant-current topographic imaging with a CO-terminated tip. The dark spots in the flat regions correspond to Cu surface atoms that allow us to register the lattice overlay in the third row [(C), (G), and (K)]. The last row [(D), (H), and (L)] shows the proposed adsorption sites, indicating top, fcc, and hcp positions. An adatom centered on a fcc site thus continues the bulk fcc structure, whereas an adatom on a hcp site would break the crystalline order of the fcc bulk. DFT calculations (21) reveal that dimers (D) adsorb with the two Fe atoms close to two next-nearest bridge sites. On-top centered trimers (H) also adsorb with the three Fe atoms close to bridge sites, and tetramers (L) adsorb on fcc sites. The top row and the rows below show different clusters.

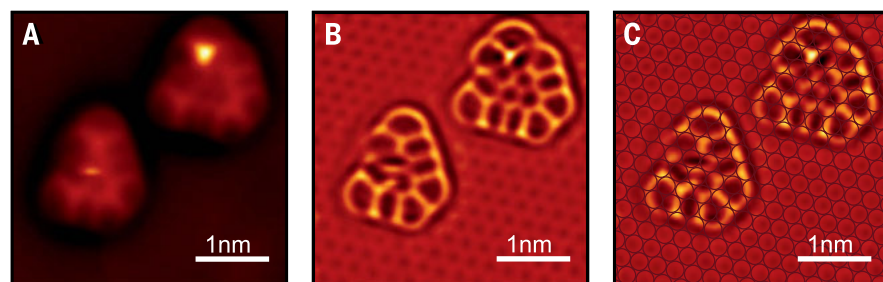
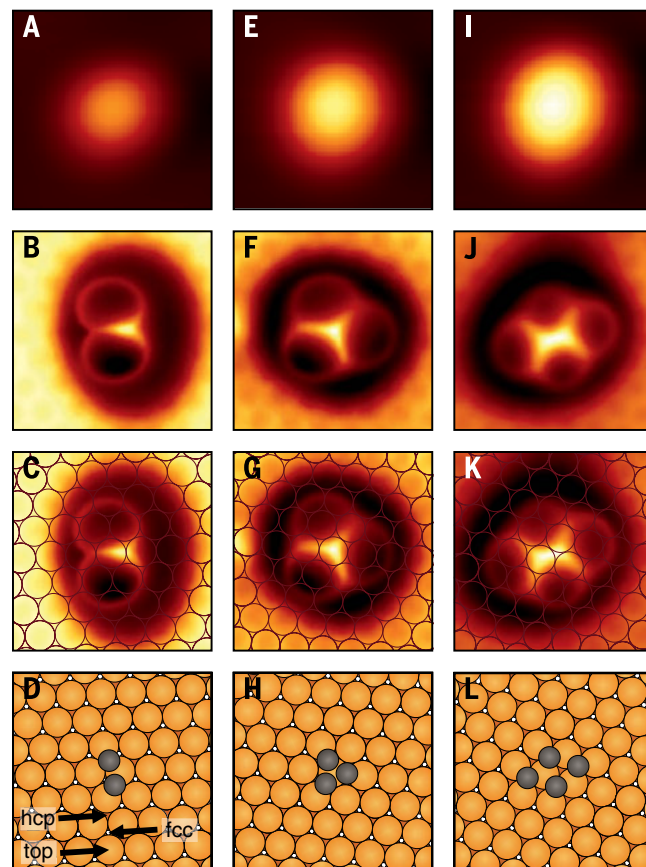


Fig. 3. Images of two nearby Fe clusters. (A) AFM image of two nearby Fe clusters. (B) Double Laplace-filtered image of (A). (C) Same image as (B), including a lattice overlay that shows the adsorption geometry. Both clusters have an additional atom on top; this atom has moved during scanning in the left cluster. The edges of the clusters appear strongly distorted because of CO bending; the center parts show that the Fe adatoms comprising the cluster adsorb on fcc sites.

REFERENCES AND NOTES

- G. Binnig, C. F. Quate, C. Gerber, *Phys. Rev. Lett.* **56**, 930–933 (1986).
- F. J. Giessibl, S. Hembacher, H. Bielefeldt, J. Mannhart, *Science* **289**, 422–425 (2000).
- H. J. Hug et al., *Science* **291**, 2509a (2001).
- F. J. Giessibl, H. Bielefeldt, S. Hembacher, J. Mannhart, *Ann. Phys. (Berl.)* **10**, 887–910 (2001).
- M. Herz, F. J. Giessibl, J. Mannhart, *Phys. Rev. B* **68**, 045301 (2003).
- A. N. Chaika, A. N. Myagkov, *J. Phys. Conf. Ser.* **100**, 012020 (2008).
- S. Hembacher, F. J. Giessibl, J. Mannhart, *Science* **305**, 380–383 (2004).
- J. Welker, F. J. Giessibl, *Science* **336**, 444–449 (2012).
- T. Hofmann, F. Pielmeier, F. J. Giessibl, *Phys. Rev. Lett.* **112**, 066101 (2014).
- M. Ternes, C. P. Lutz, C. F. Hirjibehedin, F. J. Giessibl, A. J. Heinrich, *Science* **319**, 1066–1069 (2008).
- A. Zangwill, *Physics on Surfaces* (Cambridge Univ. Press, Cambridge 1988).
- Submolecular resolution is defined as the ability to resolve atomic positions within molecules. Here, we refer to subatomic resolution as the ability to image single atoms as nontrivial features such as tori or multiple extrema, in contrast to single protrusions or single depressions.
- L. Gross, F. Mohn, N. Moll, P. Liljeroth, G. Meyer, *Science* **325**, 1110–1114 (2009).
- L. Bartels, G. Meyer, K. H. Rieder, *Appl. Phys. Lett.* **71**, 213 (1997).
- L. Gross et al., *Science* **337**, 1326–1329 (2012).
- D. G. de Oteyza et al., *Science* **340**, 1434–1437 (2013).
- N. Moll, L. Gross, F. Mohn, A. Curioni, G. Meyer, *New J. Phys.* **12**, 125020 (2010).
- R. G. Gordon, Y. S. Kim, *J. Chem. Phys.* **56**, 3122 (1972).
- A. J. Weymouth, T. Hofmann, F. J. Giessibl, *Science* **343**, 1120–1122 (2014).
- J. C. Slater, *Phys. Rev.* **36**, 57–64 (1930).
- Supplementary materials are available on Science Online.
- R. Smoluchowski, *Phys. Rev.* **60**, 661–674 (1941).
- M. Schneiderbauer, M. Emmrich, A. J. Weymouth, F. J. Giessibl, *Phys. Rev. Lett.* **112**, 166102 (2014).
- M. Feng et al., *ACS Nano* **5**, 8877–8883 (2011).
- P. Hapala, R. Temirov, F. S. Tautz, P. Jelinek, *Phys. Rev. Lett.* **113**, 226101 (2014).
- G. Kresse, J. Hafner, *Phys. Rev. B* **47**, 558–561 (1993).
- M. Huang, M. Čuma, F. Liu, *Phys. Rev. Lett.* **90**, 256101 (2003).
- L. A. Zotti, W. A. Hofer, F. J. Giessibl, *Chem. Phys. Lett.* **420**, 177–182 (2006).
- C. A. Wright, S. D. Solares, *Nano Lett.* **11**, 5026–5033 (2011).
- H. Brune, J. Wintterlin, G. Ertl, R. J. Behm, *Europhys. Lett.* **13**, 123–128 (1990).
- J. Repp, G. Meyer, K.-H. Rieder, P. Hyldgaard, *Phys. Rev. Lett.* **91**, 206102 (2003).
- D. M. Eigler, E. K. Schweizer, *Nature* **344**, 524–526 (1990).
- J. A. Strosio, R. J. Celotta, *Science* **306**, 242–247 (2004).
- M. F. Crommie, C. P. Lutz, D. M. Eigler, *Science* **262**, 218–220 (1993).
- A. Biedermann, W. Rupp, M. Schmid, P. Varga, *Phys. Rev. B* **73**, 165418 (2006).
- M. Pivetta, G. E. Pacchioni, U. Schlickum, J. V. Barth, H. Brune, *Phys. Rev. Lett.* **110**, 086102 (2013).
- A. A. Khajetoorians et al., *Science* **339**, 55–59 (2013).
- B. Schuler et al., *Phys. Rev. Lett.* **111**, 106103 (2013).
- F. Pielmeier, F. J. Giessibl, *Phys. Rev. Lett.* **110**, 266101 (2013).
- Our initial experiments of evaporating Fe atoms on Cu(111) appeared to confirm the findings of the inverse of the threefold tip 3 of (8), because we found many threefold structures that we first misinterpreted as single atoms. It turned out that upon extended Fe evaporation, the copper crystal heated up to ~15 K and the Fe monomers became mobile enough to form an abundance of trimers.

ACKNOWLEDGMENTS

We thank G. Binnig, J. Repp, and A. J. Weymouth for discussions and the Deutsche Forschungsgemeinschaft for funding under Graduiertenkolleg 1570 and Sonderforschungsbereich 689, as well as M. Grifoni (speaker of GRK) and D. Weiss (speaker of SFB) for support. F.J.G. thanks A. Heinrich for hosting several visits at the IBM Almaden Research Center from 2005 until 2010, where first attempts to resolve metallic adatoms with subatomic resolution were performed together with C. Lutz, C. Hirjibehedin, and M. Ternes. Author contributions: M.E. performed most of the measurements and data analysis, constructed the low-temperature scan head, and prepared most figures; F.H. optimized the electronics and performed crucial measurements; J.W. performed measurements on Cu adatoms on Cu(111); T.H. and F.P. performed measurements on Cu/Cu(110) and inverse measurements using

CO/Cu(111) to characterize Cu and Fe tips; M.S. constructed most of the vacuum system and sample-preparation facilities; D.M. performed the AFM measurements on Si; D.K., S.P., S.M., and H.E. performed the DFT calculations; and F.J.G. initiated and directed the project, employed the STO model, and wrote the manuscript.

SUPPLEMENTARY MATERIALS

www.sciencemag.org/content/348/6232/308/suppl/DC1
Materials and Methods
Supplementary Text
Figs. S1 to S13
References (41–47)

19 December 2014; accepted 20 February 2015
Published online 19 March 2015;
10.1126/science.aaa5329

ACTIVE GALAXIES

A strong magnetic field in the jet base of a supermassive black hole

Ivan Martí-Vidal,* Sébastien Muller, Wouter Vlemmings, Cathy Horellou, Susanne Aalto

Active galactic nuclei (AGN) host some of the most energetic phenomena in the universe. AGN are thought to be powered by accretion of matter onto a rotating disk that surrounds a supermassive black hole. Jet streams can be boosted in energy near the event horizon of the black hole and then flow outward along the rotation axis of the disk. The mechanism that forms such a jet and guides it over scales from a few light-days up to millions of light-years remains uncertain, but magnetic fields are thought to play a critical role. Using the Atacama Large Millimeter/submillimeter Array (ALMA), we have detected a polarization signal (Faraday rotation) related to the strong magnetic field at the jet base of a distant AGN, PKS 1830–211. The amount of Faraday rotation (rotation measure) is proportional to the integral of the magnetic field strength along the line of sight times the density of electrons. The high rotation measures derived suggest magnetic fields of at least tens of Gauss (and possibly considerably higher) on scales of the order of light-days (0.01 parsec) from the black hole.

The AGN jets, related to the accretion mechanism in supermassive black holes, consist of relativistic plasma driven by strong and ordered magnetic fields. As a result of the magnetic interaction of the plasma, nonthermal (synchrotron) emission is produced (1). Studying the polarization of this nonthermal emission from AGN is a direct way to probe the structure and strength of magnetic fields in the vicinity of a black hole. Of particular importance is the observation of the rotation measure, RM , defined as the change of polarization angle as a function of wavelength squared. This quantity is directly related to the plasma density and the strength of the magnetic field along the line of sight.

To date, it has been extremely difficult to obtain accurate polarimetric information from the innermost (subparsec) regions of AGN; only emission at submillimeter wavelengths can escape from these regions, due to a large synchrotron self-absorption (SSA) that blocks the emission

at longer wavelengths. Unfortunately, the sensitivity of polarization observations at submillimeter wavelengths has so far been strongly limited by the instrumentation.

Previous attempts to detect Faraday rotation at submillimeter (submm) wavelengths from AGN have yielded only upper limits (2, 3) and marginal detections (4) that require strong assumptions about the absence of variability on time scales of weeks. There is a more robust detection for the Galactic center (5), although the activity in this source is much lower than in AGN. Recently, measurements of Faraday rotation in the nearby AGN 3C 84 (redshift $z = 0.018$) have been reported at mm wavelengths (6).

We have obtained measurements of Faraday rotation at frequencies up to 300 GHz (about 1 THz in the rest frame of the source) from PKS 1830–211, a powerful gravitationally lensed AGN located at a redshift of $z = 2.5$ (7). At these frequencies, SSA is negligible in the whole jet of PKS 1830–211 (8), and the maximum emission originates at the jet region closest to the black hole; the zone where the plasma is being injected and accelerated into the main jet stream. At lower frequencies, SSA hides this jet acceleration zone

Department of Earth and Space Sciences, Chalmers University of Technology, Onsala Space Observatory, SE-43992, Onsala, Sweden.

*Corresponding author. E-mail: mivan@chalmers.se

from view. These results are thus fundamental to better understand the role of magnetic fields in the AGN accretion and jet production, which are intimately related to the growth and evolution of supermassive black holes.

This detection has been possible thanks to the high resolution (sub-arcsec) of our observations with ALMA and to the use of a new differential polarimetry technique, which we briefly describe in the following lines (see supplementary text section 1).

The ALMA receivers detect the signal in two orthogonal linear polarizations, X and Y, where X is received from a horizontal dipole and Y from a vertical dipole in the frame of the antenna mount. The two lensed images of PKS 1830–211, which we call northeast (NE, upper-left in projection on sky) and southwest (SW, lower-

right), are separated by 1". In Fig. 1, we show an example of snapshot images in XX and YY of the two components of the gravitational lens, as well as their difference. The difference image contains information about the difference between NE and SW in Stokes parameters Q and U . Our analysis makes use of the polarization ratio, R_{pol} , which is defined as

$$R_{\text{pol}} = \frac{1}{2} \left(\frac{R_{\text{XX}}^{1.2}}{R_{\text{YY}}^{1.2}} - 1 \right)$$

where $R_{\text{XX}}^{1.2}$ and $R_{\text{YY}}^{1.2}$ are the flux-density ratios between the two lensed images of the AGN, obtained separately from the XX and YY polarization products. R_{pol} is a function of the parallactic angle of the antennas, ψ , and the observing wavelength, λ , and encodes information about the

difference of polarization between the two images, via the approximately constant parameters p_{dif} and α (supplementary text section 1), as well as their rotation measure RM ,

$$R_{\text{pol}} = p_{\text{dif}} \cos(2\phi_1^0 - \alpha + 2RM(\lambda^2 - \psi/RM)) \quad (1)$$

where ϕ_1^0 is the position angle of the polarization of image 1 at zero wavelength in the plane of the sky. The technique of differential polarimetry essentially enables estimation of RM via fitting the observed sinusoidal dependence of R_{pol} as a function of λ^2 and ψ , using Eq. 1.

Our results are based on ALMA observations at sky frequencies around 100, 250, and 300 GHz (8). Correcting for the cosmological redshift, these frequencies correspond to 350, 875, and 1050 GHz

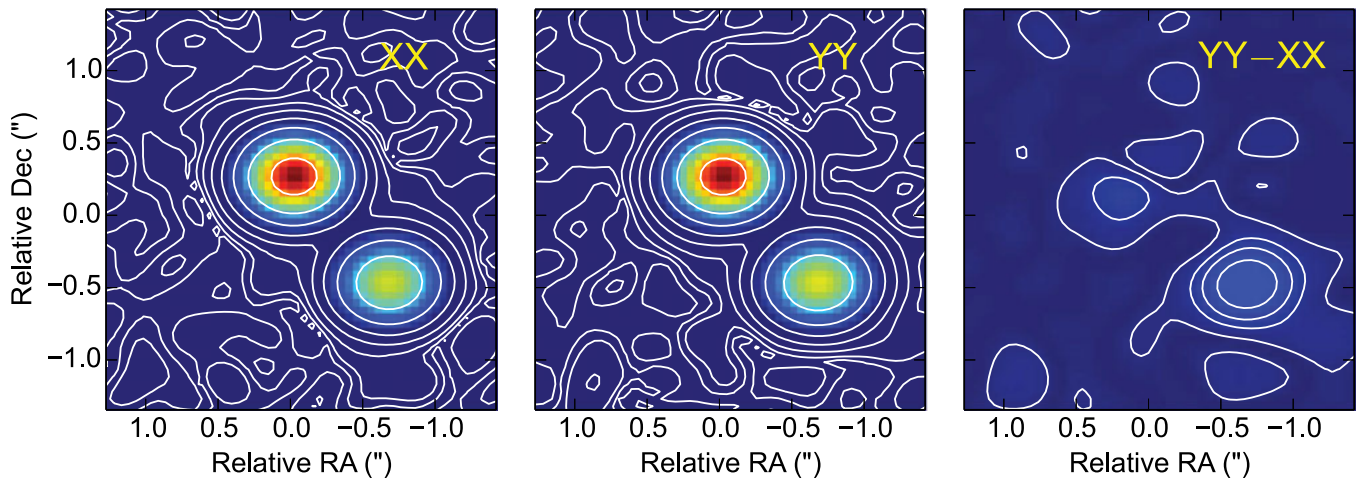


Fig. 1. ALMA image of the gravitationally lensed AGN PKS 1830–211 at 250 GHz, taken on 30 June 2014. Left, in XX polarization; center, in YY polarization (with the peak normalized to that of the XX image); right, the difference between polarizations. Notice the small residual in the southwest lensed image, which encodes differential polarization information among the northeast and southwest images. The contours are set at 0.625, 1.25, 2.5, 5, 10, 20, 50, and 99% of the peak intensity.

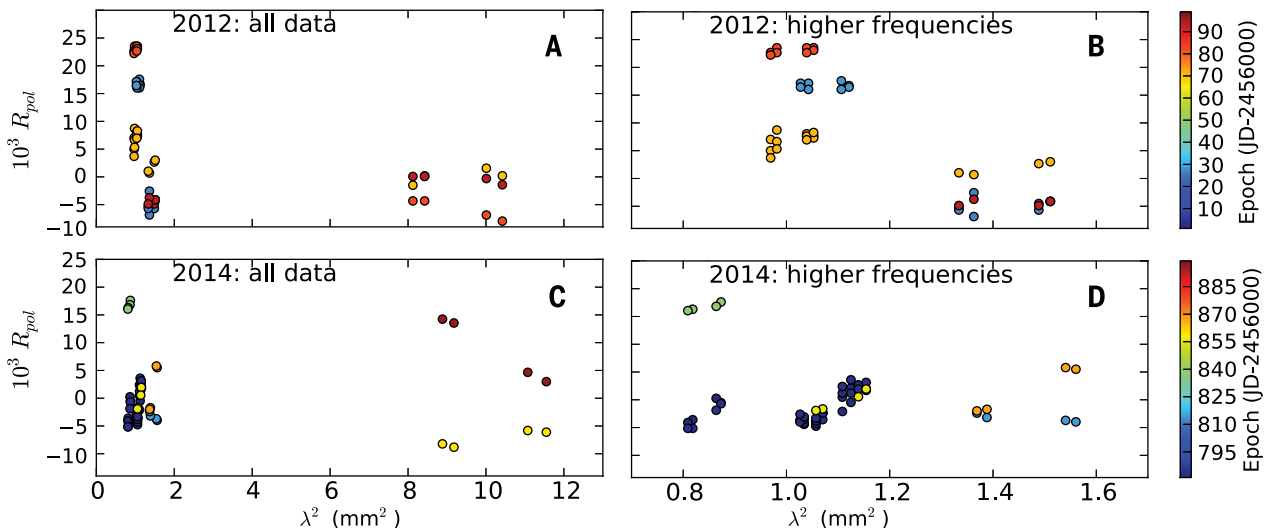


Fig. 2. Polarization ratio, R_{pol} , as a function of the wavelength squared for all our ALMA observations. Left panels (A and C) are all data; right panels (B and D) are enlargements of the region of shorter wavelengths. The uncertainties, estimated from the postfit covariance matrix as described in (10), are of the order of the symbol sizes.

in the frame of the source. More details on these observations, and a summary of the main goals of this ALMA project, can be found elsewhere (9). We also summarize all the observations in the supplementary text (section 2). Our observations can be divided in two data sets, one consisting of six epochs in 2012 (9 April to 16 June) and the other of nine epochs in 2014 (3 May to 27 August). In Fig. 2, we show the measured R_{pol} between the two lensed images of PKS 1830–211. These measurements have been obtained from the R_{XX} and R_{YY} values fitted with the visibility-modeling software presented in (10). The uncertainties have been obtained with the standard error propagation approach, using the uncertainties in R_{XX} and R_{YY} that were derived from the co-

variance matrix of the visibility fitting, as described in (10).

The derivatives of R_{pol} versus λ^2 , which are related to RM (supplementary text section 1.3), are clearly different for different wavelength ranges. Between $\lambda^2 = 8$ and 12 mm^2 , the maximum derivative is $4.4 \times 10^{-3} \text{ mm}^{-2}$, whereas between 0.8 and 1.6 mm^2 it is $70 \times 10^{-3} \text{ mm}^{-2}$. Because the maximum observed R_{pol} ratios are, in absolute value, similar at all wavelengths, the different derivatives of R_{pol} versus λ^2 must be due to larger RM at shorter wavelengths (see supplementary text section 1.3 for a more detailed discussion). Large variations of RM with wavelength have been reported in other AGN (11), although at much longer wavelengths (cm), related

to larger spatial scales in the jets. Our finding cannot be explained easily if the RM is only caused by an external (e.g., spherically symmetric) screen of material being accreted onto the black hole [as in the case of the RM detected in the Galactic center (5)] and/or by external clouds. The size of the submm emitting region (estimated as the distance to the black hole at which the submm intensity is maximum) is only of the order of 0.01 pc (8). Hence, if the Faraday screen were extended and located far from the jet base, the rotation measure at submm wavelengths should not depend on the observing frequency, because the extent of the Faraday screen would be similar for all the submm jet emission. The Faraday screen must thus be close to the jet base and change substantially on sub-parsec scales (Fig. 3). An increase of the RM at shorter wavelengths would then be explained naturally as an increase of the magnetic field strength and/or electron density as we approach the black hole. Indeed, observations of other AGN at long wavelengths (cm) show changes of RM across the jets, both longitudinal and transversal (12–14), that have been attributed to changes in particle density and magnetic fields in the jets, independent of a more distant external medium.

We have three sets of observing epochs at 250 and 300 GHz separated by a short time interval (1 to 2 days). In these three cases, we can directly estimate RM and p_{dif} by fitting R_{pol} to the model given by Eq. 1. The parameter estimates in these three data sets have been performed by least-squares minimization, comparing the measured R_{pol} to the model predictions. The data at our lowest-frequency band (i.e., 100 GHz) have been discarded from the fit, because they trace different rotation measures from different regions of the jet, as we have already discussed. We show the fitting results in Fig. 4 and the estimated parameters in Table 1. Our estimated source-rest-frame RM s are about two orders of magnitude higher than the highest values reported previously for other AGN, which are $\sim 10^6 \text{ rad/m}^2$ (4, 6).

Although the two RM measurements in 2012 are compatible, the estimate in 2014 is higher by more than a factor of 2. Regarding the amplitude of R_{pol} , which is related to the fractional polarization and to the relative polarization angles among the NE and SW images, we find different values for the two observations in 2012. These two observations were serendipitously taken before and after a strong γ -ray flare, which had a very weak radio counterpart (8). This leads us to speculate that the change in polarization may be correlated to the radio counterpart of that flare. Another γ -ray flare was detected in 2014 (15), also coincident with the time range of our 2014 observations. The new flare had a strong radio counterpart, which may also be related to the higher RM that we measure in 2014. The high variability in RM and p_{dif} in connection to the γ -ray flaring events, points toward a co-spatial origin of the γ -ray emission and the 250- to 300-GHz rotation measures, hence favoring our interpretation of the RM being caused at the region very close to the jet base.

Fig. 3. Sketch of the jet launch/acceleration region in PKS 1830–211 (not to scale). Emission at higher frequencies comes from material closer to the black hole, at subparsec scales. At these frequencies, the main contribution to RM must come from a zone close to the jet, in order to explain the different RM values between 350 GHz and 0.8 to 1 THz (source frame).

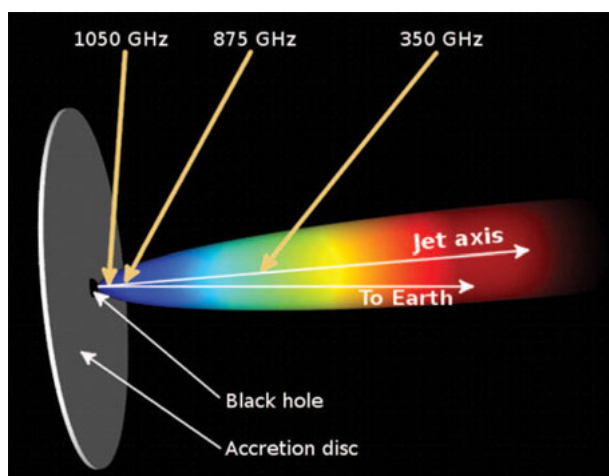


Fig. 4. Fits of our three epochs with quasi-simultaneous observations at 250 and 300 GHz to the model given in Eq. 1. We show R_{pol} versus λ^2 corrected by $-\psi/RM$, to obtain a sinusoidal behavior.

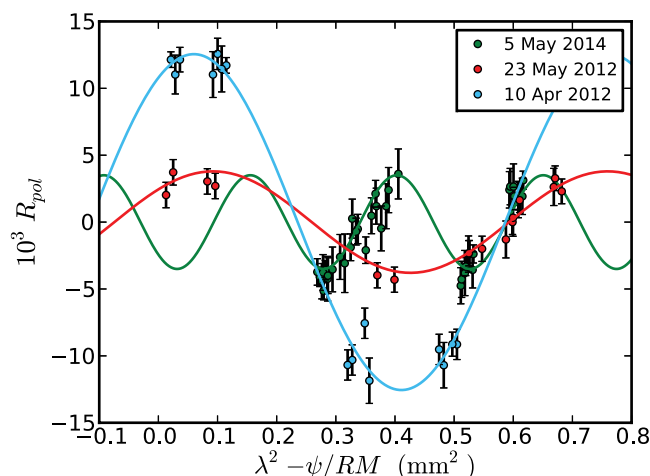


Table 1. Best-fit polarization values for the three epochs with quasi-simultaneous observations at 250 and 300 GHz. RM_{obs} are the rotation measures in the observer's frame and RM_{true} are the rotation measures in the rest frame of the source. RM_{true} is $(1+z)^2$ times larger than RM_{obs} .

	Epoch		
	10 April 2012	23 May 2012	5 May 2014
RM_{obs} (10^6 rad/m^2)	9.0 ± 0.3	9.4 ± 0.4	25.3 ± 0.8
RM_{true} (10^7 rad/m^2)	11 ± 0.4	11.5 ± 0.5	31.2 ± 1.0
p_{dif} (10^{-3})	12.6 ± 0.4	3.8 ± 0.3	3.5 ± 0.3
$2\phi_0 - \alpha$ (deg)	59 ± 27	40 ± 23	25 ± 20

The RM is related to the line-of-sight integral of the electron density times the magnetic field, corrected for the cosmological redshift (16). In units of rad/m^2 ,

$$RM = 8.1 \times 10^5 \frac{1}{(1+z)^2} \int n B_{\parallel} dl \quad (2)$$

where dl is the differential path along the line of sight (in pc), z is the redshift ($z = 2.5$), n is the particle density (in cm^{-3}), and B_{\parallel} is the magnetic field projected in the line of sight (in Gauss). Our RM will be an important test for detailed magnetohydrodynamical (MHD) models at the jet base, but such analysis is beyond the scope of this paper. At a more basic level, it is impossible to unambiguously disentangle the contributions of the magnetic field, electron density, and path length to the integral determining the rotation measure. This difficulty is exacerbated by the absence of direct information about the electron density or path length from observations, leading to the need to extrapolate from larger scales, which introduces additional uncertainty. The rotation measures derived here, $RM \sim 10^8 \text{ rad}/\text{m}^2$ in the rest frame of the source, are about a factor of 10^5 greater than the rest-frame RM values measured for parsec-scale AGN cores, where the derived magnetic fields have been independently measured to be ~ 0.05 to 0.10 G (11, 17); this suggests that the magnetic fields in the sub-parsec regions that we are probing are at least a few tens of Gauss, and possibly much higher. More exact estimates of these magnetic fields will require a separate dedicated study.

In any case, our results are a clear indication of very high magnetic fields at the jet base, which should be dynamically important near the black hole and should in turn affect the accretion process. A similar conclusion was drawn from a statistical analysis of jet core shifts from a complete sample of AGN, using high-resolution radio observations at centimeter wavelengths (18). In the near future, our differential polarimetry technique can be used to further measure and monitor RM s at very short wavelengths, from this and other AGN. The monitoring of magnetic fields and particle densities at the jet regions closest to the black holes, via submm polarimetry, will allow us to study the tight connection between black-hole accretion and relativistic jets, the two fundamental pieces of the fascinating cosmic puzzle of AGN.

REFERENCES AND NOTES

- A. P. Marscher, *Astrophys. J.* **235**, 386 (1980).
- I. Agudo, C. Thum, J. L. Gómez, H. Wiesenmeyer, *Astron. Astrophys.* **566**, A59 (2014).
- C. Y. Kuo, K. Asada, R. Rao, M. Nakamura, J. C. Algaba, H. B. Liu, M. Inoue, P. M. Koch, P. T. P. Ho, S. Matsushita, H.-Y. Pu, K. Akiyama, H. Nishioka, N. Pradel, *Astron. Astrophys.* **783**, 33 (2014).
- S. Trippe et al., *Astron. Astrophys.* **540**, A74 (2012).
- D. P. Marrone, J. M. Moran, J.-H. Zhao, R. Rao, *Astrophys. J.* **654**, L57–L60 (2007).
- R. L. Plambeck et al., *Astrophys. J.* **797**, 66 (2014).
- C. Lidman et al., *Astrophys. J.* **514**, L57–L60 (1999).
- I. Martí-Vidal et al., *Astron. Astrophys.* **558**, A123 (2013).
- S. Muller et al., *Astron. Astrophys.* **566**, A112 (2014).
- I. Martí-Vidal, W. Vlemmings, S. Muller, S. Casey, *Astron. Astrophys.* **563**, A136 (2014).
- S. P. O'Sullivan, D. C. Gabuzda, *Mon. Not. R. Astron. Soc.* **393**, 429–456 (2009).
- S. M. Croke, S. P. O'Sullivan, D. C. Gabuzda, *Mon. Not. R. Astron. Soc.* **402**, 259–270 (2010).
- M. Mahmud, D. Gabuzda, V. Bezrukovs, *Mon. Not. R. Astron. Soc.* **400**, 2–12 (2009).
- D. C. Gabuzda, V. A. Chernetskii, *Mon. Not. R. Astron. Soc.* **339**, 669–679 (2003).
- S. Ciprini, *The Astronomers Telegram* **4158** (2012).
- M. L. Bernet, F. Miniati, S. Lilly, *Astrophys. J.* **761**, 144 (2012).
- S. P. O'Sullivan, D. C. Gabuzda, *Mon. Not. R. Astron. Soc.* **400**, 26–42 (2009).
- M. Zamaninasab, E. Clausen-Brown, T. Savolainen, A. Tchekhovskoy, *Nature* **510**, 126–128 (2014).
- ADS/JAO.ALMA#2013.1.00020.S. ALMA is a partnership of the European Southern Observatory (ESO) (representing its member states), U.S. National Science Foundation (NSF), and National Institutes of Natural Sciences (NINS) of Japan, together with the National Research Council of Canada (NRC) and National Science Council of Taiwan (NSC) and Academia Sinica Institute of Astronomy and Astrophysics (ASIAA) (Taiwan), in cooperation with the Republic of Chile. The Joint ALMA Observatory is operated by ESO, Associated Universities, Inc.–National Radio Astronomy Observatory, and National Astronomical Observatory of Japan. W.V. acknowledges support from the European Research Council (ERC) under ERC grant 614264.

SUPPLEMENTARY MATERIALS

www.sciencemag.org/content/348/6232/311/suppl/DC1

Supplementary Text

Figs. S1 to S4

Tables S1 to S3

Reference (19)

28 October 2014; accepted 12 March 2015

10.1126/science.aal784

GALAXY EVOLUTION

Evidence for mature bulges and an inside-out quenching phase 3 billion years after the Big Bang

S. Tacchella,^{1*} C. M. Carollo,^{1*} A. Renzini,² N. M. Förster Schreiber,³ P. Lang,³ S. Wuyts,³ G. Cresci,⁴ A. Dekel,⁵ R. Genzel,^{3,6,7} S. J. Lilly,¹ C. Mancini,² S. Newman,⁶ M. Onodera,¹ A. Shapley,⁸ L. Tacconi,³ J. Woo,¹ G. Zamorani⁹

Most present-day galaxies with stellar masses $\geq 10^{11}$ solar masses show no ongoing star formation and are dense spheroids. Ten billion years ago, similarly massive galaxies were typically forming stars at rates of hundreds solar masses per year. It is debated how star formation ceased, on which time scales, and how this “quenching” relates to the emergence of dense spheroids. We measured stellar mass and star-formation rate surface density distributions in star-forming galaxies at redshift 2.2 with ~ 1 -kiloparsec resolution. We find that, in the most massive galaxies, star formation is quenched from the inside out, on time scales less than 1 billion years in the inner regions, up to a few billion years in the outer disks. These galaxies sustain high star-formation activity at large radii, while hosting fully grown and already quenched bulges in their cores.

At the epoch when star-formation activity peaks in the universe [redshift $z \sim 2$ (1, 2)], massive galaxies typically lie on the so-called “star-forming main sequence.” Their star-formation rates (SFRs) tightly correlate with the mass in stars (stellar mass M), reaching up to several hundred solar masses (M_{\odot}) per

year and producing a characteristic specific SFR (sSFR = SFR/ M) that declines only weakly with mass (3, 4). In contrast, at the present epoch, such massive galaxies are spheroids with old stellar populations, which reach central surface stellar densities well above $10^{10} M_{\odot} \text{ kpc}^{-2}$ and host virtually no ongoing star formation. Although the most massive ellipticals at $z = 0$ bear the clear signatures of a gas-poor formation process (5, 6), the more typical population, at a mass scale of $M \sim 10^{11} M_{\odot}$, consists of fast rotators (7) with disk-like isophotes (8), steep nuclear light profiles (9), and steep metallicity gradients (10): all features that indicate a gas-rich formation process.

The full cessation of star-formation activity in these typical massive galaxies (here referred to as the quenching process) is not well understood, nor is its relation with the emergence of their spheroidal morphologies. Several quenching mechanisms have been proposed. The so-called halo-quenching scenario predicts that circumgalactic gas is shock-heated to high temperatures and

¹Department of Physics, Institute for Astronomy, ETH Zurich, CH-8093 Zurich, Switzerland. ²Istituto Nazionale di Astrofisica (INAF) Osservatorio Astronomico di Padova, Vicolo dell'Osservatorio 5, I-35122 Padova, Italy. ³Max-Planck-Institut für Extraterrestrische Physik, Giessenbachstrasse 1, D-85748 Garching, Germany. ⁴INAF Osservatorio Astronomico di Arcetri, Largo Enrico Fermi 5, I-50125 Firenze, Italy. ⁵Racah Institute of Physics, The Hebrew University, Jerusalem 91904, Israel. ⁶Department of Astronomy, Campbell Hall, University of California, Berkeley, CA 94720, USA. ⁷Department of Physics, Le Conte Hall, University of California, Berkeley, CA 94720, USA. ⁸Department of Physics and Astronomy, University of California, Los Angeles, CA 90095-1547, USA. ⁹INAF Osservatorio Astronomico di Bologna, Via Ranzani 1, I-40127 Bologna, Italy.

*Corresponding author. E-mail: sandro.tacchella@phys.ethz.ch (S.T.); marcella.carollo@phys.ethz.ch (C.M.C.)

stops cooling in dark matter halos above a critical mass [$\sim 10^{12} M_{\odot}$ (17)]. Morphological/gravitational quenching proposes that the growth of a central mass concentration (i.e., a massive bulge) stabilizes a gas disk against fragmentation (12, 13). Feedback from an accreting supermassive black hole transfers either radiative (14) to the surrounding gas, thereby suppressing gas accretion onto the galaxy, or kinetic energy and momentum (15), which causes the expulsion of gas from the galaxy.

Quenching must soon occur in the most massive, and thus formidably star-forming, galaxies on the main sequence at $z \sim 2$, to avoid dramatically overshooting the highest observed masses of $z = 0$ galaxies (16). Yet no general consensus has emerged on which of the above-mentioned processes is primarily responsible for halting this star formation as early as a few billion years after the Big Bang. Determining the distributions of the stellar mass and SFR densities within individual $z \sim 2$ galaxies at high spatial resolution is central to resolving these issues. Together these distributions reveal how stellar mass builds up and SFR is progressively switched off inside these high- z galaxies, which, given their high masses, will have to evolve into “red and dead” systems by $z = 0$.

We measured such quantities for a sample of 22 star-forming galaxies at a median z of 2.2 [(17) and section S1]. The sample spans a wide range in stellar mass $M \sim 4 \times 10^9$ to $5 \times 10^{11} M_{\odot}$ and SFR ~ 20 to $300 M_{\odot} \text{ year}^{-1}$ and broadly traces the

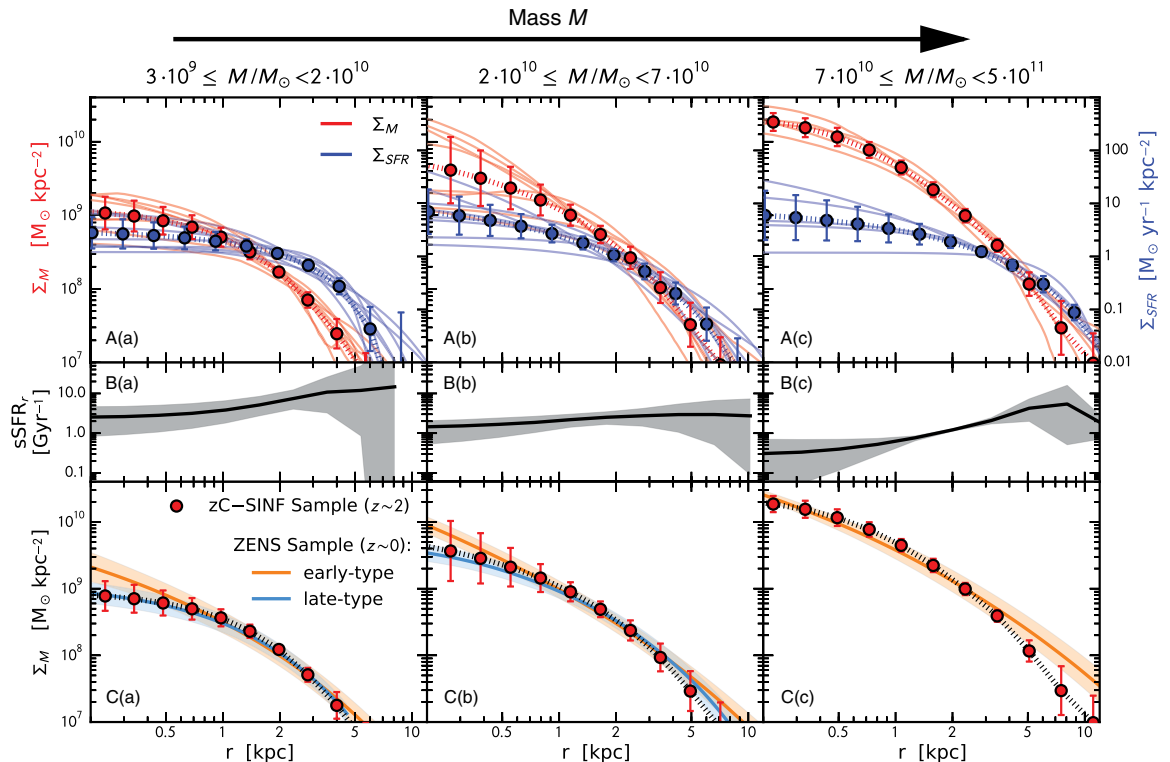
main sequence at these redshifts. The five most massive galaxies lie slightly below the average main sequence, a point we explore in more detail in section S1.

For all galaxies we obtained adaptive optics SINFONI (Spectrograph for INtegral Field Observations in the Near Infrared) spectroscopy on the European Southern Observatory’s Very Large Telescope, mapping the two-dimensional rest-frame H α emission at ~ 1 kpc spatial resolution. These data reflect the gas ionized by young stars within individual galaxies, which allows us to construct spatially resolved distributions of ionized gas kinematics and SFR surface densities internal to the galaxy. We also obtained Hubble Space Telescope (HST) imaging in the J and H passbands (17, 18). At the redshifts of the sample, the J and H filters straddle the rest-frame Balmer/4000 Å break. This spectral feature is strong in relatively old stars and therefore provides a robust estimate of the stellar mass already assembled in older stellar populations. Thus, at a similar kiloparsec resolution as the SINFONI SFR maps, the HST images provide maps of the stellar mass density that is stored in such older underlying populations. Visual inspection of the two-dimensional SFR distributions immediately reveals their notoriously irregular appearance, with bright clumps at large radii, in contrast with their centrally peaked and smooth stellar mass distributions (figs. S4 to S6).

The shapes of the average surface SFR density (Σ_{SFR}) profiles (Fig. 1, top panels) are very similar regardless of total mass and are well fitted by a Sérsic profile $\Sigma \propto \exp(-\beta \times r^{1/n})$, with the $n \sim 1$ value typical of disk-like systems. In contrast, the surface stellar mass density (Σ_M) profiles become progressively more centrally concentrated with increasing total stellar mass. The Sérsic index of the Σ_M profiles increases from $n = 1.0 \pm 0.2$ in the low-mass bin, to $n = 1.9 \pm 0.6$ in the intermediate-mass bin, up to $n = 2.8 \pm 0.3$ in the high-mass bin (uncertainties indicate the 1σ scatter). Within each mass bin, the mean Σ_M profiles are always more centrally concentrated than the SFR density profiles.

We then compared the Σ_M profiles of our sample of $z \sim 2.2$ galaxies with a mass-matched sample of local $z = 0$ galaxies (Fig. 1, bottom panels) (19). Consistent with the Sérsic fits, the low-mass $z \sim 2.2$ galaxies have the same radial stellar mass profiles of late-type disks in the local universe. The $z \sim 2.2$ galaxies in the most massive bin, however, have stellar mass profiles that overlap with those of $z = 0$ early-type galaxies out to galactocentric distances of a few kiloparsecs, corresponding to typically ~ 2 effective radii. At these high stellar masses ($\sim 10^{11} M_{\odot}$), our sample of galaxies on the $z \sim 2.2$ have therefore already saturated their central stellar mass densities to those of galaxies of similar mass at $z = 0$, which are quenched systems with a bulge-dominated morphology. Thus the

Fig. 1. Stellar mass and star-formation rate surface density distributions. The three panels of (a) to (c) show results for the three bins of stellar mass indicated at the top of each column, containing 9, 8, and 5 galaxies, respectively. (A) (upper row) The stellar surface mass density profiles (red, scale on the left vertical axis) and SFR surface density profiles (blue, scale on the right vertical axis) for our $z \sim 2.2$ sample. Thin lines represent individual galaxies; the mean values are given by the solid circles (with error bars indicating the 1σ scatter). The derivations of these profiles are described in detail in the supplementary materials (17). (B) (middle row) The mean sSFR as a function of radius r (sSFR $_r$; black line). In gray we show the 1σ scatter. (C) (bottom row) The average surface stellar mass density profiles of the star-forming $z \sim 2.2$ galaxies (red points with dashed line; error bars indicate the 1σ scatter) overplotted on the average profiles for the mass-matched samples of $z = 0$ galaxies (colors indicate morphological types: orange for early types, blue for late types).



bulge components of these massive galaxies are already fully in place while their hosts are still vigorously forming stars farther out in the surrounding (disk) regions [Figs. 1 and 2, center panels; see also (13)].

Specifically, the ratio between the star formation rate and stellar mass surface density profiles [i.e., $\text{sSFR}_r = \Sigma_{\text{SFR}}(r)/\Sigma_M(r)$] indicates suppression of the inner sSFR_r at the highest masses and generally outward-increasing radial profiles of sSFR_r (Fig. 1, center panels). By examining the surface stellar mass density within 1 kpc, $\Sigma_{M,1\text{kpc}}$, as a function of total stellar mass M , we see that the massive galaxies at $z \sim 2.2$ in our sample have substantially suppressed star-formation activity in their centers relative to lower-mass galaxies at the same epochs. We show in the supplementary materials (17) that this cannot be entirely due to dust effects. The $\text{sSFR}_{1\text{kpc}}$ values range from $\text{sSFR}_{1\text{kpc}} \sim 5$ per billion years (Gyr^{-1}) (corresponding to a mass-doubling time of ~ 200 My at a galaxy stellar mass of $10^{10} M_\odot$) down to negligible values of $\sim 0.1 \text{ Gyr}^{-1}$ at $10^{11} M_\odot$. The key conclusion is therefore that these galaxies sustain their high total SFRs at large radii, far from their central dense cores, whereas in such cores the sSFR_r is about two orders of magnitude lower.

A further important consideration that emerges from the analysis of Fig. 2 is that our galaxies lie around the identical tight $\Sigma_{M,1\text{kpc}}-M$ sequence that is traced by galaxies at $z \sim 0$ (20). This implies that the increase in total M of individual galaxies along the main sequence must be accompanied by a synchronized increase in central $\Sigma_{M,1\text{kpc}}$ until the maximal central stellar densities of today's massive spheroids are reached at a stellar mass scale on the order of $\sim 10^{11} M_\odot$. Below this galaxy mass scale, dense stellar bulges are therefore built concurrently with the outer galactic regions. At $z = 0$, the global relation curves, because the quenched galaxies have a shallower slope than the star-forming galaxies, and a clear “ridge” emerges (Fig. 2) (21). We have too few galaxies to track this curvature at earlier times, but this trend would be consistent with $z \sim 2.2$ galaxies slightly increasing their total M through declining star-formation at large radii while maintaining their already quenched inner $\Sigma_{M,1\text{kpc}}$ values.

These results provide insight into the bulge formation process. The high stellar densities that are already present in their cores indicate that at least some massive star-forming galaxies at $z \sim 2.2$ have today's massive spheroids as their descendants. We are seeing, however, neither classical bulges formed by dissipationless merging nor pseudo-bulges formed by the slow secular evolution of a stellar disk. Such a dichotomy is often invoked to explain the structural variety observed in nearby galactic bulges [(22); see, however, (23)]. The high central stellar densities of the massive galaxies in our sample argue for a gas-rich, dissipative bulge formation process at even earlier epochs. This is consistent with theoretical predictions (24) that either mergers or violent disk instabilities in gas-rich galactic structures at high redshifts lead to a compaction

phase of the gas component, which possibly even drags any preexisting stellar component within the inner few kiloparsecs.

Furthermore, the suppressed central sSFRs in such massive systems argue for a quenching engine also at work. As this apparently acts from the inner galactic regions outward, it echoes findings recently reported for massive galaxy pop-

ulations in a more recent era, at $z \sim 0.5$ to 1.5 , or ~ 1.5 to 5.5 Gy later (25, 26). Our results reveal that similar signatures are seen as early as $z \sim 2.2$, implying that the same physical processes that lead to a phase of suppressed star formation from the inside out started acting on massive star-forming galaxies as early as ~ 3 Gy after the Big Bang. We also estimate the time scale for an

Fig. 2. Central stellar mass density sequence.

We plot the stellar mass surface density within 1 kpc, $\Sigma_{M,1\text{kpc}}$, as a function of the total stellar mass M . The black points show the $z \sim 0$ ZENS sample, and the blue and red contours their density on the $\Sigma_{M,1\text{kpc}}-M$ plane split for star-forming (blue) and quiescent (red) galaxies. The correspondingly colored solid lines indicate the best fits to these $z = 0$ star-forming ($\Sigma_{M,1\text{kpc}} \propto M^{-1.0}$) and quiescent ($\Sigma_{M,1\text{kpc}} \propto M^{-0.7}$) galaxies. The dashed black line

shows the fit to the ridge of passive galaxies in the Sloan Digital Sky Survey $z = 0$ sample of Fang *et al.* (20). The error bars at the bottom right indicate the systematic uncertainty in the derivation of $\Sigma_{M,1\text{kpc}}$ and M . The large points are the $z \sim 2.2$ galaxies, color coded according to specific star-formation rate within 1 kpc, $\text{sSFR}_{1\text{kpc}}$. The $z \sim 2.2$ galaxies lie on the tight $\Sigma_{M,1\text{kpc}}-M$ locus traced by the $z = 0$ population. In contrast with total SFRs increasing with stellar mass along the main sequence, the $z \sim 2.2$ galaxies have central sSFRs that strongly decrease with stellar mass.

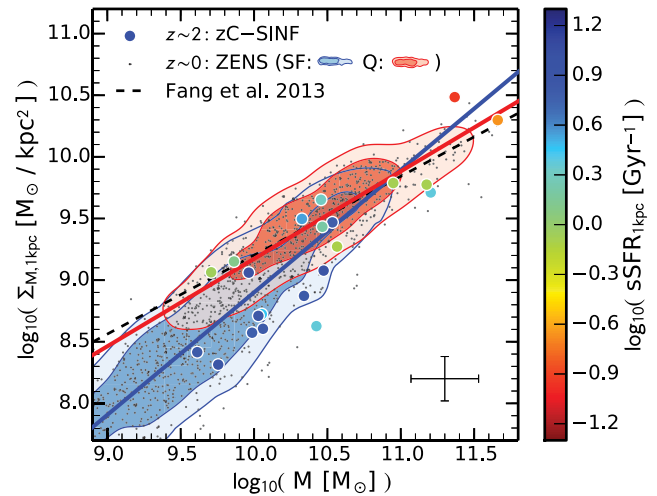


Fig. 3. Outward progression of the quenching wave.

The quenching time τ_{quench} in star-forming $\sim 10^{11} M_\odot$ galaxies at $z \sim 2.2$ as a function of galactocentric distance. Such galaxies quench from inside out on time scales in the inner cores much shorter than 1 Gy after observation, up to a few billion years in the galactic peripheries. The galaxies will be fully quenched by $z \sim 1$. The solid orange line indicates the mean quenching time for all galaxies in the highest-mass bin, whereas the orange-shaded region marks the 1σ scatter.

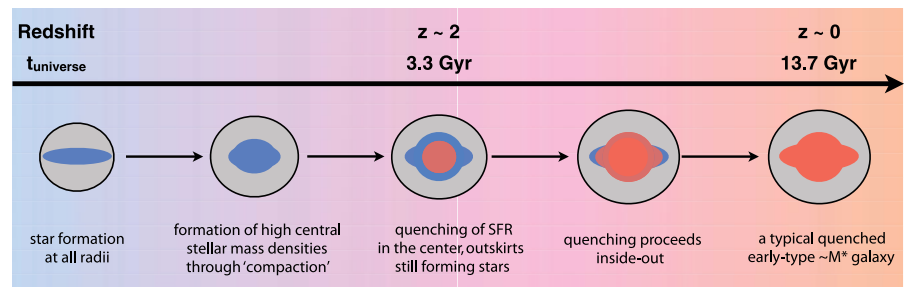
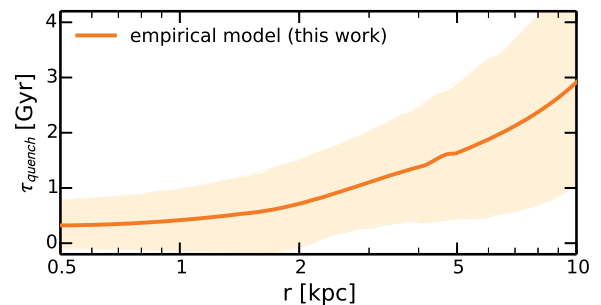


Fig. 4. Proposed sketch of the evolution of massive galaxies. Our results suggest a picture in which the total stellar mass and bulge mass grow synchronously in $z \sim 2$ main sequence galaxies, and quenching is concurrent with their total masses and central densities approaching the highest values observed in massive spheroids in today's universe.

inside-out quenching wave to propagate across $\sim 10^{11} M_{\odot}$ galactic bodies (Fig. 3). The estimate assumes that our galaxies keep forming stars with their observed radial profiles of surface SFR density until their $\Sigma_M(r)$ reaches the value observed in $z = 0$ passive galaxies of similar stellar mass. This allows quenching time scales substantially less than 1 Gy in the galaxy centers and roughly 3 Gy in the outer disk/ring regions. These give rise to a stellar age gradient of $d\log(\text{age})/d\log(r) \sim -0.5$ dex per radial decade (17). This predicted age gradient in the stellar population implies a negative color gradient in passive $z \sim 1$ to 2 spheroids, which is found in several studies (27, 28); with flat metallicity gradients, the inferred average age gradients range between about -0.1 and -0.4 dex per radial decade. A contribution to the color gradient from either dust or metallicity effects would imply that such estimates are lower limits to such photometrically estimated stellar age. The galaxies will be fully quenched by $z \sim 1$; subsequent passive evolution down to $z = 0$ will produce quenched $z = 0$ remnants with the dissipative properties of typical $\sim M^*$ spheroids, such as disk-like isophotes and fast-rotating kinematics (Fig. 4).

Our results also provide insight into quenching mechanisms. Clearly, an external process such as a large-scale shutdown of gas supply caused by a hot halo or a low cosmological accretion rate may still contribute to inside-out quenching. The fact that we observe a phase of inside-out quenching in very massive galaxies at early epochs suggests, however, also a prominent role of an internal process operating from the inner galaxy regions. The most massive galaxies in our sample exhibit fast nuclear outflows, which may indeed signify that active galactic nuclei feedback is also a factor (29). By setting the condition for sustenance of star formation, the local stellar density within galaxies may also be acting as the internal process that regulates the rate at which SFR is locally suppressed (30). The current analysis cannot identify the direction of the causality between the presence of a high stellar mass density and the cessation of star formation, but it is clear from our data that such high stellar density is present when quenching starts. Our study therefore highlights either, or possibly both, of these two internal processes as key contributors to the downfall of the most massive and most star-forming galaxies at the peak of galaxy formation.

REFERENCES AND NOTES

- S. J. Lilly, L. Tresse, F. Hammer, D. Crampton, O. Le Fevre, *Astrophys. J.* **455**, 108 (1995).
- P. Madau et al., *Mon. Not. R. Astron. Soc.* **283**, 1388–1404 (1996).
- K. J. Noeske et al., *Astrophys. J.* **660**, L43 (2007).
- E. Daddi et al., *Astrophys. J.* **670**, 156–172 (2007).
- T. Naab, A. Burkert, *Astrophys. J.* **597**, 893–906 (2003).
- T. J. Cox et al., *Astrophys. J.* **650**, 791–811 (2006).
- M. Cappellari et al., *Mon. Not. R. Astron. Soc.* **379**, 418–444 (2007).
- R. Bender, S. Doebereiner, C. Moellenhoff, *Astron. Astrophys.* **74**, 385 (1988).
- S. M. Faber et al., *Astron. J.* **114**, 1771 (1997).
- C. M. Carollo, I. J. Danziger, L. Buson, *Mon. Not. R. Astron. Soc.* **265**, 553–580 (1993).
- A. Dekel, Y. Birnboim, *Mon. Not. R. Astron. Soc.* **368**, 2–20 (2006).
- M. Martig, F. Bournaud, R. Teyssier, A. Dekel, *Astrophys. J.* **707**, 250–267 (2009).
- R. Genzel et al., *Astrophys. J.* **785**, 75 (2014).
- T. Di Matteo, V. Springel, L. Hernquist, *Nature* **433**, 604–607 (2005).
- D. J. Croton et al., *Mon. Not. R. Astron. Soc.* **365**, 11–28 (2006).
- A. Renzini, *Mon. Not. R. Astron. Soc.* **398**, L58 (2009).
- Materials and methods are available as supplementary materials on Science Online.
- S. Tacchella et al., *Astrophys. J.* **802**, 101 (2015).
- C. M. Carollo et al., *Astrophys. J.* **776**, 71 (2013).
- P. Saracco, A. Gargiulo, M. Longhetti, *Mon. Not. R. Astron. Soc.* **422**, 3107–3117 (2012).
- J. J. Fang, S. M. Faber, D. C. Koo, A. Dekel, *Astrophys. J.* **776**, 63 (2013).
- J. Kormendy, R. C. Kennicutt Jr., *Annu. Rev. Astron. Astrophys.* **42**, 603–683 (2004).
- C. M. Carollo, C. Scarlata, M. Stiavelli, R. F. G. Wyse, L. Mayer, *Astrophys. J.* **658**, 960–979 (2007).
- A. Dekel, A. Burkert, *Mon. Not. R. Astron. Soc.* **438**, 1870–1879 (2014).
- E. J. Nelson et al., *Astrophys. J.* **763**, L16 (2013).
- S. Wuyts et al., *Astrophys. J.* **779**, 135 (2013).
- Y. Guo et al., *Astrophys. J.* **735**, 18 (2011).
- A. Gargiulo, P. Saracco, M. Longhetti, F. La Barbera, S. Tamburri, *Mon. Not. R. Astron. Soc.* **425**, 2698–2714 (2012).
- N. M. Förster Schreiber et al., *Astrophys. J.* **787**, 38 (2014).
- J. Woo, A. Dekel, S. M. Faber, D. C. Koo, *Mon. Not. R. Astron. Soc.* **448**, 237–251 (2015).

ACKNOWLEDGMENTS

S.T. thanks B. Trakhtenbrot for stimulating discussions. We thank the reviewers for their thorough review, comments, and suggestions. We acknowledge support by the Swiss National Science Foundation, grant 200020_140952. This research made use of NASA's Astrophysics Data System; the arXiv.org preprint server; the Python plotting library matplotlib; and astropy, a community-developed core Python package for Astronomy. A.R., G.C., and G.Z. acknowledge support from an INAF PRIN-2012. Based on observations made with the NASA/European Space Agency Hubble Space Telescope, obtained at the Space Telescope Science Institute, which is operated by the Association of Universities for Research in Astronomy, Inc., under NASA contract NAS 5-26555, and on observations obtained at the Very Large Telescope of the European Southern Observatory, Paranal, Chile. The data used in this paper are archived at <https://archive.stsci.edu/hst/> under program ID G09822, G010092, G010924, G011694, G012578, G012060, G012061, G012062, G012063, G012064, G012440, G012442, G012443, G012444, and G012445; and <http://archive.eso.org/cms.html> under program ID 075.A-0466, 076.A-0527, 079.A-0341, 080.A-0330, 080.A-0339, 080.A-0635, 081.A-0672, 183.A-0781, 087.A-0081, 088.A-0202, 088.A-0209, and 091.A-0126.

SUPPLEMENTARY MATERIALS

www.sciencemag.org/content/348/6232/314/suppl/DC1
Materials and Methods S1 to S3
Supplementary Text S4 and S5
Figs. S1 to S10
Table S1
References (31–58)

10 September 2014; accepted 10 March 2015
10.1126/science.1261094

SUPERCONDUCTIVITY

Quasiparticle mass enhancement approaching optimal doping in a high- T_c superconductor

B. J. Ramshaw,^{1*} S. E. Sebastian,² R. D. McDonald,¹ James Day,³ B. S. Tan,² Z. Zhu,¹ J. B. Betts,¹ Ruixing Liang,^{3,4} D. A. Bonn,^{3,4} W. N. Hardy,^{3,4} N. Harrison¹

In the quest for superconductors with higher transition temperatures (T_c), one emerging motif is that electronic interactions favorable for superconductivity can be enhanced by fluctuations of a broken-symmetry phase. Recent experiments have suggested the existence of the requisite broken-symmetry phase in the high- T_c cuprates, but the impact of such a phase on the ground-state electronic interactions has remained unclear. We used magnetic fields exceeding 90 tesla to access the underlying metallic state of the cuprate $\text{YBa}_2\text{Cu}_3\text{O}_{6+\delta}$ over a wide range of doping, and observed magnetic quantum oscillations that reveal a strong enhancement of the quasiparticle effective mass toward optimal doping. This mass enhancement results from increasing electronic interactions approaching optimal doping, and suggests a quantum critical point at a hole doping of $p_{\text{crit}} \approx 0.18$.

In several classes of unconventional superconductors, superconductivity has been linked to a quantum critical point (QCP). At a QCP, the system undergoes a phase transition and a change in symmetry at zero temperature; the associated quantum fluctuations enhance interactions, which can give rise to (or enhance) superconductivity (1, 2). As the QCP is approached, these fluctuations produce increasingly stronger electronic correlations, resulting

in an experimentally observable enhancement of the electron effective mass (3–5). It is widely believed that spin fluctuations in the vicinity of an antiferromagnetic QCP are important for superconductivity in many heavy-fermion, organic, and pnictide superconductors (2, 6), leading to the ubiquitous phenomenon of a superconducting dome surrounding a QCP. The role of quantum criticality in cuprate high-temperature superconductors is more controversial (7): Do

the collapsing experimental energy scales (8), enhanced superconducting properties (see Fig. 1), and evidence for a change in ground-state symmetry near optimal doping (9–16) support the existence of strong fluctuations that are relevant to superconductivity (2, 17–19)? Alternative explanations for the phenomenology of the cuprate phase diagram focus on the physics of a lightly doped Mott insulator (7, 20) rather than that of a metal with competing broken-symmetry phases. Several investigations, both theoretical and experimental, suggest that competing order is present in the cuprates and is associated with the charge (rather than spin) degree of freedom [such as charge density wave (CDW) order, orbital current order, or nematicity; see Fig. 1] (12, 15–18, 21–28). What has been missing is direct, low-temperature evidence that the disappearance of competing order near optimal doping, and the associated change in ground-state symmetry, are accompanied by enhanced electronic interactions in the ground state.

A powerful technique for measuring low-temperature Fermi surface properties is the magnetic quantum oscillation phenomenon, which directly accesses quasiparticle interactions through the effective mass (29). Such measurements have been successful in identifying mass enhancements near QCPs in lower- T_c materials [e.g., CeRhIn_5 and $\text{Ba}(\text{FeAs}_x\text{P}_{1-x})_2$ (3, 5)], but the robustness of superconductivity near optimal doping in the cuprates has impeded access to the metallic ground state. The Fermi surface in underdoped cuprates is known to be relatively small and electron-like (30–34), in contrast to overdoped cuprates, in which a much larger hole-like surface is observed (35). This suggests the existence of broken translational symmetry in the underdoped cuprates that “reconstructs” the large hole-like surface into the smaller electron-like surface, and this translational symmetry breaking is likely related to the charge order observed in the same doping range as the small Fermi pockets (15, 27). Thus, it is desirable to perform a systematic study of the doping dependence of these small pockets as optimal doping is approached within a single cuprate family. We used high magnetic fields, extending to >90 T, to suppress superconductivity and access quantum oscillations of the underlying Fermi surface for a range of underdoped $\text{YBa}_2\text{Cu}_3\text{O}_{6+\delta}$ compositions with T_c s of up to 91 K (Fig. 1).

We observed quantum oscillations in $\text{YBa}_2\text{Cu}_3\text{O}_{6+\delta}$ at $\delta = 0.75, 0.80$, and 0.86 (corresponding to hole doping $p = 0.135, 0.140$, and 0.152) (Fig. 2A). Three regimes are clearly seen in the data: zero resistance in the vortex solid state; finite resistance that increases strongly with field in the crossover to the normal state; and magneto-

resistance accompanied by quantum oscillations in the normal state. Subtracting a smooth and monotonic background from the magnetoresistance yields the oscillatory component (36). One can make two immediate observations: (i) At higher doping, the oscillation amplitude grows faster with decreasing temperature; and (ii) the oscillation frequency changes very little between $p = 0.135$ and $p = 0.152$. The first observation directly indicates an increasing effective mass; the second observation constrains the doping where the reconstruction from a large to a small Fermi surface takes place. We quantify these observations below.

The evolution of the cyclotron effective mass with doping, and how it relates to the temperature dependence of the quantum oscillations, can be understood quantitatively within the Lifshitz-Kosevich formalism, which has been used successfully to analyze oscillations in cuprates at lower hole doping (23, 32–34, 37). The effective mass extracted from the quantum oscillation amplitude (36) is plotted as a function of doping in Fig. 3C, which reveals an increase in the mass by almost a factor of 3 from $p = 0.116$ to $p = 0.152$. Note that electron-phonon coupling is generally observed to decrease with increasing hole doping in the cuprates, ruling it out as the mechanism of mass enhancement (38) and suggesting instead that the mass enhancement comes from increased electron-electron interactions. The enhancement of the effective mass toward $p \approx 0.18$ is consistent with the doping-dependent maxima observed in the upper critical field H_{c2} (39) and in the jump in specific heat ($\Delta\gamma$) at T_c (40, 41), both of which are

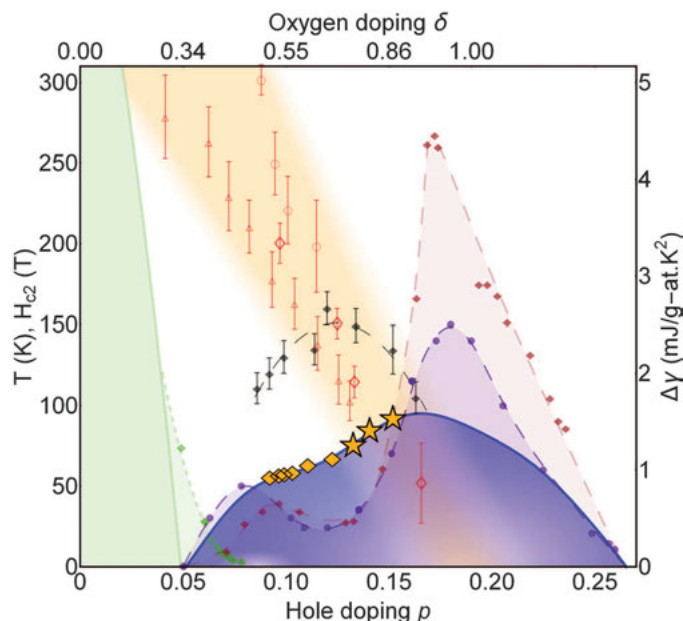
expected to be enhanced by the effective mass through the density of states (see Fig. 1). Maxima in thermodynamic quantities are typical of quantum critical systems at their QCPs, having been observed in many heavy-fermion systems (42) and in an iron pnictide superconductor (5). Some physical quantities, such as superfluid density, do not show an enhancement toward optimal doping in $\text{YBa}_2\text{Cu}_3\text{O}_{6+\delta}$ (43); this is possibly because different physical properties experience different renormalizations from interactions (44) or because they are measured in the superconducting state, where the gap may serve as a cutoff.

The quantum oscillation frequency F gives the Fermi surface area through the Onsager relation (29), $A_k = (2\pi e/h)F$, where A_k is the Fermi surface area in momentum space perpendicular to the magnetic field and h is Planck's constant divided by 2π . In contrast to the effective mass, which is enhanced by almost a factor of 3, the Fermi surface area only evolves weakly toward optimal doping: Fig. 2B shows F increasing by roughly 20% from $p \approx 0.09$ to $p \approx 0.152$. The observation of the small Fermi surface pocket up to $p \approx 0.152$ requires that the reconstruction of the Fermi surface also persists up to this doping, which strongly suggests that the reconstruction is related to the incommensurate charge order also observed in this doping range (15, 25–27). The large increase in effective mass with no accompanying large change in Fermi surface area is reminiscent of what is seen on approach to QCPs in CeRh_2Si_2 , CeRhIn_5 , and $\text{BaFe}_2(\text{As}_{1-x}\text{P}_x)_2$ (5, 42).

The connection between the mass enhancement we observe in quantum oscillations and

Fig. 1. Cuprate temperature-doping phase diagram.

Long-range antiferromagnetic order (solid green line) gives way to superconductivity (solid blue line) near $p = 0.05$. Orange diamonds designate dopings where quantum oscillations have been observed previously (52, 53); stars denote the dopings presented in this report. Short-range antiferromagnetic order (green diamonds) terminates at a QCP at $p = 0.08$ (46, 54); beyond $p = 0.08$, short-range charge order is observed above T_c



[solid black diamonds (15, 27)]. The charge order, the onset of the pseudogap as defined by neutron spin-flip scattering (open red circles) (12), the polar Kerr effect (open red diamonds) (13), and the change in the slope of resistivity with temperature (open red triangles) (55) terminate near $p = 0.18$, suggesting the possibility of a QCP at this doping. Two thermodynamic quantities show enhancement near the critical dopings: the jump in the specific heat at T_c ($\Delta\gamma$, maroon diamonds) (40, 41) and the upper critical field (H_{c2} , solid purple circles) (39).

¹Mail Stop E536, Los Alamos National Laboratory, Los Alamos, NM 87545, USA. ²Cavendish Laboratory, Cambridge University, Cambridge CB3 0HE, UK. ³Department of Physics and Astronomy, University of British Columbia, Vancouver V6T 1Z4, Canada. ⁴Canadian Institute for Advanced Research, Toronto M5G 1Z8, Canada.

*Corresponding author. E-mail: bradramshaw@gmail.com

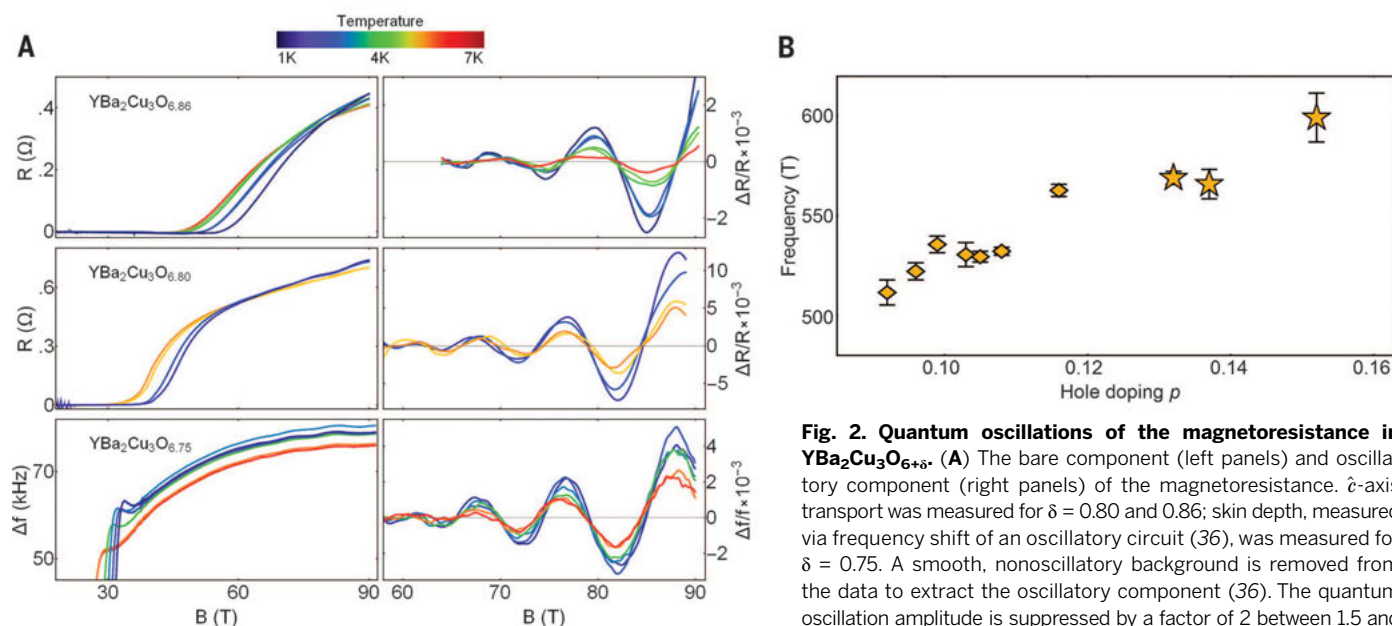


Fig. 2. Quantum oscillations of the magnetoresistance in YBa₂Cu₃O_{6+δ}. (A) The bare component (left panels) and oscillatory component (right panels) of the magnetoresistance. \hat{z} -axis transport was measured for $\delta = 0.80$ and 0.86 ; skin depth, measured via frequency shift of an oscillatory circuit (36), was measured for $\delta = 0.75$. A smooth, nonoscillatory background is removed from the data to extract the oscillatory component (36). The quantum oscillation amplitude is suppressed by a factor of 2 between 1.5 and 6 K in YBa₂Cu₃O_{6.75}, versus a factor of 5 over the same temperature range in YBa₂Cu₃O_{6.86}, indicating an increased effective mass for the higher-doped sample. (B) Quantum oscillation frequency, proportional to Fermi surface area, as a function of hole doping, with dopings below $p = 0.12$ taken from (56). The frequencies and their uncertainties were obtained as described in (36) and the symbols parallel those in Fig. 1.

high- T_c superconductivity is evident in Fig. 4, which shows successive T_c curves in increasing magnetic field. By 30 T—the third-highest curve in Fig. 4—superconductivity persists only in two small domes centered around $p \approx 0.08$ and $p \approx 0.18$; by 50 T, only the region around $p = 0.18$ remains. This phase diagram of YBa₂Cu₃O_{6+δ} in high field, with T_c first suppressed to zero around $p \approx 0.125$, closely resembles that of La_{2-x}Ba_xCuO₄ in zero field, where static charge and stripe order are observed (45). To emphasize the enhancement of the effective mass, we plot $1/m^*$ on this phase diagram [including previous m^* measurements at lower doping (46)]. This shows a trend toward maximum mass enhancement at $p \approx 0.08$ and $p \approx 0.18$ —the same dopings at which superconductivity is the most robust to applied magnetic fields. One possible scenario for YBa₂Cu₃O_{6+δ} is that critical fluctuations surrounding $p_{\text{crit}} \approx 0.08$ and $p_{\text{crit}} \approx 0.18$ provide two independent pairing mechanisms, analogous to the two superconducting domes in CeCu₂Si₂ that originate at antiferromagnetic and valence-transition QCP (47). A second scenario is a single underlying pairing mechanism whose strength varies smoothly with doping (7, 48), but where T_c is enhanced at $p_{\text{crit}} \approx 0.08$ and $p_{\text{crit}} \approx 0.18$ by an increased density of states and/or by quantum critical dynamics.

Our observed mass increase establishes the enhancement of electronic interactions approaching $p_{\text{crit}} \approx 0.18$. It is natural to ask whether this enhancement is caused by a QCP at $p_{\text{crit}} \approx 0.18$ and, subsequently, what is the associated broken-symmetry phase. The hole doping $p_{\text{crit}} \approx 0.18$ represents the juncture of several doping-dependent phenomena associated with underdoped cuprates. First, $p \approx 0.19$ represents the collapse to zero of energy scales associated with the formation of the pseudogap and its onset temper-

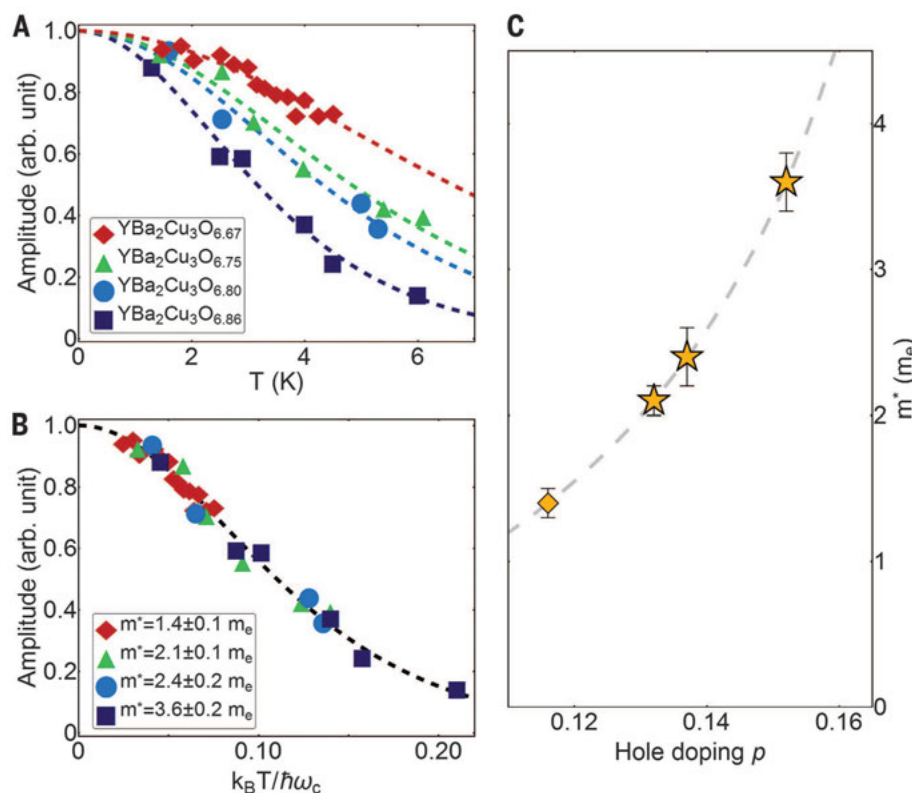


Fig. 3. The quasiparticle effective mass in YBa₂Cu₃O_{6+δ}. (A and B) Quantum oscillation amplitude as a function of temperature (A) and as a function of the ratio of thermal to cyclotron energy $k_B T / \hbar \omega_c$ (B). Also included is detailed temperature dependence of YBa₂Cu₃O_{6.67}, a composition at which oscillations have previously been reported (53). (A) illustrates the increase in m^* with increased hole doping, with fits to Eq. 1; (B) shows the same data versus $k_B T / \hbar \omega_c$, where $\omega_c = eB / m^*$. This scaling with m^* shows the robustness of the fit across the entire doping and temperature range. (C) Effective mass as a function of hole doping; error bars are SE from regression of Eq. 1 to the data, and the symbols parallel those in Figs. 1 and 2. The dashed line is a guide to the eye.

Fig. 4. A quantum critical point near optimal doping. The solid blue circles correspond to T_c as defined by the resistive transition (right axis), at magnetic fields of 0, 15, 30, 50, 70, and 82 T [some data points taken from (39, 57); solid blue curves are a guide to the eye]. As the magnetic field is increased, the superconducting T_c is suppressed. By 30 T, two separate domes remain, centered around $p \approx 0.08$ and $p \approx 0.18$; by 82 T, only the dome at $p \approx 0.18$ remains. The inverse of

the effective mass has been overlaid on this phase diagram (left axis), extrapolating to maximum mass enhancement at $p \approx 0.08$ and $p \approx 0.18$ [white diamonds taken from (56)]. This makes explicit the connection between effective mass enhancement and the robustness of superconductivity. Yellow symbols parallel those in Figs. 1 to 3. Error bars are SE from regression of Eq. 1 to the data.

ature T^* . Second, the onset of an anomalous polar Kerr rotation and neutron spin flip scattering both terminate at $p \approx 0.18$ (12, 13), representing an unidentified form of broken symmetry (which persists inside the superconducting phase for the Kerr experiment). Third, in high magnetic fields, the sign change of the Hall coefficient in $\text{YBa}_2\text{Cu}_3\text{O}_{6+\delta}$ from positive to negative, and the anomaly in the Hall coefficient in $\text{Bi}_2\text{Sr}_{0.51}\text{La}_{0.49}\text{CuO}_{6+\delta}$, occur near $p \approx 0.18$ (11, 49), which suggests that Fermi surface reconstruction from electron-like to hole-like occurs at this doping. Finally, $p \approx 0.18$ represents the maximum extent of incommensurate CDW order reported in several different experiments (15, 26, 27). Although the Fermi surface reconstruction is likely related to this CDW order, its short correlation length and the weak doping dependence of its onset temperature appear to be at odds with the standard picture of long-range order collapsing to $T = 0$ at a QCP (50). Two scenarios immediately present themselves. In the first scenario, the suppression of superconductivity by an applied magnetic field allows the CDW to transition to long-range order, as suggested by x-ray, nuclear magnetic resonance, and pulsed-echo ultrasound experiments (25, 26, 51). In this first scenario, we would be observing a field-revealed QCP. In the second scenario, CDW order is coexistent with another form of order that also terminates near $p_{\text{crit}} \approx 0.18$. Such a coexistence is suggested by multiple experimental results, including but not limited to Nernst anisotropy (22), polarized neutron scattering (12), and the anomalous polar Kerr effect (13). In this second scenario, the CDW reconstructs the Fermi surface and the other hidden form of order drives quantum criticality. Regardless of the specific mechanism, and regardless of whether $p_{\text{crit}} = 0.18$ is a QCP in the traditional sense, the observation of an enhanced

effective mass coincident with the region of most robust superconductivity establishes the importance of competing broken symmetry for high- T_c superconductivity.

REFERENCES AND NOTES

- P. Coleman, C. Pepin, Q. M. Si, R. Ramazashvili, *J. Phys. Condens. Matter* **13**, R723–R738 (2001).
- L. Taillefer, *Annu. Rev. Condens. Matter Phys.* **1**, 51–70 (2010).
- H. Shishido, R. Settai, H. Harima, Y. Onuki, *J. Phys. Soc. Jpn.* **74**, 1103–1106 (2005).
- P. Gegenwart, Q. Si, F. Steglich, *Nat. Phys.* **4**, 186–197 (2008).
- P. Walmsley *et al.*, *Phys. Rev. Lett.* **110**, 257002 (2013).
- P. Monthoux, D. Pines, G. G. Lonzarich, *Nature* **450**, 1177–1183 (2007).
- P. W. Anderson *et al.*, *J. Phys. Condens. Matter* **16**, R755–R769 (2004).
- J. L. Tallon, J. W. Loram, *Physica C* **349**, 53–68 (2001).
- G. S. Boebinger *et al.*, *Phys. Rev. Lett.* **77**, 5417–5420 (1996).
- Y. Ando, K. Segawa, S. Komiya, A. N. Lavrov, *Phys. Rev. Lett.* **88**, 137005 (2002).
- F. F. Balakirev *et al.*, *Nature* **424**, 912–915 (2003).
- B. Fauqué *et al.*, *Phys. Rev. Lett.* **96**, 197001 (2006).
- J. Xia *et al.*, *Phys. Rev. Lett.* **100**, 127002 (2008).
- A. Shekhter *et al.*, *Nature* **498**, 75–77 (2013).
- S. Blanco-Canosa *et al.*, *Phys. Rev. B* **90**, 054513 (2014).
- K. Fujita *et al.*, *Science* **344**, 612–616 (2014).
- C. M. Varma, *Phys. Rev. Lett.* **83**, 3538–3541 (1999).
- S. Chakravarty, R. B. Laughlin, D. K. Morr, C. Nayak, *Phys. Rev. B* **63**, 094503 (2001).
- S. Sachdev, *Quantum Phase Transitions* (Wiley Online Library, 2007).
- P. A. Lee, *Rep. Prog. Phys.* **71**, 012501 (2008).
- S. A. Kivelson, E. Fradkin, V. J. Emery, *Nature* **393**, 550–553 (1998).
- R. Daou *et al.*, *Nature* **463**, 519–522 (2010).
- B. J. Ramshaw *et al.*, *Nat. Phys.* **7**, 234–238 (2011).
- G. Ghiringhelli *et al.*, *Science* **337**, 821–825 (2012).
- J. Chang *et al.*, *Nat. Phys.* **8**, 871–876 (2012).
- T. Wu *et al.*, *Nat. Commun.* **4**, 2113 (2013).
- M. Hückler *et al.*, *Phys. Rev. B* **90**, 054514 (2014).

- R. Comin *et al.*, *Science* **343**, 390–392 (2014).
- D. Shoenberg, *Magnetic oscillations in metals* (Cambridge Univ. Press, Cambridge, 1984).
- N. Doiron-Leyraud *et al.*, *Nature* **447**, 565–568 (2007).
- D. LeBoeuf *et al.*, *Nature* **450**, 533–536 (2007).
- E. A. Yelland *et al.*, *Phys. Rev. Lett.* **100**, 047003 (2008).
- A. F. Bangura *et al.*, *Phys. Rev. Lett.* **100**, 047004 (2008).
- N. Barišić *et al.*, *Nat. Phys.* **9**, 761–764 (2013).
- B. Vignolle *et al.*, *Nature* **455**, 952–955 (2008).
- See supplementary materials on Science Online.
- S. E. Sebastian *et al.*, *Phys. Rev. B* **81**, 140505 (2010).
- Z.-X. Shen, A. Lanzara, S. Ishihara, N. Nagaosa, *Philos. Mag. B* **82**, 1349–1368 (2002).
- G. Grissonnanche *et al.*, *Nat. Commun.* **5**, 3280 (2014).
- J. W. Loram, K. A. Mirza, J. R. Cooper, W. Y. Liang, *Phys. Rev. Lett.* **71**, 1740–1743 (1993).
- J. W. Loram, K. A. Mirza, J. R. Cooper, J. L. Tallon, *J. Phys. Chem. Solids* **59**, 2091–2094 (1998).
- R. Settai, T. Takeuchi, Y. Onuki, *J. Phys. Soc. Jpn.* **76**, 051003 (2007).
- J. E. Sonier *et al.*, *Phys. Rev. B* **76**, 134518 (2007).
- A. J. Leggett, *Ann. Phys.* **46**, 76 (1968).
- M. Hückler *et al.*, *Phys. Rev. B* **83**, 104506 (2011).
- S. E. Sebastian *et al.*, *Proc. Natl. Acad. Sci. U.S.A.* **107**, 6175–6179 (2010).
- H. Q. Yuan *et al.*, *Science* **302**, 2104–2107 (2003).
- M. Le Tacon *et al.*, *Nat. Phys.* **7**, 725–730 (2011).
- D. LeBoeuf *et al.*, *Phys. Rev. B* **83**, 054506 (2011).
- L. Nie, G. Tarrus, S. A. Kivelson, *Proc. Natl. Acad. Sci. U.S.A.* **111**, 7980–7985 (2014).
- D. LeBoeuf *et al.*, *Nat. Phys.* **9**, 79–83 (2013).
- B. Vignolle *et al.*, *C. R. Phys.* **12**, 446–460 (2011).
- J. Singleton *et al.*, *Phys. Rev. Lett.* **104**, 086403 (2010).
- F. Coneri, S. Sanna, K. Zheng, J. Lord, R. De Renzi, *Phys. Rev. B* **81**, 104507 (2010).
- Y. Ando, S. Komiya, K. Segawa, S. Ono, Y. Kuriita, *Phys. Rev. Lett.* **93**, 267001 (2004).
- S. E. Sebastian, N. Harrison, G. G. Lonzarich, *Rep. Prog. Phys.* **75**, 102501 (2012).
- B. J. Ramshaw *et al.*, *Phys. Rev. B* **86**, 174501 (2012).

ACKNOWLEDGMENTS

This work was performed at the National High Magnetic Field Laboratory and was supported by the U.S. Department of Energy Office of Basic Energy Sciences “Science at 100 T” program, NSF grant DMR-1157490, the State of Florida, the National Science and Engineering Research Council of Canada, and the Canadian Institute for Advanced Research. S.E.S. acknowledges support from the Royal Society and the European Research Council under the European Union’s Seventh Framework Programme (FP7/2007-2013)/ERC Grant Agreement 337425. We thank S. Chakravarty, S. Kivelson, M. Le Tacon, K. A. Modic, C. Proust, A. Shekhter, and L. Taillefer for discussions; J. Baglo for sharing his results on the effect of quenched oxygen disorder on the microwave scattering rate in $\text{YBa}_2\text{Cu}_3\text{O}_{6+\delta}$, without which oscillations would not have been observed; and the entire 100 T operations team at the pulsed-field facility for their support during the experiment. Full resistivity curves are available in the supplementary materials. B.J.R., S.E.S., R.D.M., B.T., Z.Z., J.B.B., and N.H. performed the high-field resistivity measurements at the National High Magnetic Field Laboratory Pulsed Field Facility. B.J.R., J.D., R.L., D.A.B., and W.N.H. grew and prepared the samples at the University of British Columbia. B.J.R. analyzed the data and wrote the manuscript, with contributions from S.E.S., R.D.M., N.H., J.D., D.A.B., and W.N.H.

SUPPLEMENTARY MATERIALS

www.sciencemag.org/content/348/6232/317/suppl/DC1
Materials and Methods
Supplementary Text
Figs. S1 to S15
References (58–69)

15 December 2014; accepted 16 March 2015
Published online 26 March 2015;
10.1126/science.aaa4990

LUNAR FORMATION

Dating the Moon-forming impact event with asteroidal meteorites

W. F. Bottke,^{1*} D. Vokrouhlický,² S. Marchi,¹ T. Swindle,^{3,4} E. R. D. Scott,⁵ J. R. Weirich,⁶ H. Levison¹

The inner solar system's biggest and most recent known collision was the Moon-forming giant impact between a large protoplanet and proto-Earth. Not only did it create a disk near Earth that formed the Moon, it also ejected several percent of an Earth mass out of the Earth-Moon system. Here, we argue that numerous kilometer-sized ejecta fragments from that event struck main-belt asteroids at velocities exceeding 10 kilometers per second, enough to heat and degas target rock. Such impacts produce ~1000 times more highly heated material by volume than do typical main belt collisions at ~5 kilometers per second. By modeling their temporal evolution, and fitting the results to ancient impact heating signatures in stony meteorites, we infer that the Moon formed ~4.47 billion years ago, which is in agreement with previous estimates.

Insights into the last stages of terrestrial planet formation can be gleaned from the abundances and chondritic signatures of highly siderophile elements (HSEs) (such as Re, Os, Ir, Ru, Pt, Rh, Pd, and Au) found in the mantles of Earth and the Moon (1). Consider that the “giant impact” (GI) that formed the Moon probably sent all HSEs in Earth and the Moon to their respective metallic cores. If true, HSEs measured in the terrestrial and lunar mantles today were added late, with ~0.5 and ~0.02% of the planetary masses of Earth and the Moon, respectively, delivered by ancient chondritic projectiles after the GI (1). These low values imply that the GI took place near the endgame of planet formation. In addition, the ratio of accreted mass on Earth compared with the Moon, ~700 to 1200, is also curious; this value is much larger than the ratio of the gravitational crosssections of Earth and the Moon, ~20 (1, 2). This difference can be explained if terrestrial and lunar HSEs were delivered by a few very large bodies rather than numerous small bodies (1). A key additional implication, however, is that the number of small leftover planetesimals in the inner solar system at the time of the GI was also likely to be limited.

Taken together, these inferences open the door for GI ejecta to dominate the population of kilometer-sized bodies in the terrestrial planet region during the late stages of planet formation. As evidence, consider that GI simulations,

capable of reproducing Earth-Moon system constraints, often eject several percent of an Earth mass out of Earth's gravitational sphere of influence (3–5). If a considerable fraction of this mass were solid debris, as described by many GI simulations (3–5), and the GI ejecta size frequency distribution had a steep slope, which we infer from modeling work (6) and data (7), numerous kilometer-sized bodies could plausibly have struck main-belt asteroids at velocities $V > 10$ km/s (Fig. 1) (8). Impact heating here is accentuated, with numerical hydrocode impact experiments

showing that the volume of target material obtaining a ^{40}Ar - ^{39}Ar shock degassing age (8–11) at $V > 10$ km/s is nearly three orders of magnitude higher than at typical main-belt collision velocities of ~5 km/s (8, 12). Moreover, these velocities are only obtained by projectiles on highly eccentric and/or inclined orbits, such as leftover planetesimals (13) or GI ejecta (Fig. 1) (14). Thus, a record of ancient GI ejecta impact events could be observable in stony meteorites.

To test this possibility, we constructed models of ^{40}Ar - ^{39}Ar reset age profiles for stony meteorites that included contributions from both leftover planetesimals and GI ejecta. Our results were then compared with ^{40}Ar - ^{39}Ar ages for chondrites derived from large collisions between 4.35 to 4.567 billion years ago (Ga) (Fig. 2A) (9–11). The older age is that of the calcium-aluminum-rich inclusions (CAIs), the first-formed solids (15). The younger age marks the start of a relative lull in ^{40}Ar - ^{39}Ar reset ages; few are found between ~4.1 and 4.4 Ga, whereas many exist between 3.5 to 4.1 Ga, the time of the late heavy bombardment (8–10, 12). Our goal is to deduce both the timing of the GI and the relative magnitude of the bombardment by GI ejecta and that by leftover planetesimals.

The evidence that the GI ejecta size frequency distribution was steep enough to produce a large number of kilometer-sized fragments can be inferred in part from the ancient lunar impact record. Using numerical simulations to track GI ejecta, and assuming that the bodies were not strongly affected by collisional evolution or non-gravitational dynamical forces, we found that

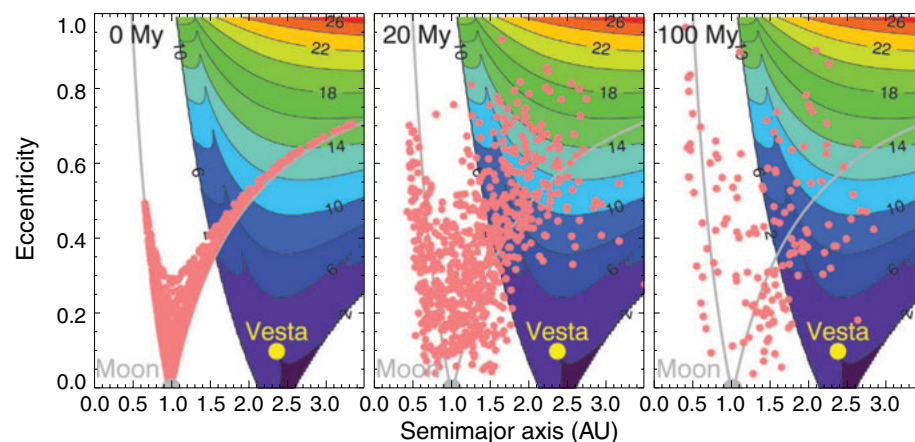


Fig. 1. The dynamical evolution of GI ejecta. Here, we show a sample of our 30,000 test bodies, all which were tracked for 600 My by using the numerical integrator SWIFT-RMVS3 (29). The planets Venus through Neptune were included in the integrations, with orbits as described in (17). The initial orbits of the ejecta test bodies were defined by placing them on Earth's Hill sphere, with a random isotropic trajectory away from Earth's center. They were then assigned an initial ejection velocity “at infinity” of 1, 3, 5, 7, or 9 km/s, respectively. These results were used to calculate impact frequencies on the Moon and terrestrial planets as well as the collision probability and impact velocity distributions between our test bodies and our representative main-belt target asteroid Vesta (8). Our results were combined by setting the initial velocity distribution of GI ejecta to values corresponding to GI hydrocode simulations; 14, 27, 26, 18, and 15% of the objects were assumed to be ejected at 1, 3, 5, 7, and 9 km/s, respectively (14). A sample of 1000 test bodies that use these velocity values are shown at several evolution times after the GI, with 38 and 6.5% left at 20 and 100 My, respectively. The color contours show the collision velocities of objects with Vesta in kilometers per second if their inclinations were 10° (12, 23).

¹Southwest Research Institute and NASA Solar System Exploration Research Virtual Institute (SSERVI)—Institute for the Science of Exploration Targets (ISET), Boulder, CO, USA.

²Institute of Astronomy, Charles University, V Holešovičkách 2, CZ-18000, Prague 8, Czech Republic.

³Lunar and Planetary Laboratory, University of Arizona, Tucson, AZ, USA.

⁴SSERVI Center for Lunar Science Exploration, Houston, TX, USA.

⁵Hawai'i Institute of Geophysics and Planetology, University of Hawai'i at Manoa, Honolulu, Hawai'i 96822, USA.

⁶Department of Earth Sciences, Western University, London, ON, Canada.

*Corresponding author. E-mail: bottke@boulder.swri.edu

~1% come back to strike the Moon within 400 million years (My) (Fig. 1) (8). Because the Moon only has ~25 ancient (Pre-Nectarian) lunar basins (16), probably made by the impact of diameter $D > 20$ km projectiles >4.1 Ga (13, 17), an impact probability of ~1% implies the GI ejecta population could—at best—only contain a few thousand $D > 20$ km bodies (the order of 25/0.01). Mass balance therefore requires the majority of GI ejecta to be in a steep size frequency distribution dominated by $D < 20$ km bodies (8). This leads us to predict that $\sim 10^{10}$ -km-sized projectiles were thrown out of the Earth-Moon system (fig. S8) (8).

Although GI simulations lack the resolution to confirm the nature of this steep size frequency distribution, insights gleaned from numerical impact experiments on $D = 100$ km bodies show that such steep slopes are common outcomes when the targets are largely left intact (6). An analog in nature for this may be the formation of the ~500-km Rheasilvia basin on the $D = 530$ km asteroid Vesta; the largest body in Vesta's family of fragments is $D \sim 8$ km, a factor of 70 smaller than Vesta itself, whereas the exponents of its cumulative power law size distribution are extremely steep, with -3.7 and -8 observed for $D > 3$ km and > 5 km fragments, respectively (fig. S6) (7, 8, 18). The shape of this size distribution implies that much of the mass of GI ejecta was initially in the form of $0.1 < D < 20$ km fragments rather than of dust and small debris (8).

A consequence of a steep GI ejecta size frequency distribution is that the fragments should undergo vigorous collisional evolution with themselves. Tests using collision evolution codes (13, 19) indicate that $D < 1$ km bodies rapidly demolished themselves, enough so to reduce the population by several orders of magnitude in mass within 0.1 to 1 My of the GI (fig. S8) (8). This would lead to a huge dust spike, with small particles either thrown out of the solar system via radiation pressure or lost to the Sun via Poynting-Robertson drag (14, 20). The surviving fragments were depleted enough that they settled into a quasi-collisional steady state, with subsequent mass loss dominated by dynamical processes. The net effect is that $\sim 10^5$ to 10^7 $D > 1$ km bodies were left in the GI ejecta population for many tens of millions of years (fig. S8).

A substantial fraction of GI ejecta reached asteroid belt-crossing orbits after the GI, either by being launched onto such orbits or by dynamically evolving there via planetary perturbations and resonances (Fig. 1 and fig. S1). We explored their impact consequences for large main-belt asteroids by calculating how they affected a representative main belt target, Vesta. Vesta was chosen because it is a likely source of the eucrite meteorites (21), Vesta's fragments have access to the gravitational resonances thought to provide most meteorites to Earth (22), and its eccentricity and inclination are close to average main-belt values (23). By calculating collision probability and impact velocity distributions over time between GI ejecta and Vesta (fig. S2) (8, 23), we found that many fragments should have hit

Fig. 2. Compilations of impact ages found within chondritic meteorites.

(A) A representation of ^{40}Ar - ^{39}Ar shock degassing ages for 34 ordinary and enstatite chondrites whose mean ages are between ~4.32 billion and 4.567 billion years (9–11). All samples were heavily shocked, shock-melted, or otherwise had some evidence for having been part of a large collision. To create this age-probability distribution, we separated the sample ages by parent body (EL, EH, E-melt/Aubrites, L, LL, and H chondrites) and computed the sum probability of ages within each class by adding Gaussian profiles, with centers and widths corresponding to the most probable age and 1σ errors of each dated sample (8). The profiles were then normalized before they were summed in order to prevent any single class from dominating the distribution (fig. S9A). We caution that systematic errors in measured Ar decay rates could make these ages slightly older (8). (B) The age-probability distribution of U-Pb ages for 24 L, LL, and H chondrites (table S1) created by using the same method (fig. S9B). U-Pb ages >60 My after CAIs are interpreted to be from impact heating alone, whereas those <60 My after CAIs are an unknown mixture of formation, metamorphic, and impact ages (26). Both distributions show a feature ~80 to 120 My after CAIs (~4.45 to 4.49 Ga).

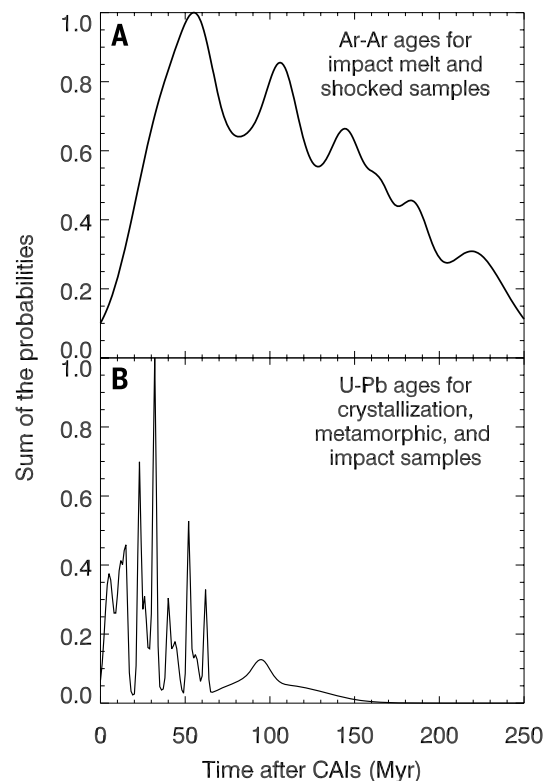
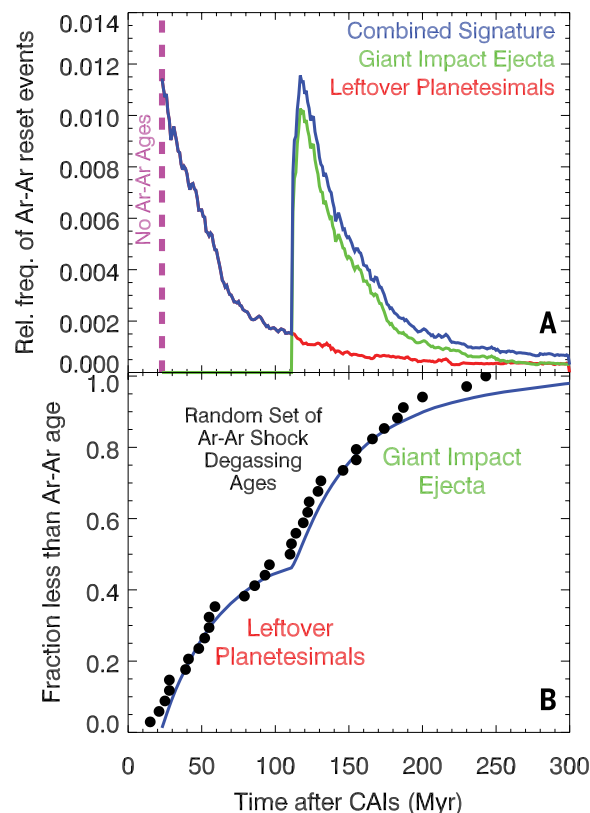


Fig. 3. A sample comparison between our model and randomly derived ^{40}Ar - ^{39}Ar shock degassing ages for asteroidal meteorites. (A) The combined ^{40}Ar - ^{39}Ar age distribution, in blue, was created by assuming that leftover planetesimals and giant impact ejecta struck main belt asteroids such as Vesta early in solar system history (8). Both model contributions have the same shape, with the former (red) ~1.8 times as large as the latter (green), respectively. (B) A single representation of our model results, shown as a blue line, compared with 34 ^{40}Ar - ^{39}Ar shock reset ages randomly drawn from Fig. 2A. In this example, the giant impact takes place at 112 My after CAIs. The plotted results are close to our derived age for the giant impact, 105 ± 25 My after CAIs (equivalently 4.46 ± 0.03 Ga), and our derived contribution ratio of 1.9 ± 0.9 between leftover planetesimals and giant impact ejecta.



large main-belt asteroids. Two types of meteorite impact signatures were likely produced.

The first signature involves numerous kilometer-sized and smaller projectiles hitting Vesta and other very large asteroids ~0.1 to a few My after the GI. Many tens of $D > 10$ km craters and numerous smaller craters were potentially produced on Vesta during this interval. Their primary effect would have been to dredge up warm material heated at depth by early parent body metamorphism. This suddenly quenched material would have yielded a spike of impact ages from this time, with many samples showing little or modest shock effects. The second signature comes from impact heating within a crater's breccia lens or ejecta blanket, which would have been dominated by $V > 10$ km/s projectiles (Fig. 1). This mechanism should have produced ^{40}Ar - ^{39}Ar shock reset ages on the target bodies for ~100 My after the GI. Subsequent impacts, such as the ~1-billion-year-old Rheasilvia basin formation event, excavated some of this material and placed it off-world, where collisions, nongravitational forces, gravitational resonances, and planetary encounters delivered it to Earth (24). Additional isotopic chronometers may also record these impacts (such as U-Pb), although this may involve higher-threshold temperatures and different heating durations than for Ar.

For our model ^{40}Ar - ^{39}Ar reset age profiles created by GI ejecta, we combined these collisional and dynamical outcomes with impact heating relationships derived in (8, 12) (fig. S4). The GI ejecta age profile was found to peak ~8 My after the GI, before slowly fading over the subsequent ~100 My (Fig. 3A and fig. S5). The leftover planetesimal ^{40}Ar - ^{39}Ar reset age profile was more complicated to assess, mainly because existing planet formation models are uncertain and incomplete. As a compromise, we took advantage of insights from (13) that show that leftover planetesimal populations quickly decimate themselves through collisional evolution. The survivors, left in a quasi-steady state with limited mass in small bodies, are then slowly lost from high eccentricity and inclination orbits over time. Although our tests with different starting size distributions and dynamical populations yielded a range of ^{40}Ar - ^{39}Ar reset age profiles, the tails of the age profiles showed shapes similar to those computed for GI ejecta. These profiles, when scaled appropriately, also provided an excellent fit to our oldest ^{40}Ar - ^{39}Ar data (Fig. 3B). We therefore assumed for simplicity that the shape of the leftover planetesimals' reset age profile tail mimicked that found for GI ejecta.

Our model results were compared with a representation of ancient ^{40}Ar - ^{39}Ar shock degassing ages from 34 chondritic samples derived from at least five or six asteroid parent bodies (Fig. 2A and fig. S9) (8–11). Using a Monte Carlo method, we randomly selected sample ages from an age-probability distribution (Fig. 2A and fig. 3B) and used a Kolmogorov-Smirnov test (K-S) statistical test to determine the quality of fit between model and data over 1000 trials. In each trial, we tested all possible combinations

of our model GI ages, varied between 0 and 300 My after CAIs, and the ratio of the contributions of the reset age profiles of leftover planetesimals to that of GI ejecta varied between 0.01 and 100. The leftover planetesimal reset age profile was defined as starting from 0 My after CAIs, whereas the GI ejecta reset age profile was started at the model GI age. The two profiles were then scaled, added, and then compared against the sample data. By collecting and analyzing the high goodness of fit cases, we estimate that the GI took place 105 ± 25 My after CAIs (equivalently 4.46 ± 0.03 Ga, 1σ confidence limits). The ratio of the leftover planetesimal contribution to that of giant impact ejecta was 1.9 ± 0.9 .

Although this solution is promising, insufficient data exist to statistically argue it is unique. For this reason, we examined additional data sets for evidence that our inferred GI age was reasonable. Among the eucrite meteorites, there is a spike of ^{40}Ar - ^{39}Ar ages between 4.47 and 4.49 Ga from at least nine unbrecciated samples (fig. S10) (8, 9, 12, 25). They are interpreted to be impact by products, and their nature corresponds well to our GI quench age predictions. Similarly, a compilation of chondrite U-Pb ages (table S1) shows a prominent feature ~95 My after CAIs (~4.47 Ga) (Fig. 2B) that appears comparable with a ^{40}Ar - ^{39}Ar shock degassing age feature at ~106 My after CAIs (~4.46 Ga) (Fig. 2A). We cannot yet apply our model to U-Pb data, however, because only the U-Pb ages >60 My after CAIs are considered to have been solely created by impact (26).

The intersection of these ages indicates that the likely timing of the giant impact was ~4.47 Ga. This value is a good match to the oldest lunar crust ages as well as several predicted ages found by other means (fig. S11) (8). It also indicates that the interval between the GI and the oldest collectable lunar samples was relatively short.

These results also offer the appealing possibility that remnants of GI ejecta—perhaps in the form of clasts with compositions akin to the crust, mantle, or core expected from the proto-Earth or the Moon-forming impactor—might be identified within ancient asteroid meteorite breccias. They also suggest that the GI was the most recent impact event of this scale in the terrestrial planet region. Other putative large-impact events, such as those taking place on early Earth or Venus, probably had to occur within the first few tens of millions of years after CAI formation, when their impact signatures could be most easily hidden among the ^{40}Ar - ^{39}Ar ages provided by leftover planetesimals. Alternatively, these collisions, or comparatively smaller ones such as the putative impact event that produced Mars's ancient Borealis basin (27), either produced too little kilometer-sized ejecta fragments to be noticed in the available data or they occurred so close in time to the GI that the signature of their ejecta cannot yet be distinctly distinguished (28). Last, although the importance of GI ejecta returning to strike the Moon has yet to be quantitatively evaluated, the values computed here suggest that it could play

an intriguing role in the earliest phase of lunar bombardment.

REFERENCES AND NOTES

- W. F. Bottke, R. J. Walker, J. M. D. Day, D. Nesvorný, L. Elkins-Tanton, *Science* **330**, 1527–1530 (2010).
- S. Marchi et al., *Nature* **511**, 578–582 (2014).
- R. M. Canup, *Icarus* **196**, 518–538 (2008).
- M. Čuk, S. T. Stewart, *Science* **338**, 1047–1052 (2012).
- R. M. Canup, *Science* **338**, 1052–1055 (2012).
- D. D. Durda et al., *Icarus* **186**, 498–516 (2007).
- D. Nesvorný, Nesvorný HCM Asteroid Families V2.0 NASA Planetary Data System, (2012).
- Materials and methods are available as supplementary materials on Science Online.
- D. D. Bogard, *Chem. Erde Geochem.* **71**, 207–226 (2011).
- T. D. Swindle, D. A. Kring, J. R. Wierich, *Advances in $^{40}\text{Ar}/^{39}\text{Ar}$ Dating: from Archaeology to Planetary Sciences*, Geological Society of London, Special Publications, **378**, 333–347 (2013).
- J. Hopp, M. Tieloff, U. Ott, E. V. Korochantseva, A. I. Buykin, *Meteorit. Planet. Sci.* **49**, 358–372 (2014).
- S. Marchi et al., *Nat. Geosci.* **6**, 303–307 (2013).
- W. F. Bottke, H. F. Levison, D. Nesvorný, L. Dones, *Icarus* **190**, 203–223 (2007).
- A. P. Jackson, M. C. Wyatt, *Mon. Not. R. Astron. Soc.* **425**, 657–679 (2012).
- J. N. Connolly et al., *Science* **338**, 651–655 (2012).
- D. E. Wilhelms, *U.S. Geol. Surv. Prof. Pap.*, paper 1348 (1987).
- W. F. Bottke et al., *Nature* **485**, 78–81 (2012).
- P. Schenk et al., *Science* **336**, 694–697 (2012).
- A. Morbidelli, W. F. Bottke, D. Nesvorný, H. F. Levison, *Icarus* **204**, 558–573 (2009).
- J. A. Burns, P. L. Lamy, S. Soter, *Icarus* **40**, 1–48 (1979).
- H. Y. McSweeney Jr. et al., *Meteorit. Planet. Sci.* **48**, 2090–2104 (2013).
- A. Morbidelli, B. Gladman, *Meteorit. Planet. Sci.* **33**, 999–1016 (1998).
- W. F. Bottke, M. C. Nolan, R. Greenberg, R. A. Kolvoord, *Icarus* **107**, 255–268 (1994).
- W. F. Bottke Jr., D. Vokrouhlický, D. P. Rubincam, D. Nesvorný, *Annu. Rev. Earth Planet. Sci.* **34**, 157–191 (2006).
- T. Kennedy, F. Jourdan, A. W. R. Bevan, M. A. Mary Gee, A. Frew, *Geochim. Cosmochim. Acta* **115**, 162–182 (2013).
- R. H. Jones et al., *Geochim. Cosmochim. Acta* **132**, 120–140 (2014).
- M. M. Marinova, O. Aharonson, E. Asphaug, *Nature* **453**, 1216–1219 (2008).
- F. Nimmo, S. D. Hart, D. G. Korycansky, C. B. Agnor, *Nature* **453**, 1220–1223 (2008).
- H. F. Levison, M. J. Duncan, *Icarus* **108**, 18–36 (1994).

ACKNOWLEDGMENTS

We thank R. Canup, B. Cohen, A. Jackson, A. Parker, P. Renne, and J. Salmon for many useful discussions and our referees for their numerous constructive comments. W.F.B., S.M., and T.S.'s participation was supported by NASA's SSERVI program through institute grant numbers NNA14AB03A and NNA14AB07A. The work of D.V. was partially supported by research grant P209-13-01308S of the Czech Grant Agency. Resources supporting this work were provided by the NASA High-End Computing Program through the NASA Advanced Supercomputing Division at Ames Research Center. Data are available in the main text, supplementary materials, or upon request.

SUPPLEMENTARY MATERIALS

www.sciencemag.org/content/348/6232/321/suppl/DC1
Materials and Methods
Figs. S1 to S11
Table S1
References (30–70)

10 October 2014; accepted 9 March 2015
10.1126/science.aaa0602

CLIMATE CHANGE

The weakening summer circulation in the Northern Hemisphere mid-latitudes

Dim Coumou,^{1,*} Jascha Lehmann,^{1,2} Johanna Beckmann^{1,2}

Rapid warming in the Arctic could influence mid-latitude circulation by reducing the poleward temperature gradient. The largest changes are generally expected in autumn or winter, but whether significant changes have occurred is debated. Here we report significant weakening of summer circulation detected in three key dynamical quantities: (i) the zonal-mean zonal wind, (ii) the eddy kinetic energy (EKE), and (iii) the amplitude of fast-moving Rossby waves. Weakening of the zonal wind is explained by a reduction in the poleward temperature gradient. Changes in Rossby waves and EKE are consistent with regression analyses of climate model projections and changes over the seasonal cycle. Monthly heat extremes are associated with low EKE, and thus the observed weakening might have contributed to more persistent heat waves in recent summers.

Enhanced warming in the Arctic could change circulation patterns in the mid-latitudes by reducing the pole-to-mid-latitude thermal gradient (1–3). This hypothesis, which was first proposed in the 1970s based on model experiments (4, 5), has recently received considerable attention due to rapid observed warming in the Arctic (6–9), associated with a decline in sea ice and other factors (1, 3, 10).

Most studies addressing the link between Arctic change and mid-latitude weather have focused on winter circulation. The extra heat stored in the ocean owing to sea-ice loss is released into the atmosphere by late autumn or early winter, when air temperatures drop below sea surface temperatures. Consequently, the largest absolute increases in Arctic geopotential height have been detected in autumn and winter (6), consistent with climate model simulations (11). Autumn has, at least in the western half of the hemisphere,

also seen a reduction in the zonal-mean flow (6, 12). This might cause a slowdown in wave propagation (6), but the results are sensitive to the exact metrics used to describe waves (12, 13). Thus, whether observed changes in geopotential height have affected mid-latitude Rossby waves remains disputed (6, 12–14).

We studied changes in mid-latitude circulation in boreal summer instead. Although the oceanic heat flux is smaller in this season (17), Arctic amplification has reduced the pole-to-mid-latitude temperature gradient (1), and Arctic geopotential heights have increased (6). These changes are likely to be related to the earlier loss of snow cover over land and increased Arctic sea surface temperatures where sea ice has been lost (7). In recent summers, mid-latitude circulation has been dominated by a negative Arctic Oscillation index; i.e., anomalously small pressure differences between mid- and high-latitudes (7, 15–17). Moreover, several recent heat waves, such as in Russia in 2010, were associated with persistent hemispheric circulation patterns (15, 16, 18).

Generally, the large-scale mid-latitude atmosphere dynamics [supplementary materials (SM

text S4] are characterized by (i) fast-traveling free Rossby waves (the so-called synoptic transients) with zonal wave numbers typically larger than 6, and (ii) quasi-stationary Rossby waves with normally smaller wave numbers as a response to quasi-stationary diabatic and orographic forcing (15, 19–21). We focus on the first. These waves are associated with synoptic-scale cyclones (storms) and anticyclones (high-pressure systems), which form the storm track regions in the mid-latitudes. They have a relatively fast phase velocity (i.e., eastward propagation) and cause weather variability on time scales of less than a week. Typically, the intensity of synoptic-scale wave (or eddy) activity is estimated by applying a 2.5- to 6-day bandpass filter to high-resolution wind field data (22–24). This way, the total eddy kinetic energy (EKE) is extracted, which is a measure of the interplay between the intensity and frequency of high- and low-pressure systems associated with fast-traveling Rossby waves. Due to the quasi-stationary nature of thermally and orographically forced waves, as analyzed in related studies (15, 16, 25, 26), they have lower frequencies and are thus excluded from our EKE computations (SM text S4).

We calculated EKE in the Northern Hemisphere from daily ERA-Interim wind fields (27), using a 2.5- to 6-day bandpass filter [see (23, 24, 28)]. We limited our analysis to the satellite-covered period (after 1979) to minimize the effects of changes in the observing system (SM text S2). The 1979–2013 period has seen a steady decline in summertime EKE (Fig. 1A). This decline is statistically significant at the 1% level and observed at all pressure levels, with the strongest relative changes in the lower to mid-troposphere (figs. S1 to S4 and table S1). Moreover, it occurs over the full hemisphere and over all relevant latitudes (fig. S5). The observed changes are thus not due to a north-south shift of storm tracks but due to a spatially homogeneous weakening. Other reanalysis products give similar results (figs. S6 to S11). For the other seasons, trends in EKE are also downward, but none are significant (figs. S12 to S17).

The decline in summer EKE is accompanied by a long-term decline in the zonal-mean zonal wind (U , Fig. 1B). Again, this weakening of the

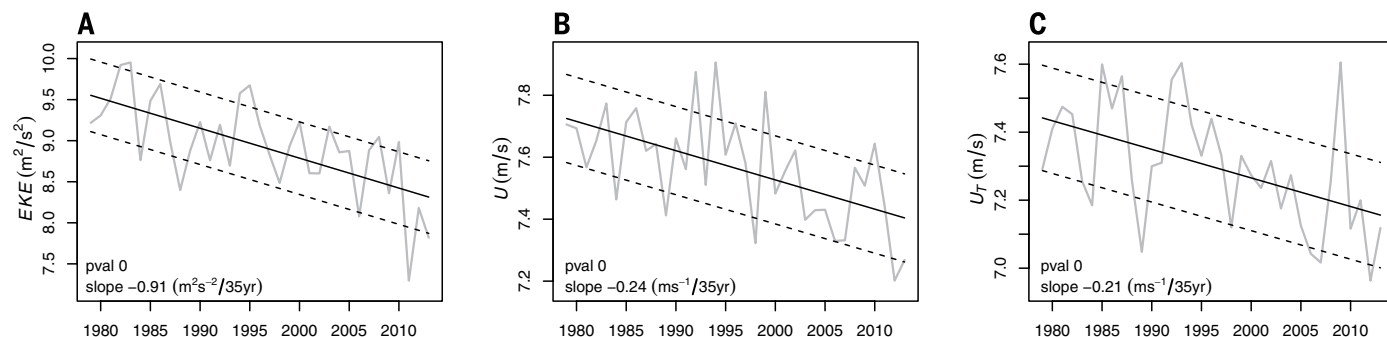


Fig. 1. Weakening summer circulation in the mid-latitudes. Absolute changes in (A) EKE, (B) zonal wind U , and (C) thermal wind U_T over 1979–2013 in summer (June, July, and August). Variables are calculated at 500 mb and averaged over 35°N to 70°N and all longitudes, with gray lines plotting observations, solid black lines the linear trend, and dashed black lines the ± 1 residual SE range. Slope and P values for the trend estimates are given in the panels.

zonal flow is seen at all altitudes and in different reanalysis products (figs. S1 to S4 and S6 to S10). The long-term weakening of the zonal flow is consistent with the decline in the pole-to-mid-latitude thermal gradient. This is shown by the downward trend of similar magnitude in thermal wind U_T (Fig. 1C), which depends on changes in the temperature gradient only (eq. S2).

Although the relative decrease in EKE has been by 8 to 15% (depending on pressure level) over the 35-year period, the zonal flow weakened by only 4 to 6% (table S1). A similar relationship between changes in EKE and zonal flow is seen in future projections of CMIP5 (Coupled Model Intercomparison Project Phase 5) climate models. Under a high-emission scenario, summer EKE

declines primarily because of decreased vertical wind shear associated with weakening of the zonal-mean flow (24). This projected reduction in EKE is spatially homogeneous, similar to the observed changes. Regression analysis of future changes in EKE and in zonal flow for individual CMIP5 models reveals a significant linear relationship (Fig. 2). The regression slope of ~ 1.4 indicates that a reduction in U is associated with a more pronounced reduction in EKE. This is seen at all pressure levels, with the regression slope increasing with altitude (fig. S18). Increased static stability plays a role as well (24, 29), which explains why the linear regression crosses the y axis at negative values: Even for zero change in U , increased static stability in a warmer climate causes EKE to decline. The observed rela-

tive changes in U and EKE over the past 35 years map reasonably well on the regression of projected future changes (Fig. 2).

The pronounced weakening in EKE should also be reflected in changed wave characteristics. To test this, we applied spectral analysis to the north-south wind component v in daily wind field data and calculated amplitude (A_v), phase speed, and period for wave numbers 1 to 15 (SM text S1.1). This way, fast-moving and quasi-stationary waves are not explicitly separated (as in EKE by using bandpass filtering), but because we used daily data, the mean wave amplitudes are dominated by fast-moving waves (SM text S4). The results are therefore comparable with EKE. We determined the wave quantities for the north-south wind component v averaged over 35°N to 70°N, and A_v thus reflects wind speeds with units of meters per second.

The amplitudes of all wave numbers except 7 have declined, with significant reductions in waves 1, 3, 4, 6, and 10 and in the mean amplitude of all waves. These changes are robust, detected in ERA-Interim and NCEP-NCAR (National Centers for Environmental Prediction–National Center for Atmospheric Research) data and for different pressure levels, with the strongest changes in the mid-troposphere (Fig. 3A and fig. S19). This vertical pattern is consistent with the more pronounced changes in EKE, U (table S1), and poleward temperature gradient (T) in the lower troposphere. The mean amplitude declined by $\sim 5\%$ over 1979–2013 (Fig. 3A), similar to the relative reduction in U (fig. S1B). This is consistent with the seasonal correlation of these quantities (Fig. 3B), which shows that, to a first order, daily anomalies in mean A_v scale with those in U . This positive correlation is expected as daily wind fields, and thus A_v , will be dominated by transient eddies, because their kinetic energy is nearly an order of magnitude larger than that of quasi-stationary waves (30). Transient eddies are not only forced by the zonal flow via vertical shear (and thus baroclinicity) but can also accelerate it via the eddy-driven jet (1, 31), explaining the positive correlation between U and A_v (SM text S4). The reduction of $\sim 5\%$ in mean wind speed (A_v) implies a $\sim 10\%$ reduction

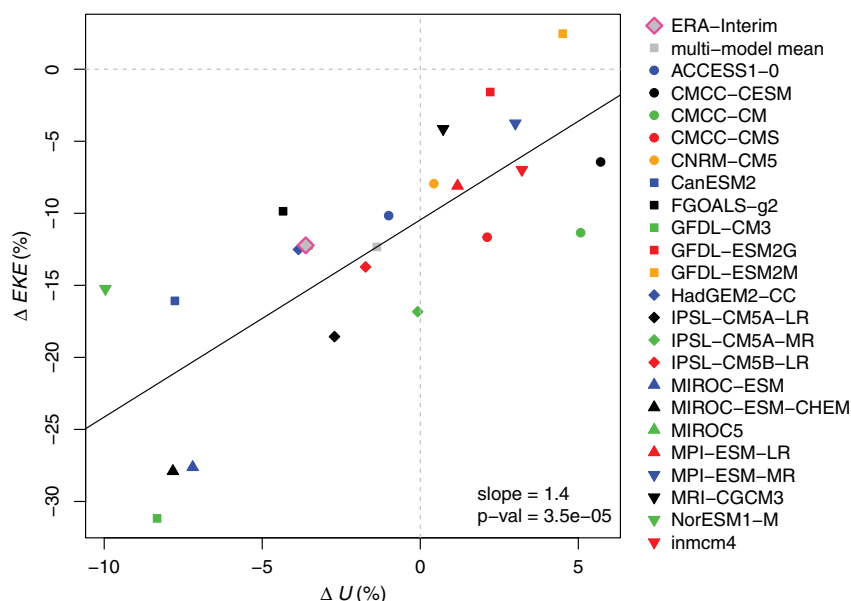
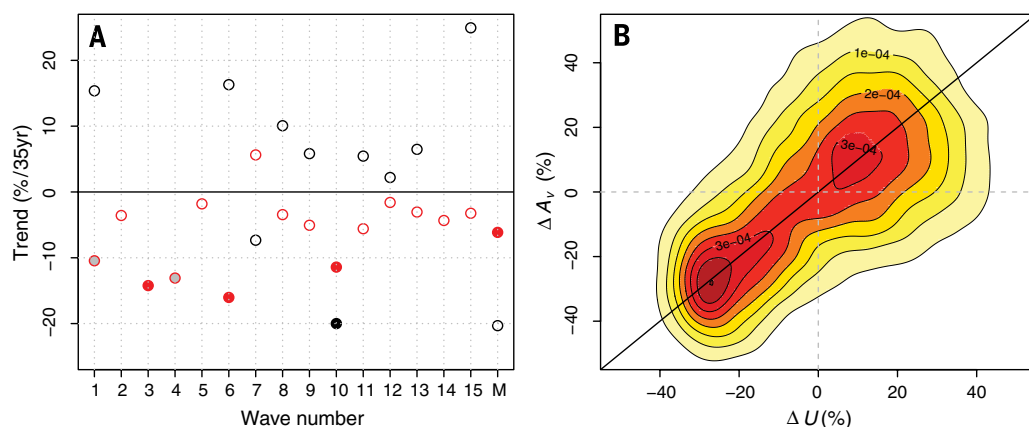


Fig. 2. Relationship between relative changes (Δ) in EKE and U in climate model projections.

The percentage change in the future (2081–2100, under scenario RCP8.5) relative to 1981–2000 for individual CMIP5 climate models is shown. Both quantities are averaged over 35°N to 70°N, all longitudes, and over 850 to 250 mb (mass-weighted). The solid black line shows the linear fit, with slope and P value given at lower right. Relative changes in EKE and U in the ERA-Interim data are given for the 1979–2013 period.

Fig. 3. (A) Trends in planetary wave amplitudes (A_v , red) and phase speed (black) at 500 mb in summer for wave numbers 1 to 15 and for the mean of all waves (M) in units of percentage change per 35 years; i.e., the period 1979–2013. Solid circles indicate 5% statistical significance, gray-filled circles indicate 10% statistical significance, and open circles are not significant. **(B)** Two-dimensional probability density distribution of daily deviations (in percentage change of their annual mean climatological values) of the zonal flow and the mean amplitude of waves 1 to 15. The bisecting line is shown in black.



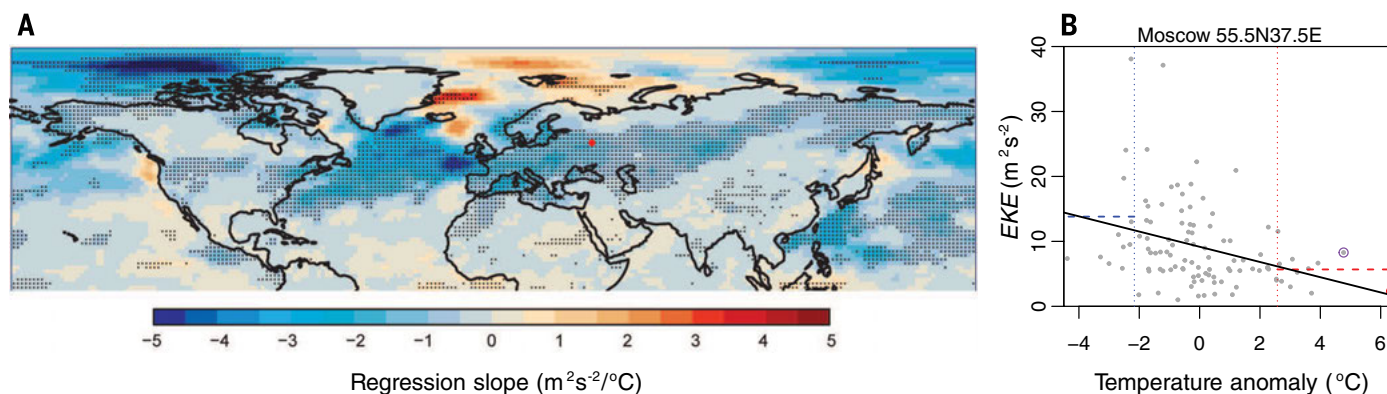


Fig. 4. Regression analysis between EKE and near-surface temperature during the summer months (June, July, and August). (A) Slope of the regression analysis. Both variables were linearly detrended, and stippling indicates significance at the 5% level. (B) EKE plotted against near-surface temperature anomaly for Moscow [red dot in (A)] for individual summer months, showing that the 10% coldest summer months (left of the vertical blue dotted line) have a substantially higher EKE ($14 \text{ m}^2/\text{s}^2$; i.e., the horizontal blue dashed line) and the 10% warmest months (right of the vertical red dotted line) a substantially lower EKE ($5.7 \text{ m}^2/\text{s}^2$; i.e., the horizontal red dashed line). Red and purple circles indicate, respectively, July and August 2010.

in kinetic energy, which is in good agreement with the bandpass-filtered results.

Wave 10 has seen a significant reduction in both amplitude and phase speed (Fig. 3A), which dropped respectively by $\sim 11\%$ and $\sim 20\%$ over the 1979–2013 period, with both negative trends acting to reduce EKE. A reduction in amplitude means lower wind speeds associated with weaker high- and low-pressure synoptic weather systems and thus lower EKE. A reduced phase speed implies more-persistent synoptic weather systems and fewer of them over the full season. The probability-density distribution of the wave period shows that wave periods in the EKE-relevant range (2.5 to 6 days) are dominated by wave 10 (fig. S21). During roughly half of all summer days, wave 10 had a wave period within this range. This suggests that the reduction in amplitude and phase speed of wave 10 contributed substantially to the reduction in EKE.

Summer EKE declined by 8 to 15% over the past decades, whereas the CMIP5 models project similar changes only by the end of the 21st century under a high-emission scenario (24). Either the climate models underpredict dynamical changes, or multidecadal variability played a role in the observed changes. In the other seasons, dynamics weakened as well, but here significant changes are only detected for the zonal-mean flow in autumn (SM text S3). Although the Arctic has warmed most in winter (1), the strongest changes in the meridional temperature gradient within the mid-latitudes occurred in summer, followed by autumn (fig. S17). Therefore, U_T and U itself weakened most in those seasons (fig. S17). The smaller year-to-year variability in those seasons (and especially in summer), as compared to winter, improves signal-to-noise ratios, making trend detection possible at an earlier stage (fig. S15). Likewise, variability in summer EKE is only half that of the other seasons (fig. S16B), and hence the signal-to-noise ratio is much larger for summer. In fact, summer EKE has weakened by more than two standard deviations over 1979–2013 (fig. S16C). Therefore, contrary to previous sug-

gestions (1–3), the influence of Arctic amplification on mid-latitude weather is unlikely to be limited to autumn and winter only.

In summer, synoptic storms transport moist and cool air from the oceans to the continents, bringing relief during periods of oppressive heat. Low cyclone activity over Europe in recent years has led to more-persistent weather (32, 33) contributing to prolonged heat waves. Regression analysis between EKE and near-surface temperature for summer months reveals that over mid-latitude continental regions, these quantities are negatively correlated (Fig. 4A). Thus, hot summer months are associated with low EKE (SM text S5). Over most of Eurasia and the United States, the negative regression slope is significant at the 5% level. In these storm track-affected regions, EKE in the 10% hottest months was only about half its summer climatological value (Fig. 4B and figs. S22 to S24). Low cyclone activity (and thus low EKE) imply that cool maritime air masses become less frequent, creating favorable conditions for the buildup of heat and drought over continents. This probably prolongs the duration of blocking weather systems, as, for example, during the Russian heat wave of 2010 (18, 34). In particular, the record-breaking July temperatures over Moscow were associated with extremely low EKE (Fig. 4B).

Recent studies have emphasized the importance of quasi-stationary waves for summer heat extremes (15, 16, 25, 35), showing that the frequency of wave-resonance events associated with high-amplitude quasi-stationary waves has increased since the onset of rapid Arctic amplification in 2000 (16). Here we show that the amplitude of fast-moving waves has steadily decreased, and also that the rate in this weakening seems to have increased since 2000 (fig. S25). Both of these observations are consistent with more-persistent summer weather (SM text S6). Low monthly EKE implies low weather variability within that month, indicating persistent weather conditions, consistent with quasi-stationary waves. The long-term reduction in EKE should lead

to a reduction in weather variability on short time scales (less than a week), in agreement with the reduced intraseasonal daily temperature variance observed (36) and theoretical arguments (37). However, our results show that low EKE is associated with heat extremes on monthly time scales. Therefore, on such longer time scales, variability might actually increase due to a reduction in EKE. This seems consistent with Huntingford *et al.* (38), who report that the largest increase in interannual seasonal temperature variance occurred in the mid-latitude boreal summer. To test this hypothesis, studies are needed that quantify both interannual and intraannual variability on all relevant subseasonal time scales.

This study shows that boreal summer circulation has weakened, together with a reduction in the pole-to-mid-latitude temperature gradient. This has made weather more persistent and hence favored the occurrence of prolonged heat extremes.

REFERENCES AND NOTES

1. J. Cohen *et al.*, *Nat. Geosci.* **7**, 627–637 (2014).
2. D. Budikova, *Global Planet. Change* **68**, 149–163 (2009).
3. J. E. Walsh, *Global Planet. Change* **117**, 52–63 (2014).
4. R. L. Newson, *Nature* **241**, 39–40 (1973).
5. M. Warshaw, R. R. Rapp, *J. Appl. Meteorol.* **12**, 43–49 (1973).
6. J. A. Francis, S. J. Vavrus, *Geophys. Res. Lett.* **39**, L06801 (2012).
7. J. E. Overland, J. A. Francis, E. Hanna, M. Wang, *Geophys. Res. Lett.* **39**, L19804 (2012).
8. R. Jaeger, K. Dethloff, D. Handorf, A. Rinke, J. Cohen, *Tellus Ser. A Dyn. Meteorol. Oceanogr.* **64**, 1–11 (2012).
9. J. L. Cohen, J. C. Furtado, M. A. Barlow, V. A. Alexeev, J. E. Cherry, *Environ. Res. Lett.* **7**, 014007 (2012).
10. F. Pithan, T. Mauritsen, *Nat. Geosci.* **7**, 181–184 (2014).
11. J. A. Screen, I. Simmonds, C. Deser, R. Tomas, *J. Clim.* **26**, 1230–1248 (2013).
12. E. A. Barnes, *Geophys. Res. Lett.* **40**, 4734–4739 (2013).
13. J. A. Screen, I. Simmonds, *Geophys. Res. Lett.* **40**, 959–964 (2013).
14. E. Kintisch, *Science* **344**, 250–253 (2014).
15. V. Petoukhov, S. Rahmstorf, S. Petri, H. J. Schellnhuber, *Proc. Natl. Acad. Sci. U.S.A.* **110**, 5336–5341 (2013).
16. D. Coumou, V. Petoukhov, S. Rahmstorf, S. Petri, H. J. Schellnhuber, *Proc. Natl. Acad. Sci. U.S.A.* **111**, 12331–12336 (2014).

17. J. A. Screen, *Environ. Res. Lett.* **8**, 044015 (2013).
18. S. Schubert, H. Wang, M. Suarez, *J. Clim.* **24**, 4773–4792 (2011).
19. J. Pedlosky, *Geophysical Fluid Dynamics* (Springer, New York, 1979).
20. K. Fraedrich, H. Böttger, *J. Atmos. Sci.* **35**, 745–750 (1978).
21. G. J. Boer, T. G. Shepherd, *J. Atmos. Sci.* **40**, 164–184 (1983).
22. M. Blackmon, *J. Atmos. Sci.* **33**, 1607–1623 (1976).
23. D. Coumou, V. Petoukhov, A. V. Eliseev, *Nonlinear Process. Geophys.* **18**, 807–827 (2011).
24. J. Lehmann, D. Coumou, K. Frieler, A. V. Eliseev, A. Levermann, *Environ. Res. Lett.* **9**, 084002 (2014).
25. H. Teng, G. Branstator, H. Wang, G. Meehl, W. M. Washington, *Nat. Geosci.* **6**, 1–6 (2013).
26. K. E. Trenberth, J. T. Fasullo, G. Branstator, A. S. Phillips, *Nat. Clim. Change* **4**, 911–916 (2014).
27. D. P. Dee *et al.*, *Q. J. R. Meteorol. Soc.* **137**, 553–597 (2011).
28. M. Murakami, *Mon. Weather Rev.* **107**, 994–1013 (1979).
29. J. Lu, G. Chen, D. M. W. Frierson, *J. Clim.* **21**, 5835–5851 (2008).
30. J. P. Peixoto, A. H. Oort, *Physics of Climate* (American Institute of Physics, New York, 1992).
31. T. Woollings, M. Blackburn, *J. Clim.* **25**, 886–902 (2012).
32. J. Kyselý, R. Huth, *Theor. Appl. Climatol.* **85**, 19–36 (2005).
33. J. Kyselý, *Global Planet. Change* **62**, 147–163 (2008).
34. R. Dole *et al.*, *Geophys. Res. Lett.* **38**, L06702 (2011).
35. J. A. Screen, I. Simmonds, *Nat. Clim. Change* **4**, 704–709 (2014).
36. J. A. Screen, *Nat. Clim. Change* **4**, 577–582 (2014).
37. T. Schneider, T. Bischoff, H. Plotka, *J. Clim.* **28**, 2312–2331 (2014).
38. C. Huntingford, P. D. Jones, V. N. Livina, T. M. Lenton, P. M. Cox, *Nature* **500**, 327–330 (2013).

ACKNOWLEDGMENTS

We thank the CMIP5 climate modeling groups and the European Centre for Medium-Range Weather Forecasts and NCEP-NCAR for making their model and reanalysis data available. Comments

by three anonymous reviewers, S. Rahmstorf, and P. Eickemeier have considerably improved the manuscript. Data presented in this manuscript will be archived for at least 10 years by the Potsdam Institute for Climate Impact Research. The work was supported by the German Research Foundation (grant no. CO994/2-1) and the German Federal Ministry of Education and Research (grant no. 01LN1304A). D.C. designed the research; D.C., J.L., and J.B. performed the analysis; and D.C., J.L., and J.B. wrote the manuscript.

SUPPLEMENTARY MATERIALS

www.sciencemag.org/content/348/6232/324/suppl/DC1
Text S1 to S6
Figs. S1 to S25
Table S1
References
Data Deposition

26 September 2014; accepted 26 February 2015
Published online 12 March 2015;
10.1126/science.1261768

ICE SHEETS

Volume loss from Antarctic ice shelves is accelerating

Fernando S. Paolo,^{1*} Helen A. Fricker,¹ Laurie Padman²

The floating ice shelves surrounding the Antarctic Ice Sheet restrain the grounded ice-sheet flow. Thinning of an ice shelf reduces this effect, leading to an increase in ice discharge to the ocean. Using 18 years of continuous satellite radar altimeter observations, we have computed decadal-scale changes in ice-shelf thickness around the Antarctic continent. Overall, average ice-shelf volume change accelerated from negligible loss at 25 ± 64 cubic kilometers per year for 1994–2003 to rapid loss of 310 ± 74 cubic kilometers per year for 2003–2012. West Antarctic losses increased by ~70% in the past decade, and earlier volume gain by East Antarctic ice shelves ceased. In the Amundsen and Bellingshausen regions, some ice shelves have lost up to 18% of their thickness in less than two decades.

The Antarctic Ice Sheet gains mass through snowfall and loses mass at its margin through submarine melting and iceberg calving. These losses occur primarily from ice shelves, the floating extensions of the ice sheet. Antarctica's grounded-ice loss has increased over the past two decades (1, 2), with the most rapid losses being along the Amundsen Sea coast (3) concurrent with substantial thinning of adjoining ice shelves (4, 5) and along the Antarctic Peninsula after ice-shelf disintegration events (6). Ice shelves restrain ("buttress") the flow of the grounded ice through drag forces at the ice-rock boundary, including lateral stresses at side-walls and basal stresses where the ice shelf rests on topographic highs (7, 8). Reductions in ice-shelf thickness reduce these stresses, leading to a speed-up of ice discharge. If the boundary between the floating ice shelf and the grounded ice (the grounding line) is situated on a retro-

grade bed (sloping downwards inland), this process leads to faster rates of ice flow, with potential for a self-sustaining retreat (7, 9, 10).

Changes in ice-shelf thickness and extent have primarily been attributed to varying atmospheric and oceanic conditions (11, 12). Observing ice-shelf thickness variability can help identify the principal processes influencing how changing large-scale climate affects global sea level through the effects of buttressing on the Antarctic Ice Sheet. The only practical way to map and monitor ice-shelf thickness for this vast and remote ice sheet at the known space and time scales of ice-shelf variability is with satellite altimetry. Previous studies have reported trends based on simple line fits to time series of ice-shelf thickness (or height) averaged over entire ice shelves or broad regions (4, 13) or for short (~5-year) time intervals (5, 14, 15). Here, we present a record of ice-shelf thickness that is highly resolved in time (~3 months) and space (~30 km), using the longest available record from three consecutive overlapping satellite radar altimeter missions (ERS-1, 1992–1996; ERS-2, 1995–2003; and Envisat, 2002–2012) spanning 18 years from 1994 to 2012.

Our technique for ice-shelf thickness change detection is based on crossover analysis of satellite radar altimeter data, in which time-separated height estimates are differenced at orbit intersections (13, 16, 17). To cross-calibrate measurements from the different satellite altimeters, we used the roughly 1-year overlap between consecutive missions. The signal-to-noise ratio of altimeter-derived height differences for floating ice in hydrostatic equilibrium is roughly an order of magnitude smaller than over grounded ice, requiring additional data averaging to obtain comparable statistical significance. We aggregated observations in time (3-month bins) and space (~30-km cells). Because the spatial distribution of crossovers changes with time (due, for example, to nonexact repeat tracks and nadir mispointing), we constructed several records at each cell location and stacked them in order to produce a mean time series with reduced statistical error (18). We converted our height-change time series and rates to thickness changes by assuming that observed losses occurred predominantly at the density of solid ice (basal melting) (4, 5, 17). This is further justified by the relative insensitivity of radar measurements to fluctuations in surface mass balance (18). For volume changes, we tracked the minimum (fixed) area of each ice shelf (18). We assessed uncertainties for all estimates using the bootstrap approach (resampling with replacement of the residuals of the fit) (19), which allows estimation of formal confidence intervals. All our uncertainties are stated at the 95% confidence level [discussion of uncertainties are provided in (18) and the several corrections applied are stated in (20)].

We estimated 18-year trends in ice-shelf thickness by fitting low-order polynomials (degree $n \leq 3$) to the data using a combination of lasso regularized-regression (21) and cross-validation for model-parameter selection (the shape of the fit is determined by the data). This combined approach allowed us to minimize the effect of short-term variability on the 18-year trends. Relative to previous studies (4, 5, 13, 22), we have improved estimations by (i) using 18-year continuous records, (ii) implementing a time series averaging

¹Scripps Institution of Oceanography, University of California, San Diego, CA, USA. ²Earth & Space Research, Corvallis, OR, USA.

*Corresponding author. E-mail: fpaolo@ucsd.edu

Fig. 1. Eighteen years of change in thickness and volume of Antarctic ice shelves. Rates of thickness change (meters per decade) are color-coded from -25 (thinning) to +10 (thickening). Circles represent percentage of thickness lost (red) or gained (blue) in 18 years. Only significant values at the 95% confidence level are plotted (table S1). (Bottom left) Time series and polynomial fit of average volume change (cubic kilometers) from 1994 to 2012 for the West (in red) and East (in blue) Antarctic ice shelves. The black curve is the polynomial fit for All Antarctic ice shelves. We divided Antarctica into eight regions (Fig. 3), which are labeled and delimited by line segments in black. Ice-shelf perimeters are shown as a thin black line. The central circle demarcates the area not surveyed by the satellites (south of 81.5°S). Original data were interpolated for mapping purposes (percentage area surveyed of each ice shelf is provided in table S1). Background is the Landsat Image Mosaic of Antarctica (LIMA).

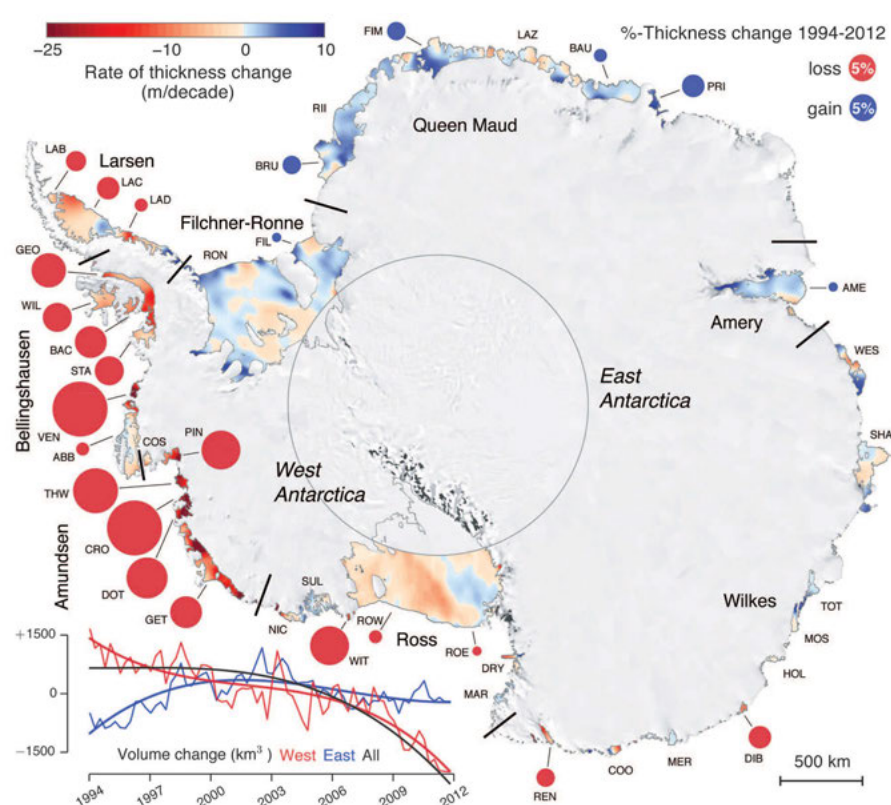
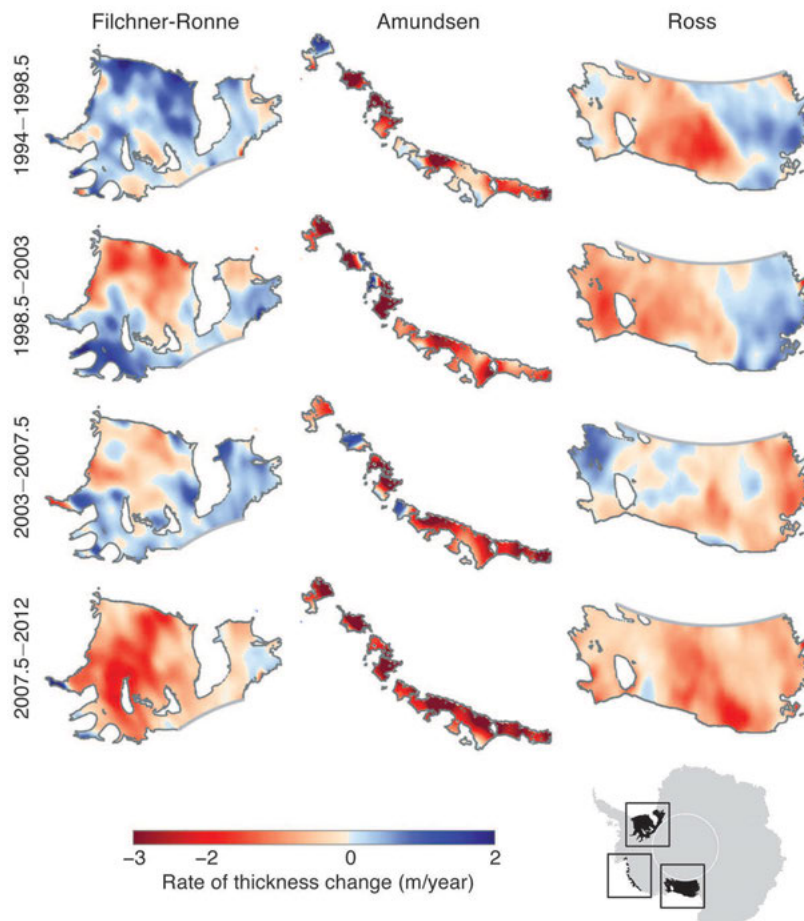


Fig. 2. Variability in the rate of Antarctic ice-shelf thickness change (meters per year). Maps for (columns from left to right) Filchner-Ronne, Amundsen, and Ross ice shelves (locations in the bottom right corner) showing average rate of thickness change for (rows) four consecutive 4.5-year intervals (1994–1998.5, 1998.5–2003, 2003–2007.5, and 2007.5–2012). Shorter-term rates can be higher than those from an 18-year interval. Ice-shelf perimeters are thin black lines, and the thick gray line demarcates the limit of satellite observations.



scheme so as to enhance the signal-to-noise ratio, and (iii) using a robust approach to trend extraction.

The 18-year average rate of thickness change varies spatially (Fig. 1). On shorter time scales, trends are highly variable but spatially coherent (Fig. 2 and movie S1). We divided our data set into eight regions on the basis of spatial coherence of long-term ice-shelf behavior and calculated time series of ice-shelf thickness change (relative to series mean) for each region (Fig. 3). The largest regional thickness losses were in the Amundsen and Bellingshausen seas, with average (and maximum) thinning rates of 19.4 ± 1.9 (66.5 ± 9.0) m/decade and 7.4 ± 0.9 (64.4 ± 4.9) m/decade, respectively. These values correspond to ~8 and 5% of thickness loss over the 18 years for the two regions, respectively. These two regions account for less than 20% of the total West Antarctic ice-shelf area but, combined, contribute more than 85% of the total ice-shelf volume loss from West Antarctica. The area-averaged time records of ice-shelf thickness and volume for the West and East Antarctic sectors (Fig. 1, bottom left), broad regions (Fig. 3), and single ice shelves (fig. S1) at 3-month time intervals show a wide range of temporal responses with large interannual-to-decadal fluctuations, stressing the importance of long records for determining the long-term state of the ice shelves. Comparing our long records with simple linear trends obtained for the periods of single satellite missions [such as the 5-year ICESat time span used in (5)] shows that it is often not possible to capture the persistent signals in the shorter records (Fig. 3 and fig. S1).

Ice-shelf average thinning rates from the 18-year polynomial fits in the Amundsen Sea region (AS) range from 1.5 ± 0.9 m/decade for Abbot to 31.1 ± 5.4 m/decade for Crosson, with local maximum thinning of 66.5 ± 9.0 m/decade on Getz (fig. S1 and table S1). Crosson and Getz have lost ~18 and 6% of their thicknesses, respectively, over the 18-year period. If this thinning persists for these two ice shelves, we can expect volume losses of ~100 and 30%, respectively, in the next 100 years. Getz is the single largest contributor to the overall volume loss of Antarctic ice shelves, with an average change of -54 ± 5 km³/year, accounting for ~30% of the total volume loss from the West Antarctic ice shelves (table S1). We find the most dramatic thickness reduction on Venable Ice Shelf in the Bellingshausen Sea (BS), with an average (and maximum) thinning rate of 36.1 ± 4.4 (64.4 ± 4.9) m/decade, respectively (fig. S1 and table S1). This ice shelf has lost 18% of its thickness in 18 years, which implies complete disappearance in 100 years.

For the ice shelves in the AS, observed rates are highest near the deep grounding lines, with lower rates found toward the shallower ice fronts (Fig. 2, table S1, and movie S1). This pattern is consistent with enhanced melting underneath the ice shelf forced by an increased flux of circumpolar deep water (CDW) from across the continental shelf and into the sub-ice-shelf cavity (22, 23, 24). The consequent loss of ice-shelf but-

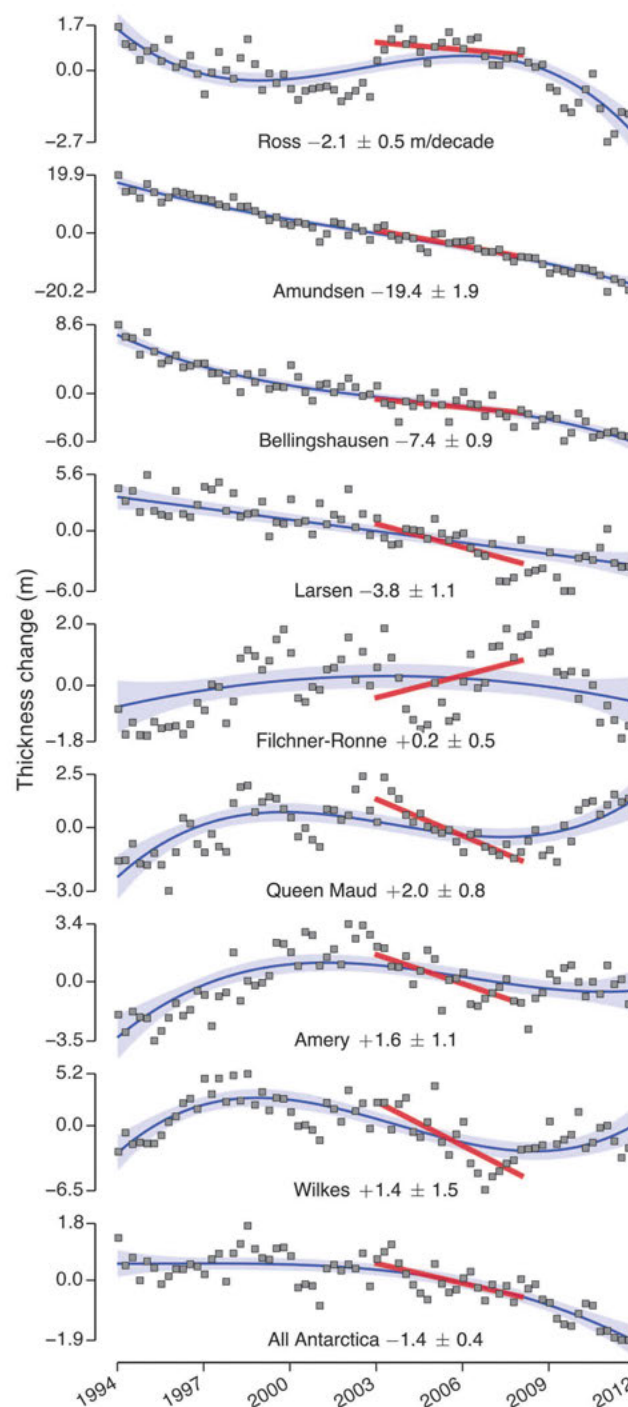


Fig. 3. Time series of cumulative thickness change relative to series mean for Antarctic ice-shelf regions (1994–2012).

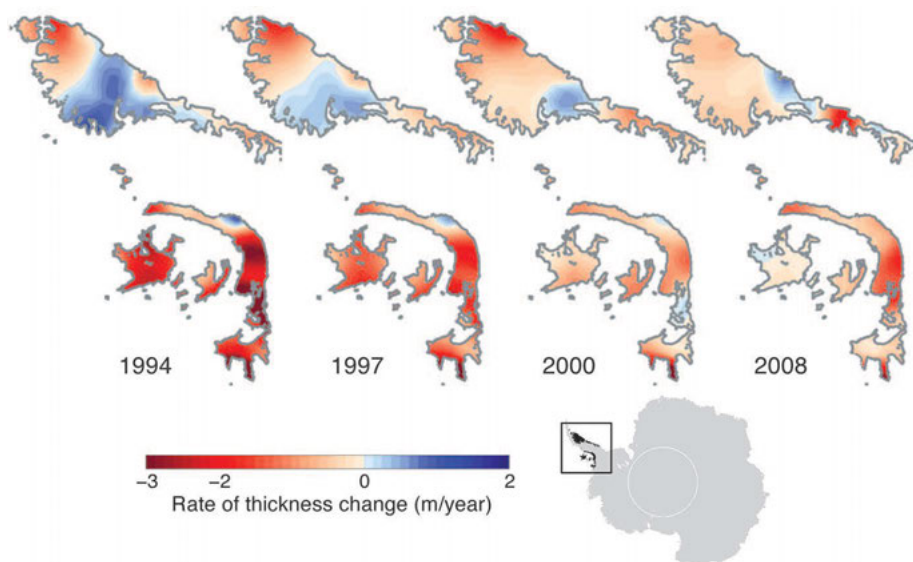
Time series correspond to averages for all ice-shelf data within the Antarctic regions defined in Fig. 1. Dots represent average thickness change every 3 months. Error bars are small (in many cases, smaller than the symbols themselves, thus omitted from the plots), making the interannual fluctuation shown by the dots significant. The blue curve is the long-term trend from polynomial regression with the 95% confidence band (18), and the red line shows the regression line to the segment of our data set that overlaps with the period used for a prior ICESat-based analysis (2003–2008) (5). Average rates (in meters per decade) are derived from the end points of the polynomial models.

tredding from increased ocean-forced melting may have driven the grounding lines inland (25) to a point on a retrograde bed slope at which the marine ice-sheet instability mechanism can take over the dynamics of ice export (7, 26). Hence, observed ice-shelf thinning reflects both ocean-induced basal melting and increased strain rates resulting from faster flows. Our analysis shows that thinning was already under way at a substantial rate at the start of our record in 1994.

On the eastern side of the Antarctic Peninsula [comprising Larsen B (Scar Inlet remnant), Larsen

C, and Larsen D], the regional ice-shelf thinning rate of 3.8 ± 1.1 m/decade (Fig. 3) is about half of that on the western side (BS) (Fig. 1). The onset of thinning for Larsen C has progressed southward (Fig. 4), which is consistent with climate-driven forcing discussed in earlier studies (22, 27). The highest thinning rates on Larsen C (with local maximum thinning of 16.6 ± 8.1 m/decade) are near Bawden Ice Rise (Figs. 1 and 4). Assuming that half of this observed thinning is due to air loss within the firn column, and considering that the ice shelf is ~40 m above flotation over

Fig. 4. Evolution of the rate of thickness change in the Antarctic Peninsula. Instantaneous rate-of-thickness change (meters per year) for four specific times (1994, 1997, 2000, and 2008) is calculated as the derivative of the polynomial fit to the thickness-change time series. The rate increases spatially with time from north to south in the Larsen Ice Shelf (movie S1). The eastern (Weddell Sea) side of the Antarctic Peninsula (top) shows independent behavior from the western (Bellingshausen Sea) side (bottom).



the ice rise (28), we can expect Larsen C to fully unground from this pinning point within the next 100 years, with potential consequences on the ice-shelf stability (29).

The regional time-varying trends for the ice shelves in the three East Antarctic regions (Queen Maud, Amery, and Wilkes) are coherent (Fig. 3). Ice shelves in the Wilkes region are challenging for conventional radar altimeters because many of them are small, contained in narrow embayments, and have rough surfaces so that altimeter-derived height changes do not necessarily reflect thickness change accurately. Our estimate of overall thickness change for the Wilkes ice shelves is 1.4 ± 1.5 m/decade, which is not significantly different from zero. The Queen Maud region ice shelves show an overall increase in thickness of 2.0 ± 0.8 m/decade.

Like the AS ice shelves, Totten and Moscow University ice shelves in the Wilkes region buttress a large marine-based section of the East Antarctic ice sheet so that their stability is potentially important to grounded-ice loss. Although these ice shelves were previously reported as thinning (5) on the basis of a straight-line fit to a 5-year record from a satellite laser altimeter (ICESat, 2003–2008), our results show that those estimates are not representative of the longer-term trends (fig. S1B). Our estimate of thickness loss during 2003–2008 is similar to the ICESat-based result, but the full 18-year period shows thickness trends that are not significantly different from zero (fig. S2).

For most ice shelves, our estimates are significantly different from previous results (table S2). Several factors contribute to this. (i) The areas of ice shelves over which measurements are averaged vary between studies, affecting estimates on small ice shelves with large thickness-change signals. (ii) Because of our grid resolution, ice shelf mask, and limited data coverage, we cannot sample near the grounding line of some ice shelves (such as Pine Island or Dotson); in such cases,

our estimated changes are likely to represent a lower bound (changes could be larger). (iii) Radar altimeters are less sensitive than are laser altimeters to variations in surface mass balance owing to penetration of the radar signal into the firn layer. (iv) Short records and previous trend-extraction approaches could not capture and account for fluctuations in the underlying trend (fig. S3). This is the dominant factor affecting comparisons between our results and previous studies.

The total volume of East Antarctic ice shelves increased during 1994–2003 by 148 ± 45 km³/year, followed by moderate loss (56 ± 37 km³/year), whereas West Antarctic ice shelves exhibited persistent volume loss over the 18 years, with marked acceleration after 2003 (Fig. 1). Before and after 2003, this region lost volume by 144 ± 45 and 242 ± 47 km³/year, respectively, corresponding to $\sim 70\%$ increase in the average loss rate. The total circum-Antarctic ice-shelf volume loss was negligible (25 ± 64 km³/year) during 1994–2003 and then declined rapidly by 310 ± 74 km³/year after 2003. Overall, from 1994 to 2012 Antarctic ice-shelf volume changed on average by -166 ± 48 km³/year, with mean acceleration of -31 ± 10 km³/year² (-51 ± 33 km³/year² for the period 2003–2012).

We have shown that Antarctic ice-shelf volume loss is accelerating. In the Amundsen Sea, some ice shelves buttressing regions of grounded ice that are prone to instability have experienced sustained rapid thinning for almost two decades. If the present climate forcing is sustained, we expect a drastic reduction in volume of the rapidly thinning ice shelves at decadal to century time scales, resulting in grounding-line retreat and potential ice-shelf collapse. Both of these processes further accelerate the loss of buttressing, with consequent increase of grounded-ice discharge and sea-level rise. On smaller scales, ice-shelf thickness variability is complex, demonstrating that results from single satellite missions with typical durations of a few years are

insufficient to draw conclusions about the long-term response of ice shelves. Large changes occur over a wide range of time scales, with rapid variations of ice-shelf thickness suggesting that ice shelves can respond quickly to changes in oceanic and atmospheric conditions.

REFERENCES AND NOTES

1. A. Shepherd *et al.*, *Science* **338**, 1183–1189 (2012).
2. T. C. Sutterley *et al.*, *Geophys. Res. Lett.* **41**, 8421–8428 (2014).
3. I. Joughin, R. B. Alley, *Nat. Geosci.* **4**, 506–513 (2011).
4. A. Shepherd *et al.*, *Geophys. Res. Lett.* **37**, L13503 (2010).
5. H. D. Pritchard *et al.*, *Nature* **484**, 502–505 (2012).
6. T. A. Scambos, J. A. Bohlander, C. A. Shuman, P. Skvarca, *Geophys. Res. Lett.* **31**, L18402 (2004).
7. C. Schoof, *J. Geophys. Res.* **112**, F03S28 (2007).
8. D. Goldberg, D. M. Holland, C. Schoof, *J. Geophys. Res.* **114**, F04026 (2009).
9. L. Favier *et al.*, *Nat. Clim. Change* **4**, 117–121 (2014).
10. I. Joughin, B. E. Smith, B. Medley, *Science* **344**, 735–738 (2014).
11. T. Scambos, C. Hulbe, M. Fahnestock, in *Antarctic Peninsula Climate Variability: Historical and Paleoenvironmental Perspectives*, E. Domack *et al.*, Eds. (American Geophysical Union, Washington, DC, 2003), vol. 79, pp. 79–92.
12. P. Dutrieux *et al.*, *Science* **343**, 174–178 (2014).
13. H. J. Zwally *et al.*, *J. Glaciol.* **51**, 509–527 (2005).
14. E. Rignot, S. Jacobs, J. Mouginot, B. Scheuchl, *Science* **341**, 266–270 (2013).
15. M. A. Depoorter *et al.*, *Nature* **502**, 89–92 (2013).
16. C. H. Davis, A. C. Ferguson, *IEEE Trans. Geosci. Rem. Sens.* **42**, 2437–2445 (2004).
17. D. J. Wingham, D. W. Wallis, A. Shepherd, *Geophys. Res. Lett.* **36**, L17501 (2009).
18. Materials and methods are available as supplementary materials on Science Online.
19. B. Efron, R. J. Tibshirani, *An Introduction to the Bootstrap*, vol. 57 of *Monographs on Statistics and Applied Probability* (Chapman and Hall, New York, 1993).
20. Corrections include lag of the satellite's leading-edge tracker (retracking), surface scattering variations, surface slope, dry atmospheric mass, water vapor, the ionosphere, solid Earth tide, ocean tide and loading, atmospheric pressure, and regional sea-level variation (18).
21. R. Tibshirani, *J. R. Stat. Soc. B* **58**, 267–288 (1996).

22. H. A. Fricker, L. Padman, *J. Geophys. Res.* **117**, C02026 (2012).
23. S. S. Jacobs, A. Jenkins, C. F. Giulivi, P. Dutrieux, *Nat. Geosci.* **4**, 519–523 (2011).
24. M. Thoma, A. Jenkins, D. Holland, S. Jacobs, *Geophys. Res. Lett.* **35**, L18602 (2008).
25. E. Rignot, J. Mouginot, M. Morlighem, H. Seroussi, B. Scheuchl, *Geophys. Res. Lett.* **41**, 3502–3509 (2014).
26. J. Weertman, *J. Glaciol.* **13**, 3–11 (1974).
27. A. J. Cook, D. G. Vaughan, *Cryosphere* **4**, 77–98 (2010).
28. P. R. Holland *et al.*, *Cryosphere Discuss.* **9**, 251–299 (2015).

29. C. P. Borstad, E. Rignot, J. Mouginot, M. P. Schodlok, *Cryosphere* **7**, 1931–1947 (2013).

ACKNOWLEDGMENTS

This work was funded by NASA [awards NNX12AN50H 002 (93735A), NNX10AG19G, and NNX13AP60G]. This is ESR contribution 154. We thank J. Zwally's Ice Altimetry group at the NASA Goddard Space Flight Center for distributing their RA data sets for all satellite radar altimeter missions (<http://icesat4.gsfc.nasa.gov>). We thank C. Davis and D. Wingham for RA-processing advice. We thank A. Shepherd and anonymous reviewers for their comments on the manuscript.

SUPPLEMENTARY MATERIALS

www.sciencemag.org/content/348/6232/327/suppl/DC1
Materials and Methods
Figs. S1 to S4
Table S1 and S2
References (30–46)
Movie S1

17 October 2014; accepted 11 March 2015
Published online 26 March 2015;
10.1126/science.aaa0940

OCEAN CHEMISTRY

Dilution limits dissolved organic carbon utilization in the deep ocean

Jesús M. Arrieta,^{1,2*} Eva Mayol,¹ Roberta L. Hansman,³ Gerhard J. Herndl,^{3,4} Thorsten Dittmar,⁵ Carlos M. Duarte^{1,2,6}

Oceanic dissolved organic carbon (DOC) is the second largest reservoir of organic carbon in the biosphere. About 72% of the global DOC inventory is stored in deep oceanic layers for years to centuries, supporting the current view that it consists of materials resistant to microbial degradation. An alternative hypothesis is that deep-water DOC consists of many different, intrinsically labile compounds at concentrations too low to compensate for the metabolic costs associated to their utilization. Here, we present experimental evidence showing that low concentrations rather than recalcitrance preclude consumption of a substantial fraction of DOC, leading to slow microbial growth in the deep ocean. These findings demonstrate an alternative mechanism for the long-term storage of labile DOC in the deep ocean, which has been hitherto largely ignored.

The accepted paradigm is that recalcitrant dissolved organic carbon (DOC) is ubiquitous in the ocean and makes up the bulk of the DOC pool at depths of >1000 m and at DOC concentrations below 42 $\mu\text{mol C liter}^{-1}$ (1). However, most of the components of the recalcitrant DOC pool remain unidentified (1, 2), and there is little evidence of structural properties that could make these compounds unavailable to microbial degradation. Conversely, the dilution hypothesis (3, 4) postulates that most organic substrates in the deep ocean are labile but cannot be used by prokaryotes at concentrations below the levels matching the energetic investment required for their uptake and degradation.

An early study (5) tested the dilution hypothesis by looking for microbial consumption in concentrations of natural DOC from deep waters, but found no substantial changes in DOC concentrations after a 2-month incubation. Those results led to the conclusion that deep-water DOC is composed of recalcitrant molecules and therefore to the dismissal of the dilution hypothesis. Here, we revisit the dilution hypothesis using a simple experimental approach, similar to that used by Barber in 1968 (5) but using methodologies not available at that time. Specifically, we tested the hypothesis that no significant increase in prokaryotic growth should be detectable when increasing DOC concentrations, which is as expected if deep oceanic DOC were structurally refractory.

Natural prokaryotic communities collected at 14 stations between 1000 to 4200 m in the Pacific and Atlantic Ocean (fig. S1) were exposed to ambient, 2-, 5- and 10-fold concentrations of natural DOC collected from their original location by means of solid phase extraction (6, 7) and incubated at in situ temperature. A consistent increase in prokaryotic abundance over time was observed in response to increasing concentrations of DOC in all 14 experiments (Fig. 1 and fig. S2). Maximum prokaryotic abundances obtained at ~10-fold DOC concentrations were 3.6 to 11.7 times higher than those observed in the corresponding controls (Fig. 1 and fig. S2). Unamended

controls showed much lower, sometimes undetectable, prokaryotic growth, comparable with the values observed in deep layers of the ocean in other studies (8, 9), whereas specific growth rates in the higher DOC enrichments showed values up to 0.4 days⁻¹, which is typical of productive surface waters (Fig. 2 and fig. S3). No significant differences (*t* test, *P* > 0.05) in prokaryotic growth were observed between unamended controls and extraction controls, confirming that the observed growth was due to the materials being extracted from seawater and not the result of a contamination with labile organics during the extraction procedure (fig. S4). The solid phase extraction method used to concentrate natural dissolved organic matter (DOM) may have introduced some compositional bias toward small and polar compounds while losing a substantial part of the DOM pool (extraction efficiency ~40%), but this does not change the fact that increasing the concentration of the extractable components of natural DOC resulted in enhanced prokaryotic growth. Chemical alterations of DOC, such as the disruption of supramolecular arrangements (10) or mild hydrolysis produced during the concentration procedure, are an unlikely explanation for the observed response because the treatments in which DOC concentration was doubled by adding concentrated DOC showed little or no enhancement of prokaryotic growth as compared with that of controls. Hence, we validated the dilution hypothesis tested, showing that dilution limits C utilization in the deep ocean.

Specific growth rates increased with DOC concentrations following a classical Monod model [coefficient of determination (*R*²) of 0.71 to 0.98] at all the locations studied (Fig. 2, fig. S3, and table S2), further confirming the hypothesis that prokaryotic growth in deep waters is limited by the concentration of DOC. In 9 out of 14 experiments, the initial in situ DOC concentration was low enough to capture the lower part of the curve and thus to give an estimate of the minimum DOC concentration necessary to support prokaryotic maintenance metabolism (Fig. 2, fig. S3, and table S2). According to these estimates, concentrations of natural DOC below 30.7 ± 5.4 $\mu\text{mol C L}^{-1}$ (average ± SE, *n* = 9 measurements) would not be sufficient to support prokaryotic metabolism, a value not significantly different (*t* test, *P* > 0.05) from the lowest concentrations of DOC around 34 $\mu\text{mol C liter}^{-1}$ reported for the deep ocean (11).

¹Department of Global Change Research, Institut Mediterrani d'Estudis Avançats (IMEDEA), Consejo Superior de Investigaciones Científicas (CSIC)/Universidad de las Islas Baleares (UIB), 07190 Esporles, Spain. ²Red Sea Research Center, King Abdullah University of Science and Technology (KAUST), Thuwal 23955-6900, Kingdom of Saudi Arabia.

³Department of Limnology and Bio-Oceanography, Division Bio-Oceanography, University of Vienna, Althanstr. 14, 1090 Vienna, Austria. ⁴Department of Biological Oceanography, Royal Netherlands Institute for Sea Research (NIOZ), 1790AB Den Burg, Netherlands. ⁵Research Group for Marine Geochemistry (ICBM-MPI Bridging Group), Institute for Chemistry and Biology of the Marine Environment (ICBM), Carl von Ossietzky University Oldenburg, and Max Planck Institute for Marine Microbiology (MPI), Bremen, Germany. ⁶The UWA Oceans Institute, University of Western Australia (UWA), Crawley, WA, Australia.

*Corresponding author. E-mail: txetxu@mail.com

Prokaryotic growth efficiency (PGE) in the unamended controls was always lower than 3%, which is similar to the values reported for deep-water masses (9). No statistically significant differences among treatments were detected in our PGE estimates because of the accumulation of errors propagating from the original measurements (one-way analysis of variance, $P > 0.05$). However, growth efficiency estimates show a consistent tendency to increase with increasing DOC concentration in all the experiments (fig. S5), suggesting a positive effect of concentration that could be related to a relief from substrate limitation (12). An increasing growth efficiency with increasing DOC concentrations cannot be explained if the bulk of the DOC components were structurally recalcitrant. The differences between our results and those reported by Barber in 1968 are probably due to a combination of methodological improvements. We used only dissolved materials, whereas Barber used a concentrate of everything with nominal size >500 daltons, including particulate matter. Thus, true DOC concentrations in Barber's experiments were probably not as high as intended. Also, a large fraction of marine DOC consists of molecules <500 daltons (fig. S7) (13, 14); thus, the composition was biased toward higher-molecular-weight compounds in Barber's experiments, meaning that the molar enrichment in his fivefold C concentration treatment was probably much lower than in our experiments.

In the four experiments carried out in the North Atlantic, incubations were kept on the ship for an additional month after the cruise until the ship returned to the harbor (fig. S2, K to N). Prokaryotic abundance remained essentially constant during the additional month in all but one of the experiments (M), in which a second phase of intense growth was observed in the most concentrated treatments (fig. S2). Although it is unclear why this happened, we can rule out contamination because growth occurred in all replicates, and a pronounced decrease in DOC was found in these samples (fig. S6). The appearance of large cells in the flow cytograms, indicating substantial growth of heterotrophic protists (15) in the late stages of the more concentrated cultures, and the fact that the prokaryotic carbon demand inferred from the increase in abundance and growth efficiency was much lower than the measured decrease in DOC concentration indicate that labile DOC was still being consumed at the end of the experiments, even when no increase in prokaryotic abundance was detectable owing to enhanced prokaryotic mortality.

A corollary to the dilution hypothesis is that bulk DOC is composed of a large diversity of individual molecules. Indeed, molecular characterization by means of Fourier-transform ion cyclotron resonance mass spectrometry (FT-ICR-MS) (fig. S7) (13, 14) shows that marine DOC is composed of a very large variety of small molecules (200 to 700 daltons) present in very low concentrations and adding up to a large pool of apparently recalcitrant DOC. We characterized the changes caused by microbial activity on the molecular composition of deep oceanic DOM in

two additional experiments (O and P) in unamended seawater and in samples in which the concentration of in situ DOC was raised to approximately five times the original concentration. Molecular characterization by means of FT-ICR-MS showed a highly reproducible pattern of microbial utilization among replicate-independent incubations (fig. S8), affecting a large number of different molecules (fig. S9). Significant utilization (relative signal in replicate incubations significantly lower than in the corresponding initial samples; t test $P < 0.05$) was found for 2095 and 1753 different compounds in the controls and for 2846 and 936 different compounds in the 5 \times -concentrated samples for experiments O and P,

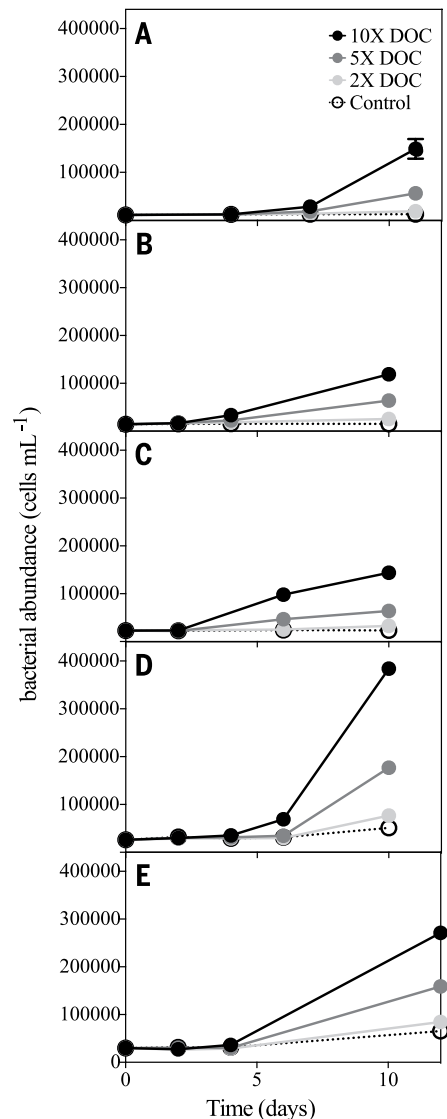


Fig. 1. Prokaryotic abundance in experimental treatments containing approximately 2, 5, and 10 times the in situ DOC concentration versus controls containing unamended seawater. (A to E) Error bars represent the standard error of the mean of triplicate cultures. Only the five experiments carried out in the North Pacific (experiments A to E) are represented. The results of the 14 experiments are shown in fig. S2.

respectively. Consistent differences could be observed between the set of molecules used in concentrated versus unamended samples, resulting in a total of 3950 different molecules consumed in either the concentrated samples or the controls for experiment O and 2140 in experiment P. Moreover, the sum of the normalized signal of all the peaks in the FT-ICR-MS fingerprint in which significant consumption was detected in either concentrates or controls was $>70\%$ in experiment O and $>40\%$ in experiment P, indicating that a major fraction of the original DOC consisted of labile compounds.

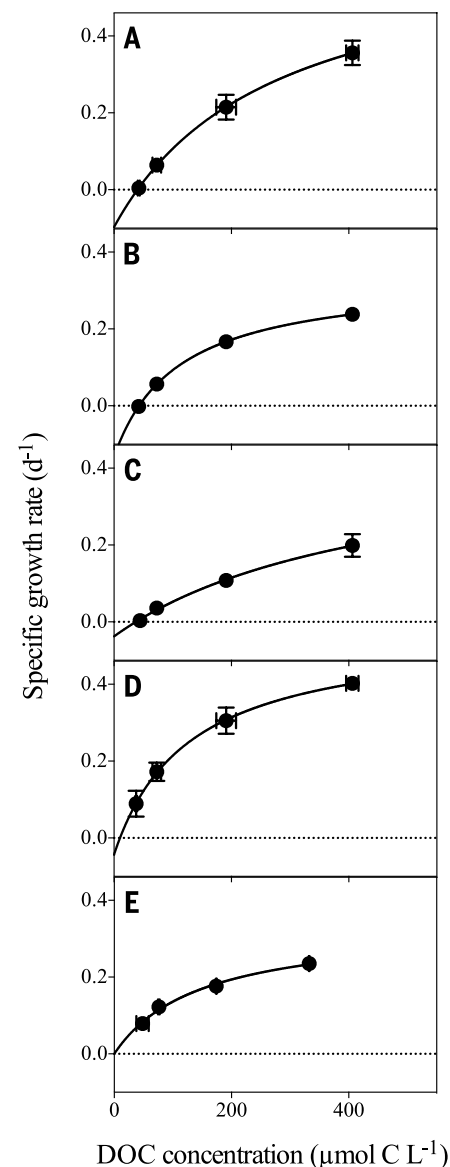


Fig. 2. Specific growth rates at different concentrations of DOC. Horizontal error bars represent the standard deviation of the mean initial DOC concentration measured in the triplicate cultures, and vertical error bars represent the standard deviation of the mean of the specific growth rates estimated for each of the triplicate cultures. Only the five experiments carried out in the North Pacific (experiments A to E) are shown. The results of the 14 experiments are available in figure S3.

The dilution hypothesis provides an alternative framework with which to explain observations of the apparent recalcitrance of DOC and lends a physiological meaning to the operationally defined “semi-labile” and “semi-refractory” fractions (16, 17). We hypothesize that under the dilution hypothesis, very heterogeneous mixtures of labile compounds appear semirefractory, whereas increasingly less diverse DOM assemblages containing larger concentrations of some substrates will present higher microbial growth and DOC turnover rates, resulting in increasing degrees of apparent lability. The microbial generation of apparently recalcitrant material (18) from labile substrates in a process recently dubbed the “microbial carbon pump” (19) can also be explained with the dilution hypothesis. Microbial utilization of abundant, labile compounds results in hundreds of different metabolites (20), which are subsequently consumed down to the lowest utilizable concentration. This mechanism explains observations of relatively concentrated, labile materials being transformed into apparently recalcitrant matter through microbial consumption (18) but does not necessarily imply the formation of structurally recalcitrant molecules. Indeed, “recalcitrant” DOC is not defined structurally, but operationally, as the DOC pool remaining after long experimental incubations or as the fraction transported in an apparently conservative manner with the ocean circulation (1). Thus, the dilution hypothesis severely limits the feasibility of geoengineering efforts to enhance carbon storage in the deep ocean (21) by using the microbial carbon pump.

FT-ICR-MS characterization of DOC from different oceans (13, 14, 22, 23) and also from this study (fig. S5) shows no indication of prevalent, intrinsically recalcitrant compounds accumulating in substantial amounts. Conversely, FT-ICR-MS data show that oceanic DOC is a complex mixture of minute quantities of thousands of organic molecules, which is in good agreement with the dilution hypothesis. Mean radiocarbon ages of deep oceanic DOC in the range of 4000 to 6000 years have been considered as evidence for its recalcitrant nature (24, 25). However, these are average ages of a pool containing a mixture of very old molecules >12,000 years old but also featuring a large proportion of contemporary materials (26). Moreover, elevated radiocarbon ages only demonstrate that these old molecules are not being newly produced at any appreciable rate—because that would lower their isotopic age—but does not necessarily imply that they are structurally recalcitrant. Furthermore, it is unlikely that natural organic molecules can accumulate in the ocean in substantial concentrations and remain recalcitrant or be preserved for millennia when degradation pathways for novel synthetic pollutants evolve soon after these compounds are released in nature (27).

Although there might be a truly recalcitrant component in deep oceanic DOC, our results clearly show that the concentration of individual labile molecules is a major factor limiting the utilization of a substantial fraction of deep oceanic DOC. These results provide, therefore, a robust and parsimonious explanation for the long-term pre-

servation of labile DOC into one of the largest reservoirs of organic carbon on Earth, opening a new avenue in our understanding of the global carbon cycle.

REFERENCES AND NOTES

1. D. A. Hansell, *Annu. Rev. Mar. Sci.* **5**, 421–445 (2013).
2. E. B. Kujawinski, *Annu. Rev. Mar. Sci.* **3**, 567–599 (2011).
3. H. W. Jannasch, *Limnol. Oceanogr.* **12**, 264–271 (1967).
4. H. W. Jannasch, *Global Planet. Change* **9**, 289–295 (1994).
5. R. T. Barber, *Nature* **220**, 274–275 (1968).
6. Materials and methods are available as supplementary materials on Science Online.
7. T. Dittmar, B. Koch, N. Hertkorn, G. Kattner, *Limnol. Oceanogr. Methods* **6**, 230–235 (2008).
8. D. L. Kirchman, X. A. G. Morán, H. Ducklow, *Nat. Rev. Microbiol.* **7**, 451–459 (2009).
9. T. Reinthaler et al., *Limnol. Oceanogr.* **51**, 1262–1273 (2006).
10. A. Nebbioso, A. Piccolo, *Anal. Bioanal. Chem.* **405**, 109–124 (2013).
11. D. A. Hansell, C. A. Carlson, D. J. Repeta, R. Schlitzer, *Oceanography (Wash. D.C.)* **22**, 202–211 (2009).
12. A. Konopka, *Curr. Opin. Microbiol.* **3**, 244–247 (2000).
13. G. Kattner, M. Simon, B. Koch, in *Microbial Carbon Pump in the Ocean*, N. Jiao, F. Azam, S. Sanders, Eds. (Science/AAAS, Washington, DC, 2011), pp. 60–61.
14. T. Dittmar, J. Paeng, *Nat. Geosci.* **2**, 175–179 (2009).
15. M. V. Zubkov, P. H. Burkhill, J. N. Topping, *J. Plankton Res.* **29**, 79–86 (2007).
16. C. A. Carlson, H. W. Ducklow, A. F. Michaels, *Nature* **371**, 405–408 (1994).
17. J. H. Sharp et al., *Estuaries Coasts* **32**, 1023–1043 (2009).
18. H. Ogawa, Y. Amagai, I. Koike, K. Kaiser, R. Benner, *Science* **292**, 917–920 (2001).
19. N. Jiao et al., *Nat. Rev. Microbiol.* **8**, 593–599 (2010).
20. R. P. Mahajan, S. Seeto, T. Ferenci, *J. Bacteriol.* **189**, 2350–2358 (2007).
21. R. Stone, *Science* **328**, 1476–1477 (2010).
22. R. Flerus et al., *Biogeosciences* **9**, 1935–1955 (2012).
23. O. J. Lechtenfeld et al., *Geochim. Cosmochim. Acta* **126**, 321–337 (2014).

24. P. M. Williams, E. R. M. Druffel, *Nature* **330**, 246–248 (1987).
25. J. E. Bauer, in *Biogeochemistry of Marine Dissolved Organic Matter*, D. A. Hansell, C. A. Carlson, Eds. (Academic Press, San Diego, CA, 2002), pp. 405–453.
26. C. L. Follett, D. J. Repeta, D. H. Rothman, L. Xu, C. Santinelli, *Proc. Natl. Acad. Sci. U.S.A.* **111**, 16706–16711 (2014).
27. S. D. Copley, *Trends Biochem. Sci.* **25**, 261–265 (2000).

ACKNOWLEDGMENTS

This is a contribution to the Malaspina 2010 Expedition project, funded by the CONSOLIDER-Ingenio 2010 program of the from the Spanish Ministry of Economy and Competitiveness (Ref. CSD2008-00077). J.M.A. was supported by a “Ramón y Cajal” research fellowship from the Spanish Ministry of Economy and Competitiveness. E.M. was supported by a fellowship from the Junta para la Ampliación de Estudios program of CSIC. G.J.H. and R.L.H. were supported by the Austrian Science Fund (FWF) projects I486-B09 and P23234-B11 and by the European Research Council (ERC) under the European Community’s Seventh Framework Programme (FP7/2007-2013)/ERC grant agreement 268595 (MEDEA project). We thank A. Dorsett for assistance with DOC analyses, participants in the Malaspina Expedition and the crews of the BIO Hespérides, and RV Pelagia and the personnel of the Marine Technology Unit of CSIC for their invaluable support. Original data sets are available online at <http://digital.csic.es/handle/10261/111563>. J.M.A. designed the experimental setup, carried out part of the experiments, measured prokaryotic abundance, analyzed the data, and wrote the manuscript. E.M. carried out part of the experiments and data analysis. C.M.D. designed the Malaspina 2010 Expedition, was responsible for DOC analyses, and together with G.J.H. contributed to the design of the experiments and discussion of results. R.L.H. and T.D. analyzed the FT-ICR-MS samples. All authors discussed the results and contributed to the manuscript.

SUPPLEMENTARY MATERIALS

www.sciencemag.org/content/348/6232/331/suppl/DC1
Materials and Methods
Figs. S1 to S9
Tables S1 and S2
References (28–35)

18 July 2014; accepted 4 March 2015

Published online 19 March 2015;

10.1126/science.1258955

SOCIAL EVOLUTION

Oxytocin-gaze positive loop and the coevolution of human-dog bonds

Miho Nagasawa,^{1,2} Shouhei Mitsui,¹ Shiori En,¹ Nobuyo Ohtani,¹ Mitsuaki Ohta,¹ Yasuo Sakuma,³ Tatsushi Onaka,² Kazutaka Mogi,¹ Takefumi Kikusui^{1*}

Human-like modes of communication, including mutual gaze, in dogs may have been acquired during domestication with humans. We show that gazing behavior from dogs, but not wolves, increased urinary oxytocin concentrations in owners, which consequently facilitated owners’ affiliation and increased oxytocin concentration in dogs. Further, nasally administered oxytocin increased gazing behavior in dogs, which in turn increased urinary oxytocin concentrations in owners. These findings support the existence of an interspecies oxytocin-mediated positive loop facilitated and modulated by gazing, which may have supported the coevolution of human-dog bonding by engaging common modes of communicating social attachment.

Dogs are more skillful than wolves and chimpanzees, the closest respective relatives of dogs and humans, at using human social communicative behaviors (1). More specifically, dogs are able to use mutual gaze as a communication tool in the context of needs of affiliative help from others (2). Conver-

gent evolution between humans and dogs may have led to the acquisition of human-like communication modes in dogs, possibly as a by-product of temperament changes, such as reduced fear and aggression (1). This idea yields interesting implications that dogs were domesticated by coopting social cognitive systems in humans that

The dilution hypothesis provides an alternative framework with which to explain observations of the apparent recalcitrance of DOC and lends a physiological meaning to the operationally defined “semi-labile” and “semi-refractory” fractions (16, 17). We hypothesize that under the dilution hypothesis, very heterogeneous mixtures of labile compounds appear semirefractory, whereas increasingly less diverse DOM assemblages containing larger concentrations of some substrates will present higher microbial growth and DOC turnover rates, resulting in increasing degrees of apparent lability. The microbial generation of apparently recalcitrant material (18) from labile substrates in a process recently dubbed the “microbial carbon pump” (19) can also be explained with the dilution hypothesis. Microbial utilization of abundant, labile compounds results in hundreds of different metabolites (20), which are subsequently consumed down to the lowest utilizable concentration. This mechanism explains observations of relatively concentrated, labile materials being transformed into apparently recalcitrant matter through microbial consumption (18) but does not necessarily imply the formation of structurally recalcitrant molecules. Indeed, “recalcitrant” DOC is not defined structurally, but operationally, as the DOC pool remaining after long experimental incubations or as the fraction transported in an apparently conservative manner with the ocean circulation (1). Thus, the dilution hypothesis severely limits the feasibility of geoengineering efforts to enhance carbon storage in the deep ocean (21) by using the microbial carbon pump.

FT-ICR-MS characterization of DOC from different oceans (13, 14, 22, 23) and also from this study (fig. S5) shows no indication of prevalent, intrinsically recalcitrant compounds accumulating in substantial amounts. Conversely, FT-ICR-MS data show that oceanic DOC is a complex mixture of minute quantities of thousands of organic molecules, which is in good agreement with the dilution hypothesis. Mean radiocarbon ages of deep oceanic DOC in the range of 4000 to 6000 years have been considered as evidence for its recalcitrant nature (24, 25). However, these are average ages of a pool containing a mixture of very old molecules >12,000 years old but also featuring a large proportion of contemporary materials (26). Moreover, elevated radiocarbon ages only demonstrate that these old molecules are not being newly produced at any appreciable rate—because that would lower their isotopic age—but does not necessarily imply that they are structurally recalcitrant. Furthermore, it is unlikely that natural organic molecules can accumulate in the ocean in substantial concentrations and remain recalcitrant or be preserved for millennia when degradation pathways for novel synthetic pollutants evolve soon after these compounds are released in nature (27).

Although there might be a truly recalcitrant component in deep oceanic DOC, our results clearly show that the concentration of individual labile molecules is a major factor limiting the utilization of a substantial fraction of deep oceanic DOC. These results provide, therefore, a robust and parsimonious explanation for the long-term pre-

servation of labile DOC into one of the largest reservoirs of organic carbon on Earth, opening a new avenue in our understanding of the global carbon cycle.

REFERENCES AND NOTES

1. D. A. Hansell, *Annu. Rev. Mar. Sci.* **5**, 421–445 (2013).
2. E. B. Kujawinski, *Annu. Rev. Mar. Sci.* **3**, 567–599 (2011).
3. H. W. Jannasch, *Limnol. Oceanogr.* **12**, 264–271 (1967).
4. H. W. Jannasch, *Global Planet. Change* **9**, 289–295 (1994).
5. R. T. Barber, *Nature* **220**, 274–275 (1968).
6. Materials and methods are available as supplementary materials on Science Online.
7. T. Dittmar, B. Koch, N. Hertkorn, G. Kattner, *Limnol. Oceanogr. Methods* **6**, 230–235 (2008).
8. D. L. Kirchman, X. A. G. Morán, H. Ducklow, *Nat. Rev. Microbiol.* **7**, 451–459 (2009).
9. T. Reinthaler et al., *Limnol. Oceanogr.* **51**, 1262–1273 (2006).
10. A. Nebbioso, A. Piccolo, *Anal. Bioanal. Chem.* **405**, 109–124 (2013).
11. D. A. Hansell, C. A. Carlson, D. J. Repeta, R. Schlitzer, *Oceanography (Wash. D.C.)* **22**, 202–211 (2009).
12. A. Konopka, *Curr. Opin. Microbiol.* **3**, 244–247 (2000).
13. G. Kattner, M. Simon, B. Koch, in *Microbial Carbon Pump in the Ocean*, N. Jiao, F. Azam, S. Sanders, Eds. (Science/AAAS, Washington, DC, 2011), pp. 60–61.
14. T. Dittmar, J. Paeng, *Nat. Geosci.* **2**, 175–179 (2009).
15. M. V. Zubkov, P. H. Burkhill, J. N. Topping, *J. Plankton Res.* **29**, 79–86 (2007).
16. C. A. Carlson, H. W. Ducklow, A. F. Michaels, *Nature* **371**, 405–408 (1994).
17. J. H. Sharp et al., *Estuaries Coasts* **32**, 1023–1043 (2009).
18. H. Ogawa, Y. Amagai, I. Koike, K. Kaiser, R. Benner, *Science* **292**, 917–920 (2001).
19. N. Jiao et al., *Nat. Rev. Microbiol.* **8**, 593–599 (2010).
20. R. P. Mahajan, S. Seeto, T. Ferenci, *J. Bacteriol.* **189**, 2350–2358 (2007).
21. R. Stone, *Science* **328**, 1476–1477 (2010).
22. R. Flerus et al., *Biogeosciences* **9**, 1935–1955 (2012).
23. O. J. Lechtenfeld et al., *Geochim. Cosmochim. Acta* **126**, 321–337 (2014).

24. P. M. Williams, E. R. M. Druffel, *Nature* **330**, 246–248 (1987).
25. J. E. Bauer, in *Biogeochemistry of Marine Dissolved Organic Matter*, D. A. Hansell, C. A. Carlson, Eds. (Academic Press, San Diego, CA, 2002), pp. 405–453.
26. C. L. Follett, D. J. Repeta, D. H. Rothman, L. Xu, C. Santinelli, *Proc. Natl. Acad. Sci. U.S.A.* **111**, 16706–16711 (2014).
27. S. D. Copley, *Trends Biochem. Sci.* **25**, 261–265 (2000).

ACKNOWLEDGMENTS

This is a contribution to the Malaspina 2010 Expedition project, funded by the CONSOLIDER-Ingenio 2010 program of the from the Spanish Ministry of Economy and Competitiveness (Ref. CSD2008-00077). J.M.A. was supported by a “Ramón y Cajal” research fellowship from the Spanish Ministry of Economy and Competitiveness. E.M. was supported by a fellowship from the Junta para la Ampliación de Estudios program of CSIC. G.J.H. and R.L.H. were supported by the Austrian Science Fund (FWF) projects I486-B09 and P23234-B11 and by the European Research Council (ERC) under the European Community’s Seventh Framework Programme (FP7/2007-2013)/ERC grant agreement 268595 (MEDEA project). We thank A. Dorsett for assistance with DOC analyses, participants in the Malaspina Expedition and the crews of the BIO Hespérides, and RV Pelagia and the personnel of the Marine Technology Unit of CSIC for their invaluable support. Original data sets are available online at <http://digital.csic.es/handle/10261/111563>. J.M.A. designed the experimental setup, carried out part of the experiments, measured prokaryotic abundance, analyzed the data, and wrote the manuscript. E.M. carried out part of the experiments and data analysis. C.M.D. designed the Malaspina 2010 Expedition, was responsible for DOC analyses, and together with G.J.H. contributed to the design of the experiments and discussion of results. R.L.H. and T.D. analyzed the FT-ICR-MS samples. All authors discussed the results and contributed to the manuscript.

SUPPLEMENTARY MATERIALS

www.sciencemag.org/content/348/6232/331/suppl/DC1
Materials and Methods
Figs. S1 to S9
Tables S1 and S2
References (28–35)

18 July 2014; accepted 4 March 2015

Published online 19 March 2015;

10.1126/science.1258955

SOCIAL EVOLUTION

Oxytocin-gaze positive loop and the coevolution of human-dog bonds

Miho Nagasawa,^{1,2} Shouhei Mitsui,¹ Shiori En,¹ Nobuyo Ohtani,¹ Mitsuaki Ohta,¹ Yasuo Sakuma,³ Tatsushi Onaka,² Kazutaka Mogi,¹ Takefumi Kikusui^{1*}

Human-like modes of communication, including mutual gaze, in dogs may have been acquired during domestication with humans. We show that gazing behavior from dogs, but not wolves, increased urinary oxytocin concentrations in owners, which consequently facilitated owners’ affiliation and increased oxytocin concentration in dogs. Further, nasally administered oxytocin increased gazing behavior in dogs, which in turn increased urinary oxytocin concentrations in owners. These findings support the existence of an interspecies oxytocin-mediated positive loop facilitated and modulated by gazing, which may have supported the coevolution of human-dog bonding by engaging common modes of communicating social attachment.

Dogs are more skillful than wolves and chimpanzees, the closest respective relatives of dogs and humans, at using human social communicative behaviors (1). More specifically, dogs are able to use mutual gaze as a communication tool in the context of needs of affiliative help from others (2). Conver-

gent evolution between humans and dogs may have led to the acquisition of human-like communication modes in dogs, possibly as a by-product of temperament changes, such as reduced fear and aggression (1). This idea yields interesting implications that dogs were domesticated by coopting social cognitive systems in humans that

are involved in social attachment. The development of human-unique social cognitive modes may depend on specific temperament and social affiliation changes and may have consequently evolved differently from those of chimpanzees and bonobos (3). Thus, although humans and dogs exist on different branches of the evolutionary tree, both may have independently acquired tolerance of one another because of alterations in neural systems that mediate affiliation (1). These alterations may be related to paedomorphic characteristics in dogs, which enabled them to retain a degree of social flexibility and tolerance similar to that of humans (4, 5); therefore, it is plausible that a specific affiliative relationship developed between humans and dogs despite interspecies differences. This common social relationship change may have enabled cohabitation between humans and dogs and the eventual development of human-like modes of social communication in dogs.

Gaze plays an important role in human communication. Gaze not only facilitates the understanding of another's intention but also the establishment of affiliative relationships with others. In humans, "mutual gaze" is the most fundamental manifestation of social attachment between a mother and infant (6), and maternal oxytocin is positively associated with the duration of mother-to-infant gaze (7). Oxytocin plays a primary role in regulating social bonding between mother and infants and between sexual partners in monogamous species (8, 9). Moreover, activation of the oxytocin system enhances social reward (10) and inhibits stress-induced activity of the hypothalamic-pituitary-adrenal axis (11). It has therefore been suggested that these functions may facilitate dyadic interaction, such as an oxytocin-mediated positive loop of attachment and maternal behaviors between mother and infant (12, 13): Maternal nurturing activates the oxytocinergic system in the infant, thus enhancing attachment; this attachment then stimulates oxytocinergic activity in the mother, which facilitates further maternal behavior (9). Because the establishment of such an oxytocin-mediated positive loop requires the sharing of social cues and recognition of a particular partner, the study of oxytocin-mediated bonding has been restricted to intraspecies relationships.

The human-dog relationship is exceptional because it is an interspecies form of attachment. Dogs can discriminate individual humans (14, 15). Furthermore, dogs show distinctly different behavior toward caregivers as compared with hand-raised wolves (14), and interaction with dogs confers a social buffering effect to humans. Likewise, dogs also receive more social buffering effects from interacting with humans than from conspecifics (16). Tactile interaction between humans and dogs increases peripheral oxytocin concentrations in both humans and dogs (17, 18).

Further, social interaction initiated by a dog's gaze increases urinary oxytocin in the owner, whereas obstruction of the dog's gaze inhibits this increase (19). These results demonstrate that the acquisition of human-like social communication improves the quality of human-dog affiliative interactions, leading to the establishment of a human-dog bond that is similar to a mother-infant relationship. We hypothesized that an oxytocin-mediated positive loop, which originated in the intraspecies exchange of social affiliation cues, acts on both humans and dogs, and facilitates human-dog bonding. However, it is not known whether an oxytocin-mediated positive loop exists between humans and dogs as has been postulated between mother and infants, and whether this positive loop emerged during domestication.

We tested the hypothesis that an oxytocin-mediated positive loop exists between humans and dogs that is mediated by gaze. First, we examined whether a dog's gazing behavior affected urinary oxytocin concentrations in dogs and owners during a 30-min interaction. We also conducted the same experiment using hand-raised wolves, in order to determine whether this positive loop has been acquired by coevolution with humans. Second, we determined whether manipulating oxytocin in dogs through intranasal administration would enhance their gazing behavior toward their owners and whether this gazing behavior affected oxytocin concentrations in owners.

In experiment 1, urine was collected from the dogs and owners right before and 30 min after the interaction, and the duration of the follow-

ing behaviors was measured during the interaction: "dog's gaze at owner (dog-to-owner gaze)," "owner's talking to dog (dog-talking)," and "owner's touching of dog (dog-touching)." Dog owners were assigned to one of two groups: long gaze or short gaze (fig. S1). Wolves were tested with the same procedure and were compared with the two dog groups. Dogs in the long-gaze group gazed most at their owners among the three groups. In contrast, wolves rarely showed mutual gazing to their owners (Fig. 1A and fig. S2). After a 30-min interaction, only owners in the long-gaze group showed a significant increase in urinary oxytocin concentrations and the highest change ratio of oxytocin (Fig. 1, B and C). The oxytocin change ratio in owners correlated significantly with that of dogs, the duration of dog-to-owner gaze, and dog-touching. Moreover, the duration of the dog-to-owner gaze correlated with dog-talking and dog-touching (table S2A); however, through multiple linear regression analysis, we found that only the duration of dog-to-owner gaze significantly explained the oxytocin change ratio in owners. The duration of dog-touching showed a trend toward explaining oxytocin concentrations in owners (Table 1A). Similarly, a significantly higher oxytocin change ratio was observed in the dogs of the long-gaze group than in those of the short-gaze group (Fig. 1, D and E). The duration of dog-to-owner gaze also significantly explained the oxytocin change ratio in dogs, and the duration of dog-touching showed a trend toward explaining oxytocin concentrations in dogs by multiple linear regression analysis (Table 1A). In wolves, in contrast, the duration of wolf-to-owner gaze did

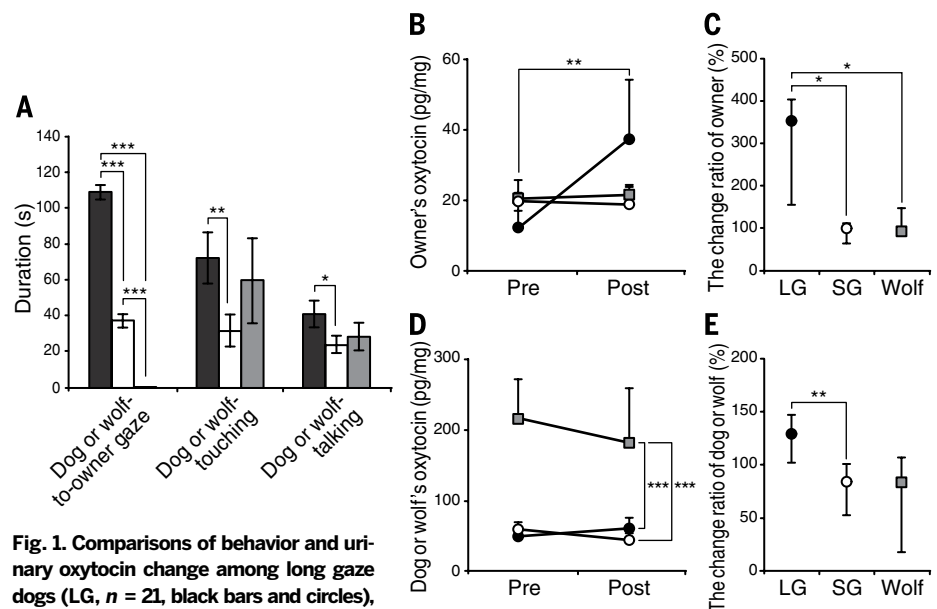


Fig. 1. Comparisons of behavior and urinary oxytocin change among long gaze dogs (LG, $n = 21$, black bars and circles), short gaze dogs (SG, $n = 9$, white bars and circles), and wolves (wolf, $n = 11$, gray bars and square). (A) Behavior during the first 5-min interaction. (B) and (D) Changes of urinary oxytocin concentrations after a 30-min interaction. Urinary oxytocin concentrations in owners (B) and dogs or wolves (D) collected before and after a 30-min interaction are shown. (C) and (E) Comparisons of the change ratio of urinary oxytocin among LG, SG, and wolf for owners (C) and dogs or wolves (E). The results of (A), (B), and (D) are expressed as mean \pm SE. (C) and (E) reflect median \pm quartile. * $P < 0.001$, ** $P < 0.01$, * $P < 0.05$.**

¹Department of Animal Science and Biotechnology, Azabu University, Sagamihara, Kanagawa, Japan. ²Department of Physiology, Jichi Medical University, Shimotsuke, Tochigi, Japan. ³University of Tokyo Health Sciences, Tama, Tokyo, Japan. *Corresponding author. E-mail: kikusu@azabu-u.ac.jp

not correlate with the oxytocin change ratio in either owners or wolves, and wolf-to-owner gaze did not explain the oxytocin change ratio in owners and wolves (tables S2B and S3). These results suggest that wolves do not use mutual gaze as a form of social communication with humans, which might be expected because wolves tend to use eye contact as a threat among conspecifics (20) and avoid human eye contact (27). Thus, dog-to-owner gaze as a form of social communications probably evolved during domestication and triggers oxytocin release in the owner, facilitating mutual interaction and affiliative communication and consequently activation of oxytocin systems in both humans and dogs in a positive loop.

In experiment 2, we evaluated the direct evidence of whether oxytocin administration enhanced dog gazing behavior and the subsequent increase in urinary oxytocin concentration in owners. This experiment involved 27 volunteers and their dogs, and participants unfamiliar to the dogs. A solution containing oxytocin or saline was administered to the dog and the dog then entered the experimental room, where the owner and two unfamiliar people were seated (fig. S4). Human behavior toward dogs was restricted to prevent the influence of extraneous stimuli on dog behavior and/or urinary oxytocin concentration. They were forbidden to talk to each other or to

touch the dog voluntarily. Urine samples from the owner and the dog were collected before and after the interaction and were later compared. The total amount of time that the dog gazed at, touched, and was close to the owner and the unfamiliar participants was also measured.

Oxytocin administration to dogs significantly increased the duration that the dog gazed at the owner in female dogs but not male dogs (Fig. 2A). Further, urinary oxytocin concentration significantly increased in the owners of female dogs that received oxytocin versus saline, even though oxytocin was not administered to the owners (Fig. 2D). No significant effect of oxytocin administration was observed in the other measured dog behaviors (Fig. 2, B and C). Furthermore, multiple linear regression analysis revealed that the

duration of gazing behavior significantly explained the oxytocin change ratio in owners (Table 1B). Thus, oxytocin administration enhances the gazing behavior of female dogs, which stimulates oxytocin secretion in their owners. Conversely, when interaction from humans was limited, no significant difference in urinary oxytocin concentrations in dogs was observed after the interaction in either the oxytocin or the saline conditions, and no significant oxytocin change ratio was found in dogs (Fig. 2, F and G). These results thus suggest that, although oxytocin administration may enhance dog gazing behavior and lead to an oxytocin increase in owners, limited owner-to-dog interaction may prevent the increased oxytocin secretion in dogs by breaking the oxytocin-mediated positive loop.

Table 1. Results of multiple linear regression analysis of oxytocin change ratio and behavioral variables in owners and dogs. * $P < 0.05$, $^{\dagger}P < 0.1$; R , multiple correlation coefficient; **, $P < 0.01$.

(A) Experiment 1

	Oxytocin change ratio	
	Owners	Dogs
Owner talking to dog	-0.107	-0.264
Owner touching dog	0.321 [†]	0.335 [†]
Dog-to-owner gaze	0.458*	0.388*
R	0.619	0.575
Adjusted R^2	0.306	0.247
P	0.008	0.020

(B) Experiment 2

	Oxytocin change ratio	
	Owners	Dogs
Dog's sex	0.090	0.138
Oxytocin administration	0.202	0.234
Dog-to-owner gaze	0.458**	0.030
Dog touching owner	-0.040	-0.054
Proximity to owner	0.048	-0.023
R	0.574	0.275
Adjusted R^2	0.248	-0.046
P	0.005	0.686

Sex: Female = 1, male = 0; oxytocin administration: oxytocin = 1, saline = 0.

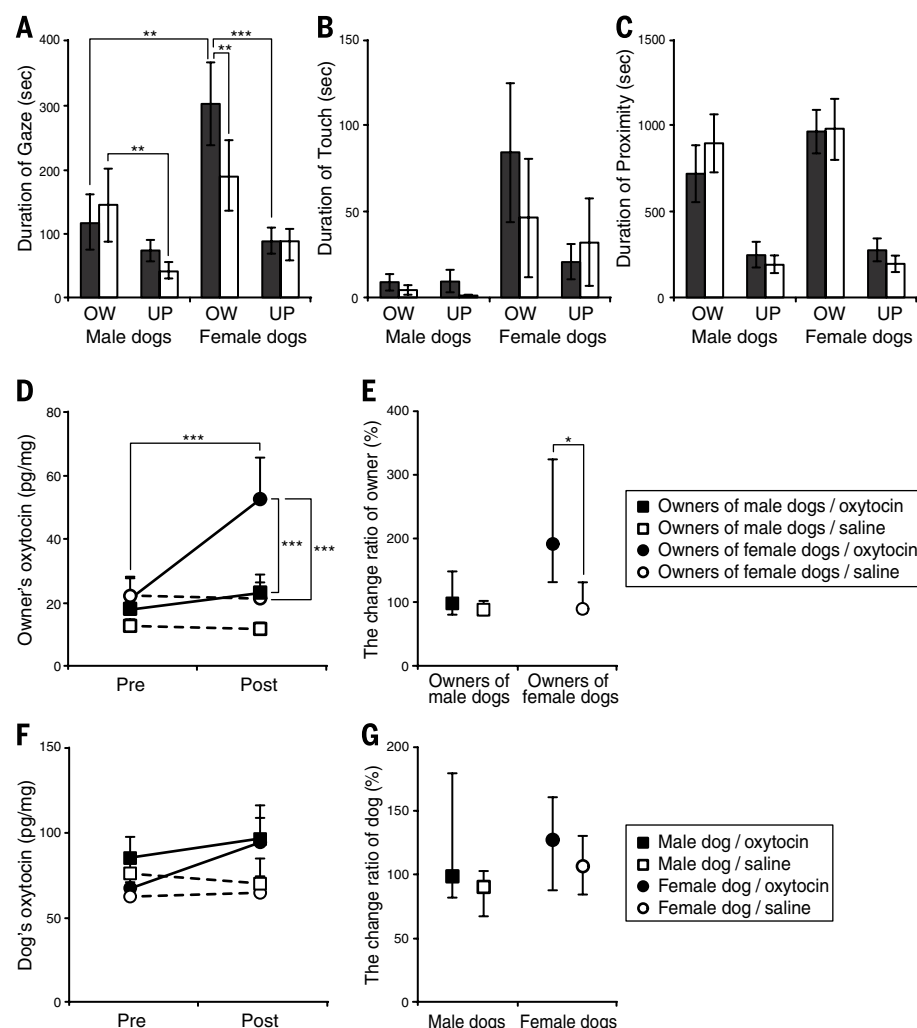


Fig. 2. Comparisons of behavior and urinary oxytocin between oxytocin and saline treatment conditions. (A) to (C) The effects of oxytocin administration on dog behaviors. Panels show the mean duration of dogs' gaze at participants (A), touching participants (B), and time spent in the proximity of less than 1 m from each participant (C). Black and white bars indicate, respectively, oxytocin- and saline treatment conditions. OW, owner; UP, unfamiliar person. (D) to (G) Change in urinary oxytocin concentrations after a 30-min interaction after oxytocin or saline administration. Urinary oxytocin concentrations of owners (D) and dogs (F) before and after a 30-min interaction are shown for oxytocin and saline groups. The change ratio of urinary oxytocin in owners (E) and dogs (G) is compared between male and female dogs. *** $P < 0.001$, ** $P < 0.01$, * $P < 0.05$. The results of (A) to (D) and (F) are expressed as mean \pm SE. (E) and (G) reflect median \pm quartile.

Interestingly, oxytocin administration only increased mutual gaze duration in female dogs, whereas sex differences were not observed in experiment 1, which did not include unfamiliar individuals. Sex differences in the effects of intranasal oxytocin have been reported in humans as well (22), and it is possible that females are more sensitive to the affiliative effects of oxytocin or that exogenous oxytocin may also be activating the vasopressin receptor system preferentially in males. Oxytocin and the structurally related vasopressin affect social bonding and aggression in sexually dimorphic manners in monogamous voles (8, 9), and oxytocin possibly increases aggression (23, 24). Therefore, the results of experiment 2 may indicate that male dogs were attending to both their owners and to unfamiliar people as a form of vigilance. The current study, despite its small sample size, implies a complicated role for oxytocin in social roles and contexts in dogs.

In human infants, mutual gaze represents healthy attachment behavior (25). Human functional magnetic resonance imaging studies show that the presentation of human and canine family members' faces activated the anterior cingulate cortex, a region strongly acted upon by oxytocin systems (26). Urinary oxytocin variation in dog owners is highly correlated with the frequency of behavioral exchanges initiated by the dogs' gaze (19). These results suggest that humans may feel affection for their companion dogs similar to that felt toward human family members and that dog-associated visual stimuli, such as eye-gaze contact, from their dogs activate oxytocin systems. Thus, during dog domestication, neural systems implementing gaze communications evolved that activate the humans' oxytocin attachment system, as did gaze-mediated oxytocin release, resulting in an interspecies oxytocin-mediated positive loop to facilitate human-dog bonding. This system is not present in the closest living relative of the domesticated dog.

In the present study, urinary oxytocin concentrations in owners and dogs were affected by the dog's gaze and the duration of dog-touching. In contrast, mutual gaze between hand-raised wolves and their owners was not detected, nor was there an increase of urinary oxytocin in either wolves or their owners after a 30-min experimental interaction (experiment 1). Moreover, the nasal administration of oxytocin increased the total amount of time that female dogs gazed at their owners and, in turn, urinary oxytocin concentrations in owners (experiment 2). We examined the association between our results and early-life experience with humans in dogs and wolves in order to test the possibility that our results were due to differences in early-life experience with humans. The results did not indicate a significant association between the animals' early-life experiences with humans and the findings of the current study (see the supplementary methods). Moreover, there were no significant differences between dogs in the long-gaze group and wolves in either the duration of dog/wolf-touching and dog/wolf-talking, suggesting that the shorter gaze of the wolves was not due to an unstable relationship. These re-

sults support the existence of a self-perpetuating oxytocin-mediated positive loop in human-dog relationships that is similar to that of human mother-infant relations. Human-dog interaction by dogs' human-like gazing behavior brought on social rewarding effects due to oxytocin release in both humans and dogs and followed the deepening of mutual relationships, which led to interspecies bonding.

REFERENCES AND NOTES

1. B. Hare, M. Tomasello, *Trends Cogn. Sci.* **9**, 439–444 (2005).
2. A. Miklósi *et al.*, *Curr. Biol.* **13**, 763–766 (2003).
3. A. P. Melis, B. Hare, M. Tomasello, *Science* **311**, 1297–1300 (2006).
4. R. Coppinger *et al.*, *Ethology* **75**, 89–108 (1987).
5. M. Somel *et al.*, *Proc. Natl. Acad. Sci. U.S.A.* **106**, 5743–5748 (2009).
6. S. Dickstein, R. A. Thompson, D. Estes, C. Malkin, M. E. Lamb, *Infant Behav. Dev.* **7**, 507–516 (1984).
7. S. Kim, P. Fonagy, O. Koos, K. Dorsett, L. Strathearn, *Brain Res.* **1580**, 133–142 (2014).
8. L. J. Young, Z. Wang, *Nat. Neurosci.* **7**, 1048–1054 (2004).
9. H. E. Ross, L. J. Young, *Front. Neuroendocrinol.* **30**, 534–547 (2009).
10. G. Dölen, A. Darvishzadeh, K. W. Huang, R. C. Malenka, *Nature* **501**, 179–184 (2013).
11. I. D. Neumann, *Prog. Brain Res.* **139**, 147–162 (2002).
12. M. Nagasawa, S. Okabe, K. Mogi, T. Kikusui, *Front. Hum. Neurosci.* **6**, 31 (2012).
13. J. K. Rilling, L. J. Young, *Science* **345**, 771–776 (2014).
14. J. Topál *et al.*, *Anim. Behav.* **70**, 1367–1375 (2005).
15. M. Nagasawa, K. Mogi, T. Kikusui, *Jpn. Psychol. Res.* **51**, 209–221 (2009).
16. D. S. Tuber, S. Sanders, M. B. Hennessy, J. A. Miller, *J. Comp. Psychol.* **110**, 103–108 (1996).

17. J. S. Odendaal, R. A. Meintjes, *Vet. J.* **165**, 296–301 (2003).
18. S. Mitsui *et al.*, *Horm. Behav.* **60**, 239–243 (2011).
19. M. Nagasawa, T. Kikusui, T. Onaka, M. Ohta, *Horm. Behav.* **55**, 434–441 (2009).
20. M. W. Fox, *The Soul of the Wolf* (Burford Books, New York, 1997).
21. M. Gácsi, J. Vas, J. Topál, Á. Miklósi, *Appl. Anim. Behav. Sci.* **145**, 109–122 (2013).
22. J. K. Rilling *et al.*, *Psychoneuroendocrinology* **39**, 237–248 (2014).
23. I. D. Neumann, *J. Neuroendocrinol.* **20**, 858–865 (2008).
24. C. K. De Dreu *et al.*, *Science* **328**, 1408–1411 (2010).
25. E. Meins, *Security of Attachment and the Social Development of Cognition* (Psychology Press, Philadelphia, 1997).
26. J. Shinozaki, T. Hanakawa, H. Fukuyama, *Neuroreport* **18**, 993–997 (2007).

ACKNOWLEDGMENTS

This study was supported in part by the Grant-in-Aid for Scientific Research on Innovative Areas (No. 4501) from the Japan Society for the Promotion of Science, in Japan. We thank all human and canine participants, Howlin' Ks Nature School, U.S. Kennel, R. Ooyama and N. Yoshida-Tsuchihashi from Azabu University, and Drs. Kato and Takeda from University of Tokyo Health Sciences. We are also grateful to Cody and Charley for their significant contributions. The analyzed data are included in the supplementary materials.

SUPPLEMENTARY MATERIALS

www.sciencemag.org/content/348/6232/333/suppl/DC1
Materials and Methods
Figs. S1 to S5
Tables S1 to S4
References (27–30)
Movies S1 to S3
Data Tables 1 and 2

9 September 2014; accepted 3 March 2015
10.1126/science.1261022

PLANT ECOLOGY

Anthropogenic environmental changes affect ecosystem stability via biodiversity

Yann Hautier,^{1,2,3*} David Tilman,^{2,4} Forest Isbell,² Eric W. Seabloom,² Elizabeth T. Borer,² Peter B. Reich^{5,6}

Human-driven environmental changes may simultaneously affect the biodiversity, productivity, and stability of Earth's ecosystems, but there is no consensus on the causal relationships linking these variables. Data from 12 multiyear experiments that manipulate important anthropogenic drivers, including plant diversity, nitrogen, carbon dioxide, fire, herbivory, and water, show that each driver influences ecosystem productivity. However, the stability of ecosystem productivity is only changed by those drivers that alter biodiversity, with a given decrease in plant species numbers leading to a quantitatively similar decrease in ecosystem stability regardless of which driver caused the biodiversity loss. These results suggest that changes in biodiversity caused by drivers of environmental change may be a major factor determining how global environmental changes affect ecosystem stability.

Human domination of Earth's ecosystems, especially conversion of about half of the Earth's ice-free terrestrial ecosystems into cropland and pasture, is simplifying ecosystems via the local loss of biodiversity (1, 2). Other major global anthropogenic changes include nutrient eutrophication, fire suppression

and elevated fire frequencies, predator decimation, climate warming, and drought, which likely affect many aspects of ecosystem functioning, especially ecosystem productivity, stability, and biodiversity (1, 3–7). However, to date there has been little evidence showing whether or how these three ecosystem responses may be mechanistically

linked. Rather, at present each anthropogenic driver of environmental change has been considered to have its own idiosyncratic syndrome of impacts on ecosystem productivity, stability, and biodiversity (1, 5–10).

This perspective was recently called into question by a study showing that the initial impacts of nutrient addition on grassland productivity were reduced through time in proportion to the extent to which nutrient addition led to the loss of plant diversity (11). In essence, that study suggested that the positive dependence of productivity on plant diversity (12–17), in combination with the negative effect of eutrophication on diversity (8, 18), caused the initial increase in productivity with nitrogen enrichment to diminish over time due to the loss of plant diversity caused by chronic nitrogen fertilization (11). This suggests the hypothesis that other drivers of global environmental change may have biodiversity-mediated effects on ecosystem functioning (19)—that changes in biodiversity resulting from anthropogenic drivers may be an intermediate cause of subsequent changes in ecosystem functioning. Here we test this hypothesis. Numerous biodiversity experiments have shown that reduced plant diversity leads to decreased temporal stability of productivity because of reductions in compensatory dynamics or in asynchronous responses to environmental fluctuations (12, 16, 20, 21). Here, our test determines how experimental manipulations of nitrogen (N), carbon dioxide (CO₂), fire, herbivory, and water affect biodiversity and productivity; and if changes in ecosystem stability associated with each environmental driver have the same dependence on biodiversity as observed in biodiversity experiments, or if each driver has an individualistic impact on stability (5, 6).

We perform this particular test because, whereas effects of anthropogenic drivers on biodiversity and productivity have been widely investigated (5, 6, 11), their long-term impacts on the temporal stability of productivity have received less attention, and the few published studies examining a single driver report mixed results (7, 9, 10, 22–25). A commonly used measure of stability among many proposed in the ecological literature (26, 27) defines the temporal stability of productivity (*S*) as the ratio of the temporal mean of productivity to its temporal variability as measured by its standard deviation (SD) (28). This measure of stability is the inverse of the coefficient of variation. Under this definition, a driver could increase stability by increasing the mean productivity relative to the SD, by decreasing the SD relative to the mean productivity, or both. Drivers that increase the SD may also increase stability if

there is a correspondingly larger proportional increase in mean productivity (or vice versa) (7, 20, 29). Importantly, given that the temporal mean and SD of productivity can depend on biodiversity (7, 21, 29), drivers might influence stability through their long-term effects on biodiversity. The simultaneous impacts of various drivers on ecosystem biodiversity, productivity, and stability have not previously been explored, thus limiting our current understanding.

Here, we determine if ecologically or societally relevant magnitudes of change in six important anthropogenic drivers influence the stability of ecosystem productivity and whether changes in stability correspond with changes in biodiversity. In particular, we test the hypothesis that changes in biodiversity, regardless of the causal factor, consistently affect the stability of ecosystem productivity.

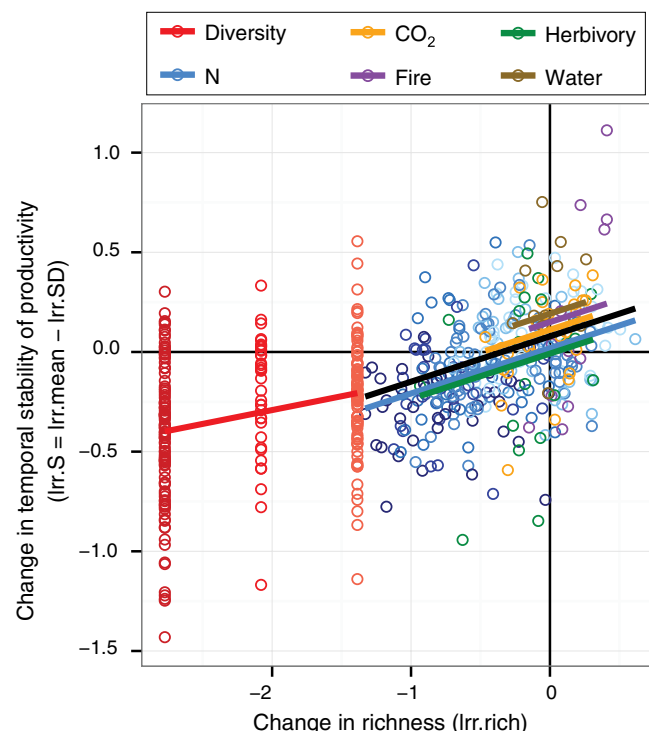
We used data from 12 experiments that manipulated one or more anthropogenic drivers over a period of 4 to 28 years (table S1). We examine both long-term stability (temporal stability determined using all 4 to 28 years of data collected on aboveground biomass in each experiment) and short-term stability (the temporal stability of each 3-year period of each experiment) and the dependence of these metrics of stability on the concurrent measures of plant species numbers.

We begin by evaluating the extent to which changes in grassland plant diversity, whether experimentally manipulated or in response to other anthropogenic drivers, including N, CO₂,

fire, herbivory, and water, predict changes in the long-term temporal stability of productivity. Our analyses control for what otherwise might be potentially confounding variables by including only experiments at the Cedar Creek Ecosystem Science Reserve on well-drained sandy soils of east-central Minnesota, USA, that used perennial grassland ecosystems of similar plant species compositions (5). We determined long-term temporal stability, *S*, as μ/σ , where μ is the average productivity of a plot across all years and σ is the temporal standard deviation in the productivity of that plot across all years. We calculated long-term stability responses as the natural logarithm of the ratio (log response ratio or *lrr*) of the long-term stability within each treatment plot divided by the average long-term stability in the reference plots (*lrr.S*). Similarly, we calculated the associated plant species richness responses as the natural logarithm of the ratio of the average richness across all years within each treatment plot divided by the average richness across all years in the reference plots (*lrr.rich*). Log response ratios quantify the proportional change in treatment plots relative to reference plots. Because *lrr.S* is the difference between the log response ratio of the temporal mean (*lrr.mean*) and the log response ratio of the temporal standard deviation (*lrr.SD*), it separates the effects of anthropogenic drivers on stability into their simultaneous effects on the mean and variance of productivity.

Reference plots were unmanipulated or otherwise had more historically typical conditions, such

Fig. 1. Human-driven environmental changes affect ecosystem stability via biodiversity. Effect of anthropogenic drivers of environmental change on the stability of productivity, as mediated by experimentally imposed changes in biodiversity [red line; slope and 95% confidence intervals (CIs): 0.14 (0.08 to 0.20)], or from biodiversity changes arising from anthropogenic drivers including N, CO₂, water, fire, and herbivory [black and other colored lines; slopes and 95% CIs: 0.22 (0.15 to 0.31)]. Black and red lines are based on separate fits; their similar slopes show that changes in biodiversity caused by anthropogenic drivers have effects on stability similar to those resulting from experimentally imposed changes in plant biodiversity ($F_{1,561} = 3.29$, $P = 0.07$). Relative changes were calculated as the natural logarithm of the ratio (*lrr*) of the variable within each treatment plot divided by the average of the variable in the reference plots. Black line is the fixed-effect linear regression slope across all anthropogenic drivers in the mixed-effects model; colored lines show trends for each driver. Colors for the points correspond to treatments in Fig. 2.



¹Department of Plant Sciences, University of Oxford, Oxford OX1 3RB, UK. ²Department of Ecology, Evolution and Behavior, University of Minnesota Twin Cities, Saint Paul, MN 55108, USA. ³Ecology and Biodiversity Group, Department of Biology, Utrecht University, Padualaan 8, 3584 CH Utrecht, Netherlands. ⁴Bren School of the Environment, University of California, Santa Barbara, CA 93106, USA. ⁵Department of Forest Resources, University of Minnesota, Saint Paul, MN 55108, USA. ⁶Hawkesbury Institute for the Environment, University of Western Sydney, Penrith, NSW 2753, Australia. *Corresponding author. E-mail: yann.hautier@plants.ox.ac.uk

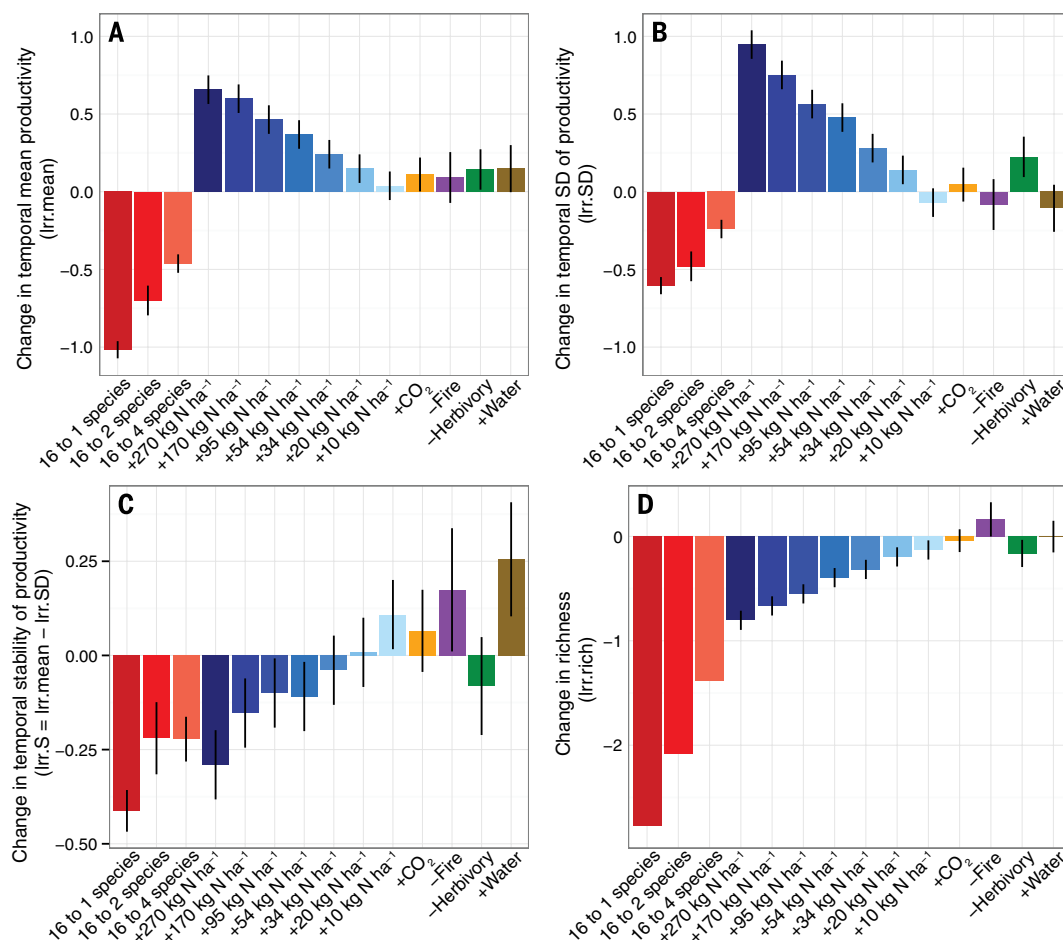


Fig. 2. Simultaneous effect of human-driven environmental changes on ecosystem productivity, stability, and biodiversity. Effect of anthropogenic drivers of environmental change on relative changes in the (A) mean, (B) standard deviation (SD), (C) stability of ecosystem productivity, and (D) plant diversity. Treatment effects are shown with their 95% CI such that treatments with intervals overlapping zero are not significantly different from zero (table S4).

as high diversity or ambient N, CO₂, herbivory, and water conditions or presettlement fire conditions. In particular, we compared biodiversity from plots planted with one, two, and four species to reference plots planted with 16 species, a level representative of a high-diversity (16.3 species m⁻²) natural grassland community in this area (5). N additions of 270, 170, 95, 54, 34, 20, and 10 kg ha⁻¹ were compared to plots receiving no N, and addition of CO₂ and water, fire suppression, and herbivore exclusion were compared to grassland plots with ambient or presettlement conditions. These treatments (except 270, 170, and 95 kg N ha⁻¹ and perhaps the monocultures of biodiversity experiments) also fall within the ranges occurring in natural grassland ecosystems of this region (5).

We found that changes in plant diversity in response to anthropogenic drivers, including N, CO₂, fire, herbivory, and water, were positively associated with changes in temporal stability of productivity (black line in Fig. 1; Fig. 2, C and D). This positive association was independent of the nature of the driver, resulting in parallel relationships (all colored lines except red in Fig. 1; table S2). This suggests that biodiversity-mediated effects on stability are independent of the factor driving changes in biodiversity. Moreover, the

positive association between changes in plant diversity and changes in stability in response to anthropogenic drivers was similar to that observed in two neighboring experiments that directly manipulated plant diversity (compare the black and red lines in Fig. 1) (2f). Thus, changes in biodiversity resulting from anthropogenic environmental changes have similar effects on stability as observed in biodiversity experiments, suggesting that changes in biodiversity may be an intermediary factor influencing how anthropogenic environmental changes affect ecosystem stability. For example, whether a 30% change in plant diversity (Irr.rich = -0.357) resulted from elevated N, CO₂, or water or from herbivore exclusion, fire suppression, or direct manipulation of plant diversity, stability tended to decrease in parallel by 8% (Irr.S = -0.082). This conclusion is supported by analyses showing that there was no remaining effect of anthropogenic drivers on changes in stability after biodiversity-mediated effects were taken into account (table S3) and that changes in stability based on biodiversity manipulations predict changes in stability in response to anthropogenic drivers (fig. S1).

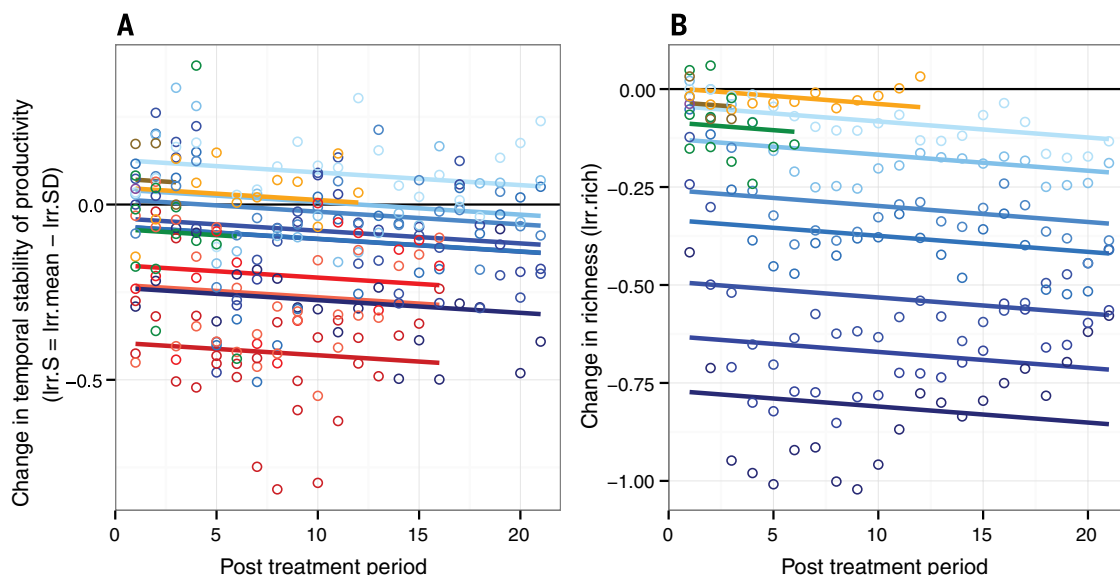
We next evaluated the extent to which changes in temporal stability of productivity in response to anthropogenic drivers were caused by change-

ing the temporal mean of productivity or the temporal variance of productivity. We found that when a driver of environmental change caused mean productivity to change, it did not consistently lead to higher or lower stability of productivity (Fig. 2 and table S4). For example, decreases in biodiversity from 16 species to one, two, and four species decreased both the temporal mean and stability of productivity (Fig. 2, A and C). By contrast, addition of N, CO₂, and water; fire suppression; and herbivore exclusion generally increased the temporal mean of productivity, although not always significantly (Fig. 2A), but either increased (N addition of 10 kg ha⁻¹, fire suppression, and water addition), reduced (N addition of 270, 170, 95, and 54 kg ha⁻¹), or had no detectable effects (N addition of 34 and 20 kg ha⁻¹, addition of CO₂, and herbivore exclusion) on stability (Fig. 2C). These differing effects on stability (Fig. 2C) were due to differences in the direction and magnitude of drivers' impact on mean productivity (Fig. 2A) compared to their variance (Fig. 2B). For example, experimental decreases in biodiversity caused a larger decrease in mean productivity than in its variance, resulting in decreased stability; whereas N addition of 10 kg ha⁻¹, fire suppression, and water addition each caused a larger increase in mean productivity

Fig. 3. Temporal trends in effect sizes of ecosystem stability and biodiversity responses to anthropogenic drivers of environmental change.

Effects of anthropogenic drivers on (A) stability ($F_{13,220} = 30.6$, $P < 0.001$) and (B) diversity ($F_{10,154} = 103.3$, $P < 0.001$) were consistent through time (Drivers \times Time: $P > 0.1$ in both cases). Stability ($F_{1,154} = 86.5$, $P < 0.001$) and diversity ($F_{1,220} = 24.8$, $P < 0.001$) had a weak tendency to decrease with increasing treatment duration. Data were divided into overlapping intervals of 3 years

reported as posttreatment period after initiation of the experiment (31), with diversity and stability determined for each interval. Colors for the points and lines correspond to treatments in Fig. 2.



than in its variance, resulting in increased stability. By contrast, N addition of 270, 170, 95, and 54 kg ha⁻¹ caused a larger increase in the variance than the mean, resulting in reduced stability. We do not expect the direction and magnitude of changes in the numerator or denominator of the stability ratio to be universal. For example, in other biodiversity experiments, decreases in biodiversity caused a larger decrease in the variance of productivity than the mean (29). Our results, however, do indicate that drivers consistently reduce stability when they reduce biodiversity.

Together, these results suggest that changes in biodiversity, whether experimentally manipulated or in response to other anthropogenic drivers, caused consistent changes in ecosystem stability of productivity (Figs. 1 and 2, C and D) not because of consistent effects of a driver or biodiversity on either the temporal mean of productivity or on its temporal variance (Fig. 2, A and B) but rather because of consistent effects on their ratio, which is stability (Figs. 1 and 2, C and D). The repeatedly observed quantitative effects of changes in biodiversity on ecosystem stability in this study are consistent with predictions of ecosystem stability by models of interactions among species that coexist because of interspecific trade-offs (30). They are also consistent with results of numerous biodiversity experiments (29).

We found no evidence that biodiversity-mediated effects on stability were caused by similar shifts in the abundances of functional groups or species (fig. S2). For example, although diversity and stability declined, native perennial C₄ grasses increased under herbivory exclusion (e.g., *Sorghastrum nutans*) and declined under high levels of chronic nitrogen enrichment (e.g., *Schizachyrium scoparium*), while non-native perennial C₃ grasses declined under herbivory exclusion (e.g., *Koeleria cristata*) and increased under high levels of chronic nitrogen enrichment (e.g., *Agropyron repens*). Thus, various drivers led to similar changes in stability

by causing changes in biodiversity, even though the various drivers had different effects on functional groups and particular species.

We also assessed whether the diversity and stability responses were consistent through time by dividing the 4 to 28 years of annual data into overlapping intervals of three consecutive years and calculating short-term stability and average species richness for each interval. This allows us to account for the effects of the different duration of the experiments (31). Effects of anthropogenic drivers on diversity and short-term stability were consistent through time. Specifically, diversity and stability had a weak tendency to decrease in unison with increasing treatment duration independently of the nature of the driver, resulting in parallel negative relationships (Fig. 3). These results further suggest that the decrease in stability over time was associated with declining plant diversity in response to anthropogenic drivers.

In total, we found that the loss of plant diversity was associated with decreased stability not only in experiments that manipulate diversity (20, 27) but also when biodiversity changed in response to other anthropogenic drivers. In combination with recent demonstrations that biodiversity is a major determinant of productivity (5, 6, 11), these findings suggest that any drivers of environmental change that affect biodiversity are likely to have long-term ecosystem impacts that result from these changes in biodiversity (19). Furthermore, biodiversity-mediated effects on stability did not qualitatively depend either on the particular factor that caused the change in biodiversity or on shifts in the abundance of particular functional groups or species. Altogether, our multiyear experiments suggest that there may be a universal impact of biodiversity change on ecosystem stability in response to anthropogenic environmental changes, with decreased plant species numbers leading to lower ecosystem stability regardless of the cause of biodiversity loss. Our

work suggests that conservation policies should encourage management procedures that restore or maintain natural levels of biodiversity or minimize the negative impacts of anthropogenic global environmental changes on biodiversity loss to ensure the stable provision of ecosystem services.

REFERENCES AND NOTES

1. P. M. Vitousek, H. A. Mooney, J. Lubchenco, J. M. Melillo, *Science* **277**, 494–499 (1997).
2. S. L. Pimm, G. J. Russell, J. L. Gittleman, T. M. Brooks, *Science* **269**, 347–350 (1995).
3. A. D. Barnosky et al., *Nature* **471**, 51–57 (2011).
4. J. Rockström et al., *Nature* **461**, 472–475 (2009).
5. D. Tilman, P. B. Reich, F. Isbell, *Proc. Natl. Acad. Sci. U.S.A.* **109**, 10394–10397 (2012).
6. D. U. Hooper et al., *Nature* **486**, 105–108 (2012).
7. Y. Hautier et al., *Nature* **508**, 521–525 (2014).
8. C. J. Stevens, N. B. Dise, J. O. Mountford, D. J. Gowing, *Science* **303**, 1876–1879 (2004).
9. Z. L. Yang, J. van Ruijven, G. Z. Du, *Plant Soil* **345**, 315–324 (2011).
10. S. L. Collins, L. B. Calabrese, *J. Veg. Sci.* **23**, 563–575 (2012).
11. F. Isbell et al., *Proc. Natl. Acad. Sci. U.S.A.* **110**, 11911–11916 (2013).
12. B. J. Cardinale et al., *Nature* **489**, 326–326 (2012).
13. A. Hector, R. Bagchi, *Nature* **448**, 188–190 (2007).
14. A. Hector et al., *Science* **286**, 1123–1127 (1999).
15. F. Isbell et al., *Nature* **477**, 199–202 (2011).
16. F. I. Isbell, H. W. Polley, B. J. Wilsey, *Ecol. Lett.* **12**, 443–451 (2009).
17. D. Tilman et al., *Science* **277**, 1300–1302 (1997).
18. Y. Hautier, P. A. Niklaus, A. Hector, *Science* **324**, 636–638 (2009).
19. M. D. Smith, A. K. Knapp, S. L. Collins, *Ecology* **90**, 3279–3289 (2009).
20. A. Hector et al., *Ecology* **91**, 2213–2220 (2010).
21. D. Tilman, P. B. Reich, J. M. H. Knops, *Nature* **441**, 629–632 (2006).
22. H. Yang et al., *Ecol. Lett.* **15**, 619–626 (2012).
23. J. Lepš, *Oikos* **107**, 64–71 (2004).
24. E. Grman, J. A. Lau, D. R. Schoolmaster Jr., K. L. Gross, *Ecol. Lett.* **13**, 1400–1410 (2010).
25. A. S. MacDougall, K. S. McCann, G. Gellner, R. Turkington, *Nature* **494**, 86–89 (2013).
26. S. L. Pimm, *Nature* **307**, 321–326 (1984).
27. A. R. Ives, S. R. Carpenter, *Science* **317**, 58–62 (2007).
28. D. Tilman, *Ecology* **80**, 1455–1474 (1999).
29. K. Gross et al., *Am. Nat.* **183**, 1–12 (2014).
30. C. L. Lehman, D. Tilman, *Am. Nat.* **156**, 534–552 (2000).
31. Materials and methods are available as supplementary materials on Science Online.

ACKNOWLEDGMENTS

The research leading to these results received funding from the European Union Seventh Framework Programme (FP7/2007-2013) under grant agreement no. 298935 to Y.H. and has been supported by the U.S. National Science Foundation (NSF) Long-Term Ecological Research (LTER) Program at Cedar Creek (DEB-8811884, DEB-9411972, DEB-0080382, DEB-0620652, and DEB-1234162), Biocomplexity Coupled Biogeochemical Cycles (DEB-0322057), Long-Term Research in Environmental Biology (DEB-0716587, DEB-1242531), and Ecosystem Sciences (NSF DEB-1120064) Programs, as well as the U.S. Department of Energy (DOE) Program for Ecosystem Research (DE-FG02-96ER62291) and

the U.S. DOE National Institute for Climatic Change Research (DE-FC02-06ER64158). We thank T. Mielke, D. Bahauddin, K. Worm, S. Barrott, E. Lind, and many summer interns for their assistance with this research. We also thank R. S. L. Veiga, W. S. Harpole, T. Züst, and M. Tanadini for suggestions that improved the manuscript. For detailed methods and original data, see www.cedar.creek.umn.edu/research/data. See table S1 for links to data for each experiment and supplementary materials for guidance on data access. The authors declare no conflict of interests. Author contributions: Y.H. and D.T. developed and framed the research question; D.T., F.I., E.W.S., E.T.B., and P.B.R. designed research; D.T., E.W.S., E.T.B., and P.B.R. performed

research; Y.H. and F.I. analyzed data; and Y.H. wrote the paper with inputs from all coauthors.

SUPPLEMENTARY MATERIALS

www.sciencemag.org/content/348/6232/336/suppl/DC1
Materials and Methods
Figs. S1 and S2
Tables S1 to S4
References (32–39)

5 November 2014; accepted 23 February 2015
10.1126/science.aaa1788

STEM CELLS

Asymmetric apportioning of aged mitochondria between daughter cells is required for stemness

Pekka Katajisto,^{1,2,3,4,*} Julia Döhla,⁴ Christine L. Chaffer,¹ Nalle Penttinen,⁴ Nemanja Marjanovic,^{1,2} Sharif Iqbal,⁴ Roberto Zoncu,^{1,2,3} Walter Chen,^{1,2,3} Robert A. Weinberg,^{1,2} David M. Sabatini^{1,2,3,5,6,†}

By dividing asymmetrically, stem cells can generate two daughter cells with distinct fates. However, evidence is limited in mammalian systems for the selective apportioning of subcellular contents between daughters. We followed the fates of old and young organelles during the division of human mammary stemlike cells and found that such cells apportion aged mitochondria asymmetrically between daughter cells. Daughter cells that received fewer old mitochondria maintained stem cell traits. Inhibition of mitochondrial fission disrupted both the age-dependent subcellular localization and segregation of mitochondria and caused loss of stem cell properties in the progeny cells. Hence, mechanisms exist for mammalian stemlike cells to asymmetrically sort aged and young mitochondria, and these are important for maintaining stemness properties.

Stem cells can divide asymmetrically to generate a new stem cell and a progenitor cell that gives rise to the differentiated cells of a tissue. During organismal aging, it is likely that stem cells sustain cumulative damage, which may lead to stem cell exhaustion and eventually compromise tissue function (1). To slow the accumulation of such damage, stem cells might segregate damaged subcellular components away from the daughter cell destined to become a new stem cell. Although nonmammalian organisms can apportion certain non-nuclear cellular compartments (2–4) and oxidatively damaged proteins (5, 6) asymmetrically during cell division, it is unclear whether mammalian stem cells can do so as well (6–9).

We used stemlike cells (SLCs) recently identified in cultures of immortalized human mam-

mary epithelial cells (10) to investigate whether mammalian stem cells can differentially apportion aged, potentially damaged, subcellular components, such as organelles between daughter cells. These SLCs express genes associated with stemness, form mammospheres, and, after transformation, can initiate tumors in vivo (10, 11). Moreover, because of their round morphology, the SLCs can be distinguished by visual inspection from the flat, tightly adherent, nonstemlike mammary epithelial cells with which they coexist in monolayer cultures (Fig. 1B).

To monitor the fate of aged subcellular components, we expressed photoactivatable green fluorescent protein (paGFP) (12) in lysosomes, mitochondria, the Golgi apparatus, ribosomes, and chromatin by fusing the fluorescent protein to the appropriate targeting signals or proteins (table S1). paGFP fluoresces only after exposure to a pulse of ultraviolet (UV) light (12), allowing us to label each component in a temporally controlled manner (Fig. 1A). Because synthesis of paGFP continues after the light pulse, cells subsequently accumulate unlabeled “young” components in addition to the labeled “old” components; these can be either segregated in distinct subcellular compartments or commingled within individual cells.

We followed the behavior of labeled components in single round SLCs or flat epithelial cells and focused on cell divisions that occurred 10 to 20 hours after paGFP photoactivation (Fig. 1B). The epithelial cells symmetrically apportioned all cellular components analyzed (Fig. 1B). In contrast, the round SLCs apportioned ~5.6 times as much ($P < 0.001$, t test) of ≥10-hour-old mitochondrial outer membrane protein 25 (paGFP-Omp25) to one daughter cell as to the other (Fig. 1B). Similarly, labeled markers for all other organelles examined were apportioned symmetrically. We designated the daughter cell that inherited more aged Omp25 from the mother cell as Progeny1 (P1) and the other as Progeny2 (P2).

To determine whether the same cells that asymmetrically apportion the mitochondrial membrane protein also allocate other membrane compartments asymmetrically, we labeled SLCs with the lipophilic dye PKH26 before photoactivation of paGFP-Omp25. PKH26 initially labels the plasma membrane and is gradually endocytosed to form distinct cytoplasmic puncta, and it is relatively symmetrically apportioned during division of hematopoietic cells (13). SLCs apportioned old mitochondria asymmetrically, but the same cells apportioned PKH26 symmetrically (Fig. 1C and movie S1). In contrast, the epithelial cells apportioned both paGFP-Omp25 and PKH26 symmetrically (Fig. 1C and movie S2), similarly to mouse embryonic fibroblasts (not shown).

To verify that SLCs indeed apportion mitochondria according to the age of the organelle, we analyzed the apportioning of paGFP-Omp25 in cell divisions that occurred at random times after the initial photoactivation. We assumed that the age of Omp25 molecules reflected the age of the mitochondria with which they were associated. Cells that divided 0 to 10 hours after photoactivation showed symmetric apportioning of paGFP-Omp25 (Fig. 1D). However, cells that divided more than 10 hours after photoactivation, and thus carried fluorescent marks only on organelles that were at least 10 hours old, apportioned their labeled mitochondria asymmetrically (Fig. 1D).

To follow the apportioning of two different age classes of mitochondria, we tagged mitochondria with mitochondrial proteins fused to a Snap-tag (14). Snap-tag is a derivatized DNA repair enzyme, O⁶-alkylguanine-DNA alkyltransferase, which can covalently link various fluorophores to the tagged fusion protein in live cells. We used two Snap-tag substrates with two different fluorophores (red

¹Whitehead Institute for Biomedical Research, Boston, MA 02142, USA. ²Department of Biology, Massachusetts Institute of Technology (MIT), Cambridge, MA 02139, USA. ³Howard Hughes Medical Institute, MIT, Cambridge, MA 02139, USA. ⁴Institute of Biotechnology, University of Helsinki, P.O. Box 00014, Helsinki, Finland. ⁵Broad Institute, Cambridge, MA 02142, USA. ⁶The David H. Koch Institute for Integrative Cancer Research at MIT, Cambridge, MA 02139, USA.
*Corresponding author. E-mail: pekka.katajisto@helsinki.fi (P.K.); sabatini@wi.mit.edu (D.M.S.) †Present address: Institute of Biotechnology, University of Helsinki, P.O. Box 00014, Helsinki, Finland.

and green) sequentially to separately label young and old organelles (Fig. 2A). Snap-tags are rendered inactive by the labeling reaction; this ensures that the two colors will mark chronologically distinct populations and, in contrast to previously used strategies (15), allows precise timing of labeling. Moreover, Snap-tags allow uniform labeling throughout the entire cell and the simultaneous labeling of multiple cells and avoid the risk of phototoxic artifacts associated with paGFP (16).

We analyzed divisions of SLCs expressing Snap-Omp25 and carrying red and green fluorophores on what we refer to as old and young mitochondria, labeled 48 to 58 and 0 to 10 hours before division, respectively (Fig. 2B and movie S3). After cell division, the old label from the mother cell was divided more asymmetrically between daughter cells than the young label (old: P1 89% versus P2 11% of the mother cell intensity, $P = 0.004$; young: 67% versus 33%, $P = 0.04$, $n = 5$) (Fig. 2, B and C, and fig. S1). This age-specific apportioning reduced the relative portion of old mitochondria in P2 to about one-fifth of those in the mother cell and one-sixth of those in the P1 daughter (fig. S2A). However, cells that inherited fewer old mitochondria contained similar total amounts of mitochondria (fig. S3), suggesting that unlabeled new mitochondria generated after the “young labeling” were differentially distributed to balance the overall mitochondrial quantity between the two daughters. We also targeted the mitochondrial inner membrane (see fig. S4 for mitochondrial constructs used) by expressing COX8A-Snap in SLCs. This inner membrane protein showed asymmetric distribution comparable to that of Omp25 (Fig. 2C), increasing our confidence that the age-selective segregation of Omp25 represented that of whole mitochondria.

Our analyses of asymmetric cell divisions indicated that the majority of mitochondria in the stemlike mother cells contained both old and young labels, whereas some mitochondria carried only young or old label (Fig. 2B). Most mitochondria carrying exclusively young label apportioned to the P2 daughter cells, whereas mitochondria containing a mix of the two labels segregated to P1 cells (Fig. 2B). Moreover, the small quantity of old label received by P2 did not colocalize with young label (Fig. 2B and fig. S2B). These findings indicate that even before cell division, the stemlike mother cell keeps new mitochondria apart from old ones and passes these younger mitochondria preferentially to the P2 daughter.

To study such segregation in greater detail, we analyzed SLCs immediately after labeling of the young mitochondria but before division (fig. S5 and Fig. 2D). Old mitochondria tended to localize perinuclearly and in some cells formed puncta containing exclusively old label (figs. S5 and S6), whereas the young label distributed throughout the mitochondrial network more evenly. To address whether such localization differences could contribute to the demonstrated age-specific apportioning, we imaged old and young mitochondria with live microscopy within the 10-hour window we used for analyses of asymmetric division (Fig. 2E). Young (green) label gradually became more perinuclear as it became older, but at 10 hours after labeling, which was the maximum time point used for the quantitation of asymmetry in cell division, there was still a significant difference in the localization of the two labels (Fig. 2E). The perinuclear localization of old label did not occur in a fibroblast cell line without stemlike properties (fig. S6), and it did not result from

old label entering and marking other subcellular components, such as lysosomes, due to mitochondrial turnover (fig. S7). However, within the interconnected mitochondrial network, we identified specific domains that were enriched for old label (Fig. 2D). These data support the notion that mother SLCs localize new and old mitochondria to specific cytoplasmic regions, ostensibly to facilitate the exclusion of old mitochondria from future P2 daughter cells.

The asymmetric apportioning and localization of mitochondria in the daughter cells suggested that daughter cells resulting from a division of a SLC might represent the founders of two lineages, one stemlike and the other more likely to differentiate. We used flow cytometry to analyze the age-selective apportioning of mitochondria in cell populations that had been synchronized to divide in concert (fig. S8 and Fig. 3A). Some divided cells received significantly fewer old mitochondria than did others, whereas the young mitochondria were more uniformly distributed. Upon fluorescence-activated cell sorting (FACS) and replating of daughter cell populations, the Pop1 cells, which received more old mitochondria, were morphologically flatter and more adherent than the Pop2 cells (Fig. 3A). Three days after cell sorting, the Pop1 cells formed clusters with a monolayer appearance, whereas the Pop2 cells regenerated both round and flat cells similar to the original parental population. However, both populations had similar rates of proliferation (fig. S9). Thus, Pop2 cells, which received fewer older mitochondria, appeared to represent the SLCs that could subsequently undergo asymmetric divisions.

We used the ability to form mammospheres in three-dimensional (3D) culture as an *in vitro* assay of mammary epithelial cell stemness (17).

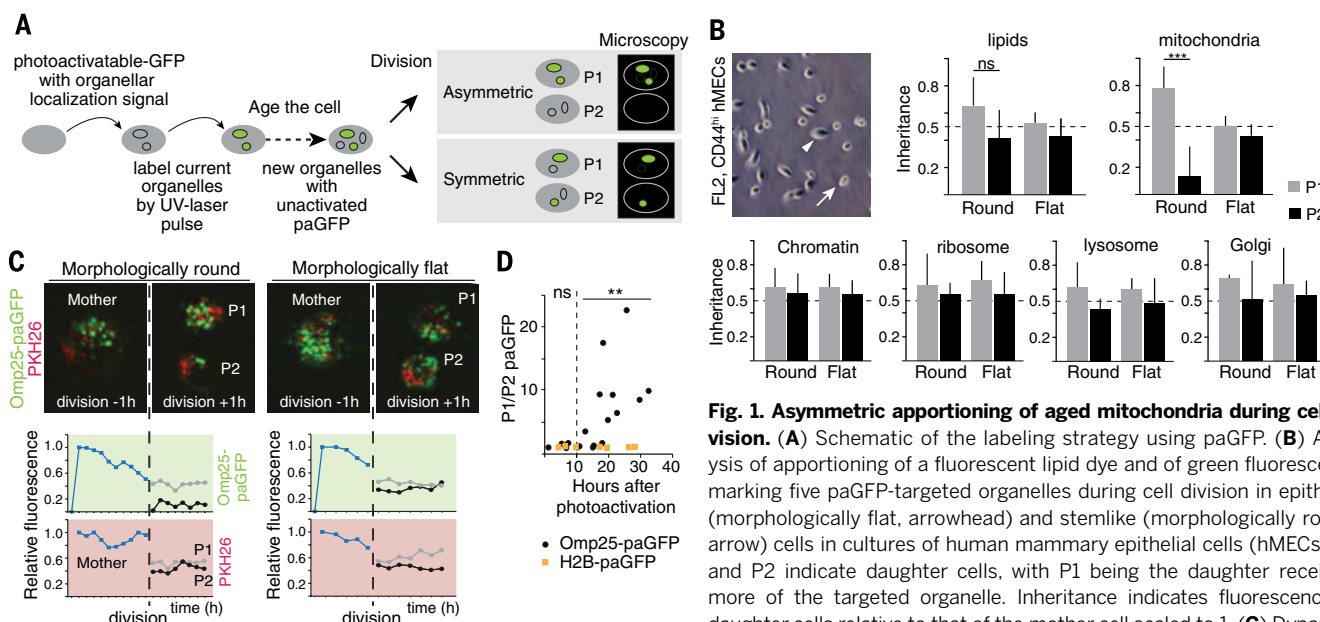


Fig. 1. Asymmetric apportioning of aged mitochondria during cell division. (A) Schematic of the labeling strategy using paGFP. (B) Analysis of apportioning of a fluorescent lipid dye and of green fluorescence marking five paGFP-targeted organelles during cell division in epithelial (morphologically flat, arrowhead) and stemlike (morphologically round, arrow) cells in cultures of human mammary epithelial cells (hMECs). P1 and P2 indicate daughter cells, with P1 being the daughter receiving more of the targeted organelle. Inheritance indicates fluorescence of daughter cells relative to that of the mother cell scaled to 1. (C) Dynamics of mitochondrial apportioning in round SLCs and flat epithelial cells.

Representative divisions are shown with mitochondria in green (paGFP-Omp25) and the lipid dye (PKH26) in red. Images are frame captures from 1 hour before and after division, and fluorescence intensity per cell is plotted at 1-hour intervals. (D) Analysis of asymmetric apportioning as a function of label age. SLCs dividing more than 10 hours after label activation show increasing asymmetric apportioning of mitochondria (Omp25) but not of chromatin label (H2B). Each data point represents an individual cell division (** $P < 0.01$, *** $P < 0.001$, *t* test).

In this assay, the Pop2 of both Snap-Omp25- and COX8a-Snap-expressing cells formed three times as many mammospheres per 1000 cells as Pop1 (Fig. 3B). Hence, the cells that inherited fewer old mitochondria during an asymmetric division were, by the criterion of mammosphere-forming ability, more stemlike.

Mitochondria that have lower membrane potential ($\Delta\Psi_m$)—an index of mitochondrial function—localize perinuclearly (18), and high $\Delta\Psi_m$ is linked to stemlike traits (19, 20). Moreover, in *Saccharomyces cerevisiae*, the $\Delta\Psi_m$ -driven selective inheritance of fit mitochondria is required for the daughter cell to maintain full replicative life span (21, 22). We analyzed the $\Delta\Psi_m$ of cells in the Pop1 and Pop2 populations to address whether their mitochondria differ functionally. Because the results with two different $\Delta\Psi_m$ indicator dyes were not consistent (fig. S10), we analyzed the age-selective apportioning of mitochondria in the presence of a mitochondrial uncoupler, carbonyl cyanide *m*-chlorophenyl hydrazone. Alterations of the $\Delta\Psi_m$ had no effect on the age-selective segregation of mitochondria in an SLC division (figs. S11 and S12). However, we did note a significant correlation between mammosphere-forming capacity and $\Delta\Psi_m$ with both dyes (fig. S10). Thus, we conclude that although $\Delta\Psi_m$ correlates with stemlike properties, it is not the signal that guides the age-selective asymmetric segregation of mitochondria during mammalian cell division.

Cells have mitochondrial quality-control mechanisms through which they specifically remove poorly functional parts of their mitochondrial network. After mitochondrial fission, which depends on the dynamin-related protein 1 (Drp1) (23), the kinase PINK1 will promote the recruitment of the Parkin E3 ubiquitin ligase to mitochondrial fragments with low $\Delta\Psi_m$ and induce their selective autophagy (24). Another PINK1/Parkin-dependent (but $\Delta\Psi_m$ - and Drp1-independent) mitochondrial quality-control mechanism is mediated by generation of mitochondrially derived vesicles that target oxidatively damaged mitochondrial components for lysosomal degradation (25).

SLCs and epithelial cells had comparable numbers of autophagosomes containing old mitochondrial label (fig. S13), indicating that degradation via the autophagosome-lysosome pathway is not directly responsible for the reduction in the numbers of old mitochondria in stemlike cells. However, SLCs had a higher mitophagy/autophagy ratio (fig. S13E), suggesting that high quality of mitochondria may be relevant for the SLC state and asymmetric apportioning during cell division. To investigate this, we transfected synchronized cells with small interfering RNAs (siRNAs) targeting Parkin or treated cells with the Drp1 inhibitor mDivi-1 (26) to inhibit mitochondrial fission. In both cases, we observed a significant and similar reduction in the number of cells inheriting mostly young mitochondria (Pop2) and

a concomitant increase in cells inheriting a mixture of old and young mitochondria (Pop1) (Fig. 4A and fig. S14). Surprisingly, fragmentation of mitochondria by Drp1 expression resulted in comparable reduction in the Pop2 with mDivi-1 or siParkin (fig. S15). However, these effects are probably not caused by the changes of the mitochondrial network status, because round SLCs and differentiated cells have similar mitochondrial network connectivity (fig. S16 and movie S5). Taken together, these data suggest that any perturbation that challenges normal mitochondrial quality-control mechanisms will either serve as a signal for an SLC to stop asymmetric segregation of mitochondria or, alternatively, overload the capacity of the SLCs to effectively apportion old mitochondria asymmetrically.

To address whether the preferential acquisition of younger mitochondria contributed to maintenance of stem cell function, we analyzed the mammosphere-forming capacity of the cells remaining in Pop2 after a division in the presence of either siParkin or mDivi-1. Both treatments eliminated the increased stemness capacity of the remaining Pop2 cells so that they formed mammospheres with the lower efficiency characteristic of the Pop1 cells (Fig. 4B). However, the cells in Pop2 from mDivi-1-treated samples proliferated similarly to control-treated cells in 2D culture (fig. S14B). Moreover, because the analysis of mammosphere formation was conducted in the absence of mDivi-1, these data suggest that

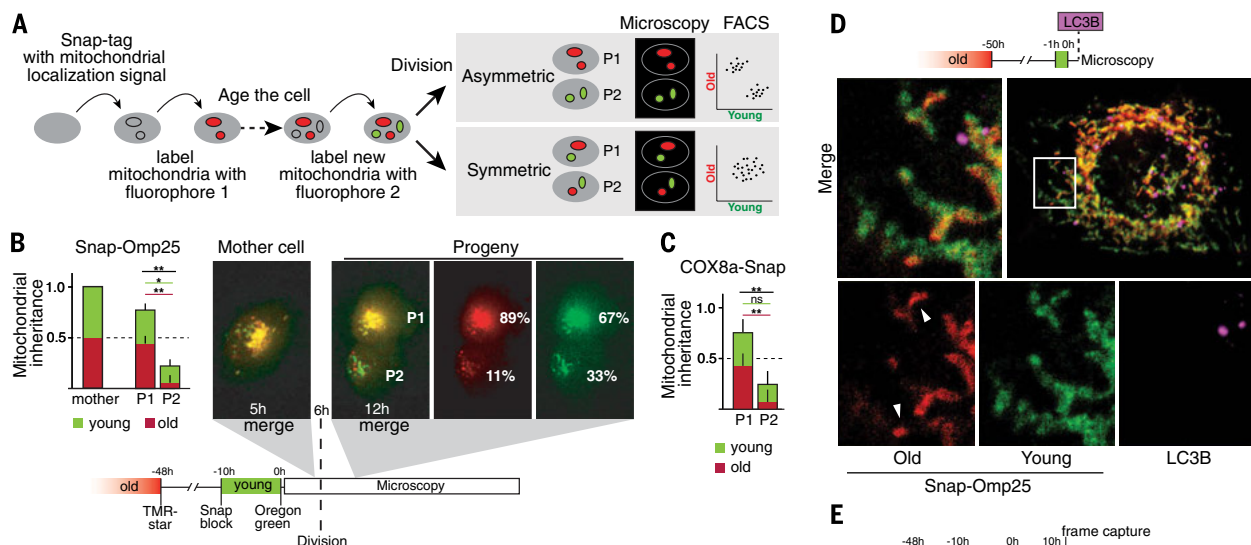


Fig. 2. Age-dependent segregation and subcellular localization of mitochondria. (A) Schematic of the labeling strategy using Snap-tag chemistry. (B and C) Analysis of mitochondrial outer membrane (B) and inner membrane (C) inheritance upon cell division. Red and green sections of bars represent the old and young labels, respectively. Values were scaled so that total intensity (red + green) of the mother cell is 1 ($n = 5$). Representative division occurring at 6 hours after the second (green) label is shown. Percent values represent the average of five divisions. Original magnification 40x. (D) Confocal microscopy of a cell with ≥ 50 -hour-old and 0- to 1-hour-old mitochondrial Snap-Omp25 labeled red and green, respectively. Mitochondrial network contains domains with different levels of enrichment for the old proteins. Mitochondrial domains enriched with old proteins (arrowheads) are not associated with autophagosomes detected by immunofluorescence for LC3B (purple) (63x, 2 μ m Z section). (E) Localization of old (red) and young (green) mitochondria (Snap-Omp25) 10 hours after labeling in an undivided cell. Squares mark regions used for measurements of the perinuclear and peripheral intensities in frames captured 10 hours after labeling for $n = 3$ (cells imaged from three separate labeling experiments) (* $P < 0.05$, ** $P < 0.01$, t test).

the failure to asymmetrically apportion old mitochondria in a single division caused a persistent loss of stemness in SLCs.

To understand how alterations of mitochondrial dynamics and quality control might eliminate the age-selective apportioning, we administered mDivi-1 to cells 46 hours after labeling old mitochondria and followed the cells with live microscopy. The old mitochondrial label that had been confined to the perinuclear region spread throughout the mitochondrial network of the cell periphery after mDivi-1 administration (Fig. 4C, fig. S14C, and movie S4). Thus, stem cells normally confine mitochondria containing old proteins to distinct subcellular domains by a Drp1-dependent mech-

anism, and such age-dependent localization of old mitochondria may be required for their asymmetric apportioning.

Our approaches for studying age-selective asymmetry during cell division show that mammalian epithelial stemlike cells allocate their mitochondria age-dependently and asymmetrically between daughters upon cell division. The mechanisms involved require normal functioning of the mitochondrial quality-control machineries and mitochondrial fission that spatially restrict old mitochondrial matter to the perinuclear region of the mother cell. Because our work was conducted on mammary epithelial stemlike cells in vitro, future work addressing

the extent of the phenomenon in other stem cell compartments and in vivo is needed. Interestingly, asymmetric cell division of mammalian embryonic stem cells depends on polarized paracrine signals (27) that could also further influence mitochondrial apportioning. Other recent evidence has implicated mitochondrial fitness in aging (4, 28, 29) and in tissue maintenance (30, 31). It will be important to determine whether the age-dependent asymmetric apportioning of mitochondria described here has a role in such physiologic processes.

Fig. 3. Stemness properties of daughter cells receiving younger mitochondria. (A)

FACS-mediated isolation of cell populations with high and low contents of old mitochondria (Pop1 and Pop2, respectively). Images show representative populations after 1 and 3 days in culture. (B) Mammosphere-forming capacity of Pop1 and Pop2 cells for $n = 5$ (scale bar, 50 μm ; $**P < 0.01$, t test).

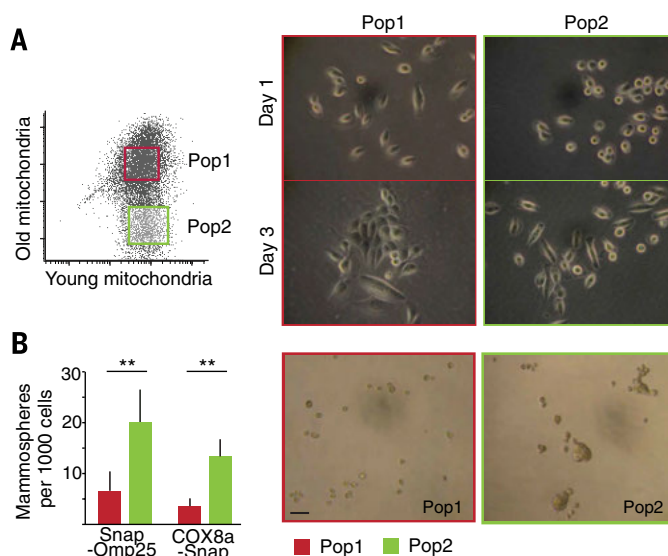
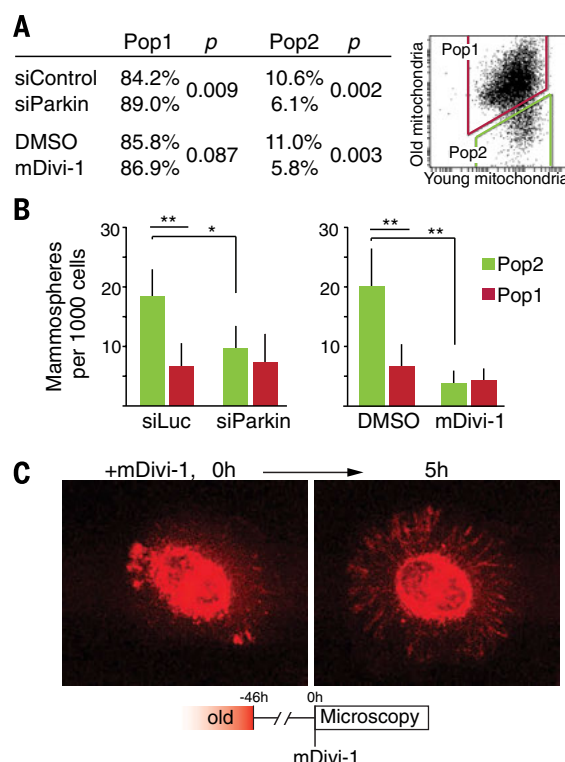


Fig. 4. Effects of mitochondrial quality control on asymmetric apportioning of old mitochondria during cell division. (A)

FACS analyses of mitochondrial apportioning in cells with defective mitochondrial quality control induced by siRNA-mediated depletion of Parkin (siParkin) or pharmacological inhibition of mitochondrial fission (mDivi-1). Table presents the percentages of cells in the two populations for $n = 3$. (B) Mammosphere-forming capacity of cells in Pop1 and Pop2 are equal after siRNA Parkin and mDivi-1 ($n = 3$). (C) Localization of old mitochondria after treatment with mDivi-1. Images are frame captures at start (0 hours) and 5 hours after mDivi-1 administration. Original magnification 63 \times . ($*P < 0.05$, $**P < 0.01$, t test)



REFERENCES AND NOTES

1. D. J. Rossi *et al.*, *Nature* **447**, 725–729 (2007).
2. F. Courmilleau, M. Fürthauer, J. A. Knoblich, M. González-Gaitán, *Nature* **458**, 1051–1055 (2009).
3. P. Fichelson *et al.*, *Nat. Cell Biol.* **11**, 685–693 (2009).
4. J. R. McFaline-Figueroa *et al.*, *Aging Cell* **10**, 885–895 (2011).
5. H. Aguilaniu, L. Gustafsson, M. Rigoulet, T. Nyström, *Science* **299**, 1751–1753 (2003).
6. R. Spokoini *et al.*, *Cell Reports* **2**, 738–747 (2012).
7. M. A. Rujano *et al.*, *PLOS Biol.* **4**, e417 (2006).
8. M. Hernebring *et al.*, *Sci. Rep.* **3**, 1381 (2013).
9. D. Vilchez *et al.*, *Nature* **489**, 304–308 (2012).
10. C. L. Chaffer *et al.*, *Proc. Natl. Acad. Sci. U.S.A.* **108**, 7950–7955 (2011).
11. A. Raouf *et al.*, *Cell Stem Cell* **3**, 109–118 (2008).
12. G. H. Patterson, J. Lippincott-Schwartz, *Science* **297**, 1873–1877 (2002).
13. G. M. Lee, S. S. Fong, D. J. Oh, K. Francis, B. O. Palsson, *In Vitro Cell. Dev. Biol. Anim.* **38**, 90–96 (2002).
14. A. Keppler *et al.*, *Nat. Biotechnol.* **21**, 86–89 (2003).
15. G. Hernandez *et al.*, *Autophagy* **9**, 1852–1861 (2013).
16. K. A. Lukyanov, D. M. Chudakov, S. Lukyanov, V. V. Verkhrusha, *Nat. Rev. Mol. Cell Biol.* **6**, 885–891 (2005).
17. G. Dontu *et al.*, *Genes Dev.* **17**, 1253–1270 (2003).
18. K. Okatsu *et al.*, *Genes Cells* **15**, 887–900 (2010).
19. C. Mantel, S. Messina-Graham, H. E. Broxmeyer, *Cell Cycle* **9**, 2008–2017 (2010).
20. A. Charruyer *et al.*, *J. Invest. Dermatol.* **132**, 2522–2533 (2012).
21. R. Higuchi *et al.*, *Curr. Biol.* **23**, 2417–2422 (2013).
22. C. Y. Lai, E. Jaruga, C. Borghouts, S. M. Jazwinski, *Genetics* **162**, 73–87 (2002).
23. E. Smirnova, L. Griparic, D. L. Shurland, A. M. van der Blik, *Mol. Biol. Cell* **12**, 2245–2256 (2001).
24. C. Vives-Bauza *et al.*, *Proc. Natl. Acad. Sci. U.S.A.* **107**, 378–383 (2010).
25. G. L. McLelland, V. Soubannier, C. X. Chen, H. M. McBride, E. A. Fon, *EMBO J.* **33**, 282–295 (2014).
26. A. Cassidy-Stone *et al.*, *Dev. Cell* **14**, 193–204 (2008).
27. S. J. Habib *et al.*, *Science* **339**, 1445–1448 (2013).
28. A. L. Hughes, D. E. Gottschling, *Nature* **492**, 261–265 (2012).
29. S. M. Rafelski *et al.*, *Science* **338**, 822–824 (2012).
30. A. Vazquez-Martin *et al.*, *Aging* **4**, 393–401 (2012).
31. B. DuBoff, J. Götz, M. B. Feany, *Neuron* **75**, 618–632 (2012).

ACKNOWLEDGMENTS

We thank all members of the Sabatini and Katajisto laboratories—especially A. Efeyan, W. Comb, Y. Chudnovsky, and L. Schweitzer—for comments on this manuscript; K. Birsoy and E. Salminen for help and reagents; and K. Ottina for RNAi reagents. This work was supported by the U.S. National Institutes of Health (R01 CA103866, R01 CA129105, and R37 AI047389) (D.M.S.), Foundations' Post Doc Pool (P.K.), Academy of Finland (P.K.), Juselius Foundation (P.K.) and Marie Curie Actions (P.K.). D.M.S. is an Investigator of the Howard Hughes Medical Institute.

SUPPLEMENTARY MATERIALS

www.sciencemag.org/content/348/6232/340/suppl/DC1
Materials and Methods
Figs. S1 to S17
Table S1
Movies S1 to S5
References

25 August 2014; accepted 12 March 2015
Published online 2 April 2015;
10.1126/science.1260384

PROTEIN STRUCTURE

Engineering of a superhelicase through conformational control

Sinan Arslan,¹ Rustem Khafizov,¹ Christopher D. Thomas,²
Yann R. Chemla,¹ Taekjip Ha^{1,3,4,*}

Conformational control of biomolecular activities can reveal functional insights and enable the engineering of novel activities. Here we show that conformational control through intramolecular cross-linking of a helicase monomer with undetectable unwinding activity converts it into a superhelicase that can unwind thousands of base pairs processively, even against a large opposing force. A natural partner that enhances the helicase activity is shown to achieve its stimulating role also by selectively stabilizing the active conformation. Our work provides insight into the regulation of nucleic acid unwinding activity and introduces a monomeric superhelicase without nuclease activities, which may be useful for biotechnological applications.

Protein functions can be regulated by controlling protein conformation, binding of ligands and effector molecules, and interactions with other proteins. Many techniques have been developed for conformational control of protein function, mainly based on inhibition of activity and removal of that inhibition in a controlled manner (1–3). Here we demonstrate that intramolecular cross-linking of an enzyme without detectable unwinding activity can convert it to a superhelicase by stabilizing its active conformation.

Although studies have shown how various helicases can translocate on single-stranded nucleic acids directionally, the mechanism of nucleic acid unwinding and how the unwinding activity is regulated remain unclear (4). Because helicases that are free to unwind all nucleic acids encountered can be detrimental to genome integrity, it is critical to understand how their unwinding activities are regulated.

Rep, PcrA, and UvrD are structurally homologous 3'-to-5' single-stranded DNA (ssDNA) translocases and helicases that can unwind double-stranded DNA (dsDNA) using energy from adenosine triphosphate (ATP) binding and hydrolysis. However, in vitro studies showed that monomers of these helicases have a very poor activity and cannot processively unwind DNA (5–8). They require oligomerization or association with cellular partner proteins to become capable of unwinding (4, 9–11). Crystal structures revealed a flexible domain (2B) that can rotate 130° to 160° in a swiveling motion between two conformations, referred to as the “open” and “closed” forms (12–15) (Fig. 1A). Whether 2B is essential for unwinding or whether it plays a regulatory role has been debated, as well as which of the two

conformations is required for DNA unwinding (4, 12–17), but no direct evidence has been found linking these conformations to the unwinding function.

To determine which conformation is assumed during unwinding, we engineered *Escherichia coli* Rep mutants that are intramolecularly cross-linked to constrain the 2B domain in closed or open conformations, respectively, termed “Rep-X” and “Rep-Y.” Residues for the cysteine substitution mutagenesis and the length of the bis-maleimide cross-linkers were selected such that when cross-linked, 2B cannot rotate appreciably, effectively locking the protein in one conformation (Fig. 1A) (18). Mutagenesis, purification, cross-linking procedures, and validation that cross-linking was intramolecular rather than intermolecular are described in fig. S1 and the supplementary text (18). Cross-linking had only modest effects on ATPase activities of Rep-X and Rep-Y (fig. S2).

In multiple-turnover ensemble unwinding reactions using fluorescently labeled DNA, Rep-X unwound dsDNA [18 or 50 base pairs (bp)] with a 3' overhang at a much faster rate and a higher reaction amplitude than the wild-type Rep or the un-cross-linked double-cysteine mutant (fig. S2, A to C). In contrast, Rep-Y unwinding rates were similar to that of Rep (fig. S2D), indicating that the dramatic unwinding enhancement is specifically achieved in the closed conformation. To determine whether the large enhancement in unwinding activity results from the activation of a monomer or from enhanced oligomerization, we performed single-molecule fluorescence resonance energy transfer (smFRET) experiments. Proteins were immobilized to a surface through the N-terminal His₆-tag (Fig. 1B) (18) to ensure that the observed activity belonged to monomers (5). We used a 18-bp duplex DNA with a 3'-(dT)₂₀ overhang labeled with a donor (Cy3) and an acceptor (Cy5) at opposite ends of the duplex (Fig. 1B). When the DNA and ATP were added to the reaction chamber, we could observe the capture of a single DNA molecule by a single protein as the sudden appearance of fluorescence signal (Fig. 1C). Unwound ssDNA coiled up

due to high flexibility [FRET efficiency (E_{FRET}) increase] (19), full unwinding released the acceptor strand (acceptor signal disappearance and donor signal increase), and then the donor strand dissociated (loss of fluorescence). The mean duration of unwinding measured from the E_{FRET} increase to acceptor strand release was ~0.6 s, giving a lower limit on the unwinding speed of 30 bp/s for the 18-bp substrate (fig. S3, A and B). Most (82%) of the DNA molecules [661 of 809 (661/809)] that initially bound to Rep-X monomers were unwound (fig. S3, C and D). In contrast, Rep and Rep-Y showed 2% (13/847) and 16% (357/2212) unwinding yields, respectively, suggesting that constraining Rep into the closed form selectively activates the unwinding activity of a monomer. The residual activities for Rep and Rep-Y may be due to conformational constraints caused by surface tethering in a small fraction of molecules or passive helicase activity of trapping thermally melted DNA.

The unwinding processivity of Rep and related helicases is limited, even in their oligomeric forms, ranging from 30 to 50 bp (5, 8, 20). We used a dual optical tweezers assay to investigate the processivity of Rep-X (Fig. 2A) (18, 21). The two traps held submicrometer-sized polystyrene beads. The first was coated with 6-kbp dsDNA (kbp, thousand base pairs) with a 3' poly-dT ssDNA overhang [(dT)_{10,15,75}, as specified in the figures] via the blunt end. The other bead was coated with Rep-X molecules via the His₆-tag. A laminar flow cell with two streams of buffer was used to control unwinding initiation (Fig. 2B, inset). When we brought the two beads in close proximity in the first stream (buffer C with 100 μM ATP and 100 μM ATP-γS), a single Rep-X binding to the 3' overhang of the DNA formed a tether between the two beads without initiating unwinding. When we moved the tethered beads to the second stream (buffer C and 1 mM ATP), the DNA tether progressively shortened as the Rep-X monomer unwound and pulled the DNA (Fig. 2B). Unless otherwise stated, *E. coli* ssDNA binding protein (SSB) was added to the second laminar stream to prevent any subsequent interaction of unwound ssDNA with other Rep-X on the bead surface, but we did not find any difference in behavior with or without SSB (18). The DNA was held under constant force, ranging from 4 to 22 pN, as indicated. Additional controls and considerations ascertained that the observed activity stemmed from a single Rep-X, regardless of the 3'-tail length and inclusion or omission of SSB (supplementary text). Notably, 95% (38/40) of the Rep-X-DNA complexes resulted in the unwinding of the entire observable ~4-kbp region of the 6-kbp DNA in a processive manner, and the average pause-free speed was 136 bp/s (Fig. 2, B to D). In comparison, only 3% (2/61 at 4 pN, none at higher forces) of wild-type Rep and 7% (5/70) of Rep-Y complexes displayed such processive unwinding. Rep-X probably has even greater processivity than 6 kbp and is currently limited only by the length of the DNA used, because all of the initiated unwinding events proceeded to the end of the measurable range of

¹Physics Department and Center for the Physics of Living Cells, University of Illinois at Urbana-Champaign, Urbana, IL 61801, USA. ²Astbury Centre for Structural Molecular Biology, University of Leeds, Leeds LS2 9JT, UK. ³Institute for Genomic Biology, University of Illinois at Urbana-Champaign, Urbana, IL 61801, USA. ⁴Howard Hughes Medical Institute, University of Illinois, Urbana, IL 61801, USA.

*Corresponding author. E-mail: tjha@illinois.edu

our assay where we manually stopped the experiment. We confirmed that Rep-X, but not Rep, can unwind 3.5-kb DNA in the absence of force, which indicates that the tension is not needed for high processivity (fig. S4).

We determined how much force Rep-X can generate by performing measurements without maintaining a constant force. Fixing trap positions led to a rapid build-up of force in the direction opposing unwinding until the measurement was terminated due to the breakage of connection between the two beads (Fig. 2E). The highest loads achieved in this experiment were not enough to stall the helicase permanently. More detailed analysis showed that the pause-free unwinding rate of Rep-X was not impeded by increasing loads up to the limits of the linear regime of our trap (Fig. 2F): ~60 pN (18). These results suggest that Rep-X is the strongest helicase known to date (22, 23).

To test whether the generation of a super active helicase via conformational control can be reproduced for other helicases, we engineered PcrA-X from *Bacillus stearothermophilus* PcrA.

Mutations involved replacing two highly conserved cysteines (tables S1 and S2), reducing the apparent ATPase activity from ~40 ATP/s (wild type) to 5 ATP/s. Upon cross-linking in the closed form, PcrA-X retained the low-ATPase activity (4.3 ATP/s) but exhibited an enhanced helicase activity in comparison to PcrA in ensemble reactions (Fig. 3A and fig. S5, A and B). Our smFRET experiments showed that PcrA-X monomers can unwind 39% (228/578) of DNA molecules, compared with 4% (26/617) for PcrA (fig. S5, C and D). In the optical tweezers assay, PcrA-X monomers were capable of processively unwinding 1- to 6-kbp-long DNA, albeit at a much lower rate (2 to 15 bp/s) (Fig. 3B), whereas no PcrA molecule (0/51) could do the same (Fig. 3C). Despite the impaired activity levels of the PcrA mutant, conversion to PcrA-X made its monomers into highly processive helicases.

Strong helicase activity of Rep-X and PcrA-X raises the possibility that their cellular partners may switch on their unwinding activity by constraining them in the closed conformation. One such partner of PcrA is RepD, a plasmid repli-

cation initiator protein that recognizes and forms a covalent adduct with the *oriD* sequence of the plasmid and then recruits PcrA for processive unwinding (24, 25). We prepared an *oriD* DNA-RepD adduct and measured the intramolecular conformation of PcrA bound to this adduct (18). We used a double-cysteine mutant of PcrA (PcrA-DM) stochastically labeled with a mixture of donor and acceptor fluorophores that would be expected to generate high E_{FRET} in the closed form and low E_{FRET} in the open form (Fig. 3D, schematics) (26). The E_{FRET} distributions of PcrA-DM bound to the *oriD* DNA-RepD adduct and the *oriD* DNA alone showed that RepD biases PcrA toward the closed high- E_{FRET} conformation (Fig. 3D), which may be the basis for unwinding activation in vivo.

Why does constraining Rep and PcrA into the closed form convert an enzyme with undetectable unwinding activity to a super helicase? The intrinsic unwinding activity itself may require the closed form; for example, via the torque-wrench mechanism proposed for UvrD (14). Alternatively, 2B may play a regulatory role (4); more specifically, the open form may inhibit helicase function, and

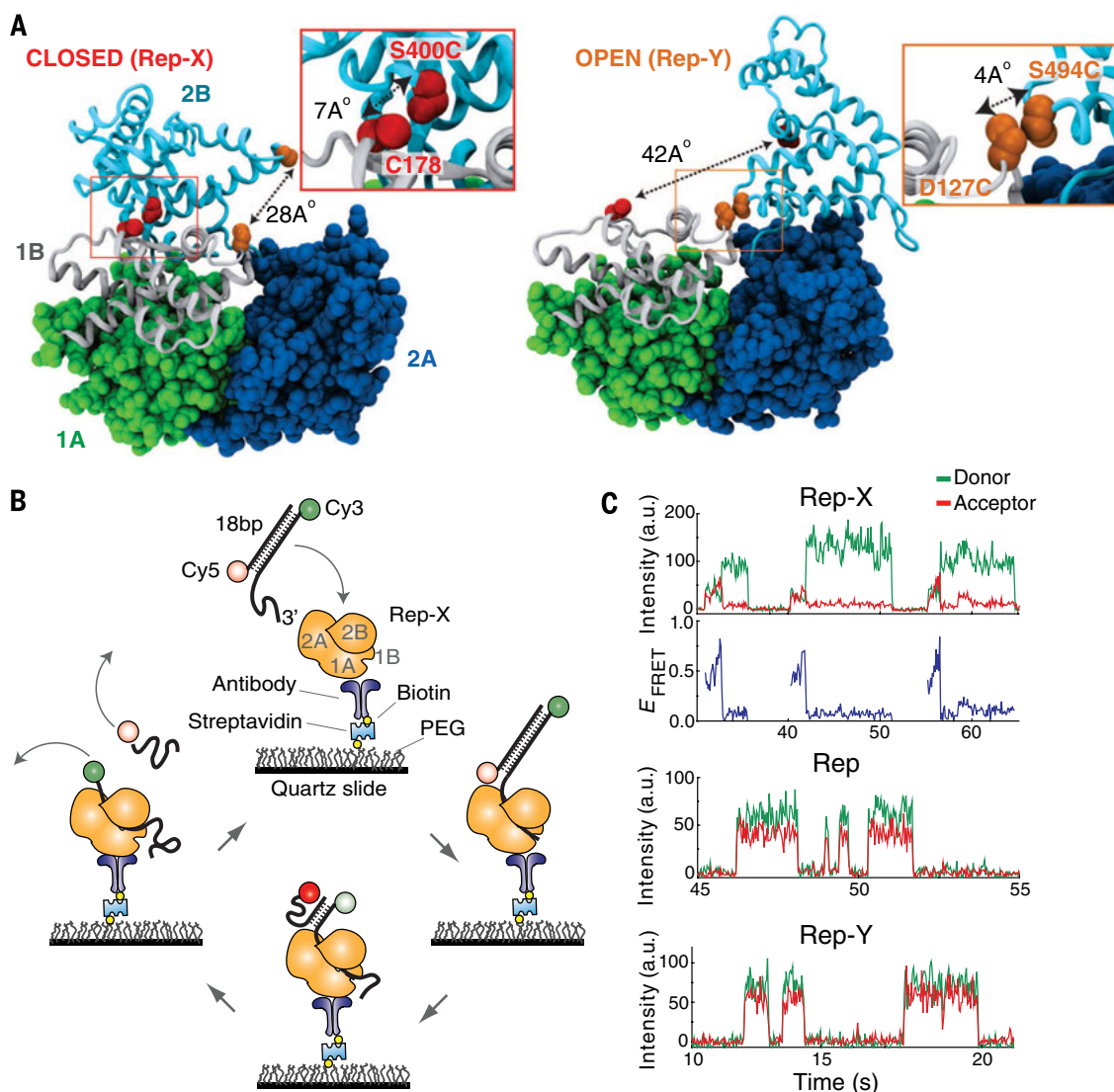


Fig. 1. Cross-link-mediated conformational control of helicase activity.

(A) Open and closed forms Rep crystal structures (Protein Data Bank entry 1UAA). Domains are colored and named. Cysteine pairs that were cross-linked to lock the protein into the closed or open conformation are shown in red or orange, respectively. Distances between the pairs are noted. Close-up views show the pairs that were cross-linked. C, Cys; S, Ser; D, Asp. (B) Schematics of smFRET analysis. The brightness of the donor (green) and acceptor (red) changes as unwinding progresses. PEG, polyethylene glycol. (C) Representative single-molecule time traces for Rep-X, Rep, and Rep-Y. a.u., arbitrary units.

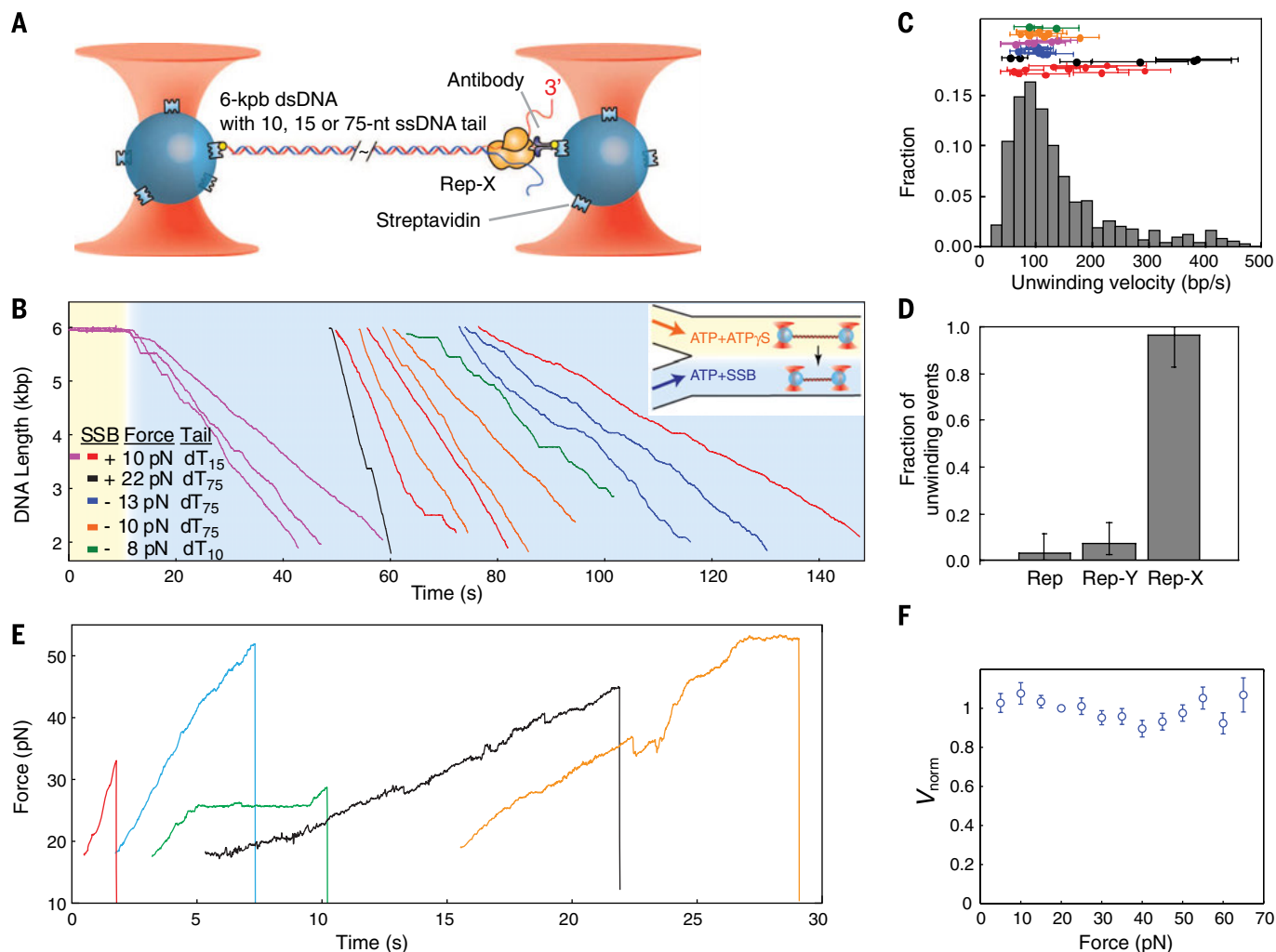


Fig. 2. Rep-X processivity and force generation. (A) Schematics of optical tweezers assay for Rep-X DNA unwinding. nt, nucleotide. (B) 6-kbp DNA unwinding traces (colored according to overhang length, SSB, and force; offset for clarity). Background colors denote two laminar flows (see inset). (C) Distribution of unwinding speed ($N = 38$ molecules). Mean speed and SD for each molecule are plotted above [colors as in (B)]. (D) Fraction of complete DNA unwinding events. Error bars represent 95% confidence bounds. (E) Unwinding traces by five Rep-X molecules in the fixed trap assay (colored and offset for clarity). (F) Normalized unwinding velocities (V_{norm}) of 58 Rep-X molecules plotted versus force. Error bars denote SEM.

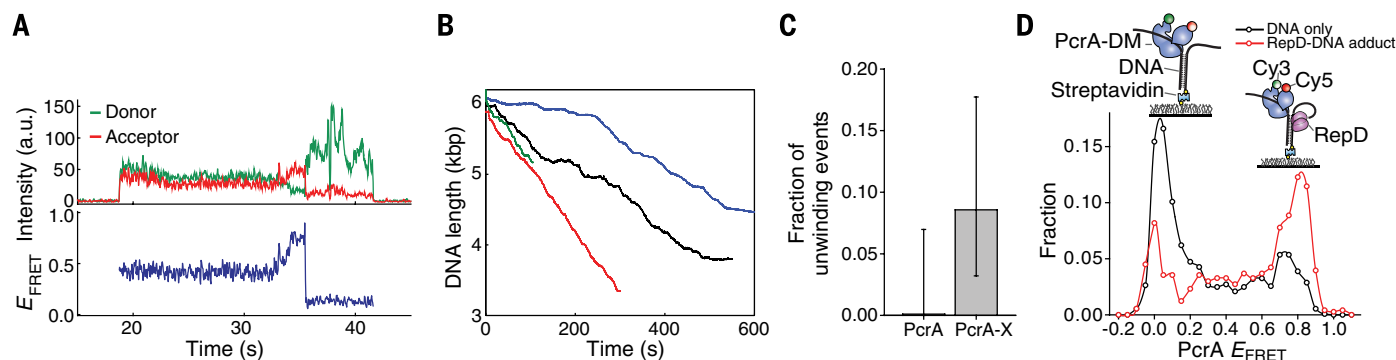


Fig. 3. Conformational control of PcrA helicase. (A) Representative smFRET time traces for a PcrA-X monomer. (B) Representative processive unwinding traces by PcrA-X in the optical tweezers assay. Each color represents a single PcrA-X molecule. (C) Fractions of enzyme-DNA binding that led to processive unwinding of 6-kbp DNA in the optical tweezers assay. Error bars represent the 95% confidence bounds. (D) The conformational effect of RepD on PcrA was measured using a smFRET assay. E_{FRET} histograms show that the PcrA bound to the RepD adduct is biased toward the closed form (high E_{FRET} population) compared with PcrA bound to the bare *oriD* DNA.

cross-linking to the closed form prevents this inhibitory mechanism. We prefer the latter for the following reasons: First, Rep-Y unwinds DNA as well as Rep when functioning as oligomers (fig. S2D), suggesting that the closed form per se is not absolutely required. Second, simultaneous measurement of unwinding and UvrD conformation showed that UvrD assumes the closed conformation during unwinding, but after it unwinds ~10 bp, it reverts to the open conformation and rewinds the DNA after strand switching (27). Therefore, we suggest that Rep-X is highly processive because the open conformation, which is required for strand switching and rewinding, is disallowed (27, 28). The deletion of 2B in Rep (RepΔ2B) makes it active in unwinding as a monomer (16), possibly by inhibiting strand switching. The poorer processivity of RepΔ2B compared with Rep-X (16) may stem from a lack of 2B, which carries its own dsDNA binding capacity. Topological enclosure of DNA in Rep-X and Rep-Y is unlikely to be the reason, because Rep-X showed at least 10-fold higher yield of highly processive unwinding than Rep-Y or Rep (Fig. 2D).

We demonstrated a conformational control that activates a naturally inhibited unwinding function to create a superhelicase with high processivity and high tolerance against force. RecBCD has similarly high processivity but contains associated nucleases. Moreover, it is known to backslide at opposing forces below 10 pN (22), whereas Rep-X can be active against forces as high as 60 pN. High processivity and high tolerance against load without nuclease activities may also be useful for biotechnological applications such as nanopore sequencing and isothermal DNA amplification.

REFERENCES AND NOTES

- B. Choi, G. Zocchi, Y. Wu, S. Chan, L. Jeanne Perry, *Phys. Rev. Lett.* **95**, 078102 (2005).
- M. Volgraf et al., *Nat. Chem. Biol.* **2**, 47–52 (2006).
- M. Tomishige, R. D. Vale, *J. Cell Biol.* **151**, 1081–1092 (2000).
- T. M. Lohman, E. J. Tomko, C. G. Wu, *Nat. Rev. Mol. Cell Biol.* **9**, 391–401 (2008).
- T. Ha et al., *Nature* **419**, 638–641 (2002).
- W. Cheng, J. Hsieh, K. M. Brendza, T. M. Lohman, *J. Mol. Biol.* **310**, 327–350 (2001).
- N. K. Maluf, C. J. Fischer, T. M. Lohman, *J. Mol. Biol.* **325**, 913–935 (2003).
- A. Niedziela-Majka, M. A. Chesnik, E. J. Tomko, T. M. Lohman, *J. Biol. Chem.* **282**, 27076–27085 (2007).
- M. S. Dillingham, *Biochem. Soc. Trans.* **39**, 413–423 (2011).
- L. E. Mechanic, B. A. Frankel, S. W. Matson, *J. Biol. Chem.* **275**, 38337–38346 (2000).
- P. Soultanas et al., *Nucleic Acids Res.* **27**, 1421–1428 (1999).
- S. S. Velankar, P. Soultanas, M. S. Dillingham, H. S. Subramanya, D. B. Wigley, *Cell* **97**, 75–84 (1999).
- S. Korolev, J. Hsieh, G. H. Gauss, T. M. Lohman, G. Waksman, *Cell* **90**, 635–647 (1997).
- J. Y. Lee, W. Yang, *Cell* **127**, 1349–1360 (2006).
- H. Jia et al., *J. Mol. Biol.* **411**, 633–648 (2011).
- K. M. Brendza et al., *Proc. Natl. Acad. Sci. U.S.A.* **102**, 10076–10081 (2005).
- W. Cheng et al., *Proc. Natl. Acad. Sci. U.S.A.* **99**, 16006–16011 (2002).
- Materials and methods are available as supplementary materials on Science Online.
- G. Lee, M. A. Bratkowski, F. Ding, A. Ke, T. Ha, *Science* **336**, 1726–1729 (2012).
- J. A. Ali, T. M. Lohman, *Science* **275**, 377–380 (1997).
- J. R. Moffitt et al., *Nature* **457**, 446–450 (2009).
- T. T. Perkins, H. W. Li, R. V. Dalal, J. Gelles, S. M. Block, *Biophys. J.* **86**, 1640–1648 (2004).
- J. G. Yodh, M. Schlierf, T. Ha, *Q. Rev. Biophys.* **43**, 185–217 (2010).
- W. Zhang et al., *J. Mol. Biol.* **371**, 336–348 (2007).
- C. Machón et al., *Nucleic Acids Res.* **38**, 1874–1888 (2010).
- J. Park et al., *Cell* **142**, 544–555 (2010).
- M. J. Comstock et al., *Science* **348**, 352–354 (2015).
- M. N. Dessinges, T. Lionnet, X. G. Xi, D. Bensimon, V. Croquette, *Proc. Natl. Acad. Sci. U.S.A.* **101**, 6439–6444 (2004).
- P. Jena, and A. Jain for helpful discussions. This work was supported by the NIH (grant GM065367) and the NSF (Physics Frontier Center grant PHY 0822613 and CAREER award MCB 09-52442 to Y.R.C.). T.H. and S.A. have filed a patent application (62/079,183) that relates to superhelicases.

SUPPLEMENTARY MATERIALS

www.sciencemag.org/content/348/6232/344/suppl/DC1
Materials and Methods
Supplementary Text
Figures S1 to S5
Tables S1 to S2
References (29–41)

9 October 2014; accepted 11 March 2015
10.1126/science.aaa0445

AXONAL REGENERATION

Systemic administration of epothilone B promotes axon regeneration after spinal cord injury

Jörg Ruschel,¹ Farida Hellal,^{1*†} Kevin C. Flynn,^{1*†} Sebastian Dupraz,^{1*} David A. Elliott,¹ Andrea Tedeschi,¹ Margaret Bates,² Christopher Sliwinski,³ Gary Brook,^{4,5} Kristina Dobrindt,⁶ Michael Peitz,⁶ Oliver Brüstle,⁶ Michael D. Norenberg,⁷ Armin Blesch,³ Norbert Weidner,³ Mary Bartlett Bunge,² John L. Bixby,² Frank Bradke^{1§}

After central nervous system (CNS) injury, inhibitory factors in the lesion scar and poor axon growth potential prevent axon regeneration. Microtubule stabilization reduces scarring and promotes axon growth. However, the cellular mechanisms of this dual effect remain unclear. Here, delayed systemic administration of a blood-brain barrier-permeable microtubule-stabilizing drug, epothilone B (epoB), decreased scarring after rodent spinal cord injury (SCI) by abrogating polarization and directed migration of scar-forming fibroblasts. Conversely, epothilone B reactivated neuronal polarization by inducing concerted microtubule polymerization into the axon tip, which propelled axon growth through an inhibitory environment. Together, these drug-elicited effects promoted axon regeneration and improved motor function after SCI. With recent clinical approval, epothilones hold promise for clinical use after CNS injury.

An ideal treatment to induce axon regeneration in the injured central nervous system (CNS) should reduce scarring (1) and growth-inhibitory factors at the lesion site (2–4), reactivate the axon growth potential (5), and be administrable as a medication after injury. Recently, a number of combinatorial approaches have led to axon regeneration (6, 7). These approaches, however, involve multiple drugs, enzymes, and interventions, rendering clinical translation difficult. Moderate microtubule stabilization by the anticancer drug Taxol promotes axon regeneration by reducing fibrotic scarring and increasing axon growth (8, 9). However, it remains elusive how microtubule stabilization induces such divergent effects. Moreover, Taxol cannot be used for clinical CNS intervention because it does not cross the blood-brain barrier (10).

We aimed to target microtubule stabilization in the injured CNS in a clinically feasible way and to decipher its distinct cellular actions. We used epothilones, a class of U.S. Food and

Drug Administration (FDA)-approved blood-brain barrier-permeable microtubule-stabilizing drugs (11). Mass spectrometry confirmed that

¹Axonal Growth and Regeneration, German Center for Neurodegenerative Diseases, Ludwig-Erhard-Allee 2, 53175 Bonn, Germany. ²The Miami Project to Cure Paralysis, University of Miami Miller School of Medicine, 1095 Northwest 14th Terrace, Miami, FL 33136, USA. ³Spinal Cord Injury Center, Heidelberg University Hospital, Schlierbacher Landstr. 200A, 69118 Heidelberg, Germany. ⁴Institute for Neuropathology, RWTH Aachen University, Steinbergweg 20, 52074, Aachen, Germany. ⁵Jülich-Aachen Research Alliance—Translational Brain Medicine. ⁶Institute of Reconstructive Neurobiology, Life&Brain Center, University of Bonn and Hertie Foundation, Sigmund-Freud-Strasse 25, 53127 Bonn, Germany. ⁷Departments of Pathology, Biochemistry and Molecular Biology, University of Miami School of Medicine, Miami, FL 33101, USA.

*These authors contributed equally to this work. †Present address: Institute for Stroke and Vascular Dementia Research, University of Munich Medical Center, Max Lebsche Platz 30, 81377 Munich, Germany. ‡Present address: Department of Molecular Medicine, Max Planck Institute of Biochemistry, Am Kloppspitz 18, 82152 Martinsried, Germany. §Corresponding author. E-mail: frank.bradke@dzne.de

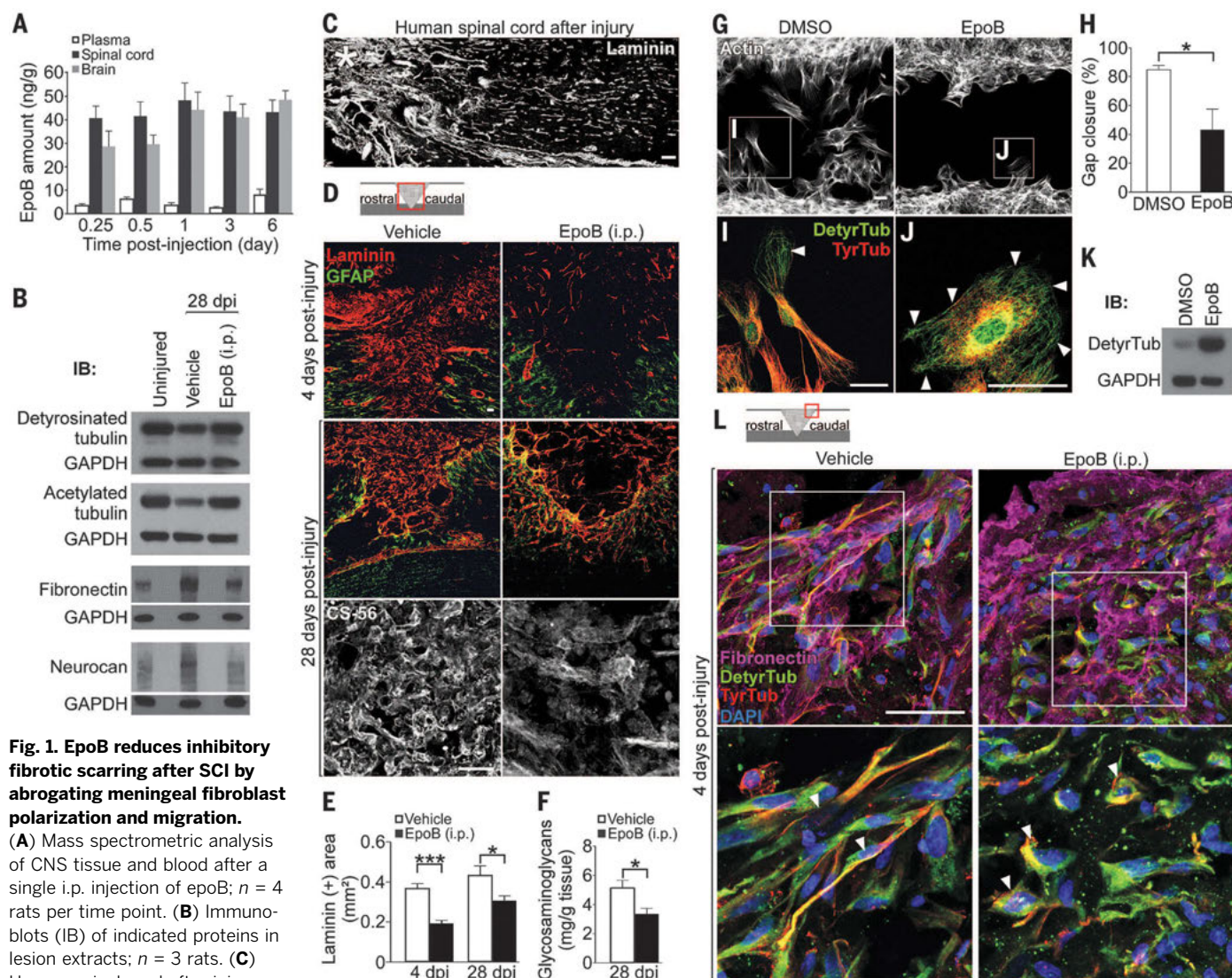
after intraperitoneal (i.p.) injection in adult rats, epoB was rapidly absorbed into the CNS and remained at comparable levels for 6 days (Fig. 1A). Rats i.p. injected with 0.75 mg of epoB per kilogram of body weight (BW) at day 1 and 15 after injury showed increased amounts of de-tyrosinated and acetylated tubulin in lesion site extracts 4 weeks after spinal cord dorsal hemisection (Fig. 1B), indicating increased microtubule stability (12). The dosage used presented no obvious adverse side effects, such as reduced animal weight or decreased white blood cell counts (fig. S1).

Fibrotic scar tissue rich in fibronectin and laminin forms at the lesion site after spinal cord

injury (SCI) in rodents (8) and humans (Fig. 1C and table S1). This scar tissue poses a key impediment to regenerating axons, because it contains axon growth-inhibitory factors, including chondroitin sulfate proteoglycans (CSPGs) (1, 8). Adult rats systemically treated after injury with 0.75 mg/kg BW epoB showed a significant reduction of fibronectin (Fig. 1B) and of laminin-positive fibrotic scar tissue even 4 weeks after dorsal hemisection (Fig. 1, D and E). We found a comparable decrease of fibrotic scarring when epoB was locally delivered to the injury site via an intrathecal catheter (fig. S2) (8). Reduction of fibrotic scar tissue by systemic epoB administration was associated with a decrease of CSPGs

(Fig. 1, D and F), including neurocan (Fig. 1B) and NG2 (13), at the injury site (fig. S3). Astrogliosis and lesion area were similar between treated and control animals (fig. S1), indicating that neuroprotective glial sealing of the injury site (14) was not affected by the treatment.

Scar reduction upon epoB treatment resulted neither from decreased cell proliferation nor from increased apoptosis (fig. S4) but from a migratory defect of scar-forming meningeal fibroblasts (15). In wound-healing assays, epoB inhibited migration of meningeal fibroblasts (Fig. 1, G and H, and movies S1 and S2) by changing their microtubular network. Control cells polarized by forming a leading edge



enriched in stable deetyrosinated microtubules and a trailing edge containing dynamic, tyrosinated microtubules (Fig. 1I), both hallmarks of directed cell migration (16). In contrast, epoB-treated fibroblasts were round and nonpolar (Fig. 1J and fig. S5) with elevated amounts of deetyrosinated microtubules (Fig. 1K) distributed throughout the cell (Fig. 1J). Similarly, systemic administration of epoB after dorsal hemisection prevented the polarization of meningeal fibroblasts at the lesion site into a bipolar, migratory shape (Fig. 1L), which reduced scar formation (Fig. 1, D and E).

In cocultures of meningeal fibroblasts and postnatal cortical neurons, epoB treatment (1 nM) perturbed fibroblast polarization while enhancing axon growth (fig. S5). Moreover, epoB re-

stored axon growth when these neurons were confronted with the inhibitory molecules Nogo-A, CSPGs, or Semaphorin 3A (Fig. 2, A and B), which are abundant at the spinal cord lesion site (2–4, 17). In neurons expressing fluorescently tagged microtubule plus-end-binding protein 3 (EB3-mCherry), which labels polymerizing microtubules (18), epoB induced rapid and concerted microtubule polymerization into the neurite tips (Fig. 2, C and D, and movie S3), causing axon elongation despite inhibitory Nogo-A (Fig. 2E and movie S3). In accordance, low doses of the microtubule-destabilizing drug nocodazole abolished microtubule protrusion in neurites (Fig. 2, D and F) and abrogated the growth-promoting effect of epoB (Fig. 2B). EpoB also promoted axon growth of human cortical neu-

rons under growth permissive as well as non-permissive conditions (fig. S6). In meningeal fibroblasts, however, epoB prevented microtubule polymerization toward the cell edges (Fig. 2G), contrasting with the microtubule dynamics found in neurons. This dichotomy was due to neuron-specific expression of the microtubule-associated protein Tau (fig. S7), which regulates microtubule dynamics, bundling, and binding of microtubule-stabilizing agents (19, 20). In fibroblasts ectopically expressing Tau, epoB induced an accumulation of bundled microtubules (fig. S8) that polymerized toward the cell edge (Fig. 2, H and I, and movie S4), mimicking the effect observed in neurons. In turn, neurons depleted of Tau, by transfection with a plasmid encoding short hairpin

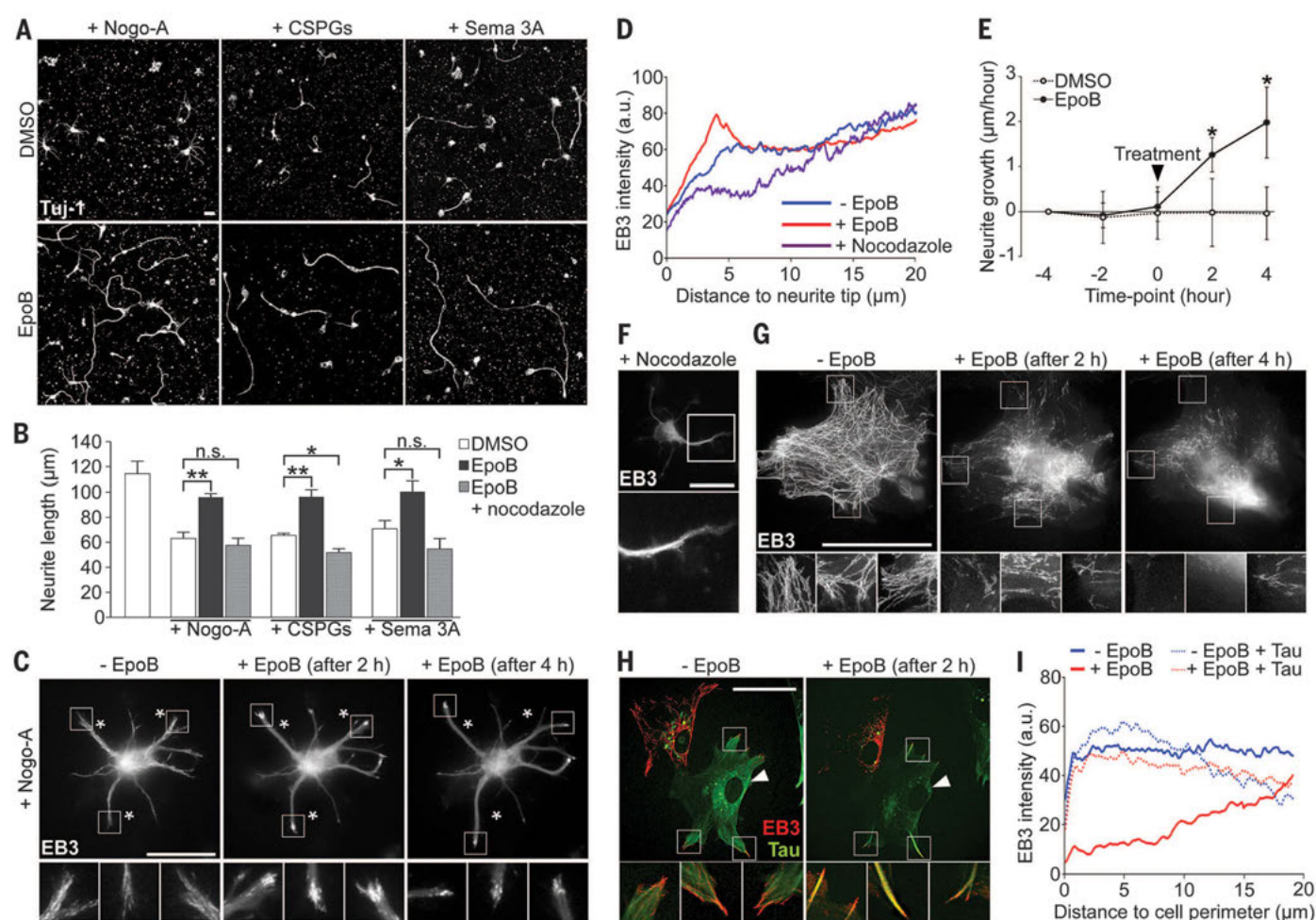


Fig. 2. EpoB promotes microtubule protrusion and axon elongation in neurons while dampening microtubule dynamics in scar-forming fibroblasts.

(A) Beta-3 tubulin (Tuj-1) immunolabeling of neurons on inhibitory substrates (CSPGs, chondroitin sulfate proteoglycans; Sema 3A, Semaphorin 3A). (B) Neurite length of cortical neurons after 48 hours under indicated conditions; $n = 3$ to 4 experiments. (C) EB3-mCherry time-lapse projections in Nogo-A exposed neuron before and after epoB treatment (asterisks, stable landmarks). Bottom panels, high magnification of boxed areas in top panels. (D) EB3-mCherry fluorescence intensity in neurites under indicated conditions; $n = 9$ to 16 neurons (from three experiments). (E) Neurite growth on Nogo-A.

Black arrowhead, time of indicated treatment. $n = 12$ to 15 neurons (from three experiments). (F and G) EB3-mCherry time-lapse projections of nocodazole-treated neuron (F) and epoB-treated meningeal fibroblast (G). Bottom panels, high magnification of boxed areas in top panels. (H) EB3-mCherry time-lapse projections before and after epoB treatment in cultured meningeal fibroblasts with (arrowhead) or without Tau-expression. Bottom panels, magnification of boxed areas in top panels. (I) EB3-mCherry fluorescence intensity in fibroblast periphery under indicated conditions; $n = 20$ cells per condition (from four experiments). Scale bars, 25 μm. Values are plotted as means [± SEM in (B) and (E)]. * $P < 0.05$, ** $P < 0.01$ by Student's t test. n.s., not significant.

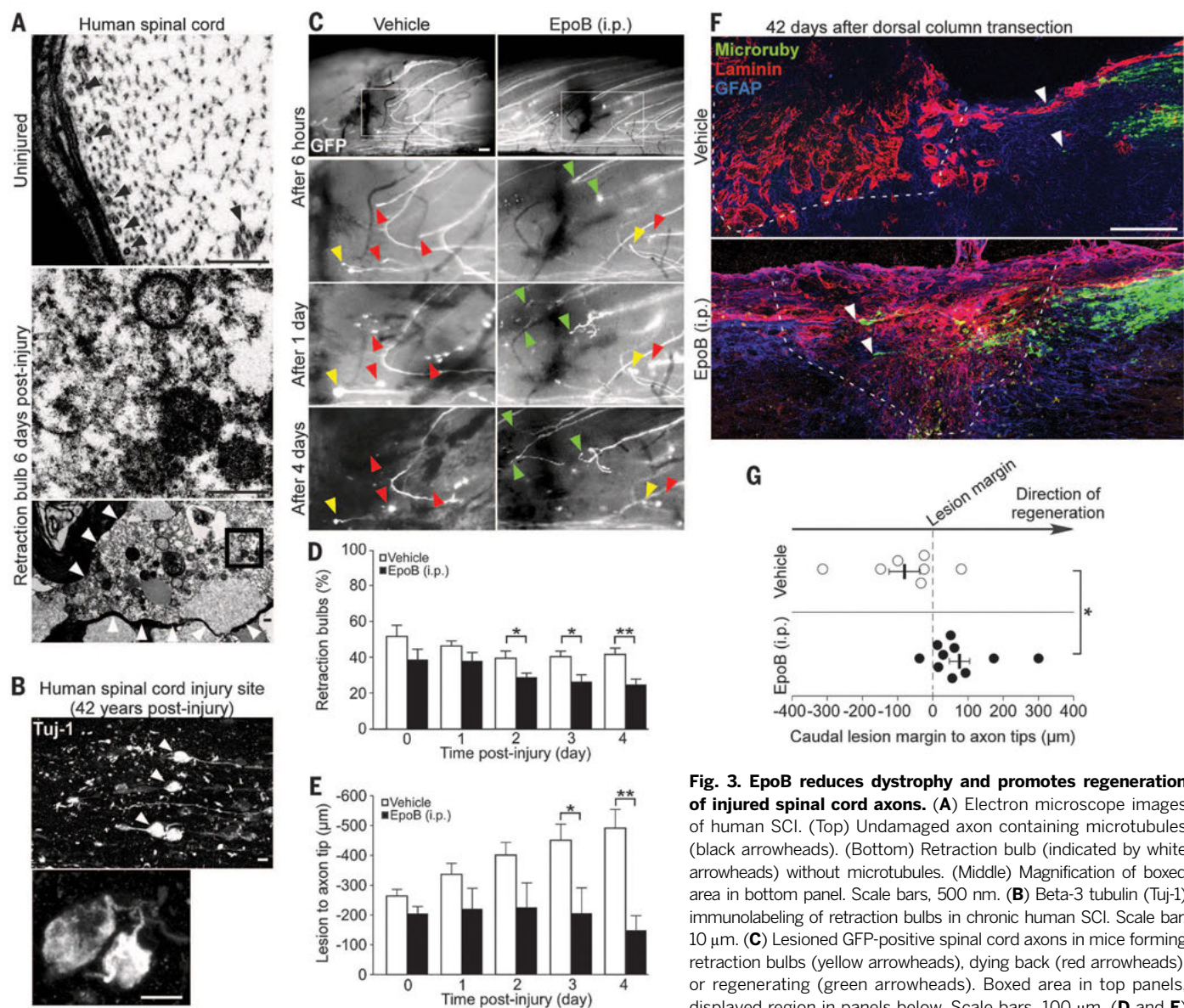


Fig. 3. EpoB reduces dystrophy and promotes regeneration of injured spinal cord axons. (A) Electron microscope images of human SCI. (Top) Undamaged axon containing microtubules (black arrowheads). (Bottom) Retraction bulb (indicated by white arrowheads) without microtubules. (Middle) Magnification of boxed area in bottom panel. Scale bars, 500 nm. (B) Beta-3 tubulin (Tuj-1) immunolabeling of retraction bulbs in chronic human SCI. Scale bar, 10 μm. (C) Lesioned GFP-positive spinal cord axons in mice forming retraction bulbs (yellow arrowheads), dying back (red arrowheads), or regenerating (green arrowheads). Boxed area in top panels, displayed region in panels below. Scale bars, 100 μm. (D and E) Percentage of injured axons forming retraction bulbs (D) and

distance between injured axons and injury site (E); $n = 8$ mice per group. Values are plotted as means + SEM. (F) Microruby-traced mouse dorsal column axons after injury (white arrowheads), laminin and GFAP immunolabeling (dashed line, lesion border). Scale bar, 100 μm. (G) Average distance between caudal lesion margin and injured axons in individual animals (circles) and group means (vertical bars) ± SEM. * $P < 0.05$, ** $P < 0.01$ by Student's t test.

RNA for tau (27), showed reduced microtubule polymerization into the distal neurite when exposed to epoB (fig. S9).

Injured axons in the rodent and human CNS form dystrophic retraction bulbs (Fig. 3, A to D, and table S2), a consequence of microtubule depolymerization and disorganization (Fig. 3, A and B) (22, 23). Because epoB induced microtubule polymerization and axon growth in cultured neurons, we assessed its ability to promote axon regeneration after SCI. In vivo imaging of adult transgenic mice, expressing green fluorescent protein (GFP) in spinal cord dorsal column axons (23, 24), revealed that transected axons of animals injected with 1.5 mg/kg BW epoB exhibited significantly fewer retrac-

tion bulbs (Fig. 3, C and D), reduced axonal dieback, and increased regenerative growth (Fig. 3, C and E). Moreover, in adult mice, systemic and postinjury treatment with epoB promoted axon regeneration after complete dorsal column transection (Fig. 3, F and G).

We then tested whether the treatment also promoted axon regrowth of descending axons important for locomotion. In adult rats injected after injury with 0.75 mg/kg BW epoB, we found a threefold increase of serotonergic fibers caudal to a dorsal hemisection (Fig. 4, A and B). Increased serotonergic innervation strongly correlates with recovery of motor function after SCI (25–27). Therefore, we asked whether the treatment improves walking of adult

rats that underwent a moderate, mid-thoracic spinal cord contusion, a clinically relevant SCI model (28). After contusion injury, epoB administration (0.75 mg/kg BW) reduced fibrotic scarring at the injury site (fig. S10) and promoted serotonergic axon regrowth in the caudal spinal cord (Fig. 4, C and D). Moreover, epoB treatment increased stride length and gait regularity and reduced external rotation of the hind paws (fig. S11), indicating improved walking balance and coordination. Accordingly, epoB-treated animals showed a 50% reduction of foot misplacements on the horizontal ladder compared to injured controls (Fig. 4E and movies S5 and S6). These functional improvements were abrogated by pharmacological

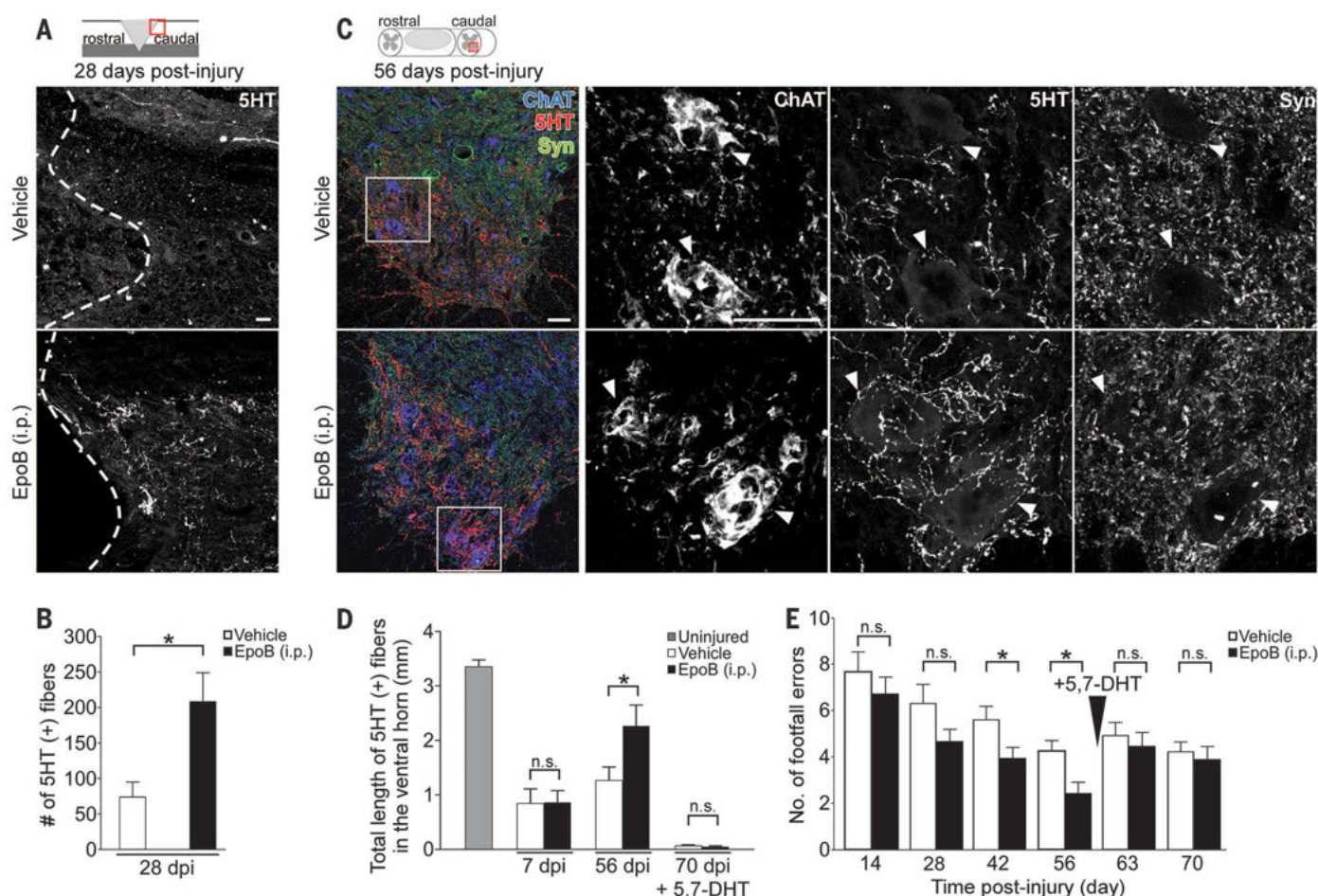


Fig. 4. EpoB promotes regrowth of raphespinal axons and improves walking after spinal cord contusion injury. (A) Serotonin (5HT) immunolabeling (dashed line, lesion border) and (B) number of 5HT-labeled (+) fibers caudal to a spinal dorsal hemisection; $n = 7$ to 8 rats per group. (C) Coronal sections of the lumbar spinal cord after contusion injury. (Left panel) Co-immunostaining of 5HT, synaptophysin (Syn), and choline acetyltransferase (ChAT). (Right panels) Magnification of each marker in boxed area (left

panel) visualizing serotonergic innervation of motor neurons (arrowheads). (D) Total length of 5HT-immunopositive fibers in the ventral horn (5,7-DHT, 5,7-dihydroxytryptamine); $n = 4$ (uninjured), 6 (7 dpi), 11 to 12 rats (56 and 70 dpi) per group. (E) Number of footfalls on the horizontal ladder; $n = 10$ to 11 rats per group. dpi, days postinjury. Scale bars, 50 μ m. Schemes in (A) and (C) indicate lesion and displayed region (red box). Values are plotted as means + SEM. * $P < 0.05$; n.s., not significant by Student's t test.

ablation of serotonergic innervation (Fig. 4, D and E, and movies S7 and S8) (25).

The finding that the stabilization of microtubules inhibits cell division established the usage of systemic microtubule-stabilizing agents as a therapeutic standard for the treatment of cancer (29). Here, at low doses, systemic administration of the microtubule-stabilizing agent epoB promoted functional recovery after SCI. Our approach differs from other experimental regenerative paradigms (1–7) by pharmacologically focusing on a single molecular target, the microtubules, yet overcoming multiple pathological obstacles. This is possible due to divergent effects of pharmacological microtubule stabilization on microtubule dynamics and, hence, the polarization of neurons and meningeal fibroblasts. This dual effect, and the efficacy after systemic and postinjury administration, give epothilones a promising translational perspective for treatment of the injured CNS.

REFERENCES AND NOTES

- N. Klapka *et al.*, *Eur. J. Neurosci.* **22**, 3047–3058 (2005).
- T. GrandPré, S. Li, S. M. Strittmatter, *Nature* **417**, 547–551 (2002).
- E. J. Bradbury *et al.*, *Nature* **416**, 636–640 (2002).
- L. Schnell, M. E. Schwab, *Nature* **343**, 269–272 (1990).
- K. Liu *et al.*, *Nat. Neurosci.* **13**, 1075–1081 (2010).
- W. J. Alilain, K. P. Horn, H. Hu, T. E. Dick, J. Silver, *Nature* **475**, 196–200 (2011).
- P. Lu *et al.*, *Cell* **150**, 1264–1273 (2012).
- F. Hellal *et al.*, *Science* **331**, 928–931 (2011).
- V. Sengottuvel, M. Leibinger, M. Pfeimer, A. Andreadaki, D. Fischer, *J. Neurosci.* **31**, 2688–2699 (2011).
- S. Fellner *et al.*, *JCI* **110**, 1309–1318 (2002).
- C. Ballatore *et al.*, *J. Med. Chem.* **55**, 8979–8996 (2012).
- C. Janke, J. C. Bulinski, *Nat. Rev. Mol. Cell Biol.* **12**, 773–786 (2011).
- J. M. Cregg *et al.*, *Exp. Neurol.* **253**, 197–207 (2014).
- J. R. Faulkner *et al.*, *J. Neurosci.* **24**, 2143–2155 (2004).
- A. L. Carbonell, J. Boya, *Brain Res.* **439**, 337–344 (1988).
- G. G. Gundersen, J. C. Bulinski, *Proc. Natl. Acad. Sci. U.S.A.* **85**, 5946–5950 (1988).
- R. J. Pasterkamp *et al.*, *Mol. Cell. Neurosci.* **13**, 143–166 (1999).
- K. C. Flynn *et al.*, *Neuron* **76**, 1091–1107 (2012).
- D. G. Drubin, M. W. Kirschner, *J. Cell Biol.* **103**, 2739–2746 (1986).
- R. Rouzier *et al.*, *Proc. Natl. Acad. Sci. U.S.A.* **102**, 8315–8320 (2005).
- H. Zempel *et al.*, *EMBO J.* **32**, 2920–2937 (2013).
- F. Bradke, J. W. Fawcett, M. E. Spira, *Nat. Rev. Neurosci.* **13**, 183–193 (2012).
- A. Ertürk, F. Hellal, J. Enes, F. Bradke, *J. Neurosci.* **27**, 9169–9180 (2007).
- C. J. Laskowski, F. Bradke, *Exp. Neurol.* **242**, 11–17 (2013).
- S. Kaneko *et al.*, *Nat. Med.* **12**, 1380–1389 (2006).
- J. E. Kim, B. P. Liu, J. H. Park, S. M. Strittmatter, *Neuron* **44**, 439–451 (2004).
- U. Stawinska *et al.*, *Exp. Neurol.* **247**, 572–581 (2013).
- J. R. Wrathall, R. K. Pettigrew, F. Harvey, *Exp. Neurol.* **88**, 108–122 (1985).
- C. Dumontet, M. A. Jordan, *Nat. Rev. Drug Discov.* **9**, 790–803 (2010).

ACKNOWLEDGMENTS

Materials and methods and other supporting materials are available on Science Online. We thank L. Meyn, K. Weisheit, D. Fleischer, and N. Thielen for technical assistance and animal care and C. Hill for teaching the spinal cord contusion injury model. We also thank C. Laskowski, C. H. Coles, A. Kania, M. Hübener, W. Jackson, and G. Tavasani for critically reading and discussing the manuscript. We are grateful for support from the Human Spinal Cord Tissue Bank and the electron microscopy core at the Miami Project, as well

as to B. Kakulas (University of Western Australia and Royal Perth) for providing anonymized postmortem sections after human spinal cord injury. This work was supported by NIH, International Foundation for Research in Paraplegia, Wings for Life, and Deutsche Forschungsgemeinschaft. H. Witte, A. Ertürk, F.H., and F.B. filed a patent on the use of microtubule-stabilizing compounds for the treatment of lesions of CNS axons (European Patent no. 1858498; European patent application EP 11 00 9155.0; U.S. patent application 11/908,118). The authors declare no competing financial interests.

SUPPLEMENTARY MATERIALS

www.sciencemag.org/content/348/6232/347/suppl/DC1
Materials and Methods
Figs. S1 to S11
Tables S1 and S2
Movies S1 to S8
References (30–37)

14 November 2014; accepted 25 February 2015
Published online 12 March 2015;
10.1126/science.aaa2958

PROTEIN STRUCTURE

Direct observation of structure-function relationship in a nucleic acid-processing enzyme

Matthew J. Comstock,^{1*} Kevin D. Whitley,¹ Haifeng Jia,² Joshua Sokoloski,² Timothy M. Lohman,² Taekjip Ha,^{1,3,4} Yann R. Chemla^{1†}

The relationship between protein three-dimensional structure and function is essential for mechanism determination. Unfortunately, most techniques do not provide a direct measurement of this relationship. Structural data are typically limited to static pictures, and function must be inferred. Conversely, functional assays usually provide little information on structural conformation. We developed a single-molecule technique combining optical tweezers and fluorescence microscopy that allows for both measurements simultaneously. Here we present measurements of UvrD, a DNA repair helicase, that directly and unambiguously reveal the connection between its structure and function. Our data reveal that UvrD exhibits two distinct types of unwinding activity regulated by its stoichiometry. Furthermore, two UvrD conformational states, termed “closed” and “open,” correlate with movement toward or away from the DNA fork.

Helicases are vectorial enzymes that play a critical role in genome maintenance, hydrolyzing nucleotide triphosphates to translocate along nucleic acids and separate the duplex strands. UvrD (DNA helicase II) is a prototypical superfamily 1 (SF 1) helicase involved primarily in nucleotide excision repair and methyl-directed mismatch repair in *Escherichia coli* (1, 2). Although a UvrD monomer is known to translocate along single-stranded DNA (ssDNA) in a 3'-to-5' direction (3–6), studies indicate that highly processive duplex DNA unwinding requires at least a dimer (4, 7–11). UvrD and structurally related SF 1 homologs (including Rep and PcrA) consist of four domains (12–16): the RecA-like motor core domains 1A and 2A and the accessory domains 1B and 2B (Fig. 1). Previous studies have shown that the 2B domain of UvrD (14, 16) and homologs (12, 13) can exhibit two

orientations—“open” and “closed” relative to the other domains (Fig. 1)—believed to regulate activity (6, 9, 14, 16). Despite detailed structural and biochemical data (4, 9–11, 14, 17), a lack of direct

evidence linking the UvrD conformational state to its function has prevented a more complete understanding of its mechanism. In this study, we used an instrument combining high-resolution optical traps and single-molecule confocal microscopy to measure simultaneously the unwinding activity and conformation of the UvrD helicase (fig. S1) (18, 19). Through these direct measurements, we demonstrate the link between UvrD oligomeric state and processivity, as well as between conformational state and unwinding versus rezipping activity.

We monitored helicase activity by detecting the unwinding of a DNA hairpin with an optical trap, as described previously (20, 21). The trap maintained a constant tension (4 to 15 pN; 10 pN for data shown unless otherwise specified) (19) and tracked the number of hairpin base pairs unwound. The composition and conformation of the same UvrD unwinding complexes, site-specifically labeled with one or two fluorophores (with labeling efficiencies ranging from 71 to 85%) (19), were detected with the confocal microscope (Fig. 1).

We observed two distinct types of DNA duplex unwinding activity, which we termed “frustrated” and “long-distance.” During frustrated activity (Figs. 2A and 3, B and C, lower panels), UvrD exhibited repetitive, bidirectional motion on DNA, during which <20 of the available hairpin

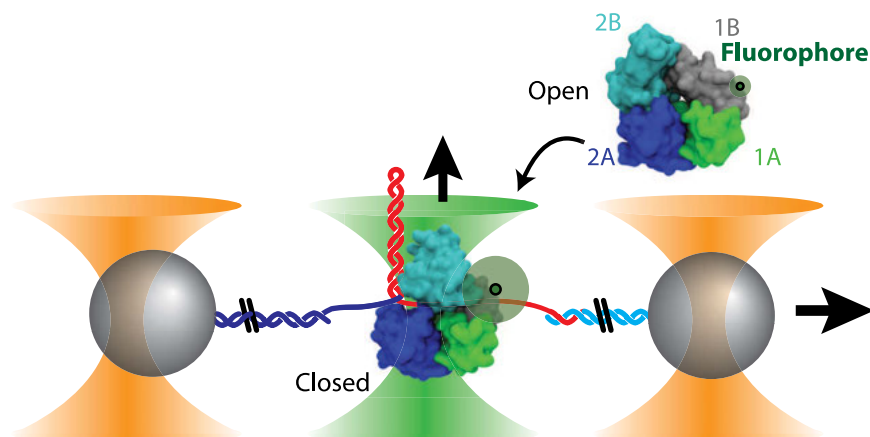


Fig. 1. Experimental layout. Structure of the UvrD monomer in the open (upper right) [Protein Data Bank identification number (PDB ID) 3LFU] (16) and closed (middle) (PDB ID 2IS2) (14) conformations with single-fluorophore location. Two microspheres (gray) in dual optical traps (orange cones) are tethered together by a DNA hairpin. One or more UvrD monomers bind ssDNA and unwind the hairpin in the presence of ATP. A confocal microscope (green cone) detects the configuration of the same fluorescently labeled UvrD unwinding complex.

¹Department of Physics, Center for the Physics of Living Cells, and Center for Biophysics and Computational Biology, University of Illinois at Urbana-Champaign, Urbana, IL 61801, USA. ²Department of Biochemistry and Molecular Biophysics, Washington University School of Medicine, St. Louis, MO 63110, USA. ³Howard Hughes Medical Institute, Urbana, IL 61801, USA. ⁴Institute for Genomic Biology, University of Illinois at Urbana-Champaign, Urbana, IL 61801, USA.

*Present address: Department of Physics and Astronomy, Michigan State University, East Lansing, MI 48824, USA. †Corresponding author. E-mail: ychemla@illinois.edu

base pairs unwound and reziped [13.6 ± 1.8 base pairs (bp), mean \pm SEM unless otherwise noted]. This bidirectional activity is distinct from the repetitive ssDNA translocation observed previously with UvrD (6) and its SF 1 homologs (22, 23). Reversals in direction occurred frequently (mean unwinding and reziping durations 0.25 ± 0.01 s and 0.23 ± 0.02 s, respectively), both mid-hairpin and after complete hairpin reziping, and typically repeated many times before UvrD dissociation (9.2 ± 1.2 repetitions for 7.8 ± 1.3 s). In

contrast, during long-distance activity (Fig. 2B, lower panel), UvrD systematically unwound >20 bp (38.9 ± 5.6 bp, on average). UvrD motion was far less repetitive, although reversals in direction did occur (mean unwinding and reziping durations 2.82 ± 0.30 s and 1.38 ± 0.13 s, respectively) at midhairpin [e.g., at 33 s (Fig. 2B)], at the end of the hairpin upon complete unwinding [89 bp (fig. S2)], and after full hairpin reziping. The mean reziping speed was dependent on adenosine triphosphate (ATP) and nearly the same as

for unwinding (fig. S3), strongly suggesting active translocation of UvrD. An alternate in which reziping results from backsliding (14, 21) would predict nearly instantaneous reziping events, inconsistent with the data. Because UvrD is a strict 3'-to-5' ssDNA translocase (4) with tight ATP coupling (24), reziping must correspond to 3'-to-5' translocation away from the ssDNA-dsDNA junction (dsDNA, double-stranded DNA), allowing the duplex to base pair in its wake. Thus, reversals in direction are probably the result of switching ssDNA strands, as first proposed by Dessinges *et al.* (25).

Our claim that frustrated and long-distance unwinding are distinct activities of UvrD is supported by measurements of the number of consecutive base pairs unwound per unwinding attempt (Fig. 2C) (19), which show a dramatic decrease past ~ 20 bp. Moreover, the two distinct activities correlate with the number of UvrD helicases present on the DNA hairpin, measured by counting singly labeled UvrD (19). When we observed frustrated unwinding activity, we usually detected only a single fluorophore, indicating a single UvrD loaded (Fig. 2A, top panel). In contrast, when we observed long-distance unwinding, we were more likely to detect two fluorophores, indicating two UvrD helicases (Fig. 2B, top panel). These trends were corroborated over many UvrD-DNA complexes (Fig. 2C, inset). These observations are consistent with previous reports that UvrD dimers are required for long-distance unwinding (4, 7–9), but they also demonstrate that monomers are competent to unwind a limited amount of DNA under tension (fig. S4) (19).

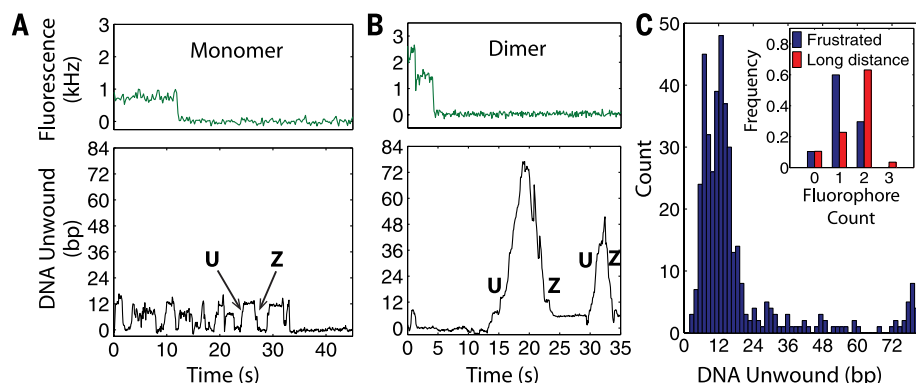


Fig. 2. Effect of UvrD oligomeric state on DNA unwinding activity. Representative time traces of unwinding activity for a UvrD monomer (A) and dimer (B), respectively. (Upper panels) Fluorescence photobleaching from a monomer (A) and a dimer (B) (240 and 120 ms per point, respectively). (Lower panels) Simultaneous measurements of hairpin unwinding (U) and reziping (Z). The UvrD monomer displays frustrated unwinding (A) (15 bp unwound), whereas the dimer displays long-distance unwinding (72 bp) (B). (C) Histogram of the maximum number of base pairs unwound per unwinding attempt ($N = 401$ replicates), showing frustrated (<20 bp) and long-distance (>20 bp) unwinding. (Inset) Distribution of fluorophore count for frustrated (blue) or long-distance (red) unwinding attempts.

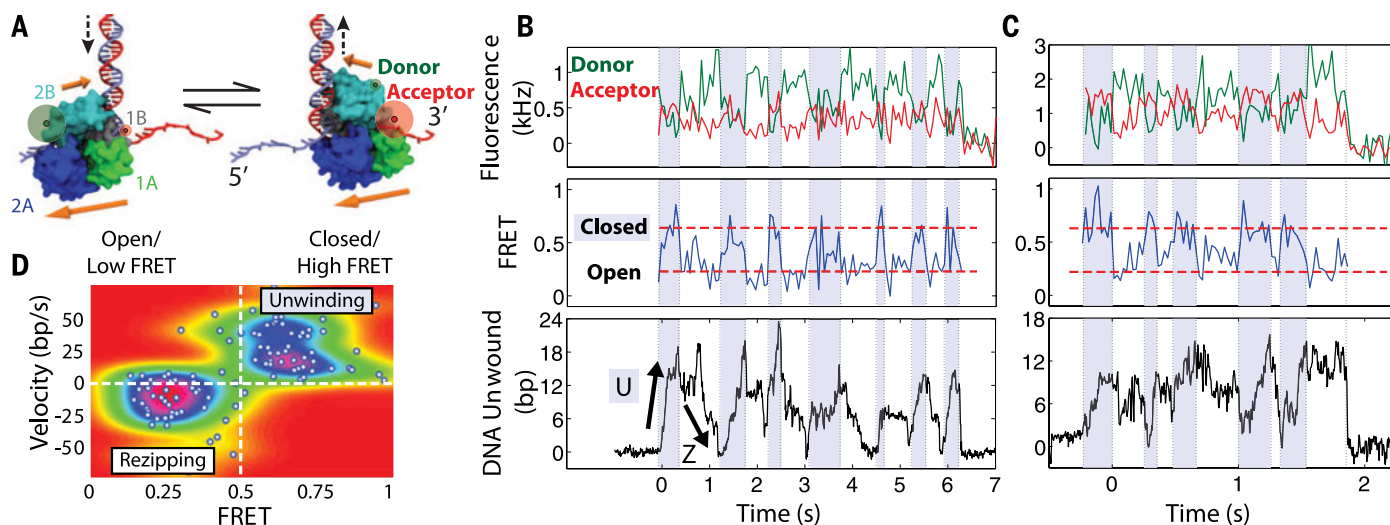


Fig. 3. Effect of open versus closed UvrD conformation on unwinding activity. (A) Location of donor and acceptor fluorophores for FRET measurement and model of UvrD conformational switching. Upper (and lower) orange arrows denote 2B (and 1A-2A) domain orientation. See text and (19) for details on the model. (B and C) Representative time traces of monomeric UvrD conformation and activity. (Upper panels) Donor (green) and acceptor (red) fluorescence intensity. (Middle panels) Corresponding FRET efficiency showing UvrD reversibly switching between open (low FRET) and closed (high FRET) conformations (dashed red lines). Fluorescence and FRET data are integrated to

60 and 50 ms per point for (B) and (C), respectively. Shaded and unshaded areas denote low- and high-FRET intervals, respectively. (Lower panels) Simultaneous measurements of unwinding (U) and reziping (Z) of the DNA hairpin. Fluorescence intensity and frustrated unwinding activity are consistent with monomeric UvrD-DNA complexes (which dissociate at 6.2 and 1.8 s). (D) Correlation between UvrD activity and conformation. The mean FRET efficiency and mean UvrD velocity determined over each time interval are plotted (white points; $N = 109$ intervals, 15 molecules). The color map represents the probability distribution of FRET state and velocity (19).

The ability of a single UvrD helicase to unwind and rezip DNA reversibly many times and in succession suggests that it can switch strands without dissociating from its DNA substrate. Previous studies showed that beyond the 1A-2A motor domains contacting ssDNA, the 2B domain can contact the junction duplex (6, 14). We thus used our instrument to detect the unwinding activity of individual UvrD monomers via optical trapping simultaneously with conformational changes of the 2B domain via single-molecule fluorescence resonance energy transfer (FRET) (26). UvrD was labeled with donor and acceptor fluorophores such that high or low FRET efficiency revealed the closed or open conformation, respectively (16, 19) (Fig. 3A).

Two example data traces of UvrD monomer conformation and unwinding activity measured simultaneously are shown in Fig. 3, B and C. The bottom panels show DNA duplex unwinding and reziping, as detected by the optical trap. The top panels show highly dynamic donor (green) and acceptor (red) fluorescence signals during activity. In the middle panels, the corresponding FRET efficiency fluctuates between high and low values (0.7 ± 0.2 and 0.3 ± 0.01 , respectively, for all molecules), consistent with the closed and open conformations, respectively (16). Dividing the unwinding and fluorescence data traces into time intervals determined by FRET state (i.e., conformation) reveals a correlation between unwinding versus reziping activity and 2B orientation. When a monomer is in the closed conformation (Fig. 3, B and C, shaded intervals), the DNA duplex unwinds, whereas the duplex rezipes upon switching to the open conformation (Fig. 3, B and C, unshaded intervals). Previously proposed models (9, 14, 16) suggested that the open versus closed conformations of UvrD correspond to moving versus stalled states; however, our direct observations demonstrate that these conformations instead correlate with UvrD reziping versus unwinding activity. Plotting the average speed versus FRET efficiency for many individual FRET-determined time intervals (Fig. 3D) corroborates our finding that unwinding (positive velocity) and reziping (negative velocity) correspond to high and low FRET states, respectively. Dividing the data traces into time intervals by unwinding speed instead yields similar results (fig. S5).

A simple model explains the correlation between 2B domain orientation and UvrD unwinding and reziping activity (Fig. 3A and movie S1) (19). In the closed conformation, the 1A-2A motor domains are oriented such that 3'-to-5' translocation occurs toward the duplex, in the unwinding direction (14). In the transition from closed to open, the 2B and 1A-2A domains rotate $\sim 150^\circ$ relative to each other (16), consistent with our

FRET efficiencies. We propose that an unwinding-to-reziping reversal is initiated by the 1A-2A domains disengaging from the ssDNA strand while 2B anchors UvrD at the DNA junction, preventing its complete dissociation. A switch from closed to open, along with rotation of 2B about the duplex, then reorients the 1A-2A domains to bind the opposing ssDNA strand in the proper orientation. 3'-to-5' translocation is now directed away from the fork junction, allowing the duplex to rezip. These steps are reversible, leading to robust back-and-forth switching between unwinding and reziping activities. Our model is compatible with previous studies of UvrD (6) and its SF1 homologs (19, 22, 23) and with the observation that intramolecular cross-linking of a Rep or PcrA monomer into the closed form allows it to unwind >1000 bp processively (27).

Although our model provides a mechanism for monomer reversals, it does not explain why these occur in the first place or why they occur less frequently during dimer unwinding. Additional measurements varying duplex stability indicate that reversals occur whenever UvrD encounters an energetic barrier to unwinding (19). UvrD dimers (and higher-order assemblies) may be more likely to overcome this barrier, leading to long-distance unwinding. Our data, together with past mutational studies (6, 28), point to strand-switching being the primary inhibitor of long-distance unwinding. For dimers, direct contact between helicases may inhibit strand-switching by the lagging UvrD, either by applying force to the leading UvrD, which stabilizes it at the duplex junction, or by preventing 2B interactions with the duplex DNA.

It is plausible that these two levels of unwinding activity play biological roles. UvrD is involved in multiple, distinct DNA maintenance processes that require different levels of processivity. During nucleotide excision repair, it is estimated that only ~ 15 bp of DNA are unwound (29). The strand-switching model above may provide a mechanism by which UvrD can unwind a small number of base pairs yet remain engaged with the DNA near the site of damage. In contrast, methyl-directed mismatch repair can require more than 1000 bp of DNA to be unwound (30). UvrD conformation and stoichiometry may be critical in enabling and regulating these disparate functions. Interactions of UvrD with accessory proteins, such as MutL (2), may also influence its conformation, stoichiometry, and activities.

REFERENCES AND NOTES

1. I. Husain, B. Van Houten, D. C. Thomas, M. Abdel-Monem, A. Sancar, *Proc. Natl. Acad. Sci. U.S.A.* **82**, 6774–6778 (1985).
2. M. Yamaguchi, V. Dao, P. Modrich, *J. Biol. Chem.* **273**, 9197–9201 (1998).
3. S. W. Matson, *J. Biol. Chem.* **261**, 10169–10175 (1986).
4. C. J. Fischer, N. K. Maluf, T. M. Lohman, *J. Mol. Biol.* **344**, 1287–1309 (2004).
5. E. J. Tomko, C. J. Fischer, A. Niedziela-Majka, T. M. Lohman, *Mol. Cell* **26**, 335–347 (2007).
6. E. J. Tomko *et al.*, *EMBO J.* **29**, 3826–3839 (2010).
7. N. K. Maluf, C. J. Fischer, T. M. Lohman, *J. Mol. Biol.* **325**, 913–935 (2003).
8. N. K. Maluf, J. A. Ali, T. M. Lohman, *J. Biol. Chem.* **278**, 31930–31940 (2003).
9. T. M. Lohman, E. J. Tomko, C. G. Wu, *Nat. Rev. Mol. Cell Biol.* **9**, 391–401 (2008).
10. H. Yokota, Y. A. Chujo, Y. Harada, *Biophys. J.* **104**, 924–933 (2013).
11. K. S. Lee, H. Balci, H. Jia, T. M. Lohman, T. Ha, *Nat. Commun.* **4**, 1878 (2013).
12. S. Korolev, J. Hsieh, G. H. Gauss, T. M. Lohman, G. Waksman, *Cell* **90**, 635–647 (1997).
13. S. S. Velankar, P. Soultanas, M. S. Dillingham, H. S. Subramanya, D. B. Wigley, *Cell* **97**, 75–84 (1999).
14. J. Y. Lee, W. Yang, *Cell* **127**, 1349–1360 (2006).
15. M. R. Singleton, M. S. Dillingham, D. B. Wigley, *Annu. Rev. Biochem.* **76**, 23–50 (2007).
16. H. Jia *et al.*, *J. Mol. Biol.* **411**, 633–648 (2011).
17. L. E. Mechanic, M. C. Hall, S. W. Matson, *J. Biol. Chem.* **274**, 12488–12498 (1999).
18. M. J. Comstock, T. Ha, Y. R. Chemla, *Nat. Methods* **8**, 335–340 (2011).
19. See materials and methods and other supplementary materials on Science Online.
20. S. Dumont *et al.*, *Nature* **439**, 105–108 (2006).
21. Z. Qi, R. A. Pugh, M. Spies, Y. R. Chemla, *eLife* **2**, e00334 (2013).
22. S. Myong, I. Rasnik, C. Joo, T. M. Lohman, T. Ha, *Nature* **437**, 1321–1325 (2005).
23. J. Park *et al.*, *Cell* **142**, 544–555 (2010).
24. E. J. Tomko, C. J. Fischer, T. M. Lohman, *J. Mol. Biol.* **418**, 32–46 (2012).
25. M. N. Dessinges, T. Lionnet, X. G. Xi, D. Bensimon, V. Croquette, *Proc. Natl. Acad. Sci. U.S.A.* **101**, 6439–6444 (2004).
26. T. Ha *et al.*, *Proc. Natl. Acad. Sci. U.S.A.* **93**, 6264–6268 (1996).
27. S. Arslan, R. Khafizov, C. D. Thomas, Y. R. Chemla, T. Ha, *Science* **348**, 344–347 (2015).
28. K. M. Brendza *et al.*, *Proc. Natl. Acad. Sci. U.S.A.* **102**, 10076–10081 (2005).
29. C. Kisker, J. Kuper, B. Van Houten, *Cold Spring Harbor Perspect. Biol.* **5**, a012591 (2013).
30. T. A. Kunkel, D. A. Erie, *Annu. Rev. Biochem.* **74**, 681–710 (2005).

ACKNOWLEDGMENTS

We thank members of the Chemla (including Z. Qi), Ha (including K.-S. Lee), and Lohman (including E. Tomko) laboratories for scientific discussion and assistance in the experimental design. Funding was provided by NSF grants MCB-0952442 (CAREER to Y.R.C.) and PHY-1430124 (Center for the Physics of Living Cells to Y.R.C. and T.H.); NIH grants R21 RR025341 (to Y.R.C. and T.H.), R01 GM065367 (to T.H.), and R01 GM045948 (to T.M.L.); and the Alfred P. Sloan Research Fellowship (to Y.R.C.). T.H. is an investigator with the Howard Hughes Medical Institute.

SUPPLEMENTARY MATERIALS

www.sciencemag.org/content/348/6232/352/suppl/DC1
Materials and Methods
Figs. S1 to S8
References (31–42)
Movie S1

8 October 2014; accepted 24 February 2015
10.1126/science.aaa0130

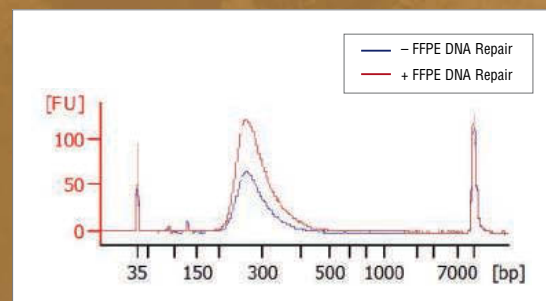
On the mend.

NEBNext[®] FFPE DNA Repair Mix from New England Biolabs[®]

While archiving of clinical materials as Formalin-Fixed, Paraffin-Embedded (FFPE) samples is common, it causes significant damage to the sample's DNA. As a result, such samples can be difficult to sequence. The cocktail of enzymes in the NEBNext FFPE DNA Repair Mix repairs multiple types of damage that are common among FFPE samples, thereby improving yields and overall library success rates.

Make sure your sample's DNA is on the mend before your next sequencing experiment!

Effect of FFPE DNA Repair Mix on library yields



An example of Agilent Bioanalyzer[®] traces of libraries prepared from stomach tumor FFPE DNA that was treated with the FFPE DNA Repair Mix, or was untreated, before library construction. Yield improvements of 101% to 458% have been observed.

Visit www.neb.com/M6630 to learn more.



American
Heart
Association®

SCIENTIFIC
SESSIONS 2015

Exhibits: November 8–10
Sessions: November 7–11

Orlando, Florida

scientificsessions.org

CALL FOR Abstracts

WEDNESDAY, APRIL 22 – WEDNESDAY, JUNE 10, 2015
5 P.M. CDT

Lead the way in scientific discovery
for heart disease & stroke.

The American Heart Association's Scientific Sessions showcases the best science and is the cardiovascular conference for **basic, translational, clinical and population science**.

- Accepted abstracts are published in AHA's *Circulation*, which receives over 2.8 billion media impressions yearly.
- Scientific Sessions 2014 had over 8 billion media impressions & 5.2 million social media impressions.
- More than 4,000 abstracts in 2014 made headlines in the *U.S. News and World Reports*, The Associated Press and Reuters.

Make sure **your science** is part of this reach.
Submit your Science today.

Abstract submission opens Wednesday, April 22,
and closes at **5 p.m. on Wednesday, June 10, 2015.**

scientificsessions.org

#AHA15



For information on how to exhibit and sponsor at
AHA's Scientific Sessions 2015 visit www.exhibitatsessions.org.



2014 Winner
Eiman Azim, Ph.D.
Columbia University
For research on skilled
limb movement

Call for Entries

Application Deadline
June 15, 2015

Eppendorf & Science Prize for Neurobiology

The annual Eppendorf & Science Prize for Neurobiology is an international award which honors young scientists for their outstanding contributions to neurobiological research based on methods of molecular and cell biology. The winner and finalists are selected by a committee of independent scientists, chaired by Science's Senior Editor, Dr. Peter Stern. To be eligible, you must be 35 years of age or younger.

You could be next to win this prize and to receive

- > Prize money of US\$25,000
- > Publication of your work in Science
- > Full support to attend the Prize Ceremony held in conjunction with the Annual Meeting of the Society for Neuroscience in the USA
- > An invitation to visit Eppendorf in Hamburg, Germany

It's easy to apply!

Learn more at: www.eppendorf.com/prize

"YOU ARE WATCHING THIS BEAUTIFUL ECOSYSTEM BE DEGRADED BY CLIMATE CHANGE OR HUMAN INTERACTION ... THEN YOU SORT OF PULL UP YOUR SOCKS AND GO SEE WHAT YOU CAN DO."

Tim
Marine conservationist and
Kenyan coral reef expert,
Tim McClanahan, AAAS Member

Every scientist has a *story*

Read his story at membercentral.aaas.org



AAAS Travels

TANZANIA
Wildlife & Eclipse Safari
August 19-September 3, 2016



**See the Annular Solar
Eclipse, September 1, 2016!**



Join us on a Wildlife & Eclipse Safari in Tanzania to see the Annular Solar Eclipse. Enjoy splendid days looking for lions, leopards, elephants, rare rhinos, hippos, spectacular birds, and other wildlife in the finest wildlife parks in East Africa! \$6,995 pp + air

For a detailed brochure, call (800) 252-4910
All prices are per person twin share + air



BETCHART EXPEDITIONS Inc.
17050 Montebello Rd, Cupertino, CA 95014
Email: AAASInfo@betchartexpeditions.com
www.betchartexpeditions.com

In the Nation, exclusive discounts are just the beginning.



AAAS members are rewarded.

With Nationwide®, you get great protection for you, your loved ones and all you've worked for in life.

As a member of AAAS, you can save with special discounts on Nationwide auto insurance. In addition, when you add rewards like **Vanishing Deductible®**,* you can take \$100 off your deductible for every year of safe driving, for up to \$500 in savings.

Call 1-866-238-1426 or visit
nationwide.com/AAAS for
a quote today!



ADVANCING SCIENCE, SERVING SOCIETY

Nationwide may make a financial contribution to this organization in return for the opportunity to market products and services to its members or customers. Products Underwritten by Nationwide Mutual Insurance Company and Affiliated Companies, Columbus, OH 43215. Not all Nationwide affiliated companies are mutual companies, and not all Nationwide members are insured by a mutual company. Subject to underwriting guidelines, review, and approval. *Vanishing Deductible is an optional feature. Annual credits subject to eligibility requirements. Max. credit: \$500. Details and availability vary by state. Products and discounts not available to all persons in all states. Nationwide, the Nationwide N and Eagle design and Vanishing Deductible are service marks of Nationwide Mutual Insurance Company. © 2014 Nationwide Mutual Insurance Company, AFC-014240 (11/14)



Diving Deep into Cell Signaling

New proteomics tools enable researchers to dive deeply into signaling networks, allowing them to tease out interactions among key molecules. But this comes with a new challenge of increased complexity. Can cell signaling scientists balance the bewildering complexity that comes with the discovery power of proteomics technology? **By Caitlin Smith**

Proteomics seems a natural discipline toward which cell signaling researchers might gravitate. Most signaling molecules studied today are proteins, after all. But proteomics presents much greater complexity than, say genomics, which many cell signaling scientists grew up learning.

“Proteins are very complex, often functioning under only a specific set of conditions, which makes multiplexing and parallel analysis difficult,” says Chris Hebel, vice president of business development at **LC Sciences**. Add to this the multi-fold interactions between these complex molecules, and you have an explosion of possible questions to ask and data to be gathered. Alterations to proteins in the form of posttranslational modifications (PTMs) such as phosphorylation, acetylation, myristoylation, glycosylation, and more, can further change the functions of these proteins, their binding partners, and their signaling properties, perhaps even initiating a cascade of other biochemical changes across the cell.

Uncovering signaling pathways with mass spectrometry

Cell signaling research has recently benefitted from a combination of serial enrichment methods and advances in mass spectrometry technology. A prime example is “affinity-based methods for selective enrichment of PTMs,” says Steven Carr,

the director of the Proteomics Platform at the **Broad Institute** of Harvard University and the Massachusetts Institute of Technology. For example, recent refinements of metal-affinity enrichment methods have helped optimize samples for serine/threonine and tyrosine phosphorylation detection. When researchers use such pre-enriched samples as their starting sample for liquid chromatography/mass spectrometry (LC/MS), they “can get much, much deeper into these samples,” says Carr. “It’s very common now to get 20,000–30,000 phosphorylation sites identified, which is really quite deep.”

The MS technologies mainly used by Carr’s lab are the new Q Exactive systems from **Thermo Fisher Scientific**. “Previously it was Orbitraps, but now we’re heavily focused on using Q Exactive Plus and Q Exactive HF instruments, because the price per performance point is very good. We run a high throughput laboratory with many concurrent projects so having many high-performance instruments is essential,” says Carr. Other high-performance MS systems are commercially available from other vendors, including **AB SCIEX** and **Waters**.

“These new generations of hybrid instruments are extremely sensitive while maintaining very high performance in terms of mass accuracy and high resolution—we take that for granted nowadays,” says Carr. Eight to 10 years ago, researchers had to pay a price. “Either you gave up sensitivity for the performance factors, or you maintained sensitivity but gave up mass accuracy and high resolution. Today, you don’t have to make those compromises.”

And MS systems continue to be refined. “Not all of them have what’s called ion funnels on the front end,” says Carr. An ion funnel is a device that makes the MS system more sensitive. Waters, **Agilent Technologies**, and Thermo Fisher Scientific offer ion funnels on certain MS systems. “Another thing that will change is more widespread availability of ion mobility in MS systems,” says Carr. Ion mobility helps to separate peptides and proteins from one another in the gas phase to make the sample less complex, which Carr likens to gas phase chromatography. “This also improves sensitivity and can increase speed,” he says.

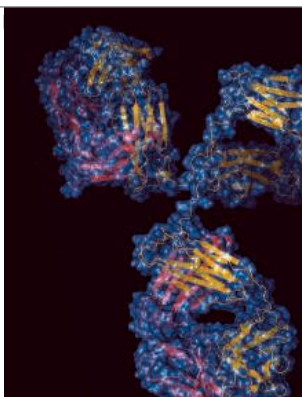
Other new developments in MS systems include the ETD option on Thermo’s Orbitrap Fusion. ETD stands for electron transfer dissociation, valuable as a “type of fragmentation that lets you map PTMs to your protein backbone,” says Andreas Huhmer, director of ‘omics marketing for life science mass spectrometry at Thermo Fisher Scientific. Thermo also offers kinase probes for pulling out kinases. The Thermo Scientific Pierce Kinase Enrichment Kit uses ActivX ATP or ADP Probes to label kinases’ active ATPase sites. The probes contain a desthiobiotin tag that allows subsequent enrichment of labeled kinases.

Mark Knepper, senior investigator in the Epithelial Systems Biology Laboratory at the National Heart Lung and Blood Institute (NHLBI), part of the **National Institutes** *continued* >

Upcoming Features

Microscopy—June 12 ■ **Transcriptomics—July 31** ■ **Proteomics—September 11**

At their best, antibodies are indispensable for molecular tagging, identification, and affinity purification.



of Health, also uses recent MS advances to study phosphoproteomics. “Progress in the development of mass spectrometers allows more spectra to be collected with greater mass resolution,” he says. “This results in remarkable increases in sensitivity.”

Knepper’s lab builds models of signaling networks by identifying specific protein kinases and phosphatases. Using the CRISPR-Cas9 genome editing system, the group can delete a particular kinase or phosphatase gene, and then study the subsequent engineered clones. “Phosphoproteomics in CRISPR clones can potentially allow conclusions about the role of specific gene products in specific signaling pathways,” says Knepper.

The power of good antibodies

At their best, antibodies are indispensable for molecular tagging, identification, and affinity purification. But antibodies come with a downside. “There’s just not enough of them,” says Carr. “Most of them don’t work in all contexts, and some of them don’t work at all. So reliance on antibodies remains very challenging.” As with MS, recent improvements in antibody technology have helped advance cell signaling and proteomics research. Yet according to Carr, “mass spectrometry has played a major role in unraveling the off-target effects of antibodies.” Not all antibodies are created equal—some work well in some experiments, such as Western blotting or immunohistochemistry, but not for others, like immunoprecipitation.

Antibody technology has improved greatly for targets with PTMs, led mainly by “motif antibodies” from **Cell Signaling Technologies** (CST). “CST developed a class of antibodies that were designed around a particular PTM sequence motif as opposed to a site-specific PTM epitope,” says Jeffrey Silva, KinomeView and PTMScan proteomics service manager at CST. Examples include phosphorylated serine/threonine targets and phosphorylated tyrosine targets. Although it does not make a motif antibody for glycosylation, CST does have antibodies against acetyl-lysine, methyl-arginine, methyl-lysine, succinyl-lysine, and phospho-histidine in the works.

Silva explains that CST developed the PTMScan Direct reagents—combinations of CST’s motif antibodies—in

response to customers’ requests for tools to pinpoint six different signaling areas: tyrosine kinases, serine/threonine kinases, apoptosis, cell cycle and DNA damage, AKT and PI3 kinase signaling, and a Multipathway Reagent that enables the identification of approximately 19 major signaling pathways. This lets researchers sample key nodes from a number of different critical signaling pathways in a multiplex LCMS assay. “It’s an efficient way to ask just which key pathways are affected by the stimulus—then they can quickly focus their efforts on the affected modulated proteins,” says Silva. All in all, the Multipathway Reagent allows researchers to identify and quantify 409 proteins and 1,006 unique phosphopeptides. CST has also developed new PTM antibodies for ubiquitination, acetylation, and cleaved caspase substrates.

Antibodies to G-protein-coupled receptors (GPCRs), which are important in multiple signaling pathways, are in high demand, but historically they have been difficult to generate. The biggest challenge is “finding antibodies of sufficiently high affinity to distinguish between closely related receptors and receptor subtypes,” according to Lora Tebbetts, product manager at **Enzo Life Sciences**, which offers over 120 antibodies for GPCRs and associated proteins. Tebbetts says that more specific antibodies are made using “peptides from the more sequence-diverse areas of N- and C-terminal regions [of GPCRs], or the third intracellular loop combined with carrier proteins as immunogens.”

Deciphering signaling networks with microchips

One of the advantages of using microchips for cell signaling research is that only small amounts of reagents and samples are needed. LC Sciences’ new phosphopeptide microarray is designed on a microchip to assess changes in expression levels of key signaling proteins in different pathways—all at once. It can “map tyrosine-phosphoproteome interaction networks by detecting the expression level of proteins containing [the] corresponding phosphoprotein-binding domains,” says Hebel. This is unique in that researchers can see at a glance where their experimental manipulations are affecting signaling pathways.

Hebel says that there are multiple reasons to use phospho-binding domains on a custom microarray instead of the more traditional antibody binding. “The probe density is much higher, which translates into higher specificity,” he explains, and the technique does not depend “on the availability of high-affinity antibodies [or] require many different antibodies with different affinities and optimal binding conditions—which would require complicated redevelopment and validation if any design change is made.”

Phosphoproteins are also the topic of study for James Heath, professor of chemistry and director of the NanoSystems Biology Cancer Center at the **California Institute of Technology**. Heath uses single cell proteomics to study phosphoprotein signaling cascades, with glioblastoma cells from brain tumors as a model system. Like many types of cancer, these tumors are not made of one kind of cancer cell,



but rather a heterogeneous population. This heterogeneity is thought to explain why single cancer drugs that target one signaling protein often fail. Heath studies the signaling cascades of glioblastoma cells to learn how to combine cancer drugs to make effective therapies.

Heath's group uses homemade microfluidic chips to study individual cells, which are positioned in their own tiny chambers inside the microchip. Each cell is separately lysed, so that its contents are captured by the waiting array of antibodies that lie within each chamber. The team then uses quantitative sandwich ELISAs that are calibrated to measure the copy number of proteins per cell. The array includes antibodies against proteins known to participate in glioblastoma signaling pathways, such as phosphoAKT, phosphoERK, phosphoSRC, and phosphoEGFR. Heath uses "targeted drugs to hit signaling pathways, like those driven by EGFR, that maintain the tumor and help it grow," he says.

Treating a tumor with a cancer drug may cause it to stop growing, or even to shrink. But in all cases of glioblastoma, says Heath, the tumor soon develops resistance to the drug and starts growing aggressively. Yet for some tumors, this isn't the result of Darwinian selection; Heath found that the resistant cells were not simply survivors—they were adapters.

"The same cells that were responding to the drug, actually developed resistance to the drug," says Heath, by activating particular signaling pathways—the same interactions that Heath saw when analyzing single cells before and after drug treatment. "If you can identify those other pathways that are activated by the drug, that tells you in principle what combination therapies you would use to treat that resistance," says Heath. In other words, if you can find a second drug to stop the adaptation response, then you can kill the tumor.

Heath's results hold promise for cancer therapy. For example, if he treats a tumor with an ERK inhibitor, or an EGFR inhibitor, the results are unimpressive. But if he treats a tumor with two inhibitors that can work together to prevent drug resistance, he says the tumor "completely shuts down."

From single cells to tissues

Studying single cells also has great value for better understanding tissues since they are communities of cells, according to Garry Nolan, director of the NHLBI Proteomics Center for Systems Immunology, and professor in the Department of Microbiology and Immunology at **Stanford University**. "They are interacting and living in the context

Featured Participants

AB SCIEX
www.absciex.com

Agilent Technologies
www.agilent.com

Broad Institute
www.broadinstitute.org

California Institute of Technology
www.caltech.edu

Cell Signaling Technologies
www.cellsignal.com

Enzo Life Sciences
www.enzolifesciences.com

Fluidigm
www.fluidigm.com

LC Sciences
www.lcsciences.com

National Institutes of Health
www.nih.gov

Stanford University
www.stanford.edu

Thermo Fisher Scientific
www.thermofisher.com

Waters
www.waters.com

of each other," he says. "Their individual biology is really about what makes us normal or dysfunctional." He sees cancer as an example of a tissue that takes on a life of its own and creates its own context or environment. "If we are to hope to understand the complexity of [the environment], and how drugs might act on that, then we need to understand how this community of players are interacting with each other," Nolan says. "That means

you have to assay as many things as you deem relevant without drowning yourself in information."

Nolan pioneered a technique called mass cytometry to measure the complement of proteins expressed in single cells simultaneously. Using antibodies against multiple proteins of interest labeled with isotopic mass tags—rather than, say, fluorescent tags—he can multiplex to a greater extent than with microscopy because spectral overlap is not an issue. When an individual cell enters a mass cytometer, it vaporizes and the isotopic tags are read by a mass spectrometer. Using this system, Nolan's lab was able to generate snapshots of signaling networks using 35–40 markers. Today they can measure about 50 parameters.

Nolan's lab uses a mass cytometry system called CyTOF 2 from **Fluidigm**. Recent improvements to the CyTOF 2 make it easier to "do experiments to help better understand the signaling properties of the proteins in different cell types," says Olga Ornatsky, principal scientist at Fluidigm. Fluidigm is adopting the CyTOF 2 system for imaging of immunohistochemistry-type stained fixed-tissue sections. While conventional immunohistochemistry assays measure three or four fluorescently labeled markers at a time, the CyTOF version can measure more than 30 markers at once. "This will widen the scope of questions that can be asked," says Ornatsky.

Increasingly, proteomics researchers are using such technologies to study more than just changes in protein levels, as they can now look into the complex interactions of signaling molecules and networks. How PTMs regulate and alter such pathways brings an additional layer to this research, with scientists having to ask: "How do these modifications affect one another?" says Carr. And as progressively more powerful proteomics tools become available, such as better antibodies and MS technologies, researchers will be able to dive even deeper into such questions.

Caitlin Smith is a freelance science writer in Portland, Oregon.
DOI: 10.1126/science.opms.p1500093



Triple A Polyclonal Antibodies

1,272 new Triple A Polyclonals are now available. All Triple A Polyclonals are recommended for immunohistochemistry, with over 700 images supplied for each antibody from a multitude of human tissues and cells, annotated by trained pathologists. A majority of them are also recommended for WB and/or ICC-IF, supported with confocal images with subcellular annotation into 19 different cellular compartments. For each Triple A Polyclonal the corresponding PrEST Antigen is also released and available as a product today. The Atlas Antibodies Advanced Polyclonal antibodies (Triple A Polyclonals) are designed using proprietary software to select the most suitable antigen for a given target protein. Combined with a unique antibody purification process, using the recombinant antigen as affinity ligand, the company achieves polyclonals with the very highest level of specificity, reproducibility, and versatility. PrEST Antigens are the recombinant protein fragments used as immunogens in the generation of Triple A Polyclonals.

Atlas Antibodies

For info: +46-(0)-85-459-58-50
www.atlasantibodies.com

Glycan Analysis Workflows

The new RapiFluor-MS Labeling Reagent and Sample Preparation Protocol greatly enhances speed, sensitivity, and simplicity of released N-Glycan profiling and characterization. The new set of technologies includes the new GlycoWorks RapiFluor-MS N-Glycan Kit, the Waters ACQUITY UPLC, the ACQUITY UPLC FLR Detector, and the ACQUITY QDa detector. These enable fast deglycosylation and labeling and a workflow that reduces sample preparation time from a day to less than one hour, allows mass detection for characterization and development with sensitivity that is 100- to 1,000-fold better than current approaches, and enables routine laboratory use supported by a simple robust protocol without involving MS experts. This approach to glycan analyses means scientists can monitor and characterize released N-glycans like never before. The new workflows take what had been a specialized and complicated activity and transform it into one that scientists and laboratories can be successful with.

Waters Corporation

For info: 800-252-4752
www.waters.com/glycans



Unified Chromatography System

The fully automated supercritical fluidic chromatography-based Nexera Unified Chromatography system (Nexera UC) can sequentially analyze up to 48 samples utilizing automatic extraction and chromatographic separation combined with high-sensitivity detection of targets by mass spectrometry. The Nexera UC system is designed to fulfill the measurement requirements of a wide range of applications including monitoring pesticides in food products, drug delivery and search for disease biomarkers, additives in forming polymers, and drug discovery research in pharmaceuticals and biopharmaceuticals along with cleaning validation. The Nexera UC system eliminates the need for complicated sample pretreatment and enables highly reliable and stable analysis of delicate samples that are prone to oxidation or dissociation if exposed to air. The state-of-the-art Nexera UC system has a much higher target analyte recovery rate and reduces the possibility of human error during analysis when compared with conventional manual systems.

Shimadzu Scientific Instruments

For info: 800-477-1227
www.ssi.shimadzu.com

Glycan Array

The largest commercially available glycan microarray is now available for profiling protein-carbohydrate interactions. This array, known as the RayBio Glycan Array 100, features 100 synthetic glycans discretely spotted onto a glass slide support. The highly diverse panel of polysaccharides was selected based on a comprehensive literature search that identified the glycan structures most frequently associated with critical cellular functions, including T cell activation, bacterial and viral binding, innate immunity, and apoptosis. Glycans are a diverse and complex family of sugar molecules that decorate the surfaces of virtually all eukaryotic cells, bacteria, and viruses. Emerging literature indicates that glycosylation of proteins is a highly complex and abundant posttranslational modification whose biological significance is only beginning to be understood. Glycan arrays permit researchers to not only profile the specificities of glycan-binding proteins, but also uncover disease-associated biomarkers and putative drug target moieties.

RayBiotech

For info: 888-494-8555
www.raybiotech.com

Bioconjugation Kits

New antibody and protein labeling kits within its Lightning-Link Rapid range enable researchers to label primary antibodies or other proteins in just 20 minutes. Dyes recently launched within this range include high sensitivity Atto dyes and Cy dyes. Innova has also released a rapid biotin conjugation kit which allows for extremely quick protein biotinylation. Despite the short incubation time, the conjugation reaction is sufficient to achieve conjugates with performance characteristics identical to, or better than, those prepared with laborious multistep conjugation procedures. Lightning-Link is an innovative technology that enables direct labeling of antibodies,

proteins, peptides, or other biomolecules. The procedure is easy to use, involves only 30 seconds of hands-on time, and no spin or separation steps are required. In addition, by circumventing the desalting or dialysis steps that commonly interrupt traditional protein labeling procedures, Lightning-Link Rapid technology can be used to label small quantities of antibody with 100% recovery.

Innova Biosciences

For info: +44-(0)-1223-496170
www.innovabiosciences.com

Electronically submit your new product description or product literature information! Go to www.sciencemag.org/products/newproducts.dtl for more information.

Newly offered instrumentation, apparatus, and laboratory materials of interest to researchers in all disciplines in academic, industrial, and governmental organizations are featured in this space. Emphasis is given to purpose, chief characteristics, and availability of products and materials. Endorsement by *Science* or AAAS of any products or materials mentioned is not implied. Additional information may be obtained from the manufacturer or supplier.

Will you be published in *Science* this December?

(If you have a recent PhD you could be.)



To be published in *Science* is a special moment for any scientist. But to do so at the very start of your career is extremely exciting indeed. If you are a recent PhD graduate you could be published in *Science* this December, and receive a very special prize in Stockholm during the week of Nobel.

The journal *Science* & SciLifeLab have established The *Science* & SciLifeLab Prize for Young Scientists, to recognize and reward excellence in PhD research and support young scientists at the start of their careers. It's about bright minds, bright ideas and bright futures.

Four winners will be selected for this international award. They will have their essays published by the journal *Science* and share a new total of 60,000 USD in prize money. The winners will be awarded in Stockholm during the second week of December when the city is alive with excitement and celebrates the new Nobel Laureates at the annual Nobel Prize ceremony. They will take part in a truly unique week of events including meeting leading scientists in their fields.

"The last couple of days have been exhilarating. It has been an experience of a lifetime. Stockholm is a wonderful city and the Award winning ceremony exceeds my wildest dreams."
—Dr. Dan Dominissini, 2014 Prize Winner

Who knows, having your work published in the journal *Science* could be a major stepping stone in your career and the *Science* & SciLifeLab Prize for Young Scientists makes this possible.

The 2015 Prize is now open. The deadline for submissions is August 1, 2015.

Enter today: www.sciencemag.org/scilifelabprize

The 2015 Prize categories are:

- Cell and Molecular Biology
- Ecology and Environment
- Genomics and Proteomics
- Translational Medicine

This prize is made possible with the kind support of the Knut and Alice Wallenberg Foundation. This Foundation grants funding in two main areas; research projects of high scientific potential and individual support of excellent scientists.

By Elisabeth Pain

En pointe

An engineer, a musician, and a dancer, Lina Colucci lives in multiple worlds. Now in the third year of a Ph.D. at the Harvard-Massachusetts Institute of Technology (MIT) Health Sciences and Technology (HST) program, she's working to develop a portable hydration sensor for patients with congestive heart failure. Since high school, she has also been redesigning the shoes used by ballerinas. Her presentation at the TEDxBussels event last December began with a ballet performance. We asked her why she continues to pursue all of her time-consuming passions. This interview was edited for brevity and clarity.

Q: Describe your pointe shoes project.

A: A hundred years ago, running shoes were just being invented—and just look at where we are now with the technology that's been put into athletic shoes. Ballet shoes, on the other hand, haven't changed much at all in the past 200 years. They are still extremely primitive. So I asked myself, "How can we make these primitive shoes better?" I've used my understanding of biomechanics to change the materials and structural design in different parts of the ballet shoes to make them more comfortable and to provide what the body needs in terms of support and flexibility.

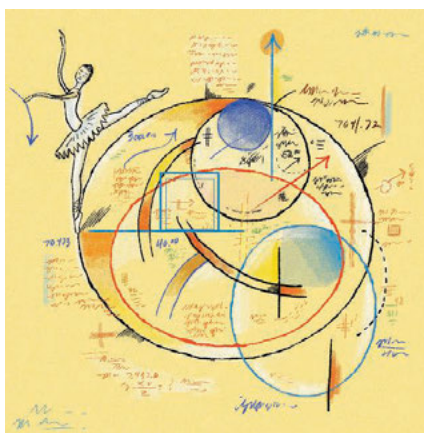
Q: How did you end up combining engineering and ballet?

A: My dad is an engineer, so I knew about engineering from a young age. I found ballet and music when I was very young as well, and I have always loved these three things. Without a doubt, my priority is engineering, but I've tried not dancing, I've tried not playing music, and it doesn't work. I have to do these other things to be more effective in my engineering work.

Q: Why? What's the connection?

A: In all these endeavors, a final product is born from feelings and fragmented ideas. Also, I think everyone needs something that feeds their mind, body, and spirit. Of course, most activities don't serve just one purpose. Dancing on stage is a spiritual experience as much as it is a physical one. Learning or choreographing new steps can be as intellectually stimulating as doing lab research.

Music and dance have also given me self-discipline and effective working methods. I have learned, for example, how to teach myself a new piece of music: sitting down for hours, starting to play slowly, and then adding differ-



*"In all these endeavors,
a final product is born
from feelings and
fragmented ideas."*

ent elements like speed, dynamics, and phrasing to build up to a final performance. This is like facing a hard engineering problem and breaking it down into smaller pieces until you are finally able to tackle the entire problem. And ballet has taught me that even if I'm not feeling well one day—even if I am exhausted—I still go to ballet class and put my best effort forward. That kind of discipline is directly transferable to any academic pursuit.

Q: Including the HST program?

A: Yes. It is hard, but it's really exciting. My classmates and I come from a variety of classical engineering disciplines. We study engineering at MIT, but we also go through some medical training at Harvard Medical School. I go from control sys-

Q: Where do you see this taking you?

A: I want to pursue entrepreneurship within health care engineering, to make the health care system a better experience for patients. I believe that technology, like the sensors I'm working on, is going to play a really big role in the health care system of the future. The idea is to free up doctors' time with technology so that they can get back to focusing on patient interaction. ■

Elisabeth Pain is Science Careers' contributing editor for Europe. For more on life and careers, visit ScienceCareers.org. Send your story to SciCareerEditor@aaas.org.

ILLUSTRATION: ROBERT NEUBECKER



There's only one **Science**

Science Careers Advertising

For full advertising details, go to ScienceCareers.org and click For Employers, or call one of our representatives.

Tracy Holmes

Worldwide Associate Director
Science Careers
Phone: +44 (0) 1223 326525

THE AMERICAS

E-mail: advertise@sciencecareers.org
Fax: 202 289 6742

Tina Burks

Phone: 202 326 6577

Nancy Toema

Phone: 202 326 6578

Marci Gallun

Sales Administrator
Phone: 202 326 6582

Online Job Posting Questions

Phone: 202 312 6375

EUROPE / INDIA / AUSTRALIA / NEW ZEALAND / REST OF WORLD

E-mail: ads@science-int.co.uk
Fax: +44 (0) 1223 326532

Axel Gesatzki

Phone: +44 (0) 1223 326529

Sarah Lelarge

Phone: +44 (0) 1223 326527

Kelly Grace

Phone: +44 (0) 1223 326528

JAPAN

Katsuyoshi Fukamizu (Tokyo)

E-mail: kfukamizu@aaas.org
Phone: +81 3 3219 5777

Hiroyuki Mashiki (Kyoto)

E-mail: hmashiki@aaas.org
Phone: +81 75 823 1109

CHINA / KOREA / SINGAPORE / TAIWAN / THAILAND

Ruolei Wu

Phone: +86 186 0082 9345
E-mail: rwu@aaas.org

All ads submitted for publication must comply with applicable U.S. and non-U.S. laws. *Science* reserves the right to refuse any advertisement at its sole discretion for any reason, including without limitation for offensive language or inappropriate content, and all advertising is subject to publisher approval. *Science* encourages our readers to alert us to any ads that they feel may be discriminatory or offensive.

Science Careers

FROM THE JOURNAL SCIENCE | AAAS

ScienceCareers.org



Tenure-Track Assistant/Associate Professor Dept. of Physiology & Biophysics

With recent approval of the NYSUNY 2020 Challenge Grant to the University and the announcement of the largest gift ever to the public higher education in the State of New York, Stony Brook Medical School is embarking on a transformational expansion of the biomedical and clinical research enterprise. The investment in cancer research will include major program development, including the development of new programs and the construction of a new state of the art 250,000 square foot research and clinical cancer center.

The Department of Physiology and Biophysics and the Stony Brook Cancer Center invite applications for a tenure-track Assistant Professor position. Exceptional candidates at the Associate Professor level will also be considered. The successful candidate is expected to have or to establish an innovative externally funded research program in an area that builds upon and extends existing strengths within the Department: cancer-related research with expertise in imaging, genomics, metabolics or therapeutics (For a description of departmental research activities, please visit: pnb.informatics.stonybrook.edu). The position includes a generous start-up package and laboratory space in the Department of Physiology and Biophysics. Departmental and institutional support facilities include cores for advanced microscopy and imaging, proteomics, microarray, metabolomics/lipidomics, and bioinformatics. The Department also has access to the facilities at Brookhaven National Laboratory. For additional information about the Cancer Center, visit: cancer.stonybrookmedicine.edu.

A Ph.D., M.D., or M.D./Ph.D. and postdoctoral research experience are required.

Those interested in this position should submit a State employment application, cover letter and resume/CV to:

Search Committee Chair
Department of Physiology and Biophysics
Basic Sciences Tower Level 6, Room 140
Stony Brook University
Stony Brook, NY 11790-8661

For a full position description, or to apply on-line, visit www.stonybrook.edu/jobs (Ref. # F-9491-15-03).

Stony Brook University is an Affirmative Action/Equal Opportunity employer. We encourage protected veterans, individuals with disabilities, women and minorities to apply.

Science Careers Cernet

“《科学》职业” 已与Cernet/赛尔互
联开展合作。中国大
陆的高校可以直接联
系Cernet/赛尔互联
进行国际人才招聘。



请访问

Sciencecareers.org/CER

点得联系信息。

Science



Vacancy: SCAR Executive Director

The Scientific Committee on Antarctic Research (SCAR) seeks an Executive Director. The successful candidate will play a leading role in the development of SCAR by implementing the vision for SCAR and Antarctic science.

Applications detailing experience, including a full CV and providing the names of three referees, should be sent by e-mail (info@scar.org) by **15th May 2015**.

For further details please see www.scar.org/secretariat/vacancy.

UNIVERSITÄT BASEL

The Faculty of Science (Philosophisch-Naturwissenschaftliche Fakultät) of the University of Basel invites applications for the position of a

Professor of Chemistry (open rank)

We are seeking for candidates with an internationally recognized research program and an outstanding publication record in

Synthetic Organic Chemistry

While all areas of organic chemistry will be considered, upon equal qualifications, preference will be given to candidates with a focus on synthetic methodology and/or target-oriented synthesis. The selected candidate is expected to participate in teaching chemistry at all levels of the BSc, MSc and PhD programs. The University of Basel has an established program for career progression allowing promotion to associate and full professor upon successful evaluation.

The Department of Chemistry is located near the centre of Basel, a town which provides a stimulating and supportive environment for interdisciplinary research thanks to the strong presence of science institutes as well as the chemical- and pharmaceutical industries. For further information see <http://www.chemie.unibas.ch>

The selected candidate is expected to commence the appointment in Spring 2016. Applications received by 31 May 2015 are guaranteed full consideration. The University of Basel is an equal opportunity and family friendly employer committed to excellence through diversity. To increase the number of women in leading academic positions, the University strongly encourages applications from women. Applications, including a *curriculum vitae*, list of publications, an outline of current and future research plans and names of four referees should be sent by email (as pdf file) to Prof. Dr. Jörg Schibler University of Basel, Dean of the Faculty of Sciences, Klingelbergstrasse 50, 4056 Basel, dekanat-philnat@unibas.ch.

For further information, please contact:
Prof. Dr. Marcel Mayor, Department of Chemistry, E-mail: marcel.mayor@unibas.ch.



UNIVERSITÄT BASEL

The Department of Pharmaceutical Sciences at the Faculty of Science, University of Basel, invites applications for a

Professorship in Molecular Pharmacy (Associate or Full Professor)

We are looking for a scientist with an outstanding track-record in the field of molecular pharmacy/medicinal chemistry. The successful candidate will help to further develop the strategic axis "Drug Sciences", for which the Department of Pharmaceutical Sciences is internationally renowned (<http://www.pharma.unibas.ch>).

The candidate is expected to:

- Establish a world-class research program in current topics of Molecular Pharmacy / Medicinal Chemistry, including drug design and synthesis, the investigation of target-ligand interactions and in vitro PK/PD evaluation
- Apply and extend available state-of-the art techniques for the drug discovery and development process (500 MHz-NMR, QQQ-LCMS, Biacore, ITC)
- Actively collaborate with colleagues in the Department of Pharmaceutical Sciences as well as in joint research projects within and outside the University of Basel
- Have teaching experience to lead undergraduate (in German) and graduate (in English) level courses on medicinal chemistry and related topics in the Bachelor and Master programs of the Department.

The position is to be filled February 1, 2017 at the latest. The University of Basel is an equal opportunity and family friendly employer committed to excellence through diversity. To increase the number of women in leading academic positions, the University strongly encourages applications from women. Please address requests for further information to Prof. Dr. Christoph Meier (christoph.meier@unibas.ch). Applications should be sent by May 15, 2015 as pdf to Prof. Dr. Jörg Schibler, Dean, Faculty of Science, University of Basel, Klingelbergstrasse 50, 4056 Basel, Switzerland, e-mail: dekanat-philnat@unibas.ch.





FUNDING OPPORTUNITIES — U.S. Department of Defense

Defense Medical Research and Development Program

Peer Reviewed Medical Research Program

The Peer Reviewed Medical Research Program (PRMRP) funds exceptional research with the goal to improve the health and well-being of all military Service Members, Veterans, and their beneficiaries. The PRMRP received **\$247.5 million** in fiscal year 2015 (FY15) and seeks grant applications in the following **topic areas**:

Acupuncture	DNA vaccine technology for post-exposure prophylaxis	Integrative medicine	Post-traumatic osteoarthritis
Acute lung injury	Dystonia	Interstitial cystitis	Psychotropic medications
Advanced prosthetics	Focal segmental glomerulosclerosis	Lupus	Pulmonary fibrosis
Arthritis	Food allergies	Malaria	Respiratory health
Burn pit exposure	Fragile X syndrome	Metals toxicology	Rheumatoid arthritis
Cardiovascular health	Healthcare-acquired infection reduction	Mitochondrial disease	Scleroderma
Chronic migraine and post-traumatic headache	Hepatitis B	Nanomaterials for bone regeneration	Sleep disorders
Congenital heart disease	Hereditary angioedema	Osteoarthritis	Tinnitus
Dengue	Hydrocephalus	Pancreatitis	Vascular malformations
Diabetes	Inflammatory bowel disease	Pathogen-inactivated dried plasma	Women's heart disease
		Polycystic kidney disease	

Descriptions of the FY15 PRMRP Program Announcements and General Application Instructions are anticipated to be posted on Grants.gov by **mid-April 2015**:

- Clinical Trial Award
- Discovery Award
- Focused Program Award
- Investigator-Initiated Research Award
- Technology/Therapeutic Development Award

All applications must conform to the Program Announcements and General Application Instructions that will be available for electronic downloading from the Grants.gov website (all viewable under CFDA number 12.420). Execution management support will be provided by the Congressionally Directed Medical Research Programs.

<http://cdmrp.army.mil>

<http://cdmrp.army.mil/funding/prmrp.shtml>

Advance your career with expert advice from Science Careers.



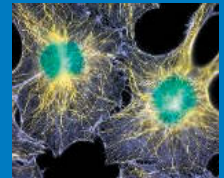
**Download Free
Career Advice Booklets!**
ScienceCareers.org/booklets

Featured Topics:

- Networking
- Industry or Academia
- Job Searching
- Non-Bench Careers
- And More



ScienceCareers
FROM THE JOURNAL SCIENCE



The NIH is the center of medical and behavioral research for the Nation —making essential medical discoveries that improve health and save lives.

Are you an exceptional candidate with proven expertise in biomedical informatics, research analysis of clinical data, and EHR systems who can provide leadership to the high-priority, trans-NIH initiatives of biomedical discovery in an era of big data? This position offers a unique and exciting opportunity to serve as a Senior Advisor for Clinical Data Science and join a team of data science specialist with significant expertise in basic research data working on: developing an enterprise-level solution to support a 1 million plus patient cohort for precision medicine; developing the “Commons” – a conceptual framework to support biomedical basic and clinical data in the cloud and beyond; developing and maintaining clinical data standards, policies, and sustainability; training; innovating data science; improving internal processes for data centric grant review; and communicating and subsequently sharing actions with all stakeholders, notably other federal agencies, philanthropic organizations, the private sector, and international partners. Given the high visibility and priority of the PMI, the Senior Advisor will interact directly with both the ADDS and the NIH Director.

Duties include: working with the PMI team to establish methods and standards for acquiring and transmitting clinical data derived from EHRs for PMI cohort research purposes; advising on issues related to the use of mobile devices and mHealth apps for acquisition and management of research data and participant reported observations; working with ADDS team to establish a synergistic exchange, such that best practices in handling unstructured research data can be translated into analogous best practices for research uses of clinical data; having a trans-NIH role in communicating and fostering developments surrounding clinical data, including the development and adoption of common clinical data elements across NIH, and developing standards on behalf of the NIH as a whole, with a particular need to interface with the efforts of the National Library of Medicine (NLM); helping to inform policies and regulatory affairs surrounding research uses of clinical data with particular emphasis on the balance of clinical data availability versus the need to protect patient privacy; advising on the development and maintenance of clinical data resources at NIH such as dbGaP, ClinVar, ClinGen and ClinicalTrials.gov; supporting the ADDS team to foster of new innovations surrounding big data, notably the establishment of the Commons; contributing to the design of intramural and extramural training programs that emphasize clinical data; contributing to the design of extramural funding programs as part of the BD2K initiative; and working closely with the Chief of the Laboratory for Informatics Development to synergize clinical informatics developments across the NIH.

The successful candidate will have a doctoral-level degree in biomedical informatics, significant research experience in handling and analyzing clinical data, proven expertise working with and developing EHR systems, and strong interpersonal skills collaborating as part of a team. Appointment will be at a salary commensurate with experience and accomplishment and includes full Federal benefits, including leave, health and life insurance, retirement and savings plan (401K equivalent).

If you are ready for an exciting leadership opportunity, please see the detailed vacancy announcement at: <http://www.jobs.nih.gov> (under Executive Careers). Application requirements apply and are due by May 11, 2015.

NIH AND DHHS ARE EQUAL OPPORTUNITY EMPLOYERS.

Programm zur Förderung der Rückkehr des hoch qualifizierten Forschungsnachwuchses aus dem Ausland

Ministerium für Innovation, Wissenschaft und Forschung des Landes Nordrhein-Westfalen



Sie stehen am Anfang Ihrer Forscherkarriere und möchten mit ihren herausragenden Ideen zur Bewältigung der großen gesellschaftlichen Herausforderungen auf den Feldern „Energie, Ressourceneffizienz, Gesundheit und Ernährung“ beitragen? Der Forschungsstandort Nordrhein-Westfalen bietet Ihnen die Chance zum Aufbau und zur Leitung einer selbstständigen Nachwuchsgruppe an einer hiesigen Hochschule Ihrer Wahl.

Im Falle einer erfolgreichen Bewerbung sind dafür über einen Zeitraum von fünf Jahren bis zu 1,25 Mio. EUR vorgesehen. Die Leitungsposition ist mit Entgeltgruppe 15 TVL – vergleichbar W2 – dotiert. Sie erhalten eine personengebundene Finanzierungszusage und etablieren Ihre Nachwuchsgruppe an einer Hochschule Ihrer Wahl in Nordrhein-Westfalen, welche Ihnen die beste Zukunftsperspektive und eventuell auch Tenure-Track bietet.

Der Beginn dieser Förderung ist zwischen Ende 2015 und Mitte 2016 vorgesehen.

Sie forschen derzeit außerhalb Deutschlands und verfügen über eine Promotion, die zum Zeitpunkt des Bewerbungsschlusses (Stichtag) mindestens zwei und höchstens sechs Jahre zurückliegt (bei Medizinerinnen und Mediziner zwei bis neun Jahre)? Ihr Lebensmittelpunkt lag vor Ihrem Auslandsaufenthalt in Deutschland? Bis zum Stichtag des Bewerbungsschlusses können Sie zwei Jahre erfolgreicher wissenschaftlicher Forschung vorweisen, davon mindestens die letzten 12 Monate außerhalb Deutschlands? Wenn dies alles auf Sie zutrifft, freuen wir uns auf Ihre Bewerbung unter

<http://www.wissenschaft.nrw.de/forschung/foerderung/wissenschaftlichen-nachwuchs-foerdern/rueckkehrprogramm/>

Nähere Informationen zu den erforderlichen Bewerbungsunterlagen sowie eine detaillierte Beschreibung des Programms finden Sie auf der angegebenen Internetseite.

Bitte reichen Sie Ihre Bewerbungsunterlagen bis zum **14. Juni 2015 (Stichtag)** online ein.

Das Land Nordrhein-Westfalen fördert die berufliche Entwicklung von Frauen. Bewerbungen von Frauen werden daher besonders begrüßt. Bewerbungen geeigneter schwerbehinderter Menschen sind erwünscht.

**WISSEN SCHAFFT
CHANCEN.NRW**

www.wissenschaft.nrw.de



Special Job Focus:
Microbiology
 May 15, 2015
 Reserve space by April 28*

THERE'S A SCIENCE TO REACHING SCIENTISTS.

For recruitment in science, there's only one **Science**

What makes *Science* the best choice?

- Read and respected by 570,400 readers around the globe
- 78% of readers read *Science* more often than any other journal
- Your ad sits on specially labeled pages to draw attention to the ad
- Your ad dollars support AAAS and its programs, which strengthens the global scientific community.

Why choose this microbiology section for your advertisement?

- Relevant ads lead off the career section with special Microbiology banner
- Bonus distribution to:
 American Society for Microbiology (ASM)
 May 30–June 2, 2015 New Orleans, LA.

Expand your exposure. Post your print ad online to benefit from:

- Link on the job board homepage directly to microbiology jobs
- Dedicated landing page for jobs in microbiology
- Additional marketing driving relevant job seekers to the job board.



* Ads accepted until May 11 on a first-come, first-served basis.

SCIENCECAREERS.ORG

ScienceCareers

FROM THE JOURNAL SCIENCE  AAAS

To book your ad: advertise@sciencecareers.org

The Americas

202-326-6582

Europe/RoW

+44 (0) 1223-326500

Japan

+81-3-3219-5777

China/Korea/Singapore/Taiwan

+86-186-0082-9345



CALL FOR NOMINATIONS

L'OREAL-UNESCO FOR WOMEN IN SCIENCE
INTERNATIONAL AWARDS
2016 EDITION, LIFE SCIENCES

Created in 1998, the L'Oréal-UNESCO For Women in Science International Awards identify and support eminent women in science throughout the world.

Each year, five Laureates are recognized for their contributions to the advancement of science, in Life or Physical Sciences in alternating years.

The 2016 Awards will designate five outstanding researchers in the Life Sciences, working in one of the following regions:

Africa & the Arab States

Asia-Pacific

Europe

Latin America

North America

Each of the five Laureates will receive an award of €100,000

More information and the nomination forms are available on the website www.fwis.fr

Deadline to submit nominations: June 16th 2015



University of Missouri ASSISTANT TEACHING PROFESSOR Division of Biological Sciences



The Division of Biological Sciences (<http://biology.missouri.edu>) at the University of Missouri invites applications for an Assistant Teaching Professor (non-tenure track). Qualifications include a doctorate in a life science or science education and independent or mentored teaching experience.

We are interested in candidates who have developed active learning strategies, particularly at the introductory level. We seek a long-term relationship with an individual who will continue to create innovative learning experiences.

The successful candidate will teach high-enrollment general biology courses and other undergraduate courses, as appropriate. The full-time appointment will begin September 1, 2015, or when the position is filled, at a salary commensurate with qualifications. We are committed to ethnic, racial and gender diversity in our faculty and strongly encourage applications from members of groups underrepresented in mathematics and science.

Application materials should include a cover letter, CV, description of teaching philosophy and experience, and evidence of teaching effectiveness and innovation. Include contact information for 3 references. Instructions for submitting application materials can be found at <http://biology.missouri.edu/NTTsearch>. Review of applications will begin **May 15, 2015** and continue until the position is filled. Questions should be addressed to **Gerald Summers (573-882-4369 or summersg@missouri.edu)**.

An Equal Opportunity/Access/Affirmative Action/Pro Disabled and Veteran Employer.

Advanced
Imaging

Cancer Biology

Cell and
Developmental
Biology

Disaster
Preparedness

Marine
Ecosystems

Network
Theory

Croucher Summer Courses 2015

A Croucher Summer Course is a residential course held over five or six days in Hong Kong. Participants have an opportunity to learn from world-renowned scientists, network with peers, participate in engaging and interactive discussions and, depending on the subject of the course, gain practical experience in the laboratory.

Each Croucher Summer Course is organised in partnership with a university in Hong Kong.

Registration fees cover course materials, accommodation, and meals. Places are limited; early application is advised:

www.croucher.org.hk

The Croucher Foundation is an independent private foundation dedicated to promoting the standard of the natural sciences, technology and medicine in Hong Kong.



Croucher Foundation
裘槎基金會